Advances in High-speed Rail Technology

He Xia
Nan Zhang
Weiwei Guo

Dynamic Interaction of Train-Bridge Systems in High-Speed Railways

Theory and Applications

北京交通大学出版社
http://press.bjtu.edu.cn

Springer

Advances in High-speed Rail Technology

More information about this series at http://www.springer.com/series/13506

He Xia · Nan Zhang · Weiwei Guo

Dynamic Interaction of Train-Bridge Systems in High-Speed Railways

Theory and Applications

北京交通大学出版社
http://press.bjtu.edu.cn

Springer

He Xia
Beijing Jiaotong University
Beijing
China

Weiwei Guo
Beijing Jiaotong University
Beijing
China

Nan Zhang
Beijing Jiaotong University
Beijing
China

ISSN 2363-5010 ISSN 2363-5029 (electronic)
Advances in High-speed Rail Technology
ISBN 978-3-662-54869-1 ISBN 978-3-662-54871-4 (eBook)
https://doi.org/10.1007/978-3-662-54871-4

Jointly published with Beijing Jiaotong University Press, Beijing, China

The print edition is not for sale in China Mainland. Customers from China Mainland please order the print book from: Beijing Jiaotong University Press

Library of Congress Control Number: 2017940357

Printed on acid-free paper

This Springer imprint is published by Springer Nature
The registered company is Springer-Verlag GmbH Germany
The registered company address is: Heidelberger Platz 3, 14197 Berlin, Germany

Preface

In recent years, the high-speed railway (HSR) has got remarkable development in China. By the end of 2016, the total length of HSR lines had been 22,000 km. In addition, there are more than tens of HSR lines being constructed. According to the "Thirteenth Five-year Plan" of China, the total length of HSR lines will reach 30,000 km by 2020, and it will be further extended to 38,000 km by 2025.

The high-speed railway has the characteristics of high speed and high traffic density of trains; thus, the problem of train-bridge coupling vibrations is very prominent. On the one hand, the high-speed train will produce a dynamic impact on the bridge structure, causing it to vibrate, which directly affects the working status and the service life of the bridge. On the other hand, the vibration of the bridge will in turn affect the running safety and stability of the on-bridge train. This makes the vibration behaviors of train-bridge system become one of the fundamental problems that need to be solved in the bridge design. It is an actual requirement for engineers to carry out comprehensive studies on the dynamic interaction of the coupled train-bridge system. This includes the dynamic analysis and assessment on the dynamic properties of the bridge structure, as well as the running safety and stability of the high-speed train. Therefore, great efforts have been continuously made to study the dynamic interaction between high-speed train and bridge. After years of development, the coupling vibration of train-bridge system has become a specialized research field.

In China, researchers have established a number of analysis models, performed systematic study on the dynamic responses of train-bridge interaction system, and achieved remarkable results for the actual engineering projects, making important contribution to the dynamic design of HSR bridges.

This book is the fruitful result of the research projects sponsored by the National Key Basic Research Program ("973" Program, 2013CB036203), the National High-technology Research and Development Program (863 Program, 2011AA11A103-3-2-1), the Natural National Science Foundations (Grant No. 51078029, 511780255, 51208027, 51208028, 51308034, 51308035, U1434205, U1434210, and 51678032), the Research Fund for Doctoral Program of Higher Education (20130009110036), and

the Supporting Program for New-century Excellent Talents in Universities (NCET-10-0219) of China, the Science and Technology Research Plans of China Railway Corporation (2013G001-A-1, 2013G001-B, 2013G004-C, 2015G002-A and 2015G006-M), and the Flanders (Belgium)-China Bilateral Project (Grant No. BIL 07/07).

In Chap. 1, starting with a general overview of HSR developments in China and abroad, the key technologies of HSR bridge construction in China are introduced, the research history and status quo of train-bridge coupling vibration are reviewed, the dynamics problems of HSR bridges are summarized, and the research contents and analysis methods for coupling vibrations of train-bridge system in HSR are expounded.

In Chap. 2, some fundamental theories and methods for vibration analysis of simply-supported beams under moving loads are presented. The analytical solutions of beam vibrations induced by a moving concentrated load, a moving harmonic load, and a moving wheel-spring-mass load with varying speed are deduced, and the vibration characteristics of them are investigated in several case studies. As one of the important phenomena related to the train-bridge coupling vibration, the mechanisms of vibration resonance, suppression, and cancellation happened in the moving-load and beam system are analyzed.

In Chap. 3, the self-excitations of train-bridge coupling vibration system are introduced. The characteristics and control standards of track irregularities, and the mechanism and description of vehicle hunting movement are summarized. The AR (auto-regressive) model simulation method of random excitations on the train-bridge system is studied.

In Chap. 4, the vibration criteria for HSR bridges and train vehicles in China are summarized, including a series of codes, standards and specifications related to the dynamic coupling analysis and test of train-bridge system, the control criteria for running safety of high-speed train due to bridge and train vibrations, the riding comfort of passengers on running train vehicles, and the structural safety serviceability of bridge due to vibrations. The conditions unnecessary to conduct coupling dynamic analysis of train-bridge system are also introduced.

Chapter 5 recapitulates the dynamic analysis models for train-bridge coupling system and the solution methods. The motion equations for the train-bridge coupling vibration system are derived. The solution methods for motion equations of train-bridge system, such as the direct coupling method, the in-time-step iteration method, and the intersystem iteration method, are studied. By taking a Pioneer EMU running through a multi-span simply-supported PC box-beam bridge on the Qinhuangdao-Shenyang HSR line as an illustrating example, the dynamic responses of train-bridge system are analyzed and the convergence in equation solution procedure is investigated.

Chapter 6 studies the vibration of coupled train-bridge system subjected to crosswinds. The influences of wind barriers on the wind velocity field around bridge structure and the aerodynamic behaviors of train vehicles are investigated. A spatial dynamic analysis model of train-bridge system subjected to crosswinds is established. The dynamic responses of the Tsing Ma Suspension Bridge in Hong

Kong are calculated, and some results are compared with the measured data, from which the threshold curve of train speed and wind velocity for ensuring the running safety of the train on the bridge is proposed. Considering the aerodynamic effect of wind barriers on a simply-supported PC girder bridge, the dynamic responses of the wind-train-bridge system are calculated, and the windbreak effect of different wind barriers is evaluated.

Chapter 7 deals with the vibration of train-bridge system subjected to earthquake action. The spectral theory-based simulation method for seismic ground motion considering spatial variation and the method for obtaining consistent earthquake record are summarized. The dynamic analysis models of a single wheel-spring-mass unit (series) passing through a simply-supported beam as well as the train-bridge system subjected to earthquakes are established. The dynamic responses of an ICE3 train passing through a steel trussed-arch bridge subjected to earthquakes are calculated, and the influences of the seismic characteristics and the input manners on the dynamic responses of train-bridge system are investigated. The running safety criteria and evaluation process of train vehicles on bridge subjected to earthquakes are proposed.

Chapter 8 is devoted to the vibration of train-bridge system subjected to collision loads. The characteristics of various collision loads on bridge are summarized. A dynamic analysis model is established for a coupled high-speed train and bridge system subjected to collision loads. An HSR double-track continuous bridge with (32+48+32) m PC box-girders is considered as an illustrative case study. The dynamic responses of the bridge and the running safety indices of the train on the bridge under three types of collision loads are analyzed. The results show that the large responses of the bridge induced by collision may strongly threaten the running safety of the train. An assessment procedure is proposed for the running safety of high-speed trains on bridges subjected to collision loads, and related threshold curves for train speed versus collision intensity are proposed.

Chapter 9 deals with the vibration of train-bridge system under differential settlement and scouring effect of foundations. The influence factors of differential settlement and the mechanism of scouring effect of pier foundations are summarized. A prediction method for cumulative settlement of bridge foundations caused by cyclic train loading is proposed, and the settlement of existing bridge foundations induced by the nearby bridge construction is calculated. The influence of differential settlement of bridge foundations on dynamic responses of train-bridge system is studied, and the train speed-settlement threshold curves for running safety and riding comfort of train are proposed. The stiffness of a single pile and the equivalent stiffness of group piles are studied, and the scouring effect on the stiffness of bridge foundations and the dynamic responses of the train-bridge system is investigated.

Chapter 10 deals with the vibration of train-bridge system under beam deformation induced by concrete creep and temperature effect. The numerical simulation method for PC beam creep camber is introduced. The vibration responses of train-bridge system excited by creep camber deformation are analyzed, and the safety threshold curves of creep camber under different train speeds are proposed, to

ensure the running safety and stability of train vehicles. By numerical simulation and field measurement, the characteristics of bridge sidewise-bending and track slab-warping deformation under non-uniform temperature field are studied, and their influences on the dynamic response and running safety of the train-bridge system are investigated.

This book will not only provide theoretical formulations and various solutions for coupling vibrations of train-bridge system, but also describe the ways to extend the life of existing bridge structures and present a guide to the rational design of new bridges. It can also be referenced for solving vehicle–structure dynamic interaction problems in the design and the research of various types of highways, railways, and other transport structures.

This book is chiefly authored by H. Xia, N. Zhang, and W.W. Guo, with Chapter 1 written by H. Xia, N. Zhang, W.W. Guo, and Y.M. Cao; Chapter 2 by H. Xia, H.L. Li, K.P. Wang, and S.Q. Wang; Chapter 3 by W.W. Guo; Chapter 4 by N. Zhang; Chapter 5 by N. Zhang and X. Wu; Chapter 6 by W.W. Guo and T. Zhang; Chapter 7 by X.T. Du; Chapter 8 by C.Y. Xia; Chapter 9 by Y.M. Cao and K.P. Wang; and Chapter 10 by J.W. Zhan and K.P. Wang. In addition, the work by Y. Tian, K.B. Li, J.J. Yang, H. Qiao, M. Xu, S. Zhou, Y.J. Wang, Q. Sun, G.H. Ge, G.L. Xiao, and other graduate students also contributed to the related chapters.

In writing this book, we drew much on the knowledge and experience acquired from collaboration with many colleagues in China and abroad. We wish to express our deep appreciation to them. We also acknowledge the information and inspiration derived from the references listed at the end of the chapters.

He Xia
Beijing, China

Contents

Chapter 1
Introduction

Since its occurrence, railway has been the focus of the world transportation. Entering the twenty-first century, railway construction has been speeded up in China to improve the passenger and freight transports. Especially, the development of high-speed railway has made remarkable achievements. As an infrastructure, bridges play a very important role in high-speed railway. With continuous raise of train speed, the bridge vibrations and their influences on running safety and stability of trains have drawn more attention. This chapter summarizes the key dynamics problems of high-speed railway bridges, reviews the research background and current status of train-bridge coupling vibration, and expounds the corresponding research contents and analysis method for coupling vibrations of train-bridge system in high-speed railway.

1.1 High-Speed Railways in China

1.1.1 Development of High-Speed Railways

The railway traffic has got great development with its safety, punctuality, and high efficiency since it appeared in England in 1825. With the progress of society and the development of science and technology, the demand for railway transport capacity is increasing, as well as for the train speed. According to UIC (Union Internationale des Chemins de Fer) in 1996, "new tracks specially constructed for high speeds, allowing a maximum running speed of at least 250 km/h, or existing tracks specially upgraded for high speeds, allowing a maximum running speed of at least 200 km/h" are defined as high-speed railway (HSR).

H. Xia et al., *Dynamic Interaction of Train-Bridge Systems in High-Speed Railways*, Advances in High-speed Rail Technology, https://doi.org/10.1007/978-3-662-54871-4_1

Fig. 1.1 Shinkansen train passing by Mountain Fuji (wikipedia 2006)

The idea of high-speed train was firstly proposed and started to try by Germany in the late nineteenth century. On October 23, 1903, the S&H-equipped railcar achieved a speed of 206.7 km/h, demonstrating the feasibility of electric high-speed railway. However, regularly scheduled electric high-speed railway travel was still more than many years away. In 1964, the first high-speed railway in the world was built in Japan, namely the Tokaido Shinkansen line connecting Tokyo and Osaka (Fig. 1.1). The Shinkansen train speed was 200 km/h and gradually speeded up to 270 $\sim$ 300 km/h and used to have a record of 443 km/h in an experiment (1996, 955 Series 300X). On April 21, 2015, the new type "L0" maglev train with seven carriages achieved the world record of train speed of 603 km/h in a test (Fig. 1.2). In 1981, the articulated high-speed train TGV (Train à Grande Vitesse) was put into service on the Paris-Lyon HSR in France, and on April 3, 2007, it created the world record of 574.8 km/h for wheeled trains (Fig. 1.3). In 1971, Germany started the construction of Hanover-Wüzburg HSR and completed it in 1991, with the operation train speed of 280 km/h (Fig. 1.4).

Up to now, high-speed railways have been constructed in many countries, such as China, Spain, Japan, Germany, France, Sweden, Italy, Korea, Belgium, Netherlands, Switzerland, and Turkey and are planned or scheduled to construct in

Fig. 1.2 "L0" maglev train in Japan (world.huanqiu 2013)

Fig. 1.3 World record of train speed by TGV (060s 2016)

Fig. 1.4 ICE high-speed train in Germany (eurail 2016)

the USA, UK, Russia, India, Indonesia, Thailand, Vietnam, South Africa, Nigeria, and other countries. By November 1, 2013, except China, the total operation mileage of high-speed railways in the world reached 11,605 km; moreover, there were 4,883 km under construction and 12,570 km in plan, according to the statistics of UIC.

The development of high-speed railway can be divided into three stages. In the initial stage, Japan, France, and Germany started and constructed their HSR lines. In the second stage, the technology for HSR was improved and got matured in Japan and several European countries and then extended to some other countries. In the third stage, high-speed railways are constructed and planned in more countries worldwide.

1.1.2 Development of High-Speed Railways in China

Since 1990s, China's railway has accelerated its modernization process. During 1997–2007, six round large-scale speed-up campaigns were conducted, raising the highest speed of passenger trains from 120 km/h to 200 km/h on more than

6,000 km rail lines. Meanwhile, theoretical and experimental researches on high-speed trains and HSR infrastructures were started.

The Qin-Shen (Qinghuangdao-Shenyang) HSR, started to construct in August 1999, was the first high-speed railway in China, with total length of 404 km and design train speed of 200 km/h (reserved to 250 km/h). In December 2002, the China made "Pioneer" EMU and "China Star" high-speed train achieved the highest test speed of 292 km/h and 321.5 km/h on this line, respectively. The Qin-Shen HSR was opened to service on October 12, 2013, being the pioneer of high-speed railways in China.

The Suining-Chongqing Railway was constructed from 2003 to 2006, with total length of 155 km and design train speed of 200 km/h. In May 2005, a test speed of 234 km/h was achieved by the "Changbai Mountain" EMU in the test section of this line.

The Guangzhou-Shenzhen Railway built in 2007 was the first four-track railway in China, with two tracks for 200 km/h high-speed trains and two for common passenger trains and freight trains, which realized the passenger\freight separation transport, being the first intercity rail transit in China.

On January 7, 2004, the first "National Medium-and-long Term Railway Development Program" was approved by the China State Council and began to implement. According to the program, by 2020, the overall railway operation mileage would reach 100,000 km; the passenger\freight separation transport would be realized on the main lines; the percentages of double-track and electrified lines should be increased to 50%; the technical standards for main railway facilities should reach or approach to advanced international level, to meet the requirement of national economy and social development on railway transport capacity. In the program, one of the important plans was to speed up the construction of high-speed railways. As shown in Fig. 1.5, the HSR network composed of "Four-vertical and Four-parallel" trunk lines and three Regional FRT (fast rail transit) systems was scheduled, to build more than 12,000 km high-speed railways.

The HSR network was planned as follows:

(1) The Four Vertical HSR Trunk Lines

- Beijing-Shanghai HSR. Total length 1,318 km, passing through three municipalities (Beijing, Tianjin, and Shanghai) and four provinces (Hebei, Shandong, Anhui, and Jiangsu), connecting two important economic zones (the Circum-Bohai Sea and the Yangzi River Delta).
- Beijing-Wuhan-Guangzhou-Shenzhen HSR. Total length 2,260 km, connecting the northern, central, and southern zones of China.
- Beijing-Shenyang-Harbin HSR. Total length 1,700 km, connecting the Northeast China to the inside Shanhaiguan zones.
- Hangzhou-Ningbo-Fuzhou-Shenzhen HSR. Total length 1,600 km, connecting the Yangzi River Delta, Pearl River Delta, and southeast coastal zones of China.

Fig. 1.5 Planned HSR network in China by 2020

(2) The Four Parallel HSR Trunk Lines

- Xuzhou-Zhengzhou-Lanzhou-Urumqi HSR. Total length 3,177 km, connecting the northwest and eastern zones of China.
- Hangzhou-Nanchang-Changsha HSR. Total length 880 km, connecting the central and eastern zones of China.
- Qingdao-Shijiazhuang-Taiyuan HSR. Total length 770 km, connecting the northern and eastern zones of China.
- Nanjing-Wuhan-Chongqing-Chengdu HSR. Total length 1,600 km, connecting the southwest and eastern zones of China.

(3) The Three Regional FRT Systems

The three regional FRT systems include the Yangtze River Delta, the Pearl River Delta, and the Circum-Bohai Zone (Beijing, Tianjin, and Hebei Province), respectively, covering the major cities in their regions.

- The Yangzi River Delta FRT System. With Shanghai, Nanjing, and Hangzhou as the centers, forming a Z-shaped traffic framework to connect nearby main cities.

- The Pearl River Delta FRT System. With the 105 km Guangzhou-Shenzhen and the 143 km Guangzhou-Zhuhai intercity lines as a main axis, forming an A-shaped traffic framework and connecting nine large and medium cities to build up the one-hour economic circle around this area including Hong Kong and Marco.
- The Circum-Bohai FRT System. With Beijing and Tianjin as the centers, and the 115 km Beijing-Tianjin intercity HSR as a main axis, forming an outward radiation traffic framework to the surrounding cities.

On November 27, 2008, according to the national development strategy and the demand for a resource-saving and environment-friendly society, the National Development and Reform Commission adjusted and optimized the scale and layout arrangement of the planned railway network issued in the "National Medium-and-long Term Railway Development Program" in 2004, increasing the development target of total railway mileage by 2020 from 100,000 km to over 120,000 km. According to the updated program, the target mileage of high-speed railway was adjusted from 12,000 km to 16,000 km. The Ningbo-Shenzhen HSR was extended northward to Shanghai, and the Hangzhou-Changsha HSR was extended westward to Kunming. To further expand the HSR network, several new HSR lines, such as Lanzhou-Urumqi, Bengbu-Hefei, Nanjing-Hangzhou, Nanchang-Jiujiang, Liuzhou-Nanning, Mianyang-Chengdu-Leshan, Harbin-Qiqihar, Harbin-Mudanjiang, Changchun-Jilin, Shenyang-Dandong, and Jinzhou-Yingkou, were scheduled to construct. Meanwhile, more regional FRT systems would be constructed for economically developed and densely populated areas, such as in Chengdu-Chongqing region, Changsha-Zhuzhou-Xiangtan region, Central China cities, Wuhan city circle, Guanzhong city group, and East coast economic zone, covering the major cities and towns within their respective regions.

During "The Eleventh Five-year Plan for National Economic and Social Development" period (2006–2010) of China, the significant investment was put into HSR construction, which not only promoted the development of HSR technologies, but also increased the construction scale and operation mileage of China's HSR to the leading position in the world. The main target of railway development in "The Eleventh Five-year Plan" was to construct 17,000 km new railway lines, including HSR lines of 7,000 km, to double-track reform existing lines of 8,000 km, and to electrify existing lines of 15,000 km.

On June 24, 2008, the China CRH3 EMU achieved a maximum speed of 394.3 km/h in the operation tests on Beijing-Tianjin Intercity HSR. On September 28, 2010, the CRH380A EMU broke the record with a maximum speed of 416.6 km/h in the operation test on Shanghai-Hangzhou Intercity HSR. On December 3, 2010, the new generation high-speed EMU renewed the record and created a speed of 486.1 km/h in the Bengbu-Zaozhuang test section located on Beijing-Shanghai HSR, which is the worldwide highest train speed on operation railway. In China, the train speed used to be 350 km/h (the highest operational train speed in the world) on Beijing-Tianjin, Wuhan-Guangzhou, Shanghai-Nanjing, and

Shanghai-Hangzhou HSR lines. Moreover, the designed operation train speed on Beijing-Shanghai HSR was up to 380 km/h.

"The Twelfth Five-year Plan" started in 2011 proposed to further speed up HSR construction. The objective was to build a rapid railway network with total length of 45,000 km, including 16,000 km HSR lines. Meanwhile, the construction standard and initial operation train speed of high-speed railways were further clarified.

In recent years, the construction of high-speed railways in China was further accelerated. A number of HSR lines have been put into operation, such as Dalian-Harbin Line (921 km), Hangzhou-Changsha Line (927 km), Lanzhou-Urumqi Line (1,776 km), Guiyang-Guangzhou Line (857 km), Nanning-Guangzhou Line (577 km), Chengdu-Chongqing Line (308 km), and Hefei-Fuzhou Line (808 km). With the opening and operation of the Shanghai-Kunming HSR line in the end of 2016, the total operation mileage of Chinese HSR reached 22,000 km, ranking first in the world. At present, the HSR operation mileage in China has far exceeded the total mileage of other countries in the world. China owns the world's most extensive HSR network with the fastest-growing, most comprehensive technology, strongest integration capability, longest operation mileage, highest operation speed, and largest construction scale.

According to the "National Medium-and-long Term Railway Development Program" and the current construction progress, by 2020, the total HSR operation mileage in China is predicted up to 25,000 km. Together with other new and existing railways, a 50,000 km rapid railway network will be completed, connecting all the provincial capitals and big cities with more than half million population, covering over 90% of the whole Chinese population. In general, the railway transport capacity will be able to meet the requirements of national economy and social development. The one-hour regional traffic networks will be established around the provincial capitals. The traveling time from Beijing to most of the provincial capitals will be less than 8 h.

According to the 2016-updated version of the "National Medium-and-long Term Railway Development Program," during the "Thirteenth Five-year Plan" period, China will continue to extend its HSR lines. The target of the program is to form an HSR framework with "eight vertical and eight horizontal channels," as shown in Fig. 1.6, and by 2025, the total mileage of China's HSR lines will reach 38,000 km.

The main contents of the HSR framework with "eight vertical and eight horizontal channels" are as follows:

(1) **The eight vertical channels**

V1: The East Coastal Channel. This channel starts from Dalian to Zhanjiang, via Shenyang, Qinhuangdao, Tianjin, Weifang, Qingdao (Yantai), Lianyungang, Yancheng, Nantong, Shanghai, Hangzhou, Ningbo, Fuzhou, Xiamen and Shenzhen, which connects the east coastal areas of China, through cities in the Eastern-Southern Liaoning Peninsula, the Beijing-Tianjin-Hebei area, the Shandong Peninsula, the east coastal areas, the Yangtze River Delta, the Pearl River Delta, and the Beibu Gulf coast.

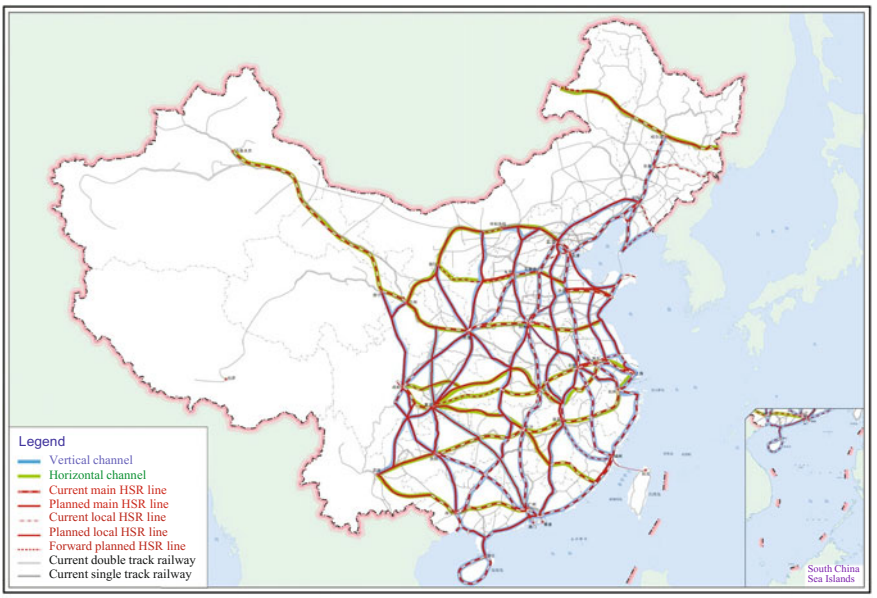

Fig. 1.6 HSR framework with "eight vertical and eight horizontal channels"

V2: The Beijing-Shanghai Channel. This channel starts from Beijing to Shanghai, and extends to Hangzhou, via Tianjin, Jinan and Nanjing, which connects the north and east areas of China, through cities in the Beijing-Tianjin-Hebei area, Shandong, Anhui and Jiangsu provinces, and the Yangtze River Delta.

V3: The Beijing-Shenzhen (Hong Kong) Channel. This channel starts from Beijing to Shenzhen, and extends to Hong Kong (Kowloon), via Hengshui, Heze, Shangqiu, Fuyang, Hefei, Jiujiang, Nanchang and Ganzhou, with a Branch Channel from Hefei to Fuzhou, via Nanchang. This channel connects the north, central, east and south areas of China, through cities in the Beijing-Tianjin-Hebei area, the middle reaches of Yangtze River, the west coast of Taiwan Strait, and the Pearl River Delta.

V4: The Harbin-Beijing-Hong Kong Channel. This channel starts from Harbin to Hong Kong, via Changchun, Shenyang, Beijing, Shijiazhuang, Zhengzhou, Wuhan, Changsha, Guangzhou and Shenzhen, including the Guangzhou-Zhuhai-Macao HSR. It connects the northeast, north, central and south areas, and the Hong Kong and Macao regions of China, through cities in Heilongjiang, Jilin and Liaoning provinces, the Beijing-Tianjin-Hebei area, the central plains, the middle reaches of Yangtze River, and the Pearl River Delta.

V5: The Hohhot-Nanning Channel. This channel starts from Hohhot to Nanning, via Datong, Taiyuan, Zhengzhou, Xiangyang, Changde, Yiyang, Shaoyang, Yongzhou and Guilin, which connects the north, central and south areas of China, through cities in the Hohhot-Baotou-Erdos area, the Central Shanxi area, the central plains, the middle reaches of Yangtze River, and the Beibu Gulf coast.

V6: The Beijing-Kunming Channel. This channel starts from Beijing to Kunming, via Shijiazhuang, Taiyuan, Xi'an and Chengdu, which connects the north, northwest and southwest areas of China, through the cities in Beijing-Tianjin-Hebei area, the Central and South Shanxi area, the Central Shaanxi plain, the Chengdu-Chongqing area, and the Central Yunnan area.

V7: The Baotou-Hainan Channel. This channel starts from Baotou to Sanya, via Yan'an, Xi'an, Chongqing, Guiyang, Nanning, Zhanjiang and Haikou, including the Yinchuan-Xi'an HSR and the Hainan island-loop HSR. It connects the northwest, southwest and south areas of China, through the cities in the Hohhot-Baotou-Erdos area, the Ningxia Along-Yellow River areas, the Central Shaanxi plain, the Chengdu-Chongqing area, the Central Guizhou area, and the Beibu Gulf coast.

V8: The Lanzhou (Xining)-Guangzhou Channel. This channel starts from Lanzhou (Xining) to Guangzhou, via Chengdu, Chongqing and Guiyang, which connects the northwest, southwest and south areas of China, through the cities in the Lanzhou-Xi'an area, the Chengdu-Chongqing area, the Central Guizhou area, and the Pearl River Delta.

(2) **The eight horizontal channels**

H1: The Suifenhe-Manzhouli Channel. This channel starts from Suifenhe to Manzhouli, via Mudanjiang, Harbin, Qiqihar and Hailar, which connects the Eastern Heilongjiang area and the Eastern Inner Mongolia area.

H2: The Beijing-Lanzhou Channel. This channel starts from Beijing to Lanzhou, via Hohhot-Yinchuan, which connects the north and northwest areas of China, through cities in Beijing-Hebei area, the Hohhot-Baotou-Erdos area, the Ningxia Along-Yellow River areas, and the Southern Gansu area.

H3: The Qingdao-Yinchuan Channel. This channel starts from Qingdao to Yinchuan, via Jinan, Shijiazhuang, Taiyuan and Zhongwei, which connects the east, north and northwest areas of China, through cities in Shandong Peninsula, Beijing, Hebei, Shanxi, Shaanxi and Ningxia provinces.

H4: The Continental-bridge Channel. This channel starts from Lianyungang to Urumqi, via Xuzhou, Zhengzhou, Xi'an, Lanzhou and Xining, which connects the east, central and northwest areas of China, through cities in east coastal area, the Central Plains, the Central Shaanxi Plain, and the Lanzhou-Tianshan Mountain corridor.

H5: The Along-Yangtze River Channel. This channel starts from Shanghai to Chengdu, via Nanjing, Hefei, Wuhan and Chongqing, including the Nanjing-Anqing-Jiujiang-Wuhan-Yichang-Chongqing HSR and the Wanzhou-Dazhou-Suining-Chengdu HSR, which connects the east, central and southwest areas of China, through cities in the Yangtze River Delta, the middle reaches of Yangtze River, and the Chengdu-Chongqing area.

H6: The Shanghai-Kunming Channel. This channel starts from Shanghai to Kunming, via Hangzhou, Nanchang, Changsha and Guiyang, which connects the east, central and southwest areas of China, through cities in the Yangtze River Delta, the middle reaches of Yangtze River, and the Guiyang-Kunming area.

H7: The Xiamen-Chongqing Channel. This channel starts from Xiamen to Chongqing, via Longyan, Ganzhou, Changsha, Changde, Zhangjiajie and Qianjiang, which connects the west coast of Taiwan Strait, and the central and southwest areas of China, through cities in the west coast of Taiwan Strait, the middle reaches of Yangtze River, and the Chengdu-Chongqing area.

H8: The Guangzhou-Kunming Channel. This is the Guangzhou-Nanning-Kunming HSR, which connects the south and southwest areas of China, through cities in the Pearl River Delta, the Beibu Gulf, and the Central Yunnan area.

In Taiwan Province, the high-speed railway was proposed in 1980s and started to construct in 1998, adopting the Japanese Shinkansen technology. The HSR line in Taiwan passes through the west coast of the island, connecting the two cities of Taipei and Kaohsiung, with the total length of 345 km. The line was opened to service on January 5, 2007, with the maximum train speed of 300 km/h.

1.2 Overview of HSR Bridges in China

1.2.1 Characteristics of HSR Bridges in China

The high-speed railway bridges in China have the following characteristics:

(1) Large proportion of elevated bridges

To meet the requirements on strict horizontal and vertical alignment parameters and the high track smoothness and stability, and for easier implementation of fully isolated operation pattern, the HSR lines usually adopt larger proportion of bridges than common railway. Especially in densely populated regions or unfavorable geological conditions, elevated bridges are used to cross the existing roads, reduce urban block segmentation, save land resource, and avoid uneven settlement of high embankment. Summarized in Tables 1.1 and 1.2 are the HSR bridges in China and abroad.

As shown in the tables, the highest proportion of HSR bridges abroad occurs in Japan, in which the percentages of bridge length on the Joetsu Shinkansen Line and Tohoku Shinkansen Line are 61.5% and 58.1%, respectively. In China, the average percentage of HSR bridges is 58.74%, in which, the percentage of bridge length on the Beijing-Shanghai HSR is 80.7%, on the Beijing-Tianjin intercity HSR is 87.7%, on the Shanghai-Hangzhou intercity HSR is 89%, and on the Guangzhou-Zhuhai intercity HSR is as high as 94.2%. By contrast, the average percentage of bridge length in common railways in China is only 4%.

(2) Mainly adopting small and medium spans

In China, HSR mainly adopts small-and-medium common-span bridges. It is not only because of the strict limits on stiffness and deformation, but also due to their advantages in standardized design, industrialized production, mechanized erection, high quality and fast construction speed that the bridge span should not be too large,

Table 1.1 Overview of HSR bridges abroad

Country	HSR lines	Line length (km)	Bridge length (km)	Percentage of bridge length (%)
Germany	Cologne-Frankfurt	177	4.8	2.7
	Hanoverian-Wurzburg	327	41	12.5
	Mannheim-Stuttgart	99	6	6.1
France	LGV Paris-Lyon	417	25	6
	LGV Atlantique	282	36	12.8
	LGV Nord-Europe	330	72	21.8
	LGV Rhône-Alpes	121	39	32.2
Japan	Tokaido Shinkansen	515	173	33.6
	Sanyō Shinkansen	554	211	38.1
	Jōetsu Shinkansen	270	166	61.5
	Tōhoku Shinkansen	493	344	58.1
	Hokuriku Shinkansen	117	39	33.3
Spain	Madrid-Sevilla	471	15	3.2
	Madrid-Barcelona	621	75.8	12.2
Italy	Rome-Florence	254	32	12.6
	Rome-Naples	204	39	19.1
	Florence-Milan	260.4	23.1	8.9
Korea	Seoul-Busan	412	111.8	27.1

generally less than 100 m. Through years of research, the series of simply-supported double-track box-beams with common spans of 32, 24, and 20 m are proposed, which can be ballasted or ballastless. According to the statistics, in the built HSR bridges, the total amount of standardized 32 m simply-supported PC box-beams is more than 300,000 spans, and the extended length is over 10,000 km, occupying 98% of the total bridge length.

In addition to the extensive application of prefabricated simply-supported PC box-beams, continuous beams, continuous rigid frames, arches, and composite beams are also adopted to cross valleys, rivers, railways, and roadways, in which the double-track PC box-section is prior to use.

(3) High rigidity and good integrity

To ensure the running safety and riding comfort of high-speed trains, HSR bridges should have sufficient stiffness and integrity in both vertical and lateral directions, to avoid too large deflection and amplitude. Besides, deformations induced by concrete creep and uneven temperature difference should be restricted, to ensure good smoothness of the track. Therefore, the design of HSR bridges is mainly controlled by stiffness rather than by strength. Although the live load for a HSR bridge is smaller than that for common railway, both the height and the weight of a HSR beam are larger than those of a common railway beam.

Table 1.2 Overview of HSR bridges in China

HSR line	Line length (km)	Bridge length (km)	Percentage of bridge length (%)
Beijing-Shanghai	1314	1060.9	80.7
Shanghai-Chengdu	1223	586	47.9
Shanghai-Kunming	2261	1207	53.4
Beijing-Wuhan	1121.7	858.7	76.5
Wuhan-Guangzhou	968.2	465.244	48.1
Nanning-Guangzhou	577.1	180.7	31.2
Hangzhou-Shenzhen	1508	565	37.5
Shijiazhuang-Taiyuan	189.93	39.2	20.6
Hefei-Nanjing	187.1	31.2	16.7
Zhengzhou-Xi'an	486.9	283.5	58.0
Beijing-Harbin	1713	1269	74.1
Harbin-Dalian	903.9	663.3	73.3
Beijing-Kowloon	2193	1384	63.1
Qingdao-Taiyuan	679	329	48.4
Xuzhou-Lanzhou	1360	822	60.5
Hainan Eastern Loop	308.11	102.95	33.4
Beijing-Tianjin	115.2	101.0	87.7
Shanghai-Nanjing	301	215.8	71.7
Guangzhou-Zhuhai	142.3	134.1	94.2
Shanghai-Hangzhou	160	142.4	89.0
Changchun-Jilin	96.26	30.3	31.5
Nanchang-Jiujiang	91.58	31.96	34.9
Taipei-Kaohsiung	345	257	74.5

(4) Extensive use of ballastless slab tracks

According to the operation experiences in China and abroad, both ballasted and ballastless tracks can meet the requirement of high-speed railway on high smoothness, reliability, and stability, but they have different characteristics. Bridges with ballastless track can reduce the secondary dead load, increase the natural frequency, and improve the dynamic behavior of train-bridge system. Therefore, the ballastless track is commonly used in HSR bridges in China. However, as a new type of track structure, the ballastless track brings new requirements on how to control the deformation, foundation settlement, and longitudinal force transmission in the bridge track system, which is one of focuses in the design of HSR bridges.

(5) High longitudinal stiffness of pier foundation

In China, most HSR lines adopt CWR (continuous welded rail). Under conditions of temperature variation, train braking, and span deflection, the bridge will produce longitudinal displacement, which induces additional stresses in the rails on

the bridge. In turn, the additional stress of rails may cause instability of CWR track on the bridge, thus affecting the running safety of trains. Therefore, the high longitudinal stiffness is required for pier foundation of HSR bridges, to minimize the additional rail stresses and the related displacement between beam and track.

(6) High structural durability and convenient maintenance

High-speed railway is an extremely important transportation facility, and any interruption of it will cause huge economic losses and social influences. Therefore, less maintenance or maintenance-free should be one of the targets for the HSR bridge construction, which requires that the structural durability should be ensured by reasonable design of structure and construction details and strict quality process control in construction. According to the design code for high-speed railways in China, as the main bearing structure, a bridge should have 100 years of durability under the predetermined actions and maintenance conditions. On the other hand, it is very difficult to maintain a HSR bridge due to the busy operation, high train speed, and limited maintenance windows of high-speed railway; therefore, the bridge structure should have efficient access for routine inspection and maintenance.

(7) Nice looking appearance and good coordination with environment

As the important modern transportation facility, in addition to safety and economy, the architecture esthetics of bridges should be taken into account in HSR design, by emphasizing the coordination of bridge structures with the natural and cultural environment, as well as the structural appearance and colors. Moreover, special attentions should be paid to ecological environment protection, by reducing train-induced noises, and avoiding pollution and damage to the ecological environment during construction and service of the bridge. Figures 1.7, 1.8, 1.9, and 1.10 give several typical HSR bridges in China.

It is seen that these bridges are designed with coordinated dimensions and fluent appearance, well-matched superstructure and substructure, open and wide clearance, and harmony with surroundings, forming a magnificent landscape.

Fig. 1.7 Nanjing Dashengguan Yangzi River Bridge

Fig. 1.8 Wuhan Tianxinzhou Yangzi River Bridge (blog. alighting 2012)

Fig. 1.9 Zhengzhou Yellow River Rail-cum-Road Bridge (Zheng et al. 2008)

Fig. 1.10 Bridge on Hainan East Circum HSR (kankanews 2014)

1.2.2 Key Technologies of HSR Bridge Construction in China

Bridges are one of the important infrastructure works constituting the high-speed railway, and also one of the key technologies in HSR construction. In addition to cross rivers, valleys, and other railway or road lines, HSR bridges are built to

support smooth and stable tracks for high-speed trains to ensure the running safety and comfort. Therefore, the superstructures of HSR bridges are supposed to have enough bending and torsional stiffness. The structure deformations induced by concrete creep and uneven temperature difference should be strictly limited, to ensure stability and maintain a highly smooth state of tracks on the bridge. Meanwhile, the substructures such as piers and abutments should have sufficient longitudinal and lateral stiffness. The superstructure of a HSR bridge can be either simply-supported or continuous, composed of either PC (prestressed concrete) box-beams, PC rigid frames, steel plate beams, steel truss beams, or steel–concrete composite beams. Sometimes, long-span structures such as trussed-arch bridges and cable-stayed bridges are also used.

Based on the successful practice of China high-speed railway, and by referencing the advanced technologies and experiences from Germany, Japan, and other countries, a set of key technologies with Chinese characteristics are created for the design and construction of HSR bridges.

(1) Design and construction technologies for common-span bridges

In China, the common-span bridges mainly adopt standardized 32 m simply-supported PC box-beams, which are prefabricated in beam yards, using pre-tensioned or post-tensioned method, transported by beam carriers, and erected by beam erection machines. In design, the stiffness of the beams is determined by train-bridge dynamic analysis, and verified by field experiments. Through continuous scientific and technological researches, engineers mastered the design theory, construction method, precise deformation control and, other key technologies in ballastless bridges, established a set of technology systems for bridge design, fabrication, transport, erection, check and acceptance, operation, and maintenance, and developed the corresponding standards.

(2) Design and construction technologies for long-span bridges

For crossing large rivers and valleys, the long-span bridges are necessary. Because the target train speed on a long-span bridge is supposed to keep consistent with the other sections of the HSR line, the design and construction of long-span bridges become more difficult. The main design and construction technologies for long-span bridges include the use of high-strength steels, adoption of new structures, development of special construction equipment, and construction of deep-water foundations.

(3) Design and construction technologies for CWR tracks on HSR bridges

The mechanism of continuous welded rail (CWR) on a bridge is different from that on the ground roadbed. The deformation and displacement of the bridge will cause additional rail stress in CWR. To ensure the running safety on the bridge, the additional rail stress induced by the combined action of beam and rail should be restricted to a safe range in designing. The additional rail stress is induced by braking force, stretching force, and bending force. After years of special study, a

mechanical model for CWR–beam interaction has been developed in China and verified by model tests and field tests, and, moreover, the related technical parameters have been proposed.

(4) Numerical simulation technology for dynamic analysis of train-track-bridge system

In order to ensure high speed, passenger comfort, and running safety of train vehicles, HSR bridges should have sufficient rigidity and integrity to avoid large defection and amplitude. The research on dynamic interaction of train-track-bridge system in China started in 1980s as early. Since then, various analytical models have been established, and the related evaluation standards developed. In a series of dynamic experiments organized by the Ministry of Railways of China, the test train speeds of over 350 km/h were repeatedly created, which verified the effectiveness of the dynamic simulation methods and the reliability of the evaluation standards.

(5) Design and construction technologies for bridges with ballastless slab tracks

The design of HSR bridges with ballastless tracks is targeting at rational structure, standardization, easy erection, and maintenance, to ensure adequate durability and good dynamic performance. To realize this target, the key technology is how to control the beam stiffness and deformation. Based on optimized design for main technical parameters, such as vertical/lateral deflection, torsion angle, vertical natural frequency, as well as the strict control of PC beam creep camber, the bridge structures can meet the laying conditions of ballastless tracks.

(6) Design and construction technologies for station bridges

Large-scale comprehensive transportation stations are used for various traffic transfers among HSR railway, common railway, subway, and ground traffic passengers, and they are designed in two structural types. The first type adopts the separated building-and-bridge system, as applied to the Beijing South Railway Station and the Shanghai Hongqiao Railway Station. In this type, the bridge and the building can be separately designed, thus the main engineering difficulties focus on the setting of thermal stress-released joint, the analysis of complicated structural stress, and the rational control of engineering quantities. The second type adopts the integrated building-bridge system, as applied to the new Wuhan Railway Station and the new Guangzhou Railway Station. In this type, the bridge needs to bear huge building weight as concentrated loads, thus the key technologies are how to realize the effective connection between the upper building and the bridge below, the rational transfer of the building loads to the piers, and the strict control on the influence of pier deformation on the upper building structure, resulting in extremely complex structural design.

(7) Fast construction technology for long elevated bridges

The proportion of bridge length in HSR lines is much higher than that in common railways. Some elevated bridges with dozens or even hundreds of

kilometers have been built. The standardly designed common-span simply-supported PC box-beams are usually prefabricated in beam yard near the railway lines and erected span by span, while the continuous beams with special spans are usually erected by in situ casting method. A series of standard technologies and equipment for beam fabrication, transportation, and erection have been developed and can be applied to the construction of superlong bridges with high quality and fast speed.

(8) Manufacture, transportation, and erection technologies for PC box-beams

To solve the problem of transportation and erection of 32 m double-track prefabricated PC box-beams, various of machines have been developed in China, such as the 450-t beam gantry crane, and the 900-t beam erecting machine, the 900-t beam carrier, the 900-t movable module bridge machine. A set of construction technologies, including beam-yard building, beam fabrication, beam transportation, and beam erection, have been developed with good efficiency, safety, and reliability.

(9) Settlement control technology for bridge foundations

Foundation settlement is the main control parameter in bridge design, especially in soft soil regions, which has important effect on the engineering investment of a HSR line. Based on the measured settlement data, several calculation methods have been developed to deal with various settlements of group pile foundations, open cutting foundations, and culvert foundation bases.

1.2.3 Common-Span HSR Bridges

According to the statistics, by the end of 2012, the operation railway bridges in China were 62,460 (including 3,658 HSR bridges), with more than 405,270 spans and total length of 10,156,500 m (including 5,070,000 m HSR bridges). The concrete bridges were more than 60,500, with 398,580 spans and about 9,944,700 m length (including 5,063,000 m HSR bridges). The steel bridges (including hybrid or composite bridges) were 1,950, with 6,690 spans and about 211,600 m length (including 7,000 m HSR steel bridges). The simply-supported PC beams with 32 m span or shorter were more than 310,440 spans, about 76.6% of the total concrete beams. The simply-supported steel beams with span less than 40 m were more than 5,150 spans, about 77.0% of the total steel beams. The simply-supported beams with small-and-medium spans are about 80% of the total number of railway bridge spans.

Listed in Table 1.3 are the main types of standardized common-span bridges in high-speed railways of China, in which s–s denotes simply-supported.

There are two types of high-speed railways in China: the passenger dedicated railway with design train speed of 350 km/h, adopting the ZK live load (standard

Table 1.3 Standardized common-span HSR bridges in China

Structure type	Span length (m)	Description
Post-tensioned PC T-beam	12, 16	Precast and erected as a whole on-site (4-pieces)
Post-tensioned PC s–s box-beam	20, 24, 32, 40	1. Mainly prefabricated in beam yard and erected by machine 2. A few are in situ casting
Continuous PC box-beam	2×24, 3×24, 3×32, 2×40, 32+48+32, 40+56+40, 40+60+40, 40+64+40, 48+80+48, 60+100+60	1. Most are in situ casting and by erection machine 2. Continuous beam with equal spans is constructed by connecting s–s spans to continuous or by erection machine
Continuous steel–concrete composite beam	32+40+32, 40+50+40, 40+56+40	
RC continuous rigid frame	12+16+12, 16+20+16, 16+24+16, 18+24+18, 16+3×24+16, 18+3×24+18	Skew angle ranges from 0° to 30°

HSR live load); and the passenger-cum-freight railway with design train speed of 250 km/h, adopting the C-Z live load (standard railway live load), with some of them reserve the condition for train speed up to 300 km/h. In design, each type of bridge has the uniform beam layout.

(1) For bridges with design train speed of 350 km/h, the distance between the lines is 5.0 m. The deck width for simply-supported box-beam is 13.4 m in Beijing-Tianjin intercity, Zhengzhou-Xi'an, and Wuhan-Guangzhou HSR lines. After optimization, the deck width is reduced to 12.0 m, which has been applied in Shijiazhuang-Wuhan, Beijing-Shijiazhuang, Shanghai-Hangzhou, Nanjing-Hangzhou, Hangzhou-Ningbo, Hefei-Bengbu, and some other HSR lines.
(2) For bridges with design train speed of 250 km/h, the distance between the lines is 4.6 m. Required by freight trains, the ballasted box-beams with deck width 13.0 m are used and applied in Hefei-Nanjing, Hefei-Wuhan, Ningbo-Taizhou-Wenzhou, Shijiazhuang-Taiyuan, Fuzhou-Xiamen, Xiamen-Shenzhen, and Nanning-Guangzhou HSR lines. After optimization, the deck width is reduced to 12.2 m. By contrast, the deck width for this train speed is 11.6 m for ballastless box-beams.

Considering structural stiffness and deformation, standardization, construction, engineering quality, economy, esthetics, and other factors, the simply-supported 32 m double-track PC box-beam is selected as the main span structure, assisted with a few 24 m beams. On the Beijing-Shanghai HSR line, for example, 32 and 24 m simply-supported PC box-beams occupy 91.8% of the total line length. Summarized in Table 1.4 are 32 and 24 m prefabricated PC box-beams adopted in HSR lines in China.

Table 1.4 Prefabricated 32 m and 24 m PC box-beams adopted in China HSR lines

HSR line	Line length (km)	Total length of bridge (km)	Percentage of bridge in length (%)	Total length of common-span bridge (km)	Percentage of common-span bridge in length (%)	Quantity of prefabricated PC box-beams	
						32 m	24 m
Beijing-Tianjin	118.0	97	82.2	93.0	95.9	2510	440
Wuhan-Guangzhou	868.0	352.1	40.6	331.0	94.0	9756	450
New Guangzhou Station	52.0	38.0	73.1	33.5	88.2	942	77
Zhengzhou-Xi'an	459.0	210.0	45.8	192.4	91.7	5393	151
Shijiazhuang-Taiyuan	118.4	40.7	34.4	30.1	74.0	957	19
Hefei-Wuhan	283.5	67.2	23.7	59.8	88.9	1736	122
Wuhan junction terminal	66.7	37.9	56.8	27.7	73.1	786	81
Hefei-Nanjing	99.1	28.4	28.7	11.6	40.9	117	317
Ningbo-Wenzhou	282.4	87.9	31.1	78.9	89.8	2336	103
Wenzhou-Fuzhou	298.0	75.0	25.1	64.9	86.5	1940	60
Fuzhou-Xiamen	263.6	72.0	27.3	48.6	67.5	1323	156
Beijing-Shanghai	1314	1060.9	80.7	723.8	68.2	19284	3549
Harbin-Dalian	903.9	662.7	73.3	613.6	92.7	16666	2777

Because HSR bridges adopt huge amount of simply-supported double-track PC box-beams, the Ministry of Railways of China set up a series of research projects, via model tests, static/dynamic prototype loading tests, and numerical simulation methods, to carry out comprehensive analysis and experimental verification on the design, construction, serving performance, long-term deformation, and other issues of this type of beams.

1.2.4 Long-Span HSR Bridges

On HSR lines, long-span bridges are adopted to cross valleys, rivers, and straits, such as cable-stayed bridges, arch bridges, PC continuous bridges, PC continuous rigid frame bridges, and rigid frame bridges with V-shape inclined legs. In order to ensure the running safety and riding comfort, strict vertical stiffness standard is proposed for long-span bridges, requiring their deflection-to-span ratios for steel bridge, steel cable-stayed bridge, and concrete bridge under the designed live loads shall be less than $L/800$, $L/650$, and $L/1000$ (L is the span of a bridge), respectively. To ensure the lateral stiffness, the width of beam bridge with 160–300 m span should be in the range of $L/18 \sim L/12$. Table 1.5 lists the long-span bridge types used in China high-speed railways.

1.2.5 Application of Train-Bridge Dynamic Analysis to HSR Design in China

Dynamic performance of the bridge is of great importance to the design of HSR bridges. The researches show that with the increase in train speed, the design of a HSR bridge is controlled by the rigidity rather than the strength, and the controlling factors are the running safety and riding comfort of train vehicles. For HSR bridges, therefore, in addition to the static analysis, the coupling train-bridge dynamic analysis should be carried out according to the actual train operation. Since the early 1980s, some Chinese institutes and universities have engaged in the research of train-bridge coupling vibration theory and its application, and a series of analysis models have been developed and verified by a large amount of measurement data. With good application and rationality, the research results have been applied in the dynamic design of HSR bridges in China.

Since 1998, organized by the Ministry of Railways, the CARS (China Academy of Railway Sciences) and three universities (Southwest Jiaotong University, Beijing Jiaotong University, and Central South University) have carried out systematic analyses of train-bridge coupling vibrations of various types of bridges, including simply-supported beam bridges, continuous beam bridges, continuous rigid frame bridges, simply-supported and continuous steel–concrete composite beam bridges,

Table 1.5 Long-span bridges in China high-speed railways

Structure type	Main span length (m)	HSR line	Case bridge	Main feature
Steel truss cable-stayed bridge	98+196+504+196+98	Beijing-Shanghai, Shanghai-Chengdu	Wuhan Tianxingzhou Bridge	1. Combined rail-cum-road bridge with four ballasted tracks 2. Triple main trusses, triple cable planes, steel box-beam 3. Two tracks for common railway, two tracks for HSR 4. Design speed of 200 km/h
	142+462+1092+462+142	Shanghai-Nantong	Hutong Yangtze River Bridge	1. Rail-cum-road bridge with four HSR tracks and six road lanes 2. Main bridge consists of a five-span two-tower cable-stayed bridge and a continuous steel truss bridge 3. Design speed of 200 km/h and 250 km/h, respectively, for Shanghai-Nantong railway and intercity railway
Continuous steel truss arch bridge	108+192+2×336+192+108	Beijing-Shanghai, Shanghai-Chengdu	Nanjing Dashengguan Yangtze River Bridge	1. Four-track railway and double-track subway with ballasted tracks 2. Triple main trusses, steel box-beam and concrete bridge deck 3. Two tracks for common railway, two tracks for HSR 4. Design speed of 300 km/h
Continuous steel truss flexible arch bridge	99+198+99	Fuzhou-Xiamen	Minjiang River Bridge	1. Trough type steel trussed-arch bridge with ballasted track 2. Passenger-cum-freight railway, reserved train speed: 300 km/h
	112+3×168+112	Beijing-Shanghai	Jinan Yellow River Bridge	Design speed: 300 km/h

(continued)

Table 1.5 (continued)

Structure type	Main span length (m)	HSR line	Case bridge	Main feature
Other arch bridge	80	Guangzhou-Shenzhen-Kowloon	Shuitian Bridge	1. Through type concrete filled steel tube arch 2. Steel box-beam
	32+140+32	Wuhan-Guangzhou	Tingsi River Bridge	1. Through tied-arch bridge with steel box-beam 2. Concrete deck and ballastless tracks 3. Design speed:300 km/h
	112		Liangjiawan Bridge	1. Concrete filled steel X-style tied-arch bridge 2. PC main beam
	128	Fuzhou-Xiamen	Mulan River Bridge	1. Tied-arch bridge with ballasted tracks 2. Passenger-cum-freight railway, reserved speed: 300 km/h
	2×90	Ningbo-Taizhou-Wenzhou	Yangdangshan Bridge	1. Through type composite steel box arch bridge 2. Design speed: 250 km/h
	32+108+32	Beijing-Shanghai	Huangcun Bridge	Half-through steel box arch bridge
	100+220+100	Guangzhou-Zhuhai	Xiaolan Bridge	1. Main span is half-trough concrete filled steel tube arch 2. Passenger-cum-freight railway
	100+2×230+100	Guangzhou-Zhuhai	Xijiang Bridge	Main span is continuous PC rigid frame and flexible steel tube arch

(continued)

Table 1.5 (continued)

Structure type	Main span length (m)	HSR line	Case bridge	Main feature
Continuous PC beam bridge	64+4×116+64	Wuhan-Guangzhou	Hengyang Xiangjiang River Bridge	Design speed: 250 km/h
Continuous PC rigid frame bridge	88+160+88	Wenzhou-Fuzhou	Tianluo Bridge	1. Ballasted tracks 2. Passenger-cum-freight railway, design speed: 250 km/h
	80+3×145+80		Baimahe River Bridge	
	108×2+185+115	Guangzhou-Zhuhai	Ronggui Waterway Bridge	Asymmetric bridge with ballastless tracks
	104+2×168+112	Guangzhou-Shenzhen-Kowloon	Zinihe River Bridge	Design speed: 350 km/h
PC rigid frame bridge with inclined legs	90	Shijiazhuang-Taiyuan	Gushan Bridge	1. Single-track ballastless railway 2. Passenger-cum-freight railway, design speed:250 km/h
Continuous V-shaped PC rigid frame bridge	48+80+48	Zhengzhou-Xi'an	Luohe Bridge	1. Ballastless tracks 2. Design speed: 350 km/h

and other types of bridges. These analyses were initially for the bridges of Qin-Shen HSR and Beijing-Shanghai HSR, and afterward successively applied to those of the Beijing-Tianjin, Wuhan-Guangzhou, Zhengzhou-Xi'an, Shijiazhuang-Taiyuan, Shanghai-Hangzhou, Beijing-Shijiazhuang, Shijiazhuang-Wuhan, and other HSRs, providing the basis for the dynamic design of these bridges.

In recent years, with rapid development of high-speed railways in China, the CARS and three universities carried out a series of field tests on more than 40 bridges located on the Hefei-Nanjing, Beijing-Tianjin, Hefei-Wuhan, Wuhan-Guangzhou, Shijiazhuang-Taiyuan, and Beijing-Shanghai HSR lines, covering more than 21 beam types and over 100 spans. The measured data indicated good dynamic performances of Chinese HSR bridges and validated the simulation methods for train-bridge dynamic analysis. These experiments are of important theoretical and practical significance to high-speed and speed-up railway bridges, especially for their design and construction, dynamic evaluation, structural reform, and reinforcement, as well as for further improvement of analysis theory and calculation method. It can be said that the analysis theory and method of train-bridge dynamic interaction in China have been at the top level in the world, and the research results have made great contributions to China's modernization and will play a more important role in the future.

1.3 Vibration Problems of Railway Bridges

With persistent development of science and technology, extensive application of high-performance materials, increasingly enlargement of bridge span, and continuous increase in train speed and vehicle load, the problem of bridge vibration becomes more prominent.

The vibration of bridge may increase internal force of the structure, cause local fatigue damage of the members, produce vibration deformation and acceleration of the bridge deck that may influence running safety and riding comfort of the on-bridge vehicles, and even in serious case completely destroy the bridge. Therefore, bridge vibration is one of the important factors that influence the safety and normal operation of traffic infrastructures, which attracts more attention in recent years.

According to the exciting sources, the bridge vibrations can be classified into five styles in two categories, see Fig. 1.11.

In the first category, bridge vibration is induced by wind forces, earthquake action, and collision of vessels, vehicles, and floating objects, which belongs to vibrations induced by various external loads.

In the second category, bridge vibration is induced by running vehicles or moving crowd, which belongs to the problem of bridge–load interaction. Since this vibration is inevitable during the normal operation of bridges, it is the fundamental issue in studying coupled vibration of train-bridge or pedestrian-bridge system.

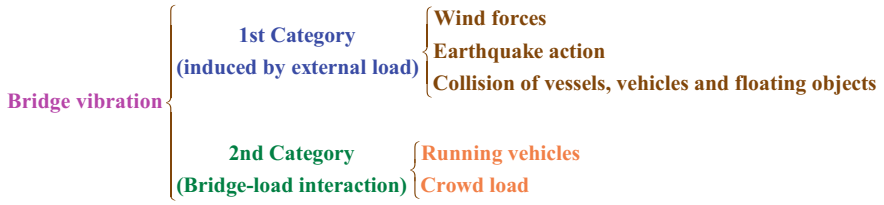

Fig. 1.11 Vibration categories of bridges

For railway bridges, the second category of vibration may occur simultaneously with the first category and thus forms the vibrations of the coupled train-bridge system subjected to wind load, earthquake action, and various collision loads. The dynamic analysis of this combined case is more complicated.

1.3.1 Bridge Vibration Induced by Wind Load

Wind is an airflow with a certain speed. When the airflow is impeded by a structure, a high-pressure air curtain will form, and the larger the wind speed, the higher the pressure on the structure. If the wind-resistant design is insufficient, the structure may produce overlarge deformation and vibration endangering its normal operation, generate local failure influencing its strength, or even collapse.

Studies about the wind-induced dynamic actions on bridges started quite early. In 1759, a British engineer named John Smitten suggested that the wind pressure should be considered during the structure design, and for the first time introduced the concept of wind load. However, at that time, the knowledge about wind pressure was quite limited. On December 28, 1879, the Tay Rail Bridge in Scotland was attacked by a violent storm and collapsed after its central spans gave way during high gales, with six carriages of a train carrying seventy-five passengers and crew plunged into the icy waters of the Tay (Fig. 1.12). The ensuing inquiry revealed that the wind-resistant strength of the bridge was only 1/12 of the due strength. After this serious accident, people paid high attention to the wind load effect, started to study wind pressures, and use them in bridge design.

However, the wind effect on structure was regarded as a static action of the wind pressure for quite a long time. In the fall of 1940, only several months after built, the 851.2 m span Tacoma Narrows Bridge in Washington State collapsed (Fig. 1.13) under a gust with velocity less than 20 m/s, shocking the field of bridge engineering. The subsequent researches showed that this accident was owing to the aerodynamic instability, which made people recognize another kind of wind effect on structure, namely the wind-induced vibration.

During the investigation of the Tacoma Bridge accident, it was surprised to find that there had been 10 suspension bridges collapsed due to strong winds in Europe and North America since 1818 (Table 1.6). All the accidents showed obvious

Fig. 1.12 Wind-induced accident of Tay Rail Bridge in Scotland (wikipedia 2016)

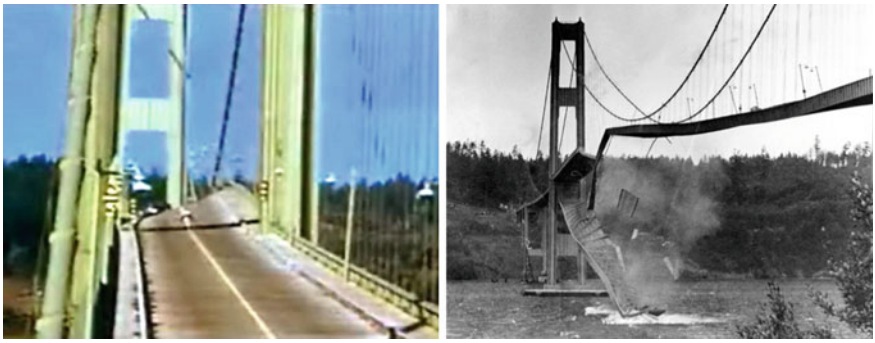

(a) Bridge deck distorted (b) Bridge broken and fell

Fig. 1.13 Wind-induced accident of Tacoma Narrows Bridge in the USA (chiuphysics.cgu 2011)

Table 1.6 Suspension bridges damaged by wind storms

No.	Bridge name	Country	Span (m)	Failure year
1	Dry burgh Abbey bridge	UK	79	1818
2	Union bridge	UK	137	1821
3	Nassou bridge	Germany	75	1834
4	Brighton bridge	UK	78	1836
5	Montrose bridge	UK	132	1838
6	Menai strait bridge	UK	177	1839
7	Roche bernard bridge	France	195	1852
8	Wheeling bridge	USA	309	1854
9	Niagara-Lewinston bridge	USA	317	1864
10	Niagara-Clifton bridge	USA	384	1889
11	Tacoma narrows bridge	USA	853	1940

characteristics of the wind-induced vibrations. However, the science and technology at that time could not solve the problem, and only the experience could be relied on. Driven by the Tacoma Bridge accident, bridge engineers started the close cooperation with the aerodynamic experts, dedicating to study the wind-induced vibration of bridge. Gradually, a new frontier branch, namely the Bridge Wind Engineering was formed in the field of bridge engineering.

The wind-induced bridge vibration is a complex aerodynamic problem. In the past, less attention was paid to study wind resistance of bridge, mainly because the wind load did not control the design for small or medium span bridges. Owing to the development of economy, progress of bridge-building technology and invention of new materials, many long-span bridges, such as suspension bridges and cable-stayed bridges, have been built in the world, with ever-longer span and ever-smaller flexibility, whose natural vibration periods reached tens of seconds. Long-span bridges are featured with light and flexibility, and susceptible to wind effect; therefore, how to control the wind-induced vibration has become the primary issue in the bridge design. For example, a measurement on the Golden Gate Bridge in 1951 reported an intensive vibration with maximum amplitude of 1.7 m at the 1/4 span under the moderate gale to fresh gale. It has been well understood that wind-induced vibration is not only harmful to the fatigue life of bridge structure, but also unsafe for pedestrians and vehicles on the bridge.

On December 28, 1986, at around 1:25 pm, a Japanese 14-series train was hit by a sudden gust from Sea of Japan when it was traveling, at a speed of 55 km/h, on the 310 m long Amarube Viaduct in Sanin region. The instantaneous wind speed on the bridge deck was about 33 m/s. All seven passenger cars of the train were blown down from the bridge, causing a serious rollover accident due to the wind force.

On December 25, 2005, at 7:15 pm, when an "Inaho 14" E653-1000 series EMU was traveling at a speed of 100 km/h near the No. 2 Mogami River bridge in Yamagata, the car-body vibrated extensively due to the strong wind, resulting in derailment of six carriages. According to statistics, five passengers were killed in the accident, and 33 people sustained injuries. The maximum instantaneous wind speed at the site was over 20 m/s.

Wind-induced vibration, also called aerodynamic action, is a structural vibration caused by turbulence of a random gust, often encountered in the nature. Some wind-induced vibrations, once formed, may cause the bridge to damage, while some others, although do not immediately damage the structure, may result in problems such as the fatigue of members or joints, and unsafety of service.

The mechanism of wind-induced bridge vibration is complicated, which can be divided into two categories. One is divergent vibration, including the classical flutter of the streamlined bridge deck, the torsional separated flow flutter of the non-streamline deck, the galloping of the rectangular-section bridge tower, and the vortex-induced vibration of suspenders and cables. The divergent vibration may induce aerodynamic instability even wind-destroyed accident of bridge, so it must be avoided through measures such as section-shape optimization, wind fairing design, and guide plate setting, based on wind tunnel test. The critical wind velocity for the designed bridge should be much higher than the most possible maximum wind velocity under the given guaranteeing probability (normally above 20%).

The other is amplitude-limited vibration, a kind of forced vibration induced by fluctuating wind, including vortex vibration and buffeting. Bridge buffeting occurs frequently under low wind velocity, producing local fatigue at member joints or bearings. Especially, excessive buffeting vibration will directly affect the running safety of trains on the bridge; therefore, the vibration amplitude should be controlled in an acceptable range in bridge design.

When a long-span railway bridge is built in a wind-prone area, the bridge will be susceptible to considerable vibration owing to aerodynamic effect, and large deformation and vibration may be induced due to its flexibility, seriously affecting the structural safety of the bridge and the running safety and riding comfort of the train vehicles. On the other hand, vehicles under wind action may change their inherent vibration properties. Therefore, the effect of wind load should be considered in running safety analysis of trains on long-span bridges crossing windy rivers, valleys, or straits.

1.3.2 Bridge Vibration Due to Earthquake Action

Earthquake is a burst and highly destructive natural disaster, being one of the three enemies with flood and hurricane for bridge engineering. There occur more than 10 times over M7.0 earthquakes each year around the world, bringing huge damage and loss to people's lives and properties. Dong et al. (2009) investigated 502 bridge collapse accidents in 66 countries, and the results showed that 119 events were due to the earthquake, 23.7% of the total (Fig. 1.14). Therefore, the seismic design of bridge has attracted more attention and been developed rapidly in recent years.

The anti-seismic engineering is the main method to mitigate the loss of people's lives and properties due to earthquakes. Since the end of World War II, the anti-seismic engineering has been developed greatly in both theories and practices. The anti-seismic calculation for bridges, buildings, and other engineering structures

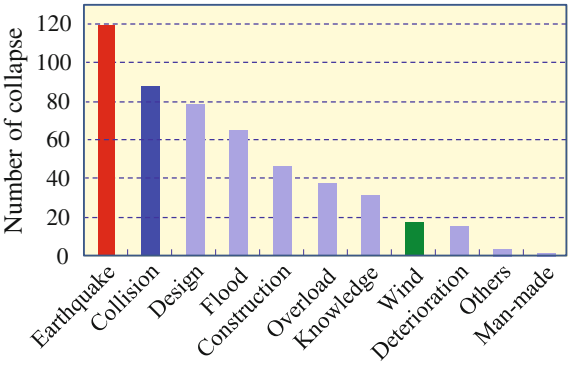

Fig. 1.14 Statistics of 502 collapse accidents of bridges in 66 countries (Dong et al. 2009)

Fig. 1.15 Bridge collapse in the Northridge earthquake (Cooper et al. 1994)

has been developed from the simple static method to the dynamic response analysis with seismic wave input, and the interaction between foundation and subsoil has been taken into consideration as well. The practicable anti-seismic design method in engineering has been established, using modern computers to analyze the nonlinear elastic–plastic seismic response of highly complex structure system, supplemented by large-scale shaking table tests as validation. It can be said that the progress and achievement in this field are remarkable.

However, in the recent decades, many intensive earthquakes occurred in the world, causing a lot of serious engineering destructions and heavy loss of people's lives and properties. For example, in 1994, the earthquake at Northridge in the USA caused 65 deaths and over 5000 injured, serious damage of commercial and residential structures, and destruction of important traffic lines, with seven bridges collapsed or partly destroyed (Fig. 1.15). It is the most costly natural disaster in the history of USA, with the overall economic loss more than $20 billion. Another example is the Great Hanshin Earthquake happened in Japan, 1995, resulted in 5466 deaths, $100 billion economic loss, and totally paralyzed almost all traffics except for aviation, bringing devastating disaster to Kobe.

China is located between the two major seismic zones: the Circum-Pacific seismic zone and the Eurasia seismic zone. Due to the squeezing by Pacific Plate, Indian Ocean Plate, and Philippine Sea Plate, the fault zone is well developed, resulting in frequent and intensive earthquakes. In the twentieth century, there occurred more than 10 times of earthquakes with M8.0 and above. One example is the famous 1976 Great Tangshan Earthquake. It happened in modern urban area, thus the loss was extremely heavy, caused 240 thousand deaths and extremely serious damage of buildings, water and power facilities, and public traffic lines. The damaged railway bridges subjected to earthquake accounted for 39.3% of the total, resulting in disruption of the Beijing-Shanhaiguan railway. The roadway bridges damaged in the earthquake accounted for 62% of the total, bringing enormous difficulty to the relief work. Another example is the Wenchuan earthquake on May 12, 2008, happened in southwest China. In this earthquake, there were 69,227 deaths, 47,277 km roadways damaged, including 19 highways, 159 trunk roads,

Fig. 1.16 Bridge collapse in the Wenchuan earthquake

and 5,560 bridges. For instance, in the 28-km railway section from Yongxing to Yuejiashan, 24 bridges were totally damaged (Fig. 1.16), and among the 384 bridges in the 370-km railway section from Weixian to Zhangming, 78 bridges suffered different degrees of damage from earthquake.

Bridges built in earthquake zones may vibrate during earthquakes, induced by up-and-down movement and horizontal swing of the ground. Especially, the horizontal swing has a great influence on tall piers and abutments, inducing large lateral displacements, which affects the safe passage of the train running on the bridge, and even in serious case causes the span to unseat and drop to the river, threatening the safety of the whole bridge. From the surveys on earthquake damage in China, Japan, USA, and some other countries, it is found that there are various types of bridge damages induced by earthquakes, including longitudinal or lateral unseat of beams, deformation or break of pier columns, local crush of masonry works, cut of support bolts, settlement or crack of conical filling on abutments, broken of U-shaped bolt on bridge deck, and collapse of sidewalk, etc.

With the upgrade of railway design standards, bridges play more and more important roles in railway engineering. Especially with the development of high-speed railways, elevated bridges stretching tens of kilometers are often built to ensure the smoothness of track and the safety and stability of running trains, which greatly increased the probability of trains on bridge when earthquakes occur. Meanwhile, the generated ground movement may cause intense bridge vibration, which would affect the safety of bridge structure and running train. On October 23, 2004, at 17:56, Niigata county of Japan was struck by an M6.8 earthquake, when a high-speed train was running at 200 km/h on the Joetsu Shinkansen. After braking, the train continued to travel for about 1.6 km, and eight of 10 carriages derailed, as shown in Fig. 1.17a. By that time, it had been the only derailment accident of Shinkansen since it opened in 1964, breaking the record that "Shinkansen train never derails" which had lasted for 40 years. On March 4, 2010, an M6.4 earthquake occurred in Kaohsiung County, when a high-speed train was heading for Taipei on a curve track. Under intense shaking, the first carriage derailed and stopped after dragging a distance of 3 km, as shown in Fig. 1.17b. Cases like this,

(a) In Japan Niigata earthquake (m.tiexue, 2014) (b) In Taiwan Kaohsiung earthquake (xmnn, 2010)

Fig. 1.17 Derailment accidents of high-speed trains due to earthquakes

as closely noticed by railway engineers, sufficiently indicate the necessity of studying the effect of earthquakes on the safety of the train running on bridge.

1.3.3 Bridge Vibration Induced by Collision of Vessels, Vehicles, and Drifters

Bridges are indispensable structures for crossing rivers, bays and other railway or highway lines, while sometimes they also become man-made obstacles against water flow or traffic underneath. With the rapid expansion of the infrastructure network in the past decades, more crossings are generated being the cause of many bridge collapse accidents due to vessel, vehicle, and other collisions.

The factors producing bridge collapses can be divided into two categories: man-made and natural. The man-made factors mainly include design fault, construction mistakes, collisions (by vessels, automobiles, and trains), overload, etc. The natural factors include earthquakes, water flow (flood, scouring, etc.), wind, collisions (by floating floes or other objects), environmental deterioration (temperature, corrosion, etc.) and some other unknowns. According to the statistics by Dong et al. (2009) based on 503 collapse accidents of bridges in 66 countries, there were 91 caused by various collisions (by vessels 56, trucks and trains 33, ice-floes 2). Only preceded by earthquakes, collisions constitute 18% of the total bridge collapses, as shown in Fig. 1.14. A similar investigation by Wardhana and Hadipriono (2003) on 503 bridge collapses in the United States from 1989 to 2000 indicated that the most frequent causes of bridge failures were attributed to floods and collisions. Collisions from trucks, barge/ships and trains were responsible for 11.73% of the total bridge failures, as shown in Fig. 1.18. A review by Hartik IE et al. (1990) on 114 bridge failures in the United States over a 38-year period (1951–1988) showed that 17 events (15%) of them were due to truck collisions.

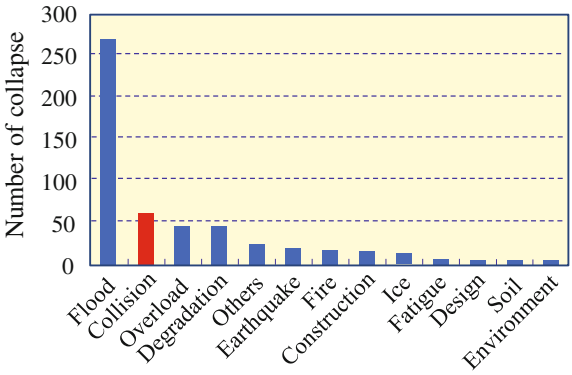

Fig. 1.18 Statistics of 503 collapse accidents of bridges in the USA (Wardhana and Hadipriono 2003)

These statistical data show that collision has become one of the leading causes for bridge failures.

Bridges built on navigable rivers may be collided by vessels. Although collision accidents are very seldom, once happen, they may cause amazing damages to life, property, society and environment.

According to an incomplete statistic, during 1960 ~ 1993, there were 29 serious vessel collisions with bridges happened in the world, resulting in more than 300 deaths. In the United States, there happened 811 accidents of ship collision on bridges in inland rivers within 5 years in the early 1970s, with the economic loss of more than 28 million US dollars. In 1980, the Sunshine Skyway Bridge in Florida was crashed by a cargo ship of 20,000 tons displacement, resulting 35 deaths and over 250 million dollars loss. In the former Soviet Union, an accident happened in 1983, when a passenger ship strayed through a side span of a railway bridge across the Volga River, the upper deck room was cut off owing to the insufficient height clearance, killing 176 persons. Another painful accident also happened on a railway bridge across the Volga River, when a train was running on the bridge, a passenger ship hit it, resulting in 4 carriages fall into water, killing more than 240 passengers.

In China, accidents of vessel collision with bridges happened frequently, and have caused very serious consequences. The Wuhan Yangtze River Bridge was completed in 1957, since then, there have been more than 70 accidents of vessel collisions on the bridge, among which a most serious one led to a traffic interruption of the Beijing-Guangzhou railway for dozens of hours. The second Wuhan Yangtze River Bridge experienced 30 ship collision accidents during the 10 years after built in 1995, resulting in direct economic loss of millions of Chinese RMB. On June 15, 2007, a pier of the Jiujiang Bridge in Guangdong Province was hit by a sand barge. The pier was promptly ruptured, and subsequently the bridge deck with a length of 140 m collapsed (Fig. 1.19). On June 6, 2011, an oil tanker fleet of over ten thousand tons displacement hit directly on the 7th pier of Wuhan Yangtze River Bridge, causing the barge bow crumpled and the pier damaged (Fig. 1.20). During the accident, people on the bridge heard a loud noise and felt a strong vibration of the deck.

Fig. 1.19 Jiujiang Bridge collapse by ship collision (tydf 2007)

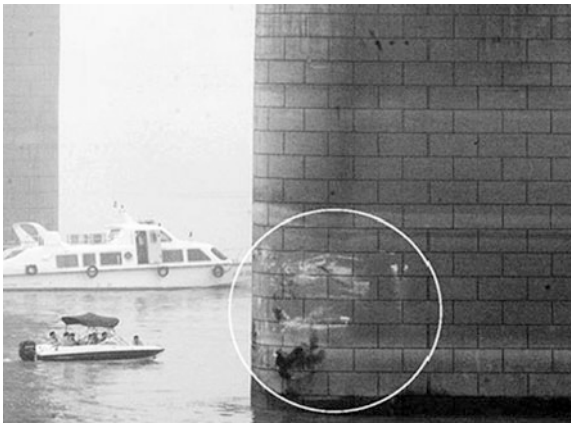

Fig. 1.20 Damaged pier of Wuhan Yangtze River Bridge

In the course of writing this book, two vessel collision with railway bridges occurred. On December 15, 2015, at 5:50 pm, when a sand dredger passed through the Zhaoqing Rail-Cum-Road Bridge on Xijiang River, the railway truss of the bridge was hit by the ultrahigh portal frame of the hull, inducing serious damage to the crossbeams, stringers and bottom lateral bracing members (Fig. 1.21). The accident caused closure of the rail traffic on the bridge, 58 trains were delayed or some others were detoured.

On January 15, 2016, at 8:00 am, when a sand carrier passed through the Xiangtan Railway Bridge on Xingjiang River, the conveyor of the ship thrust into the truss and seriously damaged the bridge, threatening the running safety of trains (Fig. 1.22). Due to this accident, more than 20 trains were delayed, and the bridge was closed for over 70 h for repair.

With rapid development of bridge construction and ship transportation, the problem of ship collision with bridges becomes more prominent. For example, there were only 7 bridges along the Yangtze River before 1990s, while up to the present, there have been more than 60 bridges in service, and many others in construction or

Fig. 1.21 Ship collision induced damage of Zhaoqing Bridge on Xijiang River (ifeng 2015)

Fig. 1.22 Ship collision induced damage of Xiangtan Bridge on Xiangjiang River (hnxttv 2016)

in planning, which greatly increases the probability of ship collision accidents on bridges. This problem is becoming more important, due to continuous enlargement of ship size, increase in shipping tonnage, raise of ship speed, and growth of dangerous goods transportation. Also, the recent rise of sea-crossing bridge construction needs to pay more attention to ship collision on bridges. Since the size and shipping tonnage of sea ships are much greater than those of river ship, and the importance and investment of sea-crossing bridge are very high, this problem and the related risk appear to be more serious. Thus it becomes more urgent to study the problem of ship collision with bridge and the corresponding countermeasures.

In addition to vessel collision, bridges may sometimes be impacted by the underpassing automobiles or trains.

A typical example was in Germany, on June 3, 1998, an ICE train from Munich to Hamburg derailed when it ran close to a small town near Hanover, and collided on the overpass bridge across the track, causing the bridge collapsed (Fig. 1.23), with 101 deaths and 88 injured, which was the most disastrous derailment accident that had occurred in Germany after the World War II.

Fig. 1.23 Derailed ICE train and collapsed bridge (blog. sina 2011)

In addition, the urban elevated or overpass bridges are often collided by the underpassing trucks, due to their overload, overheight or overspeed that may lead them out of control. On April 1, 2011, an ultrahigh truck fully loaded with steel construction members hit a railway bridge in Ashford in UK, inducing serious damage to the truck and the goods. The accident caused a 20 min train outage between Ashford and Hastings and disrupted the road traffic for several hours as well. On August 16, 2011, a lorry struck a rail bridge near the West Malling station in Kent (Fig. 1.24), which disrupted rail traffics to and from London, causing misery for thousands of commuters.

On August 8, 2002, a disastrous railway bridge collision accident by a truck took place in Taiwan Province of China. The bridge on the Lushan railway in Taichung was hit by a container truck, resulting in serious track deformation on the bridge and the derailment of a "Tze-chiang" train (Fig. 1.25).

In Mainland China, bridge accidents by vehicle collision took place from time to time. On October 15, 2008, a heavy dumper ran on a fast road in Xinjiang. When it

Fig. 1.24 Railway bridge hit by truck in England (dailymail 2011)

Fig. 1.25 Derailed "Tze-chiang" train on bridge after collided by a truck (news.sina 2011)

was about to pass beneath a railway bridge, the suddenly lifted dump box hit the beam, causing a 50 cm forward shift of the beam and therefore, the bridge had to be closed (Fig. 1.26a). On February 8, 2009 at 15:00, a bridge on the Xinxiang-Heze Railway was hit by a Scania truck with a container trailer. The bridge was equipped with two clearance frames. The overhead beam of the first frame was crashed and flew away, which further smashed the baluster, bracket and sidewalk slabs of the bridge, and then the second frame was also crashed. Finally, the truck scratched the bottom of the PC girder and then knocked down two clearance frames on the other side (Fig. 1.26b).

Apart from vessels and vehicles, bridges may also be hit by drifters in rivers. In cold areas, for example, collisions of drifting-floes on bridges often happen in spring (Fig. 1.27). In the United States, a case happened in spring 1938, when a steel arch bridge across the Niagara River near Clifton in New York State was destroyed by drifting-floe collision. The collision of floating ices may damage bridge structures, thus should be considered in the bridge design in these areas. In China, a serious case happened in March 1962, when a huge drifting-floe of about

(a) A railway bridge hit by a dumper in Xinjiang (v.ku6, 2008) (b) A railway bridge hit by container in Heze

Fig. 1.26 Vehicle collision accidents on railway bridges

(a) The Songhua River railway bridge hit by ice-floes (b) A railway bridge hit by ice-floes in Canada (Timco GW, 2011)

Fig. 1.27 Collision of drifting-floe on piers

3000 m^2 collided on a pier of the Sandaokan Yellow River Bridge, causing violent vibration of the above steel truss with maximum amplitude of 2.13 m, and leading to the whole bridge in a very dangerous state.

When a collision load acts on bridge piers, it may cause dislocation of bearings and beams, uneven deformation or fracture of expansion joints, and even collapse of beams, which have been studied by many researchers. For high-speed railway bridges, however, even if there is no beam collapse, the vibration and displacement induced by collision may deform the track and make it instable, which may further threaten the running safety of train vehicles (Laigaard et al. 1996; Xuan and Zhang 2001). The vehicle on bridge may derail from the track when the collision is intense and the train running speed is high. Therefore, the research on dynamic response of train-bridge system and running safety of train vehicles under collision loads is important for the operation safety and risk assessment of bridges.

1.3.4 Bridge Vibration Induced by Crowd Load

A footbridge is usually a slender and flexible welded structure, with small stiffness and damping, and low vibration frequency. A long-span footbridge usually vibrates in its first vertical mode induced by the crowd load, and sometimes also vibrates simultaneously with its transverse mode, which makes the pedestrians uncomfortable and nervous. When the exciting frequency of crowd load gets close to the natural frequency of a bridge, a resonance phenomenon occurs, which may amplify the vibration, panic the pedestrians, and even endanger the safety of the structure.

Crowd induced bridge vibration is an ancient and also an increasingly conspicuous problem. A famous example is the collapse of the Broughton Suspension bridge in England, which was induced by troops passing the bridge. On April 12, 1831, when the troops marching four abreast on the bridge, their regular footsteps acted on the bridge as a harmonic excitation, which caused resonant vibration of the bridge, and finally destroyed it (Bishop 1979).

A similar case occurred at the Angers Bridge in France (Peters 1987). The bridge collapsed on April 16, 1850, while a battalion of French soldiers was marching across it, killing over 200 of them, and marching was again cited as a contributing factor to the collapse.

With constant application of new materials and structural forms, footbridges become more flexible, more beautiful, and longer, which makes them more prone to serious vibration than common road bridges. Footbridges are mainly for passage of pedestrians, which are featured by that pedestrians are both vibration excitation source and vibration receiver. The vibration problem of a footbridge includes two aspects: the crowd load induces vibration of the bridge, while in turn, the vibration of the bridge affects comfort or even normal walking of pedestrians. One typical example is the crowd-induced vibration of the London Millennium Bridge.

At the turning of centuries in 2000, a new bridge, the London Millennium Bridge, appeared on the Thames River, which looked like a man with open arms to welcome tourists (Fig. 1.28 left). Compared with the huge, heavy concrete or metal piers of other bridges, this bridge only has a couple of Y-shaped hollow metal piers, and eight cables hanging between two piers with each end fixed on the bank, without any rigid girder. Two groups of cables, with four cables in each group, are, respectively, hanged on the two arms of the Y-shaped piers and connected by light metal transverse beams, on which the metal floors are laid to form the deck. However, such a slender and beautiful bridge was closed on May 13, 2000, only three days after its open to public. The reason is that on the day of opening, streams of people came to visit it, with up to 2,000 on the bridge at any one time, and when they walked through the bridge (Fig. 1.28 right), the 325 m long bridge began to ceaselessly swing over the water.

According to the theoretical research, the swing and instability of London Millennium Bridge is in fact a natural phenomenon called “collective synchronization,” rather than a design fault. This phenomenon means when people walk casually with their respective favorite speed, they will unconsciously use the same frequency to walk. The natural sway motion of people walking induces small oscillations in the bridge, which in turn causes people on the bridge to sway in

Fig. 1.28 London Millennium Bridge was closed due to crowd-induced vibration

steps, increasing the amplitude of the bridge oscillations, and continually reinforcing the effect (Strogatz et al. 2005). Now, the collective synchronous phenomenon has become a problem that should be considered in bridge design.

There are many such accidents. According to incomplete statistics, during the years of 1825 ~ 2000 there happened 39 bridge collapses related to the crowd, with 33 events reported casualties and over 800 deaths.

With the development of footbridge structures, and continuous appearance of various new types of footbridges, the crowd-induced vibration has become one of the main problems that influencing the serviceability of footbridges (Chen and Hua 2009). The characteristics of the crowd load, its vibration effect on man and the related control criteria should be considered in footbridge design. Nowadays, it has been a consensus that dynamic analysis should be applied in the design of footbridges to ensure their serviceability.

1.3.5 Bridge Vibration Induced by Running Trains

In recent years, with durative raise of train speed, steady growth of traffic density and continuous increase in vehicle load, the problem of dynamic interaction of train-bridge system becomes more and more important. On the one hand, the high-speed train will make dynamic impact on bridge structures (Fig. 1.29), causing them to vibrate, which directly affects the working status and service life of the bridge. On the other hand, the vibration of bridge will in turn affect the running stability and safety of the train, which makes the vibration state of bridge structure become an important index to evaluate the dynamic design parameters for bridge structure. Thus, it is the actual requirement for engineers to carry out comprehensive studies on dynamic interaction of coupled train-bridge system, so as to make dynamic analysis and assessment on the dynamic properties of bridge structure and

Fig. 1.29 Thalys train running through a HSR bridge (Belgium)

Table 1.7 Dynamic interaction of train-bridge system and influencing factors

Problem	Related influence factor	
	Lateral vibration	Vertical vibration
Moving gravity loading on bridge structure induced by a train running on the bridge with a certain speed	–	Composition and running speed of train; axle load and axle distance of vehicle, etc.
Impact action on bridge induced by inertial forces of car-body, bogies, and wheel-sets when a train runs on the bridge with a certain speed	Masses of car-body, bogies and wheel-sets, lateral stiffness and damping of suspension devices	Masses of car-body, bogies and wheel-sets, vertical stiffness and damping of suspension devices
Dynamic effect of bridge deformation and vibration on running vehicle	Lateral vibration of bridge; lateral deformation induced by temperature difference	Vertical deflection and vibration of bridge; vertical deformation induced by temperature difference and PC beam creep, and pier foundation settlement
Track irregularity, the random excitation source of train-bridge system vibration when a train passes bridge with certain speed	Alignment and gauge, geometric and dynamic irregularities	Vertical and cross-level, geometric and dynamic irregularities
Hunting movement of vehicle wheels, a periodic random source of self-excited forced vibration, caused by wheel-tread taper and wheel-rail gap	Wave-length and amplitude of hunting movement	–
Unevenness of wheel treads	Lateral periodical load	Vertical periodical load
Dynamic interaction of coupled train-bridge system, and resonance appearing at a certain train speed	Structural form and span of bridge; composition and axle arrangement of train; properties of lateral spring and damper; lateral and rotational frequencies of train and bridge	Structural form and span of bridge; composition and axle arrangement of train; properties of vertical spring and damper; vertical frequencies of train and bridge
Curved bridge: lateral and rotational vibration induced by centrifugal forces of moving vehicles	Lateral moving load by centrifugal force of train vehicles	–
Earthquake: the influence of earthquake spatial variability on long bridge, and safety of running train on bridge during earthquake	Lateral seismic ground motion	Vertical seismic ground motion
Wind: vibration of coupled train-bridge system induced by combined action of wind and running train, and overturn stability of train vehicles	Effect of lateral turbulent wind, dynamic action on bridge of running train with lateral wind pressure, and structural deformation induced by mean wind	Vertical vibration of bridge induced by wind, and the effect of mean wind
Collision loads: lateral or longitudinal vibration of bridge induced by collision of vessel, vehicle and floating object	Magnitude, direction and acting pattern of horizontal colliding load	Magnitude, direction and acting pattern of vertical colliding load

the running qualities of train vehicles, and to determine the service reliability of the train and the bridge.

When a train travels on a railway bridge, it will inevitably cause the bridge to vibrate. In this case, the bridge bears not only the static load, but also the moving load by loading and unloading of the train at a certain speed, and the inertial forces and other dynamic effects induced by the train and the bridge in vibration. The vibration of the bridge induced by these dynamic loads may cause fatigue of structure components, reduce their strength and stability, and even affect the safety and stability of the train running on bridge when the vibration is serious. When the loading frequency of the train equals to or approaches the natural frequency of the bridge, the resonance will occur, which will intensify the dynamic response of coupled train-bridge system, or even cause an accident. A typical example was in England in 1847, when the Chester Dee Railway Bridge was broken owing to excessive vibration induced by a train passing through it (Lewis 2007). Every serious accident provides us with disastrous experience and lesson, which promotes engineers to constantly improve the structure design, to adapt the objective laws. Therefore, the dynamic interaction of train-bridge system has been attached great importance and studied by bridge designers in many countries.

From the point of view of vehicle dynamics, each railway locomotive or vehicle is a vibration system composed of a car-body, bogies, wheel-sets and spring-damper suspension devices. The running train may produce dynamic impact on the bridge, and cause it to vibrate, while the vibration of the bridge will in turn affect the running stability and safety of the train. Therefore, the vibrations of the train and the bridge interact on and interaffect each other, forming a multi-DOFs (degrees-of-freedoms) complex vibration system.

The dynamic interaction of train-bridge system involves various problems, which are summarized in Table 1.7, with the related influence factors.

1.4 Research History and Status Quo of Train-Bridge Coupling Vibration: An Overview

1.4.1 Research on Vibration of Railway Bridges Under Moving Train

As early as in 1840s, researchers started to study the dynamic response of railway bridges. However, as the bridge vibration under moving train loads is a complex issue, many factors should be considered in the analysis to get the realistic results. These factors include the mass of car-body and bogie, the effect of dashpot and spring on the bogie, the running speed of train, the mass, stiffness and damping of pier and beam span, the structure and dynamic performance of the track on bridge, the dynamic interactions between wheel and track, track and beam, etc. as well as various random factors such as the unevenness of wheel rim, the geometric and

dynamic irregularities of track, and the hunting movement of wheel-set, making the analysis model extremely complex. Therefore, previous studies had to adopt various approximation methods, with great limitations. Only in the recent decades, with the wide application of computers and the development of a variety of numerical solution methods, was promoted the research of this problem. At present, the dynamic analysis of train-bridge coupling system has become an important research topic in the field of bridge vibration.

During the long evolution history of analysis model for train-bridge coupling vibration, the train model was developed from the simple moving force to the moving mass, and then to the moving wheel-spring-mass unit, after that to the half-vehicle model, until the spatial full train model; and the bridge model was from the single beam with constant section to the finite element model of full bridge with bearings, piers, foundations, and other accessory structures, gradually forming a complete train-bridge dynamic analysis system.

1.4.1.1 Researches Abroad

In 1849, by neglecting the bridge mass but considering the wheel mass, Willis (1849) and Stokes (1849), respectively, established the differential equation of bridge vibration under moving loads and derived its approximate and exact solutions. Later, Robinson (1887) also obtained the basic theoretical solution and conducted the related vibration tests, but the difference between the calculated results and those from the tests was large, due to neglecting the bridge mass.

In the first half of the 20th century, American engineers carried out three large-scale field tests. In first test, the maximum dynamic responses of the bridge were measured under various kinds of locomotives passing the plate beam and truss bridge at different speeds, finding that the hammer effect induced by the unbalanced wheel weight was the main excitation of bridge vibration, based on which the concept of "impact factor" was proposed. In the subsequent tests, the resonance phenomenon was found when the wheel rotation speed of the steam locomotive matched with the bridge fundamental frequency, and accordingly the concept of "critical speed" was put forward. The third test was mainly on some small span bridges, where the difference between steam locomotive and diesel locomotive was compared, and the vibration attenuating effects of pier elasticity, ballast layers, and elastic cushions were investigated.

During the same period, researchers in the former Soviet Union carried out a lot of tests, mainly studied the lateral vibration of bridge induced by locomotive and other factors, and set up the empirical formulas of the stress coefficient induced by lateral vibration with respect to train speed. Timoshenko (1922, 1927) established a bridge model under moving loads by only considering the bridge mass and obtained its analytical solution, to interpret the resonance mechanism in theory. By combining the theoretical analysis and experimental study and considering the inertial forces of both locomotive and bridge masses, Inglis (1934) used the moving periodical forces to solve the motion equation of train-bridge system, which brought

the research of train-bridge dynamic system to a new level. Subsequently, by taking into account the masses of a single wheel and bridge, Schallenkamp (1937) studied the Fourier series expansion of wheel inertia force and bridge deflection and derived the analytical solution by solving the relationship among the series coefficients. Muchnikov (1953) carried out accurate analysis on the above models by the integral equation method.

In addition, Carter (1926), as the founder of the rolling contact theory, skillfully analyzed and presented the relationship between the longitudinal and the tangential wheel-rail forces with the creep rate, according to the Hertz theory and the elastic half-space theory. On the basis of Carter's research, Johnson (1958) proposed the pure creep rolling and pure spin rolling contact theory, and generalized it to the three-dimensional rolling contact. In the 1970s, Kalker (1973, 1979) eventually proposed the three-dimensional linear creep theory for wheel-rail rolling contact, which has been widely used in the wheel-rail relationship analysis.

In this stage, although there was still a large gap between the analysis and the actual results, the moving sprung-mass model was developed, being the prototype of the modern train-bridge analysis model, and some basic concepts such as impact coefficient and resonance effect were established. All these research laid a solid foundation for the subsequent development of the modern train-bridge coupling vibration theory.

Entering the 1960s, with the aid of the structural FEM and the progress of computational technique, the research on vibration problem of train-bridge system broke through the traditional methods, stepping into the new period of system research. During this period, along with the emergence and development of high-speed railways, the needs for the dynamic analysis of train-bridge coupling system became more urgent, and meanwhile, a large number of railway constructions made the field tests more convenient. Under this background, through the systematic and in-depth efforts of researchers in various countries, the research on train-bridge coupling vibration, from mechanical model, excitation source simulation to analysis method and calculation technique, all achieved qualitative developments and obtained a lot of results in model tests and field experiments.

In the United States, Chu et al. (1979) took the lead in the research on spatial vibration of train-bridge system. They proposed the vehicle model with 11 DOFs by connecting the rigid bodies of car-body, bogies, and wheel-sets with the vertical suspensions and established the train-bridge system spatial analysis model by simplifying the truss mass into the nodes. Wiriyachai (1980) investigated the impact coefficient and the fatigue damage of truss bridge with rigid, hinged and semi-rigid nodes. Bhatti (1982) analyzed the spatial dynamic responses of the train-bridge system with the 21 DOFs' model considering the vehicle suspension nonlinearity. Later, Wang et al. (1991) improved Bhatti's vehicle model to 23 DOFs to get a more realistic simulation movement of wheel. Vu-Quoc and Olsson (1989) established the nonlinear differential equations for the vehicle and flexible structure system, using the Runge-Kutta method and the linear multi-step integral method, to predict and modify the unconditional stability of the train-bridge interaction problem.

In Japan, Matsuura (1974, 1976) studied the dynamic responses of a half-vehicle model passing the bridge, and based on the results, proposed the deflection limit for the bridge. They also established a two-layer suspension vehicle model with 10 DOFs, deduced the motion equation by the energy method and analyzed the influence of several factors (vehicle parameters, train composition and running speed, bridge span, track irregularity, etc.) on the bridge dynamic coefficients. The results showed that when the train speed reached 300 km/h, the bridge dynamic coefficient could appear abnormal value, and when the loading period induced by regularly arranged axle loads was an integer times the natural frequency of the beam, the bridge resonance would occur. Tanabe et al. (1987) established the four-axis passenger vehicle model of 31 DOFs on Shinkansen in Japan and used the FE-and-modal synthesis technology to solve the problem.

In Europe, with the development of HSR construction in the 1970s, Frýba (1972, 1976) established the vertical vibration analysis model for train-bridge system, including the moving load, moving mass, moving wheel-spring-mass unit, and vehicle element with car-body and two-layer suspensions. By considering the irregularity of bridge deck, he systematically compared the effect of different parameters, such as bridge dynamic properties, vehicle characteristics, train speed, track irregularities and wheel-rail forces, on dynamic response of the bridge. Olsson (1985, 1991) adopted the modal coordinate method to reduce the analytical DOFs of the bridge, and then derived the general vehicle element composed of time-varying, asymmetric matrices for train-bridge system, and presented the analytical expression and numerical solution of dynamic responses for simply-supported beam under moving loads.

Since the 1980s, scholars from various countries have extended the research of train-bridge coupling vibration to more application scopes. Diana and Cheli (1989) established the vehicle model of 23 DOFs considering the wheel-rail interaction, and analyzed the dynamic responses of a long-span suspension bridge under wind loads. Green and Cebon (1994, 1997) obtained the dynamic responses of the bridge through FFT transform and by convolution of the vehicle load and bridge modes in the frequency domain.

The European Railway Research Institute (ERRI) conducted a series of researches on the bridge vibration caused by high-speed trains, and the results were used to guide the dynamic design of HSR bridge (ERRI D214 Committee 1999). The D214 committee of ERRI introduced some new concepts such as the “train fingerprint” and the “bridge dynamic influence line,” and classified the factors affecting the amplification of bridge dynamic responses into two categories. One is from the train (arrangement of wheel-axles); the other is from the bridge (frequency and damping of structure). They also presented the harmonic decomposition method to calculate the maximum dynamic displacements and accelerations of the bridge. Although the harmonic decomposition method was only applied to the simply-supported beam with uniform section, it can give the upper limits of the dynamic response of the bridge under the resonance train speed while avoid the step-by-step integration of dynamic equations in the time domain. Majka and Hartnett (2008, 2009) studied in detail the influences of various parameters, such as

bridge frequency, mass, damping and span, on the dynamic responses of the single span simply-supported bridge under different train speeds.

De Roeck et al. (2000) performed systematic research on the bridge damage identification. By continuous measurement on a bridge for a whole year, they found that temperature was the most important environmental factor, as it could change the boundary conditions as well as the elastic modulus of the bridge, and the variation of vibration signals induced by bridge damage is mainly due to the decline of local stiffness. Therefore, it is necessary to eliminate the interference of environment factors when using the bridge dynamic responses as evaluation indices.

Liu et al. (2014a, b) analyzed the dynamic responses of multi-span simply-supported viaducts under the passage of train, considering the weak coupling effect between bridge and track due to ballast and rails, and found that fairly ideal analysis results of bridge dynamic behavior could be obtained by optimizing the boundary conditions of a single span beam model.

Rebelo et al. (2008) carried out dynamic tests on several medium and small span ballasted bridges in Austria, and discovered that friction forces between ballast and deck had big influence on the peak acceleration of bridge.

Rigueiro et al. (2010) studied the effect of various ballasted tracks, and found that track structure worked as a filter to the high frequency vibration of elevated railway bridges, which would reduce the maximum acceleration of the deck.

Kaliyaperumal et al. (2011) established the finite element model of a skewed steel bridge, using combined plate and beam elements. The calculated results matched well with the experience values after the model being updated by the measured characteristic parameters. It was proved that the global bridge model established with combined plate and beam elements could achieve good dynamic responses of the bridge, and can be used to estimate the average stress range of fatigue damage.

With the development of research in this field, some shortages in the analysis method and the simplification assumptions are gradually recognized, where, for example, the track structure was simplified to have the same deformation with the beam by ignoring its individual changes, and the wheel-rail relationship was mostly considered by force equilibrium and displacement compatibility, while lacked substantive physical description on real wheel-rail contact state.

In recent years, the computer simulation based on complex vehicle model and spatial bridge model has become a necessary tool for train-bridge coupling vibration research. Using more detailed wheel-rail relationship to further perfect the vehicle model and adopting more efficient calculation method to objectively simulate the real dynamic response of train-bridge system has become the common goal for all international scholars.

1.4.1.2 Researches in China

In China, studies on bridge vibration subjected to moving train loads started early in 1970s. Professor Li GH proposed the flexure-torsion theory of trussed beam, using the finite difference method to calculate the spatial free vibrations of several

bridges, and validated the results by the measured data (Li 1978). Professor Chen YJ summarized the classical and the at-the-time advanced analysis theory of train-bridge coupling vibration, and investigated the influence factors on bridge impact coefficients (Chen 1975).

Since the early 1980s, researches on the theory and the application of train-bridge coupling vibration have been carried out systematically in China.

In the China Academy of Railway Sciences, Professor Cheng QG guided his graduate students to modify the train-bridge coupling vibration model and to improve the solution algorithm (Cheng et al. 1992a, b). Xu (1988) established the freight-car model with 27 DOFs considering the deformation of bogie frame, proposed the concept of secondary track irregularity, and investigated the iteration method for solving the train-bridge motion equations of large-span railway bridges. Sun (1998) investigated the lateral vibration of a cable-stayed bridge under moving trains, considering the track irregularity, by the spectrum analysis method. Ke et al. (1991) studied the dynamic coefficient, vertical stiffness and vehicle-beam interaction of multi-span simply-supported bridges on high-speed railways. Yang (1995) solved the separated train and bridge equations by the Wilson-θ method, studied the influence of bridge deflection and track bending angle on the running performance of the train, through secondary iterations between the train and the bridge by the Seidel Iteration Method. Wang (1996) conducted linear and nonlinear dynamic analysis of the cable-stayed railway bridge on the Hongshui River. Zhang et al. (1996) carried out a series of field tests on the three speed-up railway main lines, and proposed the vertical and lateral stiffness limits for medium-and-small span HSR bridges according to the requirement on the running safety, riding comfort and car-body accelerations of train vehicle and the vibration response of bridge. Gao and Pan (1999) and Pan and Gao (2008) studied the coupling vibration of train-track-bridge system, by considering the dynamic interactions among high-speed train, track and bridge.

In Southwest Jiaotong University, the research on theory and application of train-bridge vibration system was started under the guidance of Professor Qiang SZ. Shen (1987) analyzed the spatial vibration of a steel truss bridge, and compared the calculated results of a simply-supported bridge by the load series model and the train-bridge model. He and Li (1999) and Shan and Li (2001), respectively, studied the influences of some factors, such as radius and outer-rail superelevation of curved track, on the dynamic responses of train and bridge, and proposed the stiffness limit for medium-and-small span curved HSR bridges. Li et al. (2002) separated the train-bridge system to individual train equation and bridge equation, taking displacement coordination condition at wheel-rail contact points as convergence condition, to solve the system response. Li et al. (2004) established the wind-train-bridge analysis model and analyzed the contributions of natural wind and fluctuating wind to the bridge dynamic responses, through simulating different wind speed fields. Cai (2004) established the vehicle-track-bridge coupling system model, and studied the dynamic responses of track and bridge under high-speed train by the numerical simulation method, and evaluated the running safety of train vehicles. Jin (2007) set up the spatial coupling vibration model of train-track-bridge system, considering the wheel-rail detachment and uneven compression state, and

studied the random vibration of train-bridge system, considering the randomness of track irregularity and structural parameters. Cui (2009) established the motion equations for multi-body systems, respectively, with elastic and constraint wheel-rail contact, considering the nonlinear factors, and analyzed the solution principle for the normal forces at wheel-rail contact points. Zhu (2011) used the virtual-excitation method to perform random vibration analysis of train-bridge coupling system. Li et al. (2012a, b, c, d, e) deduced the analytical expression for the vertical vibration of Euler-Bernoulli beams under random moving load series, which could be applied to preliminary HSR bridge design for fast and reliable evaluation of the maximum vibration energy.

In Central South University (the former Changsha Railway Institute), Professor Zeng QY and his research team (Zeng et al. 1990, 1991, 1999) focused on modeling the whole train-bridge system, by using the potential energy variation principle in dynamics and the "set-in-right-position" rule, and proposed the practical vibration analysis method. Taking the measured wheel hunting waves of bogie and wheel-set as the excitation source, they calculated the lateral vibrations of train-bridge system and the lateral swing forces of the train, and compared them with those related to the vertical and lateral stiffness criteria in some codes. Zhang and Zeng (1998) studied the control indices for lateral stiffness of steel truss bridge, based on the analyzed vibration results of train-bridge time-varying system and according to the safety requirement on anti-derailment. Zhu and Zeng (1994) proposed the energy-based vibration analysis method of train-bridge system, by converting the random system vibration with various stochastic factors into system vibration energy. Wang et al. (1995) generated the artificial frame hunting waves for high-speed vehicle bogies, by taking the energy variance as control condition, based on the measured data of frame structure vibration and lateral wheel-loads in China and abroad. Guo and Zeng (2000) analyzed the vibration characteristics of multi-shaped PC girders and running properties of high-speed trains by numerical simulation. Xiang et al. (2004) proposed the energy random analysis theory for vehicle derailment, and analyzed train derailment on bridge in several conditions, showing good accordance with the actual measured data.

Based on probability density evolution method, Yu et al. (2015a, b) established the random dynamic equations of train-bridge system, by introducing the random harmonic functions representing the power spectrum of track vertical irregularity to the model. The random excitation samples of track irregularity were obtained by the representative points of random frequency selected by utilizing the N-dimensional hypercube point set method. The programs for the probability density evolution and analysis of train-bridge coupled random vibration were developed. The Newmark-β integration method and the double edge difference method of TVD format were adopted to obtain the mean values, standard deviations and the evolution distributions of time-varying probability density of the train-bridge responses.

In Tongji University (the former Shanghai Railway University), Professor Cao XQ led the study on the lateral vibration of train-bridge system. Cao and Chen (1986) analyzed the lateral vibration of trussed bridge under moving trains, by the random variable simulation method, the second-order filter method and the

step-by-step integration method, to solve the random vibration equations. Cao (1991) carried out theoretical analysis and field tests on the lateral vibrations of steel truss bridge. By dividing the lateral vibration time histories into three phases as "locomotives on the bridge," "train passing the bridge" and "train leaving the bridge," he investigated the probability distribution characteristic of lateral vibration amplitudes by statistics analysis, and proposed the method for determining the spatial vibration modes and lateral swaying forces of trussed bridge. Ma and Cao (1994) established the pier-beam spatial coupling model, and analyzed the characteristics of lateral vibration and stiffness of long-span continuous bridge with PC box-girders and high piers under train passages. Wang and Cao (2000) established spatial dynamic model of train-bridge system, and analyzed the dynamic responses of a cable-stayed bridge under high-speed trains. Cao et al. (1999) did a lot of work to revise the *Code for Rating Existing Railway Bridges*, and the results were adopted in the updated version of the Code TYH2004-120 (2004).

In Beijing Jiaotong University (the former Northern Jiaotong University), Xia H started the research on train-bridge coupling vibration in 1982 guided by Professor Chen YJ (1975), and developed the theory and application of train-bridge coupling vibration (Xia 1984). By the modal comprehensive method, he established the spatial dynamic analysis model of train-bridge system including piers and bearings, considering the eccentric load on one-way track and the effects such as track irregularity, vehicle hunting, and centrifugal force of train on curved track. After that, Professor Xia and his research team carried out a series of comprehensive research in various fields of train-bridge coupling vibration, including train-bridge system, wind-train-bridge system, train-bridge system subjected to earthquake action, train-bridge system subjected to collision load, modal identification and damage detection based on train-bridge dynamic responses analysis, and environmental problems of train-bridge vibration (Xia and Chen 1992, 1994; Xia et al. 1995, 1996, 2000, 2001, 2003a, b, 2005a, b, 2006a, b, 2007, 2008a, b, 2009a, b, 2010a, b, c, 2013b, 2014b, c; Xia and De Roeck 1997; Xia 1998; Xia and Zhang 2005a, b).

Zhang N systematically studied the train-bridge coupling vibration and its engineering application (Zhang et al. 2002, 2008, 2009, 2010a, b, 2011, 2013a, b, 2014, 2015) and investigated the dynamic interaction between the articulated train and HSR bridges (Zhang 2002; Xia H et al. 2003a, b). Based on the wheel-rail interaction relations, he proposed the Inter-system Iteration Method to solve the train-bridge interaction dynamic analysis. He analyzed the dynamic responses of train-bridge system and running safety of high-speed train under seismic and wind loads, and studied the bridge deck deformations induced by concrete creep and temperature gradient and their effects on the running safety and stability of high-speed trains using the UM software.

Guo (2005) and Guo et al. (2007, 2010, 2012, 2015a, b, c) studied the dynamic responses of long-span bridges and running safety of trains under wind action, the resonance mechanism of train-bridge dynamic interaction system, the dynamic interaction of LIM (Linear Induction Motor) train and elevated bridge, and the anti-wind mechanism and windproof effects of wind barriers on bridges.

Zhan (1996) and Zhan et al. (2011) investigated structural damage identification for railway bridges based on train-induced bridge responses and sensitivity analysis. Deng (2011) and Xia and Calçada (2013) conducted dynamic analysis of coupled train-ladder track-elevated bridge system and the vibration reduction measures. Xin (2006) performed simulation analysis on dynamic responses of long-span PC continuous beam (rigid frame) train-bridge time-varying system. An et al. (2010) and An (2013) identified beam crack using the dynamic response of a moving spring-mass unit. Hou et al. (2012, 2015), Hou (2013) performed dynamic analysis and model test on steel–concrete composite beams under moving loads. Wang et al. (2013, 2015, Wang (2015) performed dynamic analysis of train-bridge coupling system considering the flexibility of vehicle car-body. Yu (2013) and Yu et al. (2016) conducted bridge damage identification from moving load induced deflection based on Wavelet Transform and Lipschitz exponent. Li et al. (2013) and Xia et al. (2014a) deduced the analytical solution for vibration response of simply-supported beam under moving load series, and derived the formulas for beam resonance effect and two types of resonance cancelation effects, by clarifying the mechanism of these two conditions. They also performed the dynamic stress analysis and fatigue performance assessment of steel bridge based on train-bridge coupling vibration (Li et al. 2015a, b; Li 2016).

Sun et al. (2013) analyzed the effect of bridge deformation induced by time-varying temperature field on the running safety and riding comfort of high-speed trains. Tian et al. (2015) proposed a multi-scale dynamic boundary approximation method based on the dynamic equilibrium equation and finite element theory, which can effectively solve the dynamic effect of orthotropic floor system on long-span railway steel bridge. Li et al. (2015) adopted the "m" method to simulate the equivalent stiffness of group-piles foundation, established the train-bridge coupling system model by imposing the spring constraints at the bottom of pile caps, and studied the effect of river scouring on the dynamic responses of the system.

During the same period, the research group actively sought for international cooperation. Many of their research results benefited from the cooperation with the Hong Kong Polytechnic University, the KU Leuven (Katholieke Universiteit Leuven) in Belgium, the Railway Technology Research Institute in Japan, the University of New South Wales in Australia, the Madrid Polytechnic University in Spain, the University of Porto in Portugal, the Keele University in England, the KTH Royal Institute of Technology in Sweden, and the Lehigh University in the US. On the basis of the research results, the group has published *Dynamic Interaction of Vehicles and Structures* (Xia 2002) and Xia and Zhang (2005a), *Traffic Environmental Vibration Engineering* (Xia et al. 2010a), *Bridge Vibration and Controls* (Xia et al. 2012a, b), *Traffic Induced Environmental Vibrations and Controls* (Xia and Calçada 2013) and *Coupling Vibrations of Train-bridge System* (Xia et al. 2014b), and other English and Chinese academic works. These academic works comprehensively reflect the contemporary research development and achievements in the field of train-bridge coupling vibration.

With the rapid development of high-speed railways in China since the beginning of this century, how to ensure the safety and comfort of high-speed trains presented an urgent demand for the study of train-bridge coupling vibration. Therefore, the Ministry of Railways of China organized the Southwest Jiaotong University, the Beijing Jiaotong University, the China Academy of Railway Sciences and the Central South University to form a research team to study the train-track-bridge coupling vibration problem. Zhai (2002), Zhai and Xia (2011) and Zhai and Wang (2012), as an academician of the Academy of Sciences of China, was appointed as the head of this team to develop the effective cooperation. Based on the fine wheel/rail dynamic coupling relationship, a perfect train-track-bridge large system model was established, and general analysis software TTBSIM was developed, which provided great help and support to the train-track-bridge system simulation analysis for HSR design in China. The explicit-implicit numerical integration method proposed by Zhai (1996) was an effective method for solving bridge equations with complex DOFs and large-scale calculation requirement, while ensuring sufficient calculation accuracy. At the same time, based on the Traction Power State Key Laboratory in Southwest Jiaotong University, this research team carried out a series of fundamental and forward-looking innovation studies for high-speed train vehicles.

In Taiwan University, Yang and Yau (1997), Yau and Yang (1999) proposed the dynamic condensation method to solve the dynamic response of the train-bridge system. The method was based on finite element theory, where the lumped mass model with attached springs and dashpots was adopted to simulate the vehicle model, and the DOFs associated with car-body were condensed into the bridge unit they contacted with, to derive the train-bridge interacting elements. By the dynamic condensation method, all the DOFs related to car-bodies in the interacting elements were eliminated, thus greatly improved the calculation efficiency. Yang et al. (2004) presented the impact coefficient formulas for simply-supported beam and continuous beam under moving loads, and analyzed the effects of parameters such as frequency ratio and bridge damping. Yau and Yang (2006) studied the vertical accelerations caused by equidistant moving load series at resonance speed, and analyzed the control parameters of resonance effect, finding that the contribution of high-order modes to accelerations often depended on the damping, while the low-order modes determined the acceleration peak value.

Yang (2003) studied the influence of running train on the environment vibration when the high-speed train travels on the elevated bridge, and using the 1/3 octave analysis method, analyzed the main influence parameters on ground vibration in lateral and vertical directions. Yang et al. (2004) investigated the vibration frequencies of bridge and train by means of the Hilbert transform, calculation algorithm, limiting factor analysis, and case studies, discovered the inherent relationship between the vibration frequencies of the bridge and the train, and proposed a new method for measuring bridge vibration frequency. Their study laid a solid theoretical foundation for the research of bridge vibration, structure service life, design, construction and other related work.

1.4.2 Study on Dynamic Responses of Train-Bridge System Under Wind Loads

The wind load applied on the bridge consists of three components, i.e., lift, drag and moment of torsion, with each component including three parts: the static wind force caused by the mean wind, the fluctuating wind force caused by buffeting wind, and the self-excited force caused by the interaction between wind and bridge structure. The research of this part has been quite developed, and already commonly used by researchers and engineers in bridge engineering.

The wind-induced bridge vibration is a very complex problem related to many interactive factors. There are several different phenomena giving rise to dynamic response of bridge structure under turbulent wind, which are flutter, buffeting, and vortex.

Under the mean wind, the oscillating structure draws energy from the airflow, and is mutually excited with the airflow, forming the self-excited vibration, known as flutter. Flutter is a kind of divergent vibration, and once occurring, it will result in flutter instability failure of the bridge. Therefore, the design wind speed of the bridge should be lower than the critical flutter wind speed.

The forced vibration caused by the wind turbulence (fluctuating wind) is called buffeting, which may occur under various wind velocities. Buffeting is a vibration with limited amplitude. Unlike the flutter with the self-excitation and divergence nature, buffeting will cause neither aerodynamic instability nor failure of the bridge. However, because the wind velocity for structural buffeting is low and frequent, it will produce local fatigue failure at the member joints or bearings of the bridge.

In addition, large bridge buffeting vibration may cause the discomfort of passengers or even endanger the running safety of high-speed train. Therefore, the buffeting analysis has become an important topic in the wind-induced vibration of train-bridge coupling system.

The vortex-induced vibration of bridge is caused by wind vortex. Although the vortex-induced vibration is also with the self-excitation nature, different from the divergence of the flutter, it usually occurs in a non-streamline bridge deck at relatively low wind velocity. The most typical vortex-induced vibration occurs in the stayed cables and hangers with circular section, which can be reduced to an allowable level by optimizing the shape of bridge deck or (and) by installing some additional aerodynamic devices on the deck.

When studying the wind-induced vibrations of train-bridge system, only the buffeting response of the system induced by turbulent wind is considered.

Bridge buffeting is an important wind-induced vibration phenomenon. There are three main bridge buffeting theories (Xiang and Ge 2002): the buffeting vibration analysis method by Davenport, the buffeting and flutter vibration analysis method by Scanlan, and the time-domain buffeting vibration analysis theory by Lin and Yang (1983), corresponding to the research work in specific issues, with respect to the methods adopted in model establishment, parameter identification, numerical simulation and calculation algorithm. Zhang et al. (2006) proposed a new

aerodynamic model for long-span bridge buffeting analysis, using quasi-steady aerodynamic stiffness and test-based unsteady aerodynamic damping to correct the model aerodynamic parameters, showing by wind tunnel test that the model can more accurately describe the aerodynamic stiffness and damping characteristics of the bridge structure. Based on the quasi-steady aerodynamic theory and the strip theory, Zhu et al. (2006) proposed a practical frequency-domain analysis method for buffeting performance of double-cantilever state of a long-span cable-stayed bridge under yawed winds, and Bao (2008) further refined this method in his doctoral dissertation to consider the dynamic behavior changes caused by the structural static wind displacement and the effects of additional wind yaw angle and attack angle on bridge buffeting. Guo and Ge (2013) studied the impulse response functions of self-excited force and performed flutter analysis in time domain for bridge.

For a train-bridge system, the wind loads may induce large bridge deformation and vibration, and the aerodynamic performances with and without train are fairly different due to the large frontal area of the train, so the dynamic analysis of train-bridge system under wind load is very complicated, where three interactions need to be considered, namely the train-bridge interaction, the wind-bridge interaction and the wind-train interaction. Li et al. (2005a, b 2012a, b, c, d, e, 2014) established a nonlinear spatial wind-train-bridge system model by regarding wind, train and bridge as an interactive and coordinated coupling dynamic system, measured the aerodynamic parameters of bridge, train and combined train-and-bridge section model by wind tunnel tests, and analyzed the train-bridge interaction under wind loads by using the self-developed bridge structural analysis software.

Wang and Guo (2012) and Liu (2014) analyzed the running safety of the train when it ran on the bridge under wind loads by numerical simulation, and conducted several case studies for practical engineering. Zhang and Xia (2013) studied the dynamic response and safety of train and bridge when the train was running on a railway suspension bridge, by applying the static wind and the simulated buffeting wind on the train and the bridge. Kwon et al. (2008) established the analysis model for the intercity maglev train running on the suspended guide rail bridge under gust load, taking the simulated track irregularity and turbulent wind velocity as the excitation, and solved the motion equations in time domain.

During 1999–2007, based on the cooperation between the Beijing Jiaotong University and the Hong Kong Polytechnic University, Xia H and Xu YL studied the train traversability of the Tsing Ma Bridge, the world's longest rail-cum-road bridge, under strong winds, and co-published a series of analysis results about the dynamic response of train and large-span suspension bridge system under wind loads (Xia et al. 2000; Xu et al. 2003, 2004, 2007). Xia and Chen (1994, 1998) proposed an analysis method for dynamic reliability of train-bridge system under random wind excitation using the Monte Carlo simulation technique. Guo et al. (2007, 2010) established a dynamic interaction model of train and large-span bridge system under turbulent wind load, studied the vibration characteristics of the Tsing Ma Bridge under wind loads and train passage, and verified the results by some measured data,

based on which they proposed the wind velocity-train speed threshold curves to ensure the running safety of train. In dynamic design of the Wuhan Tianxingzhou Yangtze River Bridge, the Nanjing Dashengguan Yangtze River Bridge and other long-span HSR bridges, Xia et al. (2008a, b) and Zhang et al. (2009) systematically analyzed the effect of wind on the safety of bridge structure and running train vehicle, providing important basis for bridge design. Wang et al. (2010, 2013), Wang (2012) established the dynamic analysis model of wind-train-bridge coupling system considering the large-displacement geometry nonlinearity, calculated the dynamic response of the Wufengshan rail-cum-road suspension bridge, and studied the effects of bridge nonlinear deformation, wind velocity, and train speed.

When a train runs at a high speed, the aerodynamic forces and moments on the car-bodies make the train at a "floating" state. Under strong crosswind, the aerodynamic performance of the train worsens dramatically, and with the enlargement of lift and lateral forces on the train, the possibility of a train derailment or overturn increases. Currently, the study on the wind-induced unsafety of high-speed train is mainly based on the deterministic methods, namely both the aerodynamic parameters of the vehicle system and the environment are determined and unchanged. Yu et al. (2012) studied the effect of uniform crosswind on running safety of high-speed train, finding that wheel offload factor was the most susceptible to exceed the limit among the safety indices and proposed the offload factor-based safety threshold of high-speed train under crosswind. Zhai et al. (2013) studied the exponentially distributed wind flow field around bridge with different heights, and by the multi-body dynamic model of high-speed train, simulated and analyzed the aerodynamic surface pressure characteristics of opposite trains crossing on the bridge under crosswind. Huang et al. (2006) analyzed the two-dimensional flow characteristics of ICE train on the standard simply-supported beam under crosswind, and theoretically investigated the flow characteristics of train-bridge system by introducing the research on cavity flow characteristics.

In order to investigate the aerodynamic characteristics of high-speed train vehicles on bridge under crosswind, Guo et al. (2015a, b, c) measured the aerodynamic forces acting on the vehicle by a wind tunnel test model with a scale of 1:20, obtained the aerodynamic force coefficients of the head car, middle cars and rear car of high-speed train and analyzed the effect of Reynolds numbers, relative position between vehicle and bridge and wind yaw angle on the aerodynamic force coefficients of vehicles.

Wind barriers, or other windproof facilities, can significantly alter the aerodynamic characteristics of the bridge, and especially decrease the critical flutter speed, owing to the vortex characteristics of the cavity swirl flow. Moreover, wind barriers play an important role in sheltering the high-speed train from wind attack, greatly reduce the lateral aerodynamic forces on the train, and increase the running stability and comfort of the train.

Zhang (2013) and Zhang et al. (2013c, d) studied the aerodynamic problem when the airflow passes through the wind barrier based on the computational fluid dynamics (CFD) simulation, and analyzed the effect of wind barriers with different parameters (screen height, porosity rate, etc.) on wind velocity. They also

quantitatively analyzed the windbreak effect and effective protection area of wind barriers and investigated the structural forms and main design parameters of wind barriers. Guo et al. (2015a, b, c) took the common-span simply-supported bridges located in the wind zones of the HSR line from Lanzhou to Urumqi as the research target, conducted wind tunnel test on the anti-wind performance of train-bridge section model with wind barrier, obtained the tri-component coefficient of vehicle and bridge under different operating conditions. They further studied the wind-sheltering effects of different wind barrier forms on train running safety, using the coupling analysis model of wind-train-bridge system. Zhang et al. (2015) assumed the aerodynamic force uniformly acting on the train, and on this basis, studied the effect of triangular wind barriers located around the towers of long-span bridge on train-bridge dynamic responses. The results showed that wind barrier had little impact on the bridge dynamic response, but could significantly reduce the dynamic response of the on-bridge train and improve its running safety.

He et al. (2016) studied a novel louver-type wind barrier with adjustable blades. The aerodynamic control mechanism of the proposed wind barrier was explored by the CFD technique, and the aerodynamic characteristics of both train and bridge due to this wind barrier were systematically investigated by wind tunnel tests. Compared to the traditional grid-type wind barrier, the novel wind barrier presented better aerodynamic performance in improving the running safety and riding comfort of train on the bridge under strong wind environment.

Li et al. (2012d, 2014) conducted the wind tunnel tests, respectively, using the three-vehicle model and the single-vehicle model to test the wind load mutation process when two opposite trains crossing near the tower, and investigated the effects of wind velocity, train speed, track location and vehicle type on the aerodynamic coefficients of the vehicle models. In addition, they measured the aerodynamic coefficients of the vehicle models on three typical bridges with different wind barriers. Li et al. (2009) simulated the dynamic responses of trains with and without considering aerodynamic forces and illustrated the effect of aerodynamic force on the dynamic characteristics of the train system when opposite high-speed trains crossing.

Tian and He (2001) and Tian (2004) simulated the crossing process of opposite high-speed trains, by the method for solving the three-dimensional compressible non-steady Navier-Stokes equation. They studied the numerical calculation method for air pressure pulse induced by train crossing, the aerodynamic model, and the real vehicle test technology. Besides establishing the relationship of the train crossing pressure wave with train speed, intertrack space, car-body shape, width and profile, and train composition, they also suggested the safety criterion for transient crossing pressure impact on car-body and window structure of various types of HSR trains in China.

Hu and Guo (2009) and Zhang et al. (2013a) analyzed the train-bridge dynamic responses under turbulent wind by the time-domain analysis method, adopting the spatially correlated cross turbulent wind velocity field, and considering both the static wind loads and the quasi-steady fluctuating wind forces of the train and the bridge. Liu (2010) established the dynamic analysis model for wind-train-track-bridge system,

by taking into account various interactions of wind-bridge, wind-train, wheel-rail and bridge track, to analyze the influence of train type, train speed, one-way or cross passage, track form, track irregularity and other factors on the train and bridge dynamic responses.

1.4.3 Study on Dynamic Responses of Train-Bridge System Subjected to Earthquake Action

With increase in bridges on railway lines in recent years, the possibility of trains running on bridges becomes larger when an earthquake happens, especially for HSR lines, where tens or even hundreds of kilometers of elevated bridges are built, and it would be extremely dangerous when an accident happens for high-speed trains. Therefore, the dynamic response of train-bridge system subjected to earthquakes has been paid great attention by scholars in China and abroad. The research on this problem mainly includes the vibration and running safety of train-bridge system under seismic action, the influence of spatial variability of earthquake ground motions on long-span bridges, and so on.

Yau and Frýba (2007) and Yau et al. (2009) studied the dynamic response of a suspension bridge subjected to moving loads and vertical earthquake action. They solved the quasi-static part of dynamic response by analytical method and the dynamic part by the Galerkin method, by modeling the traffic load as a row of equidistant moving forces, while simulating the earthquake by vertical motions of supports. The results indicated that the interaction of the moving load and the seismic action might substantially amplify the response of long-span suspended bridges in the vicinity of the supports, and appropriate measures by increasing cable sag or reducing cable stiffness could help mitigate the earthquake-induced responses of the train-bridge system.

He et al. (2011) developed an analytical approach to evaluate the influence of dynamic train-bridge interaction on the seismic response of the Shinkansen viaduct in Japan under moderate earthquakes and found that the response of bridge subsystem might be underestimated if the train load acted on the bridge only as additional mass.

Ju (2012, 2013) studied the running safety of train on the bridge subjected to earthquake, using the nonlinear finite element method, where the high-speed vehicle was modeled with nonlinear wheel elements, viscous-elastic spring-damper elements and lumped mass, and found that the derailment factor of the vehicle can be reduced by increasing the lateral stiffness of piers. Konstantakopoulos TG et al. (2012) investigated the vibration of a suspension bridge subjected to the train and seismic loads and studied the influence of bridge span, earthquake arrival time, site condition, and various other factors on the dynamic response of train-bridge coupling system.

Nishimura et al. (2010a, b) performed theoretical analysis and experimental studies on the derailment mechanism and running safety of HSR vehicles subjected to earthquake action and track excitations. Chen et al. (2014a, b) studied the seismic response of high-speed railway bridge subjected to near-fault forward directivity ground motions using a vehicle-track-bridge element, finding that the displacements at girder and pier-top as well as the bending moment at pier bottom subjected to near-fault earthquakes are larger than those subjected to far-field earthquakes, and the directivity pulse-like ground motion effect and the high-frequency component of vertical acceleration have significant influence on the hysteretic characteristics of piers.

Zhang et al. (2010a, 2011b) studied the random vibration problem of train-bridge coupling system, by combining the pseudo-excitation method and the precise integration method. The proposed pseudo-excitation method can be used to solve the non-stationary random vibrations of train-bridge system subjected to multi-support excitations, and the research results show that the wave traveling effect has significant influence on the random response of train-bridge system due to earthquake while the train speed has little influence. Zhu et al. (2014) proposed an FEM analytical framework for dynamic analysis of train-bridge coupling system subjected to non-uniform seismic excitations, and studied the influence of earthquake motion intensity, seismic wave traveling velocity, train speed, and various other factors on the random response of train-bridge system.

To study the influence of earthquakes on the running safety of high-speed train on bridge, Xia et al. (2006a, b) and Han (2005) established a dynamic model of coupled train-bridge system subjected to earthquakes, in which the non-uniform seismic waves were input from different foundations. The motion equations of the train subsystem and the bridge subsystem under earthquakes were connected by the nonlinear wheel-track interaction relation. With a high-speed train passing through a (48 + 5×80 + 48)m continuous PC bridge under earthquakes as a case study, the influences of train speed and seismic wave traveling velocity on the dynamic response of the train-bridge system were studied, based on which the critical train speed threshold curves were proposed for running safety of the train on the bridge under earthquakes with various intensities.

Zhang et al. (2010b, 2011a) established the train-bridge coupling dynamic analysis model subjected to multi-point input seismic ground motions using the large mass method, in which the train subsystem was modeled by the rigid-body dynamics method, the bridge subsystem by the FEM discretization, and the wheel-rail interaction forces were defined, respectively, according to the wheel-rail correspondence assumption in vertical direction and the simplified Kalker creep theory in lateral. With the artificial ground motion time histories and track irregularities as excitations, the whole processes of an ICE3 high-speed train passing through a (120 + 5×168 + 120)m cable-stayed bridge were simulated, to study the dynamic responses of the train-bridge system under various train speeds and earthquake intensities.

Du (2011), Du et al. (2011, 2012) and Du and Xia (2012) proposed a FEM analysis framework for dynamic responses of train-bridge coupling system under non-uniform seismic excitations, where the wheel-rail interaction and separation conditions were considered, and two input modes of ground motion, the displacement input and the acceleration input, were adopted. In a case study, the whole process of a high-speed train passing through a trussed-arch bridge during earthquakes was simulated and analyzed. The results showed that compared with only considering the wave traveling effect, when the full seismic spatial variability, which includes wave traveling effect, incoherence effect and local site effect, is considered, the peak magnitude and appearing time of the bridge displacement as well as the car-body acceleration changed obviously, which should not be neglected in seismic analysis of train-bridge system.

Ling et al. (2013) established a vehicle-track coupling dynamic model with an earthquake excitation, by simplifying the seismic wave as periodic lateral sinusoidal waves and applying the seismic displacement and velocity time histories to the bottom of track slab, and the acceleration time histories to the rail. Based on the model, the effect of seismic wave spectral characteristics is studied, in view of frequency and amplitude, on the derailment performance of a high-speed train. Lu and Qiu (2012) established the container vehicle-truss bridge coupling model under earthquakes using a free-interface component mode-synthesis method and found that the maximum lateral response of the vehicle-bridge system was amplified greatly by the earthquake action while the vertical vibration of the system was mainly caused by the moving vehicle load.

Lei et al. (2014) and Lei and Li (2015) established a coupling vibration model of train-track-bridge system under seismic action, in which the ballasted track was simulated by three-layer beams with elastic point supports, and the seismic action was input via the large mass method. The results showed the weak coupling between the in-plane and out-plane responses of a high-pier rigid-frame bridge. Afterward, they studied the influence of pseudo-static components of bridge seismic response on the running safety of high-speed train and found that compared with longitudinal and vertical pseudo-static components, the lateral one significantly enlarged the lateral displacements of bridge and track, as well as made increased the derailment factor and offload factors of train.

Taking the Shinkansen E300 as the train model and the multi-span elevated simply-supported PC elevated bridge as the bridge model, Tan and Zhu (2009) analyzed the vibration characteristics of high-speed train-bridge interaction system under earthquakes. Han (2015) proposed the lateral displacement and acceleration limits by statistical analysis for the continuous bridge commonly used in urban rail transit. Chen (2011) proposed a unified vehicle model for both road car and railway train, based on which he analyzed the coupling vibration of road car, light-rail train, and long-span cable-stayed bridge during earthquakes, and further studied the vibration control effect of several damping devices on a long-span cable-stayed bridge.

Taking CRTS II ballastless slab track in HSR as engineering background, Chen (2012) proposed a dynamic analysis method for the high-speed train-track-bridge

system under earthquake action, and analyzed the running safety limit values according to different dynamic design parameters of bridge.

The soil-structure interaction has influence on the dynamic response of train-bridge system subjected to earthquake action, but the related analysis is still in the exploration stage. Li et al. (2005a, b) established a three-dimensional train-bridge coupling model considering the soil-structure interaction, in which the pile foundation was modeled by an elastically supported beam, and the soil around piles were simulated by discrete springs and dashpots. Li et al. (2011) studied the influence of soil-structure interaction on the train-bridge system vibration, using a bridge model with pile foundation, in which each pile was modeled by an elastic foundation beam, and the pile-soil interaction was realized by elastic supports. Chen et al. (2012) established a train-bridge interaction model considering soil-structure interaction, based on the modified Penzien model with simplified pile-bottom boundary.

Bian (2006) proposed a quasi-analytical method to analyze the dynamic response of viaducts induced by high-speed train, where the train-bridge-foundation interaction system was divided into two parts by the substructure method. One was the spatial FE model of viaduct under running train, and the other was the interaction model between pile foundation and surrounding soil based on Fourier series expansion. The two parts were linked by the common nodes on pile cap, and the whole system was solved in the frequency domain. Gao et al. (2014) established an analysis model of the whole train-bridge-foundation interaction system, using the viscous-spring superposition artificial boundaries, calculated the dynamic response of the system, and studied the effect of soil-structure interaction, train speed, and other factors.

1.4.4 Study on Dynamic Responses of Train-Bridge System Subjected to Collision Load

The collision loads causing bridge vibration are mainly produced by the collision on the pier or girder by vessels, vehicles, or floating objects, which are calculated by empirical formulas in the current specifications. However, due to the type diversity and the dimension discreteness of different colliding objects, and the distinction of various pier types, the calculated results may quite differ from the reality. Therefore, the theoretical analysis and the numerical calculation on the collision mechanics are of great importance for determining the design collision forces and improving the bridge dynamic performance.

In the aspect of vessel collision with bridges, the systemic research started from the early 1980s, when a special working group organized by PIANC (the Permanent International Association of Navigation Congresses) carried out investigation on the accidents of vessel collision with bridges. In 1995, an international organization was established by 9 countries including Belgium, France, and Germany, to work

on the research of vessel-bridge collision specially. From then on, a lot of results have been achieved by researchers in this field.

The first research paper about vessel-bridge collision problem was published by Minorsky (1953) in 1953. In this paper, based on the statistical analysis of the data from 26 accidents and experiments about vessel collisions on bridges, Minorsky proposed an empirical formula to describe the linear relationship between the kinetic energy loss and the damaged vessel bodies. Woisin (1976, 1979) conducted a series of model tests and theoretical analysis, modified Minorsky's theory and applied it to the analysis of vessel collision with bridge piers. Based on these work, Woisin proposed the calculation formulas for vessel collision forces, which has been adopted by AASHTO (1991).

Derucher (1982, 1984) developed a procedure to determine the amount of pier movement (failure of the piles) that might occur when collided by vessels, assuming no spring back displacement of the vessel, then described the relationship between the impact force and the deformation of anti-collision elements by elastic constants, and investigated the vibration characteristics of vessel-bridge system during the collision. Pedersen and Zhang (1998) presented the closed-form analytical expressions for the energy released for crushing and the impact impulse during ship collisions. By consideration of friction forces at the collision contact points, the established mathematical model was applied to the analysis of different situations of collisions, such as ship-ship collision, ship collision with rigid wall, and ship collision with flexible structure.

The full-scale experiments of vessel–vessel collision have been conducted in several countries since 1960s, and obtained some valuable data. However, very few full-scale experiments have been made for vessel-bridge collision, because this type of destructive experiment is very expensive and difficult to conduct, and the tested results are limited owing to the nonlinear characteristics of collision and the uncertainty of collision conditions. Consolazio et al. (2003, 2006) used the nonlinear FE software ADINA to simulate various vessel-bridge collision situations and carried out field tests, to investigate the soil stress, vessel deformation, impact load and the accelerations/displacements of the pier under vessel collision.

In 1970s, researchers started to develop simplified analytical methods to study the collision problem, based on the upper limit theory in plastic mechanics and some important assumptions. The simplified analytical methods could solve the problems easily and fast, and produce good calculation results, thus they have been widely applied to vessel-bridge collision analysis. Ueda and Rashed (1984), Ueda et al. (1995) proposed the concept of ISUM (Ideal Structural Unit Method), by dividing the structure into "structure elements" as big as possible, with their geometric and material nonlinearity determined by the refined "analytical-numerical" method, to greatly reduce the element quantity and the overall DOFs of the calculation model. This method has been widely used in nonlinear analysis of large-scale structures. Based on ISUM, Paik and Pedersen (1996) and Paik et al. (2001) proposed a collision analysis method for the structural damage due to ship collisions, which could reduce a mass of time for modeling and calculation.

In recent years, the Chinese researchers also carried out studies on vessel-bridge collision. Considering the accident risk of vessel collision on bridge, Xiang (2002) demonstrated the necessity and reasonability to directly adopt the concept and method of probabilistic design, while in the probability-based design and the related studies, the target failure probability suitable for the anti-collision design and the synthetic load induced by vessel collision should be established. Wang and Chen (2007) and Wang (2011) investigated the dynamic responses of bridge with different pile foundations under vessel collision, analyzed and compared the static/dynamic responses of the key parts of bridge, and discussed how to determine the rational value for the equivalent static impact force of vessel collision. Chen (1995) carried out the 1:20 model test of vessel-bridge collision, for the pier anti-collision device of the Houzhu Bridge, obtained important data such as the impact force, the acceleration and displacement of the anti-collision device model and the dynamic strain at the collided region, and found out the failure modes of the anti-collision device under various collision conditions. Liu and Gu (2002, 2003) summarized several typical calculation methods for vessel-bridge collision and analyzed the characteristics of these methods, achieving useful results.

In terms of vehicle collision on bridges, the collision mechanism is very complex, involving problems of geometric nonlinearity, material nonlinearity, contact nonlinearity and various dynamic effects, which makes the theoretical analysis difficult, thus experimental study becomes a reliable method. The Arup Company in UK used to conduct a full-scale test of vehicle collision with bridge superstructure and obtained important data about the collision mechanism and impact forces. Buth et al. (2009, 2010) conducted two full-scale crush tests involving an 80,000-lb (36.32t) van-type tractor-trailer impacting a simulated bridge pier, supported by the Texas Department of Transportation Project, and obtained the force-versus-time data from the load cells installed on the pier, indicating an equivalent static design force of 400 kips (1781kN), when the force data were processed with a 0.05 s moving average filtering.

With rapid progress of the computer simulation based FEA technique, the numerical simulation method for vehicle-bridge collision was developed. Severino and El-Tawil (2003) and El-Tawil et al. (2005) adopted the inelastic transient FE simulation to study the collision effect between vehicle and pier. Sharma et al. (2012) established the analytical models to evaluate the anti-collision capacity of reinforced concrete columns against impact of vehicles with different weights. They improved the static and semi-static analysis methods and proposed a new dynamic evaluation method that could more accurately reflect the vehicle-bridge collision characteristics.

Yu and Zha (2011) adopted the FEM to simulate and verify the experimental results of a lateral drop-hammer impact on solid/hollow concrete-filled steel tube columns. Ma et al. (2009) simulated the impact processes of heavy loaded container truck and overheight vehicle with different velocities on the bridge girder, studied the deformation and stress state of the girder under collision, and analyzed the influence of vehicle load, velocity and car-body stiffness on the bridge dynamic responses. Lu et al. (2009, 2011) and Xu et al. (2012) studied the impact forces and

failure mechanism of the over height truck collision on bridge superstructure through nonlinear FE simulation and a scaled model test, analyzed the influence factors on impact forces, and proposed the simplified calculation model and the impact forces formula for vehicle-bridge collision.

Regarding floating ice-floe and drift collisions on bridges, since drift usually has smaller volume and mass than ice-floe, and thus produces smaller impact, the research was mainly focused on the ice-floe collision. Christensen et al. (1995) carried out a series of model tests to study the design load of ice-floe collision and the impact force of ice-floe on the Great Belt West Bridge, and the influence of flow velocity, impact angle, type and stiffness of collided structure on the impact force and structural response. Brown (2000, 2007) measured the ice forces and the structural response to these forces on two instrumented concrete piers of the Confederation Bridge, and analyzed the time series data for the derivation of ice loads, with an accompanying observation of the interaction, using the available video recordings, survey of ice features, and information from the sensors installed on and adjacent to the bridge. The resulting load traces were analyzed in detail to provide the best estimates of the loads.

In China, research on ice-structure interaction started in 1980s. Since then, researchers have carried out field tests to study the dynamic characteristics and compressive strength of the ice, the interaction between ice and bridges, and the impact of ice-floe on piers. Han (2000) analyzed the mechanical properties of ice-floe on bridge structure in the Songhua River and their influence factors according to experimental results, calculated the displacement response of the Songhua River Bridge under ice-floe collision by FEM, and proposed the formula to calculate the ice stress applicable to the northeast region of China. Yu et al. (2007) and Yuan (2010) carried out uniaxial compression and bending strength tests under various ice temperatures and strain rates for ices from five typical river sections in Heilongjiang Province, and established the mathematical model for the correlations between ice temperature, strain rates, strength and elastic modulus.

Wang (2007) investigated the lateral displacement of pier-top under ice-floe impact in the Huma River by a field test. Qi (2009) established the FE model for ice-bridge collision, where the hydrodynamic pressure was considered, and the ice impact forces obtained from field measurement were taken as the known input, and analyzed the dynamic responses of the bridge under ice impact forces by the refined time-domain integration method. Yue et al. (2009) conducted full-scale ice-floe collision tests on a compliant monopod platform in Bohai Bay, China, to investigate the dynamic ice forces and structural vibrations caused by crushing failure of ice sheet.

When a collision load acts on a bridge pier, it may cause dislocation of bearings and girders, uneven deformation or fracture of expansion joints, and even collapse of girders, resulting in serious accidents. For railway bridges, however, even if there is no girder collapse, the vibrations induced by collision may deform the track and make it unstable, which may further threaten the running safety of the train on the bridge. When the collision is intense and the train speed is high, the running safety

of the train may be seriously affected, and in the most serious case, the train may even derail from the track.

To this end, Xia (2012), Xia et al. (2012a, 2013a, 2014a, 2016) and Cui (2015) established the train-bridge coupling dynamic model under impact load. By taking several HSR bridges and various high-speed trains as the illustrative examples, and considering the impact forces due to ice-floe, vessel and vehicle collisions, they calculated the vibration responses of bridge structure and the running safety indices of train vehicles, finding that strong impact forces of collision could cause intense bridge vibration at pier-top and mid-span, which might threaten the running safety of high-speed trains. Based on the parameter analysis, they proposed the assessment method for the running safety of high-speed train on the bridge subjected to collision load, using the threshold curves for train speed versus collision intensity. Furthermore, Xia CY et al. studied the dynamic responses of train-bridge coupling system and running safety of train when the piers getting into plastic state under intense collision, with the vessels simulated by the elastic–plastic model of plastic hardening character and the pier modeled by common concrete stress–strain relationship, and achieved preliminary results.

With the development of general structural analysis software, the FE numerical simulation has become an effective and rational method to study the problem of vessel, vehicle, and drift collisions with bridge pier and superstructure. Based on the structural FEM, continuum mechanics, linear/nonlinear algebra and ordinary differential algorithm, instantaneous integration, software design, and other techniques, the calculations for both the external and internal mechanisms of collision can be realized in the same analysis progress, providing more accurate results. However, because the research on collision forces started later, there still remains a mass of unknown problems. Therefore, the study on the bridge vibration subjected to collision loads and the running safety of high-speed train passing through the bridge is still an urgent issue with great importance.

1.5 Research Contents of Train-Bridge Coupling Vibrations

With the raise of train speed and the increase in train load, the dynamic problem of bridge structure becomes more prominent. The issues such as structural safety, dynamic bearing capacity and operational reliability caused by running train-induced bridge vibration have attracted wide attention. The dynamic analysis of train-bridge system can be applied directly to evaluating the bridge dynamic performance, determining the dynamic reinforcement method and estimating the reinforcement effect. In order to ensure the bridge dynamic performance and the train running safety, it is important to study the train-bridge dynamic interaction, which is the engineering demand of railway bridge design and also the requirement of national economy development and people's life.

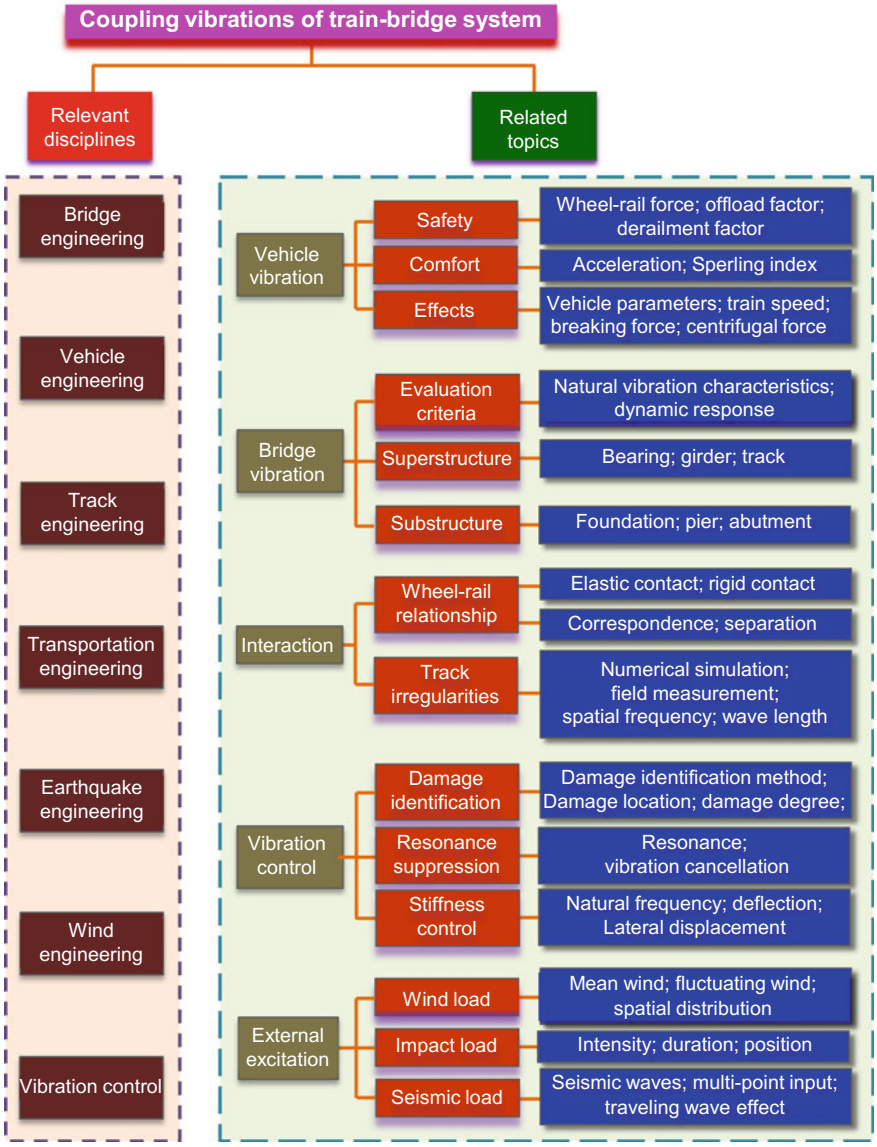

Fig. 1.30 Research system of train-bridge coupling vibration

The coupling vibration of train-bridge system is a complex research system involving bridge engineering, traffic engineering, vehicle dynamics, track mechanics, wind engineering, earthquake engineering, impact engineering, vibration control and other engineering science fields, as shown in Fig. 1.30.

The engineering problems involved in the analysis of train-bridge coupling vibration are as follows:

(1) Dynamic analysis of bridge structure and vehicle under running train load.

The dynamic responses of various types of bridge structures under running trains can be calculated with the dynamic interaction analysis model of train-bridge system, including the dynamic deflections, vibration amplitudes, accelerations and frequencies and dynamic coefficients of bridge spans, the dynamic strains of members, the dynamic reaction forces of bearings, the vibration amplitudes and accelerations of piers, the wheel-rail forces, and the accelerations of car-body. The analyzed results can be applied directly to bridge design, especially to the design of new types of bridges, and for example, have been successfully applied to the HSR bridge design in China.

(2) Dynamic analysis of train-bridge system under wind action.

For bridges with long-span or in wind-prone regions, the wind-induced vibration of train-bridge coupling system and the running safety of trains are an important problem. With wind as external excitation, the dynamic responses of the bridge and the running train can be calculated, the results can be applied to safety evaluation of bridge structure and running train, and, moreover, the thresholds for critical train speeds with respect to different wind velocities can be proposed to ensure the running safety of trains.

(3) Dynamic analysis of train-bridge system under earthquake action.

With the increase in train speed, earthquake has a growing influence on the safety of train running on the bridges in seismic prone region, especially for the long-span bridges and HSR bridges. With the input of seismic ground motion, the dynamic responses of the bridge and the running train can be calculated, the analyzed results can be applied to safety evaluation of bridge structure and running train, and the critical train speeds can be proposed to ensure the running safety of train on bridge subjected to earthquakes with various intensities.

(4) Dynamic analysis of train-bridge system subjected to collision.

For bridges crossing rivers or other traffic lines, the strong vibration of train-bridge system could be caused by collisions of vessel, vehicle, and drift, threatening the running safety of high-speed train, which has been paid important attention. With the collision force acting on the bridge pier or superstructure, the dynamic responses of the bridge and the running train can be calculated, and the analyzed results can be applied to evaluation of the running safety of trains.

(5) Dynamic analysis of train-bridge system with bridge deterioration.

With the increase in service years, damage may occur in the bridge superstructure and piers, and the foundation scouring may get deepened. Such deterioration of bridge service performance may lead to the decrease of bridge stiffness and

the change of bridge dynamic behaviors, producing a great influence on the running safety and stability of train. Evaluation of the residual service performance of damaged bridge with the dynamics-based method is one of key issues in railway bridge engineering.

(6) Dynamic analysis of train-bridge system with bridge/track quasi-static deformation.

The quasi-static deformation of bridge/track includes the creep camber of PC beam, the upwarp or side bending of beam and the center upwarp or corner warping of ballastless track slab induced by temperature gradient, and the uneven settlement of piers, which leads to the deformation of track structures, influencing the vibration behaviors of bridge and train. The quasi-static deformation of bridge is unavoidable, and the whole influence on the dynamic response of train-bridge system should be estimated in design and operation.

(7) Evaluation criteria for dynamic responses of train-bridge system.

To evaluate the running safety and stability of train and the service performance of bridge, the reasonable criteria for dynamic responses of train and bridge are

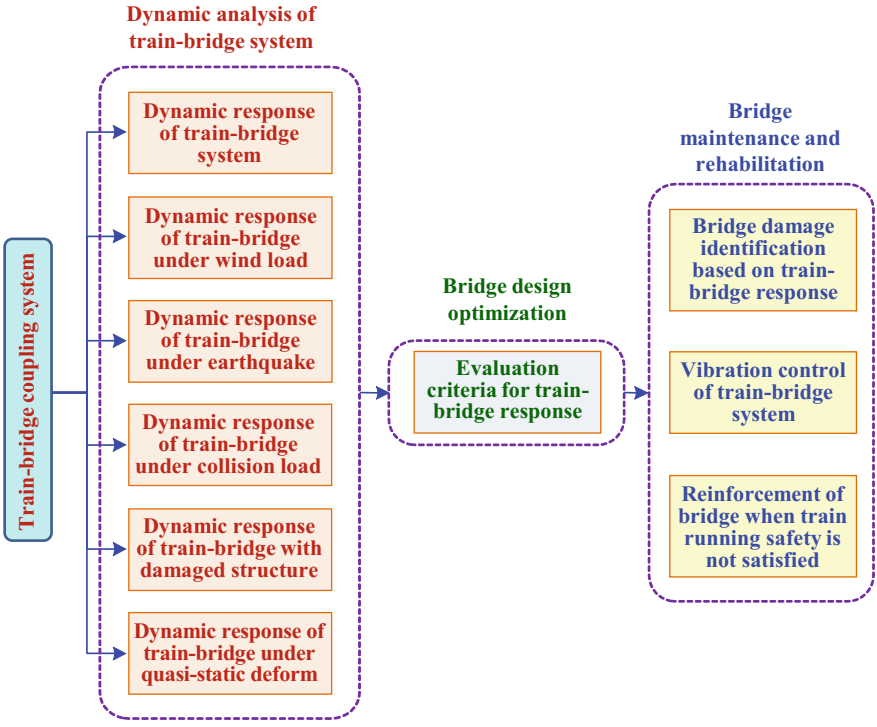

Fig. 1.31 Problems involving the dynamic analysis of train-bridge system

Table 1.8 Contents of dynamic analysis of train-bridge system

Research object	Research content	Research significance
Excitation source	(1) Moving train loads (2) Track irregularities (3) Earthquake action (4) Wind loads (5) Collision loads of vessel, vehicle and ice-floe (6) Foundation scouring (7) Creep camber of PC girder (8) Temperature deformation of girder and pier (9) Numerical simulation of various loads	(1) Dynamic design method of bridges (2) Method of reducing dynamic load effect
Bridge structure	(1) Natural vibration characteristics of bridge structure (natural frequency, mode shape and damping) (2) Dynamic coefficient of bridge under specific train load (3) Dynamic responses of bridge under moving load (dynamic deflection and amplitude of beam, dynamic strain of member, dynamic support reaction force, dynamic displacement and amplitude of pier) (4) Distribution of bridge responses and their correlations with train vehicle responses	(1) Dynamic design of bridge (2) Dynamic design of on-bridge track (3) Wind-resistant design and seismic design of bridge (4) Vibration control of bridge (5) Evaluation of dynamic performance of bridge (6) Bridge damage diagnosis (7) Dynamic reinforcement design and reinforcement effect evaluation (8) Fatigue design of structure member
Train vehicles running on the bridge	(1) Acceleration of car-body and bogie (2) Offload factor of vehicle (3) Derailment factor of vehicle (4) Overturn factor of vehicle (5) Wheel-rail interaction force (6) Distribution of vehicle safety indices with respect to train type, train composition, and running speed	(1) Control criteria for running train safety (2) Control criteria for bridge vibration (3) Train speed control threshold subjected to earthquake action (4) Train speed control threshold during strong wind (5) Train speed control threshold under collision condition
Passenger comfort	(1) Vehicle running stability (2) Vibration frequency of car-body (3) Acceleration of car-body (4) Distribution of vehicle stability indices with respect to train type, train composition, and running speed	(1) Allowable criteria for vehicle running stability indices (2) Allowable criteria for car-body acceleration (3) Allowable criteria for riding comfort of passenger

necessary. According to the evaluation criteria, the thresholds for running safety of train under wind loads, earthquake actions and collision impacts can be proposed.

(8) Vibration control of bridge structure subjected to various loads.

The vibration of bridge structure subjected to various loads can be reduced with the structural vibration control devices. The dynamic analysis model of train-bridge system can be applied to determining the control parameters and to evaluate the control effect.

(9) Bridge damage diagnosis based on dynamic analysis of train-bridge system.

The bridge damage diagnosis method based on the dynamic analysis of train-bridge system is developed, which applies to studying the inherent association mechanism between the dynamic responses and the damage of bridge, and to investigating the bridge damage localization and quantitative evaluation. The bridge modal parameters identification method and the associated signal analysis technique by directly using the bridge response and indirectly using the train response are also the research topics.

(10) Evaluation of bridge dynamic performance and reinforcement method.

The dynamic analysis of train-bridge system is also applicable to evaluation of bridge dynamic performance, selection of reinforcement method and assessment of reinforcement effect.

The above engineering problems can be classified into two categories: one is dynamic analysis of train-bridge system, belonging to dynamic analysis of bridge, the other is bridge damage diagnosis and reinforcement based on the system, belonging to bridge maintenance, as summarized in Fig. 1.31. This book focuses on the first eight problems related to the dynamic analysis of train-bridge system.

The main contents of dynamic analysis of train-bridge system are summarized in Table 1.8.

1.6 Dynamic Analysis Methods of Train-Bridge System

In the early 1980s, the Chinese scholars began to engage in the research of train-bridge coupling vibration in theory and application, and since then have established and developed various analysis models using different methods. These models have been validated by a large amount of measured data, showing good applicability and rationality, and have been applied to many engineering practices.

1.6.1 Dynamic Analysis Methods of Train-Bridge Coupling System

The research on train-bridge coupling vibrations mainly includes three types of methods, namely the analytical method, the numerical simulation method, and the experimental method.

(1) The analytical method

The analytical method describes each part of the train-bridge system by using the theoretical model, which is rigorous because it mainly relies on the theoretical derivation in mathematics and mechanics. The analytical method could not only help the researchers better understand the problem in theory, but also provide strong reference for verification of the numerical simulation and the empirical prediction results. However, for the complicated vibration analysis of train-bridge system, the theoretical modeling requires necessary simplifications on the actual situation, and some restrictions on the geometry and material properties of the structure, or the ideal conditions directly adopted on the system. Therefore, the completely accurate analytical results do not exist up to now. Even in some ideal states, the closed-form solutions for the complex theoretical formulas are difficult to obtain, unless adopting numerical integration or other methods.

(2) The numerical simulation method

For the problem of train-bridge coupling vibration, most early researches adopted the analytical method and the experimental method. With the advent of computers with high performances, various numerical methods become a highly effective tool for simulating train-bridge coupling vibration, playing an important role in this field, which are used by more and more researchers. The commonly used numerical simulation methods include the FEM (finite element method), the BEM (boundary element method) and the F-B hybrid method. Due to the limitation of calculating means and parameters conditions, the numerical simulation method has also to use some approximation assumptions to establish the simple and easy-to-calculate models. The top issue for the simplified models is to validate the rationality of them, which can only be done by experiments. Due to the complexity of the actual bridge and vehicle and the time-varying characteristics of moving load, the numerical simulation method is the mostly adopted in dynamic analysis of train-bridge coupling system.

(3) The experimental method

Experiment is one of the major means for the research of train-bridge coupling vibration. Before the FEM appeared, the field experiment had been the main method of the study, namely by measuring the responses of train and bridge to obtain the empirical formula or theory and using them to guide the bridge design. After the FEM appeared, field experiment still works, in addition to directly measure and evaluate the dynamic performances of train and bridge, which is used

to verify the theory, while using theory to guide the experiment can save a lot of work. In China, researchers conducted dynamic experiments under running trains to verify the established train-bridge coupling vibration analysis model, and according to the comparison between the simulated results and those from the experiment, to analyze and determine the main factors influencing the calculation error and thus to update the models.

In terms of test method, since the small-scale model test is difficult to simulate complicated wheel-rail interaction relations, prototype test and field experiment are often adopted to measure the vibration of the train-bridge system, and the measured results can objectively and comprehensively reflect the actual working performance of the bridge under the moving train loads. However, if the research only remains in the experimental stage but do not try to reveal the inherent law further, a large number of repeated experiments have to be conducted in order to determine the new dynamic parameters with the change of the structural type and span of bridge and the performance of vehicle, which are not only costly but a waste of time. Therefore, the pure test method is often constrained by many conditions.

On the other hand, the pure use of theoretical analysis to solve this problem is also very difficult, because the bridge vibration under train loads is a very complicated subject. In order to keep the theoretical results in accordance with the reality, many factors should be taken into account, including the masses of the car-body and bogie, the effects of dashpot and spring, the running speed of train, the masses, stiffness and damping of beam and pier, the structural type and dynamic property of track, and the dynamic interactions of wheel-rail and rail-beam, etc. In addition, the analysis is also affected by the unevenness of wheel, the geometric and dynamic irregularities of track, the hunting movement of wheel-set, and many other random factors. All these factors make the analysis model very complicated. Therefore, although mature algorithm has been available for dynamic analysis of the beam itself, various approximated methods have to be adopted to establish the train-bridge system analysis model, due to the limitation of calculating method. For example, the train axle loads are simplified into moving constant forces or deterministic harmonic excitations, the dynamic effects of the train are modeled by the steadily moving mass model, the isolated impact force model or moving springs-dashpot-mass model, etc. The first issue for these simplified models is to validate the rationality of their modeling, while this can only be realized through experiments.

Currently, the coupling vibration of train-bridge system is usually studied by combined means of theoretical analysis, numerical simulation, and experimental investigation, namely using experimental results to verify the theoretical method and numerical model, and then adopting the verified theoretical method and numerical model to analyze the train-bridge coupling vibration, to study the effect of various parameters on the vibration, and to analyze the safety of trains and bridges under various operating conditions.

1.6.2 Motion Equation and Solution of Train-Bridge System

Based on the structural dynamics theory, the train subsystem and the bridge subsystem are, respectively, regarded as an MDOF system, and the motion equations of the train-bridge system can expressed as

$$\begin{cases} \mathbf{M}_{\mathrm{v}}\ddot{\mathbf{X}}_{\mathrm{v}} + \mathbf{C}_{\mathrm{v}}\dot{\mathbf{X}}_{\mathrm{v}} + \mathbf{K}_{\mathrm{v}}\mathbf{X}_{\mathrm{v}} = \mathbf{F}_{\mathrm{v}} \\ \mathbf{M}_{\mathrm{b}}\ddot{\mathbf{X}}_{\mathrm{b}} + \mathbf{C}_{\mathrm{b}}\dot{\mathbf{X}}_{\mathrm{b}} + \mathbf{K}_{\mathrm{b}}\mathbf{X}_{\mathrm{b}} = \mathbf{F}_{\mathrm{b}} \end{cases} \tag{1.1}$$

where: $\mathbf{M}$, $\mathbf{C}$ and $\mathbf{K}$ are the global mass, damping and stiffness matrices, $\mathbf{X}$ and $\mathbf{F}$ are the displacement and force vectors, respectively, with subscripts v denoting the train subsystem and b the bridge subsystem, and each head-dot over $\mathbf{X}$ representing a derivative with respect to time.

The excitations on the train-bridge coupling system can be divided into several categories, as shown in Fig. 1.32, including track irregularity, beam creep camber, temperature and other structural deformation, wind load, collision force, structure damage, foundation scouring and settlement, and earthquake, etc. The mathematical expressions of these excitations in Eq. (1.1) are illustrated as follows.

(1) Track irregularities

Track irregularity is one of the main excitation sources for the train-bridge coupling system. The interaction force between the train subsystem and the bridge subsystem is not only the function of track irregularity, but also the function of the motion state ($\mathbf{X}_{\mathrm{v}}$ and $\mathbf{X}_{\mathrm{b}}$) of the train and the bridge, due to the coupling relationship between them. Assuming the track irregularities as $\mathbf{i}$, the motion equation of the train-bridge coupling system can be expressed as

$$\begin{cases} \mathbf{F}_{\mathrm{v}} = \mathbf{F}_{\mathrm{vi}} = \mathbf{F}_{\mathrm{vi}}\left(\mathbf{X}_{\mathrm{v}}, \dot{\mathbf{X}}_{\mathrm{v}}, \ddot{\mathbf{X}}_{\mathrm{v}}, \mathbf{X}_{\mathrm{b}}, \dot{\mathbf{X}}_{\mathrm{b}}, \ddot{\mathbf{X}}_{\mathrm{b}}, \mathbf{i}\right) \\ \mathbf{F}_{\mathrm{b}} = \mathbf{F}_{\mathrm{bi}} = \mathbf{F}_{\mathrm{bi}}\left(\mathbf{X}_{\mathrm{v}}, \dot{\mathbf{X}}_{\mathrm{v}}, \ddot{\mathbf{X}}_{\mathrm{v}}, \mathbf{X}_{\mathrm{b}}, \dot{\mathbf{X}}_{\mathrm{b}}, \ddot{\mathbf{X}}_{\mathrm{b}}, \mathbf{i}\right) \end{cases} \tag{1.2}$$

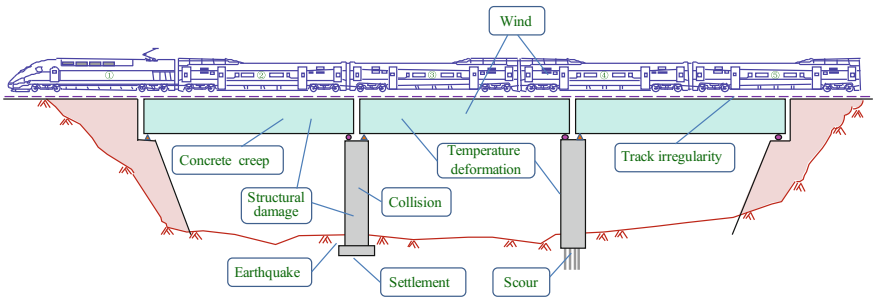

Fig. 1.32 Problems related to train-bridge coupling vibration

In the mathematical form, the train subsystem and the bridge subsystem in Eq. (1.1) are independent of each other, while in the simultaneous Eq. (1.2), the two subsystems are coupled through $\mathbf{F}_{vi}$ and $\mathbf{F}_{bi}$, thus establishing the mathematical expressions of $\mathbf{F}_{vi}$ and $\mathbf{F}_{bi}$ is the key point for the dynamic analysis of train-bridge coupling system. All these mathematical expressions depend on the wheel-rail relationship assumption adopted and the track irregularity value $\mathbf{i}$.

(2) Quasi-static bridge deformations

The quasi-static deformations of bridge are mainly induced by concrete creep of beams, temperature effect and foundation settlement, which may cause the geometry change in tracks on the bridge. The quasi-static deformations can be regarded as an additional track irregularity excitation on the train-bridge system. Assuming the additional track irregularity as $\mathbf{i}_a$, Eq. (1.2) can be expressed as

$$\begin{cases} \mathbf{F}_v = \mathbf{F}_{vi} = \mathbf{F}_{vi}\left(\mathbf{X}_v, \dot{\mathbf{X}}_v, \ddot{\mathbf{X}}_v, \mathbf{X}_b, \dot{\mathbf{X}}_b, \ddot{\mathbf{X}}_b, \mathbf{i}+\mathbf{i}_a\right) \\ \mathbf{F}_b = \mathbf{F}_{bi} = \mathbf{F}_{bi}\left(\mathbf{X}_v, \dot{\mathbf{X}}_v, \ddot{\mathbf{X}}_v, \mathbf{X}_b, \dot{\mathbf{X}}_b, \ddot{\mathbf{X}}_b, \mathbf{i}+\mathbf{i}_a\right) \end{cases} \tag{1.3}$$

It is noted that whether or not including the influence of this additional track irregularity, the expressions of the wheel-rail interaction forces in Eqs. (1.2) and (1.3) are identical, denoted by $\mathbf{F}_{vi}(\bullet)$ and $\mathbf{F}_{bi}(\bullet)$.

(3) Wind and collision loads

In the dynamic analysis of train-bridge system, when neglecting the self-excited force of the wind on the train and the bridge, or neglecting the dynamic interaction between the impact object and the bridge during collision, the wind load or the collision load can be regarded as the external force on the train and the bridge. Once the calculation conditions are given, the time histories of these external forces are known, which change only with the acting location and duration rather than the movement state of train and bridge. Assuming the external force vectors of train and bridge subsystem as $\mathbf{F}_{ve}(t)$ and $\mathbf{F}_{be}(t)$, respectively, Eq. (1.2) can be rewritten as

$$\begin{cases} \mathbf{F}_v = \mathbf{F}_{vi} = \mathbf{F}_{vi}\left(\mathbf{X}_v, \dot{\mathbf{X}}_v, \ddot{\mathbf{X}}_v, \mathbf{X}_b, \dot{\mathbf{X}}_b, \ddot{\mathbf{X}}_b, \mathbf{i}\right) + \mathbf{F}_{ve}(t) \\ \mathbf{F}_b = \mathbf{F}_{bi} = \mathbf{F}_{bi}\left(\mathbf{X}_v, \dot{\mathbf{X}}_v, \ddot{\mathbf{X}}_v, \mathbf{X}_b, \dot{\mathbf{X}}_b, \ddot{\mathbf{X}}_b, \mathbf{i}\right) + \mathbf{F}_{be}(t) \end{cases} \tag{1.4}$$

If the self-excited forces in the wind load or the interaction forces in the collision process are taken into account, these loads are associated with the movement states of the train and the bridge, which will be separately introduced in the related chapters later.

(4) Structural damage and foundation scouring

In mathematics, structural damage and foundation scouring can be regarded as the global stiffness decrease of the bridge subsystems. Structural damage causes injuries in cross section or decrease of the material elastic modulus, while foundation scouring leads to decline of constraint stiffness of pier bottom or side piles.

Considering structural damage and foundation scouring, the motion equations of train-bridge system can be expressed as

$$\begin{cases} \mathbf{M}_{\mathrm{v}}\ddot{\mathbf{X}}_{\mathrm{v}} + \mathbf{C}_{\mathrm{v}}\dot{\mathbf{X}}_{\mathrm{v}} + \mathbf{K}_{\mathrm{v}}\mathbf{X}_{\mathrm{v}} = \mathbf{F}_{\mathrm{v}} \\ \mathbf{M}_{\mathrm{b}}\ddot{\mathbf{X}}_{\mathrm{b}} + \mathbf{C}_{\mathrm{b}}\dot{\mathbf{X}}_{\mathrm{b}} + (\mathbf{K}_{\mathrm{b}} - \mathbf{K}_{\mathrm{bd}})\mathbf{X}_{\mathrm{b}} = \mathbf{F}_{\mathrm{b}} \end{cases} \tag{1.5}$$

where $\mathbf{K}_{\mathrm{bd}}$ is the reduced amount of the global stiffness after the bridge degradation.

(5) Earthquakes

For the train-bridge coupling system, earthquakes can be regarded as a set of known time histories of ground motion at the earthquake input points (the bottom of bridge pier or pile cap, or the foundation) of the bridge subsystem. In general, the seismic responses at different bridge foundations are inconsistent, resulting in the problem of non-uniform seismic excitation. By inputting the given seismic histories into Eq. (1.1), the dynamic response of train-bridge system under seismic action can be solved, and the motion equations are expressed as

$$\begin{cases} \mathbf{M}_{\mathrm{v}}\ddot{\mathbf{X}}_{\mathrm{v}} + \mathbf{C}_{\mathrm{v}}\dot{\mathbf{X}}_{\mathrm{v}} + \mathbf{K}_{\mathrm{v}}\mathbf{X}_{\mathrm{v}} = \mathbf{F}_{\mathrm{v}} \\ \mathbf{M}_{\mathrm{b}}\ddot{\mathbf{X}}_{\mathrm{b}} + \mathbf{C}_{\mathrm{b}}\dot{\mathbf{X}}_{\mathrm{b}} + \mathbf{K}_{\mathrm{b}}\mathbf{X}_{\mathrm{b}} = \mathbf{F}_{\mathrm{b}} \\ \mathbf{T}_{\mathrm{bs}}\mathbf{X}_{\mathrm{v}} = \mathbf{X}_{\mathrm{s}} \\ \mathbf{T}_{\mathrm{bs}}\dot{\mathbf{X}}_{\mathrm{v}} = \dot{\mathbf{X}}_{\mathrm{s}} \\ \mathbf{T}_{\mathrm{bs}}\ddot{\mathbf{X}}_{\mathrm{v}} = \ddot{\mathbf{X}}_{\mathrm{s}} \end{cases} \tag{1.6}$$

where: $\mathbf{X}_{\mathrm{s}}$, $\dot{\mathbf{X}}_{\mathrm{s}}$ and $\ddot{\mathbf{X}}_{\mathrm{s}}$ are displacement, velocity and acceleration vectors at the earthquake input points; $\mathbf{T}_{\mathrm{bs}}$ is the transform matrix from the displacement vector of the bridge $\mathbf{X}_{\mathrm{b}}$ to the displacement vector at the earthquake input points $\mathbf{X}_{\mathrm{s}}$.

(6) Solution of motion equations

Under the precondition of the simplified vehicle and bridge models, the motion Eq. (1.1) of train-bridge coupling system can be solved by the analytical method, where the bridge is regarded as the system with distributed parameters.

Such methods can be used for vibration analysis of the simply-supported beam under moving force, moving concentrated mass, moving distributed mass, moving wheel-spring-mass unit, variable speed loads, and the train-bridge coupling resonance and vibration cancelation mechanisms, etc. When the mass of the vehicle is far less than that of the bridge, the analytical method has better calculation accuracy, as the error produced by simplification of vehicle subsystem is quite small.

More generally, Eqs. (1.1)–(1.4) of the train-bridge coupling system and their extended forms Eqs. (1.5)–(1.6) are established by MDOF system and solved by numerical integral method. Because the current analysis methods are not limited to solve the linear system, it is not particularly required that the dynamic matrices in the equations be constant. In general, the solution for the motion equations of train-bridge coupling system is not unconditionally converged, which depends on the adopted assumption of wheel-rail interaction relationship.

References

060s, (2016) http://new.060s.com/article_pic/2016/07/26/19018.7.htm, 26 Jun 2016

AASHTO (1991) AASHTO LRFD bridge design specifications [S]. American association of state highway and transportation officials. Washington, DC, USA

An N (2013) Research on damage detection techniques based on coupled vehicle-bridge vibration responses [D]. Beijing Jiaotong University, Beijing (in Chinese)

An N, Xia H, Zhan JW (2010) Identification of beam crack using the dynamic response of a moving spring-mass unit [J]. Interact Multiscale Mech—An Int J 3(4):321–332

Bao HF (2008) Frequency-domain analysis of long-span bridge buffeting under skew winds with effect of static wind displacement [D]. Tongji University, Shanghai (in Chinese)

Bhatti MH (1982) Vertical and lateral dynamic response of railway bridges due to nonlinear vehicles and track irregularities [D]. Illinois Institute of Technology

Bian XC (2006) Analysis of viaduct-ground vibration due to high-speed train moving loads [J]. J Vib Eng 19(4):438–445 (in Chinese)

Bishop RED (1979) Vibration [M], 2nd edn. Cambridge University Press, London

blog.alighting, (2012) http://blog.alighting.cn/1266/archive/2015/5/27/267747.html fig-7 2012-03-15

blog.sina, (2011) http://blog.sina.com.cn/s/blog_66d16c570102drya.html fig-222011-7-25

Brown TG (2000) Ice loads on the piers of confederation bridge, Canada [J]. Struct Eng 78(5):18–23

Brown TG (2007) Analysis of ice event loads derived from structural response [J]. Cold Reg Sci Technol 47(3):224–232

Buth CE (2009) Guidelines for designing bridge piers and abutments for vehicle collisions [R]. Semi annual report. Texas Transportation Institute, TX, USA

Buth CE, Abu-Odeh AY, Brackin MS, Geedipally SR, Lord D, Williams WF (2010) Guidelines for designing bridge piers and abutments for vehicle collisions [R]. Project summary, texas department of transportation project. Texas Transportation Institute

Cai CB (2004) Theory and application of train-track-bridge coupling vibration in high-speed railways [D]. Southwest Jiaotong University, Chengdu (in Chinese)

Cao XQ, Chen X (1986) Analysis for random vibration of truss bridges produced by the hunting action between wheels and track [J]. J Railwa 01:89–97(1). (in Chinese)

Cao XQ (1991) Lateral vibration for steel truss bridge[M]. China Railway Publishing House, Beijing (in Chinese)

Cao XQ, Wu DJ, Luo WW (1999) The report of standard stiffness verification of railway bridges [R]. Shanghai Tiedao University, Shanghai (in Chinese)

Carter FW (1926) On the action of a locomotive driving wheel [C]. Proc. R Soc Lond A: Math Phys Eng Sc. R Soc 112(760):151–157

Chen YJ (1975) The evolution of basic theory of bridge vibration under vehicle load [J]. Bridge Construction 2:18–20 (in Chinese)

Chen ZH (1995) Preliminary research on the impact of ship to the large bridge pier and its parameter test [D]. Nanjing University of Science and Technology, Nanjing (in Chinese)

Chen DH (2011) Research on vibration control of dynamic responses for vehicle-bridge system under earthquakes [D]. Center South University, Changsha (in Chinese)

Chen LK (2012) Seismic responses of high-speed railway train-ballastless track-bridge system and train-running safety during earthquake [D]. Central South University, Changsha (in Chinese)

Chen ZQ, Hua XG (2009) Vibration and Dynamic Design of Footbridge [M]. China Communications Press, Beijing (in Chinese)

Chen LK, Jiang LZ, Tao L, Yu ZW (2012) Seismic response analysis of high-speed vehicle-bridge considering soil-structure interaction [J]. Rock Soil Mech 33(10):316–3170

Chen LK, Jiang LZ, Guo WW et al (2014a) The seismic response of high-speed railway bridges subjected to near-fault forward directivity ground motions using a vehicle-track-bridge element [J]. Shock Vib. Article ID985602

Chen LK, Zhang N, Jiang LZ et al (2014b) Near-fault directivity pulse-like ground motion effect on high-speed railway bridge [J]. Journal of Central South University 21:2425–2436
Cheng QG, Pan JY (1992a) Vertical stiffness analysis of long-span cable-stayed railway bridge [C]. In: The national academic conference on bridge structure, pp 1163–1168. (in Chinese)
Cheng QG, Xu WP (1992b) Discussion of train running property of long-span cable-stayed railway bridge [C]. In: The national academic conference on bridge structure, pp 41–45. (in Chinese)
chiuphysics.cgu (2011) http://chiuphysics.cgu.edu.tw/yun-ju/cguweb/PhyExp/Exp201Wave/Exp201Home07Bridge.html. Accessed 17 Oct 2011
Christensen FT, Timco GW, Nwogu OG (1995) Compliant model tests with the great belt west bridge piers in ice Part II: Analyses of results [J]. Cold Reg Sci Technol 23(2):165–182
Chu KH, Dhar CL, Garg VK (1979) Railway-bridge impact: simplified train and bridge model [J]. J Struct Div 105(9):1823–1844
Consolazio GR, Cowan DR (2003) Nonlinear analysis of barge crush behavior and its relationship to impact resistant bridge design [J]. Comput Struct 81(8–11):547–557
Consolazio GR, Cook RA, McVay MC et al (2006) Barge impact testing of the St. George Island causeway bridge, phase III: physical testing and data interpretation [R]. Final Report to FDOT, Contract No. BC-354, Gainsville, Fla
Cooper JD, Fiedland IM, Buckle IG, Nimis RB, McMullin-Bobb N (1994) The Northridge Earthquake: Progress Made, Lessons Learned in Seismic-Resistant Bridge Design [J]. Public Roads 58(1). https://www.fhwa.dot.gov/publications/publicroads/94summer/p94su26.cfm
Cui SA (2009) Refined simulation study between vehicle and bridge based on multi-body system dynamics and finite element method [D]. Southwest Jiaotong University, Chengdu (in Chinese)
Cui KP (2015) Research of motor collision loads and dynamic responses of high speed train-bridge system and running safety evaluation of trains subjected to motor collision loads [D]. Beijing Jiaotong University, Beijing (in Chinese)
Dailymail (2011) http://www.dailymail.co.uk/news/article-2026278/Passengers-face-massive-delays-lorry-gets-lodged-railway-bridge.html. Fig-232011-8-16
De Roeck G, Peeters B, Maeck J (2000) Dynamic monitoring of civil engineering structures [C]. In: Proceedings of IASS-IACM2000, computational methods for shell and spatial structures, Chania, Greece
Deng YS (2011) Dynamic Analysis and Vibration Reduction Research of Urban Rail Transit Viaduct with Ladder Track [D]. Beijing Jiaotong University, Beijing (in Chinese)
Derucher KN (1982) Analysis of concrete bridge piers for vessel impact [C]. In: Proceedings of the Sino-America symposium on bridge and structural engineering, pp 1–11
Derucher KN (1984) Bridge pile damage upon vessel impact [J]. Comput Struct 18(5):931–935
Diana G, Cheli F (1989) Dynamic interaction of railway systems with large bridges [J]. Veh Syst Dyn 18(1–3):71–106
Dong ZF, Guo J, Wang JJ (2009) Summary and prevention countermeasures of bridge collapse [J]. Shanghai Highw 2:30–32 (in Chinese)
Du XT (2011) Research on spatial dynamic effect of long-span bridge and running safety of train during strong earthquakes [D]. Beijing Jiaotong University, Beijing (in Chinese)
Du XT, Xia H, Yu Z (2011) Study on the input patterns of seismic ground motion in the dynamic interaction analysis of train-bridge system [J]. China Railw Sci 32(6):43–40 (in Chinese)
Du XT, Xia H (2012) Influence of spatial variation of seismic ground motion on dynamic response of train-bridge system [J]. Eng Mech 29(9):106–111 (in Chinese)
Du XT, Xu YL, Xia H (2012) Dynamic interaction of bridge-train system under non-uniform seismic ground motion [J]. Earthq Eng Struct Dyn 41(1):139–157
EL-Tawil S, Severino E, Fonseca P (2005) Vehicle collision with bridge piers [J]. J Bridg Eng 10 (3):345–353
ERRI D214 Committee (1999) Rail bridges for speeds higher than 200 km/h [R]. Research Report of the European Rail Research Institute [J]
eurail (2016) http://www.eurail.com/europe-by-train/high-speed-trains/ice-fig4. Accessed 25 Sept 2016

Frýba L (1972) Vibration of solids and structures under moving loads [J]. Springer, Dordrecht
Frýba L (1976) Non-stationary response of a beam to a moving random force [J]. J Sound Vib 46 (3):323–338
Gao MM, Pan JY (1999) The study on dynamic characteristics of prestressed concrete cable-stayed high speed bridges [J]. Traffic Eng Sci Technol 2:1–7 (in Chinese)
Gao XJ, Guo YC, Li MY, Guo XK (2014) Dynamic response analysis of the vehicle-bridge system considering soil-structure dynamic interaction [J]. World Earthq Eng 30(4):47–54 (in Chinese)
Green MF, Cebon D (1994) Dynamic response of highway bridges to heavy vehicle loads: theory and experimental validation [J]. J Sound Vib 170(1):51–78
Green MF, Cebon V (1997) Dynamic interaction between heavy vehicles and highway bridges [J]. Comput Struct 52(2):253–264
Guo WW (2005) Dynamic responses of long-span bridges and running safety of trains under wind action [D]. Beijing Jiaotong University, Beijing (in Chinese)
Guo XR, Zeng QY (2000) Analysis of dynamic characteristic and train running performance of multi-II type prestressed concrete bridge for high-speed railway [J]. J China Railw Soc 22 (1):72–78 (in Chinese)
Guo ZW, Ge YJ (2013) Impulse response functions of self-excited force and flutter analysis in time domain for bridge [J]. China J Highw Transp 26(6):103–109 (in Chinese)
Guo WW, Xu YL, Xia H, Zhang WS, Shum KM (2007) Dynamic response of suspension bridge to typhoon and trains ii: numerical results [J]. J Struct Eng ASCE 133(1):12–21
Guo WW, Xia H, Xu YL (2010) Running safety analysis of a train on the Tsing Ma Bridge under turbulent wind [J]. Earthq Eng Eng Vib 9(3):307–318
Guo WW, Xia H, De Roeck G, Liu K (2012) Integral model for train-track-bridge interaction on the Sesia viaduct: dynamic simulation and critical assessment [J]. Comput Struct 112–113:205–216
Guo WH, Zhang JW, Xiang CQ (2015a) Wind tunnel test of aerodynamic characteristics of high-speed train on bridge [J]. J Cent South Univ (Science and Technology), 08:5151–3159 (in Chinese)
Guo WW, Wang YJ, Xia H, Lu S (2015b) Wind tunnel test on aerodynamic effect of wind barriers on train-bridge system [J]. Sci China Technol Sci 58(2):219–225
Guo WW, Xia H, Karoumi R, Zhang T, Li XZ (2015c) Aerodynamic effect of wind barriers and running safety of trains on high-speed railway bridges under cross winds [J]. Wind Struct 20 (2):213–236
Han Y (2000) Study of computational method of river Ice effects on bridge pies [D]. Harbin University of Civil Engineering and Architecture, Harbin (in Chinese)
Han Y (2005) Dynamic responses of high-speed railway bridges and running safety of vehicles during earthquakes [D]. Beijing Jiaotong University, Beijing (in Chinese)
Han Y, Wang XD (2015) Research on seismic design of continuous track bridge based on running safety [J]. Railw Eng 7:1–6 (in Chinese)
Harik IE, Shaaban AM, Gesund H, Valli GYS, Wang ST (1990) United States bridge failures, 1951-1988[J]. J Perform Constr Facil ASCE 4(4):272–277
He FL, Li J (1999) Curvature and super elevation effects on coupled vibration of vehicle and curved bridge [J]. Bridge Constr 03:7–9 (in Chinese)
He XW, Kawatani MU, Hayashikawa TR, Matsumoto TS (2011) Numerical analysis on seismic response of Shinkansen bridge-train interaction system under moderate earthquakes [J]. Earthq Eng Eng Vib 10:85–97
He XH, Shi K, Wu T, Zou YF, Wang HF, Qin HX (2016) Aerodynamic performance of a novel wind barrier for train-bridge system [J]. Wind Struct 23(3):171–189
hnxttv (2016) http://www.hnxttv.com/news/2016-01/16/cms65353article.shtml fig-212016-1-16
Hou ZM (2013) Theoretical analyses and model test for dynamic behaviors and damage identification of steel-concrete Beam bridges [D]. Beijing Jiaotong University, Beijing (in Chinese)

Hou ZM, Xia H, Zhang YL (2012) Dynamic analysis and shear connector damage identification of steel-concrete composite beams [J]. Steel and Compos Struct 13(4):327–341 327
Hou ZM, Xia H, Wang YQ, Zhang YL, Zhang TS (2015) Dynamic analysis and model test on steel-concrete composite beams under moving loads [J]. Steel Compos Struct 18(3):565–582
Hu SL, Guo WH (2009) Aerodynamic characteristics of high-speed vehicle and bridge in the crosswind [J]. J Chongqing Jiaotong Univ (Natural Science), 06:1008–1010 + 1015. (in Chinese)
Huang L, Liao HL, Li YL (2006) Analysis of flow characteristics around train-bridge system under cross wind and train induced wind [J]. J Railw Sci Eng 06:61–65 (in Chinese)
ifeng (2015) http://gz.ifeng.com/fygy/detail_2015_10/16/4450588_0.shtml fig-20 2015-10-16
Inglis CE (1934) A mathematical treatise on vibrations in railway bridges [M]. Cambridge
Jin ZB (2007) Train-track-bridge system and train-bridge stochastic vibration [D]. Southwest Jiaotong University, Chengdu
Johnson KL (1958) The effect of spin upon the rolling motion of an elastic sphere on a plane [J]. J Appl Mech 25(3):332–338
Ju SH (2012) Nonlinear analysis of high-speed trains moving on bridges during earthquakes [J]. Nonlinear Dyn 69:173–183
Ju SH (2013) Improvement of bridge structures to increase the safety of moving trains during earthquakes [J]. Eng Struct 56:501–508
Kaliyaperumal G, Imam B, Righiniotis T (2011) Advanced dynamic finite element analysis of a skew steel railway bridge [J]. Eng Struct 33(1):181–190
Kalker JJ (1973) Simplified theory of rolling contact [J]. Delft Progress Rep 1(1):1–10
Kalker JJ (1979) The computation of three-dimensional rolling contact with dry friction [J]. Int J Numer Meth Eng 14(9):1293–1307
kankanews (2014) http://info.kankanews.com/c/2014-10-10/0045586100.shtml, 2014-10-10
Ke ZT, Chen XZ, Zhang D (1991) Research on dynamic performance of quasi high-speed railway bridge [J]. Railw Eng S1:62–69 (in Chinese)
Konstantakopoulos TG, Raftoyiannis IG, Michaltsos GT (2012) Suspended bridges subjected to earthquake and moving loads [J]. Eng Struct 45:223–237
Kwon SD, Lee JS, Moon JW, Kim MY (2008) Dynamic interaction analysis of urban transit maglev vehicle and guideway suspension bridge subjected to gusty wind [J]. Eng Struct 30:3445–3456
Laigaard JJ, Svensson E, Ennemark E (1996) Ship-induced derailment on a railway bridge [J]. Struct Eng Int 6(2):107–112
Lei HJ, Li XZ, Liu DJ (2014) Train running safety analysis of high-pier rigid-frame bridge under earthquake action [J]. Earthq Eng Eng Vib 34(5):87–93
Lei HJ, Li XZ (2015) Effects of structural quasi-static components on seismic responses of train-track-bridge system [J]. J Southwest Jiaotong Univ 50(1):124–130, 136 (in Chinese)
Lewis PR (2007) Disaster on the dee: Robert Stephenson's Nemesis of 1847 [M]. Tempus Publishing, Ltd
Li GH (1978) Spatial internal force, stability and vibration analysis of truss bridges [J]. China Sci 06:687–693
Li HL, Xia H, Guo WW (2013) Study on mechanism of resonance and vibration cancellation for simply supported beam under moving loads [J]. Eng Mech 30(7):47–54 (in Chinese)
Li HL, Frangopol DM, Soliman M, Xia H (2015a) Fatigue reliability assessment of railway bridges based on probabilistic dynamic analysis of a coupled train-bridge system [J]. Struct Eng ASCE 04015158:1–16
Li HL, Xia H, Soliman M et al (2015b) Bridge stress calculation based on the dynamic response of coupled train-bridge system [J]. Eng Struct 99:334–345
Li HL (2016) Dynamic stress analysis and fatigue performance assessment of steel bridges based on train-bridge coupling vibration [D]. Beijing Jiaotong University, Beijing (in Chinese)
Li KB, Zhang N, Xia H et al (2015c) Analysis on structure-borne noise of 32 m simply supported trough-girder bridge for high-speed railway [J]. China Railw Sci 04:52–59 (in Chinese)

Li XB, Hou CL, Zhang SG, Zhang JY, Zhang WH (2009) Flow-induced vibration of high-speed train in passing events [J]. J Vib Shock 28(7):81–84 (in Chinese)
Li XZ, Ma WB, Qiang SZ (2002) Coupling vibration analysis of vehicle-bridge system by iterative solution method [J]. J Vib Shock 21(3):23–27 + 92. (in Chinese)
Li YL, Zhou SH, Qiang SZ (2004) Simulation of three-dimensional fluctuating wind field for large span cable-stayed bridge [J]. China Civil Eng J 36(10):60–65 (in Chinese)
Li YL, Qiang SZ, Liao HL, Xu YL (2005a) Dynamics of wind–rail vehicle–bridge systems [J]. J Wind Eng Ind Aerodyn 93:483–507
Li ZX, Huang J, Zhang Y, Zhang GC (2005b) Influence of seismic excitation on coupled vibration of train-bridge system in light railway [J]. Earthq Eng Eng Vib 25(6):183–188
Li XZ, Liu XH, Liu DJ (2011) Coupled vibration analysis of a bridge and vehicles with railway continuous rigid-frame soil-structure interaction [J]. J Vib Shock 30(2):54–58 (in Chinese)
Li XZ, Zhang ZJ, Liu QM (2012a) Vertical dynamic response analysis of a simply supported beam bridge under successive moving loads [J]. J Vib Shock 31(20):137–142
Li YL, Dong SF, Zang Y, Qiang SZ (2012b) Coupling vibration of wind-vehicle-bridge system for long-span road-rail suspension bridge and wind-resistant criterion of running train [J]. Eng Mech 29(12):114–120 (in Chinese)
Li YL, Hu P, Zhang MJ, Xu XL (2012c) Aerodynamic characteristics of vehicle-bridge system under cross wind: parameter studies based on wind tunnel test [J]. J Southwest Jiaotong University 2:210–217 (in Chinese)
Li YL, L X, X HY, Liao HL (2012d) Coupling vibration of wind-vehicle-bridge system for long-span steel truss cable-stayed bridge [J]. J Traffic Transp Eng 12(5):22–27 (in Chinese)
Li YL, Zhu JQ, Zhao K, Qiang SZ (2012e) Coupled vibration of wind-rail vehicle-bridge system for Shanghai Yangtze River Bridge and the wind-resistant criterion of running transit [J]. China Civ Eng J 45(9):108–114 (in Chinese)
Li YL, Xiang HY, Liao HL (2014) Study on wind shielding effect of wind screens based on coupling vibration theory of wind-vehicle-bridge (lines) systems [J]. China Civ Eng J 03:97–102 (in Chinese)
Lin YK, Yang JN (1983) Multimode bridge response to wind excitations [J]. Eng Mech ASCE 109 (2):586–603
Ling L, Xiao XB, Wu L, Jin XS (2013) Effect of spectrum characteristics of seismic wave on derailment of high-speed train [J]. Eng Mech 30(1):384–393, 431. (in Chinese)
Liu DJ (2010) Coupling vibration study of wind-train-track-bridge system [D]. Southwest Jiaotong University, Chengdu (in Chinese)
Liu QJ (2014) Coupled vibration research of wind-vehicle-bridge of light rail-cum-road suspension bridges [J]. J Wuhan Univ Technol 36(3):107–113 (in Chinese)
Liu JC, Gu YN (2002) A review of approaches to mechanism of ship-bridge collision and its nonlinear FEM simulation [J]. Ship Eng 5:4–9 (in Chinese)
Liu JC, Gu YN (2003) Simulation of ship-bridge head-on collision based on finite element model of whole ship-bridge [J]. Eng Mech 20(5):155–162 (in Chinese)
Liu K, Lombaert G, De Roeck G (2014a) Dynamic analysis of multi-span viaducts under the passage of the train using a substructure approach [J]. J Bridge Eng 19(1):83–90
Liu K, Zhang N, Xia H, De Roeck G (2014b) A comparison of different solution algorithms for the numerical analysis of vehicle-bridge interaction [J]. Int J Struct Stab Dyn 14(2):1–17
Lu KL, Qiu HQ (2012) Container vehicle-truss bridge coupled vibration analysis under wind and seismic load [J]. Eng Mech 29(10):313–320, 334. (in Chinese)
Lu XZ, He ST, Huang SN (2009) Collision between over-high trucks and bridge superstructures-damage mechanism and impact loads [J]. J China Highw 22(5):60–67 (in Chinese)
Lu XZ, He ST, Huang SN (2011) Collision between over-height vehicles and bridge superstructures failure mechanism, design methodology and protection measures [M]. China Architecture and Building Press, Beijing (in Chinese)
m.tiexue (2014) http://m.tiexue.net/touch/thread_7971955_1.html fig-16a 2014–7-10

Ma KQ, Cao XQ (1994) The analysis of lateral vibration of continuous box-girder bridge with high piers while a train passing on it [J]. J Shanghai Inst Railw Technol 01:9–18 (in Chinese)
Ma XL, Gao ZS, Zhang DH (2009) Dynamic response analysis of flyover under collision of ultrahigh vehicle with different speeds [J]. Shanxi Archit 35(20):304–306 (in Chinese)
Majka M, Hartnett M (2008) Effects of speed, load and damping on the dynamic response of railway bridges and vehicles [J]. Comput Struct 86(6):556–572
Majka M, Hartnett M (2009) Dynamic response of bridges to moving trains: a study on effects of random track irregularities and bridge skewness [J]. Comput Struct 87(19–20):1233–1252
Matsuura A (1974) Dynamic interaction of bridge and high-speed train [J]. Railw Res Rep 31 (5):14–17 (in Japanese)
Matsuura A (1976) A study of dynamic behavior of bridge girder for high-speed railway [J]. Proc Japan Civ Eng Soc 256:35–47 (in Japanese)
Minorsky N (1953) On interaction of non-linear oscillations [J]. J Franklin Inst 256(2):147–165
Muchnikov YM (1953) Some methods of computing vibration of elastic systems subjected to moving loads [J]. Gosstroiizdat Moscow 19(5):216–223
news.sina (2011) http://news.sina.com.cn/c/2002-08-09/1108666006.html fig-242002-8-9
Nishimura K, Terumichi Y et al (2010a) Experimental study on the vehicle safety by earthquake track excitation with 1/10 scale vehicle and roller rig [J]. J Syst Des Dyn 4(1):226–237
Nishimura K, Terumichi Y et al (2010b) Analytical study on the safety of high-speed railway vehicle on excited tracks [J]. J Syst Des Dyn 4(1):211–225
Olsson M (1985) Finite element, modal co-ordinate analysis of structures subjected to moving loads [J]. J Sound Vib 99(1):1–12
Olsson M (1991) On the fundamental moving load problem [J]. J Sound Vib 145(2):299–307
Paik JK, Pedersen PT (1996) Modeling of the internal mechanics in ship collisions [J]. Ocean Eng 23(2):107–142
Paik JK, Thayamballi AK, Pedersen PT, Park YI (2001) Ultimate strength of ship hulls under torsion [J]. Ocean Eng 28(8):1097–1133
Pan JY, Gao MM (2008) Dynamic analysis of vehicle-line-bridge in railway system [M]. China Railway Press, Beijing
Pedersen PT, Zhang SM (1998) On impact mechanics in ship collisions [J]. Mar Struct 11 (10):429–449
Peters TF (1987) Transitions in engineering: guillaume Henri Dufour and the early 19th century cable suspension bridges [M]. Birkhauser Inc, Boston
Qi N (2009) Research on Ice-induced pier vibration model test and ice load identification [D]. Dalian University of Technology, Dalian (in Chinese)
Rebelo C, Da Silva LS, Rigueiro C et al (2008) Dynamic behavior of twin single-span ballasted railway viaducts: field measurements and modal identification [J]. Eng Struct 30(9):2460–2469
Rigueiro C, Rebelo C, Da Silva LS (2010) Influence of ballast models in the dynamic response of railway viaducts [J]. J Sound Vib 329(15):3030–3040
Robinson SW (1887) Vibration of bridges [J]. Trans Am Soc Civ Eng 16(1):42–65
Schallenkamp A (1937) Schwingungen von Trägernbeibewegten Lasten [J]. Arch Appl Mech 8 (3):182–198
Severino E, El-Tawil S (2003) Collision of vehicles with bridge piers [C]. In: Proceedings of the second MIT conference on computational fluid and solid mechanics, pp 637–640
Shan DS, Li Q (2001) Introduction of reasonable bearing form of curved-girder bridge in high-speed railway [J]. J. Chongqing Jiaotong Univ 02: 1–5 + 18. (in Chinese)
Sharma H, Hurlebaus S, Gardoni P (2012) Performance-based response evaluation of reinforced concrete columns subject to vehicle impact [J]. Int J Impact Eng 43(5):52–62
Shen RL (1987) Spatial vibration analysis of truss bridge when train passing through bridges [D]. Southwest Jiaotong University, Chengdu (in Chinese)
Stokes GG (1849) Discussion of a differential equation relating to the breaking of railway bridges [J]. Trans Camb Philos Soc 8:287–319
Strogatz SH, Abrams DM, Mcrobie A, Eckhardt B, Ott E (2005) Theoretical mechanics: crowd synchrony on the millennium bridge [J]. Nature 438(7064):43–44

Sun JL (1998) Study on spatial dynamic interaction between train and long-span railway bridge [D]. China Academy of Railway Sciences, Beijing (in Chinese)
Sun Q, Zhang N, Wang XN (2013) Temperature effect on running safety of simply supported high-speed railway bridge [J]. Railw Eng 12:10–14 (in Chinese)
Tan CJ, Zhu B (2009) Coupled vibration analysis of high-speed train and bridge subjected to seismic excitation [J]. J Vib Shock 28(1):4–8
Tanabe M, Yamada Y, Hajime W (1987) Modal method for interaction of train and bridge [J]. Comput Struct 27(1):119–127
Tian HQ (2004) Research and applications of air pressure pulse from trains passing each other [J]. J Rail Sci Eng 1:83–89 (in Chinese)
Tian HQ, He DX (2001) 3-numerical calculation of the air pressure pulse from two trains passing by each other [J]. J China Railw Soc 23(3):18–22 (in Chinese)
Tian Y, Zhang N, Xia H (2015) Multi-scale dynamic boundary approximation method for orthotropic plate bridge deck [J]. Bridge Constr 04:100–106 (in Chinese)
Timco GW (2011) Isolated Ice floe impacts [J]. Cold Reg Sci Technol 68:35–48
Timoshenko SP (1922) On the forced vibrations of bridges [J]. The Lond Edinb Dublin Philos Mag J Sci 43(257):1018–1019
Timoshenko SP (1927). Vibration of bridges [J]. Am Soc Eng 53–61
tydf (2007) http://www.tydf.cn/read.php?fpage=26&tid=114670 fig-18 2007-6-16
TYH2004-120 (2004) Code for rating existing railway bridge [S]. China Railway Publishing House. (in Chinese)
Ueda Y, Rashed SMH (1984) The idealized structural unit method and its application to deep girder structures [J]. Comput Struct 18(2):277–293
Ueda Y, Rashed SMH, Paik JK (1995) Buckling and ultimate strength interaction in plates and stiffened panels under combined in plane biaxial and shearing forces [J]. Mar Struct 8(1):1–36
v.ku6 (2008) http://v.ku6.com/show/NBodfHRRP7sft17H.html?lb=1 fig-25a 2008-10-15
Vu-Quoc L, Olsson M (1989) A computational procedure for interaction of high-speed vehicles on flexible structures without assuming known vehicle nominal motion [J]. Comput Methods Appl Mech Eng 76(3):207–244
Wang GC (1996) Linear and nonlinear analysis of vehicle-bridge coupled vibration of railway cable-stayed bridges with long span [D]. China Academy of Railway Sciences, Beijing (in Chinese)
Wang JF (2007) Research on mechanics characteristic of river Ice and its impact on pier [D]. Northeast Forestry University, Harbin (in Chinese)
Wang JJ (2011) Research and engineering application on bridges against vessel impact [M]. China Communications Press, Beijing (in Chinese)
Wang SQ (2012) Nonlinear dynamic analysis of long-span bridge subjected to cross wind and train [D]. Beijing Jiaotong University, Beijing (in Chinese)
Wang KP (2015) Influence of bridge additional deformation on running performance of high-speed trains [D]. Beijing Jiaotong University, Beijing (in Chinese)
Wang G, Cao XQ (2000) Dynamic analysis of long-span cable-stayed bridge under the high-speed train [J]. J Shanghai Inst Railw Technol 08:7–11 + 21. (in Chinese)
Wang JJ, Chen C (2007) Simulation of damage for bridge pier subjected to ship impact [J]. Eng Mech 24(7):156–160
Wang L, Guo XR (2012) The wind-vehicle-bridge coupling dynamic analysis of three-tower suspension bridge [J]. J Railw Sci Eng 9(1):24–29 (in Chinese)
Wang TL, Garg VK, Chu KH (1991) Railway bridge/vehicle interaction studies with new vehicle model [J]. J Struct Eng 117(7):2099–2116
Wang RH, Guo XR, Zeng QY (1995) Random simulating method of artificial crawl wave of high-speed train frame [J]. J Changsha Railw Univ 02:1–7 (in Chinese)
Wang SQ, Xia H, Guo WW, Zhang N (2010) Nonlinear dynamic response analysis of a long-span suspension bridge under running train and turbulent wind [J]. Interact Multiscale Mech—An Int J 3(4):309–320

Wang KP, Xia H, Guo WW (2013a) A train-bridge coupling vibration model considering car-body flexibility based on Euler beam hypothesis [J]. J Beijing Jiaotong Univ 06:55–61 (in Chinese)
Wang SQ, Xia H, Guo WW, Du XT (2013b) Coupling vibration analysis of wind-train-bridge system considering geometric nonlinearity of bridge [J]. Eng Mech 4:122–128 (in Chinese)
Wang KP, Xia H, Xu M, Guo WW (2015) Dynamic analysis of train-bridge interaction system with flexible car-body [J]. J Mech Sci Technol 29(9):3572–3580
Wardhana K, Hadipriono FC (2003) Analysis of recent bridge failures in the United States [J]. J Perform Constr Facil 17(3):144–150
Willis R (1849) Appendix to the report of the commissioners appointed to inquire into the application of iron to railway structures [R]. HM Stationary Office, London
wikipedia (2006) https://en.wikipedia.org/wiki/Mount_Fuji#/media/File:Mountfujijapan.jpg –fig1 20 May 2006
wikipedia (2016) https://en.wikipedia.org/wiki/Tay_Bridge_disaster fig.11 2016-8-18 1879-12-28
Wiriyachai A (1980). Impact and fatigue in open deck railway truss bridges [D]. Illinois Institute of Technology
Woisin G (1976) The collision test of the GKSS [J]. Jahrbuch Schiffbautech Gesellsch 70:465–487
Woisin G (1979) Model testing with the collision protection structures in reactor ships [C]. In: Proceedings of the international symposium on advances in marine technology. Trondheim, pp 309–336
world.huanqiu (2013) http://world.huanqiu.com/photo/2013-08/2706819_2.html -fig2 2013-08-29
Xia H (1984) Dynamic responses of high piers under train passages and their influences on running safety of vehicles [D]. Northern Jiaotong University, Beijing (in Chinese)
Xia H (1998) Transverse vibration reinforcement and its experimental analysis of steel plate girder bridge [J]. Eng Mech (supplement) 438–478
Xia H (2002) Dynamic interaction of vehicles and structures [M]. Science Press, Beijing (in Chinese)
Xia CY (2012) Dynamic responses of train-bridge system subjected to collision loads and running safety evaluation of high-speed trains [D]. Beijing Jiaotong University, Beijing (in Chinese)
Xia H, Chen YJ (1992) Analysis of the lateral dynamic interaction in vehicle-girder-pier system [J]. China Civ Eng J 25(2):3–12 (in Chinese)
Xia H, Chen YJ (1994) Dynamic reliability analysis of train-bridge system under wind action [J]. China Civ Eng J 27(2):14–21 (in Chinese)
Xia H, De Roeck G (1997) System identification of mechanical structures by a high-order multivariate autoregressive model [J]. Comput Struct 64(1–4):341–351
Xia H, Chen YJ (1998) Dynamic analysis of train-bridge system under random excitations [C]. Proc Stoch Struct Dyn, Notre Dame, pp 535–543
Xia H, Zhang N (2005a) Dynamic interaction of vehicles and structures, 2nd edn [M]. Science Press, Beijing (in Chinese)
Xia H, Zhang N (2005b) Dynamic analysis of railway bridges under high-speed trains [J]. Comput Struct 83(1–4):1891–1901
Xia H, Calçada R (2013a) Traffic induced environmental vibrations and controls: theory and application [M]. Nova Science Publishers Inc, New York
Xia H, Yan GP, Chen YJ (1995) Dynamic responses of train and cable-stayed bridge system under wind action [J]. J Beijing Jiaotong Univ 19(2):131–136 (in Chinese)
Xia H, Chen YJ, Zhang D, Ke ZT (1996) Dynamic analysis of steel truss bridges under increased train speeds [J]. J China Railw Soc 05:79–86 (in Chinese)
Xia H, Xu YL, Chan THT (2000) Dynamic interaction of long suspension bridges with running trains [J]. J Sound Vib 237(2):263–280
Xia H, De Roeck G, Zhang HR, Zhang N (2001) Dynamic analysis of train-bridge system and its application in steel girder reinforcement [J]. Comput Struct 79:1851–1860
Xia H, De Roeck G, Zhang N, Maeck J (2003a) Experimental analysis of high-speed railway bridge under Thalys trains [J]. J Sound Vib 268:103–113
Xia H, Zhang N, De Roeck G (2003b) Dynamic analysis of high-speed railway bridge under articulated trains [J]. Comput Struct 81:2467–2478

Xia H, Zhang N, Gao R (2005a) Experimental analysis of railway bridges under high-speed trains [J]. J Sound Vib 282(2):517–528
Xia H, Zhang N, Cao YM (2005b) Experimental study of train-induced vibrations of environments and buildings [J]. J Sound Vib 280:1017–1029
Xia H, Han Y, Guo WW (2006a) Dynamic analysis of train-bridge system subjected to non-uniform seismic excitations [J]. J Earthq Eng Struct Dyn 35:1563–1579
Xia H, Zhang N, Guo WW (2006b) Analysis of resonance mechanism and conditions of train-bridge system [J]. J Sound Vib 297(2):810–822
Xia H, Cao YM, Zhang N (2007) Numerical analysis of vibration effects of metro trains on surrounding environment [J]. Int J Struct Stab Dyn 7(1):154–166
Xia H, Guo WW, Wu X, Pi YL, Bradford MA (2008a) Lateral dynamic interaction analysis of a train-girder-pier system [J]. J Sound Vib 318:927–942
Xia H, Guo WW, Zhang N, Sun GJ (2008b) Dynamic analysis of a train-bridge system under wind action [J]. Comput Struct 86:1845–1855
Xia H, Guo WW, Xia CY, Pi YL, Bradford MA (2009a) Dynamic interaction analysis of a LIM train and elevated bridge system [J]. J Mech Sci Technol 23(3):3257–3270
Xia H, Chen JG, Wei PB, Xia CY, Roeck De, Degrande G (2009b) Experimental investigation of railway train-induced vibrations of surrounding ground and nearby multi-story buildings [J]. J Earthq Eng Eng Vib 8(1):137–148
Xia H et al (2010a) Traffic induced environmental vibrations and controls [M]. Science Press, Beijing (in Chinese)
Xia H, Cao YM, De Roeck G (2010b) Theoretical modeling and characteristic analysis of moving-train induced ground vibrations [J]. J Sound Vib 329:819–832
Xia H, Chen JG, Xia CY, Inoue H, Zenda Y, Qi L (2010c) Experimental study of train-induced structural and environmental vibrations of rail transit elevated bridge with ladder tracks [J]. J Rail Rapid Transit 224(304):115–224
Xia CY, Lei JQ, Zhang N, Xia H, De Roeck G (2012a) Dynamic analysis of a coupled high-speed train and bridge system subjected to collision load [J]. J Sound Vib 331:2334–2347
Xia H, De Roeck G, Goicolea JM (2012b) Bridge vibration and controls: new research [M]. Nova Science Publishers Inc, New York
Xia CY, Xia H, Zhang N, Guo WW (2013a) Effect of truck collision on the dynamic response of train-bridge systems and running safety of high-speed trains [J]. Int J Struct Stab Dyn 13(3): 1–18
Xia H, Deng YS, Xia CY, De Roeck G, Qi L, Sun L (2013b) Dynamic analysis of coupled train-ladder track-elevated bridge system [J]. Struct Eng and Mech 47(5):661–678
Xia CY, Xia H, De Roeck G (2014a) Dynamic response of a train-bridge system under collision loads and running safety evaluation of high-speed trains [J]. Comput Struct 140:23–38
Xia H, Zhang N, Guo WW (2014b) Coupling vibrations of train-bridge system [M]. Science Press, Beijing
Xia H, Li HL, Guo WW, De Roeck G (2014c) Vibration resonance and cancellation of simply supported bridges under moving train loads [J]. J Eng Mech ASCE 140(5):04014015-1-11
Xia CY, Zhang N, Xia H, Ma Q, Wu X (2016) A framework for carrying out train safety evaluation and vibration analysis of a trussed-arch bridge subjected to vessel collision [J]. Struct Eng Mech 59(4):683–701
Xiang HF, Ge YJ (2002) Refinements on aerodynamic stability analysis of super long-span bridges [J]. J Wind Eng Ind Aerodyn 90(12–15):1493–1515
Xiang HF (2002) State-of-art of ship collision design for bridges and future research [J]. J Tongji Univ 30(4):386–392 (in Chinese)
Xiang J, Zeng QY, Zhou ZH (2004) Mechanical mechanism and random energy analysis theory of train derailment on the bridge and its application [J]. J China Railw Soc 02:97–104 (in Chinese)
xmnn (2010). http://www.xmnn.cn/dzbk/xmwb/20100305/201003/t20100305_1347608.htm fig-16b 2010-3-5

Xin XZ (2006) Dynamic analysis of long-span PC continuous Beam (Rigid Structure) bridge-train time-varying system [D]. Beijing Jiaotong University, Beijing (in Chinese)
Xu WP (1988) Study on space dynamic interaction between train and long-span railway bridge [D]. China Railway Science, Beijing (in Chinese)
Xu LJ, Lu XZ, Smith ST, He ST (2012) Scaled model test for collision between over-height truck and bridge superstructure [J]. Int J Impact Eng 39(2012):31–42
Xu YL, Xia H, Yan QS (2003) Dynamic response of suspension bridge to high wind and running train [J]. J Bridge Eng ASCE 8(1):46–55
Xu YL, Zhang N, Xia H (2004) Vibration of coupled train and cable-stayed bridge systems in cross winds [J]. Eng Struct 26(10):1389–1406
Xu YL, Guo WW, Chen J, Shum KM, Xia H (2007) Dynamic response of suspension bridge to typhoon and trains. I: field measurement results [J]. J Struct Eng ASCE 133(1):3–11
Xuan Y, Zhang D (2001) Derailment of train caused by collision between ships and railway bridge pier [J]. Foreign Bridges 4:60–64 (in Chinese)
Yang YM (1995) Theoretical and experimental studies on dynamic interaction between train and long span railway bridge [D]. China Railway Science, Beijing. (in Chinese)
Yang YB (2003) Ground vibration induced by high-speed trains over viaducts [C]. Proc ISEV: 147–157
Yang YB, Yau JD (1997) Vehicle-bridge interaction element for dynamic analysis [J]. J Struct Eng
Yang YB, Lin CW, Yau JD (2004) Extracting bridge frequencies from the dynamic response of a passing vehicle [J]. J Sound Vib 272(3):471–493
Yau ZD, Yang YB (1999) Theory of vehicle-bridge interaction for high-speed railway [M]. Publishing technology service co. LTD., Taipei (in Chinese)
Yau JD, Yang YB (2006) Vertical accelerations of simple beams due to successive loads traveling at resonant speeds [J]. J Sound Vib 289(1):210–228
Yau JD, Frýba L (2007) Response of suspended beams due to moving loads and vertical seismic ground excitations [J]. Eng Struct 29:3255–3262
Yau JD (2009) Dynamic response analysis of suspended beams subjected to moving vehicles and multiple support excitations [J]. J Sound Vib 325:907–922
Yu Z (2013) Research on bridge damage detection based on moving load induced structural response and wavelet analysis [D]. Beijing Jiaotong University, Beijing (in Chinese)
Yu M, Zha XX (2011) Behavior of solid and hollow concrete filled steel tube columns under vehicle impact [J]. Prog Steel Build Struct 13(1):57–64 (in Chinese)
Yu MG, Zhang JY, Zhang WH (2012) Running safety of high-speed trains on bridges under strong crosswinds [J]. Chin J Mech Eng 18:104–111 (in Chinese)
Yu TL, Wang JF, Du F (2007) Experimental research on ice disaster in Huma River [J]. J Nat Disasters 16(4):43–48 (in Chinese)
Yu Z, Xia H, Goicolea JM, Xia CY (2016) Bridge damage identification from moving load induced deflection based on Wavelet Transform and Lipschitz exponent [J]. Int J Struct Stab and Dyn 16(5):1550003: 1–22
Yu ZW, Mao JF, Tan S, Zeng ZP (2015a) Probability density evolution analysis of vertical random vibration of train-bridge system [J]. J Cent South China Univ (Science and Technology) 46 (04):1420–1427
Yu ZW, Mao JF, Tan S, Zeng ZP (2015b) Vertical random vibration analysis of vehicle parameters [J]. J Cent South China Univ (Science and Technology) 38(01):97–104
Yuan ZG (2010) Research on Inland river Ice mechanical property and Ice impact force on bridge pier [D]. Northeast Forestry University, Harbin (in Chinese)
Yue QJ, Guo FW, Kärnä T (2009) Dynamic ice forces of slender vertical structures due to ice crushing [J]. Cold Reg Sci Technol 56:77–83
Zeng QY, Luo NA, Jiang F (1990) Preliminary study on lateral oscillation force of train on the bridge [J]. Bridge Constr 01:28–36 (in Chinese)
Zeng QY, Yang Y, Luo NG, Jiang F, Zhang Q (1991) Lateral vibration analysis of train-bridge time varying system [J]. J China Railw Soc 02:38–46 (in Chinese)

Zeng QY, Guo XR et al (1999) Analysis theory and application of time-variant train-bridge vibration system [M]. China Railway Publishing House, Beijing (in Chinese)
Zhai WM (1996) Two simple fast integration methods for large-scale dynamic problems in engineering [J]. Int J Numer Methods Eng 39(24):4199–4214
Zhai WM (2002) New advance in vehicle-track coupling dynamics [J]. China Railw Sci 02:1–14 (in Chinese)
Zhai WM, Wang SL (2012) Influence of bridge structure stiffness on the dynamic performance of high-speed train-track-bridge coupled system [J]. China Railw Sci 01:19–26 (in Chinese)
Zhai WM, Xia H et al (2011) Train-track-bridge dynamic interaction: theory and engineering application [M]. Science Press, Beijing (in Chinese)
Zhai JP, Li M, Zhang JY, Lv FM (2013) Influence of bridge height on passing performance of high-speed trains under crosswind [J]. Comput Aided Eng 03:1–8
Zhan JW (1996) Soundness evaluation and experiment method studies on existing railway piers [D]. Beijing Jiaotong University, Beijing (in Chinese)
Zhan JW, Xia H, Chen SY, De Roeck G (2011) Structural damage identification for railway bridges based on train-induced bridge responses and sensitivity analysis [J]. J Sound Vib 330:757–770
Zhang N (2002) Theoretical analysis and experimental study on dynamic interaction of high-speed railway bridge and articulated trains [D]. Beijing Jiaotong University, Beijing (in Chinese)
Zhang T (2013) Study on running safety of trains and windproof measures for high-speed railway bridges in strong wind field [D]. Beijing Jiaotong University, Beijing (in Chinese)
Zhang L, Zeng QY (1998) An approach to control index of lateral rigidity of steel truss bridges [J]. Bridge Constr 01:3–6 (in Chinese)
Zhang N, Xia H (2013a) A vehicle-bridge interaction dynamic system analysis method based on inter-system iteration [J]. China Railw Sci 05:32–38 (in Chinese)
Zhang N, Xia H (2013b) Dynamic analysis of coupled vehicle-bridge system based on inter-system iteration method [J]. Comput Struct 114–115:26–34
Zhang D, Ke ZT, Zheng R (1996) Evaluation study on the behavior of existing bridges due to speed raise up to 160 km/h [J]. China Railw Sci 01:9–20 (in Chinese)
Zhang N, Xia H, Guo WW (2008) Vehicle-bridge vibration analysis under high-speed trains [J]. J Sound Vib 268:103–113
Zhang N, Xia H, Guo WW (2009) Analysis on the wind-vehicle-bridge coupling vibration for Nanjing Dashengguan Yangtze River Bridge of Beijing-Shanghai High-Speed Railway [J]. China Railway. Science 30(1):41–48 (in Chinese)
Zhang N, Xia H, Guo WW, De Roeck G (2010a) A vehicle-bridge linear interacted model and its validation [J]. Int J Struct Stab Dyn 9(2):335–361
Zhang N, Xia H, De Roeck G (2010b) Dynamic analysis of a train-bridge system under multi-support seismic excitations [J]. J Mech Sci Technol 24(11):2181–2188
Zhang ZC, Lin JH, Zhang YH et al (2010c) Non-stationary random vibration analysis for train-bridge systems subjected to horizontal earthquakes [J]. Eng Struct 32:3571–3582
Zhang N, Xia H, De Roeck G (2011a) Analysis of a vehicle-bridge-earthquake interactive system under multi-support excitations [J]. J Harbin Eng Univ 32(1):26–32 (in Chinese)
Zhang ZC, Zhang YH, Lin JH, Zhao Y, Howson WP, Williams FW (2011b) Random vibration of a train traversing a bridge subjected to traveling seismic waves [J]. Eng Struct 33:3546–3558
Zhang JW, Guo WH, Xiang CQ (2013a) Simulation of stochastic wind field based on covariance proper transformation and weighted amplitude wave superposition [J]. J Vib Shock 21:197–203 (in Chinese)
Zhang M, Zhang N, Xia H (2013b) Analysis on wind-vehicle-bridge dynamic interaction for long-span railway suspension bridge [J]. China Railw Sci 34(4):14–21 (in Chinese)
Zhang T, Guo WW, Xia H (2013c) Aerodynamic characteristics of vehicle-bridge system under crosswinds and effect of wind barriers [J]. J China Railw Soc 35(7):102–106 (in Chinese)
Zhang T, Xia H, Guo WW (2013d) Analysis on running safety of train on bridge with wind barriers subjected to cross wind [J]. Wind Struct 17(3):203–225

Zhang N, Zhou S, Xia H, Sun L (2014) Evaluation of vehicle-track-bridge interacted system for the continuous CRTS-II non-ballast track slab [J]. Sci China Technol Sci 57(10):1895–1901
Zhang N, Ge GH, Xia H, Li XZ (2015) Dynamic analysis of coupled wind-train-bridge system considering tower shielding and triangular wind barriers [J]. Wind Struct 21(3):311–329
Zhang ZT, Ge YJ, Chen ZQ (2006) A new aerodynamic method for long-span bridge buffeting analysis [J]. Eng Mech 23(6):94–101
Zheng J et al (2008) The high-speed railway bridges in China [M]. Higher Education Press, Beijing
Zhu Y (2011) Research on theory and application of Train-bridge coupling system stochastic [D]. Southwest Jiaotong University, Chengdu (in Chinese)
Zhu HH, Zeng QY (1994) The energy random analysis of train-bridge time varying system vibration [J]. J Changsha Railw Univ 04:6–10 (in Chinese)
Zhu LD, Wang M, Guo ZS, Ding SQ (2006) Buffeting performance of double-cantilever state of a long-span cable-stayed bridge under yawed wind [J] Eng Mech 04:86–92. (in Chinese)
Zhu DY, Zhang YH, Kennedy D et al (2014) Stochastic vibration of the vehicle-bridge system subjected to non-uniform ground motions [J]. Veh Syst Dyn 52(3):410–428

Chapter 2
Fundamental Theories and Analytical Methods for Vibrations of Simply-Supported Beams Under Moving Loads

In this chapter, some fundamental theories and methods for vibration analysis of simply-supported beams under moving loads are presented. The analytical solutions of vibrations induced by a moving concentrated load, a moving harmonic load, and a moving wheel-spring-mass (WSM) load with varying speed are deduced, respectively, and the vibration characteristics of them are investigated in several case studies. In addition, as one of the important phenomena related to the train-bridge coupling vibration, the mechanisms of vibration resonance, suppression, and cancellation happened in the moving load and beam system are analyzed.

2.1 Vibrations of Simply-Supported Beam Under Moving Loads

2.1.1 Analysis Model

For a simply-supported beam subjected to a moving load, if the mass of the load is much smaller than that of the beam, the inertial force caused by the mass of the load can be neglected, and the load becomes a moving concentrated force varying with time, denoted as $P(t)$. In this case, a simplified analysis model is established, as shown in Fig. 2.1.

Assuming the simply-supported beam has a uniform cross section with constant bending stiffness EI, a uniformly distributed mass $\bar{m}$ per unit length, a viscous damping with the damping force proportional to the vibration velocity, and the small and elastic deformation during its vibration excited by a moving concentrated load $P(t)$ with the constant speed V, as shown in the coordinates shown in Fig. 2.1, the motion equation for the beam subjected to the moving concentrated load can be expressed as

H. Xia et al., *Dynamic Interaction of Train-Bridge Systems in High-Speed Railways*, Advances in High-speed Rail Technology, https://doi.org/10.1007/978-3-662-54871-4_2

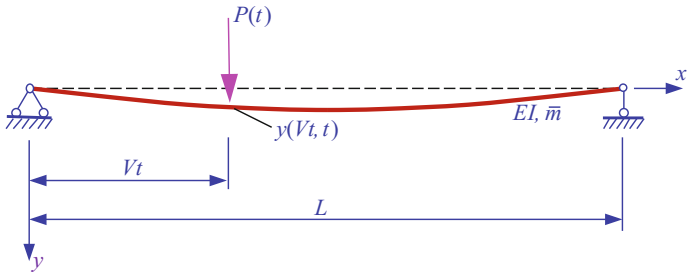

Fig. 2.1 Simply-supported beam under a moving concentrated load

$$EI\frac{\partial^4 y(x,t)}{\partial x^4}+\bar{m}\frac{\partial^2 y(x,t)}{\partial t^2}+c\frac{\partial y(x,t)}{\partial t}=\delta(x-Vt)P(t) \tag{2.1}$$

where c is the damping coefficient of the beam; δ is the Dirac function, a useful function for this analysis, which has the following characteristics

$$\delta(x-\eta)=\begin{cases}\infty, & (x=\eta)\\ 0, & (x\neq\eta)\end{cases} \tag{2.2a}$$

$$\int_{-\infty}^{\infty}\delta(x-\eta)f(x)\mathrm{d}x=f(\eta) \tag{2.2b}$$

$$\int_{a}^{b}\delta(x-\eta)f(x)\mathrm{d}x=\begin{cases}0, & (\eta<a<b)\\ f(\eta), & (a\leq\eta\leq b)\\ 0, & (a<b<\eta)\end{cases} \tag{2.2c}$$

Equation (2.1) is a partial differential equation. It can be solved by the modal decomposition method, namely the separation of variables in mathematics. In this method, the geometric coordinates of the structure are transformed into the modal coordinates or the generalized coordinates. Accordingly, the motion of the structure can be represented by the superposition of modal movements (Clough and Penzien 2003). For a one-dimensional continuous structure, the transformation can be described by

$$y(x,t)=\sum_{i=1}^{\infty}\phi_i(x)\cdot q_i(t) \tag{2.3}$$

where $q_i(t)$ is the generalized coordinate varying with time t, and $\phi_i(x)$ is the modal function. Equation (2.3) shows that any rational displacement of the structure can be expressed by superposition of the corresponding amplitudes of all the modes.

The modal component of any deformation of the structure can be acquired by using the orthogonality of the modes. For a beam with uniform section, the contribution of the nth mode to the displacement $y(x, t)$ can be obtained by multiplying $\phi_n(x)$ on both sides of Eq. (2.3) and integrating them along the axle of the beam as

$$\int_0^L \phi_n(x) y(x,t) \mathrm{d}x = \sum_{i=1}^{\infty} q_i(t) \int_0^L \phi_n(x) \phi_i(x) \mathrm{d}x \tag{2.4}$$

Due to the orthogonality of modes, the right-hand side of Eq. (2.3) equals to zero when $i \neq n$, and only one term of the infinite series is left. Consequently, the generalized coordinates of the nth mode can be expressed as

$$q_n(t) = \frac{\int_0^L \phi_n(x) y(x,t) \mathrm{d}x}{\int_0^L \phi_n^2(x) \mathrm{d}x} \tag{2.5}$$

By decomposing the motion equation of the simply-supported beam based on the above principle, and substituting Eq. (2.3) into Eq. (2.1), we obtain

$$EI \sum_{i=1}^{\infty} q_i(t) \frac{\mathrm{d}^4 \phi_i(x)}{\mathrm{d}x^4} + \bar{m} \sum_{i=1}^{\infty} \phi_i(x) \frac{\mathrm{d}^2 q_i(t)}{\mathrm{d}t^2} + c \sum_{i=1}^{\infty} \phi_i(x) \frac{\mathrm{d}q_i(t)}{\mathrm{d}t} = \delta(x - Vt) P(t) \tag{2.6}$$

By multiplying each term of Eq. (2.6) with the nth modal function $\phi_n(x)$, conducting integration along the length of the beam, and considering the orthogonality of modes, the motion equation in generalized coordinate corresponding to the nth mode is given by

$$\begin{aligned} EIq_n(t) \int_0^L \phi_n(x) \frac{\mathrm{d}^4 \phi_n(x)}{\mathrm{d}x^4} \mathrm{d}x + \bar{m} \frac{\mathrm{d}^2 q_n(t)}{\mathrm{d}t^2} \int_0^L \phi_n^2(x) \mathrm{d}x + c \frac{\mathrm{d}q_n(t)}{\mathrm{d}t} \int_0^L \phi_n^2(x) \mathrm{d}x \\ = \int_0^L \delta(x - Vt) P(t) \phi_n(x) \mathrm{d}x \end{aligned} \tag{2.7}$$

For the simply-supported beam with uniform section, the modal function can be assumed as a trigonometric function

$$\phi_n(x) = \sin \frac{n\pi x}{L} \tag{2.8}$$

Substituting it into Eq. (2.7), and noting the following formulas

$$\int_0^L \sin^2 \frac{n\pi x}{L} \mathrm{d}x = \frac{L}{2}$$
$$\int_0^L \delta(x - Vt) P(t) \sin \frac{n\pi x}{L} \mathrm{d}x = P(t) \sin \frac{n\pi Vt}{L}$$

The following motion equation can be obtained

$$\frac{L}{2}\bar{m}\frac{\mathrm{d}^2 q_n(t)}{\mathrm{d}t^2} + \frac{L}{2}c\frac{\mathrm{d}q_n(t)}{\mathrm{d}t} + \frac{L}{2}\frac{n^4\pi^4}{L^4}EIq_n(t) = P(t)\sin\frac{n\pi Vt}{L} \tag{2.9}$$

For the simply-supported beam with uniform section, the nth circular frequency and the nth damping coefficient are $\omega_n = \frac{n^2\pi^2}{L^2}\sqrt{\frac{EI}{\bar{m}}}$ and $c_n = 2\xi_n\bar{m}\omega_n$, respectively. Dividing both sides of Eq. (2.9) by $\frac{\bar{m}L}{2}$ and introducing $\dot{q} = \frac{\mathrm{d}q}{\mathrm{d}t}$ and $\ddot{q} = \frac{\mathrm{d}^2 q}{\mathrm{d}t^2}$, the standard form of the nth modal equation for the simply-supported beam under moving load can be written as

$$\ddot{q}_n(t) + 2\xi_n\omega_n\dot{q}_n(t) + \omega_n^2 q_n(t) = \frac{2}{\bar{m}L}P(t)\sin\frac{n\pi Vt}{L} \tag{2.10}$$

For convenience of discussion, two parameters are introduced herein, the critically damped circular frequency $\omega_b = c/2\bar{m} = \xi_n\omega_n$ (Frýba 1999) and the circular frequency $\bar{\omega} = \pi V/L$ of excitation (Xia et al. 2006). Accordingly, Eq. (2.10) can be rewritten as

$$\ddot{q}_n(t) + 2\omega_\mathrm{b}\dot{q}_n(t) + \omega_n^2 q_n(t) = \frac{2}{\bar{m}L}P(t)\sin n\bar{\omega}t \tag{2.11}$$

Equation (2.11) is a linear differential equation with constant coefficients, and obviously, the equations for different modes are independent. By using the Duhamel integral, the particular solution can be obtained as

$$q_n(t) = \frac{2}{\bar{m}L\omega_\mathrm{D}^n}\int_0^t P(\tau)\sin n\bar{\omega}\tau \mathrm{e}^{-\omega_\mathrm{b}(t-\tau)}\sin\omega_\mathrm{D}^n(t-\tau)\mathrm{d}\tau \tag{2.12}$$

where $\omega_\mathrm{D}^n = \omega_n\sqrt{1-\xi_n^2}$ is the nth natural frequency of the damped structure. Equation (2.12) is suited for structures in undercritically damped and critically damped cases.

For a simple load, such as a moving constant load $P(t) = P$ or a moving harmonic load $P(t) = P\sin\omega t$, the closed-form solution of Eq. (2.12) can be obtained by integration. In the following sections, the analytical solutions for the simply-supported beam under the above two types of simple loads are deduced, with emphasis on the discussion of several special cases related to the moving constant load.

2.1.2 Vibration of Simply-Supported Beam Under a Moving Concentrated Load

In the case of a moving constant load, i.e., $P(\tau) = P$, Eq. (2.12) can be expressed as

$$q_n(t) = \frac{2P}{\bar{m}L\omega_{\mathrm{D}}^n}\int_0^t \sin n\bar{\omega}\tau \, \sin\omega_{\mathrm{D}}^n(t-\tau)\mathrm{e}^{-\omega_{\mathrm{b}}(t-\tau)}\mathrm{d}\tau \tag{2.13}$$

By using the following triangular transformation formula (Rade and Westergren 2010)

$$\sin n\bar{\omega}\tau \, \sin\omega_{\mathrm{D}}^n(t-\tau) = \frac{1}{2}\left\{\cos[\omega_{\mathrm{D}}^n t - (\omega_{\mathrm{D}}^n + n\bar{\omega})\tau] - \cos[\omega_{\mathrm{D}}^n t - (\omega_{\mathrm{D}}^n - n\bar{\omega})\tau]\right\} \tag{2.14}$$

and the exact solutions of the following two integrations

$$\int_0^t \sin(a+b\tau)\mathrm{e}^{(c+d\tau)}\mathrm{d}\tau = \frac{1}{b^2+d^2}\left\{[d\,\sin(a+b\tau) - b\,\cos(a+b\tau)]\mathrm{e}^{(c+d\tau)}\right\}\Big|_0^t \tag{2.15a}$$

$$\int_0^t \cos(a+b\tau)\mathrm{e}^{(c+d\tau)}\mathrm{d}\tau = \frac{1}{b^2+d^2}\left\{[b\,\sin(a+b\tau) + d\,\cos(a+b\tau)]\mathrm{e}^{(c+d\tau)}\right\}\Big|_0^t \tag{2.15b}$$

and substituting Eq. (2.14) into Eq. (2.13), and by utilizing Eq. (2.15a, 2.15b), the solution of Eq. (2.13) can be obtained as

$$\begin{aligned} q_n(t) &= \frac{P}{\bar{m}L\omega_{\mathrm{D}}^n}\left\{\int_0^t \cos[\omega_{\mathrm{D}}^n t - (\omega_{\mathrm{D}}^n + n\bar{\omega})\tau]\,\mathrm{e}^{-\omega_{\mathrm{b}}(t-\tau)}\mathrm{d}\tau\right. \\ &\quad \left. - \int_0^t \cos[\omega_{\mathrm{D}}^n t - (\omega_{\mathrm{D}}^n - n\bar{\omega})\tau]\mathrm{e}^{-\omega_{\mathrm{b}}(t-\tau)}\mathrm{d}\tau\right\} \\ &= \frac{P}{\bar{m}L\omega_{\mathrm{D}}^n}\left\{\frac{1}{(\omega_{\mathrm{D}}^n + n\bar{\omega})^2 + \omega_{\mathrm{b}}^2}\left\{[(\omega_{\mathrm{D}}^n + n\bar{\omega})\sin n\omega t + \omega_{\mathrm{b}}\cos n\bar{\omega}t]\right.\right. \\ &\quad \left.\left. + [(\omega_{\mathrm{D}}^n + n\bar{\omega})\sin\omega_{\mathrm{D}}^n t - \omega_{\mathrm{b}}\cos\omega_{\mathrm{D}}^n t]\mathrm{e}^{-\omega_{\mathrm{b}}t}\right\}\right. \\ &\quad \left. - \frac{1}{(\omega_{\mathrm{D}}^n - n\bar{\omega})^2 + \omega_{\mathrm{b}}^2}\left\{[-(\omega_{\mathrm{D}}^n - n\bar{\omega})\sin n\omega t + \omega_{\mathrm{b}}\cos n\bar{\omega}t]\right.\right. \\ &\quad \left.\left. + [(\omega_{\mathrm{D}}^n - n\bar{\omega})\sin\omega_{\mathrm{D}}^n t - \omega_{\mathrm{b}}\cos\omega_{\mathrm{D}}^n t]\mathrm{e}^{-\omega_{\mathrm{b}}t}\right\}\right\} \end{aligned} \tag{2.16}$$

Note that $\omega_{\mathrm{D}}^{n2} = \omega_n^2 - \omega_{\mathrm{b}}^2$ and $\omega_{\mathrm{D}}^{n2} = 0$ are, respectively, valid in the undercritically damped case and the critically damped case, and Eq. (2.16) is rewritten separately for the two cases as

$$q_n(t) = \frac{2P}{\bar{m}L}\frac{1}{(\omega_n^2 - n^2\bar{\omega}^2)^2 + 4\omega_{\mathrm{b}}^2 n^2\bar{\omega}^2}\Big\{(\omega_n^2 - n^2\bar{\omega}^2)\sin n\bar{\omega}t - \frac{n\omega[(\omega_n^2 - n^2\bar{\omega}^2) - 2\omega_{\mathrm{b}}^2]}{(\omega_n^2 - \omega_{\mathrm{b}}^2)^{1/2}}\mathrm{e}^{-\omega_{\mathrm{b}}t}\sin\omega_{\mathrm{D}}^n t - 2\omega_{\mathrm{b}} n\bar{\omega}(\cos n\bar{\omega}t - \mathrm{e}^{-\omega_{\mathrm{b}}t}\cos\omega_{\mathrm{D}}^n t)\Big\} \tag{2.17a}$$

$$q_n(t) = \frac{2P}{\bar{m}L}\frac{1}{(\omega_n^2 + n^2\bar{\omega}^2)^2}\Big\{(\omega_n^2 - n^2\bar{\omega}^2)\sin n\omega t - 2\omega_n n\bar{\omega}\cos n\bar{\omega}t + \mathrm{e}^{-\omega_{\mathrm{b}}t}[(\omega_n^2 + n^2\bar{\omega}^2)n\bar{\omega}t + 2\omega_n n\bar{\omega}]\Big\} \tag{2.17b}$$

For convenience of discussing the influences of load moving speed and structural damping on the vibration responses of the bridge, two dimensionless parameters, i.e., speed parameter α and damping parameter μ, are introduced, which are defined by

$$\alpha = \frac{\bar{\omega}}{\omega_1} = \frac{VL}{\pi}\left(\frac{\bar{m}}{EI}\right)^{1/2} = \frac{V}{V_{\mathrm{cr}}} \tag{2.18a}$$

$$\mu = \frac{\omega_{\mathrm{b}}}{\omega_1} = \frac{\omega_{\mathrm{b}}L^2}{\pi}\left(\frac{\bar{m}}{EI}\right)^{1/2} \tag{2.18b}$$

where $V_{\mathrm{cr}} = \frac{2f_n L}{n^2} = \frac{\pi}{L}\left(\frac{EI}{\bar{m}}\right)^{1/2}$ (n = 1, 2, 3, …) means the critical speed, f_n is the nth natural frequency of the beam, and EI is the bending stiffness of the bridge. When the load moving speed is n times of the critical speed, the resonance of the nth mode will be induced. More details can be found in Sect. 2.3.

By introducing Eq. (2.18a, 2.18b), Eq. (2.17a, 2.17b) becomes

$$q_n(t) = y_0\frac{1}{n^2[n^2(n^2 - \alpha^2)^2 + 4\alpha^2\mu^2]}\Big\{n^2(n^2 - \alpha^2)\sin n\bar{\omega}t - \frac{n\alpha[n^2(n^2 - \alpha^2) - 2\mu^2]}{(n^4 - \mu^2)^{1/2}}\mathrm{e}^{-\omega_{\mathrm{b}}t}\sin\omega_{\mathrm{D}}^n t - 2n\alpha\mu(\cos n\bar{\omega}t - \mathrm{e}^{-\omega_{\mathrm{b}}t}\cos\omega_{\mathrm{D}}^n t)\Big\} \tag{2.19a}$$

$$q_n(t) = y_0\frac{1}{n^2(n^2 + \alpha^2)^2}\Big\{(n^2 - \alpha^2)\sin n\bar{\omega}t - 2n\alpha\cos n\bar{\omega}t + \mathrm{e}^{-\omega_n t}[(n^2 + \alpha^2)n\bar{\omega}t + 2n\alpha]\Big\} \tag{2.19b}$$

where $y_0 = \frac{PL^3}{48EI} \approx \frac{2PL^3}{\pi^4 EI} = \frac{2P}{\bar{m}L\omega_1^2}$, indicating the displacement of the bridge at mid-span where a concentrated force P is applied.

By the modal decomposition method, the particular solution to the displacement response of the simply-supported beam in undercritically damped case can be expressed as

$$y(x,t) = y_0 \sum_{n=1}^{\infty} \frac{1}{n^2[n^2(n^2-\alpha^2)^2 + 4\alpha^2\mu^2]} \{n^2(n^2-\alpha^2)\sin n\bar{\omega}t - \frac{n\alpha[n^2(n^2-\alpha^2)-2\mu^2]}{(n^4-\mu^2)^{1/2}} e^{-\omega_b t}\sin\omega_D^n t - 2n\alpha\mu(\cos n\bar{\omega}t - e^{-\omega_b t}\cos\omega_D^n t)\} \sin\frac{n\pi x}{L} \tag{2.20}$$

in which $q_n(t)$ is the generalized coordinate of the nth mode given by Eq. (2.19a, 2.19b).

Based on Eq. (2.20), several special cases are discussed hereinbelow.

2.1.2.1 Static Load Case ($\alpha = 0$)

When the speed parameter $\alpha = 0$, Eq. (2.20) becomes

$$y(x,t) = y_0 \sum_{n=1}^{\infty} \frac{1}{n^4} \sin\frac{n\pi x}{L} \sin n\bar{\omega}t = y_0 \sum_{n=1}^{\infty} \frac{1}{n^4} \sin\frac{n\pi x}{L} \sin\frac{n\pi Vt}{L} \tag{2.21}$$

In this case, the problem becomes the solution of the bridge displacement at position x when a static load P acts at position Vt. Herein, Vt indicates the moving distance of the load on the bridge. Equation (2.21) can be regarded as the Fourier expansion of the influence line of bridge displacement at position x, or the Fourier expansion of the bridge deflection curve when a concentrated load P acts at the position Vt.

2.1.2.2 Undamped Case ($\mu = 0$)

(1) $\alpha \neq k$, $\mu = 0$

As will be demonstrated later, when the speed parameter of the load meets $\alpha = k$, the resonance with the nth mode can be caused. Hence, the load speed corresponding to $\alpha = k$ is called as the resonant speed.

First, consider the case where the load moves on the bridge at non-resonance speed, i.e., $\alpha \neq k$.

In the undamped case $\mu = 0$, Eq. (2.20) becomes

$$y(x,t) = y_0 \sum_{n=1}^{\infty} \sin\frac{n\pi x}{L} \frac{1}{n^2(n^2-\alpha^2)} \left(\sin n\bar{\omega}t - \frac{\alpha}{n}\sin\omega_n t\right) \tag{2.22}$$

According to this equation, the first-order mode contributes most to the displacement, which means high precision can be reached by using the first-order vibration mode when solving the bridge displacement under dynamic loads.

Considering the terms within the parentheses of Eq. (2.22), and letting them equal to zero at the time when the load is about to leave the bridge, namely at $t = L/V$, the following equation is obtained

$$\left(\sin n\bar{\omega}t - \frac{\alpha}{n}\sin\omega_n t\right)\Big|_{t=\frac{L}{V}} = \sin n\pi - \frac{\alpha}{n}\sin\frac{n^2\pi}{\alpha} = 0 \tag{2.23}$$

It is easy to see when $\alpha = n^2/k$ ($k = 1, 2, 3, \ldots, k \neq n$), Eq. (2.23) is valid. Assuming $\alpha = n^2/k$ corresponds to a speed V_{can}, we have

$$\alpha = \frac{V_{can}}{V_{cr}} \Rightarrow V_{can} = \alpha V_{cr} \tag{2.24}$$

By substituting Eq. (2.18a) into Eq. (2.24), and using the theoretical frequency of the simply-supported beam $f_1 = f_n/n^2$, V_{can} can be expressed as

$$V_{can} = \alpha V_{cr} = \frac{n^2}{k} \cdot \frac{2f_n L}{n^2} = 2n^2 f_1 L/k \tag{2.25}$$

Equations (2.22) and (2.23) show that when $\alpha = n^2/k$, the bridge displacement component of the nth vibration mode becomes null at the time $t = L/V$, and thus, V_{can} is called the cancellation speed corresponding to the nth vibration mode of the beam.

When the load moves out of the bridge, i.e., when $t > L/V$, the beam is in free vibration. The displacement solution of the bridge will be

$$y(x,t) = \sum_{n=1}^{\infty} \left[\frac{\dot{y}_n(x, L/V)}{\omega_n}\sin\omega_n t + y_n(x, L/V)\cos\omega_n t\right] \tag{2.26}$$

where $y_n(x, L/V)$ and $\dot{y}_n(x, L/V)$ are, respectively, displacement and velocity of the bridge at $t = L/V$, which can be expressed as

$$y_n(x, L/V) = \frac{y_0}{n^2(n^2-\alpha^2)} \left(\sin\frac{n\bar{\omega}L}{V} - \frac{\alpha}{n}\sin\frac{\omega_n L}{V}\right) \sin\frac{n\pi x}{L} \tag{2.27a}$$

$$\dot{y}_n(x, L/V) = \frac{n\bar{\omega}y_0}{n^2(n^2-\alpha^2)}\left(\cos\frac{n\bar{\omega}L}{V} - \cos\frac{\omega_n L}{V}\right)\sin\frac{n\pi x}{L} \tag{2.27b}$$

At the moment when the load moves out of the bridge at the cancellation speed V_{can}, the vibration velocity of the bridge is not necessarily equal to zero, while it can be expressed as

$$\begin{aligned}\dot{y}(x,t)|_{t=\frac{L}{V}} &= \left(V\frac{\partial y(x,t)}{\partial x} + \frac{\partial y(x,t)}{\partial t}\right)\Bigg|_{t=L/V} \\ &= y_0\sum_{n=1}^{\infty}\sin\frac{n\pi x}{L}\frac{n\bar{\omega}}{n^2(n^2-\alpha^2)}(\cos n\pi - \cos k\pi)\end{aligned} \tag{2.28}$$

It can be observed from Eq. (2.28) that when n and k have the same parity, Eq. (2.26) equals zero, indicating no displacement and velocity exist on the bridge after the load leaves the bridge, namely the bridge becomes motionless. When n and k are with different parity, only the displacement is zero, while the velocity is not, which makes the bridge continue to vibrate, namely as a residual vibration. Correspondingly, V_{can} given in Eq. (2.25) is defined as full cancellation speed in the case with same parity and as the displacement cancellation speed with different parity.

When a series of loads travels at full cancellation speed, the vibration of the bridge will totally disappear after all the loads leave the bridge, due to the linear superposition of all null displacements induced by the loads.

(2) $\alpha = k$, $\mu = 0$

In the case of $\alpha = k$ and $\mu = 0$, Eq. (2.20) becomes an indeterminate form due to 0/0, and its extreme value can be evaluated by applying the L'Hospital's rule. Thus, the particular solution of the bridge displacement can be expressed as

$$\begin{aligned}y(x,t) = {} & y_0\frac{1}{2k^4}(\sin k\bar{\omega}t - k\bar{\omega}t\cos k\bar{\omega}t)\sin\frac{k\pi x}{L} \\ & + y_0\sum_{n=1,n\neq k}^{\infty}\sin\frac{n\pi x}{L}\frac{1}{n^2(n^2-\alpha^2)}\left(\sin n\bar{\omega}t - \frac{\alpha}{n}\sin\omega_n t\right)\end{aligned} \tag{2.29}$$

It is found that when $\alpha = k$ and $\mu = 0$, the bridge displacement at any position x increases with the time t and reaches to the maximum value at $t = L/V$, but not to infinity.

This situation is equivalent to the occurrence of resonance between the bridge and the moving load P. When $k = n$, i.e., $\sin(n\pi Vt/L) = \sin n\bar{\omega}t$, the loading frequency of the moving load coincides with the natural frequency of the nth bridge mode. Moreover, in the case of $k = 1$, the dynamic amplification factor of resonant displacements reaches the maximum, which again indicates that the first mode contributes most to the displacement.

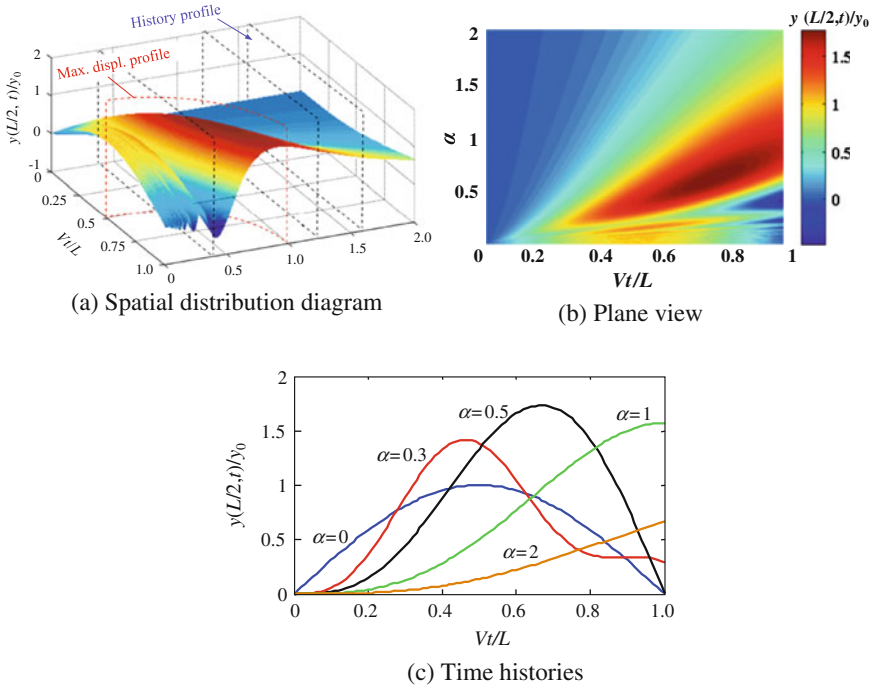

(a) Spatial distribution diagram

(b) Plane view

(c) Time histories

Fig. 2.2 Distributions of mid-span displacement $y(L/2, t)/y_0$ versus time Vt/L and load speed α ($\mu = 0$)

Shown in Fig. 2.2a is the spatial distribution of bridge mid-span displacement subjected to a single moving load, herein expressed with the relative displacement $y(L/2, t)/y_0$ versus time parameter Vt/L and speed parameter α, and in Fig. 2.2b is its plane view. In Fig. 2.2a, the intersecting lines of the curved surfaces with the planar α are the displacement time histories of the bridge, respectively, related to various load speeds of $\alpha = 0$, 0.3, 0.5, 1, 2, as shown in Fig. 2.2c. It is found that at low speed, the maximum mid-span displacement appears when the load is near the bridge center. With the increase of speed, the load position producing the maximum mid-span displacement shifts toward the beam-end, and at certain speed, the mid-span displacement reaches the maximum just at the moment when the load is leaving the bridge.

Shown in Fig. 2.3 is the variation of maximum relative displacement $y_{max}(L/2, t)/y_0$ of the bridge at mid-span versus load speed parameter α. It is found that the maximum displacement does not increase monotonously with the load speed, while some peaks appear at certain speeds, fluctuating in a pattern similar to half sine wave series.

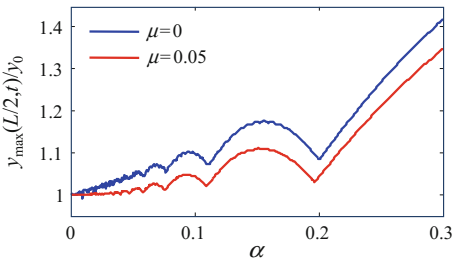

Fig. 2.3 Relation of maximum mid-span displacements with load speed α ($\mu = 0$ and $\mu = 0.05$)

2.1.2.3 Undercritically Damped Case

(1) $\alpha \neq k$, $\mu \ll 1$

When the bridge is undercritically damped, μ and μ^2 in Eq. (2.20) can be neglected, and the following formula similar to Eq. (2.22) can be obtained

$$y(x,t) \approx y_0 \sum_{n=1}^{\infty} \sin\frac{n\pi x}{L} \frac{1}{n^2(n^2-\alpha^2)} \left(\sin n\bar{\omega}t - \frac{\alpha}{n} e^{-\omega_b t} \sin \omega_n t\right) \tag{2.30}$$

Equation (2.30) is very practical in engineering, because the damping of bridges is usually very small, and the driving speed of actual vehicles can never achieve the case of $\alpha = k$ ($V = kV_{cr}$). For example, for the bridge with the span of $L = 32$ m, the first natural frequency $f_1 = 4.5$ Hz, and $k = 1$, the critical speed is calculated as $V_{cr} = 2f_1L = 288$ m/s (1036.8 km/h), which is much higher than the current train speed.

When the train speed is low, there is $\alpha \ll 1$. If the vehicle mass is small compared to the bridge mass, the vehicle can be modeled as a series of moving concentrated loads by ignoring its mass. In this case, the bridge displacement under train loads can be solved by considering only the first-order mode. Thus, the simplified solution of bridge displacement under a single moving load is expressed as

$$y(x,t) \approx y_0 \sin\frac{\pi x}{L} \sin n\bar{\omega}t \tag{2.31}$$

(2) $\alpha = k$, $\mu \ll 1$

The derivation in this case is similar to that when $\alpha = k$, $\mu = 0$, and the bridge displacement is directly given by

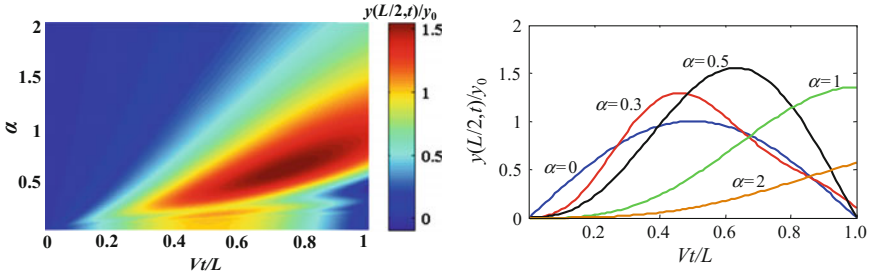

(a) Plane view (b) Time history

Fig. 2.4 Distribution of mid-span displacement $y(L/2, t)/y_0$ versus time Vt/L and velocity α ($\mu = 0.05$)

$$y(x,t) \approx y_0 \frac{1}{2k^4}\left[e^{-\omega_b t}\sin k\bar{\omega}t - \frac{k^2}{\mu}(1-e^{-\omega_b t})\cos k\bar{\omega}t\right]\sin\frac{k\pi x}{L} + y_0\sum_{n=1,n\neq k}^{\infty}\frac{1}{n^2(n^2-\alpha^2)}\left(\sin n\bar{\omega}t - \frac{\alpha}{n}e^{-\omega_b t}\sin\omega_n t\right)\sin\frac{n\pi x}{L} \tag{2.32}$$

Shown in Fig. 2.4a is the plane view of mid-span displacement distribution of the undercritically damped bridge ($\mu = 0.05$) varying with time Vt/L and load speed α, and in Fig. 2.4b are the time history curves of $y(L/2, t)/y_0$ versus Vt/L in various speed parameters. The variation of maximum displacement $y_{max}(L/2, t)/y_0$ versus load speed α is demonstrated in Fig. 2.3. By comparing the curves in the two damping cases, it can be found that the damping effect decreases the bridge displacement, but does not obviously change the variation trend of maximum displacement with speed parameter.

2.1.2.4 Critically Damped Case ($\mu = \mu_{cr} = k^2$)

When the damping ratio ξ_k is equal to 1, the kth mode of the bridge is critically damped, and thus, the critical damping parameter becomes

$$\mu_{cr} = \frac{\omega_b}{\omega_1} = \frac{\xi_k\omega_k}{\omega_1} = k^2 \tag{2.33}$$

In this case, the generalized coordinate $q_k(t)$ of the kth mode of the simply-supported beam can be described by Eq. (2.19b), and the contribution of the kth mode to the displacement is

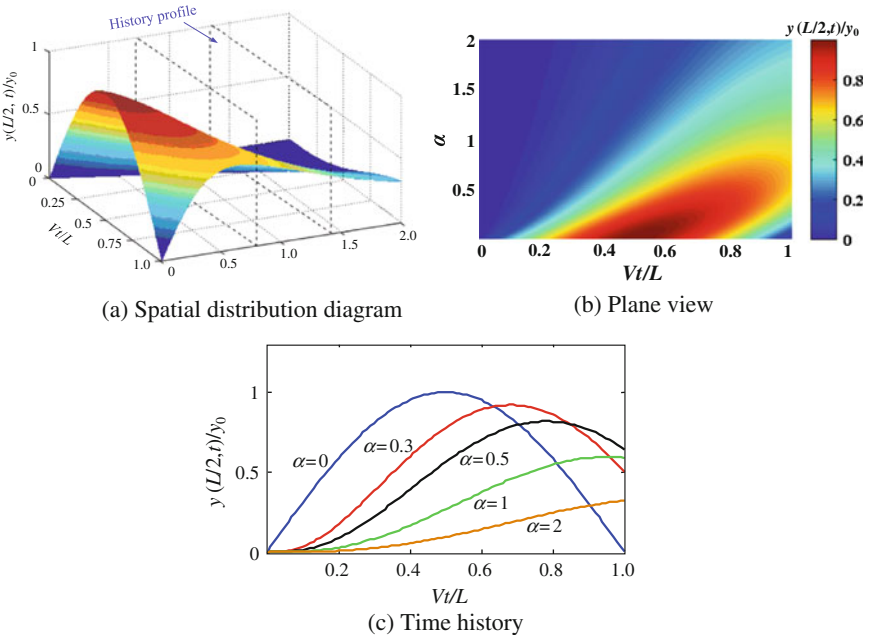

(a) Spatial distribution diagram

(b) Plane view

(c) Time history

Fig. 2.5 Distributions of mid-span displacement $y(L/2, t)/y_0$ versus time Vt/L and load speed α ($\mu = 1$)

$$y_k(x,t) = q_k(t)\sin\frac{k\pi x}{L} = y_0\frac{1}{k^2(k^2+\alpha^2)^2}\left\{(k^2-\alpha^2)\sin k\bar{\omega}t - 2k\alpha\cos k\bar{\omega}t + \mathrm{e}^{-\omega_k t}\left[(k^2+\alpha^2)k\bar{\omega}t + 2k\alpha\right]\right\}\sin\frac{k\pi x}{L} \tag{2.34}$$

When the bridge is critically damped, there is $\mu = \mu_{cr} = k^2$, which is not the critical damping for all the modes. When $n > k$, the nth mode is undercritically damped, and the corresponding generalized coordinate $q_n(t)$ can be solved by Eq. (2.17a). When $n < k$, the nth mode is overcritically damped, and the corresponding generalized coordinate $q_n(t)$ will be discussed in the next section.

Shown in Fig. 2.5a is the critically damped case, the spatial distribution of mid-span displacements of the bridge versus time parameter Vt/L, and load speed parameter α, in Fig. 2.5b is its plane view, and in Fig. 2.5c are the displacement time histories of the bridge related to various load speeds of $\alpha = 0, 0.3, 0.5, 1, 2$.

2.1.2.5 Overcritically Damped Case ($\mu > \mu_{cr} = k^2$)

According to the previous discussion, if the kth mode of the bridge is critically damped, the nth mode ($n < k$) will be overcritically damped, namely

$$\xi_n = \frac{\xi_k \omega_k}{\omega_n} = \frac{\omega_k}{\omega_n} > 1, \quad n < k \tag{2.35}$$

In the overcritically damped case, Eq. (2.12) is no longer valid, so the Duhamel integral solution to Eq. (2.11) becomes

$$q_n(t) = \frac{2}{\bar{m} L \omega_{\mathrm{D}}^n} \int_0^t P(\tau) \sin n\bar{\omega}\tau \cdot \mathrm{e}^{-\omega_{\mathrm{b}}(t-\tau)} \cdot \sinh \omega_{\mathrm{D}}^n (t-\tau) \mathrm{d}\tau \tag{2.36}$$

where $\omega_{\mathrm{D}}^n = \omega_n \sqrt{\xi_n^2 - 1}$ is the damped natural frequency of the nth mode, and $\sinh \omega_{\mathrm{D}}^n (t-\tau) = [\mathrm{e}^{\omega_{\mathrm{D}}^n (t-\tau)} - \mathrm{e}^{-\omega_{\mathrm{D}}^n (t-\tau)}]/2$.

The solution to the nth general coordinate is given by

$$\begin{aligned} q_n(t) = y_0 & \frac{1}{n^2[n^2(n^2-\alpha^2)^2 + 4\alpha^2\mu^2]} \left\{ n^2(n^2-\alpha^2) \sin n\bar{\omega}t - 2n\alpha\mu \cos n\bar{\omega}t \right. \\ & + \frac{n\alpha \mathrm{e}^{-\omega_{\mathrm{b}}t}}{2(\mu^2 - n^4)^{1/2}} \left\{ \left[2\mu^2 - n^2(n^2-\alpha^2) + 2\mu(\mu^2 - n^4)^{1/2} \right] \mathrm{e}^{\omega_{\mathrm{D}}^n t} \right. \\ & \left. \left. - \left[2\mu^2 - n^2(n^2-\alpha^2) - 2\mu(\mu^2 - n^4)^{1/2} \right] \mathrm{e}^{-\omega_{\mathrm{D}}^n t} \right\} \right\} \end{aligned} \tag{2.37}$$

and the displacement component of the simply-supported beam related to the nth ($n < k$) mode can be expressed as

$$\begin{aligned} y_n(x,t) = y_0 & \frac{1}{n^2[n^2(n^2-\alpha^2)^2 + 4\alpha^2\mu^2]} \left\{ n^2(n^2-\alpha^2) \sin n\bar{\omega}t - 2n\alpha\mu \cos n\bar{\omega}t \right. \\ & + \frac{n\alpha \mathrm{e}^{-\omega_{\mathrm{b}}t}}{2(\mu^2 - n^4)^{1/2}} \left\{ \left[2\mu^2 - n^2(n^2-\alpha^2) + 2\mu(\mu^2 - n^4)^{1/2} \right] \mathrm{e}^{\omega_{\mathrm{D}}^n t} \right. \\ & \left. \left. - \left[2\mu^2 - n^2(n^2-\alpha^2) - 2\mu(\mu^2 - n^4)^{1/2} \right] \mathrm{e}^{-\omega_{\mathrm{D}}^n t} \right\} \right\} \sin \frac{n\pi x}{L} \end{aligned} \tag{2.38}$$

Demonstrated in Fig. 2.6 is, in the overcritically damped ($\mu = 2$) case, the relationship between the relative displacement at the mid-span and the time parameter Vt/L and load speed parameter α.

2.1.3 Displacement of Bridge Subjected to a Moving Load Series

The analytical solutions above are valid for the bridge displacements induced by a single constant moving load. When performing dynamic analysis of the train-bridge system, the train load can be modeled as a moving load series composed of N loads

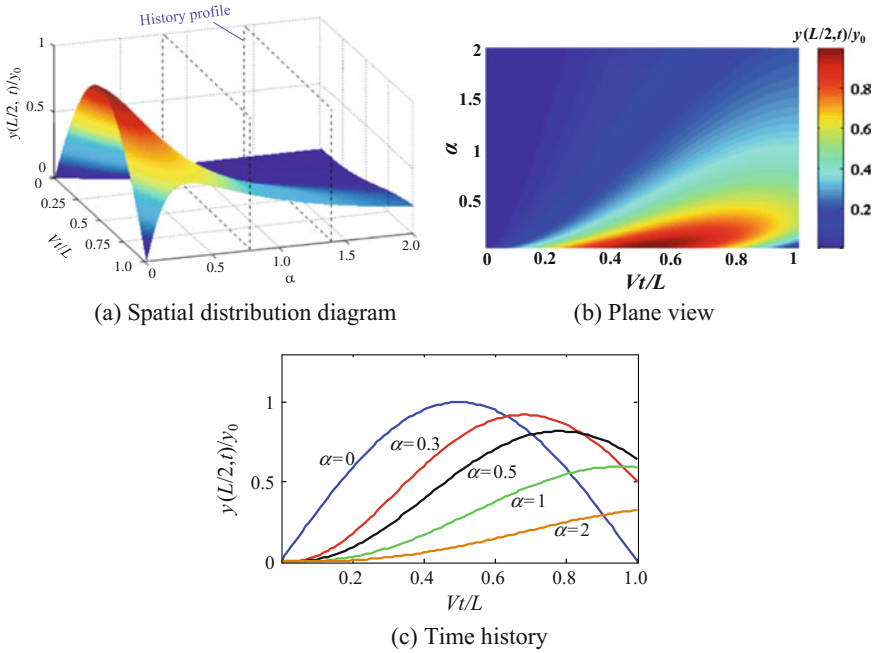

(a) Spatial distribution diagram

(b) Plane view

(c) Time history

Fig. 2.6 Distributions of mid-span displacement $y(L/2, t)/y_0$ versus time Vt/L and load speed α ($\mu = 2$)

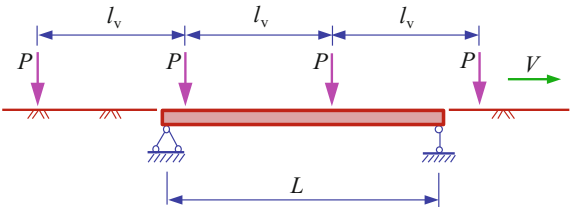

Fig. 2.7 Train load series moving on a simply-supported beam

with identical intervals equal to the vehicle length l_v, as shown in Fig. 2.7. By assuming small deformation for the beam, the displacement of the bridge under the load series can be directly written as the superposition of all responses induced by individual moving loads

$$y(x,t) = \sum_{i=0}^{N-1} y_i \left[x, \left(t - \frac{i \cdot l_v}{V} \right) \right] \tag{2.39}$$

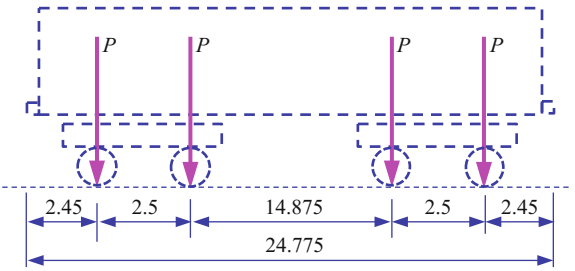

Fig. 2.8 Wheelbases of a German ICE3 car (Unit: m)

where $y_i(x, t)$ is the bridge displacement induced by the ith load of the moving load series.

Assuming the initial status of the bridge is still, the response of the bridge induced by each force of the moving load series can be analyzed in three phases. Before the force enters, the bridge does not vibrate, and $y_i(x, t)$ is zero. During the force moves on the beam, the bridge is in forced vibration, and $y_i(x, t)$ can be obtained by Eq. (2.19a, 2.19b). After the force leaves, the bridge is in free vibration, and $y_i(x, t)$ can be solved by Eq. (2.26).

Using the above method, the mid-span displacements of a simply-supported bridge under moving load series are calculated. The span of the bridge is $L = 32$ m, the fundamental frequency is $f_1 = 4.5$ Hz, and two damping ratios are considered as $\xi = 0, 0.05$, namely $\mu = 0, 0.05$. The moving load series consists of 32 concentrated forces, which are arranged according to the axle loads and wheelbases of the German ICE3 high-speed train composed of (3 motor-cars +1 trailer car) $\times$ 2, and each car has four wheel-sets, as shown in Fig. 2.8. The calculated displacement time histories of the bridge at mid-span are shown in Fig. 2.9.

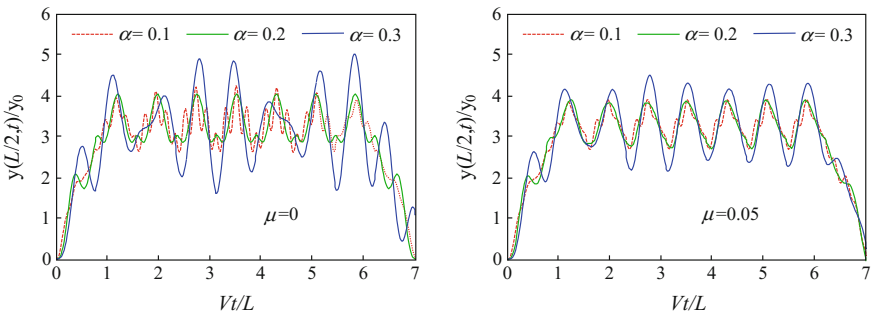

Fig. 2.9 Mid-span displacement time histories of the bridge

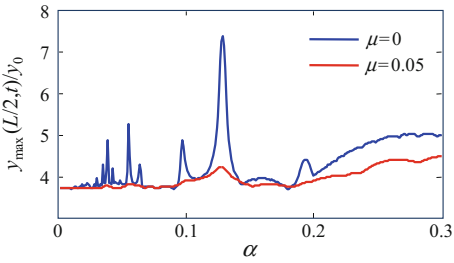

Fig. 2.10 Maximum defections at mid-span versus velocity and damping

Shown in Fig. 2.10 are the variations of maximum relative displacement $y_{\max}(L/2, t)/y_0$ of the bridge at mid-span versus load speed parameter α. It can be found that the periodic excitations by successive action of the concentrated force series induce several displacement peaks at certain speeds, indicating the resonant responses of the bridge, which are quite different from the regularity by a single moving load. The damping effect can reduce the maximum displacement and obviously depress the resonant response of the bridge. Detailed derivation of bridge resonance induced by moving load series can be found in Sect. 2.3.

2.1.4 *Analytical Solution for Vibration of Simply-Supported Beam Under a Moving Harmonic Load*

In this case, $P(t) = P \sin \theta t$, and thus, Eq. (2.12) can be expressed as

$$q_n(t) = \frac{2P}{\bar{m}L\omega_{\mathrm{D}}^n} \int_0^t \sin\theta\tau \sin n\bar{\omega}\tau \sin\omega_{\mathrm{D}}^n(t-\tau)\mathrm{e}^{-\omega_{\mathrm{b}}(t-\tau)}\mathrm{d}\tau \tag{2.40}$$

The following triangle transformation formula is utilized for the above integral

$$\begin{aligned}\sin\theta\tau \sin n\bar{\omega}\tau \sin\omega_{\mathrm{D}}^n(t-\tau) = \frac{1}{4}\{&\sin\left[\omega_{\mathrm{D}}^n t + \left(r_2 - \omega_{\mathrm{D}}^n\right)\tau\right] + \sin\left[\omega_{\mathrm{D}}^n t - \left(r_2 + \omega_{\mathrm{D}}^n\right)\tau\right] \\ &- \sin\left[\omega_{\mathrm{D}}^n t + \left(r_1 - \omega_{\mathrm{D}}^n\right)\tau\right] - \sin\left[\omega_{\mathrm{D}}^n t - \left(r_1 + \omega_{\mathrm{D}}^n\right)\tau\right]\}\end{aligned} \tag{2.41}$$

where $r_1 = \theta + n\bar{\omega}$, and $r_2 = \theta - n\bar{\omega}$.

Substituting Eq. (2.41) into Eq. (2.40), and using Eq. (2.15a, 2.15b), the precise integral solution of Eq. (2.40) can be deduced as

$$
\begin{aligned}
q_n(t) &= \frac{P}{2\bar{m}L\omega_{\mathrm{D}}^n}\left\{\int_0^t \sin\left[\omega_{\mathrm{D}}^n t + (r_2 - \omega_{\mathrm{D}}^n)\tau\right]\mathrm{e}^{-\omega_{\mathrm{b}}(t-\tau)}\mathrm{d}\tau + \int_0^t \sin\left[\omega_{\mathrm{D}}^n t - (r_2 + \omega_{\mathrm{D}}^n)\tau\right]\mathrm{e}^{-\omega_{\mathrm{b}}(t-\tau)}\mathrm{d}\tau\right. \\
&\quad \left. - \int_0^t \sin\left[\omega_{\mathrm{D}}^n t + (r_1 - \omega_{\mathrm{D}}^n)\tau\right]\mathrm{e}^{-\omega_{\mathrm{b}}(t-\tau)}\mathrm{d}\tau - \int_0^t \sin\left[\omega_{\mathrm{D}}^n t - (r_1 + \omega_{\mathrm{D}}^n)\tau\right]\mathrm{e}^{-\omega_{\mathrm{b}}(t-\tau)}\mathrm{d}\tau\right\} \\
&= \frac{P}{2\bar{m}L\omega_{\mathrm{D}}^n}\left\{\frac{1}{(r_2 - \omega_{\mathrm{D}}^n)^2 + \omega_{\mathrm{b}}^2}\left\{\left[\omega_{\mathrm{b}}\sin r_2 t - (r_2 - \omega_{\mathrm{D}}^n)\cos r_2 t\right] - \left[\omega_{\mathrm{b}}\sin\omega_{\mathrm{D}}^n t - (r_2 - \omega_{\mathrm{D}}^n)\cos\omega_{\mathrm{D}}^n t\right]\mathrm{e}^{-\omega_{\mathrm{b}}t}\right\}\right. \\
&\quad + \frac{1}{(r_2 + \omega_{\mathrm{D}}^n)^2 + \omega_{\mathrm{b}}^2}\left\{\left[-\omega_{\mathrm{b}}\sin r_2 t + (r_2 + \omega_{\mathrm{D}}^n)\cos r_2 t\right] - \left[\omega_{\mathrm{b}}\sin\omega_{\mathrm{D}}^n t + (r_2 + \omega_{\mathrm{D}}^n)\cos\omega_{\mathrm{D}}^n t\right]\mathrm{e}^{-\omega_{\mathrm{b}}t}\right\} \\
&\quad - \frac{1}{(r_1 - \omega_{\mathrm{D}}^n)^2 + \omega_{\mathrm{b}}^2}\left\{\left[\omega_{\mathrm{b}}\sin r_1 t - (r_1 - \omega_{\mathrm{D}}^n)\cos r_1 t\right] - \left[\omega_{\mathrm{b}}\sin\omega_{\mathrm{D}}^n t - (r_1 - \omega_{\mathrm{D}}^n)\cos\omega_{\mathrm{D}}^n t\right]\mathrm{e}^{-\omega_{\mathrm{b}}t}\right\} \\
&\quad \left. - \frac{1}{(r_1 + \omega_{\mathrm{D}}^n)^2 + \omega_{\mathrm{b}}^2}\left\{\left[-\omega_{\mathrm{b}}\sin r_1 t + (r_1 + \omega_{\mathrm{D}}^n)\cos r_1 t\right] - \left[\omega_{\mathrm{b}}\sin\omega_{\mathrm{D}}^n t + (r_1 + \omega_{\mathrm{D}}^n)\cos\omega_{\mathrm{D}}^n t\right]\mathrm{e}^{-\omega_{\mathrm{b}}t}\right\}\right\}
\end{aligned}
\tag{2.42}
$$

In the undercritically damped case, $\omega_{\mathrm{D}}^{n2} = \omega_n^2 - \omega_{\mathrm{b}}^2$, Eq. (2.42) can be rearranged as

$$
\begin{aligned}
q_n(t) = \frac{P}{\bar{m}L}&\left\{\frac{1}{(\omega_n^2 - r_2^2)^2 + 4\omega_{\mathrm{b}}^2 r_2^2}\left[(\omega_n^2 - r_2^2)\left(\cos r_2 t - \mathrm{e}^{-\omega_{\mathrm{b}}t}\cos\omega_{\mathrm{D}}^n t\right)\right.\right. \\
&\left. + 2\omega_{\mathrm{b}} r_2 \sin r_2 t - \frac{\omega_{\mathrm{b}}}{\omega_{\mathrm{D}}^n}(\omega_n^2 + r_2^2)\mathrm{e}^{-\omega_{\mathrm{b}}t}\sin\omega_{\mathrm{D}}^n t\right] \\
&- \frac{1}{(\omega_n^2 - r_1^2)^2 + 4\omega_{\mathrm{b}}^2 r_1^2}\left[(\omega_n^2 - r_1^2)\left(\cos r_1 t - \mathrm{e}^{-\omega_{\mathrm{b}}t}\cos\omega_{\mathrm{D}}^n t\right)\right. \\
&\left.\left. + 2\omega_{\mathrm{b}} r_1 \sin r_1 t - \frac{\omega_{\mathrm{b}}}{\omega_{\mathrm{D}}^n}(\omega_n^2 + r_1^2)\mathrm{e}^{-\omega_{\mathrm{b}}t}\sin\omega_{\mathrm{D}}^n t\right]\right\}
\end{aligned}
\tag{2.43}
$$

Based on the generalized coordinates obtained from Eq. (2.43), the particular solution for the displacement of the simply-supported beam under a moving harmonic load can be written as

$$
\begin{aligned}
y(x,t) = \frac{y_0}{2}\sum_{n=1}^{\infty}&\left\{\frac{\omega_1^2}{(\omega_n^2 - r_2^2)^2 + 4\omega_{\mathrm{b}}^2 r_2^2}\left[(\omega_n^2 - r_2^2)\left(\cos r_2 t - \mathrm{e}^{-\omega_{\mathrm{b}}t}\cos\omega_{\mathrm{D}}^n t\right)\right.\right. \\
&\left. + 2\omega_{\mathrm{b}} r_2 \sin r_2 t - \frac{\omega_{\mathrm{b}}}{\omega_{\mathrm{D}}^n}(\omega_n^2 + r_2^2)\mathrm{e}^{-\omega_{\mathrm{b}}t}\sin\omega_{\mathrm{D}}^n t\right] \\
&- \frac{\omega_1^2}{(\omega_n^2 - r_1^2)^2 + 4\omega_{\mathrm{b}}^2 r_1^2}\left[(\omega_n^2 - r_1^2)\left(\cos r_1 t - \mathrm{e}^{-\omega_{\mathrm{b}}t}\cos\omega_{\mathrm{D}}^n t\right)\right. \\
&\left.\left. + 2\omega_{\mathrm{b}} r_1 \sin r_1 t - \frac{\omega_{\mathrm{b}}}{\omega_{\mathrm{D}}^n}(\omega_n^2 + r_1^2)\mathrm{e}^{-\omega_{\mathrm{b}}t}\sin\omega_{\mathrm{D}}^n t\right]\right\}\sin\frac{n\pi x}{L}
\end{aligned}
\tag{2.44}
$$

in which $q_n(t)$ is the generalized coordinate of the nth mode.

According to engineering practice, some additional conditions are herein introduced to simplify Eq. (2.44). For example, for solution of bridge displacement, sufficiently precise can be obtained by considering the first-order mode, so only

$n = 1$ is taken. For a real bridge, the dimensionless parameters α and μ are usually very small, i.e., $\alpha \ll 1$ and $\mu \ll 1$. Accordingly, Eq. (2.44) can be rewritten as

$$y(x,t) = y_0 \frac{\omega_1^2}{\theta^2} \frac{1}{\left(\frac{\omega_1^2}{\theta^2} - 1\right)^2 + 4\left(\frac{\bar{\omega}^2}{\theta^2} + \frac{\omega_b^2}{\theta^2}\right)} \left\{ \left[\left(\frac{\omega_1^2}{\theta^2} - 1\right)^2 + 4\frac{\omega_b^2}{\theta^2} \right]^{1/2} \sin(\theta t + \varphi) \sin \bar{\omega} t \right.$$
$$\left. + 2\frac{\bar{\omega}}{\theta}(\cos\theta t \cos\bar{\omega} t - e^{-\omega_b t} \cos\omega_1 t) \right\} \sin\frac{\pi x}{L} \tag{2.45}$$

where $\varphi = \tan^{-1}\left(-\frac{2\omega_b/\theta}{\omega_1^2/\theta^2 - 1}\right)$.

To better describe the frequency effect of the harmonic load, a dimensionless parameter, frequency ratio, is introduced, expressed as

$$\gamma = \frac{\theta}{\omega_1} \tag{2.46}$$

where θ is the frequency of the harmonic load, and μ_1 is the fundamental frequency of the bridge.

Under $\mu = 0.05$ and various frequency ratios, the distributions of mid-span displacement $y(L/2, t)/y_0$ of the bridge versus time parameter Vt/L and load speed parameter α are shown in Fig. 2.11.

According to Eq. (2.46), when the loading frequency θ is close or equal to the first-order frequency ω_1 of the bridge, the maximum bridge dynamic response can be observed. In this case, Eq. (2.45) can be rewritten as

$$y(x,t) = y_0 \frac{\omega_1}{2} \frac{\cos\omega_1 t}{\bar{\omega}^2 + \omega_b^2} [\omega(\cos\bar{\omega} t - e^{-\omega_b t}) - \omega_b \sin\bar{\omega} t] \sin\frac{\pi x}{L} \tag{2.47}$$

Dynamic amplification factor

Herein, the dynamic amplification factor (DAF) is defined as the ratio of the maximum mid-span deflection of the bridge caused by the moving harmonic load $P(t) = P \sin\theta t$ to the deflection induced by the static load P, denoted as

$$D_{1/2} = \frac{\max[y(L/2, t)]}{y_0} \tag{2.48}$$

To investigate the variations of the bridge DAF versus loading frequency ratio γ and load speed parameter α, the maximum mid-span displacements of the bridge are calculated, considering different loading frequencies and load speeds in the undercritically damped case ($\mu = 0.05$), and the results are shown in Fig. 2.12.

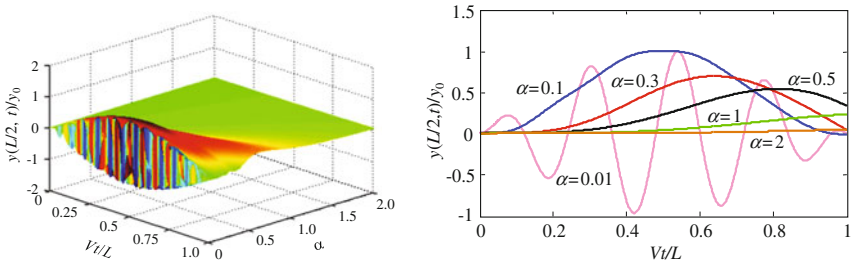

(a) $\gamma = 0.1$

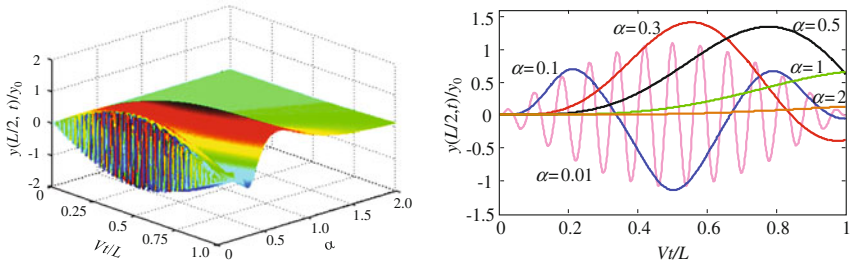

(b) $\gamma = 0.3$

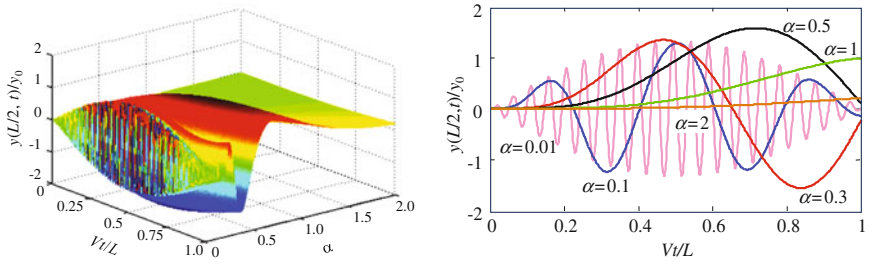

(c) $\gamma = 0.5$

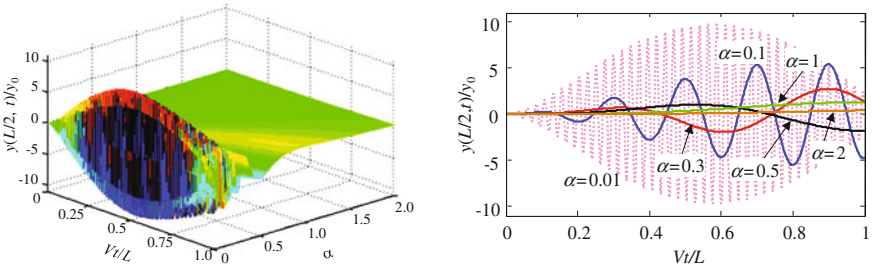

(d) $\gamma = 1.0$

Fig. 2.11 Distributions of mid-span displacement $y(L/2, t)/y_0$ of the bridge versus Vt/L and α under a harmonic load with various frequencies ($\mu = 0.05$)

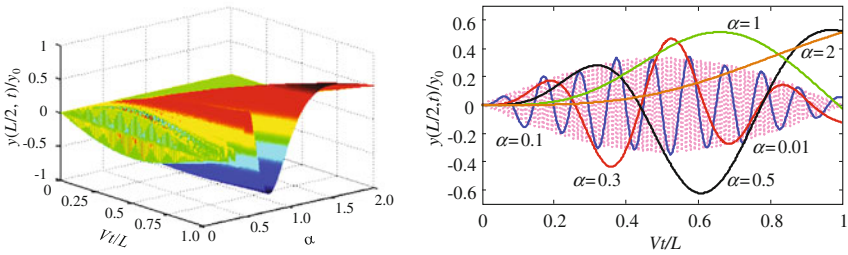

(e) γ = 2.0

Fig. 2.11 (continued)

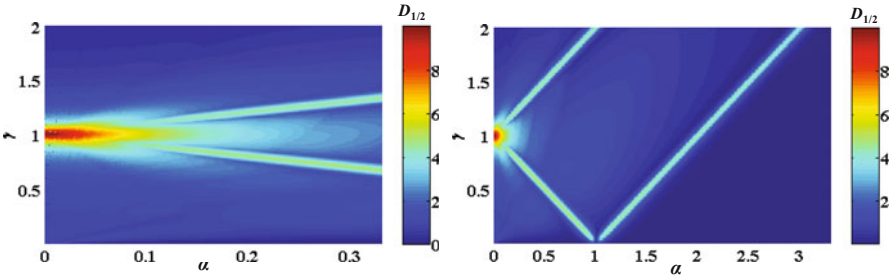

(a) $\alpha = 0 \sim 0.3$ (b) $\alpha = 0 \sim 3$

Fig. 2.12 Variations of bridge DAF versus loading frequency ratio γ and speed parameter α ($\mu = 0.05$)

It can be found that when the load speed is small, the loading frequency has little influence, and thus, the displacement response is similar to that under static load and reaches the maximum at $\gamma = 1$. With the increase of load speed, the influence of loading frequency on bridge displacement enlarges, the bridge DAF at $\gamma = 1$ gradually decreases, and the loading frequency corresponding to the maximum DAF changes, no longer at $\gamma = 1$.

An interesting phenomenon associated with the bridge displacement response can be observed in Fig. 2.12b. Considering the two axis planes as a mirror, the line connecting the maximum displacement points is equivalent to a ray with 45° incident, producing a peak displacement at the intersection position ($\alpha = 0$, $\gamma = 1$) with the mirror. This phenomenon is called the ray reflection effect of the maximum displacement response. In the figure, $D_{1/2}$ is nearly zero when γ is around null (i.e., $\theta \approx 0$), since $P(t) = P \sin \theta t \approx 0$. Hence, the displacement induced by a moving constant load cannot be directly obtained from Eq. (2.44) for the moving harmonic load by setting $\gamma = 0$.

2.2 Vibration of Simply-Supported Beam Under Moving Loads with Variable Speed

In the previous sections, the analysis method and the dynamic response characteristics of a simply-supported beam under moving concentrated load and harmonic load were introduced, and in Xia and Zhang (2005) and Xia et al. (2012), the cases considering moving uniformly distributed mass and the moving vehicle with sprung-mass were discussed. All the above-mentioned loads are moving at constant speed, while in fact, moving vehicles are usually subjected to acceleration and deceleration. In this section, the investigation is extended to a more general case, i.e., the vibration of a simply-supported beam subjected to a moving wheel-spring-mass (WSM) load with variable speed.

2.2.1 *Calculation Model*

The calculation model of the simply-supported beam under a moving WSM load with variable speed is shown in Fig. 2.13. The moving WSM load is composed of a wheel (unsprung-mass) M_1, a sprung-mass M_2, a spring k_1, and a dashpot c_1.

In the analysis, the initial speed of the load is V_0, the acceleration is $a(t)$, the speed at time t is $V(t)$, the moved distance is $s(t)$, the dynamic deflection of the beam is $y(x, t)$, and the movement of the sprung-mass M_2 is $Z(t)$. By assuming the wheel M_1 moves along the beam without detachment, the deflection of the wheel M_1 is consistent with that of the beam at the position of the wheel.

The sprung-mass M_2 is subjected to the inertial force $P_{I2} = M_2\ddot{Z}(t)$, the elastic force $P_S = k_1[Z(t) - y(x,t)]|_{x=s(t)}$ due to the relative displacement between M_2 and M_1, and the damping force $P_D' = c_1[\dot{Z}(t) - \dfrac{\mathrm{d}y(x,t)}{\mathrm{d}t}]|_{x=s(t)}$ due to the relative velocity between M_2 and M_1. By considering the equilibrium of forces on M_2 shown in Fig. 2.13, the motion equation for the sprung-mass M_2 can be derived as

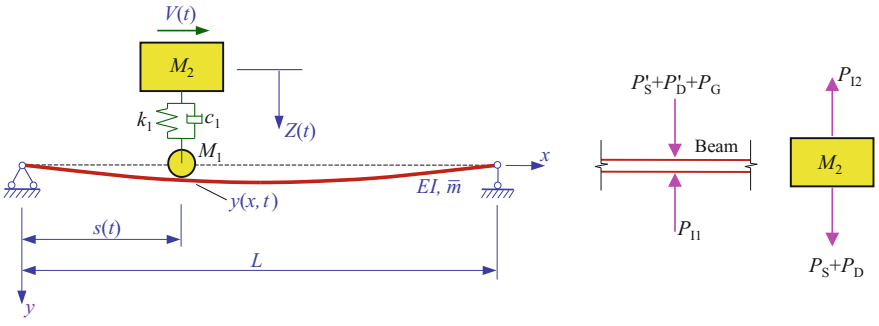

Fig. 2.13 Model of simply-supported bridge with a speed-varying WSM load

$$M_2\ddot{Z}(t) + k_1\left[Z(t) - y(x,t)|_{x=s(t)}\right] + c_1\left[\dot{Z}(t) - \frac{\mathrm{d}y(x,t)}{\mathrm{d}t}\bigg|_{x=s(t)}\right] = 0 \tag{2.49}$$

where $\dfrac{\mathrm{d}y}{\mathrm{d}t} = \dfrac{\partial y(x,t)}{\partial t} + \dfrac{\partial y(x,t)}{\partial x}V(t)$. Since the load speed is not constant, both terms should be considered. The motion equation of the mass M_2 becomes

$$M_2\ddot{Z}(t) + k_1[Z(t) - y(x,t)|_{x=s(t)}] + c_1\left\{\dot{Z}(t) - \left[\frac{\partial y(x,t)}{\partial t} + \frac{\partial y(x,t)}{\partial x}V(t)\right]\bigg|_{x=s(t)}\right\} = 0 \tag{2.50}$$

When the WSM load moves on the beam at the speed of $V(t)$, the beam is subjected to the inertial force $P_{\mathrm{I1}} = M_1\dfrac{\mathrm{d}^2y(t)}{\mathrm{d}t^2}|_{x=s(t)}$ from the mass M_1, the gravity $P_{\mathrm{G}} = (M_1 + M_2)g$ of the masses, the elastic force $P_{\mathrm{S}}^{'} = P_{\mathrm{S}}$, and the damping force $P_{D}^{'} = P_{\mathrm{D}}$. Thus, the force applied on the beam can be expressed as

$$\begin{aligned} P(x,t) &= \delta[x - s(t)][P_{\mathrm{G}} - P_{\mathrm{I}} + P_{\mathrm{S}} + P_{\mathrm{D}}] \\ &= \delta[x - s(t)]\left\{(M_1 + M_2)g - M_1\frac{\mathrm{d}^2y(x,t)}{\mathrm{d}t^2} + k_1[Z(t) - y(x,t)] + c_1\left[\dot{Z}(t) - \frac{\mathrm{d}y(x,t)}{\mathrm{d}t}\right]\right\} \end{aligned} \tag{2.51}$$

Note that $\dfrac{\mathrm{d}^2y}{\mathrm{d}t^2} = \dfrac{\partial^2y}{\partial t^2} + 2\dfrac{\partial^2y}{\partial x\partial t}V(t) + \dfrac{\partial y}{\partial x}a(t) + \dfrac{\partial^2y}{\partial x^2}V^2(t), \dfrac{\mathrm{d}y}{\mathrm{d}t} = \dfrac{\partial y(x,t)}{\partial t} + \dfrac{\partial y(x,t)}{\partial x}V(t)$, and $a(t) = \frac{\mathrm{d}V(t)}{\mathrm{d}t}$ is the moving acceleration of the load, and Eq. (2.51) can be rewritten as

$$\begin{aligned} P(x,t) = \delta[x - s(t)]\Bigg\{&(M_1 + M_2)g - M_1\left[\frac{\partial^2y(x,t)}{\partial t^2} + 2\frac{\partial^2y(x,t)}{\partial x\partial t}V(t) + \frac{\partial y(x,t)}{\partial x}a(t)\right. \\ &\left. + \frac{\partial^2y(x,t)}{\partial x^2}V^2(t)\right] + k_1[Z(t) - y(x,t)] + c_1\left\{\dot{Z}(t) - \left[\frac{\partial y(x,t)}{\partial t} + \frac{\partial y(x,t)}{\partial x}V(t)\right]\right\}\Bigg\} \end{aligned} \tag{2.52}$$

The motion equation of the simply-supported beam under loads with variable speed can be expressed as

$$EI\frac{\partial^4y(x,t)}{\partial x^4} + \bar{m}\frac{\partial^2y(x,t)}{\partial t^2} + c\frac{\partial y(x,t)}{\partial t} = P(x,t) \tag{2.53}$$

When Eq. (2.53) is solved with the modal decomposition method, by substituting $y(x,t) = \sum_{i=1}^{\infty} q_i(t) \cdot \phi_i(x)$ into the equation, multiplying each term by the mode shape function $\phi_n(x) = \sin\frac{n\pi x}{L}$, integrating along the beam, and considering the orthogonality of modes, Eq. (2.53) becomes

$$\ddot{q}_n(t) + 2\xi_n\omega_n\dot{q}_n(t) + \omega_n^2 q_n(t) = \frac{2}{\bar{m}L}P_n(t) \quad (n = 1, 2, \ldots\ldots) \tag{2.54}$$

in which $P_n(t)$ is the generalized force of the nth mode, expressed as

$$P_n(t) = P_{n1}(t) + P_{n2}(t) \tag{2.55}$$

where

$$\begin{aligned} P_{n1}(t) &= \int_0^L \delta[x - s(t)]\left\{(M_1 + M_2)g - M_1\left[\sum_{i=1}^{\infty}\ddot{q}_i(t)\phi_i(x) + 2\sum_{i=1}^{\infty}\dot{q}_i(t)\phi_i'(x)V(t)\right.\right. \\ &\quad \left.\left. + \sum_{i=1}^{\infty} q_i(t)\phi_i'(x)a(t) + \sum_{i=1}^{\infty} q_i(t)\phi_i''(x)V^2(t)\right]\right\}\phi_n(t)\mathrm{d}x \\ &= (M_1 + M_2)g\,\sin\frac{n\pi s(t)}{L} - M_1\sum_{i=1}^{\infty}\ddot{q}_i(t)\left[\frac{i\pi}{L}a(t)\cos\frac{i\pi s(t)}{L} - \left(\frac{i\pi}{L}\right)^2 V^2(t)\sin\frac{i\pi s(t)}{L}\right] \\ &\quad \times \sin\frac{n\pi s(t)}{L} - 2M_1\sum_{i=1}^{\infty}\dot{q}_i(t)\frac{i\pi}{L}V(t)\cos\frac{i\pi s(t)}{L}\sin\frac{n\pi s(t)}{L} \\ &\quad - M_1\sum_{i=1}^{\infty}\ddot{q}_i(t)\sin\frac{i\pi s(t)}{L}\sin\frac{n\pi s(t)}{L} \end{aligned} \tag{2.56a}$$

$$\begin{aligned} P_{n2}(t) &= \int_0^L \delta[x - s(t)]\left\{k_1 Z(t) + c_1\dot{Z}(t)\right. \\ &\quad \left. - \sum_{i=1}^{\infty}\left\{k_1 q_i(t)\phi_i(x) + c_1\left[\dot{q}_i(t)\phi_i(x) + q_i(t)\phi_i'(x)V(t)\right]\right\}\right\}\phi_n(x)\mathrm{d}x \\ &= \left[k_1 z(t) + c_1\dot{Z}(t)\right]\sin\frac{n\pi s(t)}{L} - \sum_{i=1}^{\infty}\dot{q}_i(t)c_1\sin\frac{i\pi s(t)}{L}\sin\frac{n\pi s(t)}{L} \\ &\quad - \sum_{i=1}^{\infty} q_i(t)\left[k_1\sin\frac{i\pi s(t)}{L} + c_1 V(t)\cos\frac{i\pi s(t)}{L}\right]\sin\frac{n\pi s(t)}{L} \end{aligned} \tag{2.56b}$$

By moving the unknown displacement, velocity, and acceleration terms from the right-hand side of Eq. (2.52) to the left, the following equation can be obtained

$$\begin{aligned}
&\ddot{q}_n(t)+\frac{2M_1}{\bar{m}L}\sum_{i=1}^{\infty}\ddot{q}_i(t)\sin\frac{i\pi s(t)}{L}\sin\frac{n\pi s(t)}{L}+2\xi_n\omega_n\dot{q}_n(t)\\
&\quad+\frac{2c_1}{\bar{m}L}\sum_{i=1}^{\infty}\dot{q}_i(t)\sin\frac{i\pi s(t)}{L}\sin\frac{n\pi s(t)}{L}+\frac{4M_1}{\bar{m}L}\sum_{i=1}^{\infty}\dot{q}_i(t)\frac{i\pi}{L}V(t)\cos\frac{i\pi s(t)}{L}\sin\frac{n\pi s(t)}{L}\\
&\quad+\omega_n^2q_n(t)+\frac{2M_1}{\bar{m}L}\sum_{i=1}^{\infty}q_i(t)\left[\frac{i\pi}{L}a(t)\cos\frac{i\pi s(t)}{L}\sin\frac{n\pi s(t)}{L}-\left(\frac{i\pi}{L}\right)^2V^2(t)\sin\frac{i\pi s(t)}{L}\sin\frac{n\pi s(t)}{L}\right]\\
&\quad+\frac{2k_1}{\bar{m}L}\sum_{i=1}^{\infty}q_i(t)\sin\frac{i\pi s(t)}{L}\sin\frac{n\pi s(t)}{L}+\frac{2c_1}{\bar{m}L}\sum_{i=1}^{\infty}q_i(t)\frac{i\pi}{L}V(t)\cos\frac{i\pi s(t)}{L}\sin\frac{n\pi s(t)}{L}\\
&\quad-\frac{2}{\bar{m}L}\left[k_1Z(t)+c_1\dot{Z}(t)\right]\sin\frac{n\pi s(t)}{L}\\
&=\frac{2}{\bar{m}L}(M_1+M_2)g\sin\frac{n\pi s(t)}{L}
\end{aligned}\tag{2.57}$$

When the bridge displacement at the load position is expressed with the modal decomposition method, the motion equation of the sprung-mass M_2 becomes

$$\begin{aligned}
&M_2\ddot{Z}(t)+c_1\dot{Z}(t)+k_1Z(t)-c_1\sum_{i=1}^{\infty}\dot{q}_i(t)\sin\frac{i\pi s(t)}{L}\\
&\quad-c_1\sum_{i=1}^{\infty}q_i(t)\frac{i\pi}{L}V(t)\cos\frac{i\pi s(t)}{L}-k_1\sum_{i=1}^{\infty}q_i(t)\sin\frac{i\pi s(t)}{L}=0
\end{aligned}\tag{2.58}$$

The motion equation of the system can be obtained by combining Eqs. (2.57) and (2.58). For a simply-supported beam, if N terms of displacement series are used, and the sprung-mass M_2 has one DOF $Z(t)$, the motion equations of the system can be expressed in terms of matrices with $(N + 1)$ orders as

$$\mathbf{M}\{\ddot{X}\}+\mathbf{C}\{\dot{X}\}+\mathbf{K}\{X\}=\{F\}\tag{2.59}$$

where $\{X\}$ is the generalized displacement vector; **M**, **C,** and **K** are the generalized mass, damping, and stiffness matrices, respectively; and $\{F\}$ is the generalized load vector. They are expressed as follows

$$\{X\}=[q_1(t),q_2(t),\cdots,q_N(t),Z(t)]^{\mathrm{T}}\tag{2.60}$$

$$\mathbf{M}=\begin{bmatrix}
1+\rho_{\mathrm{M}}\Phi_{11} & \rho_{\mathrm{M}}\Phi_{12} & \cdots & \rho_{\mathrm{M}}\Phi_{1N} & 0\\
\rho_{\mathrm{M}}\Phi_{21} & 1+\rho_{\mathrm{M}}\Phi_{22} & \cdots & \rho_{\mathrm{M}}\Phi_{2N} & 0\\
\cdots & \cdots & \ddots & \cdots & 0\\
\rho_{\mathrm{M}}\Phi_{N1} & \rho_{\mathrm{M}}\Phi_{N2} & \cdots & 1+\rho_{\mathrm{M}}\Phi_{NN} & 0\\
0 & 0 & 0 & 0 & M_2
\end{bmatrix}\tag{2.61}$$

$$\mathbf{C}=\begin{bmatrix} 2\xi_1\omega_1+\varphi_{11}+\rho_C\Phi_{11} & \varphi_{12}+\rho_C\Phi_{12} & \cdots & \varphi_{1N}+\rho_C\Phi_{1N} & -\rho_C\phi_1 \\ \varphi_{21}+\rho_C\Phi_{21} & 2\xi_2\omega_2+\varphi_{22}+\rho_C\Phi_{22} & \cdots & \varphi_{2N}+\rho_C\Phi_{2N} & -\rho_C\phi_2 \\ \cdots & \cdots & \ddots & \cdots & \cdots \\ \varphi_{N1}+\rho_C\Phi_{N1} & \varphi_{N2}+\rho_C\Phi_{N2} & \cdots & 2\xi_N\omega_N+\varphi_{NN}+\rho_C\Phi_{NN} & -\rho_C\phi_N \\ -c_1\phi_1 & -c_1\phi_2 & \cdots & -c_1\phi_N & c_1 \end{bmatrix} \tag{2.62}$$

$$\mathbf{K}=\begin{bmatrix} \omega_1^2+\psi_{11}+\rho_K\Phi_{11} & \psi_{12}+\rho_K\Phi_{12} & \cdots & \psi_{1N}+\rho_K\Phi_{1N} & -\rho_K\phi_1 \\ \psi_{21}+\rho_K\Phi_{21} & \omega_2^2+\psi_{22}+\rho_K\Phi_{22} & \cdots & \psi_{2N}+\rho_K\Phi_{2N} & -\rho_K\phi_2 \\ \cdots & \cdots & \ddots & \cdots & \cdots \\ \psi_{N1}+\rho_K\Phi_{N1} & \psi_{N2}+\rho_K\Phi_{N2} & \cdots & \omega_N^2+\psi_{NN}+\rho_K\Phi_{NN} & -\rho_K\phi_N \\ \Gamma_1-k_1\phi_1 & \Gamma_2-k_1\phi_2 & \cdots & \Gamma_N-k_1\phi_N & k_1 \end{bmatrix} \tag{2.63}$$

$$\{F\}=[\rho_F\phi_1,\ \rho_F\phi_2,\ \cdots,\ \rho_F\phi_N,\ 0]^T \tag{2.64}$$

where:

$\rho_M=\frac{2M_1}{\bar{m}L}, \rho_C=\frac{2c_1}{\bar{m}L}, \rho_K=\frac{2k_1}{\bar{m}L}, \rho_F=\frac{2(M_1+M_2)}{\bar{m}L}g, \phi_n=\sin\frac{n\pi s(t)}{L}, \Phi_{nm}=\phi_n\phi_m,$
$\beta_n=\cos\frac{n\pi s(t)}{L}, \varphi_{nm}=\frac{2m\pi}{L}\rho_M\phi_n\beta_m V(t), \Gamma_n=-c_nV(t)\frac{n\pi}{L}\beta_n,$ and
$\psi_{nm}=\rho_M\left[\frac{m\pi}{L}\phi_n\beta_m a(t)-\frac{m^2\pi^2}{L^2}V^2(t)\Phi_{nm}\right]+\frac{m\pi}{L}\rho_C V(t)\phi_n\beta_m.$

The multiplier φ_{nm} in the damping matrix and ψ_{nm} and Γ_n in the stiffness matrix represent the influence of variable speed of the moving load.

The results show that for the simply-supported beam subjected to a moving WSM load, the generalized mass matrix **M** is non-diagonal, but the coupling terms with M_2 are zeros. Both **K** and **C** are non-diagonal full matrices, through which the equations for the beam and the moving load are coupled. Although the equations for the whole system cannot be completely decoupled by modal decomposition, the order of the equations can be reduced by adopting an appropriate order number N.

Since the WSM load is moving on the beam, the coefficients Φ_{nm}, φ_{nm}, $\psi_{nm,}$ and Γ_n in the generalized mass matrix **M**, stiffness matrix **K,** and damping matrix **C** are time-varying. Therefore, Eq. (2.59) is a second-order linear differential equations with time-varying coefficients, which is usually solved by the step-by-step numerical integration method.

2.2.2 Case Study

Based on the above theory and analysis method, a computation program is developed to analyze the dynamic response of a three-span simply-supported bridge subjected to a moving WSM load with constant acceleration.

The bridge consists of 3×32 m PC box-beams. The beam is made of C50 concrete with elastic modulus of 34.5 MPa and mass density of 2500 kg/m^3.

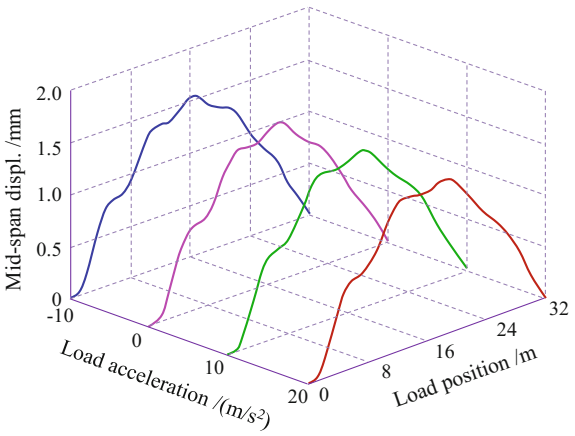

Fig. 2.14 Displacement time histories of the bridge under the speed-varying WSM load

The cross section of the beam has an area of 8.97 m^2 and an inertia moment of 11.1 m^4. In the WSM model, the wheel mass M_1 is 10.68 t, the sprung-mass M_2 is 73.32 t, the spring coefficient k_1 is 7.48 MN/m, and the damping coefficient c_1 is 240 kNs/m.

In the calculation, the first five vibration modes are considered for the bridge, the damping ratio is 0.05, the Newmark parameters are $\lambda = 0.5$ and $\beta = 0.25$, and the integration time step is 0.0005 s.

Shown in Fig. 2.14 are the dynamic displacement histories of the bridge at the central mid-span, when the WSM load enters the bridge at initial speed of 40 m/s and then moves on the bridge at a constant speed, variable speeds with accelerations of 10 m/s^2, 20 m/s^2, and -10 m/s^2, respectively. It can be observed that when the load moves on the bridge with different accelerations, the displacement time history curves are quite similar, but the maximum displacements are slightly different.

To further investigate the influence of load moving acceleration, some representative points on the maximum displacement curve of the bridge versus load moving speed are discussed in detail. The load speeds are divided into four categories according to the variation feature of the curve, as shown in Fig. 2.15, which are represented by speed points 1–6. Listed in Table 2.1 are the initial speeds, the accelerations of the load, and the maximum mid-span displacements of the bridge adopted in the calculation.

Based on Fig. 2.15 and the calculated results in Table 2.1, the influences of speed variations at these points on bridge maximum displacements are analyzed from the view of load-bridge resonance.

(1) Category I. Points 1 and 4 belong to this category, which are the load speeds yielding peak displacement responses. Corresponding to these points, when the load arrives at the mid-span, the speeds do not equal those yielding the maximum displacements; thus, in both the acceleration and deceleration cases, the maximum displacements become smaller.

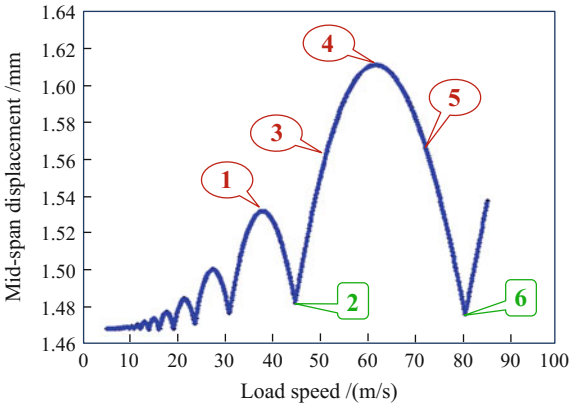

Fig. 2.15 Calculated representative load speeds

Table 2.1 Maximum displacements of bridge under speed-varying WSM load

Item		Maximum displacement (mm)					
Point number		1	2	3	4	5	6
Category		I	II	III	I	IV	II
Initial speed V_0 (m/s)		37.8	44.6	50.0	61.5	72.0	80.0
Acceleration a (m/s^2)	0	1.532	1.482	1.552	1.611	1.566	1.476
	5	1.530	1.492	1.558	1.610	1.560	1.479
	10	1.526	1.502	1.564	1.609	1.554	1.484
	15	1.519	1.502	1.570	1.608	1.548	1.488
Deceleration a (m/s^2)	0	1.532	1.482	1.552	**1.611**	1.566	1.476
	−5	1.531	1.496	1.545	**1.612**	1.572	1.484
	−10	1.528	1.508	1.534	**1.612**	1.577	1.493
	−15	1.522	1.518	1.529	**1.611**	1.582	1.501

(2) Category II. Points 2 and 6 belong to this category, which are the load speeds yielding valley displacement responses. Corresponding to these points, when the load arrives at the mid-span, the speeds do not equal those yielding the minimum displacements; thus, in both the acceleration and deceleration cases, the maximum displacements become larger.

(3) Category III. Point 3 belongs to this category, which is the load speed located in the upward segment of the displacement curve. Corresponding to this point, the load acceleration yields larger maximum displacement, while the deceleration yields smaller.

(4) Category IV. Point 5 belongs to this category, which is the load speed located in the downward segment of the displacement curve. Corresponding to this point, the load acceleration yields smaller maximum displacement, while the deceleration yields larger.

The change of maximum displacement should increase with acceleration variation. Most of the data in Table 2.1 comply with this law, indicating the load-bridge resonance theory is valid for load with variable speed, while a few data in bold do not. These exceptions can be explained as follows.

(1) Due to the influence of speed incremental step, the calculated representative speeds yielding the peaks and valleys are not precise enough, so they are only the approximations of the real ones.
(2) When the load moves at variable speeds, the load position on the bridge yielding the maximum mid-span displacement is slightly different from that at constant speeds, and thus, the maximum displacement will be different.

It can be concluded that the maximum displacement of the bridge is associated with the initial speed and acceleration of the load, as well as the speed and position of the load corresponding to the maximum displacement. The conclusions above are confirmed by the analysis of the 3×32 m simply-supported bridge subjected to the moving WSM load, showing that

(1) When the load moves with different accelerations, the displacement time history curves of the bridge are almost the same, with difference less than 3% among their peak values. Therefore, the assumption of constant load speed is sufficient for usual analysis.
(2) When the load moves at a variable speed, the maximum mid-span displacement of the bridge is associated with the speed and position of the load arriving near the mid-span. The variation characteristics of maximum displacement versus load speed are in accordance with that when the load moves at a constant speed.

2.3 Resonance Analysis of a Simply-Supported Beam Subjected to Moving Loads

According to the fundamental theorems of structural dynamics, when a row of train vehicles travels over a railway bridge, the loading frequency (dependent on the train speed, bridge span, and composition of train vehicles) will change with the train speed and a resonant vibration will occur when the loading frequency coincides with the natural frequency of the bridge. The strong vibration induced by the resonance not only directly affects the working state and serviceability of the bridge, but also reduces the running safety of the train, diminishes the riding comfort of the passengers, and sometimes even destabilizes the ballasted track on the bridge. Therefore, it is necessary to develop methods to predict the resonant speeds of the running train and to assess the dynamic behavior of the bridge under resonance conditions.

In the past decades, researchers offered a lot of efforts to study the resonance problem of bridges under moving loads, such as by Matsuura (1976), Xia and Chen

(1992), Frýba (1999, 2001), Diana and Cheli (1989), Yang et al. (1997, 2004a, b), Yau and Yang (1999), Cheung et al. (1999), Li and Su (1999), Yau (2001), Savin (2001), Pesterev et al. (2003), Kwark et al. (2004), Xia et al. (2006, 2012), Ju and Lin (2003), Garinei and Risitano (2008), Hamidi and Danshjoo (2010), Michaltsos and Raftoyiannis (2010), Zambrano (2011), Rocha et al. (2012), Lee et al. (2012), Luu et al. (2012), and Lavado et al. (2014), and many of these models have been validated by field experiments (Liu et al. 2009; Xia and Zhang 2005; and Xia et al. 2012).

There are various factors associated with the resonance of the train-bridge system under moving loads, such as the periodic loading on the bridge by the regularly arranged wheel-axle loads due to vehicle gravity or centrifugal force, the periodic impact on the bridge caused by wheel scars, the periodic excitations induced by local track irregularities, the lateral periodic loading by hunting movement and centrifugal forces of train vehicles, the lateral moving load series caused by winds on car-bodies, and the periodical actions on moving vehicles by deflections of long bridge with identical multi-spans. The excitation frequencies by all the above factors are associated with the train speed. Consequently, investigation on the train-bridge resonance is significant in theory as well as in engineering practice.

2.3.1 Bridge Resonance Induced by a Moving Load Series

The resonance of train-bridge system is affected by the span, total length, lateral stiffness and vertical stiffness of the bridge, the compositions of the train, and the axle arrangements and natural frequencies of the vehicles. The general mechanism of bridge resonance induced by moving load series can be described as follows.

2.3.1.1 Fundamental Analysis Model

A simply-supported beam subjected to a train load is analyzed herein. The beam has a span L, a uniform mass $\bar{m}$, a bending stiffness EI, and a zero damping. The train consists of several identical cars with the full length l_v of each car, the rated distance l_c between the two bogies of the car, and the fixed wheelbase l_w between the two wheel-axles of the bogie, as shown in Fig. 2.16a. To explain the general principles and to facilitate the derivation, the train axle loads are simplified as N moving concentrated constant loads with identical interval d_v, as shown in Fig. 2.16b.

Suppose the load series travels on the beam from left to right at a uniform speed V, and the traveled distance of the first force is $x = Vt$. For the load series with identical intervals, there exists a time delay $\Delta t = d_v/V$ between any two successive forces. The motion equation for the beam acted on by such moving load series can be written as

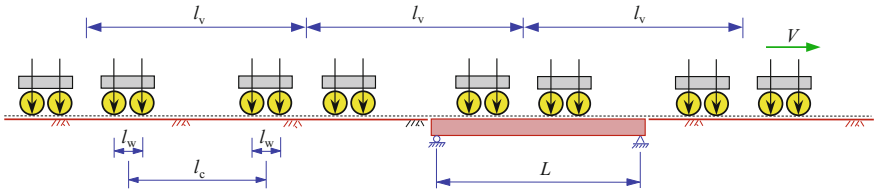

(a) Arrangement of wheel-axle loads of a train

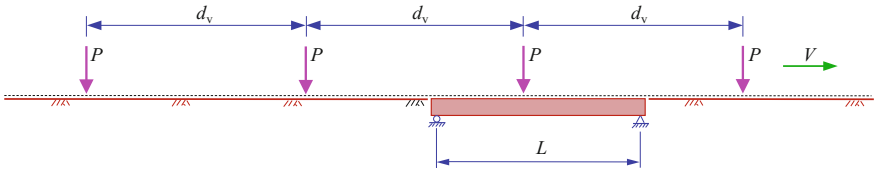

(b) Simplified moving load series

Fig. 2.16 Moving load series of a train on the bridge

$$EI\frac{\partial^4 y(x,t)}{\partial x^4}+\bar{m}\frac{\partial^2 y(x,t)}{\partial t^2}=\sum_{k=0}^{N-1}\delta\left[x-V(t-\frac{k\cdot d_v}{V})\right]P \tag{2.65}$$

It can be expressed in terms of the generalized coordinates as

$$\ddot{q}_n(t)+\omega_n^2 q_n(t)=\frac{2}{\bar{m}L}P\sum_{k=0}^{N-1}\sin\frac{n\pi V}{L}\left(t-\frac{k\cdot d_v}{V}\right) \tag{2.66}$$

Equation (2.66) is the motion equation of a SDOF system subjected to harmonic load series. The particular solution of Eq. (2.66) is

$$q(t)=\frac{2PL_b^3}{EI\pi^4}\frac{1}{1-\beta^2}\sum_{k=0}^{N-1}\left[\sin\bar{\omega}\left(t-\frac{k\cdot d_v}{V}\right)-\beta\sin\omega_1\left(t-\frac{k\cdot d_v}{V}\right)\right] \tag{2.67}$$

where $\bar{\omega}=\pi V/L$ is the exciting circular frequency of the moving load, and $\omega_1=\frac{\pi^2}{L^2}\sqrt{\frac{EI}{\bar{m}}}$ is the fundamental circular frequency of the beam. The displacement response of the beam where only the first mode is considered can thus be expressed as

$$y(x,t)=\frac{2PL_b^3}{EI\pi^4}\frac{1}{1-\beta^2}\sin\frac{\pi x}{L}\cdot\left[\sum_{k=0}^{N-1}\sin\bar{\omega}\left(t-\frac{k\cdot d_v}{V}\right)-\beta\sum_{k=0}^{N-1}\sin\omega_1\left(t-\frac{k\cdot d_v}{V}\right)\right] \tag{2.68}$$

where $\beta = \bar{\omega}/\omega_1$ is the ratio of exciting frequency to the fundamental frequency of the beam, and $1/(1-\beta^2)$ is the dynamic magnification factor.

The first term of the right-hand side of Eq. (2.68) represents the forced response of the beam due to the moving loads, while the second term represents the transient response due to its free vibration. According to their different mechanisms, the resonant responses of a simply-supported beam subjected to moving load series can be divided into two types.

2.3.1.2 Bridge Resonance Induced by Periodically Loading of Moving Load Series

First, the discussion is made for the second progression term of Eq. (2.68), to explain how the transient response in common sense may induce the resonance of the beam.

Before considering the second progression series, it is instructive to introduce the necessary transformation of triangular progression. For the sum of a finite triangular progression $\sin(a-ix)$, (i = 1, 2, …, m), it can be expressed as

$$\sum_{i=1}^{m} \sin(a-ix) = \sum_{i=1}^{m} [\sin a \, \cos ix - \cos a \, \sin ix] \tag{2.69}$$

The two terms of Eq. (2.69) can be further expressed as (Rade and Westergren 2010)

$$\begin{cases} \sum\limits_{i=1}^{m} \sin ix = \sin 0.5mx \cdot \sin 0.5(m+1)x \cdot \csc 0.5x \\ \sum\limits_{i=1}^{m} \cos ix = \sin 0.5mx \cdot \cos 0.5(m+1)x \cdot \csc 0.5x \end{cases} \tag{2.70}$$

Introducing them into Eq. (2.69) leads to

$$\sum_{i=1}^{m} \sin(a-ix) = \frac{\sin 0.5mx \cdot \sin[a-0.5(m+1)x]}{\sin 0.5x} \tag{2.71}$$

Now, let $i = k, m = N-1, x = \omega_1 d_v/V$, and $a = \omega_1 t$; the progression term of the transient response in Eq. (2.68) becomes as the form

$$\begin{aligned} \sum_{k=0}^{N-1} \sin \omega_1 \left(t - \frac{k \cdot d_v}{V} \right) &= \sin \omega_1 t + \sum_{k=1}^{N-1} \sin \omega_1 \left(t - \frac{k \cdot d_v}{V} \right) \\ &= \sin \omega_1 t + \frac{\sin\left[(N-1) \cdot \frac{\omega_1 d_v}{2V}\right] \cdot \sin\left[\omega_1 t - N \cdot \frac{\omega_1 d_v}{2V}\right]}{\sin \frac{\omega_1 d_v}{2V}} \end{aligned} \tag{2.72}$$

For $\frac{\omega_1 d_v}{2V} = \pm i\pi$, the second term of Eq. (2.72) becomes an indeterminate form 0/0, but when the L'Hospital's rule is applied, the limit solution is found to be

$$\lim_{\frac{\omega_1 d_v}{2V} \to \pm i\pi} \frac{\sin\left[(N-1)\cdot\frac{\omega_1 d_v}{2V}\right]\cdot \sin\left[\omega_1 t - N\cdot\frac{\omega_1 d_v}{2V}\right]}{\sin\frac{\omega_1 d_v}{2V}} = (N-1)\sin\omega_1\left[t - N\cdot\frac{d_v}{2V}\right] \tag{2.73}$$

Obviously, the extreme condition with physical significance for Eq. (2.73) is

$$\frac{\omega_1 d_v}{2V} = i\pi \quad (i = 1, 2, 3, \cdots) \tag{2.74}$$

Substituting this condition into Eq. (2.71), the limit value of the transient response term in Eq. (2.67) is obtained as

$$\sum_{k=0}^{N-1} \sin\omega_1\left(t - \frac{k\cdot d_v}{V}\right)\Big|_{\frac{\omega_1 d_v}{2V} = i\pi} = N\sin\omega_1 t \tag{2.75}$$

It can be seen that each force in the moving load series may induce the transient response of the structure, and the successive forces form a series of periodical excitations. The response of the structure will be successively amplified with the increase of N, the number of forces traveling through the beam, resulting in the structural resonance.

Similar results can be obtained for higher modes of the bridge. Considering all of these modes and letting $\omega_n = 2\pi f_{bn}$, the resonant condition of the bridge under a moving load series can be derived from Eq. (2.72) as

$$V_{br} = \frac{3.6\cdot f_{bn}\cdot d_v}{i} \quad (n = 1, 2, 3, \cdots)(i = 1, 2, 3, \cdots) \tag{2.76}$$

where V_{br} is the resonant train speed (km/h); f_{bn} is the nth vertical or lateral natural frequency of the bridge (Hz); d_v is the intervals of the moving loads (m); and the multiplicator i = 1, 2, 3 is determined by the extreme condition Eq. (2.74).

Equation (2.76) indicates that when a train moves on the bridge at speed V, the regularly arranged wheel-axle loads may produce periodical dynamic actions on the bridge with the loading period d_v/V. The bridge resonance occurs when the loading period is close to the nth natural vibration period of the bridge or its i times. A series of resonant responses related to different bridge natural frequencies may occur corresponding to different train speeds. The appearance of this phenomenon is determined by the time of the load traveling through the distance d_v. Equation (2.76) is called as ***the first resonant condition*** of simply-supported bridge. Detailed illustration on the physical meaning of the bridge resonance induced by the moving load series will be presented in Sect. 2.4.3.

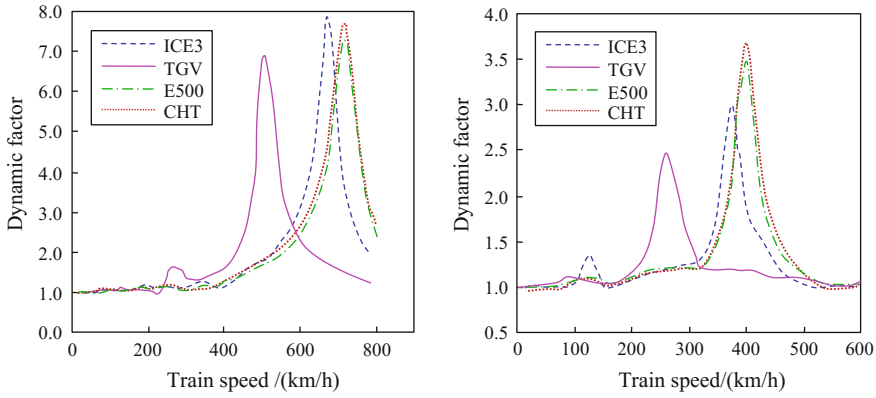

(a) L=20m (b) L=32m

Fig. 2.17 Dynamic factors of simply-supported beams versus train speed

During the dynamic analysis of the bridges on the Beijing-Shanghai HSR, the dynamic interaction model of train-bridge system was used to study the resonant responses induced by various high-speed trains, such as Germany ICE3, France TGV, Japan E500, and China CHT. Shown in Fig. 2.17 are the simulated distribution curves of dynamic factors versus train speed for the PC box-beams with 20 and 32 m spans, where the dynamic factor is defined as the ratio of the maximum dynamic to the maximum static deflection of the beam under the same loading.

It is given that the natural frequencies of the 20 m and 32 m PC box-beams are 7.73 Hz and 4.23 Hz, respectively. By using Eq. (2.76), the corresponding resonant train speeds can be estimated as 520 km/h and 284.8 km/h for TGV whose average car length is l_v = 18.7 m, and 285 km/h and 400 km/h for ICE3, E500, and CHT whose average car lengths are all $l_v \approx 26$ m. In this example, the calculation is based on $d_v = l_v$; namely, the full length of vehicle is taken as the load interval, where the four axle loads of the rear bogie at the previous car and the front bogie at the following car are combined as one concentrated load. The resonant train speeds estimated by Eq. (2.76) are in good accordance with the critical train speeds from the simulated results, as compared in Fig. 2.17.

Equation (2.76) can also be used to analyze the lateral response of bridge under the first resonant condition. The lateral resonance analysis has special significance for bridges with high piers under a moving load series induced by centrifugal forces or lateral wind pressures. Since the lateral frequency of the bridge system is usually smaller than the vertical frequency, the critical train speed for lateral resonance is also lower.

A simply-supported steel truss with the span of 48 m is analyzed as an example. The moving load series are the lateral axle loads induced by wind pressures acting on car-bodies.

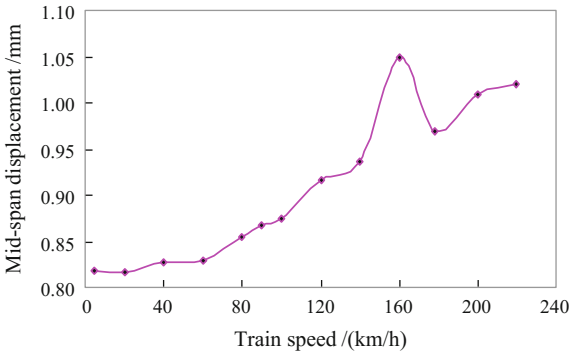

Fig. 2.18 Lateral displacements of steel truss versus train speed

The lateral natural frequency of the truss is 1.86 Hz. The train concerned is composed of one locomotive followed by 18 passenger cars. The full length of each car is 26.57 m. The resonant train speed for the first resonant condition estimated by Eq. (2.76) is

$$i = 1 : V_{\mathrm{br}1} = \frac{1.86 \times 26.57}{1} \times 3.6 \approx 178\,\mathrm{km/h}$$
$$i = 2 : V_{\mathrm{br}2} = \frac{1.86 \times 26.57}{2} \times 3.6 \approx 89\,\mathrm{km/h}$$
$$i = 3 : V_{\mathrm{br}3} = \frac{1.86 \times 26.57}{3} \times 3.6 \approx 60\,\mathrm{km/h}$$

According to the predicted results, the dynamic responses of the truss under various train speeds are analyzed by the whole history simulations of train-bridge system, with the calculation train speeds in the range of 5–220 km/h. Figure 2.18 shows the distribution curve of lateral mid-span displacements of the truss versus train speed.

It can be found that during the train passage, an obvious peak appears at the speed of 160 km/h, and two small peaks appear at the speeds of 80 and 40 km/h, showing significant harmonic resonances of the first order. Considering that the natural frequency of the bridge will decrease when loaded by the train, the estimated results obtained from Eq. (2.76) are in accordance with those from the whole history simulations of train-bridge system.

2.3.1.3 Bridge Resonance Induced by Loading Rate of a Moving Load Series

As for the first progression term of Eq. (2.68) which represents the forced response of the bridge, the solution is almost the same as the second term except that it misses the multiplicator β and uses $\bar{\omega}$ instead of ω_1; thus, an extreme condition similar to Eq. (2.74) can be directly written as

$$\frac{\bar{\omega} d_{\mathrm{v}}}{2V} = i\pi \, (i = 1, 2, 3, \ldots) \tag{2.77}$$

Substituting $\bar{\omega} = \pi V/L$ into Eq. (2.77), the train speed V in the numerator is counteracted with that in the denominator and thus results in the extreme condition

$$d_{\mathrm{v}} = 2iL \quad (i = 1, 2, 3, \ldots) \tag{2.78}$$

The limit value of the steady-state response progression can be obtained by using this extreme condition

$$\sum_{k=0}^{N-1} \sin \bar{\omega} \left(t - \frac{k \cdot d_{\mathrm{v}}}{V} \right) \Big|_{\frac{\bar{\omega} d_{\mathrm{v}}}{2V} = i\pi} = N \sin \bar{\omega} t \tag{2.79}$$

There is no train speed V expressed in Eq. (2.78); namely, no resonant train speed exists. Equations (2.78) and (2.79) show that when the interval of loads equals to $2i$ times of the bridge span, i.e., the half-wavelength formed by the beam deflection, the successive increase of the number of passing wheel-axles may gradually enlarge the bridge response. However, since the minimum axle intervals of real vehicles are much smaller than two times of the bridge span length, and the actual arrangement of train wheel-axles is never identical, this solution is only of mathematical significance. Therefore, the resonant train speed cannot be derived in this way.

In fact, the second resonance of the simply-supported beam under moving train loads can be directly determined from Eq. (2.68) by the dynamic magnification factor $1/(1 - \beta^2)$. For the nth bridge modes, $\bar{\omega}_n = n\pi V/L$ is the nth exciting frequency. Obviously, when the frequency ratio β_n is equal to 1, i.e., $\omega_n = \bar{\omega}_n$, the dynamic magnification factor $1/(1 - \beta_n^2)$ will become infinitive. At this time, the nth resonant vibration of the bridge is excited. For the simply-supported beam under moving loads, the nth natural frequency of the beam $\omega_n = 2\pi f_{\mathrm{b}n}$, and thus, the resonant train speed V_{br} can be described as

$$V_{\mathrm{br}} = \frac{7.2 \cdot f_{\mathrm{b}n} \cdot L}{n} \quad (n = 1, 2, 3, \ldots) \tag{2.80}$$

where V_{br} is the resonant train speed (km/h); $f_{\mathrm{b}n}$ is the nth vertical or lateral natural frequency of the bridge (Hz); and L_{b} is the span of the bridge (m).

Equation (2.80) indicates that bridge resonance occurs when the traveling time of the train through the bridge equals to $0.5n$ times the nth vibration period of the bridge. The appearance of this phenomenon is determined by the loading rate of moving loads related to the bridge span. Equation (2.80) is called as ***the second resonant condition*** of simply-supported bridge, in which V_{br} is nothing less than the resonant speed derived at $\alpha = k$ in Sect. 2.1.

The resonant train speed calculated from Eq. (2.80) is rather high. For instance, the lowest natural frequencies for the simply-supported beams with moderate or small spans are 80/L and 120/L, respectively, given in the Chinese codes *Interim Provisions on Design of New 200* km/h *Passenger-cum-freight Railways* (TJS 2005-285 2005a, b) and the *Interim Provisions on Design of Beijing-Shanghai HSR* (TJS 2003-13 2003), by which the resonant train speeds can be estimated by Eq. (2.80) as 576 and 864 km/h. These values are far higher than the current train speeds in operation. Thus, currently, the vertical resonance of a simply-supported beam is analyzed mainly based on the first resonant condition, while for trains with higher speed, e.g., a maglev train, the second resonant condition is of certain significance in resonance analysis.

When the train is running on the bridge, the centrifugal forces or the lateral wind pressures on the car-bodies will be transferred via wheel-sets to the bridge structure. These actions can be represented by a series of lateral moving loads. When the excitation frequency of the moving load series is equal or close to the bridge natural frequency, the second resonant response will occur. The corresponding critical train speed V_{br} can be estimated through Eq. (2.80). The relationship between the bridge lateral resonant response induced by a moving load series due to mean wind pressure on the vehicle and critical train speeds is illustrated through a realistic example.

For bridges with high piers often encountered in engineering, owing to their low natural frequencies, the analysis on both the first and the second lateral resonances is of significance. Since a pier cannot directly support train loads, a bridge composed of two 32 m simply-supported beams and a 56 m high pier is analyzed as an example. The moving load series are formed by the same lateral wind loads as in the previous example. Modal analysis shows that the first three modes of the bridge are dominated by the lateral vibrations of the pier. With respect to the bridge lateral frequencies 0.95, 2.52, and 5.02 Hz, the resonant train speeds estimated by the first resonant condition Eq. (2.74) include

$$\begin{aligned}
f_{\mathrm{b1}} = 0.95\,\mathrm{Hz}: &\quad V_{\mathrm{br1}} = 91\,\mathrm{km/h}, &\quad V_{\mathrm{br2}} = 46\,\mathrm{km/h}, &\quad V_{\mathrm{br3}} = 31\,\mathrm{km/h}\\
f_{\mathrm{b2}} = 2.52\,\mathrm{Hz}: &\quad V_{\mathrm{br1}} = 240\,\mathrm{km/h}, &\quad V_{\mathrm{br2}} = 120\,\mathrm{km/h}, &\quad V_{\mathrm{br3}} = 81\,\mathrm{km/h}\\
f_{\mathrm{b3}} = 5.02\,\mathrm{Hz}: &\quad V_{\mathrm{br1}} = 481\,\mathrm{km/h}, &\quad V_{\mathrm{br2}} = 240\,\mathrm{km/h}, &\quad V_{\mathrm{br3}} = 161\,\mathrm{km/h}
\end{aligned}$$

For the 2×32 m bridge, the lateral loading length to the pier is L = 64 m, so the possible resonant train speeds estimated from the second resonant condition Eq. (2.80) include

$$\begin{aligned}
n = 1: V_{\mathrm{br1}} &= \frac{7.2 \times 0.95 \times 64}{1} \approx 438\,\mathrm{km/h}\\
n = 2: V_{\mathrm{br2}} &= \frac{7.2 \times 2.52 \times 64}{2} \approx 581\,\mathrm{km/h}\\
n = 3: V_{\mathrm{br3}} &= \frac{7.2 \times 5.02 \times 64}{3} \approx 771\,\mathrm{km/h}
\end{aligned}$$

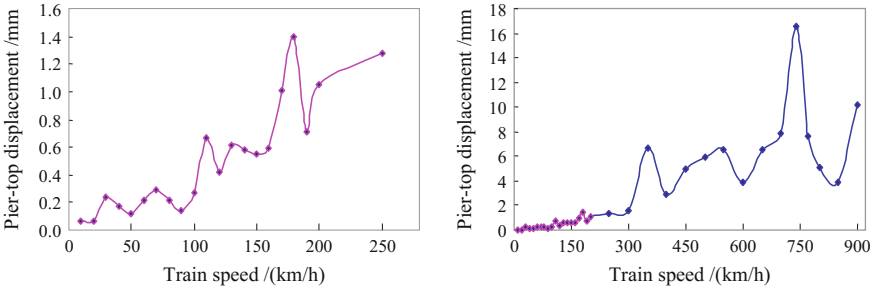

Fig. 2.19 Lateral displacement of the pier-top versus train speed

The dynamic responses of the bridge under various train speeds are analyzed by the whole history simulations of train-bridge system, with the calculation train speeds in the range of 10–900 km/h. Figure 2.19 shows the distribution curves of lateral displacements of the pier-top versus train speed.

The curves show that the lateral resonance of the pier is obvious: The peak values of lateral displacement are found in the positions slightly lower than the estimated critical velocities by the first resonant condition, and also the peak displacements at 380 and 740 km/h, which are close to the corresponding resonant train speeds estimated by the second resonant condition. Considering the natural frequency of bridge will decrease when loaded by the train, the estimated results by Eqs. (2.76) and (2.80) are in accordance with those from the whole history simulations of train-bridge system.

Furthermore, one can estimate the responses of the bridge under vehicle centrifugal forces. As moving load series, the vehicle centrifugal forces have the same mechanism to induce the lateral vibration of the bridge as the mean wind pressures acting on the car-bodies. Thus, the calculated curves in Fig. 2.19 can also be used for estimating centrifugal forces. According to the Chinese code *Fundamental Code for Design on Railway Bridge and Culvert* (TB10002.1-2005 2005), $\bar{m}$ force can be 15% of the static load of vehicles, which is about 2.5 times of the vehicle design wind load. Therefore, when considering the vehicle centrifugal forces, much greater pier-top displacements will be excited than those shown in Fig. 2.19.

2.3.1.4 Bridge Resonance Owing to the Sway Forces of Train Vehicles

The third bridge resonance is induced by the periodical actions of lateral moving load series on the bridge owing to the sway forces of train vehicles. The sway forces of vehicles may be excited by track irregularities and wheel hunting movements. The resonant train speed in this case can be determined by

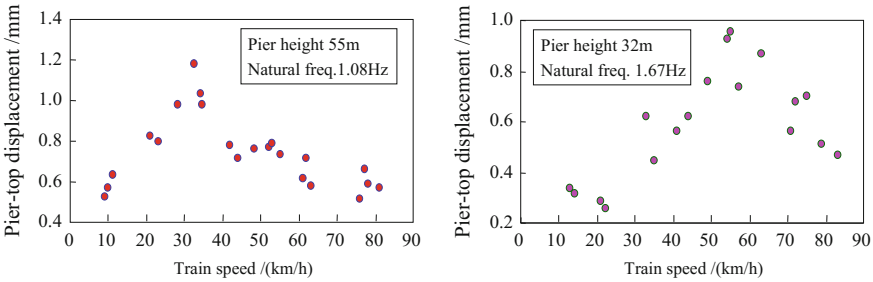

Fig. 2.20 Lateral displacements of high piers versus train speed

$$V_{\mathrm{br}} = \frac{3.6 \cdot f_{\mathrm{b}n} \cdot L_{\mathrm{s}}}{i} (n = 1, 2, 3, \cdots; i = 1, 2, 3, \cdots) \tag{2.81}$$

where $f_{\mathrm{b}n}$ is the nth vertical or lateral natural frequency of the bridge (Hz); L_{s} is the dominant wavelength of track irregularities or wheel hunting movement. The multiplicators i = 1, 2, 3,… show that when the dominant frequency of track irregularities or wheel hunting movement equals to the nth natural frequency or higher harmonic frequencies, the resonance of the bridge occurs. This is called ***the third resonant condition*** of bridge.

Although both track irregularities and wheel hunting movement are of random properties, Eq. (2.81) can still be used to estimate the lateral resonance of bridge induced by their dominant wavelengths. A good example is presented in Fig. 2.20, the distributions of the lateral displacements of two high piers versus train speed. The data in the figure were measured in the field experiments at two real bridges on the Chengdu-Kunming Railway in China. One can find peak values appearing at certain train speeds, which are in good accordance with the estimated resonant train speeds of 33 km/h and 51.1 km/h, respectively. The estimated resonant train speeds are calculated by Eq. (2.81), using the hunting wavelength L_{s} = 8.5 m for wheels with worn threads, the given pier heights H = 55 m and 32 m, and the corresponding bridge frequencies f = 1.08 Hz and 1.67 Hz, respectively.

2.3.1.5 Application Scopes of Resonance Conditions

Based on the analysis above, the resonant vibrations of bridges induced by moving trains have been classified into three mechanisms. The first is related to the intervals of the moving load series, which form the periodically loading on the bridge. The second is induced by the loading rate, i.e., the relative moving speed of the load series to the bridge. The third is owing to the swing forces of the train vehicles excited by track irregularities and wheel hunting movement.

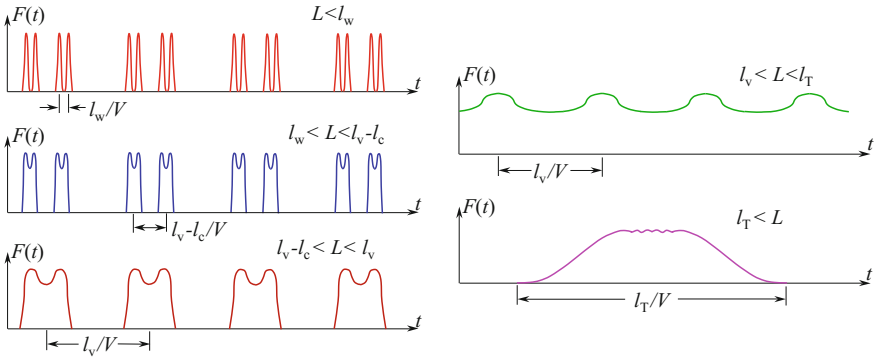

Fig. 2.21 Time histories of load series moving on bridge

In the above resonant conditions, the axle loads of the train vehicles are assumed to be in equidistance. While in reality, there exist several axle intervals in a train: the full length l_v of a car, the rated center-to-center distance l_c between two bogies of a car, the fixed wheelbase l_w between two wheel-sets of a bogie, and the different compositions of these distances. According to the relative lengths between the beam span or the bridge length and the above loading intervals, when Eq. (2.76) is used to analyze the first resonance induced by moving trains, the application scopes can be further discussed as follows (ref. Figs. 2.16 and 2.21):

(1) $L<l_w$: When the bridge length L is shorter than the fixed wheelbase l_w of a bogie, there can be only one wheel-set at any moment on the bridge, with the shortest excitation period $l_w = V$ and some other longer periods as $(l_v - l_c)/V$ and l_v/V. However, it is only an extreme situation in theory, for there exists no such short bridge in reality.

(2) $l_w < L < l_v - l_c$: When the bridge length L is longer than the fixed wheelbase l_w of a bogie but shorter than the distance $l_v - l_c$ between the rear bogie of the previous car and the front bogie of the following car, there can still be only one wheel-set at any moment on the bridge, with the main excitation period $(l_v - l_c)/V$ and some longer periods as l_v/V, while the shorter period l_w/V is not obvious. This situation may occur for the bridges with very short spans.

(3) $l_v - l_c < L < l_v$: When the bridge length L is longer than the distance $l_v - l_c$ between the rear bogie of the previous car and the front bogie of the following car, but shorter than the full length l_v of the car, there can be two wheel-sets simultaneously on the bridge, with the main excitation period l_v/V, while the shorter periods as l_w/V and $(l_v - l_c)/V$ are not obvious. Since the full lengths are about 25 m for passenger car and 15 m for freight car, this situation may occur for common bridges with small spans.

(4) $l_v < L < l_T$: When the bridge length L is longer than the full length l_v of a car but shorter than the total length l_T of the whole train, there can be more than one cars and two wheel-sets simultaneously on the bridge, neither of the above

excitation periods as l_w/V, $(l_v - l_c)/V$ nor l_v/V is obvious. This situation may occur for common bridges with moderate spans or for lateral resonance analysis of the bridge as a whole.

(5) $l_T < L$: When the bridge length L is longer than the total length l_T of a train, there can be several cars with many wheel-sets simultaneously on the bridge; thus, the load series cannot form periodical loading to the bridge system. This situation may occur for long-span bridges, or for lateral resonance analysis of the bridge as a whole. However, the resonant conditions proposed in this section cannot be directly used to analyze the resonant conditions for long-span bridges, because the whole course of a train traveling over the bridge longer than the total length of the train is equivalent to a half-loading period, and thus, no harmonic load forms. Therefore, Eqs. (2.76) and (2.80) cannot be directly used to estimate the resonant train speeds. As for the third resonant condition where the bridge resonance is excited by track irregularities or wheel hunting, no obvious resonance can be observed for long-span bridges because of the counteractions between the forces from the wheel-sets moving with different phases.

Thus, it can be seen that when using the above equations to analyze the train-induced resonance of the bridge, the loading intervals can be the full length l_v of a car, the rated center-to-center distance l_c between two bogies of a car, the fixed wheelbase l_w of a bogie, and the various compositions of these distances. While for a row of train vehicles, the arrangement of the axle loads is not in equidistance, and neither equal are the values of all axle forces which are affected by the bridge damping, track irregularities, and other complicated factors. Accordingly, a series of resonant vibrations may be excited with different response levels when the train moving at various speeds on the bridge, and a series of corresponding resonant train speeds could be found. Therefore, the precise resonance analysis usually depends on the simulation calculations of the train-bridge dynamic interaction system according to the real conditions of train composition, wheel arrangement, and vehicle loads.

2.3.2 *Resonance Analysis of Train Vehicles*

As a train runs on a long bridge at the speed V, the periodical actions on the vehicle can be excited by successive deflections of the bridge that consists of a series of identical spans (see Fig. 2.22), which can be considered as periodic track irregularities with frequency V/L_b. Resonance occurs to the vehicle when this loading frequency coincides with the natural frequency of the vehicle, and the dynamic responses of the vehicle will be greatly amplified. The critical train speed in this case can be written as

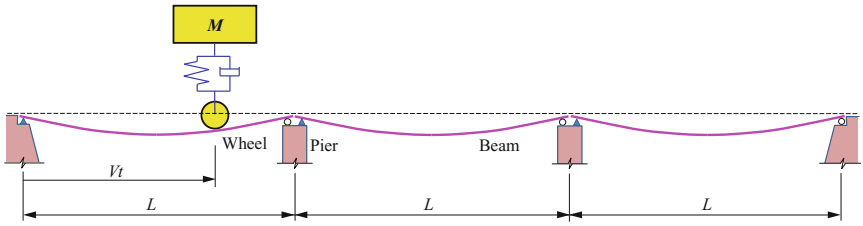

Fig. 2.22 Vehicle vibration induced by bridge deflections

$$V_{\mathrm{vr}} = 3.6 \cdot f_{\mathrm{v}} \cdot L \tag{2.82}$$

where V_{vr} is the critical train speed (km/h); f_{v} is the natural vertical frequency of vehicle (Hz); and L_{b} is the span length of bridge (m).

The excitation of bridge deflections on the vehicle is equivalent to a wheel-spring-mass system on the ground in harmonic motions. The transmissibility between the amplitudes of the mass and the deflection of the beam can be estimated as (Clough and Penzien 2003)

$$\mathrm{TR} = \sqrt{\frac{1 + (2\xi\beta)^2}{(1 - \beta^2)^2 + (2\xi\beta)^2}} \tag{2.83}$$

For a half-vehicle model with sprung-mass M = 24 t, equivalent spring stiffness k = 800 kN/m, and damping ratio ξ = 0.2, the natural frequency is calculated as 0.92 Hz. At the critical train speed, i.e., β = 1, the transmissibility can be calculated as TR = 2.69. It means when the deflection of the bridge is 2 mm, the amplitude of the vehicle will be as large as 5.38 mm. Moreover, the resonance of vehicles will in turn enlarge the dynamic impact on the bridge.

The fundamental vertical natural frequencies of train vehicles are usually between 0.8 and 1.5 Hz. For the railway bridges with 20 m $\sim$ 40 m spans, the corresponding critical train speeds could thus be estimated as V_{vr} = 57 km/h $\sim$ 216 km/h. To prevent or to suppress vehicle resonance due to bridge deflections, therefore, attentions should be paid in design to avoid long series of identical spans, or to reduce the deflection by strengthening structural stiffness.

2.4 Vibration Suppression and Cancellation Analysis of Train-Bridge System

In studying the train-bridge resonance, Yang et al. (1997) found that resonance of the bridge may not occur at certain ratios between span length and characteristic load distance. Savin (2001) discovered that when a single load passing a

simply-supported bridge at different speeds, the amplitude of free vibration changes and declines to null at some speeds. This interesting finding interprets the vibration cancellation effect; namely, when a single load passes the bridge at a cancellation speed, the residual free vibration of the bridge will be null after the load leaves it.

Unlike the resonance effect that enlarges the bridge response, the cancellation effect may suppress the vibration of the bridge, which is favorable for train running safety and bridge service. Therefore, an insight investigation into the cancellation effect is of important significance, and some further investigations have been done, such as those by Yau et al. (2001), Pesterev et al. (2003), Yang et al. (2004a, b), Museros et al. (2013), and Xia et al. (2014).

In this section, vibrations of the simply-supported beam under a moving single force, equidistant load series, and train loads are theoretically analyzed, in terms of bridge free vibration after each load leaving the bridge. By analysis of the vibration responses, the occurrence conditions of resonance and two types of vibration cancellation effects on the simply-supported beam are derived for any mode. Additionally, the influence of vibration cancellation on resonance is investigated, and conditions for resonance disappearance are obtained. The resonance and cancellation mechanisms and characteristics of bridge response are illustrated through numerical case study.

2.4.1 Resonance and Cancellation of Simply-Supported Beam Under Moving Equidistant Load Series

2.4.1.1 Analysis Model

A simply-supported beam bridge subjected to a train load is analyzed herein, using the same model as shown in Fig. 2.16. The train is simplified as a series of moving loads with identical interval, each force P represents a concentrated constant car load, and the interval l_v denotes the full length of a car. Thus, a train composed of N_v cars can be considered as N_v moving forces, numbered as P_k ($k = 1, 2, 3, \ldots N_v$). If the initial time is defined as the moment when the first load gets onto the bridge, the time of the kth load entering the bridge can be expressed as

$$t_k = (k-1)l_v/V \tag{2.84}$$

where V is the moving speed of the train.

2.4.1.2 Analytical Solution for Bridge Vibration Response

Ignoring the damping effect, the motion equation of the bridge under moving equidistant loads can be expressed as

$$\bar{m}\frac{\partial^2 y(x,t)}{\partial t^2}+EI\frac{\partial^4 y(x,t)}{\partial x^4}=\sum_{k=1}^{N_v}P\delta[x-V(t-t_k)] \tag{2.85}$$

where $\bar{m}$ and EI are, respectively, the mass per unit length and the bending stiffness of the bridge; $y(x, t)$ is the displacement of the bridge at position x and time t; and δ is the Dirac delta function.

Equation (2.85) is a partial differential equation, whose initial and boundary conditions can be expressed as

$$\begin{cases} y(x,0)=\dot{y}(x,0)=0 \\ y(0,t)=y(L,t)=0 \\ EIy''(0,t)=EIy''(L,t)=0 \end{cases} \tag{2.86}$$

For a simply-supported beam, Eq. (2.85) can be solved through the modal decomposition method. The displacement of the beam can be expressed by $y(x,t)=\sum_{n=1}^{\infty}q_n(t)\sin\frac{n\pi x}{L}$, namely the product of generalized coordinates $q(t)$ and mode shapes. Thus, Eq. (2.85) can be rewritten in terms of generalized coordinates as

$$\ddot{q}_n(t)+\omega_n^2 q_n(t)=\frac{2P}{\bar{m}L}\sum_{k=1}^{N_v}\sin\left(\frac{n\pi V(t-t_k)}{L}\right) \tag{2.87}$$

where $\omega_n=\left(\frac{n\pi}{L}\right)^2\sqrt{\frac{EI}{\bar{m}}}$ is the nth circular frequency of the bridge.

Equation (2.87) is the motion equation of the simply-supported beam under a moving load series. Its particular solution is ($\beta_n \neq 1$)

$$y(x,t)=\frac{2P}{\bar{m}L}\sum_{n=1}^{\infty}\left\{\sin\left(\frac{n\pi x}{L}\right)\frac{1}{\omega_n^2(1-\beta_n^2)}\sum_{k=1}^{N_v}[\sin\bar{\omega}_n(t-t_k)-\beta_n\sin\omega_n(t-t_k)]\right\} \tag{2.88}$$

where $\bar{\omega}_n = n\pi V/L$ is the exciting frequency; $\beta_n = \bar{\omega}_n/\omega_n$ is the ratio of the exciting frequency of moving loads to the natural frequency of bridge, which can be expressed in terms of speed parameter α as $\beta_n = \alpha/n$. The case $\beta_n = 1$ corresponds to the second resonant condition, which has been discussed in Sects. 2.1 and 2.3, and is not described again herein.

Considering the case when the first (N−1) (N = 1, 2, 3, …, N_v) forces have left, and the Nth force is on the bridge, the displacement response of the bridge can be expressed by the following equation

$$y(x,t) = \frac{2P}{\bar{m}L}\sum_{n=1}^{\infty}\sin\left(\frac{n\pi x}{L}\right)\frac{1}{\omega_n^2(1-\beta_n^2)}Q_N(V,t) \tag{2.89}$$

where

$$\begin{aligned} Q_N(V,t) = {} & [\sin\bar{\omega}_n(t-t_N) - \beta_n\sin\omega_n(t-t_N)] \\ & - \beta_n\sum_{k=1}^{N-1}\left[\sin\omega_n(t-t_k) + (-1)^{n-1}\sin\omega_n\left(t-t_k-\frac{L}{V}\right)\right] \end{aligned} \tag{2.90}$$

The first term of $Q_N(V, t)$ represents steady and transient responses induced by the Nth force moving on the bridge. The second term is associated with the total residual responses (free vibration) induced by the first ($N-1$) forces that have left the bridge, which is derived from Eq. (2.88) as follows:

During $t_k \le t \le t_k + L/V$, the kth force is on the bridge, and the forced vibration response of the bridge induced by it can be written as

$$y_k(x,t) = \frac{2P}{\bar{m}L}\sum_{n=1}^{\infty}\sin\left(\frac{n\pi x}{L}\right)\frac{1}{\omega_n^2(1-\beta_n^2)}[\sin\bar{\omega}_n(t-t_k) - \beta_n\sin\omega_n(t-t_k)] \tag{2.91}$$

During $t > t_k + L/V$, the kth load has left the bridge, and the free vibration response of the bridge induced by it can be expressed as

$$\begin{aligned} y_k(x,t) = {} & \sum_{n=1}^{\infty} y_k^n(x, t_k + L/V)\cos\omega_n(t - t_k - L/V) \\ & + \sum_{n=1}^{\infty}\frac{\dot{y}_k^n(x, t_k + L/V)}{\omega_n}\sin\omega_n(t - t_k - L/V) \end{aligned} \tag{2.92}$$

where $y_k^n(x, t_k + L/V)$ and $\dot{y}_k^n(x, t_k + L/V)$ are, respectively, displacement and velocity of the nth mode at $t = t_k + L/V$, which are the initial conditions of the free vibration and can be derived from Eq. (2.91).

Substituting $y_k^n(x, t_k + L/V)$ and $\dot{y}_k^n(x, t_k + L/V)$ into Eq. (2.92), the total residual response of the bridge induced by the first $N-1$ forces can be expressed as

$$y_k(x,t) = -\frac{2P}{\bar{m}L}\sum_{n=1}^{\infty}\sin\left(\frac{n\pi x}{L}\right)\frac{1}{\omega_n^2(1-\beta_n^2)}\beta_n\sum_{k=1}^{N-1}\left[\sin\omega_n(t-t_k) + (-1)^{n-1}\sin\omega_n(t-t_k-L/V)\right] \tag{2.93}$$

From Eq. (2.93), the second term in the $Q_N(V, t)$ can be extracted. By applying the trigonometric transformation, Eq. (2.90) can be expressed as

$$Q_N(V,t) = [\sin \bar{\omega}_n(t - t_N) - \beta_n \sin \omega_n(t - t_N)] - 2\beta_n \sum_{k=1}^{N-1} \left[\cos \frac{\omega_n L}{2V} \sin \omega_n \left(t - t_k - \frac{L}{2V}\right)\right] \quad (n = 1, 3, 5, \ldots) \tag{2.94a}$$

$$Q_N(V,t) = [\sin \bar{\omega}_n(t - t_N) - \beta_n \sin \omega_n(t - t_N)] - 2\beta_n \sum_{k=1}^{N-1} \left[\sin \frac{\omega_n L}{2V} \cos \omega_n \left(t - t_k - \frac{L}{2V}\right)\right] \quad (n = 2, 4, 6, \ldots) \tag{2.94b}$$

It is not easy to observe the significant physical meanings of this equation. Therefore, by introducing Eqs. (2.84) and (2.70) into Eq. (2.94a, 2.94b), a more interesting expression for $Q_N(V,t)$ can be obtained as

$$Q_N(V,t) = [\sin \bar{\omega}_n(t - t_N) - \beta_n \sin \omega_n(t - t_N)] - 2\beta_n \cos \frac{\omega_n L}{2V} \left\{ \sin \omega_n \left(t - \frac{L}{2V} - \frac{t_{N-1}}{2}\right) \frac{\sin(N-1)\frac{\omega_n L_v}{2V}}{\sin \frac{\omega_n L_v}{2V}} \right\} \quad (n = 1, 3, 5, \ldots) \tag{2.95a}$$

$$Q_N(V,t) = [\sin \bar{\omega}_n(t - t_N) - \beta_n \sin \omega_n(t - t_N)] - 2\beta_n \sin \frac{\omega_n L}{2V} \left\{ \cos \omega_n \left(t - \frac{L}{2V} - \frac{t_{N-1}}{2}\right) \frac{\sin(N-1)\frac{\omega_n L_v}{2V}}{\sin \frac{\omega_n L_v}{2V}} \right\} \quad (n = 2, 4, 6, \ldots) \tag{2.95b}$$

2.4.1.3 Resonance and Cancellation

It is observed from Eq. (2.95a, 2.95b) that the residual free vibration in terms of generalized coordinates for the bridge induced by the first ($N-1$) forces can be expressed by a sinusoidal function (for odd-order modes) or a cosine function (for even-order modes).

For $\sin(\omega_n L_v/2V) = i\pi$, Eq. (2.95a, 2.95b) becomes an indeterminate form 0/0; however, when the L'Hospital's rule is applied, the limit solution is found to be

$$Q_N(V,t) = [\sin \bar{\omega}_n(t - t_N) - \beta_n \sin \omega_n(t - t_N)] - 2(N-1)\beta_n \cos\left(\frac{\omega_n L}{2V}\right) \sin \omega_n \left(t - \frac{L}{2V}\right) \quad (n = 1, 3, 5, \ldots) \tag{2.96a}$$

$$Q_N(V,t) = [\sin\bar{\omega}_n(t-t_N) - \beta_n \sin\omega_n(t-t_N)] - 2(N-1)\beta_n \sin\left(\frac{\omega_n L}{2V}\right)\cos\omega_n\left(t-\frac{L}{2V}\right) \quad (n=2,4,6,\ldots) \tag{2.96b}$$

It can be seen from Eq. (2.96a, 2.96b) that the displacement of bridge will be successively amplified with the increase of the number N of forces traveling on the bridge. Therefore, by using the extreme condition $\omega_n L_v/2V = i\pi$, the resonant speed V_{res} (km/h) for the bridge under the moving load series can be expressed as

$$V_{res} = \frac{3.6 f_n L_v}{i} \quad (i=1,2,3,\cdots) \tag{2.97}$$

where f_n is the nth-order natural frequency of the bridge (Hz). Equation (2.97) has been defined as the first resonant condition in Sect. 2.3, where more details on the bridge resonance induced by the moving load series can be found.

When $\cos(\omega_n L/2V) = 0$ or $\sin(\omega_n L/2V) = 0$, the second term of $Q_N(V, t)$ in Eq. (2.94a, 2.94b) becomes zero and only the first term is left

$$Q_N(V,t) = [\sin\bar{\omega}_n(t-t_N) - \beta_n \sin\omega_n(t-t_N)] \tag{2.98}$$

In this case, the total residual response (free vibration) of the bridge excited by the first ($N-1$) forces is equal to null, while the vibration is determined only by the Nth force acting on the bridge. This phenomenon is herein defined as ***the first cancellation effect of vibration*** with the following conditions

$$\frac{\omega_n L}{2V} = i\pi - \frac{\pi}{2} \quad (n=1,\ 3,\ 5,\ldots;\ i=1,\ 2,\ 3,\ldots) \tag{2.99a}$$

$$\frac{\omega_n L}{2V} = i\pi \quad (n=2,4,6,\cdots;i=1,2,3,\ldots) \tag{2.99b}$$

It can be observed from Eq. (2.90) that when Eq. (2.99a, 2.99b) is satisfied, there is a $(2i\text{-}1)\pi$ or a $2i\pi$ phase difference between the two sinusoidal terms within the second part of $Q_N(V, t)$. This means that the two parts of the residual free vibration induced by a single moving load are canceled out.

The conditions in terms of load speed V_{canI}(km/h) for the first type of cancellation can be further derived from Eq. (2.99a, 2.99b) as

$$V_{canI} = \frac{7.2 f_n L}{2i-1}, \quad (n=1,3,5,\cdots; \quad i=1,2,3,\cdots; \quad \text{and } n \neq 2i-1) \tag{2.100a}$$

$$V_{canI} = \frac{7.2 f_n L}{2i}, \quad (n=2,\ 4,\ 6,\cdots; \quad i=1,\ 2,\ 3,\ldots; \quad \text{and } n \neq 2i) \tag{2.100b}$$

Note that the restriction conditions $n \neq 2i-1$, (n = 1, 3, 5,…) and $n \neq 2i$ (n = 2, 4, 6,…) are given in Eq. (2.100a, 2.100b), because under these values β_n becomes 1 and the second resonance condition is satisfied, which is beyond the assumption of Eq. (2.88). The speed from Eq. (2.100a, 2.100b) coincides with the cancellation speed $\alpha = n^2/k$ in Sect. 2.1.

It can be found from Eq. (2.100a, 2.100b) that the cancellation effect takes place when the force travels on the bridge at a certain speed. This type of cancellation is induced by each individual load and is independent of the number and composition of load series. The cancellation speed is related to the order of vibration mode. Because the fundamental mode provides the largest contribution to the mid-span displacement of a simply-supported bridge, it seems feasible to use Eq. (2.100a) with n = 1 to predict the cancellation speed. This is also assumed in the subsequent section.

2.4.2 *Resonance and Cancellation of Simply-Supported Beam Under a Series of Train Loads*

2.4.2.1 Analysis Model Considering Train Load Series

For a real train composed of several cars, as mentioned previously, there exist different geometric intervals: the full length l_v of the car, the rated axle distance l_c between bogie centers of a car, and the wheelbase l_w between the two wheel-sets of a bogie. Thus, an analysis model shown in Fig. 2.23 is adopted to study the influence of these intervals on the resonance and cancellation effects of a simply-supported bridge.

In this model, the loads of a train composed of N_v cars with four axles are represented by $4N_v$ moving concentrated forces expressed as P_{kj} (k = 1, 2, 3,…,N_v; j = 1, 2, 3, 4), where subscript k indicates the car number of the train and j indicates the axle number of each car. Thus, the train is modeled as groups of four moving

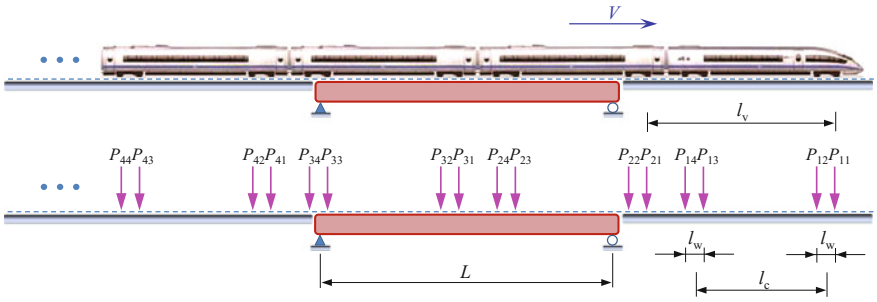

Fig. 2.23 Analysis model of train load series

concentrated forces P_{k1}, P_{k2}, P_{k3}, and P_{k4} with an identical interval l_v between similar forces of each group.

Owing to the time delays between load groups P_{k2}, P_{k3}, P_{k4}, and P_{k1}, the time for the kth force in group j traveling on the bridge can be defined as

$$\begin{cases} t_{k1}=t_k \\ t_{k2}=t_k+l_w/V \\ t_{k3}=t_k+l_c/V \\ t_{k4}=t_k+(l_c+l_w)/V \end{cases} \tag{2.101}$$

Note that $t_k = (k-1)l_v/V$ is still valid herein.

In this case, the motion equation for the bridge can be written as

$$\bar{m}\frac{\partial^2 y(x,t)}{\partial t^2}+EI\frac{\partial^4 y(x,t)}{\partial x^4}=\sum_{k=1}^{N_v}\sum_{j=1}^{4}P\delta\left[x-V(t-t_{kj})\right] \tag{2.102}$$

Considering the case when the first $(N-1)$ cars have left the bridge and only the Nth car is traveling on the bridge, the solution of Eq. (2.102) can be given directly referring to the previous analysis in Sect. 2.4.1 as

$$y(x,t)=\frac{2P}{\bar{m}L}\sum_{n=1}^{\infty}\sin\left(\frac{n\pi x}{L}\right)\frac{1}{\omega_n^2(1-\beta_n^2)}\sum_{j=1}^{4}Q_{Nj}(V,t) \tag{2.103}$$

where

$$\sum_{j=1}^{4}Q_{Nj}(V,t)=\sum_{j=1}^{4}\left[\sin\bar{\omega}_n(t-t_{Nj})-\beta_n\sin\omega_n(t-t_{Nj})\right] -2\beta_n\sum_{k=1}^{N-1}\sum_{j=1}^{4}\cos\frac{\omega_n L}{2V}\left[\sin\omega_n\left(t-t_{kj}-\frac{L}{2V}\right)\right] \quad (n=1,3,5,\ldots) \tag{2.104a}$$

$$\sum_{j=1}^{4}Q_{Nj}(V,t)=\sum_{j=1}^{4}\left[\sin\bar{\omega}_n(t-t_{Nj})-\beta_n\sin\omega_n(t-t_{Nj})\right] -2\beta_n\sum_{k=1}^{N-1}\sum_{j=1}^{4}\sin\frac{\omega_n L}{2V}\left[\cos\omega_n\left(t-t_{kj}-\frac{L}{2V}\right)\right] \quad (n=2,4,6,\ldots) \tag{2.104b}$$

By applying trigonometric transformation formulas $\sin A+\sin B=2\cos\frac{A+B}{2}\sin\frac{A-B}{2}$ and $\cos A+\cos B=2\cos\frac{A+B}{2}\cos\frac{A-B}{2}$ to the second term of the

right side of Eq. (2.104a, 2.104b), the following expressions can be obtained after rearrangement as

$$\sum_{j=1}^{4} Q_{Nj}(V,t) = \sum_{j=1}^{4} \left[\sin \bar{\omega}_n(t-t_{Nj}) - \beta_n \sin \omega_n(t-t_{Nj})\right] - 8\beta_n \cos\frac{\omega_n L}{2V}\cos\frac{\omega_n l_w}{2V}\cos\frac{\omega_n l_c}{2V} \times \sum_{k=1}^{N-1}\left[\sin\omega_n\left(t - t_{k1} - \frac{L}{2V} - \frac{l_w}{2V} - \frac{l_c}{2V}\right)\right] \quad (n = 1,3,5,\ldots) \tag{2.105a}$$

$$\sum_{j=1}^{4} Q_{Nj}(V,t) = \sum_{j=1}^{4} \left[\sin \bar{\omega}_n(t-t_{Nj}) - \beta_n \sin \omega_n(t-t_{Nj})\right] - 8\beta_n \sin\frac{\omega_n L}{2V}\cos\frac{\omega_n l_w}{2V}\cos\frac{\omega_n l_c}{2V} \times \sum_{k=1}^{N-1}\left[\cos\omega_n\left(t - t_{k1} - \frac{L}{2V} - \frac{l_w}{2V} - \frac{l_c}{2V}\right)\right] \quad (n = 2,4,6,\ldots) \tag{2.105b}$$

By again introducing Eq. (2.70), the above equations can be further rewritten as

$$\sum_{j=1}^{4} Q_{Nj}(V,t) = \sum_{j=1}^{4} \left[\sin \bar{\omega}_n(t-t_{Nj}) - \beta_n \sin \omega_n(t-t_{Nj})\right] - 8\beta_n \cos\frac{\omega_n L}{2V}\cos\frac{\omega_n l_w}{2V}\cos\frac{\omega_n l_c}{2V} \times \left\{\sin\omega_n\left(t - \frac{L}{2V} - \frac{l_w}{2V} - \frac{l_c}{2V} - \frac{t_{N-1}}{2}\right)\frac{\sin(N-1)\frac{\omega_n l_v}{2V}}{\sin\frac{\omega_n l_v}{2V}}\right\} \quad (n = 1,3,5,\ldots) \tag{2.106a}$$

$$\sum_{j=1}^{4} Q_{Nj}(V,t) = \sum_{j=1}^{4} \left[\sin \bar{\omega}_n(t-t_{Nj}) - \beta_n \sin \omega_n(t-t_{Nj})\right] - 8\beta_n \sin\frac{\omega_n L}{2V}\cos\frac{\omega_n l_w}{2V}\cos\frac{\omega_n l_c}{2V} \times \left\{\cos\omega_n\left(t - \frac{L}{2V} - \frac{l_w}{2V} - \frac{l_c}{2V} - \frac{t_{N-1}}{2}\right)\frac{\sin(N-1)\frac{\omega_n l_v}{2V}}{\sin\frac{\omega_n l_v}{2V}}\right\} \quad (n = 2,4,6,\ldots) \tag{2.106b}$$

2.4.2.2 Resonance and Cancellation Induced by a Train Load Series

The resonant conditions derived from Eq. (2.106a, 2.106b) are not different from Eq. (2.97) in Sect. 2.3. Obviously, two more cancellation conditions can be extracted from Eq. (2.106a, 2.106b) as

$$\cos(\omega_n l_w/2V) = 0 \tag{2.107a}$$

$$\cos(\omega_n l_c/2V) = 0 \tag{2.107b}$$

The corresponding cancellation train speeds V_{canII}(km/h) can be expressed as

$$V_{\text{canII}} = \frac{7.2 f_n l_{\text{w}}}{2i-1}, \quad (i = 1, 2, 3, \cdots) \tag{2.108a}$$

$$V_{\text{canII}} = \frac{7.2 f_n l_{\text{c}}}{2i-1}, \quad (i = 1, 2, 3, \cdots) \tag{2.108b}$$

The cancellation effect will be expected if conditions associated with the wheelbase l_{w} and the axle distance l_{c} between the bogie centers in Eq. (2.108a, 2.108b) are met. However, the mechanism herein is different from that described in previous section, because in this case, the cancellation occurs due to the offset of free vibrations of the bridge induced by the moving loads of different groups. Equation (2.107a) indicates that the free vibrations induced by the two axle loads of one bogie cancel each other out, while Eq. (2.107b) indicates that the free vibrations induced by the two axle loads spaced l_{v} apart cancel each other out. As a result, the residual free vibrations of the bridge become null after the first car leaves the bridge. This type of cancellation is determined by load intervals.

A more general formula can be obtained through extension of the cancellation conditions of Eq. (2.107a, 2.107b), and the corresponding cancellation train speed can be expressed as

$$V_{\text{canII}} = \frac{7.2 f_n L_{\text{ch}}}{2i-1}, \quad (i = 1, 2, 3, \cdots). \tag{2.109}$$

where L_{ch} is the characteristic interval of the load series.

This cancellation effect is herein defined as ***the second cancellation effect of vibration***. For a railway train with two bogies and four axles, the characteristic interval may be l_{c} or l_{w}. In fact, L_{ch} can be any regular interval between the axle loads in the load series; hence, l_{v} is included as well, as shown in Fig. 2.23.

Thus far, two types of cancellation effects and their conditions have been proposed, as expressed in Eqs. (2.100a, 2.100b) and (2.109), respectively. When only the fundamental mode of the bridge is concerned, the cancellation speed equation can be written in a unified form as function of the bridge span L

$$V_{\text{can}} = \frac{7.2 \alpha f_1 L}{2i-1}, \quad (i = 1, 2, 3, \cdots) \tag{2.110}$$

where f_1 is the fundamental frequency of the bridge; α is the dimensionless length parameter, which may take the value of 1 or L_{ch}/L, indicating the first or second type of cancellation, respectively.

2.4.2.3 Resonance Disappearance

The second term of Eq. (2.106a, 2.106b) will be null once cancellation conditions are satisfied even with the resonant condition synchronously met. Therefore, cancellation plays a more dominant role, and resonance disappearance may be expected when a train speed coincides simultaneously with the conditions of resonance and cancellation. When $V_{can} = V_{res}$, namely combining Eqs. (2.97) and (2.110), a new mathematical expression is obtained as

$$\frac{l_v}{L} = \frac{2\alpha k}{2j-1}, \quad (j,k = 1,2,3,\cdots) \tag{2.111}$$

where j and k are, respectively, the resonance and cancellation order for the first bending mode of the bridge. In theory, when the ratio of car length l_v to span L meets the conditions of Eq. (2.111), both the cancellation and resonance conditions may simultaneously appear at certain train speeds, and the resonance of the bridge at its fundamental mode will be avoided. Therefore, this interesting phenomenon is named as ***resonance disappearance***.

2.4.3 Numerical Verification

To verify the theoretical expressions, by using the FEM, a computation program is developed to analyze the vibration response of a single span simply-supported bridge under moving train loads.

The bridge has a span of 31.1 m, a uniform mass density of 19.1 Mg/m, and a uniform cross-sectional bending stiffness of $EI = 1.66 \times 10^8$ kN·m^2, and the first natural frequency is calculated by $f_1 = \frac{\pi}{2L^2}\sqrt{\frac{EI}{m}}$ as 4.79 Hz.

A high-speed train composed of four cars is adopted for analysis, simplified as 16 concentrated forces. The forces take the axle loads of the ICE3 high-speed train, which are 160 kN for the first and the last motor-cars ($P_1 \sim P_4$, $P_{13} \sim P_{16}$) and 146 kN for the intermediate trailer cars ($P_5 \sim P_8$, $P_9 \sim P_{12}$), respectively, as shown in Fig. 2.24.

According to the train axle intervals and the bridge span shown in Fig. 2.24, the characteristic interval L_{ch} of the load series can be $l_v = 24.775$ m, $l_c = 17.375$ m, and $l_w = 2.5$ m, and thus, the dimensionless length parameter α in Eq. (2.110) can be identified as 1.0 for the first cancellation condition, and as $l_w/L = 0.08$, $l_c/L = 0.56$, and $l_v/L = 0.79$ for the second cancellation condition. On the basis of these parameters, the resonance and cancellation speeds V_{res} and V_{can} corresponding to the fundamental mode of the bridge are calculated by Eqs. (2.97) and (2.110), and the results of the first eight orders are listed in Table 2.2.

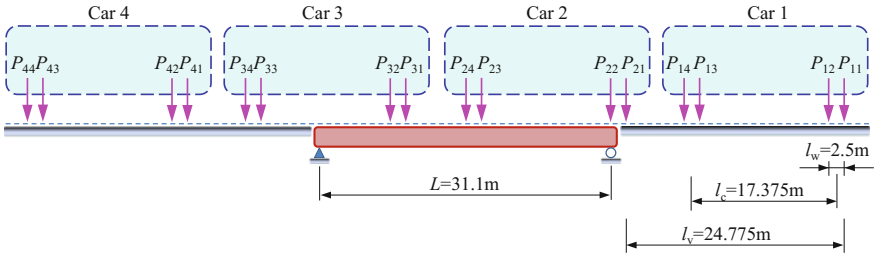

Fig. 2.24 Simply-supported bridge subjected to a moving train load series

Table 2.2 Resonance and cancellation train speeds for the 31.1 m span simply-supported bridge

Order i		1	2	3	4	5	6	7	8
Resonance train speed V_{res} (km/h)		427	214	142	107	85	71	61	–
Cancellation train speed V_{can} (km/h)	α = 1.00	N/A	358	215	153	119	98	83	72
	α = 0.08	86	–	–	–	–	–	–	–
	α = 0.56	601	200	120	86	67	–	–	–
	α = 0.79	847	282	169	121	94	77	65	–

Note "–" indicates the speeds lower than 60 km/h, which are not listed in this table

2.4.3.1 Time History Analyses of the Bridge Under Resonance and Cancellation Conditions

Resonance effect

It is known that a resonance may appear when a certain relationship is satisfied among the load moving speed, load interval, and bridge natural frequency. Herein, the first-order resonance speed 427 km/h is taken as an example to illustrate how the ICE3 train load series induces the resonance of the bridge.

Because the ICE3 load series is composed of several different intervals, the analysis is conducted in two stages, as shown in Fig. 2.25.

In the first stage, a group of loads composed of the first axle loads (P_{11}, P_{21}, P_{31}, and P_{41}) of the four cars is considered. The time delay between any two successive loads is determined by load interval l_v and resonant speed V_{res}, which can be calculated as

$$t_{res} = \frac{l_v}{V_{res}} = \frac{il_v}{f_n l_v} = iT_{bn}, \quad (i = 1, 2, 3, \cdots) \tag{2.112}$$

When only the first mode of the bridge is considered, and for the resonant speed related to $i = 1$, the time delay is equal to the bridge natural period T_b, thus producing a 2π phase difference between the free vibrations of the bridge induced by any two successive loads in this group. In this case, the amplitudes of the bridge in

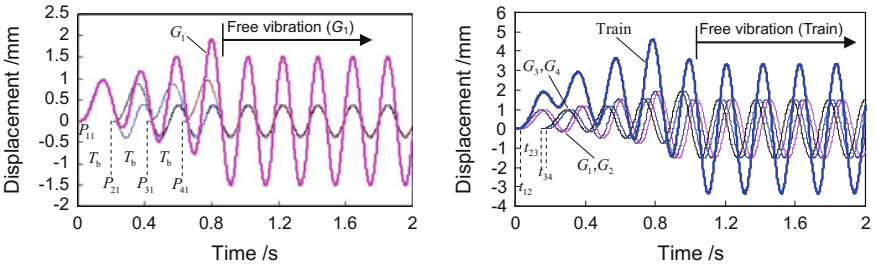

(a) Induced by equidistance loads (b) Superposition of various loads

Fig. 2.25 Displacement histories of the bridge at mid-span under V_{res} = 427 km/h

the free vibration stage will be directly superposed to form a resonant displacement curve G_1, as shown in Fig. 2.25a.

Similarly, the resonant displacement curve G_2 induced by the load series composed of the second axle loads (P_{12}, P_{22}, P_{32}, and P_{42}) of the four cars can be obtained and so for G_3 and G_4.

In the second stage, the four resonant displacement curves ($G_1 \sim G_4$) induced by the four groups of load series are superposed together according to the time delays determined by their intervals l_w, l_c, and $l_w + l_c$. Thus, the bridge displacement induced by the whole train can be obtained, as shown in Fig. 2.25b.

It is easy to see that under the resonant speed, the displacement of the bridge will be successively amplified with an increasing number of loads, which explains the physical meaning of Eq. (2.96a, 2.96b).

The first cancellation effect

Parameter $\alpha = 1$ corresponds to the first type of cancellation. The third-order ($\alpha = 1$, $i = 3$) cancellation speed 215 km/h in Table 2.2 is selected as an example to illustrate how the first cancellation effect appears. Shown in Fig. 2.26 are the calculated displacement histories of the bridge induced by the train (four cars), the first car, and its four individual axle loads $P_{11} \sim P_{14}$.

The mechanism for the first type of cancellation can be observed clearly in these displacement histories. It is found that each moving load induces a forced vibration

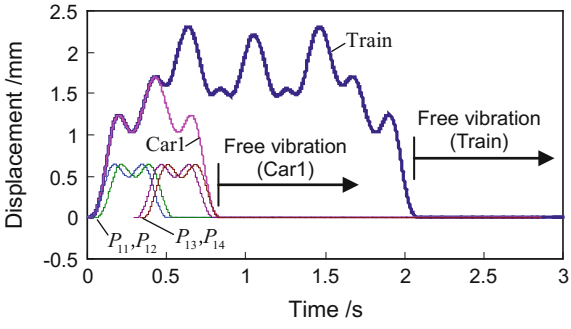

Fig. 2.26 Displacement histories of the bridge induced by the train, Car 1, and its four individual loads ($P_{11} \sim P_{14}$) under V_{can1} = 215 km/h

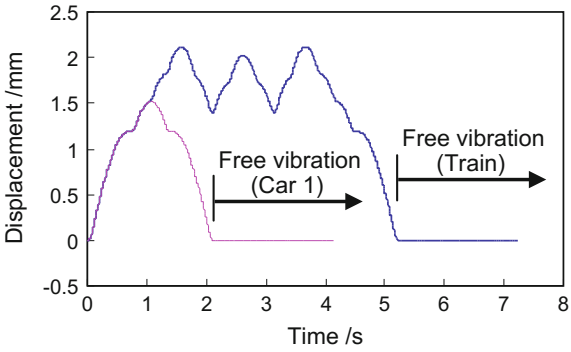

Fig. 2.27 Displacement histories of the bridge induced by the train and Car 1 under V_{canII} = 86 km/h

of the bridge, but when it leaves, the free vibration of the bridge is null. As a result, the free vibration of the bridge remains zero when the first car as well as the train leaves the bridge. This numerical example explains the physical meaning of Eq. (2.100a, 2.100b).

The second cancellation effect

In Table 2.2, $\alpha = 0.08$ and $\alpha = 0.56$ correspond to the second type of cancellation speeds, which are derived from wheelbase l_w of a bogie and axle distance l_c between the bogie centers of a car, respectively.

Obviously, $V_{canII} = 86$ km/h is the most opportune cancellation speed for comparison, for it appears twice in the table at $\alpha = 0.08$ ($i = 1$) and $\alpha = 0.56$ ($i = 4$), respectively, so it is selected as an example to illustrate the effect of the second cancellation. The mechanism of this type of cancellation is clearly illustrated in Fig. 2.27, which gives the displacement histories of the bridge at mid-span induced by the train and the first car only.

It is seen that at this cancellation speed no free vibration of the bridge appears when the first car as well as the train leaves the bridge, because the cancellation speed $V_{canII} = 86$ km/h is the first-order cancellation speed ($\alpha = 0.08$) related to l_w and also the fourth-order cancellation speed ($\alpha = 0.56$) related to L_c. When $\alpha = 0.08$ and $i = 1$, the free vibrations induced by P_{11} and P_{12} cancel each other out, same for P_{13} and P_{14}. When $\alpha = 0.56$ and $i = 4$, the free vibrations induced by P_{11} and P_{13} cancel each other out and also P_{12} and P_{14}. As a result, no free vibration remains when each car leaves the bridge, and the displacement of the bridge is determined only by the loads still on it.

The mechanism of the second type of vibration cancellation is further explained in Fig. 2.28. At $V_{can} = 86$ km/h, the cancellation effect appears between the two axle loads separated by l_w or l_c.

Figure 2.28a illustrates the mechanism of the second cancellation effect corresponding to P_{11} and P_{12} with a wheelbase l_w. It can be found that the displacement of the bridge induced by P_{12} has a time delay of $T_b/2$ related to P_{11}, producing a phase difference π between them and causing the free vibrations by P_{11} and P_{12} having the same amplitudes but opposite phases. The result is null vibration when this pair of loads leaves the bridge.

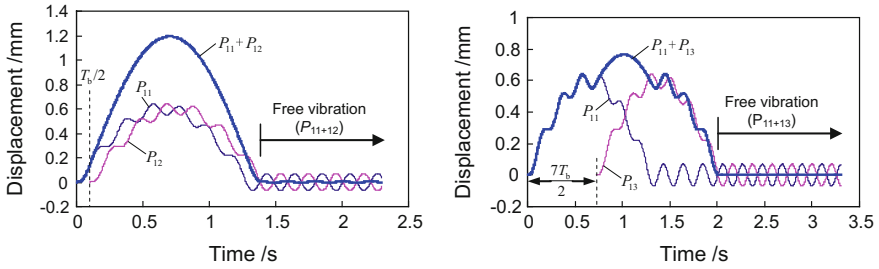

(a) V_{can}=86 km/h, l_w=2.5 m, i=1 (b) V_{can}=86 km/h, l_c=17.375 m, i=4

Fig. 2.28 Displacement histories of the bridge under V_{canI} = 86 km/h

Figure 2.28b shows the mechanism of the second cancellation effect corresponding to P_{11} and P_{13} with an interval l_c. In this case, the time delay between P_{13} and P_{11} becomes 7 $T_b/2$, and the phase difference becomes 7π; thus, the free vibrations induced by the two loads cancel each other out. Similar cancellation effects exist between the other pairs of loads (P_{12} + P_{14}).

The time delay between the two loads can be calculated by the interdistance and cancellation speed of the loads as follows:

$$t_{can} = \frac{L_{ch}}{V_{can}} = \frac{(2i-1)L_{ch}}{2f_n L_{ch}} = \frac{(2i-1)}{2} T_{bn}, \quad (i = 1, 2, 3, \ldots) \tag{2.113}$$

When only the first mode of the bridge is considered, it is calculated from Eq. (2.113) that at V_{canII} = 86 km/h, the time delays for the two pairs of loads are $T_b/2$ (i = 1) and 7 $T_b/2$ (i = 4), respectively, as marked in Fig. 2.28, and thus, the displacements of the bridge induced by them completely cancel out.

2.4.3.2 Relationship Between Resonance and Cancellation Effects

It was mentioned previously that the condition of cancellation is more dominant over that of resonance. Therefore, cancellation plays a more dominant role and resonance disappearance may be expected when the train speeds coincide with both conditions of resonance and cancellation. In the subsequent section, the relationship between resonance and cancellation effects is discussed.

Suppression of resonance by the first cancellation effect

It is interesting to notice from Table 2.2 that the cancellation speed V_{canI} = 215 km/h is very close to the resonance speed V_{res} = 214 km/h (i = 2), which means this resonant speed approximately meets the cancellation condition. To better describe what will happen, the time histories of bridge mid-span displacements induced by a single load P_{11}, the first car, and the whole train under V_{res} = 214 km/h are calculated, as shown in Fig. 2.29a.

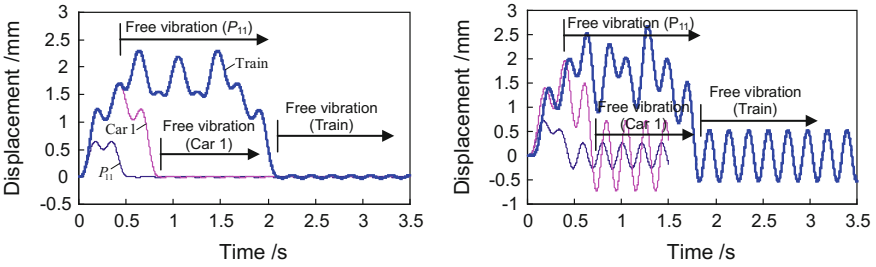

(a) V_{res}=214 km/h (b) V=250 km/h

Fig. 2.29 Displacement histories of the bridge induced by single load P_{11}, Car 1, and train

The resonant speed determined by Eq. (2.97) corresponds to the resonance effect that is provoked by the successive amplification of the bridge displacement with an increasing number of loads on the bridge. As shown in Fig. 2.29a, because the speed 214 km/h is very close to the first type of cancellation speed V_{canI} = 215 km/h, the free vibration of the bridge induced by each individual load is approximately equal to zero, and thus, the bridge displacement induced by a series of loads after superposition of all effects of them is also very small. Therefore, when the resonant speed is close to the cancellation speed, the resonance effect is suppressed by the cancellation effect, resulting in small bridge vibrations.

For comparison, the time histories of the bridge displacement at the train speed of 250 km/h, which is neither a resonance speed nor a cancellation one, are shown in Fig. 2.29b. It is clear that neither the free vibrations induced by the first axle load nor by the car 1 is zero. Hence, after the whole train leaves the bridge, there remains a high residual response (free vibration) on the bridge.

Suppression of resonance by the second cancellation effect

According to Table 2.2, the cancellation speed V_{canII} = 86 km/h is very close to the resonance speed V_{res} = 85 km/h (i = 5). To better describe what will happen in this situation, the time histories of bridge displacements induced by two loads, P_{11} and P_{21}, are calculated, as shown in Fig. 2.30a.

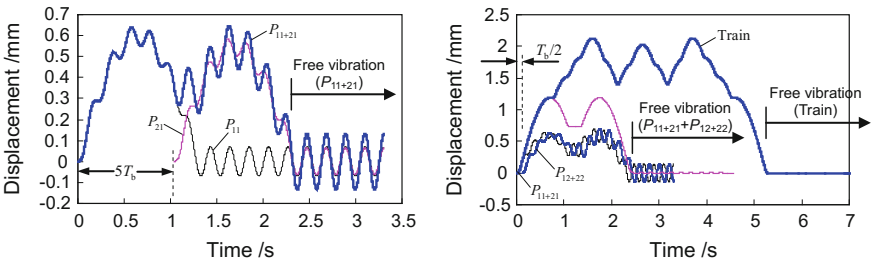

(a) Resonance effect (V_{res}=85 km/h, i=5) (b) Resonance suppression (V_{can} =86 km/h, i=4)

Fig. 2.30 Displacement histories of the bridge at mid-span

Using Eq. (2.112), it is calculated that under 85 km/h, the time delay between the two loads P_{11} and P_{21} is 5 T_b (i = 5). In this case, the phase gap between free vibrations induced by P_{11} and P_{21} is 10π, which indicates five vibration periods, and thus, the free vibrations induced by the two loads superpose each other.

However, in this special case, because the resonant speed 85 km/h is very close to the cancellation speed 86 km/h, the resonance will be suppressed. The mechanism of resonance suppression is shown in Fig. 2.30b, where P_{11} and P_{21} reflect the resonance effect of P_{11+21}, and P_{12} and P_{22} reflect the resonance effect of P_{12+22}. Because the time delay between P_{11+21} and P_{12+22} at 85 km/h is quite close to $T_b/2$, the resultant free vibrations of the bridge subjected to these two pairs of loads almost cancel each other out. When the whole train leaves the bridge, the free vibration remains very small.

Influence of cancellation effect on resonance

To further investigate the relationship between the derived theoretical resonance and cancellation conditions, a numerical analysis is carried out for the dynamic responses of the bridge subjected to the train load series shown in Fig. 2.24, within the speed range of 70 ∼ 500 km/h.

Shown in Fig. 2.31 is the distribution of the calculated DAF (Dynamic Amplification Factor) of the bridge mid-span deflection versus train speed.

It is observed that the DAF does not increase monotonously with the train speed, while there appear several peaks at particular train speeds. When the resonance and cancellation speeds listed in Table 2.2 are marked on the DAF curve, the influence of resonance and cancellation conditions can be clearly observed.

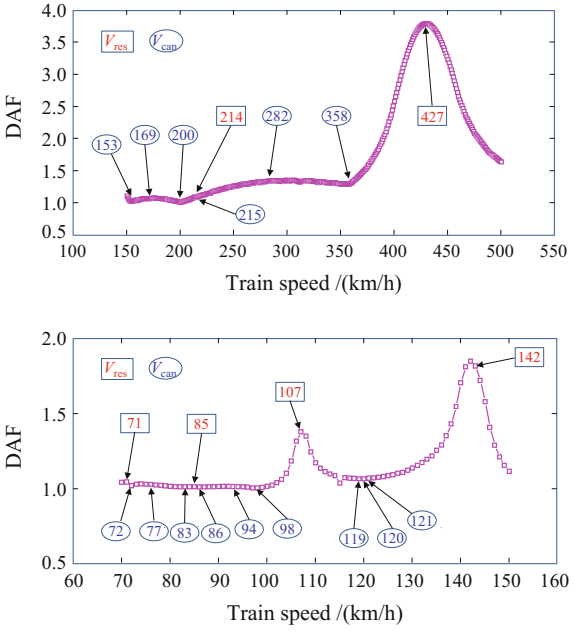

Fig. 2.31 Distribution curves of bridge deflection DAF versus train speed

Obvious peaks on the DAF curves appear at the resonance train speeds 427, 142, and 107 km/h, indicating the resonance phenomena indeed happen at these speeds.

At the resonance speeds of 214, 85, and 71 km/h, however, similar cancellation speeds of 215, 86, and 72 km/h exist, resulting in relatively small DAF values. This numerically proves that when a load series speed simultaneously meets both the resonance and cancellation conditions, the cancellation effect plays a dominant role and the resonance effect will be suppressed; namely, a resonance disappearance occurs. Hence, when the ratio of car length l_v to bridge span L meets the conditions of Eq. (2.111), there will be $V_{res} = V_{can}$ at certain speeds, which provides the possibility of eliminating the resonance. For the considered 31.1 m span simply-supported bridge and the ICE3 train, if the resonance at speed 214 km/h is counteracted, the dynamic responses of the bridge will remain at a low level in the whole speed range of 150 $\sim$ 350 km/h, which is of practical significance in bridge design and the running safety of high-speed trains.

2.4.3.3 Influence of Damping on the Cancellation Effect

In the previous theoretical and numerical analyses, the influence of damping was ignored. In reality, the free vibration of a bridge will attenuate gradually because of the existence of damping. Thus, in the second cancellation effect, the free vibrations induced by a pair of loads will not completely cancel each other out, even if they have the same amplitude and opposite phases. To illustrate the influence of damping on the second type of cancellation, the cancellation speed of 86 km/h is taken again as an example, which corresponds to $\alpha = 0.08$ ($i = 1$) and $\alpha = 0.56$ ($i = 4$). A damping ratio of 0.05 is used to calculate the displacement of the bridge subjected to two loads, as shown in Fig. 2.32.

It can be found that the existence of damping only changes the amplitudes of the free vibration of the bridge, while it affects little the vibration period because the difference between damped and undamped periods is very small. Thus, under the cancellation speed of 86 km/h, the time delay between P_{11} and P_{12} is $T_b/2$ ($i = 1$)

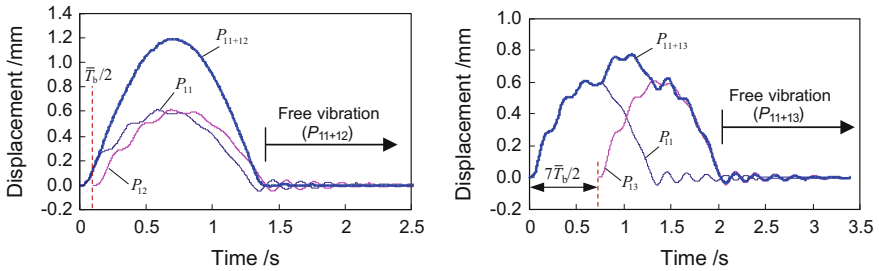

(a) V_{can}=86km/h, L_w=2.5m, i=1 (b) V_{can}=86km/h, L_c=17.375m, i=4

Fig. 2.32 Displacement histories of the bridge considering damping ratio 0.05 under V_{can} = 86 km/h

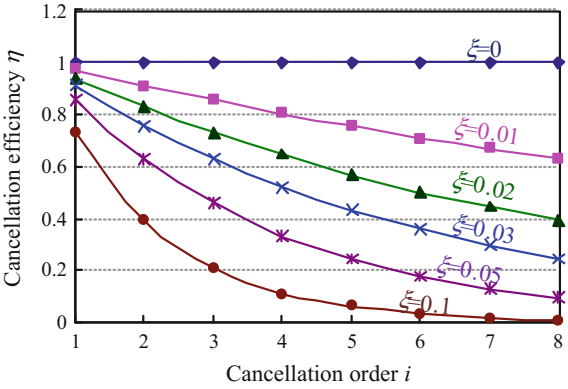

Fig. 2.33 Distributions of cancellation efficiency versus cancellation order for different damping ratios

and that between P_{11} and P_{13} is $7T_b/2$ ($i = 4$), which are approximately equal to those in the undamped case. However, the displacements of free vibration induced by the two loads cannot perfectly cancel each other out despite their opposite phases. This is because they have different absolute values as a result of the unequal time of damping attenuations. It can be concluded that the time delay between the two loads affects the canceling extent of the bridge free vibration, and obviously, the longer the time delay, the less the free vibration can be canceled, thus lowering the cancellation effect.

Of course, the value of damping has a direct influence on the cancellation effect. Figure 2.33 illustrates the distribution of the cancellation efficiency η (defined as the ratio of the maximum free vibration displacement of the bridge that has been canceled out to the one without cancellation) with respect to the cancellation order under several different damping ratios. It can be found that the higher the damping, and the longer the delay time (reflected by the cancellation order) between the two loads, the lower is the cancellation efficiency. Despite this, the cancellation efficiency η is greater than 0.5 for the first two cancellation orders with the bridge damping ratio in the range of $0 \sim 0.05$.

2.4.3.4 Conclusions

The mechanisms of vibration resonance and cancellation for a simply-supported bridge subjected to a moving load series are investigated theoretically and are verified through finite-element numerical simulations. The following conclusions can be drawn:

(1) A resonant vibration may occur because of the superposition of vibrations induced by a series of moving loads passing over a simply-supported bridge when the time interval between two adjacent loads equals the natural period of the bridge or its ith ($i = 1, 2, 3,\ldots$) multiples.

(2) The free vibration of the bridge induced by a single moving load may be canceled out to null by itself when the load speed satisfies a certain relationship with the span length and the natural frequencies of the bridge. This is defined as the first cancellation effect. The first cancellation condition is related to a single load behavior, while it is independent of the numbers and arrangement of loads. The critical cancellation speed expression is associated with the order n of the vibration mode.
(3) The free vibrations of the bridge induced by a series of moving loads may cancel each other out when the load speed satisfies a certain relationship with the load interval and the natural frequencies of the bridge. This is defined as the second cancellation effect, which is related to the interval between any two loads, namely the arrangement of the load series. The second cancellation condition is related to the characteristic interval of loads.
(4) The damping of the bridge has an influence on the efficiency of the second type of cancellation: The higher the damping and the longer the delay time between two loads, the lower is the cancellation efficiency.
(5) In some cases, a certain train speed may simultaneously satisfy both resonance and cancellation conditions. If this occurs, the cancellation plays a dominant role and a resonance disappearance can be expected. This provides the possibility of avoiding bridge resonance via proper design, which is of theoretical as well as practical significance in the dynamic design of high-speed railway bridges.

References

Cheung YK, Au FTK, Zheng DY, Cheng YS (1999) Vibration of multi-span bridges under moving vehicles and trains by using modified beam vibration functions [J]. J Sound Vib 228 (3):611–628

Clough RW, Penzien J (2003) Dynamics of structures [M]. McGraw Hill Inc, New York

Diana G, Cheli F (1989) Dynamic interaction of railway systems with large bridges [J]. Veh Sys Dyn 18:71–106

Frýba L (1999) Vibration of solids and structures under moving loads [M]. Thomas Telford, London

Frýba L (2001) A rough assessment of railway bridges for high speed trains [J]. Eng Struct 23 (5):548–556

Garinei A, Risitano G (2008) Vibrations of railway bridges for high-speed trains under moving loads varying in time [J]. Eng Struct 30(3):724–732

Hamidi SA, Danshjoo F (2010) Determination of impact factor for steel railway bridges considering simultaneous effects of vehicle speed and axle distance to span length ratio [J]. Eng Struct 32(5):1369–1376

Ju SH, Lin HT (2003) Resonance characteristics of high-speed trains passing simply-supported bridges [J]. J Sound Vib 267(5):1127–1141

Kwark JW, Choi ES, Kim YJ et al (2004) Dynamic behavior of two-span continuous concrete bridges under moving high-speed train [J]. Comput Struct 82(4–5):463–474

Lee HH, Jeon JC, Kyung KS (2012) Determination of a reasonable impact factor for fatigue investigation of simple steel plate girder railway bridges [J]. Eng Struct 36:316–324

Li JZ, Su MB (1999) The resonant vibration for a simply-supported girder bridge under high speed trains [J]. J Sound Vib 224(5):897–915
Liu K, Reynders E, De Roeck G, Lombaert G (2009) Experimental and numerical analysis of a composite bridge for high-speed trains. J Sound Vib 320(1–2):201–220
Luu M, Zabel V, Könke C (2012) An optimization method of multi-resonant response of high-speed train bridges using TMDs [J]. Finite Elem Anal Des 53:13–23
Lavado J, Doménech A, Martínez-Rodrigo MD (2014) Dynamic performance of existing high-speed railway bridges under resonant conditions following a retrofit with fluid viscous dampers supported on clamped auxiliary beams [J]. Eng Struct 59:355–374
Matsuura A (1976) A study of dynamic behavior of bridge girder for high speed railway [J]. Proc Jpn Civil Eng Soc 256:35–47 (in Japanese)
Michaltsos GT, Raftoyiannis IG (2010) The influence of a train's critical speed and rail discontinuity on the dynamic behavior of single-span steel bridges [J]. Eng Struct 32(2):570–579
Museros P, Moliner E, Martínez-Rodrigo MD (2013) Free vibrations of simply-supported beam bridges under moving loads: maximum resonance, cancellation and resonant vertical acceleration [J]. J Sound Vib 332(2):326–345
Pesterev AV, Yang B, Bergman LA, Tan CA (2003) Revisiting the moving force problem. J Sound Vib 261(1):75–91
Rade L, Westergren B (2010) Mathematics handbook for science and engineering. Springer
Rocha JM, Henriques AA, Calçada R (2012) Safety assessment of a short span railway bridge for high-speed traffic using simulation techniques [J]. Eng Struct 40:141–154
Savin E (2001) Dynamic amplification factor and response spectrum for the evaluation of vibrations of beams under successive moving loads [J]. J Sound Vib 248(2):267–288
TB10002.1-2005 (2005) Fundamental code for design on railway bridge and culvert [S]. China Railway Publishing House, Beijing
TJS 2003-13 (2003) Interim provisions on design of Beijing-Shanghai HSR [S]. China Railway Publishing House, Beijing (in Chinese)
TJS 2005-285 (2005a) Interim provisions on design of 200 km/h new railways for passenger and freight trains [S]. China Railway Publishing House, Beijing (in Chinese)
TJS 2005-285 (2005b) Commentary on interim provisions on design of 200 km/h new railways for passenger and freight trains [S]. China Railway Publishing House, Beijing (in Chinese)
Xia H, Chen YJ (1992) Dynamic interaction analysis of train-beam-pier system [J]. China Civil Eng J 25(2):3–12 (in Chinese)
Xia H, Zhang N (2005) Dynamic interaction of vehicles and structures [M]. Beijing Science Press (in Chinese)
Xia H, Zhang N, Guo WW (2006) Analysis of resonance mechanism and conditions of train-bridge system [J]. J Sound Vib 297(3–5):810–822
Xia H, De Roeck G, Goicolea JM (2012) Bridge vibration and controls: new research [M]. Nova Science Publishers Inc, New York
Xia H, Li HL, Guo WW, De Roeck G (2014) Vibration resonance and cancellation of simply-supported bridges under moving train loads [J]. J Eng Mech ASCE 140 (5):04014015-1-11
Yang YB, Yau JD, Hsu LC (1997) Vibration of simple beams due to trains moving at high speeds [J]. Eng Struct 19(11):936–944
Yang YB, Yau JD, Wu YS (2004a) Vehicle-bridge interaction dynamics [M]. World Scientific Publishing, Singapore
Yang YB, Lin CL, Yau JD, Chang DW (2004b) Mechanism of resonance and cancellation for train-induced vibrations on bridges with elastic bearings [J]. J Sound Vib 269(1–2):345–360
Yau JD (2001) Resonance of continuous bridges due to high speed trains [J]. J Mar Sci Technol 9 (1):14–20
Yau JD, Wu YS, Yang YB (2001) Impact response of bridges with elastic bearings to moving loads [J]. J Sound Vib 248(1):9–30

Yau JD, Yang YB (1999) Theory of vehicle-bridge interaction for high-speed railway [M]. DNE Press, Taipei

Zambrano A (2011) Determination of the critical loading conditions for bridges under crossing trains [J]. Eng Struct 33(2):320–329

Chapter 3
Self-excitations of Train-Bridge Coupling Vibration System

In this chapter, the self-excitations of train-bridge coupling vibration system are introduced. The characteristics and control standards of track irregularities, and the mechanism and description of vehicle hunting movement are summarized. The AR (auto-regressive) model simulation method of random excitations on the train-bridge system is studied.

There are various excitation sources causing vibrations of train-bridge system, which can be divided into two categories: external environmental excitations and internal self-excitations, as shown in Fig. 3.1. The external environmental excitations primarily include wind load, earthquake action, impact load, water wave action, and other external loads on the train-bridge system. The internal self-excitations include track irregularities, wheel-set hunting movement, gravity and centrifugal forces of train vehicles, and various permanent deformations, such as initial deformation of bridge deck, creep camber of PC girders, folding angle at beam-end, uneven settlement, and water flow scouring at foundations of bridge abutments and piers. This chapter mainly focuses on the causes of track irregularity and wheel-set hunting movement and their influence on the train-bridge system. The other internal excitations and the external excitations of the system will be separately introduced in the later relevant chapters.

3.1 Track Irregularities

3.1.1 Definition of Track Irregularities

Track irregularities refer to the deviations of the rails that support and guide the wheels from the ideal rail surface along the track (Cass et al. 1969; Garg and Dukkipati 1984; Wang 1983, 1994; Haigermoser et al. 2015), which include the static irregularity at unloaded status and the dynamic irregularity under train loading.

H. Xia et al., *Dynamic Interaction of Train-Bridge Systems in High-Speed Railways*, Advances in High-speed Rail Technology, https://doi.org/10.1007/978-3-662-54871-4_3

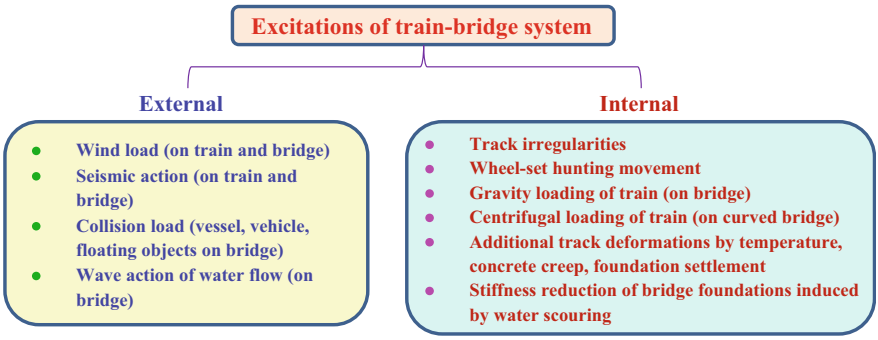

Fig. 3.1 Excitation sources of train-bridge coupling system

According to the directions at the track section, track irregularities in train-bridge dynamic analysis can be divided into four common geometrical parameters, as illustrated in Fig. 3.2, which are the alignment y_i, the vertical profile z_i, the cross-level Δz_i, and the gauge Δy_i. The cross-level irregularity can also be expressed in terms of the angle formed by the level difference between the left rail and the right rail, namely $\theta_i = \Delta z_i / 2b$.

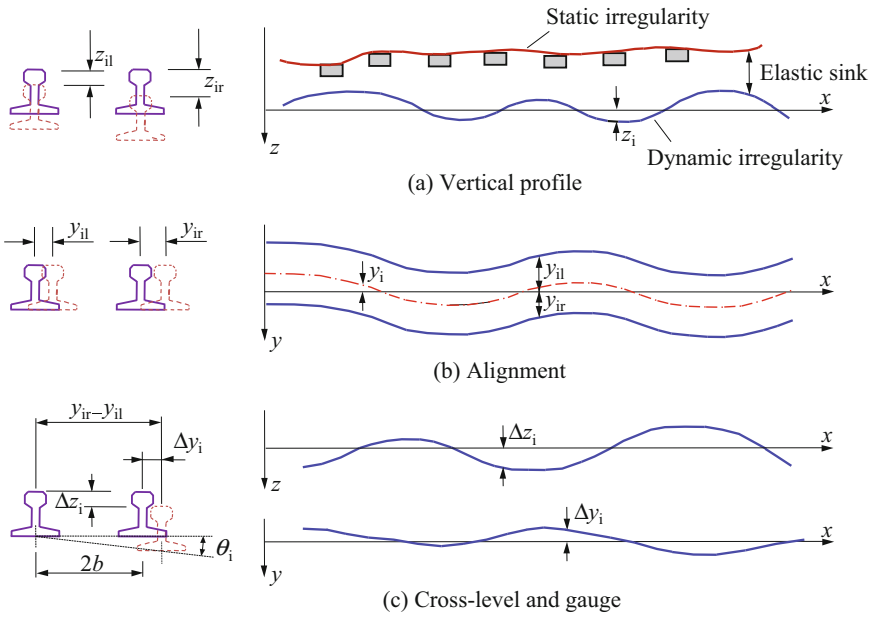

Fig. 3.2 Illustration of track irregularities

Using y_{il} and y_{ir} to represent the track irregularities of the left and the right rails in the y-direction, while z_{il} and z_{ir} in the z-direction, respectively, the four track irregularities are defined as follows:

$$\text{Vertical profile} : z_i = \frac{z_{il} + z_{ir}}{2} \tag{3.1}$$

$$\text{Alignment} : y_i = \frac{y_{il} + y_{ir}}{2} \tag{3.2}$$

$$\text{Cross} - \text{level} : \Delta z_i = z_{il} - z_{ir} \tag{3.3a}$$

$$\text{or} : \theta_i = \frac{\Delta z_i}{2b} \tag{3.3b}$$

$$\text{Gauge deviation} : \Delta y_i = y_{ir} - y_{il} \tag{3.4}$$

According to the wavelength characteristics, shape features, dynamic properties, and the acting directions of excitations on the train vehicles, track irregularities can be classified into several types, as described hereinbelow.

1. ***Classification by the direction of excitations on the train vehicles***

(1) Vertical track irregularities

The vertical track irregularities include vertical profile, cross-level, track twist, short-wave irregularity, and rail vertical periodic irregularity.

The vertical profile irregularity refers to the vertical fluctuating of rail surface along the track, which is caused by elevation deviations due to construction and maintenance of the track, deflection of the bridge, uneven residual settlement of the track bed and roadbed, unequal gap among the track components, existence of hidden sag and blinded hanging rail, and vertical elasticity inconsistence of the track.

The cross-level irregularity means the variation of altitude difference between the left and right rail tops at each cross section of track. The amplitude of cross-level irregularity refers to the altitude difference excluding the superelevation of the outer rail on the curved track.

Track twist, also known as level distortion, refers to the top-surface distortion of the left and right rails with respect to the track level, which is measured by the level difference between the two rails at two cross sections in a certain distance. The International Union of Railways (UIC B55RP 3 1966) defines the "a certain distance" as "the acting distance" which refers to the wheelbase of the vehicle or the center-to-center distance between the two bogies.

Short-wave irregularity of the track refers to the irregularity at the top surface of the rail within a small range, which is formed by uneven surface wear, scratch, peeling off, rough welds, and stagger joints of the rail, wherein the rail surface

scratches, peeling off, rough welds, and stagger joints are isolated and without periodicity, while uneven surface wear, especially corrugated abrasion and wave abrasion, has periodic characteristics.

The vertical periodic irregularity is caused by the roller error, scratch, rough welds, and uneven rolling pressure during the rolling and straightening process of the rail.

(2) Lateral track irregularities

Lateral track irregularities include alignment irregularity, gauge deviation, and lateral periodic irregularity of rail.

Alignment irregularity, also known as direction irregularity, means the transverse concave-convex fluctuation of the rail head at the inner side along the track, which is formed due to the deviation of the track centerline, accumulation of lateral uneven residual deformation of track panel, side uneven wear of rail head, and lateral elasticity inconsistence of the track.

Gauge deviation is that of the minimum inner distance between the left rail and the right rail with respect to the standard gauge, which is measured at 16 mm (in China, while in European and some other countries, it is 14 mm) below the top surface of rails at the same cross section.

Lateral periodic irregularity refers to the lateral periodic bending deformation of the rail during its rolling and straightening process.

(3) Composite track irregularity

Composite track irregularity is the bidirectional irregularity composed of vertical and lateral irregularities at the same location of the rail, in which the more harmful ones are the alignment and level reversely composited irregularity and the geometrical deviation at the endpoints of a curved track.

The alignment and level reversely composited irregularity means that at the same location, there exist simultaneously both alignment irregularity and cross-level irregularity where a reverse superelevation status is formed at the outer rail on the convex side of the track.

The geometrical deviations, which are caused by inconsistence or mismatch of the initial and/or endpoints of superelevation, versine, gauge and longitudinal slope in the curve-transition section and transition-straight section, have a non-negligible influence on the running stability, comfort, and safety of the train.

2. ***Classification by the wavelength characteristics of track irregularities***

There exist many wavelength components in the measured track irregularities, with a wide range from 0.01 to 200 m. Track irregularities with different wavelengths have various effects on the vibration of train-bridge system, so it is necessary to classify the track irregularities according to wavelength. The standards for classifying track irregularity with wavelength in different countries are similar, but the wavelength ranges for classification are not the same. Shown in Table 3.1 is the

Table 3.1 Track irregularity classification with wavelength characteristics

Wavelength types	Wavelength range	Amplitude	Common track irregularities
Short-wave irregularity	A few mm to dozens of mm	≤ 1 mm	Rail surface irregularities such as rail head abrasion, scratch, peeling off, rough joint welds, and corrugated wear
	Hundreds of millimeters	≤ 2 mm	Wave wear and uneven sleeper spaces
Medium-wave irregularity	1–3.5 m	0.1–1 mm	Track irregularity formed in rolling process
	3–30 m	1–35 mm	Vertical profile, alignment, distortion and cross-level irregularities, and gauge deviation
Long-wave irregularity	30–150 m	1–60 mm	Vertical profile and alignment irregularities

track irregularity classification with their wavelength characteristics (Luo et al. 2006).

3. ***Classification by the shape characteristics of track irregularities***

The tracks are long rails welded or fishplate connected with rail segments of a certain length. Track irregularities in common subgrade and some special sections such as joint area, welds zone, grade crossing, turnout area, bridge-subgrade and tunnel-subgrade transitions have different characteristics in their shapes. Based on the field measurement and statistical analysis, the track irregularities can be divided into several forms according to their approximate shape features: (1) sinusoidal or cosinusoidal form (including partial isolated and continuous periodic); (2) parabola form; (3) convex form (including reverse and forward step shaped, mostly as local irregularity); (4) triangular form (including partial isolated and continuous periodic); (5) S-shaped form (including local isolated and continuous periodic).

4. ***Static and dynamic track irregularities***

There exist static and dynamic irregularities in railway track. Generally, the geometry shapes for the static and dynamic track irregularities are quite different at the same location, and the worse the track condition, the greater the difference.

(1) Static track irregularities

The static track irregularities are those measured under no load. In this case, the rails and the sleepers do not bend following the uneven residual deformations and hidden sags of the track bed in a short distance, so the static irregularities cannot reflect the local deformation of the track caused by the hidden sags, uneven elasticity, etc., but can partially reflect the accumulated irregularities caused by uneven

residual deformation of the bed and the subgrade. Static irregularities are usually measured by manual work or light measuring cart.

(2) Dynamic track irregularity

The dynamic track irregularities are those measured under train load. Dynamic irregularities have direct influence on the running safety, wheel-rail forces, and vehicle vibration of the train, so the amplitudes of dynamic irregularities are taken as the control standards for track irregularities, especially the safety management standards, in China as well as in other countries.

Dynamic irregularities are measured when a track inspection car runs on the track. Shown in Figs. 3.3 and 3.4 are, respectively, the track irregularity curves measured at the N102 Bridge and the Shihe River Bridge on the Qin-Shen (Qinhuangdao-Shenyang) high-speed railway (Cao and Xia 2005), which were widely used in dynamic analysis of train-bridge system in Chinese high-speed railway design.

Some researchers believe that the track irregularities measured by track inspection car at different speeds are not real track irregularities, because they contain various additional track deformations as well as wheel vibration responses. In theory, only the track irregularities measured under quasi-static wheel loads can

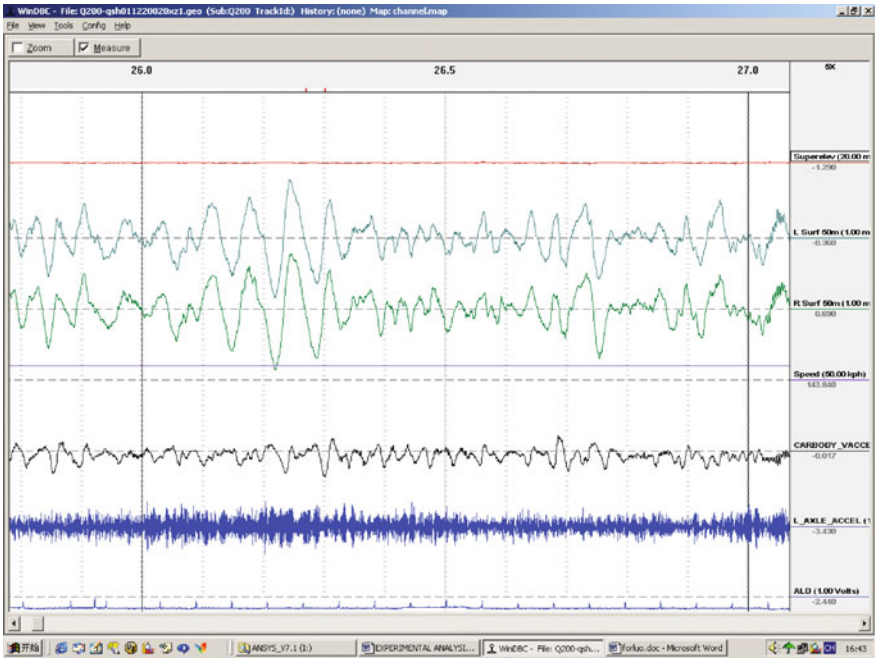

Fig. 3.3 Track irregularity curves measured at the N102 Bridge on the Qin-Shen HSR

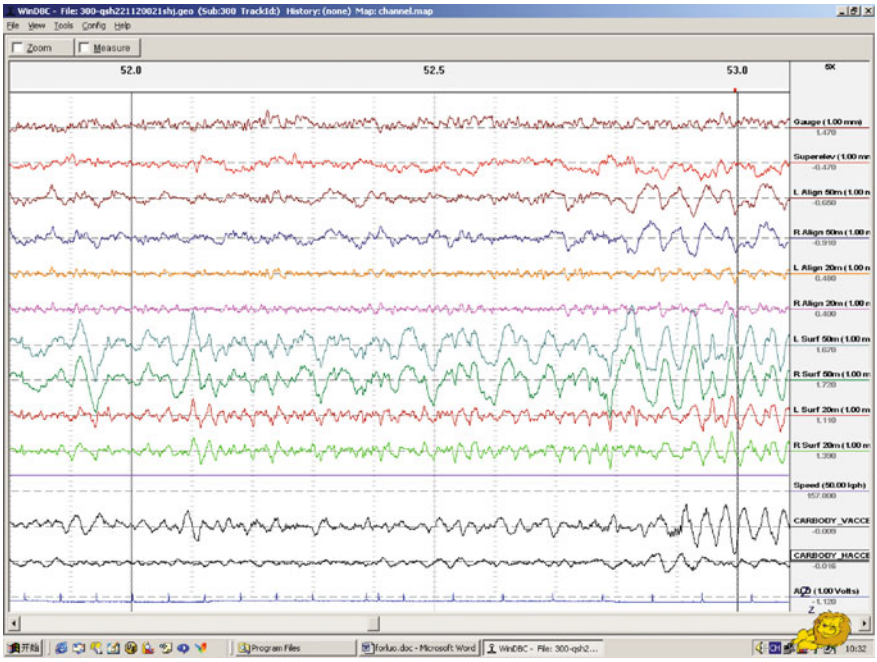

Fig. 3.4 Track irregularity curves measured at the Shihe River Bridge on the Qin-Shen HSR

reflect the inherent true state of the track. Indeed, only when the car moves at low speed and under constant quasi-static wheel load, can the real vertical track irregularity be described by the quasi-static movement of the wheel. While in fact, the additional sinkage of the track and the vibration displacement of the wheel at different speeds are very small, usually less than the resolution of inspection system on the track inspection car; therefore, the speed of track inspection car has little substantial influence on the authenticity of the measured results.

3.1.2 Excitation Function of Track Irregularities in the Train-Bridge Vibration System

When a railway vehicle runs on the track, the track irregularities may induce the floating and lateral vibrations and the wheel-rail forces of the vehicle, so they are the main self-exciting source of train-bridge coupling vibration system. Taking the floating vibration as an example, the basic principle of this excitation is shown in Fig. 3.5.

A vehicle can be simplified as a system composed of a sprung-mass M, a wheel m, a spring k, a damper c, which has two degrees-of-freedom, namely the

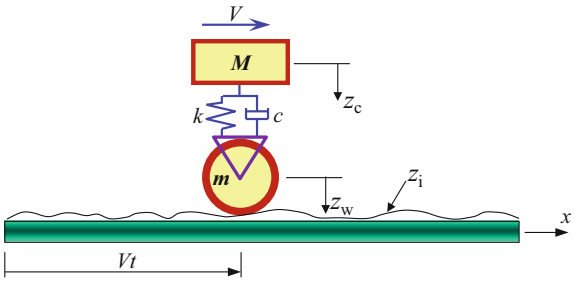

Fig. 3.5 Forced vibration caused by track irregularity

displacement z_c of mass M and displacement z_w of wheel. The vehicle moves on the track with an irregularity expressed by z_i.

In this system, the equation of motion for the sprung-mass M is

$$M\ddot{z}_c = -k(z_c - z_w) - c(\dot{z}_c - \dot{z}_w) \tag{3.5}$$

For convenience of analysis, the correspondence contact relationship is assumed between the wheel and the track, and the track deformation is not considered temporarily. In this case, the motion of the unsprung-mass m can be determined by the track irregularity at its location, which can be expressed as

$$z_w = z_i(x) = z_i(Vt) \tag{3.6}$$

By substituting Eq. (3.6), Eq. (3.5) becomes

$$M\ddot{z}_c + c\dot{z}_c + kz_c = kz_i + c\dot{z}_i \tag{3.7}$$

Because z_i and $\dot{z}_i$ in this equation are known, the displacement of the sprung-mass M can be directly written by the Duhamel integral (Clough and Penzien 2003)

$$\begin{aligned} z_c(t) = {} & e^{-\xi\omega t}(A \sin \omega_d t + B \cos \omega_d t) \\ & + \frac{1}{M\omega_d}\int_0^t [kz_i(V\tau) + c\dot{z}_i(V\tau)]e^{-\xi\omega(t-\tau)} \sin \omega_d(t-\tau)d\tau \end{aligned} \tag{3.8}$$

When the vehicle moves on the track at a certain speed, the unsprung-mass m will also produce an inertial force due to the irregularity

$$F_I = m\ddot{z}_w(x) = m\ddot{z}_i(Vt) \tag{3.9}$$

In reality, the track is elastic, which will deform and vibrate when it is acted on by the elastic force $k(z_c - z_w)$ of the spring, the damping force $c(\dot{z}_c - \dot{z}_w)$ of the damper, and the inertial force F_I of the unsprung-mass m.

Similarly, the alignment track irregularity may cause the wheel and the track to produce lateral vibration.

Therefore, track irregularity is one of the main excitations for the train vehicle vibration, and an important cause to produce the wheel-rail interaction forces and the dynamic effect of the track structure.

The existence of track irregularities may change the wheel-rail contact relation, and affect the dynamic characteristics of the wheel-rail system. Train vehicles vibrate when they are excited by the track irregularities and other external excitations, and the vibration is transmitted to the track and the bridge structure through the wheel-rail contact points, forming the dynamic interaction process of the train-track-bridge system. Therefore, track irregularities play a very important role in dynamic analysis of train-bridge interaction system, and they are considered as one of the main self-excitations for the train-track or train-bridge vibration system (Yasojima 1981; Garg and Dukkipati 1984; Chen and Zhai 2001; Zhang 2001; Xia et al. 2012; Zhai 2014; Anderson et al. 2015; Yang et al. 2015; Wang et al. 2015). When the track is in poor condition, the vehicle vibration and wheel-rail forces excited by the irregularities may seriously increase with train speed, which, in the serious case, may even cause a train to derail from the track. The superposition of bridge deformation and track irregularities has a non-negligible influence on the analysis results for the train-bridge coupling vibration system, so it is important to choose the reasonable track irregularity spectra for acquiring true and reliable results.

3.1.3 Mathematical Description of Random Irregularity Characteristics

The geometric state of a track has strong randomness, because it is affected by various factors. These factors include the initial bending, wear and damage of rails, uneven spacing and varying quality of sleepers, uneven grading and strength, loose, dirt, and compaction of track bed, uneven subsidence, and varying stiffness of roadbed. In fact, the track irregularity is composed of random irregularity waves with different wavelengths, phases, and amplitudes, which is a complex stochastic process along the track mileage. The track irregularity in any particular section can be regarded as a sample of the random process: For the infinitely long track, it is an approximate ergodic weak stationary process, while for the local irregularity, it is a non-stationary process. Therefore, the track irregularity cannot be clearly expressed by a mathematical formula with definite amplitude, wavelength, and phase, but be described by statistical parameters in the random vibration theory (Cooperider et al. 1975; Pater 1988; Xin 2005; Liu et al. 2006; Xu et al. 2015; Zacher et al. 2015). The stochastic statistical properties of track irregularity include two aspects: the amplitude statistics and power spectrum statistics of track irregularity.

3.1.3.1 Statistical Characteristics of Track Irregularity Amplitude

The amplitude of track irregularity refers to the deviation value of the actual track state from the theoretical one. The maximum positive value or maximum negative value of the irregularity in a certain track section is called the peak or half-peak of the irregularity, and the difference between the adjacent maximum positive value and the maximum negative value is known as the peak-to-peak value.

The amplitude of track irregularity in a special position cannot represent the overall status for the consecutive irregularity in a track section. Generally, the amplitude and wavelength variations of the consecutive track irregularity within a specific section can be described and evaluated with the statistical characteristics such as mean square value and standard deviation.

(1) Mean square value and standard deviation of track irregularity

For a track section of $0 \sim L$, the mean square value ψ_η^2 and the variance σ_η^2 of the track irregularity $\eta(x)$ can be expressed as

$$\psi_\eta^2 = \frac{1}{L}\int_0^L \eta^2(x)\mathrm{d}x \tag{3.10}$$

$$\sigma_\eta^2 = \frac{1}{L}\int_0^L [\eta(x) - \mu_\eta]^2\mathrm{d}x = \frac{1}{L}\int_0^L \eta^2(x)\mathrm{d}x - \mu_\eta^2 = \psi_\eta^2 - \mu_\eta^2 \tag{3.11}$$

where x is the mileage location of the track; μ_η is the mean value of track irregularity in this section.

As can be seen from the above equation, the mean square value of track irregularity is composed of the mean and the variance, which are related to the excitation energy.

Variance indicates the amplitude deviation of a random irregularity from the baseline, whose square root is standard deviation. The standard deviation of a track irregularity describes the dispersion degree of its amplitude. The standard deviation of track irregularity σ_η can be expressed as

$$\sigma_\eta = \sqrt{\frac{1}{n}\sum_{i=1}^{n}(\eta_i - \mu_\eta)^2} \tag{3.12}$$

The variance or standard deviation is adopted to evaluate the maintenance quality of the track in China and some European countries. In China, for example, the track quality index (TQI) is used to evaluate the statistical properties of track irregularity amplitude (TYH2004-120 2004). The basic method of using TQI is to divide the measured track irregularities in a section into several segments with a certain length (200 m in China), then calculate the standard deviations for the

irregularities in each segment, and sum these standard deviations with different weights to compose the TQI, and use the TQI as the standard to evaluate the quality state of the track irregularity in this section.

(2) P index of track irregularity

In Japan, the P index method is used for track irregularity management. The P index is the percentage of the number of sampling points exceeding a certain standard (3 mm) among the total samples of irregularity in a certain length of track (500 m in Japan), expressed as

$$P = \frac{\text{number of sampling points exceeding a certain standard}}{\text{total number of sampling points}} \times 100\% \tag{3.13}$$

Clearly, the P index reflects the amplitude state of track irregularities in the specific track section.

(3) Moving average value e of track irregularity

In France, SNCF (Société Nationale des Chemins de Fer) performs not only routine inspections and evaluations on local track irregularities with different management levels, but also comprehensive examination and management on the overall state of the track irregularity. The moving average value e (i.e., the average deviation or comprehensive index) of absolute deviation of track irregularity in a 300 m section is used to manage the quality state of track. The method is to calculate the average amplitude of track irregularity in the range of 150 m before and after the calculating point, and take it as the e value of this point. Therefore, the calculated e value reflects the overall state of the track irregularity amplitudes in the 300 m section. The relationship between the moving average value e and the standard deviation σ is

$$\sigma = 1.38e \tag{3.14}$$

3.1.3.2 Power Spectral Densities of Track Irregularity

In addition to amplitudes, the wavelengths and their variation rates of track irregularities also have important effect on the wheel-rail interforces and dynamic interaction of train-bridge system.

The most effective way to describe the wavelength characteristics of track irregularities is to apply power spectrum, namely to describe and assess track irregularities with the power spectral density function (PDF) (RGRV 1985; Railway Construction Institute 1999; Xiao et al. 2008; Zhang et al. 2008; Wei 2011). Power spectral density, also known as mean square spectral density, is used to describe the frequency feature of random data with spectral density of their mean square values. Power spectral density is an effective statistical parameter to describe the wavelength components or frequency components (as an excitation of vehicle-track

interaction, the wavelength can be converted into frequency according to the speed of the vehicle) and other characteristics of track irregularities, which can fully reflect the distributions of track irregularity amplitudes in various wavelengths.

Since the differences in transport conditions, maintenance states, track structures, natural climates, etc., among different lines or various locations of a same railway, track irregularities are neither strictly ergodic nor really stationary. However, it is confirmed by the stationary test that except those on the sections of rail joints, welds, turnout zones, etc., most track irregularities are stationary or weak stationary, which can be handled as stationary random process, and their wavelength characteristics can be described by the power spectral densities.

(1) Definition of track irregularity power spectrum

Assuming $\eta(t)$ and $\eta(x)$ are samples of a track irregularity, the estimate of power spectral density is defined as

$$\hat{G}_\eta(f) = \frac{\hat{\psi}_\eta^2(f, \Delta f)}{\Delta f} \tag{3.15}$$

where $\hat{\psi}_\eta^2(f, \Delta f)$ is the mean square value of $\eta(t)$ or $\eta(x)$ in the frequency range of $[f, f + \Delta f]$, and Δf is the bandwidth.

If the bandwidth $\Delta f \to 0$, and the statistical period $T \to \infty$ or the distance $X \to \infty$, the exact expression of power spectral density can be obtained as

$$\hat{G}_\eta(f) = \lim_{\Delta f \to 0} \frac{\hat{\psi}_\eta^2(f, \Delta f)}{\Delta f} = \lim_{\Delta f \to 0} \frac{1}{\Delta f} \left[\lim_{T \to \infty} \frac{1}{T} \int_0^T \eta^2(t, f, \Delta f) \mathrm{d}t \right] \tag{3.16}$$

or:

$$\hat{G}_\eta(f) = \lim_{\Delta f \to 0} \frac{1}{\Delta f} \left[\lim_{X \to \infty} \frac{1}{X} \int_0^X \eta^2(x, f, \Delta f) \mathrm{d}x \right] \tag{3.17}$$

where $\eta(t, f, \Delta f)$ and $\eta(x, f, \Delta f)$ represent the values of $\eta(t)$ and $\eta(x)$ in the frequency range of $[f, f + \Delta f]$, respectively.

It can be seen from Eqs. (3.15)–(3.17) that power spectral density is the mean square value of $\eta(t)$ or $\eta(x)$ per unit frequency bandwidth. It should be noted that f in Eq. (3.16) is the time frequency with $f = 1/T$ (Hz), while in Eq. (3.17), f is the spatial frequency with $f = 1/\lambda$ (1/m). It is more convenient to describe track irregularity with spatial frequency, while vibrations of vehicle and track can also be

described with time frequency. The unit of power spectral density of track irregularity is $mm^2/(1/m)$.

The power spectral densities defined in Eqs. (3.15)–(3.17) only exist for positive frequencies and are called the single-side power spectral densities, which can be obtained by filtering, squaring, or averaging method.

In numerical analysis, the power spectral densities are expressed in a different way, where the power spectral densities of track irregularity are calculated with the fast Fourier transform (FFT), expressed as

$$G_\eta(f) = \lim_{T\to\infty} \frac{1}{T}\left[\int_0^T \eta(t)\mathrm{e}^{-j2\pi ft}\mathrm{d}t\right]^2 \tag{3.18}$$

$$G_\eta(f) = \lim_{X\to\infty} \frac{1}{X}\left[\int_0^X \eta(x)\mathrm{e}^{-j2\pi fx}\mathrm{d}x\right]^2 \tag{3.19}$$

Power spectral density $G_\eta(f)$, also known as self-spectral density, is used to describe the frequency characteristics of the random data by the spectrum density of mean square value of the data. $G_\eta(f)$ is the most important statistical function to study various random information, such as the statistics of frequency or wavelength components and the variations of amplitudes in random vibrations, and to describe the characteristics of track irregularities.

(2) Power spectrum density diagram of track irregularity

The power spectrum density of track irregularity $G_\eta(f)$ can be expressed with a power spectrum density diagram, which is a continuous curve in a coordinate system, with the spatial frequency or wavelength as the abscissa and the power spectral density value as the ordinate. Power spectrum density diagram can clearly show various wavelength components in the track irregularity.

The area below a power spectral density curve between f_1 and f_2 equals to the mean square value ψ_η^2 of various wavelength components in the frequency band (or wavelength band), that is

$$\psi_\eta^2(f_1,f_2) = \int_{f_1}^{f_2} G_\eta(f)\mathrm{d}x, \quad (0 \le f_1 \le f_2) \tag{3.20}$$

As the power spectral densities of track irregularity are distributed in a wide range, the power spectral density diagram is expressed with logarithmic coordinates to show the variations of power spectral densities in the entire wavelength range.

Shown in Fig. 3.6 are the power spectral densities of vertical profile irregularities measured in China's main railways. It can be seen that each power spectral density diagram consists of continuous downward sloping curves, which contains

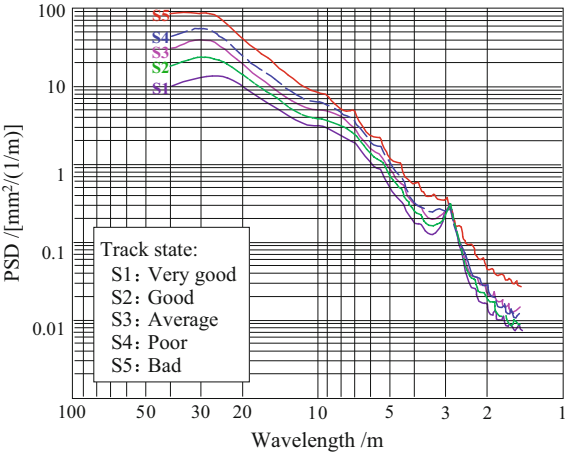

Fig. 3.6 Power spectral densities of vertical profile irregularities in China

the amplitude and wavelength information for a certain section of track irregularity, and has the spectrum characteristics of broadband random wave. In most cases, the longer the wavelength component, the bigger the power spectrum density amplitude. Sometimes, the power spectral density curve may also contain a convex peak of narrow-band random wave and/or periodic spikes. According to the spectral characteristics of track irregularities, the excitation environment of train vehicles can be well identified, and the diseases in track structure can be analyzed and detected. The differences among the PSD curves indicate the quality status of various tracks: The lower the curve's position, the smaller the area under the spectrum, and the better the track status. So it is an effective method to describe the characteristics of track irregularities by power spectral densities, which is important for assessing the state of track regularities, studying the vehicle vibration excited by track irregularities, and designing the running and suspension system of train vehicles.

(3) Fitting expression of power spectral density curves

The power spectral density diagram of track irregularity is a statistic characteristic curve based on a large number of measured samples, which generally cannot be expressed by a definitive analytical function. While in practice, for convenience of description and application, a fitting function formula closing to the spectral density curve is usually required. There are various kinds of fitting curve formulas of track spectra proposed in China and other countries. Generally, a complicated formula is closer to the actual spectral density curve, but it needs more characteristic parameters for fitting the curve. Some typical track spectra will be introduced in detail in the next section of this chapter.

3.1.3.3 Description of Local Track Irregularity

In track inspection, when the track is found to have big irregularity amplitude or abnormal deformation at a local section, which is significantly different from those at the adjacent section, special attention should be paid, for such particular local irregularities often cause large transient response of the rail and the wheel-set when the train passes.

Researchers have conducted surveys and statistical analyses on various local track irregularities, and divided them based on their waveform characteristics into three categories as regular local irregularity, deterministic irregular local irregularity, and random local irregularity. Regular local irregularity and deterministic irregular local irregularity can be described by definite functions such as sinusoidal function, cosine function, trigonometric function, and jump function or the combinations of these functions.

In American railways, the waveforms of local track irregularity are summarized into eight types, and the proportion and probability of irregularity with different waveforms are analyzed. Table 3.2 shows the waveform characteristics and the occurring locations of these eight types of local track irregularities.

Track irregularities with different waveform characteristics may exist individually, or in pairs, in treble and in multiple, may be continuous and also be periodic. For some typical local irregularity waveforms, they can also be described approximately by function expressions.

Random local irregularity waveforms are complex, so they are usually approximately described with their characteristic parameters such as amplitudes, half-wavelengths, 1/4 wavelengths, average variation rates, and wave numbers.

As shown in the local random track irregularity curve in Fig. 3.7, the distance between adjacent peak positions with the same sign is defined as wavelength λ, the distance between a positive peak and the adjacent negative peak is half-wavelength L, and the distance between a peak and the adjacent zero point is l equaling to 1/4

Table 3.2 Waveform characteristics and occurring locations of local track irregularity

Characteristics	Location
Sharp-curved	Joints, frogs, interlocking devices, hard bends, buffer rails, insulation joints of SWR, fishplate joints of rails, piers
Circle-curved	Soft soil sections, scouring places, mud-pumping points, dirty ballasts, joints, transition curves, level crossings, bridges, overpasses, loose bolts, frog, interlocking devices
S-curved	Transition curves, bridges, crossings, interlocking devices, cutting-subgrade transition zones
Stepped	Bridges, level crossings, local repaired places
Slotted	Soft soil points, soft and unstable subgrades, transition curves
Sine-wave curved	Transition curves, soft soil points, bridges
Decayed sine-wave curved	Easement curve, frog, local soft soil place
Sinusoidal curved	Local soft soil places, insulation joints

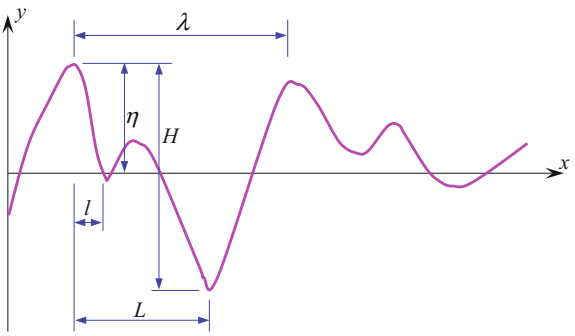

Fig. 3.7 Description of a random local track irregularity form

wavelength. The wavelength λ of local irregularity is usually difficult to determine, so it is usually taken as $4l$ which is easier to distinguish.

The average variation rate can approximately reflect both wavelength and amplitude. It is either defined as η/l, the ratio of half-peak amplitude η to l, called the average variation ratio of 1/4 wavelength, or H/L, the ratio of peak-to-peak amplitude H to half-wavelength L, called the average variation ratio of peak-to-peak amplitude.

3.1.4 Typical Track PSD

The statistics for spectral characteristics of track irregularities have long been paid attention. For example, the UK railway department began this research as early in 1964. UK, Japan, Germany, USA, the former Soviet Union, India, Czech Republic, and some other countries have proposed, respectively, their own power spectral densities of track irregularity or related PSD functions. In the early stage of development of China's high-speed railways, the track spectra from other countries were adopted for dynamic analysis of train-bridge coupling system. In 2014, based on a large number of measurements on high-speed railway lines, the track irregularity spectra of high-speed railway were proposed in the China code *PSD of Ballastless Track Irregularities of High-speed Railway* (TB/T 3352 2014), which have been gradually applied in dynamic analysis of high-speed railway bridges.

1. ***British track irregularity spectra***

The track spectra used in British railway are

$$\begin{cases} \text{Vertical profile} : S_{\text{v}}(f) = \frac{1}{1.33f^2 + 7.81f^3 + 22.94f^4} \\ \text{Alignment} : S_{\text{a}}(f) = \frac{1}{100.8f^3} \\ \text{Cross} - \text{level} : S_{\text{c}}(f) = \frac{1}{7.72f^2 - 6.30f^3 + 15.69f^4} \end{cases} \tag{3.21}$$

where $S(f)$ is the PSD function of track irregularities [mm^2/(1/m)], and f is the spatial frequency (1/m).

2. ***American track irregularity spectra***

The power spectral densities of track irregularity were proposed by the Federal Railroad Administration (FRA) on the basis of a large number of measured data, which are fitted with the even functions expressed by cutoff frequencies and roughness constants as follows.

(1) Vertical profile track irregularity

$$S_{\mathrm{v}}(\Omega) = \frac{kA_{\mathrm{v}}\Omega_{\mathrm{c}}^2}{\Omega^2(\Omega^2 + \Omega_{\mathrm{c}}^2)} \tag{3.22}$$

where $S_{\mathrm{v}}(\Omega)$ is the PSD function of vertical profile track irregularity [cm^2/(rad/m)], A_{v} is the roughness constant (cm^2·rad/m), Ω_{c} is the cutoff frequency (rad/m), and k is the safety factor which is between 0.25 and 1.0 according to the requirement, and generally taken as 0.25.

(2) Alignment track irregularity

$$S_{\mathrm{a}}(\Omega) = \frac{kA_{\mathrm{a}}\Omega_{\mathrm{c}}^2}{\Omega^2(\Omega^2 + \Omega_{\mathrm{c}}^2)} \tag{3.23}$$

where $S_{\mathrm{a}}(\Omega)$ is the PSD function of alignment track irregularity [cm^2/(rad/m)], and A_{a} is the roughness constant (cm^2·rad/m).

(3) Cross-level and gauge track irregularities

$$S_{\mathrm{c}}(\Omega) = S_{\mathrm{g}}(\Omega) = \frac{4kA_{\mathrm{v}}\Omega_{\mathrm{c}}^2}{(\Omega^2 + \Omega_{\mathrm{c}}^2)(\Omega^2 + \Omega_{\mathrm{s}}^2)} \tag{3.24}$$

where $S_{\mathrm{c}}(\Omega)$ and $S_{\mathrm{g}}(\Omega)$ are, respectively, PSD functions of cross-level and gauge track irregularities [cm^2/(rad/m)], and Ω_{s} is the cutoff frequency (rad/m).

The standard track spectra are divided into 1–6 grades, and the related parameters in Eqs. (3.22)–(3.24) are listed in Table 3.3. In the table, the maximum allowable train speeds related to different grades in accordance with the running safety standard are also given.

Table 3.3 Parameters of track spectra given in FRA standard (Grade 1–6)

Item		Grade of track					
		Grade-1	Grade-2	Grade-3	Grade-4	Grade-5	Grade-6
A_v (cm^2·rad/m)		1.2107	1.0181	0.6816	0.5376	0.2095	0.0339
A_a (cm^2·rad/m)		3.3634	1.2107	0.4128	0.3027	0.0762	0.0339
Ω_s (rad/m)		0.6046	0.9308	0.8520	1.1312	0.8209	0.4380
Ω_c (rad/m)		0.8245	0.8245	0.8245	0.8245	0.8245	0.8245
Train speed allowance (km/h)	Freight train	16	40	64	96	128	176
	Passenger train	24	48	96	128	144	176

3. ***German track irregularity spectra***

The track irregularity spectra in German high-speed railways are currently applied in European railways, which are also adopted in China to analyze the running stability of trains according to the overall technical conditions for high-speed trains. The German track irregularity spectra are expressed as

$$S_v(\Omega) = \frac{A_v\Omega_c^2}{(\Omega^2+\Omega_r^2)(\Omega^2+\Omega_c^2)} \tag{3.25a}$$

$$S_a(\Omega) = \frac{A_a\Omega_c^2}{(\Omega^2+\Omega_r^2)(\Omega^2+\Omega_c^2)} \tag{3.25b}$$

$$S_c(\Omega) = \frac{A_v\cdot b^{-2}\cdot\Omega_c^2\cdot\Omega^2}{(\Omega^2+\Omega_r^2)(\Omega^2+\Omega_c^2)(\Omega^2+\Omega_s^2)} \tag{3.25c}$$

$$S_g(\Omega) = \frac{A_g\Omega_c^2\Omega^2}{(\Omega^2+\Omega_r^2)(\Omega^2+\Omega_c^2)(\Omega^2+\Omega_s^2)} \tag{3.25d}$$

where $S_v(\Omega)$, $S_a(\Omega)$, and $S_g(\Omega)$ are, respectively, the PSD functions of vertical profile, alignment, and gauge irregularities [m^2/(rad/m)], and $S_c(\Omega)$ is the PSD function of cross-level irregularity [1/(rad/m)]; A_v, A_a, and A_g are the roughness coefficients [m^2·rad/m]; Ω_c, Ω_r, and Ω_s are the cutoff frequencies (rad/m); b is the half of the distance between the right and left rail centers.

The cutoff frequencies and roughness constants in Eqs. (3.25a, 3.25b, 3.25c, and 3.25d) are shown in Table 3.4, where A_g are the reference values based on the variations of gauge irregularity in the range of −3 to +3 mm.

Table 3.4 Cutoff frequencies and roughness coefficients of the German track spectra

Track level	Ω_c (rad/m)	Ω_r (rad/m)	Ω_s (rad/m)	A_a(m^2·rad/m)	A_v (m^2·rad/m)	A_g (m^2·rad/m)
Low disturbance	0.8246	0.0206	0.4380	2.119×10^{-7}	4.032×10^{-7}	5.32×10^{-8}
High disturbance	0.8246	0.0206	0.4380	6.125×10^{-7}	1.08×10^{-6}	1.032×10^{-7}

In the table, parameters in "low disturbance" are applicable for high-speed railways with train speed greater than 250 km/h, and those in "high disturbance" for ordinary railways.

4. ***Track spectra of ordinary railways in China***

In the late 1990s, the China Academy of Railway Science (CARS) systematically studied the track irregularity states in China. Aiming to speed up the three main railway lines to 160 km/h, the CARS measured 40,000 km track irregularities by inspection cars and some others by ground surveys, and based on statistics of the test data, proposed the PSD functions of track irregularities for China's ordinary railways as follows

$$S(f) = \frac{A(f^2 + Bf + C)}{f^4 + Df^3 + Ef^2 + Ff + G} \tag{3.26}$$

where f is the spatial frequency (1/m); A, B, C, D, E, F, and G are the characteristic parameters, which have different values for vertical profile, alignment, and cross-level irregularities in various types of railway lines. Listed in Table 3.5 are the characteristic parameters for ordinary railway lines in China.

Table 3.5 Characteristic parameters of track irregularity PSD functions for ordinary railway lines in China

Parameters	A	B	C	D	E	F	G
Vertical profile of left rail	1.1029	−1.4709	0.5941	0.8480	3.8016	−0.2500	0.0112
Vertical profile of right rail	0.8581	−1.4607	0.5848	0.0407	2.8428	−0.1989	0.0094
Alignment of left rail	0.2244	−1.5746	0.6683	−2.1466	1.7665	−0.1506	0.0052
Alignment of right rail	0.3743	−1.5894	0.7265	0.4353	0.9101	−0.0270	0.0031
Cross-level	0.1214	−2.1603	2.0214	4.5089	2.2227	−0.0396	0.0073

Note The speedup target of the three main railway lines is 160 km/h

5. *Track spectra of high-speed railways in China*

In recent years, the CARS, using track inspection cars, measured the geometric track irregularities of ballastless slab tracks on Beijing-Tianjin, Wuhan-Guangzhou, and some other high-speed railways. By analyzing the measured data and using the periodogram method, the CARS proposed the track irregularity spectral diagrams with various percentiles of the Beijing-Tianjin intercity railway, and analyzed the characteristics of the spectra (Zhang et al. 2008). Figure 3.8 shows the 50% point spectra.

In 2014, the China Railway Corporation officially issued the track irregularity spectra with various percentiles for high-speed railways, in which the PSD functions for irregularities of vertical profile, alignment, cross-level, and gauge deviation are expressed with segmentally fitted power functions

$$S(f) = \frac{A}{f^k} \tag{3.27}$$

where f is the spatial frequency (1/m), the coefficients A and k in various segments corresponding to the average spectra can be obtained in Table 3.6, in which the wavelengths at the spatial frequency segmenting points are listed in Table 3.7, and

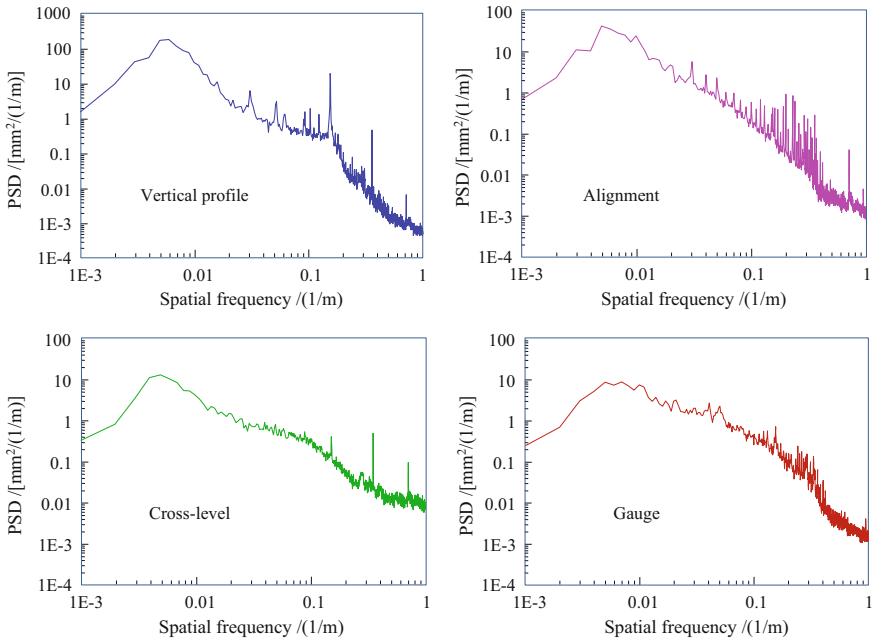

Fig. 3.8 Track irregularity PSD diagrams of Beijing-Tianjin intercity railway (50% point spectrum)

Table 3.6 Fitting formula coefficients for average spectra of HSR ballastless track irregularities

Irregularity type	Segment 1		Segment 2		Segment 3		Segment 4	
	A	k	A	k	A	k	A	k
Vertical profile	1.0544×10^{-5}	3.3891	3.5588×10^{-3}	1.9271	1.9784×10^{-2}	1.3643	3.9488×10^{-4}	3.4516
Alignment	3.9513×10^{-3}	1.8670	1.1047×10^{-2}	1.5354	7.5633×10^{-4}	2.8171	–	–
Cross-level	3.6148×10^{-3}	1.7278	4.3685×10^{-2}	1.0461	4.5867×10^{-3}	2.0939	–	–
Gauge	5.4978×10^{-2}	0.8282	5.0701×10^{-3}	1.9037	1.8778×10^{-4}	4.5948	–	–

Table 3.7 Spatial frequencies and corresponding wavelengths at segmenting points for HSR ballastless track irregularity spectra

Irregularity type	Segment 1, 2		Segment 2, 3		Segment 3, 4	
	Spatial freq. (1/m)	Wavelength (m)	Spatial freq. (1/m)	Wavelength (m)	Spatial freq. (1/m)	Wavelength (m)
Vertical profile	0.0187	53.5	0.0474	21.1	0.1533	6.5
Alignment	0.0450	22.2	0.1234	8.1	–	–
Cross-level	0.0258	38.8	0.1163	8.6	–	–
Gauge	0.1090	9.2	0.2938	3.4	–	–

Table 3.8 Conversion factors from average spectra to percentile spectra of track irregularity

Percentile	10.0	20.0	25.0	30.0	50.0	60.0	63.2	70.0	75.0	80.0	90.0
Conversion factor C	0.105	0.223	0.288	0.357	0.693	0.916	1.000	1.204	1.386	1.609	2.303

the conversion factor C from average spectra to percentile spectra is shown in Table 3.8.

6. ***Track irregularities and PSD curves measured on Qin-Shen HSR***

In 2002, upon the completion of the Qin-Shen high-speed railway with design speed 200 km/h, the China's Ministry of Railways organized two large-scale comprehensive field tests. In the second test, the maximum speed of the China-star train reached 321.5 km/h.

Shown in Fig. 3.9 are the 1200 m samples of vertical profile, alignment, and cross-level irregularities and their PSD curves measured on the Qin-Shen HSR (Cao and Xia 2005), whose maximum amplitudes are 7.73, 3.59, and 2.22 mm, respectively.

7. ***Comparison of track spectra from various countries***

The comparisons of track irregularity spectra from British, Germany, USA, and China's ordinary railway lines and high-speed railway are shown in Fig. 3.10, in which the measured spectra from Shinkansen line in Japan and Qin-Shen HSR in China are also plotted for reference. The Japanese track spectra are provided by the Japan Railway Technical Research Institute based on a section of measured track irregularities, which have no statistical significance, but can reflect some wavelength characteristics of Shinkansen track irregularities. The track spectra from Qin-Shen HSR were measured by the track inspection car in the comprehensive experimental section K30–K72 where France-made rails were laid.

It can be seen that among the track spectra in various countries, the British track spectrum values are large and the Japanese Shinkansen track spectrum values are

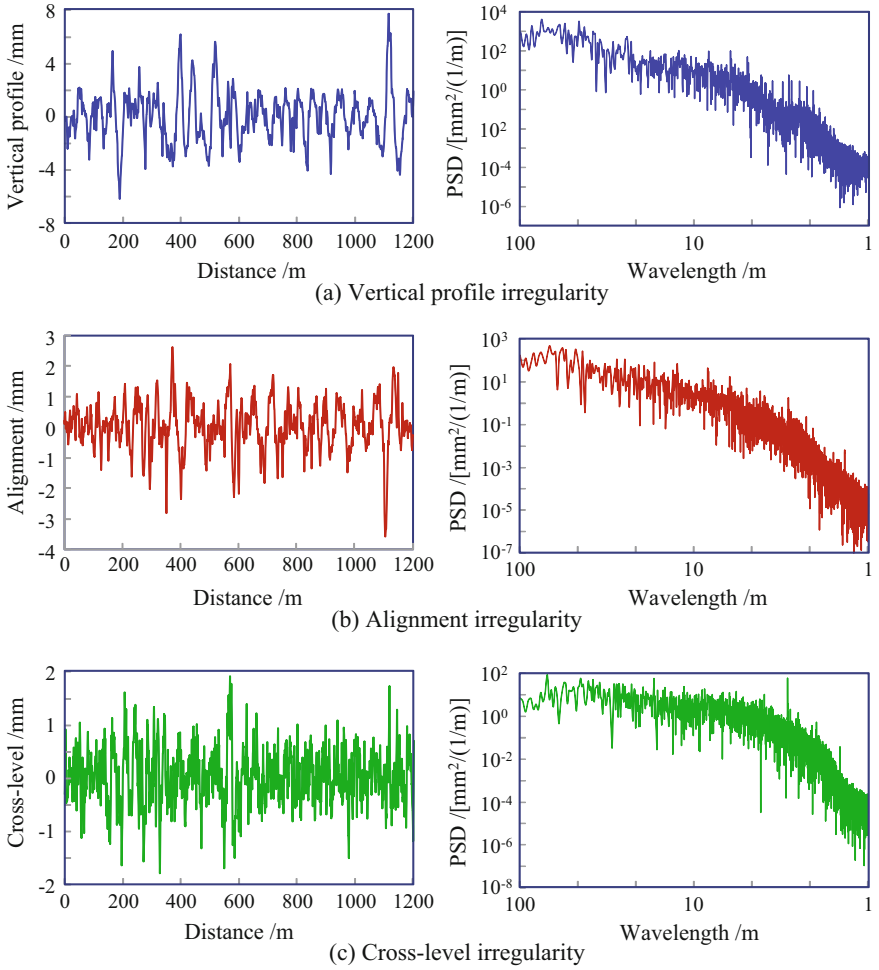

Fig. 3.9 Track irregularity samples and PSD curves measured on Qin-Shen HSR

small, because the British track spectra are for general railway, while the Japanese ones are for very good tracks, so the these two spectrum curves are less used in simulation analysis. The American Grade-6 spectrum curves have the same forms, respectively, with the German low disturbance curves, but have bigger values, which is mainly because that the allowable train speed for the American track spectra is only 176 km/h while the German ones are for high-speed railway. The alignment and cross-level irregularity spectra in China HSR are almost equal to the average values of the Japanese Shinkansen ones, and the vertical profile irregularity spectrum is smaller than that of the Japanese one, because the ballastless slab tracks with better smoothness are adopted in China.

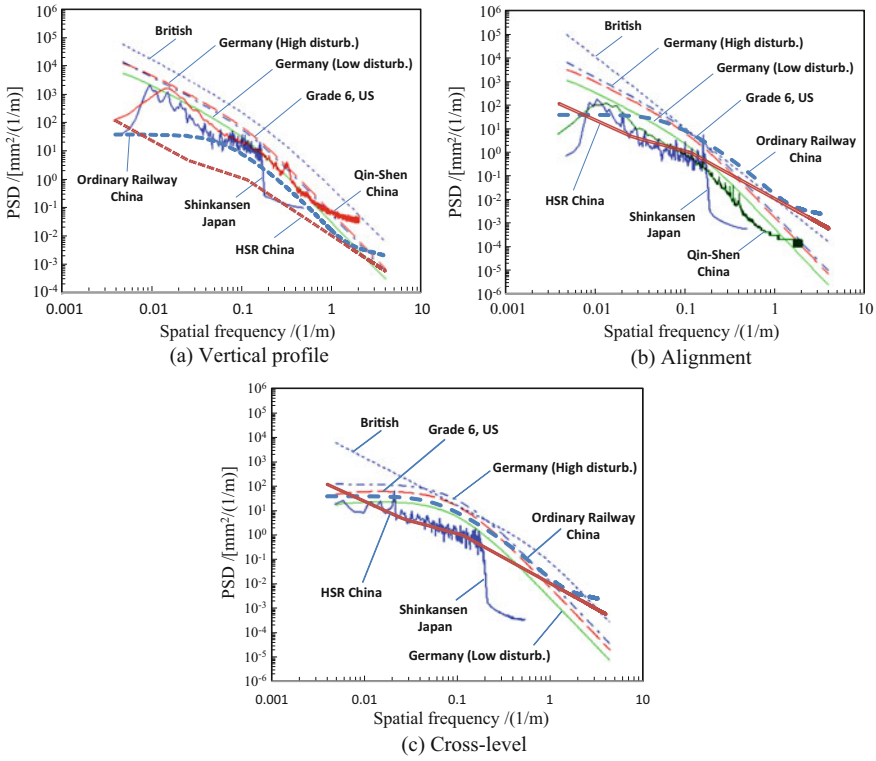

Fig. 3.10 Comparisons of track irregularity spectra from specifications and measurements in various countries

3.1.5 Control Standards of Track Irregularities

A lot of researches on the control of track irregularities have been carried out in China and abroad, and fruitful results achieved. In some countries, especially in those with developed railways such as France, Japan, and Germany, based on the characteristics of their railways and the practical conditions of track structures and plane/longitudinal track sections, series of monitoring and management standards and control measures for track irregularities have been studied and developed, such as job acceptance criteria, routine maintenance standards, emergency repair standards, and train speed-limit management standards of tracks. These criteria and standards play important roles in track quality controls of these countries, and provide technical assurances for running safety and comfort of trains and the development of high-speed railways.

In China, researches on control of track irregularities started relatively late, and systematic studies had not been conducted until the mid-1980s. Projects on track irregularity controls were proposed and approved as the state science and

Table 3.9 Management standard for track irregularities of Shinkansen lines (200 km/h and up) in Japan

Item		Target of management			
		Job acceptance	Maintenance plan	Comfort	Safety
Track irregularity	Vertical profile (mm/10m)	≤4	6	7	10
	Alignment (mm/10m)	≤3	4	4	6
	Gauge (mm)	≤±2	+6 −4	+6 −4	+6 −4
	Cross-level (mm)	≤3	5	5	7
	Planarity (mm/2.5m)	≤3	4	5	6
Shaking acceleration	Vertical (Peak-to-peak) (*g*)	–	0.25	0.25	0.35
	Lateral (Peak-to-peak) (*g*)	~0.20	0.20	0.20	0.30

technology key projects from "The 6th Five-Year Plan" to "The 12th Five-Year Plan." With the development of more than 30 years, a lot of practical results have been obtained, and some standards on track irregularity controls for China's main railways put forward, related to routine maintenances and repairs, job acceptances, emergency repairs, and train speed-limit management of tracks, and especially the track quality index TQI standard for track geometric state control. These standards provide a technical basis for speedup of trains in existing railways and design of subgrades, tracks, and bridge structures of high-speed railways in China.

There are two main factors limiting the train speed: The first is plane/longitudinal section, and the second is smooth state of track, which have been proved through studies and practices in China and abroad. If the track smooth state is poor, the vehicle vibration and the wheel-rail interforces induced by track irregularities will increase sharply with the train speed, which may even cause a train derailment accident in serious case. Therefore, high-speed railways require much more strict standards on track irregularities than those for ordinary railways.

Listed in Tables 3.9, 3.10, and 3.11 are, respectively, the management standards for track irregularity of high-speed railways in Japan and France, the dynamic management standard for track irregularity of speeding up main railways in China, and the standard of track irregularity for the 200 km/h and up test on Zhengzhou-Wuhan railway line in 1998.

To ensure the high smoothness of high-speed railway tracks, the precision criteria for laying tracks are specified in the Chinese standard "Interim Regulations for Design of New Railway Subgrades, Bridges, Tunnels and Stations with the 200 km/h Speed," as shown in Table 3.12, which are in accordance with those required in the standards for 200 km/h railways in other countries.

In the Chinese standard *Code for Design of high-speed railway* (TB10621 2014), the laying precisions for HSR main line tracks should meet the requirements in Table 3.13.

Table 3.10 Management standard for track irregularities of TGV lines in France

Type	Lateral acceleration (m/s^2)		Vertical profile (mm)		Alignment (mm)	
	Car-body	Bogie	Half-peak value (12.2 m base)	Peak-to-peak value (31 m base)	Half-peak value (10 m base)	Peak-to-peak value (33 m base)
VO	—	—	3		2	
VA	1.2	3.5	5	10	6	12
VI	2.2	6	10	18	8	16
VR	2.8	8	15	24	12	20

Note VO new built; VA maintenance; VI operation; VR emergency repair

3.1.6 Numerical Simulation of Track Irregularities

According to the statistical characteristics of measured track irregularities, the PSD functions of track irregularities for different grades of railway can be determined, based on which the simulated track irregularity curves can be obtained by numerical methods.

A track irregularity random function can be regarded as a stationary Gauss random process. There are several methods to produce track irregularity samples with a given track irregularity power spectrum, such as trigonometric series superposition method, secondary filter method, AR model method, or ARMA model.

When using the trigonometric series superposition method, a sample of track irregularity can be generated by the following formula

$$w(x) = \sqrt{2}\sum_{k=1}^{N}\sqrt{S(\omega_k)\Delta\omega}\cos(\omega_k x + \phi_k) \tag{3.28}$$

where $w(x)$ is the generated track irregularity series; $S(\omega_k)$ is the given PSD function of track irregularity; $\omega_k, (k = 1, 2, \ldots, N)$, in which ω_1 and ω_N are, respectively, the lower and upper limits of frequency concerned; $\Delta\omega$ is the bandwidth of frequency interval; ϕ_k is the phase related to the kth frequency which is uniformly distributed in 0–2π.

For the simulated irregularity samples, it is necessary to test whether they have the same characteristics with the given PSD function $S(\omega)$. The basic test method is to use FFT transform to get the simulated PSD function $S^*(\omega)$ from the simulated irregularity series $w(x)$ (x = 1, 2,…), then compare it with the theoretical one $S(\omega)$, observe the closeness between them, to verify the reliability of simulated samples.

The wavelength range of track irregularity spectra has great influence on the analyzed results of train-bridge dynamic system. In general, short-wave irregularities influence the safety indices of vehicles such as derailment coefficients and

Table 3.11 Dynamic management standard for track irregularities of speeding up railways in China

Train speed (km/h)	Vertical profile (mm)	Alignment (mm)	Gauge (mm)	Cross-level (mm)	Torsion (mm) (2.4 m base)	Car-body acceleration (g)	
						Lateral	Vertical
$120 < V \leq 140$	6	5	+6 −4	6	5	0.06	0.10
	10	8	+10 −7	10	8	0.10	0.15
	15	12	+15 −8	14	12	0.15	0.20
$140 < V \leq 160$	6	5	+6 −4	6	5	0.06	0.10
	8	7	+8 −6	8	7	0.10	0.15
	12	10	+12 −8	10	10	0.15	0.20
Allowance in Zhengzhou-Wuhan test section	7	6	+6 −4	6	6	0.15	0.20
Allowance in circular test line	8	7	+7 −4	7	7	0.15	0.20

Table 3.12 Track laying precision criteria for new-built high-speed railways (ballasted track)

Item	Vertical profile	Alignment	Cross-level	Torsion (twist warp)	Gauge
Amplitude	3 mm	2 mm	3 mm	1‰ (3 m base)	±2 mm
Management wavelength	40–50 m	40–50 m	40–50 m	–	–

Table 3.13 Track laying precisions for HSR main line tracks

Item	Ballasted track		Ballastless slab track	
Gauge	±1 mm	Standard gauge 1435 mm	±1 mm	Standard gauge 1435 mm
	1/1500	Change rate	1/1500	Change rate
Alignment	2 mm	Chord length 10 m	2 mm	Chord length 10 m
	2 mm/5 m	30 m base	2 mm/8*a* (m)	8*a* (m) base
	10 mm/150 m	300 m base	10 mm/240*a* (m)	240*a* (m) base
High-low	2 mm	Chord length 10 m	2 mm	Chord length 10 m
	2 mm/5 m	30 m base	2 mm/8*a* (m)	8*a* (m) base
	10 mm/150 m	300 m base	10 mm/240*a* (m)	240*a* (m) base
Cross-level	2 mm	Excluding super elevation of curve and transition curve	2 mm	Excluding super elevation of curve and transition curve
Torsion	2 mm	3 m base, including those produced by super elevation slope of transition curve	2 mm	3 m base, including those produced by super elevation slope of transition curve
Deviation from design track elevation/center	10 mm	Rail surface elevation at platform should not lower than the design value	10 mm	Rail surface elevation at platform should not lower than the design value

Note a in the table is fastener spacing (m)

offload factors of wheels, while long-wave irregularities affect the vibration acceleration of car-body, thus affecting the riding comfort of passengers. In dynamic analysis of train-bridge system, the selection of wavelengths for track irregularity spectra should consider the vibration frequencies of locomotive, vehicle, track, and bridge, and the train speed range in calculation.

For track irregularities with long wavelengths that produce low-frequency excitation, as the natural frequencies of bridge structures are generally higher than those of vehicles, the vibration standard on vehicles is the control factor to determine the long-wave component considered for track irregularities. Considering the most unfavorable situation of car-body vibration, the wavelength L of long-wave track irregularity considered in simulation analysis should satisfy

$$L \geq \frac{V}{3.6f}(\mathrm{m}) \tag{3.29}$$

where V is the maximum calculating train speed (km/h), and f is the natural frequency of car-body (Hz).

The natural frequencies of high-speed train vehicles are generally in the range of 1.0–1.5 Hz, so the comfort standard is the control factor to determine the wavelength of long-wave track irregularity. The lower frequency limit in ISO2631 is 0.89 Hz and that recommended in ORE/C116 is 0.5 Hz; therefore, if the calculating train speed is 400 km/h (111.1 m/s), the wavelength of long-wave track irregularity should be longer than 120 m, and if the train speed is 300 km/h (83.3 m/s), the long-wave wavelength should reach 85 m. The management wavelengths of track irregularity at different train speeds are shown in Table 3.14, where it can be found that the management wavelength of track irregularities should be in the range of 45–85 m at the train speed of 250–300 km/h.

For track irregularities with short-wave wavelengths, as the sampling interval of track irregularity by the inspection car in China and abroad is generally 0.25 or 0.3048 m (1 ft), the shortest effective wavelength of track irregularity is about 1.0 m. When the train speed is 400 km/h, therefore, the excitation frequency is higher than 100 Hz.

Shown in Fig. 3.11 are the vertical profile track irregularity spectra measured on the Gou River Bridge of the Qin-Shen high-speed railway, which are filtered with different wavelengths. The figure shows that the track irregularities contain various wavelengths in a certain range, and the PSD curves filtered with 30 and 50 m are quite close to each other. In dynamic analysis of train-bridge system for high-speed railway, the long-wave cutoff wavelength for track irregularity sample is 80 m, and the sampling interval is 0.25 m, namely the shortest effective wavelength is about

Table 3.14 Management wavelengths of track irregularities at different train speeds (m)

Natural frequency of vehicle	Train speed		
	250 km/h	270 km/h	300 km/h
1.0 Hz	70	75	83
1.5 Hz	46	50	55

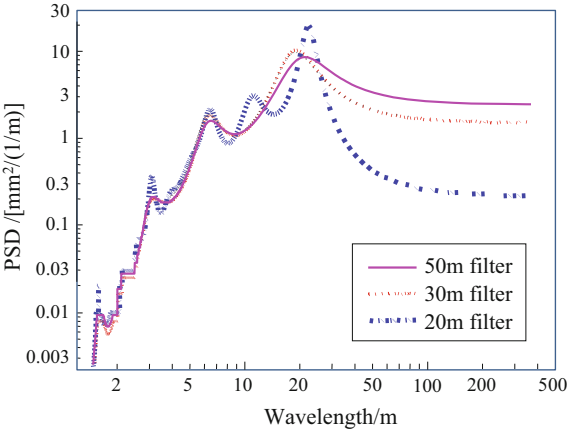

Fig. 3.11 Vertical profile track irregularity PSDs of Gou River Bridge on the Qin-Shen HSR

1.0 m. This wavelength covers the possible wavelength range of track irregularities on bridge, and remains a certain allowance.

Taking the Germany low disturbance track spectrum as an example, the random track irregularity samples are generated by the above-mentioned numerical simulation method (the PSD-based equivalent algorithm), using the PSD functions given in Eq. (3.18).

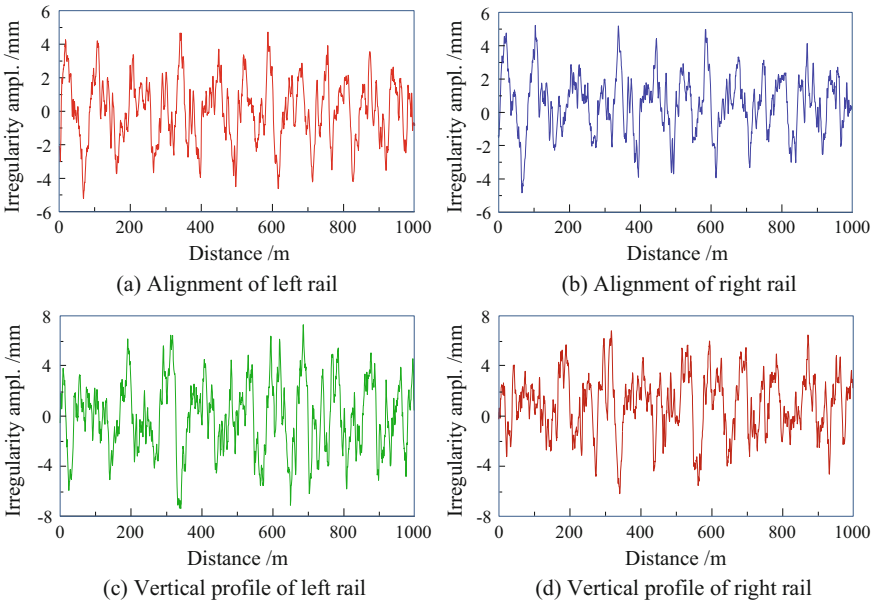

Fig. 3.12 Track irregularity curves generated from German low disturbance PSD

Figure 3.12 shows the simulated track irregularity curves with wavelength range 1–120 m, which are adopted in the train-bridge dynamic analysis of Qin-Shen HSR and Beijing-Shanghai HSR. The results show that when the wavelength is 1–120 m, the amplitude of vertical profile track irregularity generated from German low disturbance PSD varies in the range of −7.5–7.5 mm, and that of the alignment track irregularity in the range of −6–5 mm.

3.2 Vehicle Hunting Movement

3.2.1 Mechanism of Vehicle Hunting Movement

When a railway vehicle runs on a track, the wheel-set rolling along the track produces, simultaneously, a lateral movement and a yawing movement in horizontal plane, forming a motion trajectory of sinusoid curve (Wang 1983, 1994; Kalker 1979; Yang 1990; Xia et al. 2012), as shown in Fig. 3.13. This phenomenon is due to the conic wheel tread and the gap between the wheel rim and the rail side. During the movement, when the wheel-set drifts off the central line of the track, whose left wheel and right wheel will roll along the track at different rolling radii. For example, when the wheel-set drifts towards the right side, due to the conic wheel tread, the right wheel rolls with a larger radius, and thus moves a longer distance than the left one, and the unequal moving distances of the two wheels make the wheel-set drift to the left side of the track, and vice versa. This is the so-called hunting movement of wheel-set. The hunting movement of wheel-set forces the bogie and further the car-body to move in horizontal plane, producing the hunting movements of bogie and car-body. In dynamic analysis of train-bridge system, wheel-set hunting movement can be defined as a given relative motion between wheel-set and track, which is regarded as a self-excitation source of the system.

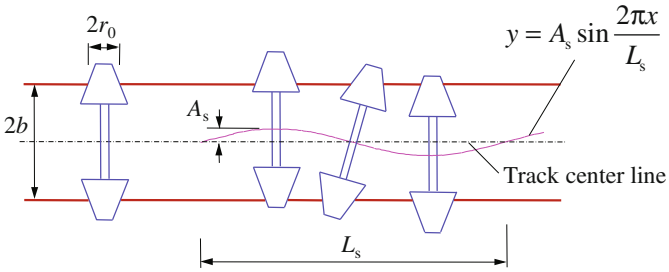

Fig. 3.13 Illustration of wheel-set hunting movement

When a vehicle runs on an ideal straight track, if the wheel-set has a good positioning stiffness, and the suspension system has appropriate matching parameters, or under other specific conditions, the amplitude of hunting movement generated in a certain speed range will attenuate with time, in which the movement is known as the stable hunting movement. When the train speed exceeds a critical value, the amplitude of the hunting movement will increase with time, so that the wheel-set will swing from side to side until the wheel rim collides with the rail, and thus, the bogies and the car-body also undergo severe vibration, in which case the movement is called unstable hunting movement.

When an unstable hunting movement occurs, it may not only worsen the running performance of vehicle, debase the comfort of passengers, increase the dynamic loads on vehicle parts, but also induce serious wheel-rail collision, causing damage to the vehicle and the track structure, and even vehicle derailment. Therefore, the hunting movement of vehicle is one of the main obstacles to realize high-speed running of trains.

3.2.2 *Hunting Movements of Wheel-Set in Free and Actual States*

There are two types of hunting movement when a vehicle runs on the track: one occurs in the wheel-set, the other occurs in the bogie, which are very complicated. The study starts from the simplest case, namely the hunting movement of a free wheel-set with conical tread, by assuming (1) the free wheel-set moves at a uniform speed along the straight track with constant rail gauge and rigid subgrade; (2) the wheel continuously contacts with the rail, and the lateral displacement of the wheel-set is very small.

The wheel-set movement can be regarded as rotating around the instantaneous center of rotation with the radius ρ, as shown in Fig. 3.14.

When the movement speed is very low and the force (moment) of inertia can be neglected, the hunting movement of free wheel-set can be described with simple harmonic motion as

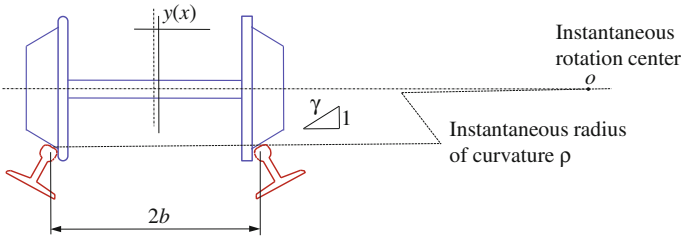

Fig. 3.14 Illustration of wheel-set movement

$$y(x) = A_w \sin\frac{2\pi x}{L_w} = A_w \sin\frac{2\pi V}{L_w} t \tag{3.30}$$

where x is the traveling distance of the wheel-set along the track; A_w is the hunting amplitude of free wheel-set; L_w is the hunting wavelength of free wheel-set, which can be expressed as

$$L_w = 2\pi\sqrt{\frac{br_0}{\lambda}} \tag{3.31}$$

where b is half of the distance between the right and left wheels at their rolling circles, approximately equals to half of track gauge; r_0 is the rolling radius of wheel, approximately equals to radius of the wheel; λ is taper of wheel tread; V is the traveling speed of the vehicle. Thus, the hunting frequency of the free wheel-set can be derived as

$$f_w = \frac{V}{L_w} = \frac{V}{2\pi}\sqrt{\frac{\lambda}{br_0}} \tag{3.32}$$

In fact, due to the positioning device of bogie, the displacement of the wheel-set with respect to the bogie is restrained, resulting in the hunting wavelength movement of bogie whose wavelength is different from the free wheel-set. Assuming the two wheel axles on the bogie are parallel to each other and perpendicular to the longitudinal axis of the bogie (as shown in Fig. 3.15), and the two wheel-sets are rigidly fixed on the bogie, the hunting wavelength and frequency of the bogie movement can be expressed as

$$L_t = 2\pi\sqrt{\frac{br_0}{\lambda}\left[1 + \left(\frac{S_0}{2b}\right)^2\right]} \tag{3.33}$$

$$f_t = \frac{V}{L_t} = \frac{V}{2\pi\sqrt{\frac{br_0}{\lambda}\left[1 + \left(\frac{S_0}{2b}\right)^2\right]}} \tag{3.34}$$

where S_0 is the wheelbase of bogies.

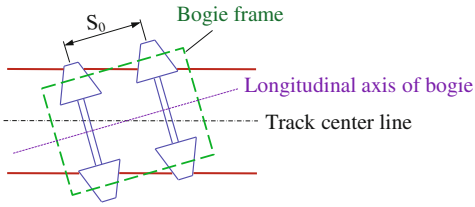

Fig. 3.15 Illustration of bogie hunting movement

It can be seen that the law of the vehicle hunting movement is related to the slope of tread, the radius, and the distance between the rolling circles of the wheels. The hunting frequency is proportional to the vehicle speed. The hunting wavelength of bogie is longer than that of free wheel-set, while the hunting frequency is lower than that of the free wheel-set.

For the bogies of main passenger cars in China, S_0 = 2400 mm, $2r_0$ = 915 mm, $2b$ = 1.493 m, and for the new wheels, λ = 1/20; thus, the hunting wavelengths of free wheel-set and bogie can be calculated as L_w = 16.4 m and L_t = 31.1 m, respectively.

For the bogies of CRH2 high-speed EMU, S_0 = 2500 mm, $2r_0$ = 860 mm, $2b$ = 1.493 m, and for the new wheels, λ = 1/40; thus, the hunting wavelengths of free wheel-set and bogie can be calculated as L_w = 22.5 m and L_t = 43.9 m, respectively.

For the bogies of main freight cars in China, S_0 = 1750 mm, $2r_0$ = 840 mm, $2b$ = 1.493 m, and for the new wheels, λ = 1/20; thus, the hunting wavelengths of free wheel-set and bogie can be calculated as L_w = 15.7 m and L_t = 24.2 m, respectively.

The actually measured hunting wavelengths of bogies are between L_w and L_t, depending on the positioning stiffness of wheel-sets on the bogie, and the hunting amplitude of wheel-set also varies during its movement.

Shown in Fig. 3.16a is the comparison of theoretical and measured wheel hunting frequencies of passenger cars in China. It can be seen that the hunting frequencies increase linearly with train speed, which is in accordance with the theoretical result. However, the measured frequencies are distributed between the theoretical values of free wheel-set and rigidly fixed bogie, for the connection of wheel-set with bogie is actually neither free nor rigidly fixed, but elastically positioned.

Shown in Fig. 3.16b is the comparison of theoretical and measured wheel hunting frequencies of freight cars. Different from passenger cars, the measured

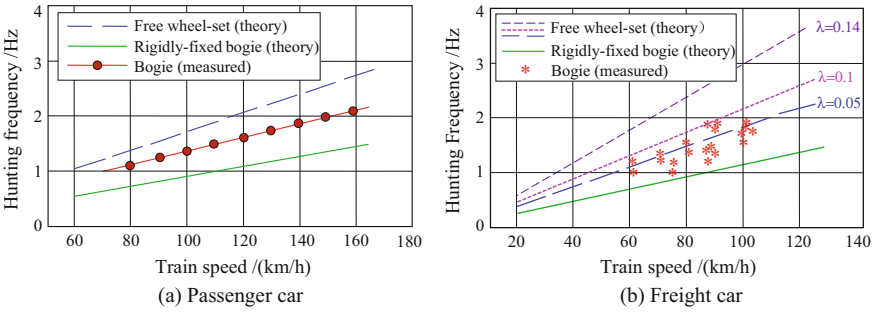

Fig. 3.16 Relationship between wheel-set hunting frequencies and train speed

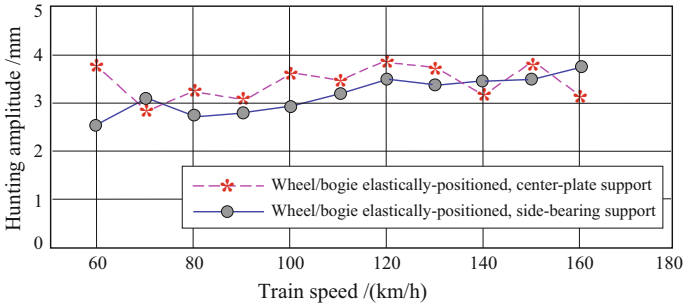

Fig. 3.17 Distribution of measured wheel hunting amplitudes of passenger vehicles

frequencies distribute around the theoretical curve in a scattered way, but show largely a linear trend versus train speed, and nearly half of the measured values are higher than theoretical ones of free wheel-set ($\lambda = 0.05$), which is not only because the wheel-sets are elastically positioned on the bogie, but also owing to the inevitable abrasion of wheel treads after a period of use.

For a new wheel, the slope of wheel tread is $\lambda = 0.05$ for common bogies and $\lambda = 0.025$ for high-speed bogies. According to Zhang (1996), the slope of wheel tread will reach $\lambda = 0.28$ when a wheel wears to extremity, and the corresponding hunting wavelength will be $L_w = 6.65$ m. Suppose the slope of wheel tread is worn to $\lambda = 0.14$ and $\lambda = 0.1$, the related hunting wavelengths will be $L_w = 9.4$ m and $L_w = 12.5$ m, respectively. When plotting these two corresponding frequency distribution curves in Fig. 3.16, it can be seen that the curve with $\lambda = 0.1$ can envelope the measured data.

Experimental investigation shows that for common-speed vehicles, the variation law of actual hunting frequencies agrees basically with that of theoretical ones, while for high-speed vehicles, the hunting movement becomes much more complicated, and the influence of dynamic action should be taken into account.

Shown in Fig. 3.17 are the distributions of measured wheel hunting amplitudes of passenger cars (Wang 1983). As shown in the figure, in the train speed range of 60–160 km/h, the hunting amplitudes of wheel-sets are between 2.5 and 4 mm, and have little relation with train speed.

For various types of bogies, the distribution curves of wheel hunting frequencies and amplitudes are different. During the whole process of a vehicle running, the wheel hunting movement is continuously excited by track irregularity; thus, the hunting frequency and amplitude are affected by the property and working state of the track. Therefore, the actual hunting movement is very complicated.

3.2.3 Description of Wheel Hunting Movement in Train-Bridge System

In dynamic analysis of train-bridge system, the hunting movement of a wheel on the track can be expressed with the following formula

$$y_s(x) = A_s \sin\left(\frac{2\pi x}{L_s} + \varphi_s\right) = A_s \sin\left(\frac{2\pi V}{L_s} t + \varphi_s\right) \tag{3.35}$$

where L_s, φ_s, and A_s are, respectively, the wavelength, initial phase, and amplitude of hunting movement.

As discussed previously, the value of L_s should consider the wearing degree of the wheel tread: For a new wheel with λ = 1/20, L_s = 15.7 m; for a wheel wore to extremity, λ = 0.28, L_s = 6.65 m. In fact, the wearing degrees of wheel tread for all vehicles are arbitrary, and for each wheel-set, it can be treated individually as a random variable with uniform distribution, namely $L_s \sim R$ (6.65, 15.7 m).

According to the site survey, the initial hunting phase angles of various wheel-sets on a train are different, which can be assumed as random variables with uniform distribution in the range of 0–2π, namely $\varphi_s \sim R(0, 2\pi)$.

Up to now, there have been few measurements on amplitudes of wheel hunting movement, so A_s can be taken as a random variable according to the measured results in Fig. 3.17, that is, $A_s \sim R$ (2.5, 4 mm) for any wheel-set.

3.3 AR Model Simulation of Random Excitations on Train-Bridge System

When a train runs on the track, the hunting movement of the wheel and the movement excited by track irregularities exist simultaneously, forming the resultant motion of the wheel-set. The resultant motion can be regarded as the random excitation of train-bridge coupled vibration system, which can be obtained by measuring the vibration responses of the wheel-set. The following example illustrates the principle and method to simulate the random excitation of train-bridge system by measuring the vibration accelerations.

3.3.1 Measurement of Random Excitation

To measure the random excitation, a test was carried out on the circular railway test section of the China Academy of Railway Sciences. Firstly, accelerometers are installed on the axle boxes of two bogies of the test car to measure the accelerations of wheel-sets, and then the resultant displacement response can be obtained by

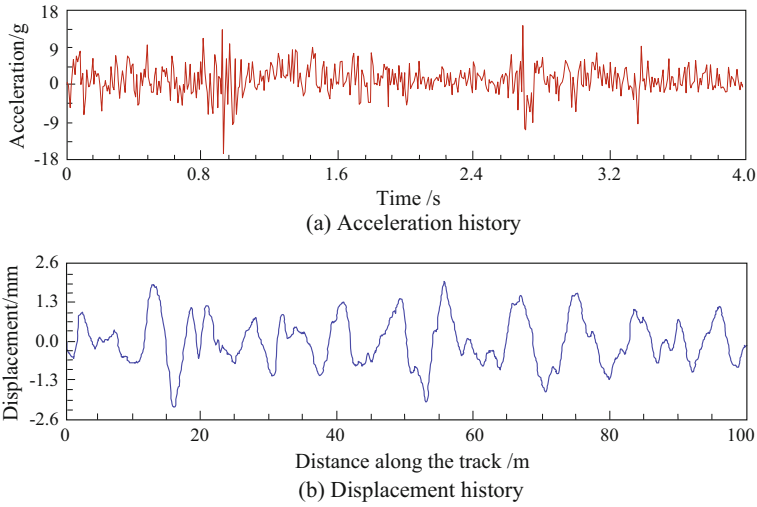

Fig. 3.18 Measured acceleration and displacement curves of wheel-set

twice integrating the measured acceleration histories. A group of measurements were conducted in the test, at different train speeds from 40 to 155 km/h. The statistical properties of the system excitation can be obtained by repeated observations and analysis on the measured vibration data.

Figure 3.18a shows a measured acceleration histories of the wheel-set when the train runs at the speed of 100 km/h. To obtain the excitation function for the system, the displacement time history Δx has to be transformed into the discrete data series $Y(x_i)$ which is a function of distance x,

$$Y(x_i) = Y(t)|_{t=i\Delta x/V} \tag{3.36}$$

where x_i is the position of the ith sampling point along the track length, Δx is the sampling interval, and V is the train speed.

Figure 3.18b shows the displacement of the wheel-set along the track after twice numerical integration on the acceleration histories.

3.3.2 AR Model Simulation of System Excitation

Due to the time-varying characteristics of train-bridge dynamic interaction and the nonlinearity of wheel-rail contact relation, the motion equations of the train-bridge system can only be solved by the step-by-step integration method, which determines that the system input should adopt time-domain function or time-domain samples (Xia and Chen 1993; Xia and De Roeck 1997).

Considering the low-frequency properties of the system excitation, a time series model, the higher-order vector AR model, is adopted, which has distinct advantage compared with the FFT analysis in the frequency domain.

According to the time series analysis theory, an ordered discrete set $Y(x_0),\ldots Y(x_i),Y(x_n)$ is called the discrete digital time series, which can be obtained by sampling the signal at a series of discrete time points $x_0,x_1,\ldots,x_n$ (where x_i is the independent variable, and $x_0<x_1<\cdots<x_i<\cdots<x_n$). When $\mathbf{Y}$ is a vector, this set becomes a multivariate vector time series $\mathrm{Y}_x=[\,\mathrm{Y}_{1,x}\quad \mathrm{Y}_{2,x}\quad \ldots\quad \mathrm{Y}_{N,x}\,]^{\mathrm{T}}$, which can be expressed by a vector AR model as

$$\mathbf{Y}_x+\boldsymbol{\Phi}_1\mathbf{Y}_{x-1}+\cdots+\boldsymbol{\Phi}_P\mathbf{Y}_{x-P}=\boldsymbol{\varepsilon}_x \tag{3.37}$$

where $\mathbf{Y}_x$ is the zero-mean stationary random series of N-variates; $\boldsymbol{\Phi}_1,\boldsymbol{\Phi}_2,\ldots\boldsymbol{\Phi}_P$ are auto-regressive matrices of $N\times N$ order; $\boldsymbol{\varepsilon}_x=[\,\varepsilon_{1,x}\quad \varepsilon_{2,x}\quad \ldots\quad \varepsilon_{P,x}\,]^{\mathrm{T}}$ is an N-variate white noise series that satisfies $E[\boldsymbol{\varepsilon}_x\boldsymbol{\varepsilon}_s^{\mathrm{T}}]=\mathbf{Q}$ for $x=s$, where $\mathbf{Q}$ is the covariance matrix, and $E[\boldsymbol{\varepsilon}_x\boldsymbol{\varepsilon}_s^{\mathrm{T}}]=0$ for $x\neq s$.

Suppose a series of $L+P+1$ observations with zero mean have been sampled from the wheel-set vibration responses at the time of $t_0,t_1,\ldots,t_{L+P}$, and are to be fitted by an N-AR(P) model, the auto-regressive matrix $\boldsymbol{\Phi}$ can be estimated by least squares minimizing

$$\begin{aligned}T_\varepsilon&=\sum_{k=P}^{L+P}\sum_{i=1}^{N}[w_i(k)]\\&=\sum_{k=P}^{L+P}\mathbf{W}(k)\cdot\mathbf{W}^{\mathrm{T}}(k)=\mathrm{trace}(\boldsymbol{\varepsilon}\cdot\boldsymbol{\varepsilon}^{\mathrm{T}})=\mathrm{trace}[(\mathbf{U}-\boldsymbol{\Phi}\mathbf{V})(\mathbf{U}-\boldsymbol{\Phi}\mathbf{V})^{\mathrm{T}}]\end{aligned} \tag{3.38}$$

To minimize T_ε, we can differentiate it with respect to $\boldsymbol{\Phi}$ and make the result equal to zero, that is

$$\left.\frac{\partial T_\varepsilon}{\partial\boldsymbol{\Phi}}\right|\boldsymbol{\Phi}=\hat{\boldsymbol{\Phi}}=\mathbf{0}-\mathbf{U}\mathbf{V}^{\mathrm{T}}-\mathbf{V}\mathbf{U}^{\mathrm{T}}+2\hat{\boldsymbol{\Phi}}\mathbf{V}\mathbf{V}^{\mathrm{T}}=\mathbf{0} \tag{3.39}$$

Note that $\mathbf{U}\mathbf{V}^{\mathrm{T}}=\mathbf{V}\mathbf{U}^{\mathrm{T}}$, the discrete auto-regressive matrix $\hat{\boldsymbol{\Phi}}$ ($2N\times 2P$ order) can be estimated as

$$\hat{\boldsymbol{\Phi}}=\left[\,\hat{\boldsymbol{\Phi}}_1\quad\hat{\boldsymbol{\Phi}}_2\quad\ldots\quad\hat{\boldsymbol{\Phi}}_P\,\right]=(\mathbf{U}\mathbf{V}^{\mathrm{T}})(\mathbf{V}\mathbf{V}^{\mathrm{T}})^{-1} \tag{3.40}$$

where

$$\mathbf{U}=[\,X(P)\quad X(P+1)\quad\cdots\quad X(P+L)\,] \tag{3.41}$$

$$\mathbf{V} = \begin{bmatrix} X(P-1) & X(P-2) & \cdots & X(P-1+L) \\ X(P-2) & X(P-1) & \cdots & X(P-2+L) \\ \cdots & \cdots & \cdots & \cdots \\ X(0) & X(1) & \cdots & X(L) \end{bmatrix} \tag{3.42}$$

In order to obtain the interrelation of random excitations of the system (especially the phase difference between the wheel-sets on the front and the rear bogies of a vehicle), a two-variate high-order AR model is adopted in the analysis.

The wheel-set displacement series obtained after twice integration on the acceleration data recorded at various train speeds is normalized by sampling interval $\Delta x = 0.5$ m, which can be well fitted by a two-variate AR(12) model. Then, the estimated auto-regressive matrices from different data records are calculated, and finally are averaged to acquire the statistical auto-regressive matrices $\mathbf{\Phi}_1$ to $\mathbf{\Phi}_{12}$.

By substituting them into Eq. (3.37), the 2-AR(12) model of the system excitation can be expressed as

$$\begin{aligned} \begin{Bmatrix} Y_m^1 \\ Y_m^2 \end{Bmatrix} &= \begin{bmatrix} 2.678 & 0.225 \\ -0.023 & 2.654 \end{bmatrix} \begin{Bmatrix} Y_{m-1}^1 \\ Y_{m-1}^2 \end{Bmatrix} + \begin{bmatrix} -3.221 & -0.691 \\ 0.058 & -3.123 \end{bmatrix} \begin{Bmatrix} Y_{m-2}^1 \\ Y_{m-2}^2 \end{Bmatrix} + \begin{bmatrix} 2.871 & 1.085 \\ -0.068 & 2.758 \end{bmatrix} \begin{Bmatrix} Y_{m-3}^1 \\ Y_{m-3}^2 \end{Bmatrix} \\ &+ \begin{bmatrix} -2.54 & -1.32 \\ 0.07 & -2.47 \end{bmatrix} \begin{Bmatrix} Y_{m-4}^1 \\ Y_{m-4}^2 \end{Bmatrix} + \begin{bmatrix} 2.18 & 0.99 \\ -0.08 & 2.21 \end{bmatrix} \begin{Bmatrix} Y_{m-5}^1 \\ Y_{m-5}^2 \end{Bmatrix} + \begin{bmatrix} -1.73 & -0.41 \\ 0.07 & -1.99 \end{bmatrix} \begin{Bmatrix} Y_{m-6}^1 \\ Y_{m-6}^2 \end{Bmatrix} \\ &+ \begin{bmatrix} 1.30 & 0.08 \\ -0.06 & 1.75 \end{bmatrix} \begin{Bmatrix} Y_{m-7}^1 \\ Y_{m-7}^2 \end{Bmatrix} + \begin{bmatrix} -0.94 & 1.86 \\ 0.08 & -1.52 \end{bmatrix} \begin{Bmatrix} Y_{m-8}^1 \\ Y_{m-8}^2 \end{Bmatrix} + \begin{bmatrix} 0.62 & 0.25 \\ -0.11 & 1.26 \end{bmatrix} \begin{Bmatrix} Y_{m-9}^1 \\ Y_{m-9}^2 \end{Bmatrix} \\ &+ \begin{bmatrix} -0.39 & -0.06 \\ 0.09 & -0.99 \end{bmatrix} \begin{Bmatrix} Y_{m-10}^1 \\ Y_{m-10}^2 \end{Bmatrix} + \begin{bmatrix} 0.27 & 0.23 \\ -0.03 & 0.66 \end{bmatrix} \begin{Bmatrix} Y_{m-11}^1 \\ Y_{m-11}^2 \end{Bmatrix} + \begin{bmatrix} -0.12 & -0.08 \\ 0.01 & -0.23 \end{bmatrix} \begin{Bmatrix} Y_{m-12}^1 \\ Y_{m-12}^2 \end{Bmatrix} + \begin{Bmatrix} \varepsilon_m^1 \\ \varepsilon_m^2 \end{Bmatrix} \end{aligned} \tag{3.43}$$

The random excitation series groups can then be generated by continuously inputting random numbers with white noise properties into the estimated AR

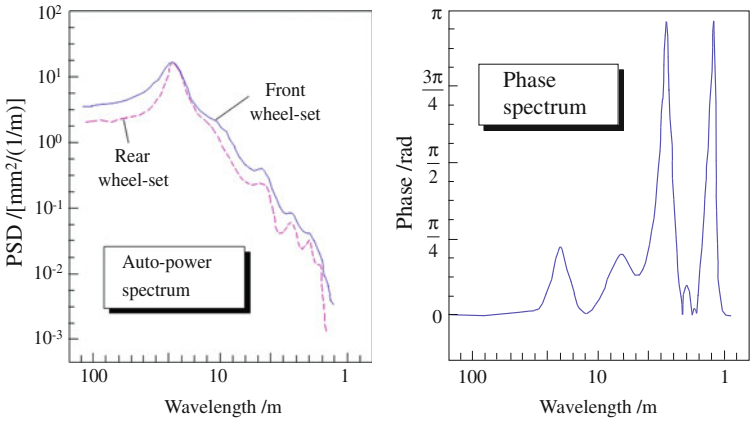

Fig. 3.19 Auto-power spectrum and phase spectrum of system excitation

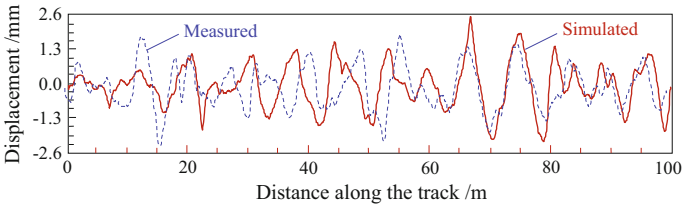

Fig. 3.20 Simulated and measured curves of system excitation

model. At each time $t = m$, a group of random displacement $\left[Y_m^1, Y_m^2\right]^{\mathrm{T}}$ are determined by the white noise $[\varepsilon_m^1, \varepsilon_m^2]^{\mathrm{T}}$ at the same time and the displacements $[Y_{m-k}^1, Y_{m-k}^2]^{\mathrm{T}}$ $(k = 1, 2, \ldots 12)$ at the previous times. The frequency properties of the random excitation series are determined by the parameter matrices of the AR model.

The power and the phase spectra of system excitation obtained by the above method are shown in Fig. 3.19.

The frequency characteristics of the system excitation can be seen from the auto-power spectra, whose predominant frequency is slightly higher than that of the common track irregularities, and the corresponding wavelength is about 22 m which is between the theoretical hunting wavelengths for the free and the rigidly fixed wheel-sets.

The phase spectrum indicates the phase relationship between the wheel-set on the front and the rear bogies. It can be seen that the phase difference at the predominant frequency is about $\pi/4$.

The random excitation curves are generated by the 2-AR(12) model, and one of them is shown in Fig. 3.20, in which the measured curve in Fig. 3.18b is also given. It can be seen that the measured and the simulated curves are in good consistence.

In this method, it is easy to see that the AR model works as a filter, and its coefficient matrices reflect the frequency characteristics of the filter, while the matrices themselves are obtained by fitting and statistically analyzing the measured data. Therefore, the random series generated by the AR model can well reflect the statistical characteristics of the system excitation. Such a random series varying with distance can be used as the self-excitation to simulate the whole history of a train passing through a bridge.

In fact, this method can be used to generate a random series for any known track irregularity power spectrum if it can be converted into time series model coefficients through a transformation. The so-called secondary filtering method is formed on the basis of this principle.

References

Anderson R, Torstensson PT, Kabo E, Larsson F (2015) An efficient approach to the analysis of rail surface irregularities accounting for dynamic train–track interaction and inelastic deformations [J]. Veh Syst Dyn 53(11):1667–1685

Cao XQ, Xia H (2005) Dynamic performance measurement of bridge on Qinhuangdao-Shenyang high-speed railway [R]. Part-C, Technical Report, Beijing, China Academy of Railway Sciences, pp 7–71

Cass R, Berthiaume PP, Kalita RE et al (1969) Dynamic measurement of absolute track properties [J]. J Ind Eng 91(3):855–859

Chen G, Zhai WM (2001) Influences of track irregularities on lateral random vibration response of vehicle and track system [J]. J Nanjing Univ Aeronaut Astronaut 33(3):227–232 (in Chinese)

Clough RW, Penzien J (2003) Dynamics of structures [M]. Computers and Structures Inc, Berkeley

Cooperider NK, Law EH, Hull R et al (1975) Analytical and experimental determination of nonlinear wheel/rail constraints [R]. FRA-OR&D, U.S. Department of Transportation, Interim Report No

Garg VK, Dukkipati RV (1984) Dynamics of railway vehicle system [M]. Academic Press, Canada

Haigermoser A, Luber B, Rauh J, Gräfe G (2015) Road and track irregularities: measurement, assessment and simulation [J]. Veh Syst Dyn 53(7):878–957

Kalker JJ (1979) Survey of wheel-rail rolling contact theory [J]. Veh Syst Dyn 8(4):317–358

Liu YH, Li F, Huang YH (2006) Numerical simulation methods of railway track irregularities [J]. J Traffic Transp Eng 6(1):29–33 (in Chinese)

Luo L, Zhang GM, Wu WQ, Chai XS (2006) Track irregularity control of wheel-track system [M]. China Railway Publishing House, Beijing (in Chinese)

De Pater AD (1988) The geometrical contact between track and wheel-set [J]. Veh Syst Dyn 17:127–140

Railway Construction Institute (1999) Research on track irregularity spectra in chinese main railways [R]. TY-1215, China Academy of Railway Sciences, Beijing

RGRV (1985) Research on random excitation functions of rolling stock/track system [J]. J Changsha Railw Univ 2:1–36 (in Chinese)

TB10621 (2014) Code for design of high-speed railway [S]. China Railway Publishing House, Beijing (in Chinese)

TB/T 3352 (2014) Track irregularity spectra for ballastless slab tracks of high-speed railway [S]. China Railway Publishing House, Beijing (in Chinese)

TYH2004-120 (2004) Code for rating existing railway bridges [S]. China Railway Publishing House, Beijing (in Chinese)

UIC B55 RP 3 (1966) Permissible wheel-load variations on two-axle goods wagons [R]

Wang FT (1983) Vehicle dynamics [M]. China Railway Publishing House, Beijing (in Chinese)

Wang FT (1994) Vehicle system dynamics [M]. China Railway Publishing House, Beijing (in Chinese)

Wang XL, Lai XC, Wang JN, Na H (2015) Dynamic response analysis of train-track coupling system under random irregularities [J]. J Dalian Univ Technol 55(1):81–88 (in Chinese)

Wei CF (2011) Time domain conversion and application research of track irregularity power spectrum [D]. Southwest Jiaotong University, Chengdu (in Chinese)

Xia H, De Roeck G (1997) System identification of mechanical structures by a multivariate autoregressive model [J]. Comput Struct 1–4:341–351

Xia H, Chen YJ (1993) Application of multivariate AR model to bridge modal analysis by ambient vibration measurement [J]. J Vib Shock 12(1):47–52 (in Chinese)

Xia H, De Roeck G, Goicolea JM (2012) Bridge vibration and controls: new research [M]. Nova Science Publishers Inc, New York

Xin XZ (2005) Technical analysis of ballastless track of DB and proposals [J]. Railw Stand Des 2:1–6 (in Chinese)

Xiao SN, Yang GW, Zhang WH, Zhao YX (2008) Simulation of stochastic railway track irregularity based on spectrum density function [J]. China Railw Sci 29(2):28–32 (in Chinese)

Xu JH, Wand P, Wang L, Xiao JL (2015) Research on the distribution characteristics and influence factors of sensitive wavelength of track vertical profile irregularity [J]. J China Railw Soc 37 (7):72–78 (in Chinese)

Yang G (1990) A numerical procedure for solving the nonlinear equations of the geometrical contact between wheel and track [R]. Delft University of Technology, Netherlands

Yang XW, Gu SJ, Zhou SH et al (2015) Effect of track irregularity on the dynamic response of a slab track under a high-speed train based on the composite track element method [J]. Appl Acoust 99:72–84

Yasojima Y (1981) Running stability of railway wagons on vibrating tracks [J]. JSCE 313:111–124 (in Japanese)

Zacher M, Nicklisch D, Grabner G et al (2015) A multi-national survey of the contact geometry between wheels and rails [J]. J Rail Rapid Transit 229(6):691–709

Zhai WM (2014) Vehicle-track coupled dynamics (4th Edition) [M]. China Railway Publishing House, Beijing (in Chinese)

Zhang DX (1996) System dynamics for rolling stocks and tracks [M]. China Railway Publishing House, Beijing (in Chinese)

Zhang GM (2001) Vehicle-track-bridge system dynamic analysis model and track irregularities control on quasi & high-speed railways [D]. China Academy of Railway Sciences, Beijing (in Chinese)

Zhang SG, Kang X, Liu XB (2008) Characteristic analysis of the power spectral density (PSD) of track irregularity on Beijing-Tianjin inter-city railway [J]. China Railway Science 29(5):25–30 (in Chinese)

Chapter 4
Vibration Criteria for HSR Bridges and Train Vehicles in China

In this chapter, the vibration criteria for HSR bridges and train vehicles in China are summarized, including the structural safety and durability of bridge and the stability of track due to vibration, the running safety of high-speed train due to bridge and train vibrations, and the riding comfort of passengers on running trains. The conditions unnecessary to conduct coupling dynamic analysis of train-bridge system are introduced.

The high-speed train produces impact on the bridge and causes it to vibrate, and, meanwhile, the vibration of the bridge in turn influences the running safety and stability of train vehicles. The dynamic interaction of train-bridge system is a key factor affecting the performances of both bridge structure and train vehicles. The calculated or measured dynamic response of train-bridge system reflects the dynamic characteristics and service status of the system, thus should be controlled to ensure the safety of train vehicles, the comfort of passengers, the fatigue damage of bridge members, as well as the stability of the track structures. For this purpose, therefore, it is important to establish the vibration evaluation criteria for bridges and train vehicles.

The serviceability related to train-bridge vibration involves the following problems:

(1) The structural safety and durability of bridge and the stability of track due to vibration;
(2) The running safety of high-speed train due to bridge and train vibrations;
(3) The riding comfort of passengers on running train;
(4) The running safety of high-speed train on bridge subjected to strong wind, intense earthquake, or collision;
(5) The environmental effect due to train-bridge vibration;
(6) The noise effect of bridge structure due to high-speed train.

Problems (1) to (3) are introduced in this chapter, including the evaluation criteria for bridge structures and train vehicles, with the related calculating methods, problem (4) will be discussed, respectively, in the following chapters, while problems (5) and (6) are not included in this book, which can be found in Xia and Zhang (2005) and Xia et al. (2012).

H. Xia et al., *Dynamic Interaction of Train-Bridge Systems in High-Speed Railways*, Advances in High-speed Rail Technology, https://doi.org/10.1007/978-3-662-54871-4_4

4.1 General Introduction

In the past decades, a series of codes (including standards, specifications, and regulations) were issued in China for design, construction, and safety examination of high-speed railways. The vibration criteria proposed in these codes, after validated and updated by years of design, construction, and maintenance practice in HSR, can meet the requirement of train-bridge coupling dynamic analysis and are adopted to evaluate the dynamic performances of HSR bridge structures and train vehicles. The main codes and the related criteria are summarized hereinafter, and to provide a complete conception, the ones for common railways are also introduced.

(1) *Code for Design of High-speed Railway* (TB10621-2014 2015a, b), issued by the National Railway Administration of PRC on December 1, 2014, abbreviated as HSR Code in this chapter. This code is applicable to high-speed railways of passenger trains with the design speed of 250–350 km/h, in three grades, respectively, running EMU (electrical multiple unit) train with the design speed of 250, 300, and 350 km/h. The items in this code for concrete bridges are applicable to spans no more than 96 m.

(2) *Interim Provisions on Design of 200–250 km/h New Passenger Dedicated Railways* (TJS2005-140 2005a, b), issued by the Ministry of Railways of PRC on August 10, 2005, abbreviated as Interim PR Code in this chapter. This code is applicable to high-speed railways of passenger trains with the design speed of 200–250 km/h. The items in this code for concrete bridges are applicable to spans no more than 96 m. In Item 6.1.1 of the code, it is stipulated that "In bridge design, train-bridge coupling dynamic analysis should be conducted as necessary are clearly demonstrated."

(3) *Interim Provisions on Design of 200 km/h New Railways for Passenger and Freight Trains* (TJS2005-285 2005a, b), issued by the Ministry of Railways of PRC on April 25, 2005, abbreviated as Interim PFR Code in this chapter. This code is applicable to railways for passenger trains with the design speed of 250 km/h and freight trains of 120 km/h. The provisions in this code for concrete bridges are applicable to spans no more than 96 m.

(4) *Fundamental Code for Design on Railway Bridge and Culvert* (TB10002.1-2005 2005a, b), issued by the Ministry of Railways of PRC on June 14, 2005, abbreviated as Bridge Code in this chapter. This code is applicable to the design of bridge and culvert on Grade I or Grade II railway for combined passenger and freight transport, with the passenger train speed no more than 160 km/h and the freight train speed no more than 120 km/h (80 km/h for trains with Z8A bogies). The applicable spans in this code are, respectively, no more than 96 m for concrete beams, 168 m for steel beams, and 40 m for steel plate beams.

(5) *Code for Rating Existing Railway Bridges* (TYH2004-120 2004), issued by the Ministry of Railways of PRC on March 9, 2004, abbreviated as Bridge Rating Code in this chapter. This code is applicable to the existing bridges with standard gauge for combined passenger and freight transport, with the

maximum passenger train speed of 160 km/h and the maximum freight train speed of 80 km/h. It can also be referenced when the maximum passenger train speed is 200 km/h.

(6) *Code for Rating Service Performance of High-speed Railway Bridge* (TZY2014-232 2014), issued by the China Railway Corporation on August 19, 2014, abbreviated as HSR Rating Code in this chapter. This code is applicable to rating and evaluation for double-track PC box-beam bridges with spans no more than 100 m in high-speed railways.

(7) *Railway Vehicle Specification for Evaluating the Dynamic Performance and Accreditation Test* (GB5599-85 1985), issued by the National Standard Bureau of PRC on November 25, 1986, abbreviated as Vehicle Code in this chapter. This code is applicable to the dynamic performance and accreditation test for passenger and freight vehicles on railways with standard gauge.

(8) *Railway Locomotive Specification for Evaluating the Dynamic Performance and Accreditation Test* (TB/T 2360-93 1994) issued by the Ministry of Railways of PRC on November 11, 1993, abbreviated as Locomotive Code in this chapter. This code is applicable to the dynamic performance and accreditation test and experiments for the electric and diesel locomotives on railways with standard gauge.

The applications of the criteria for dynamic responses of bridge structure and train vehicles given in the above eight codes can be divided into three categories.

(1) Criteria for calculated results of train-bridge coupling dynamic analysis

The first category of application is for the calculated results of train-bridge coupling dynamic analysis, involving the HSR Code, Interim PR Code and Interim PFR Code, which are aimed, respectively, at bridges on high-speed railways with the design speed of 250–350 km/h, passenger-dedicated railways with the design speed of 200–250 km/h, and speed-raised railways with maximum train speed of 200 km/h. In the three codes, train-bridge coupling dynamic analysis is required to be conducted, and the related criteria are given, including the derail factor, offload factor, lateral wheel/rail force, vertical and lateral car-body acceleration, riding comfort index (Sperling comfort index) limits for vehicle, and the vertical acceleration limit for bridge deck. These criteria can be directly used for evaluating the calculated dynamic response of bridge structure and train vehicles.

(2) Criteria for the measured dynamic response of train-bridge system

The second category of application is for the measured dynamic responses of train-bridge system, involving the Bridge Rating Code, HSR Rating Code, Vehicle Code, and Locomotive Code, which applies to guiding the in situ experiment for railway bridges and the dynamic performance test for vehicles. Although the criteria given in the four codes are proposed based on the measured data, they are also applicable to evaluating the calculated dynamic response of train-bridge system using the real vehicle, bridge, and track parameters, because the simulation analysis is essentially a kind of numerical experiment.

In the Bridge Rating Code, the limits for dynamic response of bridge under running train are given. Because the Bridge Rating Code is based on the experimental results mainly from typical existing railway bridges around the year of 2000, while not from HSR bridges, so the criteria in the Bridge Rating Code are not the necessary condition but can be referenced in evaluating the dynamic response of HSR bridges.

The HSR Rating Code is based on large amount of experimental data from HSR bridges, which is adopted as an important standard for evaluating both measured and calculated dynamic responses of train-bridge system in high-speed railway.

In the Vehicle Code and Locomotive Code, the limits for running safety and riding comfort of train vehicles are given. There was no railway train with speed higher than 200 km/h when the codes were issued, and the vehicles involved in the codes were quite different from the high-speed train vehicles both in performance and in structure. However, since the running safety indices of train vehicle depend on wheel-rail interaction, and the riding comfort of passengers reflects their subjective feeling, it is believed they should be similar for ordinary and high-speed vehicles. Therefore, in Interim PR Code, Interim PFR Code, and HSR Code, the safety and riding comfort criteria are proposed by referencing those from the Vehicle Code and Locomotive Code, which are also applicable in evaluation of both measured and calculated dynamic responses of train-bridge system in high-speed railway.

(3) Criteria for bridge stiffness

The third category of application is for bridge stiffness, involving four designing codes, namely HSR Code, Interim PR Code, Interim PFR Code, and Bridge Code. In these codes, the criteria for the beam vertical and lateral deformations, the vertical and lateral angles at beam-ends, and the beam torsional angles are related to the train-bridge dynamic response. In fact, the criteria were proposed for the calculation under static loads, mainly to prevent the designed bridge from too low stiffness. Because the static response of bridge is substantially different from the dynamic response, the above mentioned criteria can only be referenced for evaluating the service performance of the bridge, but not directly used for train-bridge coupling dynamic analysis.

In these codes, criteria are also proposed to control the natural frequency of bridge structure. The natural frequency refers to the bridge frequency in free vibration, which is a characteristic of the bridge itself, independent of external factors, such as the vehicle loads. In a strict sense, the bridge natural frequency is not a major factor for train-bridge dynamic response, but it reflects the stiffness of the structure which affects the dynamic performance of the bridge, thus playing an important role in bridge design.

Up to the present, the dynamic responses of train-bridge system are evaluated and controlled in design, by using the maximum values of the related indices proposed in the HSR Code, Interim PR Code, and Interim PFR Code. In these codes, however, there is lack of strict regulations on the calculation condition and

data statistic method for train-bridge coupling dynamic analysis. For example, the calculated responses may change with different integral time steps, even if all other input data of the train-bridge system are the same. This in certain extent decreased the objectivity of evaluation for the train-bridge dynamic responses. Therefore, the calculation method for the dynamic response indices of train-bridge system is studied in this chapter, by referencing the Vehicle Code and Locomotive Code.

4.2 Criteria for Train Running Safety

In the current Chinese codes, the criteria for evaluating train running safety include derail factor, offload factor, lateral wheel/rail force, and overturn coefficient (Wang 1983; Dukkipati 2000; Xia and Zhang 2005; Zhai and Xia 2011; Xia et al. 2012). The four train running safety indices can be obtained by *in-situ* measurements or from train-bridge coupling dynamic analysis, in which the derail factor, offload factor, and lateral wheel/rail force are used in evaluation of train safety in common operating status, while the overturn coefficient is used to ensure the train against being overturned by lateral wind force, centrifugal force, and lateral inertia force.

4.2.1 Derailment Factor

Derailment factor is an index to evaluate the safety of vehicle wheel against derailment. In Item 3.3.2 of Vehicle Code: Derailment factor is used to check whether the vehicle will derail due to wheel-flange climbing up the rail-head under lateral force. In Item 2.2.1 of Locomotive Code: Derailment factor is used to check the safety level of locomotive against derailment due to wheel-flange climbing the rail-head under lateral force.

Derailment factor is defined as Q/P, the ratio of the lateral force to the dynamic wheel load. By the wheel-rail relationship shown in Fig. 4.1, the critical status for derailment can be derived as

$$\frac{Q}{P} = \frac{\tan\alpha - \mu}{1 + \mu \tan\alpha} \tag{4.1}$$

where α is the wheel tread angle; μ is the friction coefficient between flange and rail.

In the figure, at the left and right contact points, the lateral forces are Q_1 and Q_2, the vertical forces are P_1 and P_2, and the derailment factors for the two wheels of the wheel-set are, respectively, Q_1/P_1 and Q_2/P_2.

The limits for derailment factor are given in the HSR Code, Interim PR Code, Interim PFR Code, Vehicle Code, and Locomotive Code, as listed in Table 4.1.

It can be seen that the limits for derailment factor are quite different in the codes, which can be explained as follows:

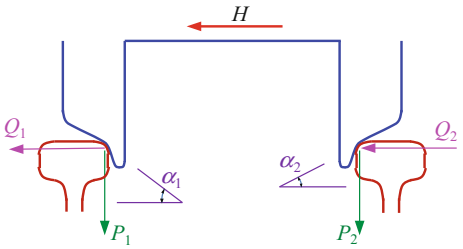

Fig. 4.1 Sketch of derailment factor

Table 4.1 Limits for derailment factors in Chinese codes

Item and code	Limit	Remark
Item 7.3.6, HSR code	0.8	
Item 6.3.6, Interim PR code	0.8	
Item 5.3.2, Interim PFR code	0.8	
Item 3.3.2.2, Vehicle code	First limit: 1.2 Second limit: 1.0	For climbing rail side only
Item 2.2.2.1, Locomotive code	Maximum value $(Q/P)_{max}$: Excellent: 0.6, Good: 0.8, Qualified: 0.9 Usual maximum value $(Q/P)_{m\cdot M}$: Excellent: 0.4, Good: 0.6, Qualified: 0.7	For guiding wheel-set only

(1) In Item 3.3.2.3 of Vehicle Code, the first limit is used to ensure the train running safety, and the second limit reserves a larger safety margin. In Item 2.1 of Locomotive Code: All the dynamic performance of the tested locomotive shall be "qualified" or higher grade.

(2) In Item 5.3.4.1 of Vehicle Code, it is required that the derailment factor is calculated by the wheel with smaller vertical force. In the Locomotive Code, no explicit information is given about how to determine the guiding wheel-set. The author suggests to reference Item 5.3.4.1 of Vehicle Code, namely, to calculate the derailment factor for the locomotives by the wheel with smaller vertical force.

(3) In Item 2.2.2.2 of Locomotive Code, there is an additional provision in evaluating the derailment factor. It states that even for $(Q/P)_{max} > 0.9$, only when one of the following conditions is matched can it be judged as "unqualified": (a) two peaks larger than 0.9 occur in succession, when the discontinuous measurement method is adopted; (b) the time duration of derailment factor larger than 0.9 is more than 0.07 s, when the continuous measurement method is adopted; (c) when the time duration is less than 0.07 s, the derailment factor shall meet the following condition

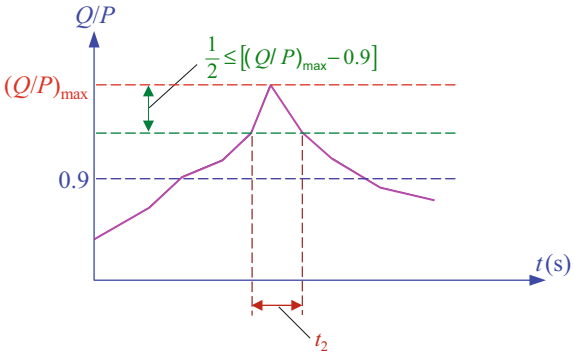

Fig. 4.2 Definition of t_2 in Eq. (4.2)

$$(Q/P)_{\max} \le 0.065 \frac{1}{t_1} \tag{4.2}$$

where $t_1 = 1.5t_2$, and t_2 is defined in Fig. 4.2.

(4) In Table 4.1, the usual maximum value $(Q/P)_{m\cdot M}$ of derailment factor is given in Item 2.2.1 of Locomotive Code as

$$(Q/P)_{m\cdot M} = \overline{Q/P} + 1.65\sigma \tag{4.3}$$

where $\overline{Q/P}$ is the statistical average; σ is the mean square deviation of the experimental samples for the derailment factor Q/P.

4.2.2 *Offload Factor*

In Item 3.3.3 of Vehicle Code: Offload factor is used to check whether the vehicle will derail due to overlarge offload at one side of wheel-set. Offload factor is defined as $\Delta P/\bar{P}$, the ratio of wheel load reduction at the offloaded side to the average load of the two wheels, in which

$$\bar{P} = \frac{1}{2}(P_{st1} + P_{st2}) \tag{4.4}$$

$$\Delta P = \bar{P} - P_1, \quad \text{when } P_1 < P_2 \tag{4.5}$$

$$\Delta P = \bar{P} - P_2, \quad \text{when } P_2 < P_1 \tag{4.6}$$

where P_{st1} and P_{st2} are static loads of the left and right wheels, respectively.

The limits for offload factor are given in the HSR Code, Interim PR Code, Interim PFR Code, and Vehicle Code, as listed in Table 4.2.

Table 4.2 Limits for offload factors in Chinese codes

Item and code	Criteria	Remark
Item 7.3.6, HSR code	0.6	–
Item 6.3.6, Interim PR code	0.6	–
Item 5.3.2, Interim PFR code	0.6	–
Item 3.3.3.1, Vehicle code	First limit 0.65 Second limit 0.60	The first limit is for evaluating vehicle safety; the second limit reserves a larger safety margin.

Because the original intention to measure the offload factor is to check the performance of the vehicle, not for the track structure, it is required that the factor is measured when the train running through a No. 9 standard turnout or a curve with small radius, so as to eliminate the effect of lateral wheel/rail force. For vehicles running on the bridge, the wheel load decreases when the wheel vibrates upside, which will, even with small or zero lateral wheel/rail force, induce derailment due to the relative lateral displacement between wheel and rail. Therefore, as a criterion for anti-derailment, offload factor has practical significance for vehicles running on the bridge, so it is adopted as an important index in evaluating the vertical dynamic performance of train-bridge system.

4.2.3 Lateral Wheel/Rail Force

In Item 3.3.4 of Vehicle Code: The criterion for wheel/rail lateral force is recommended, to evaluate whether it will enlarge the gauge or seriously deform the track. According to the criterion, limits for wheel/rail force are given, respectively, of the wheel and of the wheel-set. As shown in Fig. 4.1, the wheel/rail force produces Q_1 and Q_2 for the two wheels, and H for the wheel-set is expressed as

$$H = Q_1 + Q_2 \tag{4.7}$$

The limits for lateral wheel/rail force are given in the HSR Code, Interim PR Code, Interim PFR Code, and Vehicle Code, as listed in Table 4.3, where P_0 is the static axle load, P_{st} is the static axle load at certain side, either P_{st1} or P_{st2}, so it is obvious that $P_0 = 2P_{st}$.

In the criteria, setting limit for lateral wheel/rail force of the wheel is to ensure the track gauge (against spike yielding or pulled up), while for the wheel-set is to ensure the track structure against serious deformation (e.g., lateral sliding or overturn of rail and sleeper). There is no functional relationship between them, and thus they cannot be replaced by each other.

Table 4.3 Limits for lateral wheel/rail forces in Chinese codes

Item and code	For the wheel	For the wheel-set
Item 7.3.6, HSR code	–	10 kN + $P_0/3$
Item 6.3.6, Interim PR code	–	80 kN
Item 5.3.2, Interim PFR code	–	80 kN
Item 3.3.4, Vehicle code	For elastic stress limit against rail spike pulled up: 19 kN + $0.3P_{st}$	Wood sleeper: $0.85(10\text{ kN} + P_0/2)$
	For yield stress limit against rail spike pulled up: 29 kN + $0.3P_{st}$	PC sleeper: $0.85(15\text{ kN} + P_0/2)$

4.2.4 Overturn Coefficient

The overturn coefficient is only mentioned in the Vehicle Code, which is defined as

$$D = \frac{P_d}{P_{st}} \tag{4.8}$$

where P_d is the dynamic load of all wheels on one side of a vehicle or a bogie; P_{st} is the related static load.

The dynamic load P_d of a wheel is the difference of the instantaneous vertical wheel/rail force P and the related static load P_{st}, expressed as

$$P_d = P - P_{st} \tag{4.9}$$

Thus Eq. (4.8) can be expressed as

$$D = \frac{P - P_{st}}{P_{st}} = \frac{P}{P_{st}} - 1 \tag{4.10}$$

In Item 3.3.5.1 of Vehicle Code: The criterion of overturn coefficient is $D < 0.8$, and in Item 3.3.5.3, it is explained that only when the overturn coefficients of all concerned wheels exceed 0.8 at the same time, can the case be regarded as dangerous.

4.2.5 Discussion About Sampling Frequency of Vehicle Safety Indices

It is obvious that the values of the calculated derailment factor, offload factor, lateral and vertical wheel/rail forces, and overturn coefficient are related to the integration time step adopted. According to the sampling theorem, there is no component in the

calculated wheel/rail force with the period smaller than two times of sampling time step. Therefore, it is necessary to adopt proper time step in evaluation of vehicle safety indices, to avoid missing high-frequency components. Considering there is no statement about the calculation time step in neither HSR Code, Interim PR Code nor Interim PFR Code, a method how to select reasonable time step in evaluation of vehicle safety indices is proposed herein, by referring the measurement method in the Vehicle Code and Locomotive Code, to avoid too much weighting of individual and instantaneous peaks in the evaluation.

In high-speed railways in China, the "2 m smoothing" technique is used in data processing when the wheel/rail force is measured continuously by the EMU inspection cars, by which the instant wheel/rail force is defined as the average of the measured forces in 2 m ahead of the current wheel position. The wheel/rail force after "2 m smoothing" is expressed as

$$F_1(t) = \frac{V \int_{t_{-2}}^{t} F_0(\tau)\mathrm{d}\tau}{3.6S} \tag{4.11}$$

where $t_{-2} = 3.6\ S/V$ is the starting time of the duration being smoothed; F_0 is the measured or calculated wheel/rail force; V is the train speed in km/h; $S = 2$ m in this process.

The process of "2 m smoothing" is recommended by the author in evaluation of vehicle safety indices by HSR Code, Interim PR Code, Interim PFR Code, Vehicle Code, and Locomotive Code. Namely, the measured or calculated vertical and lateral wheel/rail forces should be "2 m smoothing" processed first, can they be used to calculate the derailment factor, offload factor, and overturn coefficient for evaluation.

4.3 Criteria for Train Running Stability

The criteria for train vehicle running stability include vertical and lateral car-body accelerations and vertical and lateral vehicle running stability indices. The car-body accelerations can be obtained by calculation or measurement, and the vehicle running stability indices can be calculated with the car-body acceleration histories.

4.3.1 Car-Body Acceleration

The vertical and lateral car-body accelerations can be measured or calculated, according to Vehicle Code and Locomotive Code.

In Item 4.2.1 of Vehicle Code: The sensors are installed at Locations 1 and 2 on the car-floor, and 1000 mm from the bogie pins, as shown in Fig. 4.3.

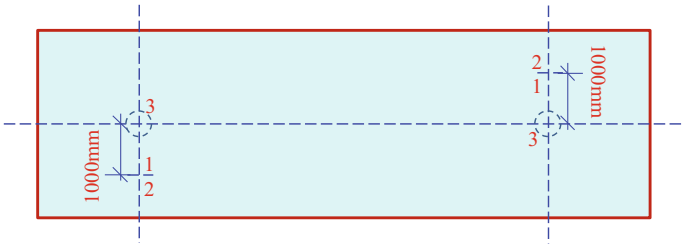

Fig. 4.3 Measuring points for car-body acceleration

In Items 4.1.2.1 and 4.1.2.2 of Locomotive Code: The measuring points for vertical and lateral car-body accelerations are on the front and rear traction beams of the vehicle underframe, and the measuring point for driver's cab is on the floor at the center. Since the car-body is considered as a rigid body and the traction beams have no independent DOF, the author suggests the output location of locomotive car-body acceleration is at Point 3 in Fig. 4.3, which is on the floor above the bogie pin.

The limits for car-body acceleration are given in the HSR Code, Interim PR Code, Interim PFR Code, Vehicle Code, and Locomotive Code, as shown in Table 4.4, in which the accelerations are half-peak values. In the Commentary on Interim PFR Code (TJS 2005-285 2005b), it is explained that the criterion in

Table 4.4 Limits for car-body accelerations in Chinese codes

Item and code	Vertical car-body acceleration			Lateral car-body acceleration		
Item 7.3.6, HSR code (m/s^2)	1.3			1.0		
Item 6.3.6, Interim PR code (g)	0.13			0.10		
Item 5.3.2, Interim PFR code (g)	0.13			0.10		
Item B.1, Vehicle code	Average max. car-body acceleration: Passenger vehicle: $(0.00027V + C)g$ Freight vehicle: $(0.00215V + C)g$			Average max. car-body acceleration: Passenger vehicle: $(0.00027V + C)g$ Freight vehicle: $(0.00135V + C)g$		
Item 2.3.2, Locomotive code	Maximum acceleration A_{max} (m/s^2)			Maximum acceleration A_{max} (m/s^2)		
	Excellent	Good	Qualified	Excellent	Good	Qualified
	2.45	2.95	3.63	1.47	1.96	2.45
	Effective acceleration A_w (m/s^2)			Effective acceleration A_w (m/s^2)		
	Excellent	Good	Qualified	Excellent	Good	Qualified
	0.393	0.586	0.840	0273	0.407	0.580

Table 4.5 Constant C

Running stability grade	Passenger vehicle		Freight vehicle	
	Vertical vibration	Lateral vibration	Vertical vibration	Lateral vibration
Excellent	0.025	0.010	0.06	0.08
Good	0.030	0.018	0.11	0.13
Qualified	0.035	0.025	0.16	0.18

Interim PFR Code is for passenger comfort, so the limits for car-body accelerations in Item 5.3.2 of it are only for the passenger train. In Table 4.4, V is train speed in km/h, and C is constant, as listed in Table 4.5.

It should be explained that

(1) There is no traditional locomotive in EMU trains. As the motor-car carries passengers, it should also be evaluated by the car-body acceleration limit in the Vehicle Code.
(2) In the Appendix B of Vehicle Code, when conducting train-bridge coupling dynamic analysis, the calculated car-body acceleration shall be low-pass filtered by 20 Hz before it is used for evaluation. This can be referenced when using the HSR Code, Interim PR Code, and Interim PFR Code.
(3) The limits in the Vehicle Code are for the average maximum car-body acceleration. Based on Item 5.2.6 and Appendix B of the code, the average maximum car-body acceleration is calculated by: dividing the acceleration signal into 6s-segments, low-pass filtering each segment by 20 Hz, and calculating the maximum value for it, then averaging the maximum values of all segments, which is the average maximum car-body acceleration concerned.
(4) In Item 2.3 of Locomotive Code, the maximum car-body acceleration is calculated by

$$A_{\max} = \bar{A} + 3\sigma_n \tag{4.12}$$

where $\bar{A}$ is the statistic average; σ_n is the mean square deviation of all the absolute peaks in the acceleration sample; and n is the total number of the peaks. In analysis, the inflexions in acceleration history are regarded as the peaks, because it is hard to find the peaks by computer software.

In Item 2.3.3 of Locomotive Code: The acceleration signal should be low-pass filtered by 40 Hz for calculating the maximum acceleration $A_{\max}$, and by 1–80 Hz for the effective acceleration A_{w}. This regulation should be obeyed in evaluating the calculated results by train-bridge coupling dynamic analysis.

The effective acceleration A_{w} is an index for evaluating the stability of locomotive by considering the human feeling and the frequency effect on human-body tiredness. In Item 2.3.1 of Locomotive Code, the effective acceleration A_{w} is defined with two equivalent methods, the time domain method and the frequency method, as follows.

By the frequency method, A_w is defined as

$$A_w = \sqrt{2\int_1^{80} G(f)B^2(f)\mathrm{d}f} \tag{4.13}$$

where $G(f)$ is the average power spectral density (PSD) of the measured acceleration sample, in (m^2/s^4/Hz); f is the frequency in Hz; $B(f)$ is the frequency weighting function, expressed as:

$$\text{Vertical vibration: } B(f) = \begin{cases} 0.5\sqrt{f} & (f = 1-4\,\text{Hz}) \\ 1 & (f = 4-8\,\text{Hz}) \\ 8/f & (f = 8-80\,\text{Hz}) \end{cases} \tag{4.14}$$

$$\text{Lateral vibration: } B(f) = \begin{cases} 1 & (f = 1-2\,\text{Hz}) \\ 2/f & (f = 2-80\,\text{Hz}) \end{cases} \tag{4.15}$$

By the time domain method, A_w is defined as

$$A_w = \sqrt{\frac{1}{T}\int_t^{t+T} a_w^2(t)\mathrm{d}t} \tag{4.16}$$

where T is the sampling period in s; $a_w(t)$ is the weighted acceleration obtained by filtering the acceleration sample with $B(f)$, in (m/s^2).

4.3.2 Sperling Comfort Index (Riding Quality Index)

The Sperling comfort index or riding quality index is used to evaluate the running stability of vehicle in train-bridge coupling dynamic analysis.

The method for calculating the Sperling comfort index is given in Items 3.2.1.1 and 5.3.1.1 of Vehicle Code and Appendix C of Locomotive Code. They are equivalent, although different units are used. Herein, the calculation method in Vehicle Code is introduced.

Before calculating the Sperling comfort index, the car-body acceleration history should be analyzed to obtain its frequency spectrum. If n frequency components of the car-body acceleration in vertical or lateral direction are considered, the resultant Sperling comfort index can be calculated as

$$W = \sqrt[10]{W_1^{10} + W_2^{10} + \cdots + W_n^{10}} \tag{4.17}$$

where

$$W_i = 7.08\sqrt[10]{\frac{A_i^3}{f_i}F(f_i)} \tag{4.18}$$

where A_i is the amplitude of acceleration component at frequency f_i, in unit of g; f_i is the ith frequency, in unit of Hz, and $F(f)$ is the frequency weighting function, expressed as:

$$\text{Vertical vibration: } F(f) = \begin{cases} 0.325f^2 & (f = 0.5-5.9\,\text{Hz}) \\ 400/f^2 & (f = 5.9-20\,\text{Hz}) \\ 1 & (f > 20\,\text{Hz}) \end{cases} \tag{4.19}$$

$$\text{Lateral vibration: } F(f) = \begin{cases} 0.8f^2 & (f = 0.5-5.4\,\text{Hz}) \\ 650/f^2 & (f = 5.4-26\,\text{Hz}) \\ 1 & (f > 26\,\text{Hz}) \end{cases} \tag{4.20}$$

The criteria for Sperling comfort indices are given in HSR Code, Vehicle Code, and Locomotive Code, as listed in Table 4.6.

The calculated Sperling comfort index is greatly affected by the length of the acceleration sample. For example, the lateral car-body acceleration history is shown in Fig. 4.4, which is recorded when a train running through a shielding area. It is obvious that the Sperling comfort index for 0–50 s is smaller than that for 18–25 s.

Table 4.6 Criteria of Sperling comfort indices in Chinese codes

Item and code	Excellent	Good	Accepted
Item 7.3.6, HSR code	2.5	2.75	3.0
Item 3.2.1.2, Vehicle code	Passenger car: 2.5	Passenger car: 2.75	Passenger car: 3.0
Item 3.2.2.2, Vehicle code	Freight car: 3.5	Freight car: 4.0	Freight car: 4.25
Item 2.3.2, Locomotive code	2.75	3.10	3.45

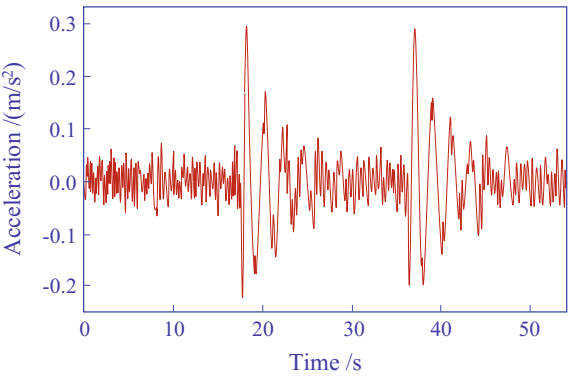

Fig. 4.4 Car-body lateral acceleration history when a train running through a shielding area

Considering this factor, the sampling length for calculating Sperling comfort index is stipulated in the Vehicle Code and Locomotive Code. In Item 5.2.6 of Vehicle Code, the sampling length is 18–20 s. In Item 4.3.1 of Locomotive Code, the sampling length is the time for the locomotive to run 300–500 m.

4.4 Criteria for Bridge Dynamic Performance

The criteria for bridge dynamic performance include the limits on the natural frequency of the bridge, the deformation, amplitude and acceleration at beam mid-span, the rotation angle at beam-ends, the distortion angle of beam-body, and the dynamic factor of structure, which are given in the HSR Code, Interim PR Code, Interim PFR Code, Bridge Code, Bridge Rating Code, and HSR Rating Code. In these six codes, the HSR Code, Interim PR Code, Interim PFR Code, and Bridge Code are design codes, in which the limits are set for evaluating the static calculation results; while the Bridge Rating Code and HSR Rating Code are rating codes, in which the limits are set for evaluation of the bridge service status.

In Item 10.0.2 of Bridge Rating Code, two criteria are provided to evaluate the service performance of the bridge:

(1) Limit to ensure vehicle running safety: The measured bridge response should meet the limit, otherwise the measures should be taken to ensure the safety of the train running through the bridge.
(2) Usual value: the upper limit of measured amplitude, the lower limit of measured frequency, and the average value of structure testing coefficient, under normal service status of the bridge. When a measured datum exceeds the given usual value, the bridge structure shall be examined to find the possible disease, and the investigation should be done to find if there exists any abnormal excitation from the train, such as loading eccentricity and bad vehicle status.

In the HSR Rating Code, only usual values are given. In Item 2.1.3 of the code, they are defined as follows: The usual values are the upper limits of measured deformation, displacement, amplitude and acceleration of beam-body, vertical rotation angle at beam-ends, and dynamic factor of structure, and the lower limit of natural frequency, and the range of damping ratio, under normal service status of the bridge.

4.4.1 Natural Frequency

Natural frequency of the bridge reflects its stiffness, which should be controlled in design and be evaluated in rating.

In Item 7.3.5 of HSR Code, Item 6.3.5 of Interim PR Code, and Item 5.3.2 of Interim PFR Code, the lower limits for vertical natural frequency of simply-supported beam are given in formulas expressed as

$$n_0 = 80/L \qquad (L \leq 20\,\text{m}) \tag{4.21}$$

$$n_0 = 23.58L^{-0.592} \qquad (20 < L \leq L_u) \tag{4.22}$$

where n_0 is the lower limit for vertical natural frequency (Hz); L is the design span of the beam; and L_u is the maximum applicable span given by the codes, being 96 m in the HSR Code and Interim PFR Code, and 80 m in the Interim PR Code.

In the Bridge Code, there is no limit for vertical natural frequency of beam, instead, whose vertical stiffness is controlled by the deformation under static design load. Item 5.1.3 of this code gives the limits for lateral natural frequencies of bridge with various structure types, as listed in Table 4.7, where the structure frequency refers to the beam itself without considering the substructure.

The usual values of lowest lateral natural frequencies of beams are given in Item 10.0.5 of Bridge Rating Code, as listed in Table 4.8. Besides, Item 10.0.6 of the code requires that the lateral natural frequencies of the beam under various train speeds should not be lower than the usual values in Table 4.9. In these two tables, the bridge structure refers to the whole bridge, not only to the superstructure. In fact, in evaluation of the measured or calculated frequencies, the output points are at the beam, so the contribution of the piers is naturally included.

There exists a conflict between the Bridge Code and the Bridge Rating Code, which can be found by comparison of the curves shown in Fig. 4.5. The curves

Table 4.7 Limits for lateral natural frequency of beams (Bridge Code)

Structure type	Span length (m)	Limit for lateral frequency (Hz)
Deck steel plate beam	24–40	$>60/L^{0.8}$
Through steel plate beam	24–32	$>55/L^{0.8}$
Half-through steel truss beam	40–48	$>60/L^{0.8}$
Through steel truss beam	48–80	$>65/L^{0.8}$
PC beam	24–40	$>55/L^{0.8}$

Table 4.8 Usual values of lateral natural frequency of bridge (Bridge Rating Code)

Structure type		Measured minimum lateral natural frequency (Hz)
Steel plate beam or steel truss beam	Common bridge steel	$\geq 100/L$
	Low alloy steel	$\geq 90/L$
PC beam		$\geq 90/L$

L is the span length (m)

Table 4.9 Limits for lateral natural frequency of bridge under various train speeds (Bridge Rating Code)

Structure type					Bridge lateral natural frequency (Hz)		
					$V \leq 60$ km/h	$V \leq 70$ km/h	$V \leq 80$ km/h
Steel beam	Steel plate beam without floor system				$50/L^{0.8}$	$55/L^{0.8}$	$60/L^{0.8}$
	With floor system	Steel plate beam			$45/L^{0.8}$	$52/L^{0.8}$	$55/L^{0.8}$
		Truss beam	Deck type	$H/L = 1/6$	$70/L^{0.8}$	$75/L^{0.8}$	$80/L^{0.8}$
				$H/L = 1/8$	$65/L^{0.8}$	$70/L^{0.8}$	$75/L^{0.8}$
			Half-through type		$48/L^{0.8}$	$55/L^{0.8}$	$60/L^{0.8}$
			Through type		$50/L^{0.8}$	$60/L^{0.8}$	$65/L^{0.8}$
PC beam					$40/L^{0.8}$	$50/L^{0.8}$	$55/L^{0.8}$

L is the span length (m); H is the truss height (m)

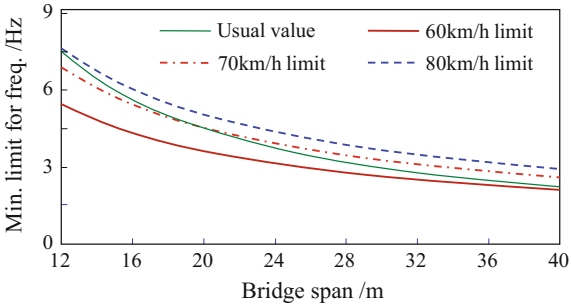

Fig. 4.5 Limits comparison for lateral natural frequencies of bridge structure

represent, respectively, the usual values under various train speeds and the limits for lateral natural frequencies of the PC beam bridge with the spans of 12–40 m.

In the figure, the usual value curve based on Table 4.8 is the reference criterion, meaning more attention should be paid when the measured data are lower than the curve, while the limit curves for various train speeds based on Table 4.9 are safety criteria that should be satisfied. In theory, the usual value curve should be higher than all the limit curves, while the figure shows that the usual value curve is lower than the limit curve of 80 km/h for all span lengths and that of 70 km/h for spans longer than 20 m. When using the Bridge Rating Code, this overlap should be noticed, and the applicable criterion is adopted according to concrete conditions.

The usual values of measured lateral natural frequencies for concrete or masonry piers with $H_1/B \geq 2.5$ are given in Item 10.0.7 of Bridge Rating Code, as listed in Table 4.10, where H is the total height of pier, from the foundation bottom or the pile cap bottom to the pier-top, in unit of m; H_1 is the pier height, from the foundation top or the pile cap-top to the pier-top, in unit of m; and B is the average

Table 4.10 Usual values of lateral natural frequency of piers with $H_1/B \geq 2.5$ (Bridge Rating Code)

Foundation type	Soil	Lateral natural frequency (Hz)	Remarks
Open foundation	Rock	$\geq \frac{24\sqrt{B}}{H_1}$	
Caisson foundation			
Pile foundation		$\geq \alpha_1 \frac{24\sqrt{B}}{H}$	α_1 is 0.8 for soft clay, 0.9 for hard clay, sand, or gravel, and 1.0 for rock-socketed pile
Open foundation	Clay, sand, or gravel	$\geq \alpha_3 \frac{24\sqrt{B}}{H_1}$	α_3 is 0.9 for gravel and coarse sand, and 0.8 for hard clay, medium sand, or fine sand

width of the pier, in unit of m. When using this item to evaluate the measured or calculated frequencies, the output point should be on the pier-top.

In the HSR Rating Code, the usual values of the first-order vertical natural frequency for simply-supported beams, and the first- and second-order natural frequencies for the continuous beams, are respectively given in Item 4.2.1, as listed in Tables 4.11 and 4.12.

4.4.2 *Deformation*

Under train loading, the bridge produces deformation of beam-body and rotation angle at beam-ends, which may change the smoothness state of the track on bridge, inducing impact by the running vehicle.

1. ***Safety limits***

To control the vertical design stiffness of beam, the limits for beam mid-span vertical deflection under design load (Excluding dynamic coefficient) are set in Item 7.3.2 of HSR Code, Item 6.3.1 of Interim PR Code, Item 5.3.1 of Interim PFR Code, and Item 5.1.2 of Bridge Code, as listed in Tables 4.13, 4.14, 4.15, and 4.16, where L is the span length, taken separately for each span for continuous beam with unequal spans.

It is noticed that the limits for vertical deflection in HSR Code and Interim PR Code are smaller than those in Interim PFR Code and Bridge Code; however, this does not imply that the designed vertical beam stiffness by PFR Code and Bridge Code is smaller than that by HSR Code and Interim PR Code, because the design loads in the codes are different: HSR Code and Interim PR Code adopt the ZK live load, while Interim PFR Code and Bridge Code adopt the C-Z live load.

Table 4.11 Usual values of the first-order natural frequency for simply-supported beams (HSR Rating Code)

Bridge design speed	Track type	Span length							
		19.5 m		23.5 m		31.5 m		39.1 m	
		Beam height (m)	Frequency (Hz)	Beam height (m)	Frequency (Hz)	Beam height (m)	Frequency (Hz)	Beam height (m)	Frequency (Hz)
250 km/h	Ballasted track	–	–	2.20	7.0	–	–	–	–
				2.50	7.8	2.50	5.0		
				2.80	8.4	2.80	5.5		
	Ballastless track	–	–	2.50	8.2	2.50	5.3	–	–
350 km/h	Ballasted track	–	–	–	–	3.05	5.9	–	–
	Ballastless track	2.45	9.9	3.05	9.6	3.05	6.2	3.75	5.5

Note (1) h is the beam height at mid-span. For 23.5 and 31.5 m simply-supported beams with design speed of 250 km/h, the usual values of 2.2 m can be adopted for beam height 2.2 m $\leq h \leq$ 2.3 m; the usual values of 2.5 m can be adopted for beam height 2.3 m $\leq h \leq$ 2.7 m; the usual values of 2.8 m can be adopted for beam height 2.7 m $\leq h \leq$ 2.9 m

(2) For the double-track simply-supported beams with similar span lengths, the usual value can be calculated by interpolation of the related ones

Table 4.12 Usual values of the first- and second-order natural frequencies for continuous beams (HSR Rating Code)

Bridge design speed (km/h)	Track structure type	First frequency (Hz)	Second frequency (Hz)	Span length (m)
250	Ballasted track	$340/L^{1.2}$		$32 \leq L \leq 100$
	Ballastless track	$360/L^{1.2}$		
350	Ballastless track	$400/L^{1.2}$		

Note (1) For span length L, the unit is m
(2) The usual values in the table can be used for 3-span continuous box-beams, the first frequency is for the middle span and the second for the side span
(3) It can be referenced by all the 3-span continuous box-beams with side span no less than 32 m and middle span no more than 100 m

Table 4.13 Limits for vertical deflection of beam-body (HSR Code)

Bridge design speed (km/h)	Range of span L		
	$L \leq 40$ m	40 m $< L \leq 80$ m	$L > 80$ m
250	$L/1400$	$L/1400$	$L/1000$
300	$L/1500$	$L/1600$	$L/1100$
350	$L/1600$	$L/1900$	$L/1500$

Note (1) Applicable to double-track simply-supported beam with 3 or more spans. For one-unit continuous beam with 3 or more spans, the limits shall be 1.1 times. For one-unit double-track continuous beam with 2 spans or simply-supported beam with 2 or less spans, the limits shall be 1.4 times; (2) For single-track simply-supported beam or continuous beam, the limits shall be 0.6 times

Table 4.14 Limits for vertical deflection of beam-body (Interim PR Code)

Span length L	$L \leq 24$ m	24 m $< L \leq 40$ m	40 m $< L <$ 96 m
Single span	$L/1300$	$L/1000$	$L/1000$
Multi-span	$L/1800$	$L/1500$	$L/1200$

Table 4.15 Limits for vertical deflection of beam-body (Interim PFR Code)

Range of span	$L \leq 20$ m	20 m $< L \leq 50$ m	50 m $< L \leq 70$ m	70 m $< L <$ 96 m
Single span	$L/1000$		$L/900$	
Multi-span	$L/1400$	$L/1200$	$L/1000$	$L/900$

To control the lateral design stiffness of beam, the limits for beam mid-span lateral deflection are set in Item 7.3.3 of HSR Code, Item 6.3.2 of Interim PR Code, Item 5.3.1 of Interim PFR Code, and Item 5.1.3 of Bridge Code. The limits for the four codes are the same: under the effect of lateral swing force, centrifugal force of

Table 4.16 Limits for vertical deflection of beam-body (Bridge Code)

Bridge superstructure		Limit of vertical deflection
Simply-supported steel truss beam		*L*/900
Continuous steel truss beam	Side span	*L*/900
	Middle span	*L*/750
Simply-supported steel plate beam		*L*/900
Simply-supported RC or PC beam		*L*/800
Continuous RC or PC beam	Side span	*L*/800
	Middle span	*L*/700

Table 4.17 Usual values of vertical deflection-to-span ratio (Bridge Rating Code)

Beam type	Structure type		Vertical deflection-to-span ratio
Steel beam	Steel plate beam	Common bridge steel	1/1200
		Low alloy steel	1/950
	Truss beam	Common bridge steel	1/1500
		Low alloy steel	1/1250
RC beam	Normal height (h/L = 1/7–1/9)		1/4000
	Low height (h/L = 1/13–1/15)		1/1900
Section steel beam			1/1250
PC beam	Normal height (h/L = 1/11–1/13)		1/1800
	Low height (h/L = 1/14–1/16)		1/1300

Note h is the beam height (m); L is span length (m)

the train, wind force and temperature, the lateral deflection of the beam shall not be more than 1/4000 of the calculated span length.

The limits for vertical and lateral deformations under design loads given in HSR Code, Interim PR Code, Interim PFR Code, and Bridge Code have close relationship with the running safety of the train; however, because the limits are set for the bridge design, they are not applicable for evaluating the calculated results by train-bridge coupling dynamic analysis.

2. ***Usual values***

To evaluate the vertical stiffness of bridge structure in service status, the usual values of vertical deflection-to-span ratio at bridge mid-span under test train load (converted to C-Z live load) are given in Item 10.0.3 of Bridge Rating Code, as shown Table 4.17.

In theory, "converted to C-Z live load" means the measured deflection-to-span ratio is multiplied by the conversion factor k:

$$k = \frac{d_{ZH}}{d_0} \tag{4.23}$$

where d_{ZH} is the deflection at bridge mid-span under the C-Z live load at the most unfavorable loading position; d_0 is the measured deflection at bridge mid-span under the test train load.

In the HSR Rating Code, the usual values of vertical deflection-to-span ratios at bridge mid-span for common-span double-track simply-supported PC box-beam and continuous beam under the static EMU load (converted to ZK live load) are given in Item 4.3.1, as shown in Tables 4.18 and 4.19.

The usual values of deflection-to-span ratio in HSR Rating Code are based on the converted static design load, which are essentially a criterion for design stiffness of HSR bridges. However, the train-bridge coupling dynamic analysis is based on the train in service instead of the static train load, so the calculated results need not necessarily meet the criteria in Tables 4.18 and 4.19.

4.4.3 Amplitude

The limits and the usual values of lateral mid-span amplitudes for various kinds of simply-supported beams are given in Item 10.0.5 of Bridge Rating Code, as listed in Tables 4.20 and 4.21, where L is the span length and B is the web spacing.

As an example, the criteria for lateral mid-span amplitude of typical bridges under loaded freight train are calculated as follows: (1) limit 3.56 mm and usual value 2.54 mm, for the 32 m simply-supported PC beam with 1.8 m web spacing; (2) limit 7.27 mm and usual value 5.26 mm, for the 40 m deck steel (common bridge steel) plate beam with 2.0 m web spacing and without floor system; (3) limit 7.71 mm and usual value 4.28 mm, for the 64 m through steel (low alloy steel) truss beam with floor system and 5.75 m main truss spacing.

The usual values of lateral pier-top amplitude are given in Item 10.0.7 of Bridge Rating Code, as listed in Tables 4.22 and 4.23.

It should be noticed that the limits and usual values of vertical mid-span deflection and lateral amplitude in Tables 4.20 and 4.21 are based on the measured data from the existing railway when the Bridge Rating Code was completed. They are not applicable for evaluation of the dynamic performance of HSR bridges.

In the HSR Rating Code, the usual values of vertical and lateral mid-span amplitudes of simply-supported and continuous double-track PC box-beams under one track load are given in Items 4.4.1 and 4.4.2, as listed in Tables 4.24, 4.25, 4.26 and 4.27.

Table 4.18 Usual values of vertical deflection-to-span ratio for simply-supported PC box-beam (HSR Rating Code)

Bridge design speed (km/h)	Track type	Span length							
		19.5 m		23.5 m		31.5 m		39.1 m	
		Beam height (m)	Deflection/span ratio	Beam height (m)	Deflection/span ratio	Beam height (m)	Deflection/span ratio	Beam height (m)	Deflection/span ratio
250	Ballasted track	–	–	2.20	1/7700	–	–	–	–
				2.50	1/9500	2.50	1/4800		
				2.80	1/12000	2.80	1/6500		
	Ballastless track	–	–	2.50	1/9700	2.50	1/5000	–	–
350	Ballasted track	–	–	–	–	3.05	1/7200	–	–
	Ballastless track	2.45	1/11000	3.05	1/15000	3.05	1/7900	3.75	1/7400

Note (1) h is the beam height. For 23.5 and 31.5-m simply-supported beams with design speed of 250 km/h, the usual value of h = 2.2 m applies to beam of 2.2 m $\leq h \leq$ 2.3 m; the usual values of 2.5 m apply to beam of 2.3 m $\leq h \leq$ 2.7 m; the usual values of 2.8 m apply to beam of 2.7 m $\leq h \leq$ 2.9 m (2) For double-track simply-supported beams with similar span lengths, the usual values can be by interpolation of the related ones

Table 4.19 Usual values of vertical deflection-to-span ratio for continuous beam (HSR Rating Code)

Bridge design speed (km/h)	Track type	Length of middle span				
		48 m	56 m	64 m	80 m	100 m
250	Ballasted track	1/5500	1/5000	1/4500	1/4000	1/3500
	Ballastless track	1/5800	1/5200	1/4700	1/4200	1/3700
350	Ballastless track	1/6000	1/5500	1/5000	1/4500	1/4000

The usual value applies to double-track continuous beam with 3 spans by general design, and can be referenced for that by non-general design (with middle span no more than 100 m)

Table 4.20 Limits for maximum lateral mid-span amplitude of simply-supported beams (Bridge Rating Code)

Structure type				Safety limit for lateral amplitude at mid-span
Steel beam	Steel plate beam or steel truss without floor system			$L/5500$
	With floor system	Steel plate beam		$L/6000$
		Steel truss beam	$L \leq 40$ m	$L/6500$
			40 m $< L \leq$ 96 m	$L/(75L + 3500)$
RC beam or PC beam				$L/9000$

The usual values of lateral pier-top amplitude under one track load are given in Item 4.4.2 of HSR Rating Code, as listed in Table 4.28.

In Table 4.28, Note (3) refers to the case when resonance occurs between the train and the bridge. The lateral dynamic performance of the bridge is related to lateral stiffness or frequency of the pier-beam structure. The lateral amplitude is enlarged when the loading frequency is closed to the natural frequency of the pier-beam structure. In HSR bridges in China, as the lateral stiffness of common-span simply-supported beams and continuous beams are designed to be quite large, it is impossible to induce intense vibration affecting the serviceability, unless the bridge is damaged. Therefore, the measured results larger than the criteria imply that the bridge, instead of the vehicle, has some possibility to be abnormal. In order to reflect the bridge vibration in the special status of resonance, twice of usual value is used to evaluate the lateral pier-top amplitude.

In fact, very little high-frequency component exists in the measured bridge amplitude, so there is no provision for filtering the signal given in the Bridge Rating Code and HSR Rating Code. Accordingly, the results of train-bridge coupling dynamic analysis need not be filtered before the evaluation.

Table 4.21 Usual values of maximum lateral mid-span amplitude of simply-supported beams (Bridge Rating Code)

Structure type			Usual value of measured max lateral amplitude under loaded freight train $V \leq 80$ km/h	Usual value of measured max lateral amplitude under passenger train			
				$V \leq 120$ km/h		$120 < V \leq 160$ km/h	$160 < V \leq 200$ km/h
				Joint rail track	CWR track		
Steel beam	Steel plate beam or steel truss beam without floor system	Common bridge steel	$\leq \frac{L}{3.8B}$	$\leq \frac{L}{9.9B}$	$\leq \frac{L}{11.4B}$	$\leq \frac{L}{9.4B}$	$\leq \frac{L}{8.0B}$
		Low alloy steel	$\leq \frac{L}{3.2B}$	$\leq \frac{L}{8.3B}$	$\leq \frac{L}{9.6B}$	$\leq \frac{L}{7.9B}$	$\leq \frac{L}{6.7B}$
	Steel plate beam or steel truss beam with floor system	Common bridge steel	$\leq \frac{L}{2.6B}$	$\leq \frac{L}{6.8B}$	$\leq \frac{L}{7.8B}$	$\leq \frac{L}{6.4B}$	$\leq \frac{L}{5.4B}$
		Low alloy steel	$\leq \frac{L}{2.2B}$	$\leq \frac{L}{5.7B}$	$\leq \frac{L}{6.6B}$	$\frac{L}{5.4B}$	$\leq \frac{L}{4.6B}$
PC beam			$\leq \frac{L}{7.0B}$	$\leq \frac{L}{18.2B}$	$\leq \frac{L}{20.9B}$	$\leq \frac{L}{17.2B}$	$\leq \frac{L}{14.7B}$

Table 4.22 Usual values of lateral pier-top amplitude (Bridge Rating Code)

Structure of pier	Pier size	Foundation and soil		Lateral amplitude at pier-top (mm)	
		Foundation type	Soil	$V \leq 60$ km/h	$V > 60$ km/h
Concrete or masonry pier	Low pier: $H_1/B < 2.5$	Open foundation	Rock	$\frac{H}{30}$	$\frac{H}{25}+0.1$
		Caisson foundation			
		Pile foundation		$\frac{H}{30}+0.2$	$\frac{H}{25}+0.4$
		Open foundation	Clay, sand, or gravel		
	Medium height pier $H_1/B \geqq 2.5$	Open foundation	Rock	$\frac{H_1^2}{100B}+0.2$	
		Caisson foundation			
		Pile foundation		$\frac{(H+\Delta h)^2}{100B}+0.2$	
		Open foundation	clay, sand, or gravel	$\alpha_2\left(\frac{H_1^2}{100B}+0.2\right)$	

Note H is the total height of the pier, from the foundation bottom or pile cap bottom to pier-top (m); H_1 is the height of the pier, from the foundation top or pile cap-top to pier-top (m); B is the average width of the pier (m); coefficients Δh and α_2 are given in Table 4.23

Table 4.23 Coefficients for lateral pier-top amplitude (mm) (Bridge Rating Code)

Coefficient	Soil	Train speed	
		$V \leq 60$ km/h	$V > 60$ km/h
Δh	Soft clay	1	2
	Hard clay, sand, or gravel	0	1
	Rock-socketed pile	0	1
α_2		1.0	1.15

Table 4.24 Usual values of vertical mid-span amplitude for double-track simply-supported beam (mm) (HSR Rating Code)

Bridge design speed (km/h)	Track type	Span length			
		19.5 m	23.5 m	31.5 m	39.1 m
250	Ballasted track	–	0.25	0.30	–
350	Ballastless track	0.30	0.20	0.35	0.25

Table 4.25 Usual values of vertical mid-span amplitude for double-track continuous beam (mm) (HSR Rating Code)

Bridge design speed (km/h)	Track type	Span length							
		32 m	40 m	48 m	56 m	60 m	64 m	80 m	100 m
250	Ballasted track	0.25	0.40	0.30	0.40	0.35	0.85	0.70	0.60
350	Ballastless track	0.25	0.30	0.40	0.65	0.35	0.45	0.45	0.45

Table 4.26 Usual values of lateral mid-span amplitude for double-track simply-supported beam (mm) (HSR Rating Code)

Bridge design speed (km/h)	Track type	Span length			
		19.5 m	23.5 m	31.5 m	39.1 m
250	Ballasted track	–	0.15		–
350	Ballastless track	0.10	0.15		0.10

Table 4.27 Usual values of lateral mid-span amplitude for double-track continuous beam (mm) (HSR Rating Code)

Bridge design speed (km/h)	Track type	Span length							
		32 m	40 m	48 m	56 m	60 m	64 m	80 m	100 m
250	Ballasted track	0.10			0.15		0.10		0.15
350	Ballastless track	0.10			0.15		0.10		0.15

Table 4.28 Usual values of lateral pier-top amplitude (mm) (HSR Rating Code)

Bridge design speed (km/h)	Usual value (mm)	Application range
250	$\frac{H_p}{55B} + 0.02$	$0.5 \leq \frac{H_p}{B} \leq 4.2$
350	$\frac{H_p}{60B} + 0.03$	

Note (1) The usual values in the table apply to solid pier, hollow pier and double-column pier in double-track bridges

(2) H_p is the total height of pier, from open foundation bottom or pile cap bottom to pier-top; B is the average width of the pier

(3) The lateral amplitude at pier-top shall not be larger than twice of the usual value, when the lateral forced frequency is closed to the natural frequency of the pier-beam structure

4.4.4 Acceleration

In Item 7.3.6 of HSR Code, Item 6.3.6 of Interim PR Code, and Item 5.3.2 of Interim PFR Code, the limits for vertical acceleration of bridge deck under strong vibration with frequency of 20 Hz and below are given as

(1) 0.35 g (or 3.5 m/s^2) for ballasted track
(2) 0.5 g (or 5.0 m/s^2) for ballastless track

When the limits specified above are not satisfied, there is a risk that resonance or excessive vibration of the bridge may occur, with a possibility of excessive deck acceleration leading to ballast instability, or excessive deflection and stress of the bridge structure. For such cases, a train-bridge coupling dynamic analysis is necessary to calculate impact and resonance effect.

In Item 10.0.5 of Bridge Rating Code, it is required that the lateral amplitude of bridge structure at the loading level shall not be larger than 0.14 g under the real train load. Obviously, this acceleration depends on the mass and stiffness of both the beam and the piers. In the Bridge Rating Code, no signal processing method is provided for lateral beam accelerations. The author suggests to refer to the HSR Code, namely, to process the calculated results by train-bridge coupling dynamic analysis, using a 20-Hz low-pass filter.

Herein, both the vertical and lateral accelerations refer to the bridge accelerations at the loading level. The concerned acceleration is at the bridge floor for RC or PC beams, at the upper flange for the deck steel plate beams, and at the lower chord members for the through steel truss beams.

The usual values of vertical mid-span acceleration (20-Hz low-pass filtered) for double-track simply-supported PC box-beams and continuous box-beams under one track EMU train are given in Item 4.4.1 of HSR Rating Code, as listed in Tables 4.29 and 4.30, but the usual values for lateral acceleration are not provided.

Table 4.29 Usual values of vertical mid-span acceleration for simply-supported beam (m/s^2) (HSR Rating Code)

Bridge design speed (km/h)	Track type	Span length			
		19.5 m	23.5 m	31.5 m	39.1 m
250	Ballasted track	–	0.40	0.40	–
350	Ballastless track	0.30	0.40	0.30	0.25

Table 4.30 Usual values of vertical mid-span acceleration for continuous beam (m/s^2) (HSR Rating Code)

Bridge design speed (km/h)	Track type	Span length							
		32 m	40 m	48 m	56 m	60 m	64 m	80 m	100 m
250	Ballasted track	0.30	0.35	0.30	0.35	0.25	0.40	0.30	0.20
350	Ballastless track	0.20	0.20	0.20	0.30	0.20	0.20	0.20	0.20

4.4.5 Rotation Angle at Beam-Ends

Under train loading, the bridge will produce vertical and horizontal rotations at beam-ends, as sketched in Fig. 4.6 and Fig. 4.7, respectively.

The vertical and horizontal rotation angles at beam-ends cause local unevenness of the on-bridge track, which may affect the safety and riding comfort of the running train. The vertical rotation angles are mainly controlled by the vertical beam stiffness, and the horizontal rotation angles by the lateral pier stiffness.

The limits for vertical rotation angle at beam-ends are given in Item 7.3.7 of HSR Code, Item 6.3.1 of Interim PR Code, and Item 5.3.1 of Interim PFR Code, as listed in Table 4.31. The limits in the table are based on static designing loads (excluding dynamic coefficient): ZK live load for HSR Code and Interim PR Code, and C-Z live load for Interim PFR Code.

In Item 7.3.9 of HSR Code and Item 6.3.2 of Interim PR Code, the limits for horizontal rotation angle at beam-ends induced by lateral displacement of pier are all set as 1‰, under the effects of ZK live load, lateral swing load, centrifugal force, wind force, and temperature.

In Item 5.3.4 of Interim PFR Code, the limit is also 1‰, but the C-Z live-load is used instead of the ZK live-load, and the rotation induced by foundation displacement is also included.

In Item 5.3.3 of Bridge Code, the limits for horizontal rotation angle of adjacent bridge decks induced by lateral displacement of pier or abutment are 1.5‰ when the bridge span is $L < 40$ m, and 1‰ when $L \geq 40$ m, under the most unfavorable loads.

It should be noted that the limits for rotation angle at beam-ends are based on static design load, mainly to prevent the beam designed from too low stiffness. In train-bridge coupling dynamic analysis, even when the calculated rotation angle is larger than the criteria, it does not imply that the bridge is unfit for the running safety and stability of the train. Because the dynamic response of bridge is substantially different from the static response, the above criteria can only be

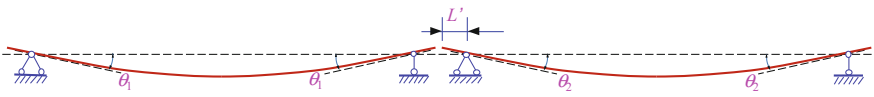

Fig. 4.6 Sketch of vertical rotation angles at beam-ends

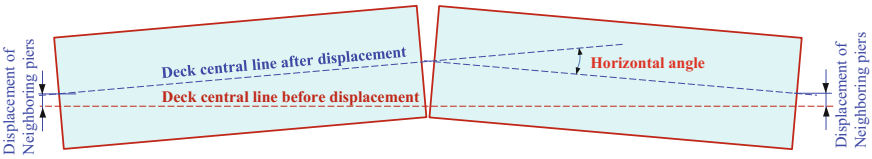

Fig. 4.7 Sketch of horizontal rotation angles at beam-ends

Table 4.31 Limits for vertical rotation angle at beam-ends in Chinese codes

Code and design load	Track type on bridge	Position	Limit (rad ‰)	Remark (m)
ZK Live load, HSR code	Ballasted track	Between abutment and beam	2	
		Between two beams	$\theta_1 + \theta_2 \leq 4$	
	Ballastless track	Between abutment and beam	1.5	$L' \leqq 0.55$
			1	$0.55 < L' \leqq 0.75$
		Between two beams	$\theta_1 + \theta_2 \leq 3$	$L' \leqq 0.55$
			$\theta_1 + \theta_2 \leq 2$	$0.55 < L' \leqq 0.75$
ZK live load, Interim PR code	Ballasted track		2	
	Ballastless track		1	
C-Z live load, Bridge code		Between abutment and beam	3	
		Between two beams	$\theta_1 + \theta_2 \leq 6$	

Note L' is the suspended length of the beam over end, ref. Fig. 4.6

referenced in evaluating the results by train-bridge coupling dynamic analysis, but not obliged.

4.4.6 *Distortion Angle of Beam-Deck*

In order to control the torsional stiffness of the beam, the limits for track surface irregularity resulted from the distortion of beam-deck under design live loads are given in Item 7.3.4 of HSR Code, Item 6.3.3 of Interim PR Code, and Item 5.3.1 of Interim PFR Code. The relative vertical deformation (t in Fig. 4.8) of the two rails on one track shall not be more than 1.5 mm for ZK live load in HSR Code and

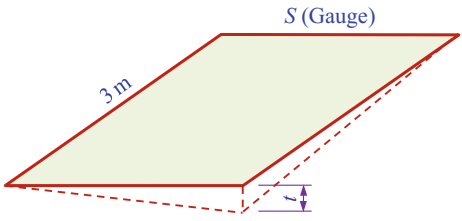

Fig. 4.8 Definition of deck distortion

Interim PR Code, and 3 mm for C-Z live load in Interim PFR Code, based on a 3 m-length track section.

The limits refer to the vertical displacement difference of the beam surface. Because the displacement difference is not related to the track structure, although the code items contain the term of track, neither the track deformation nor the track-beam interaction need to be considered in calculation.

Similar to the limits for rotation angle at beam-ends, the criteria for the distortion angle of beam-deck can only be referenced in evaluating the results by train-bridge coupling dynamic analysis, but not obliged.

4.4.7 Dynamic Coefficient

According to Item 6.4.1 of HSR Rating Code, the dynamic coefficient $1 + \mu$ of bridge can be calculated based on the dynamic deflection and strain waves measured at the control section of the beam. The dynamic coefficient from the vertical deflection reflects the global dynamic behavior of the beam, while that from the dynamic strain reflects the local dynamic behavior. The code provides two methods for calculating the dynamic coefficient, corresponding to "with quasi-static calibration" and "without quasi-static calibration". The dynamic coefficient "with quasi-static calibration" is defined as

$$1 + \mu = \frac{\delta_{\mathrm{dmax}}}{\delta_{\mathrm{smax}}} \tag{4.24}$$

where δ_{dmax} is the measured or calculated maximum dynamic deflection; δ_{smax} is the measured or calculated maximum quasi-static (or static) deflection. In train-bridge coupling dynamic analysis, δ_{smax} is obtained by the train running through the bridge at speed $V \leq 5$ km/h.

In Item 4.4.1 of HSR Rating Code, the usual value of dynamic coefficient for the double-track simply-supported PC box-beam is defined as

$$1 + \mu = 1 + \mu' + 0.5\mu'' \tag{4.25}$$

where $\mu' = \frac{K}{1-K+K^4}$; $K = \frac{V}{7.2n_0L}$; $\mu'' = \frac{1}{100}\left[56\mathrm{e}^{-\left(\frac{L}{10}\right)^2} + 50\left(\frac{n_0L}{80} - 1\right)\mathrm{e}^{-\left(\frac{L}{20}\right)^2}\right]$, V is the train speed (km/h); n_0 is the measured first-order natural frequency of the beam (Hz); L is the span length (m).

4.5 Conditions Unnecessary to Conduct Train-Bridge Coupling Dynamic Analysis

The research of UIC on dynamic response of train-bridge coupling system for high-speed railway shows that only by controlling the fundamental frequency of the beam is not sufficient to avoid the occurrence of resonance. For some early designed beams, owing to the deviations of vehicle parameter values and the absence of considering the torsional effect in analysis, although the designed fundamental frequency of the beams could meet the criterion, resonance still occurred under higher train speed. For example, in several 14–20 m bridges on the Paris-Lyons HSR line, the resonance was found under the train speed of 260 km/h, when the actual effect (real train load times the actual dynamic coefficient) was larger than the design effect (UIC load times design dynamic coefficient). Therefore, even if the vertical frequency of the beam is higher than the limit, only by static load analysis is insufficient, while the train-bridge coupling dynamic analysis should be conducted based on real operation train load.

With the development of high-speed railway, the design principle and the related criteria for HSR bridges are studied, based on train-track-bridge coupling dynamic analysis and in situ experiments, by the researchers in Germany, Japan, and some other countries. In the code *Design Requirements for Rail-bridges Based on Interaction Phenomena between Train, Track and Bridge* (UIC 776-2 2009), not only provided the dynamic design procedure for HSR bridges, but also provided the conditions unnecessary to do train-bridge coupling dynamic analysis. It is an important reference to the dynamic design of HSR bridges in China. The logic diagram to determine whether a specific dynamic analysis is required in UIC 776-2 is shown in Fig. 4.9.

Since 1990s, a lot of work has been done for train-bridge coupling dynamic analysis in China. The train-track-bridge coupling dynamic analysis has been carried out for the bridges with various structural types and all span lengths, providing important technical support to the dynamic designs of HSR bridges. A large amount of data were obtained in the debugging and commissioning tests for new HSR lines by the China Academy of Railway Science and some universities, which have been used for train-bridge coupling dynamic analysis to verify the analysis models and the calculated results, providing the basic condition to reduce the complex calculation work in dynamic design of HSR bridges. Accordingly, the conditions unnecessary to conduct train-bridge coupling dynamic analysis are proposed in the HSR Code, based on the theoretical analysis and experimental data, and by reference of the UIC code.

In UIC 776-2, there is no criterion for lateral vibration of common-span bridges, which is reasonable, because the lateral stiffness of the beams, especially for the double-track beams, is quite large. In fact, the lateral vibration of the bridge is too small to affect train running safety or passenger comfort, which has been verified by theoretical analysis and engineering practice, and become the consensus in Chinese

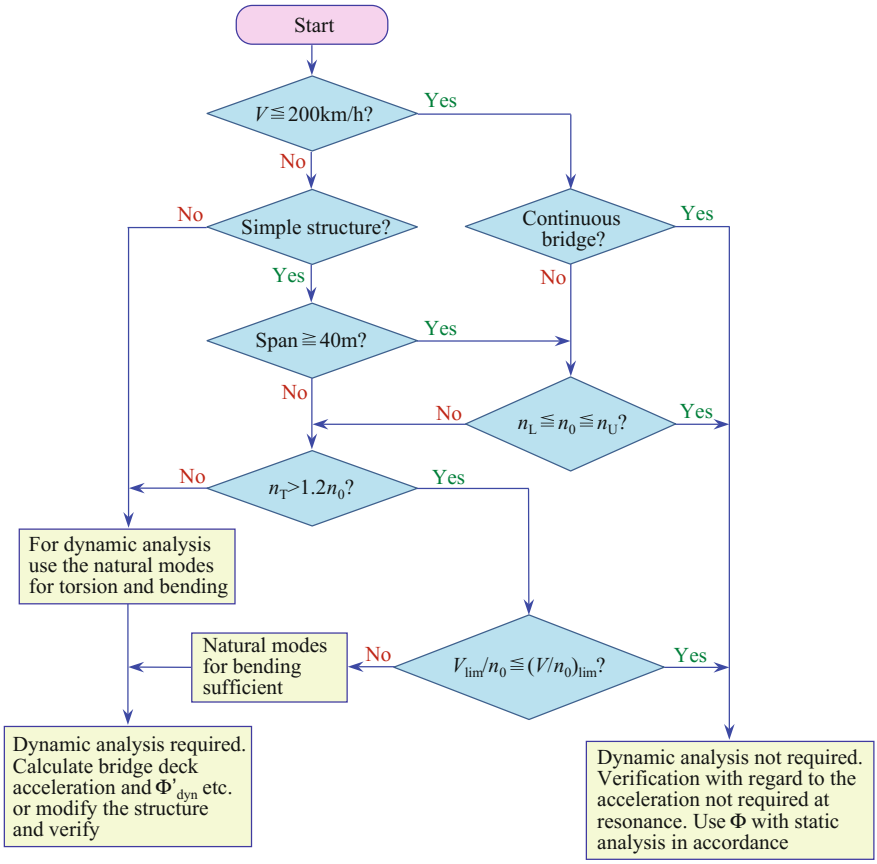

Fig. 4.9 Logic diagram to determine whether a specific dynamic analysis is required

railway. Therefore, the factors related to lateral vibration are not considered in the conditions unnecessary to conduct train-bridge coupling dynamic analysis.

There is no explicit explanation for the term "simple structure" in UIC Code 776-2, but the author believes it should include the simply-supported beam at least. The double-track simply-supported PC box-beams with small and medium spans are very common in HSR bridges in China, which covers 98% of the total bridge length, so in the HSR Code, the conditions unnecessary to conduct train-bridge coupling dynamic analysis are proposed only for the simply-supported beams.

There are also some continuous beams with 48–128 m spans used in HSR bridges in China. Considering the variousness of these beams in section and deck arrangement, it is not appropriate to make uniform provisions for them in the conditions unnecessary to conduct train-bridge coupling dynamic analysis in the HSR Code.

During the design of HSR bridges, Chinese engineers conducted a series of dynamic simulations, by both moving load models and train-bridge coupling dynamic analysis method, for the common-span simply-supported beams with various span lengths and different stiffness and verified some results with experiment data. The dynamic simulations involved the single-track and double-track simply-supported PC box-beams with span lengths of 12, 16, 20, 24, 32, and 40 m, and various train loads, including the China-made CRH series (CRH2, CRH3, and CHR5) trains, the German ICE3 train, and the HSLM A01-10 train in UIC code. Based on the simulation results, the conditions unnecessary to conduct train-bridge dynamic simulations analysis are proposed for the double-track simply-supported PC box-beams with spans no more than 40 m, based on the relations of the bridge dynamic responses with the factors such as train type (axle load, axle distance, and vehicle length), train speed, and bridge stiffness (fundamental frequency).

The research results are adopted in the HSR Code of China. In item 7.3.5 of the code, it is stipulated that for the CRH series EMU with 24–26 m car length, and the double-track simply-supported concrete or PC box-beams with $L \leq 32$ m, when the vertical natural frequency of the beam-body is not less than the limits shown in Table 4.32, train-bridge coupling dynamic analysis may not be conducted in the design of beam structure.

For simply-supported beams and other types of bridge beams, which fail to meet the requirements in Table 4.32, train-bridge coupling dynamic analysis shall be conducted according to actual conditions when the passenger trains passing bridge (the maximum calculation train speed shall be 120% of the design speed), and the following additional terms ought to be considered:

(1) The limits in Table 4.32 are applicable only to CRH series EMU trains with 25 m car length, so the train-bridge coupling dynamic analysis is required when the car length differs obviously.
(2) For the single-track simply-supported beam, since the vertical stiffness is about half that of the double-track, the vibration of the beam is larger, so the train-bridge coupling dynamic analysis is required.
(3) For simply-supported beams with non-box-sections, the torsional stiffness should be considered. Train-bridge coupling dynamic analysis is unnecessary only when the first torsional frequency of the beam is larger than 1.2 times of the vertical frequency, in addition to meet the limits in Table 4.32.

Table 4.32 Limits for vertical natural frequency when no dynamic calculation is required for double-track simply-supported beam with common spans (HSR Code)

Span L (m)	20	24	32
Design train speed (km/h)	Vertical natural frequency (Hz)		
250	100/L	100/L	120/L
300	100/L	120/L	130/L
350	120/L	140/L	150/L

References

Dukkipati RV (2000) Vehicle dynamics. Alpha Science International Ltd., Pangbourne
GB5599-85 (1985) Railway vehicles specification for evaluating the dynamic performance and accreditation test. National Bureau of Standards, Beijing (in Chinese)
TB/T 2360-93 (1994) Railway locomotive specification experiment for the dynamic performance and accreditation test. China Railway Publishing House, Beijing (in Chinese)
TB10002.1-2005 (2005a) Fundamental code for design on railway bridge and culvert. China Railway Publishing House, Beijing
TB10002.1-2005 (2005b) Commentary on fundamental code for design on railway bridge and culvert. China Railway Press, Beijing
TB10621-2014 (2015a) Code for design of high-speed railway. China Railway Publishing House, Beijing
TB10621-2014 (2015b) Commentary on code for design of high-speed railway. China Railway Publishing House, Beijing
TJS2005-140 (2005a) Interim provisions on design of 200–250 km/h new special passenger railways. China Railway Publishing House, Beijing (in Chinese)
TJS2005-140 (2005b) Commentary on interim provisions on design of 200–250 km/h new special passenger railways. China Railway Publishing House, Beijing (in Chinese)
TJS 2005-285 (2005a) Interim provisions on design of 200 km/h new railways for passenger and freight trains. China Railway Publishing House, Beijing (in Chinese)
TJS 2005-285 (2005b) Commentary on interim provisions on design of 200 km/h new railways for passenger and freight trains. China Railway Publishing House, Beijing (in Chinese)
TYH 2004-120 (2004) Code for rating existing railway bridge. China Railway Publishing House, Beijing (in Chinese)
TZY 2014-232 (2014) Code for rating operating performance of high-speed railway bridge. China Railway Publishing House, Beijing
UIC Code 776-2 (2009) Design requirements for rail-bridges based on interaction phenomena between track, train and bridge. International Union of Railways
Wang FT (1983) Vehicle dynamics. China Railway Publishing House, Beijing
Xia H, Zhang N (2005) Dynamic interaction of vehicles and structures, 2nd edn. Science Press, Beijing (in Chinese)
Xia H, De Roeck G, Goicolea JM (2012) Bridge vibration and controls: new research. Nova Science Publishers Inc., New York
Zhai WM, Xia H (2011) Train-track-bridge dynamic interaction: theory and engineering application. Science Press, Beijing (in Chinese)

Chapter 5
Dynamic Analysis of Train-Bridge Coupling System

The dynamic analysis model for train-bridge coupling system and the solution method are introduced in this chapter. The modeling methods for the train subsystem and the bridge subsystem, the Hertz elastic theory for wheel-rail normal contact, the Kalker linear creep theory for wheel-rail tangential creep and its corrected and simplified form, the wheel-rail vertical correspondence contact assumption, the wheel hunting wave assumption, and other common wheel-rail interaction models are discussed. The motion equations for train-bridge coupling vibration system are derived. The solution methods for motion equations of train-bridge system, such as the direct coupling method, the in-time-step iteration method, and the intersystem iteration method, are studied. By taking a Pioneer EMU running through a multi-span simply-supported PC box-beam bridge on the Qinhuangdao-Shenyang HSR line as an illustrating example, the dynamic responses of train-bridge system are analyzed and the convergence in equation solution procedure is investigated.

5.1 Introduction

When a high-speed train passes through the bridge, it makes the bridge vibrate, which may affect not only the service performance of the bridge structure, but also the safety and stability of the train vehicles, as well as the riding comfort of passengers. Therefore, various analysis models are developed to study the dynamic behaviors of train-bridge system.

The train-bridge dynamic interaction is a very complex issue. As shown in Fig. 5.1, when a train travels on a railway bridge, the train, track, beam structure, bearings, piers, foundations, and subsoil form an intercoupling and interexciting MDOF (multi-degree-of-freedom) vibration system. Therefore, the established model should as far as possibly reflect various dynamic interactions in the system, including those between different parts of train vehicle, between wheel and rail,

H. Xia et al., *Dynamic Interaction of Train-Bridge Systems in High-Speed Railways*, Advances in High-speed Rail Technology, https://doi.org/10.1007/978-3-662-54871-4_5

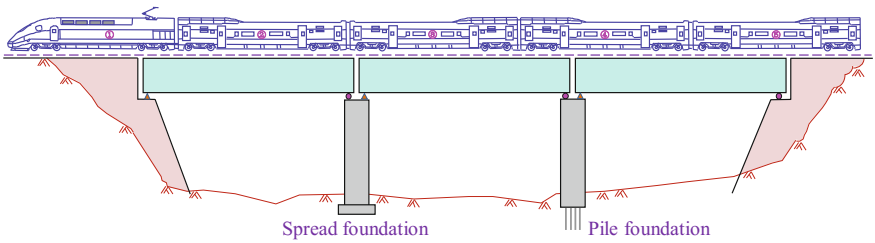

Fig. 5.1 Interaction of train-beam-pier-foundation-soil system when a train passes the railway bridge

between track and beam, between beam and piers through bearings, between pier and foundation, and between foundation and subsoil.

The dynamic behavior of a train-bridge system is a coupled, complex time-varying interaction problem. Such a problem is generally solved by numerical simulation method via establishing a dynamic interaction model for the train-bridge system.

Theoretically, the analysis model can be regarded as a unified big spatial dynamic system composed of two subsystems, the bridge subsystem and the train subsystem, which are simulated as two elastic structures, with each characterized by some patterns of vibration.

Generally, the train subsystem is modeled by the multi-body dynamics, while the bridge subsystem is modeled by the FEM (Finite Element Method). The two subsystems interact with each other through the contact forces, i.e., the forces at the contact points between the wheels of the vehicle and the rail surface on the bridge. The main self-excitation of the system is the track irregularity, and the external excitation includes the wind force, earthquake action, collision force, and other loads.

5.2 Train Subsystem

5.2.1 Fundamental Vibration Patterns of a Vehicle

Railway is a major land transportation mode. There are two types of railway trains: the centralized power train and the EMU (Electric Multiple Units) train. The centralized power train is composed of locomotives and vehicles, in which the locomotives provide traction power, while the vehicles carry cargo or passengers. The EMU train is also called distributed power train, composed of motor-cars and trailer-cars, with the motor-cars providing distributed traction power. The EMU train is only used for passenger transport.

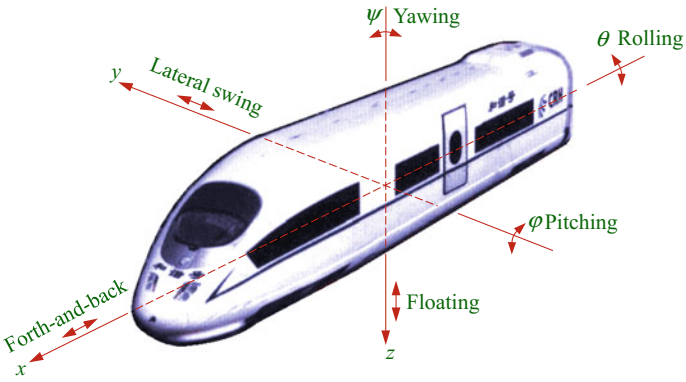

Fig. 5.2 Car-body coordinates in space

From the view of vehicle dynamics, railway locomotive and vehicle have the same characteristics. For convenience, except for specific needs, locomotive and vehicle are hereinafter collectively called "vehicle."

A railway vehicle consists of a car-body, two bogies, and four or six wheel-sets, which are connected by spring-dashpot suspension systems, forming a complex MDOF vibration system. When the vehicle in train-bridge dynamic system is modeled, a car-body (or a bogie, a wheel-set) is normally regarded as a rigid body. Thus, the spatial position of a car-body can be determined by three orthogonal coordinates (x, y, z) which intersect at the gravity center O, as shown in Fig. 5.2.

Therefore, the vibration of a car-body comprises six DOFs: three translational movements along the coordinates and three rotational vibrations around the coordinates, forming six fundamental vibration patterns:

(1) Vertical floating, $z(t)$. The car-body produces vertical vibration along the z-axis direction, with all points on it moving the same displacement at any moment, as shown in Fig. 5.3a.
(2) Lateral swing, $y(t)$. The car-body produces lateral vibration along the y-axis direction, with all points on it moving the same lateral displacement at any moment, as shown in Fig. 5.3b.
(3) Forth-and-back, $x(t)$. The car-body produces longitudinal vibration along the x-axis direction, with all points on it moving the same displacement at any moment, as shown in Fig. 5.3c.
(4) Yawing, ψ (t). The car-body produces rotary vibration of angle $\pm$ ψ around the z-axis, as shown in Fig. 5.3d.
(5) Pitching, φ (t). The car-body produces rotary vibration of angle of $\pm$ φ around the y-axis, as shown in Fig. 5.3e.
(6) Rolling, θ (t). The car-body produces rotary vibration of angle of $\pm$ θ around the x-axis, as shown in Fig. 5.3f.

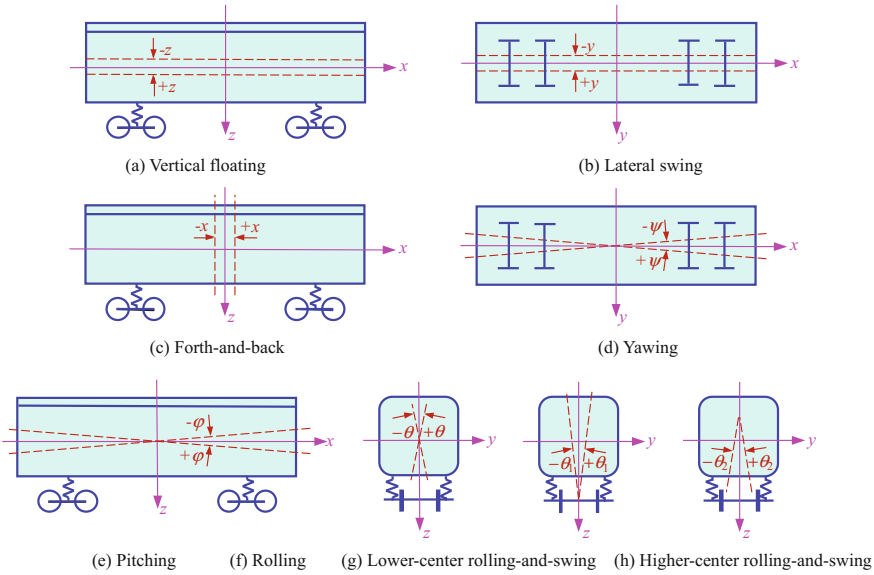

Fig. 5.3 Fundamental patterns of car-body vibration

In general, the spring stiffness and damping characteristic of suspension system on the front and rear bogies are identical, and the mass is symmetrical, thus the floating, forth-and-back, pitching, and yawing motions can occur independently. However, the lateral swing and rolling motions cannot exist independently; instead, they are coupled to form two resultant patterns: the lower-center rolling-and-swing and the upper-center rolling-and-swing, as shown in Fig. 5.3g, h.

Actually, each pattern of a car-body vibration does not occur independently. The complicated vibration of a car-body is usually coupled by the six fundamental patterns with different combinations. When a vehicle runs on the track, floating and pitching are always coupled, while lateral swing, rolling, and yawing often occur simultaneously, owing to the influence of complicated factors such as load asymmetry and randomness of track irregularity. Usually in vehicle vibration analysis, floating and pitching in the *xoz* plane are called vertical vibration, and lateral swing and yawing in the *xoy* plane and rolling in the *yoz* plane are called lateral vibration, while forth-and-back vibration along the car-body longitudinal axis is called longitudinal vibration.

The vibration patterns of other parts in a vehicle such as a bogie or a wheel-set appear different from those of a car-body. For example, the vibrations of floating, lateral swing, forth-and-back, yawing, pitching, and rolling may independently occur in a bogie or a wheel-set, owing to their geometrical symmetry.

5.2.2 *Vehicle Element Model*

The train subsystem model consists of several vehicle elements, and each vehicle element is a MDOF vibration system composed of car-body, bogies, wheel-sets, and spring-damper suspensions, as shown in Fig. 5.4.

Bogie forms. There are two types of bogies used in railway trains: (1) independent bogies, which are used in the vehicles for most of conventional and high-speed trains, where the vehicles are independent of each other; (2) articulated bogies, which are used in the vehicles for some high-speed trains such as the French TGV (train à grande vitesse) and the Korean KTX (Korea Train Express), where the vehicles are articulated with each other by the bogies.

In this chapter, only introduced is the high-speed train with independent bogies. For the articulated high-speed train sharing a bogie with two adjacent vehicles, such as the French TGV, the vehicle element model can reference the related literature (Zhang 2002; Xia et al. 2003).

Bogie suspension system. In high-speed trains, locomotives and vehicles (or motor-cars and trailer-cars in EMU) adopt two-layer suspension devices. The spring-and-dashpot assembly between the bogie and wheel is called the primary

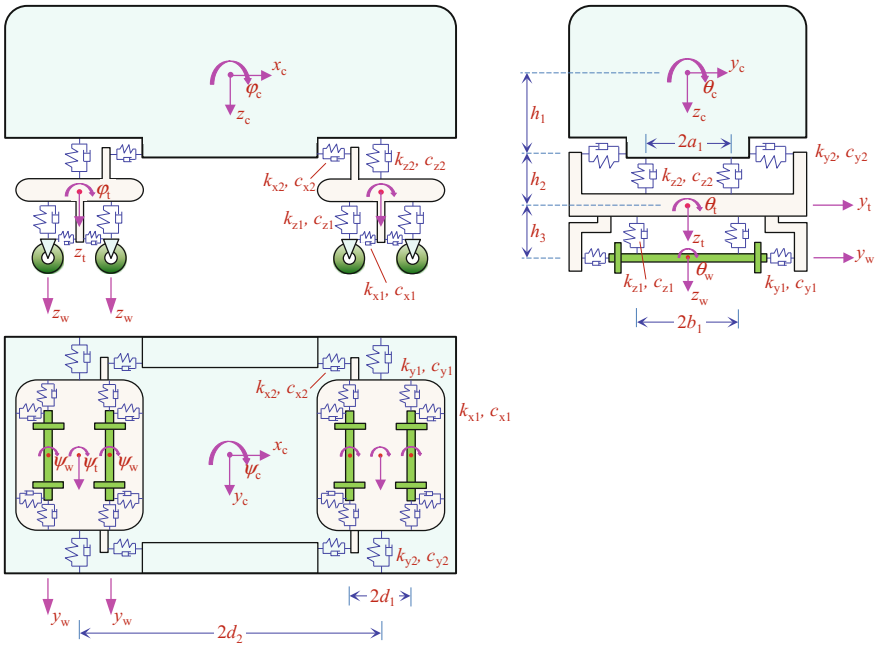

Fig. 5.4 Vehicle element model

suspension system, and that between the body and bogie is called the secondary suspension system.

Vehicle damping. There are various damping adopted for the bogie dashpot. While in vehicle element model, the viscous damping is usually assumed, which is convenient in theoretical solution. Because the train-bridge time-varying system is solved by the step-by-step integration method, other forms of damping are also applicable for the model.

Because the vehicle element is in the gravity field, the zero-coordinate in the z-axis direction is set at the gravity balance position for each component of the vehicle.

To simplify the analysis while with enough accuracy, the following assumptions are used in modeling the train subsystem:

(1) The train is modeled by several independent vehicle elements, by neglecting the interaction among them.
(2) The car-body, bogies, and wheel-sets in each vehicle element are regarded as rigid components, neglecting their elastic deformation during vibration.
(3) The vehicle element is a linear system, namely the mass, damping, and stiffness matrices of the vehicle element are regarded as constant matrices in the analysis process.
(4) The train runs on the bridge at a constant speed, while the movement of the train under starting, braking, or accelerating state is neglected, thus the DOFs in the longitudinal direction for car-body, bogies, and wheel-sets are not considered.
(5) Each car-body or bogie has 5 DOFs in directions of y, z, θ, φ, and ψ. The number of DOFs for wheel-set is determined by the assumption on wheel-rail contact, ref. Sect. 5.4 of this chapter.
(6) The springs in vehicle element are linear, and the dampers are viscous. In the primary suspension system, k_{x1}, k_{y1}, k_{z1} are spring constants, and c_{x1}, c_{y1}, c_{z1} are damping constants, on each side of a wheel-set in x-, y-, z-directions, respectively. In the secondary suspension system, $k_{x2,}$ k_{y2}, k_{z2} are spring constants, and c_{x2}, c_{y2}, c_{z2} are damping constants on each side of a bogie in x-, y-, z-directions, respectively.

Based on the above assumptions, the model of vehicle element is established, as shown in Fig. 5.4. The parameters in the figure will be introduced in Sects. 5.4 and 5.5 of this chapter.

The motion equation of vehicle element is usually established by the multi-body dynamics, which will be derived in Sect. 5.5 *Motion equations of train-bridge coupling system*.

5.3 Bridge Subsystem

The railway bridge is composed of piers, abutments, beams, floor systems, tracks, and accessory structures. When a train runs on the bridge, the forces from the wheels are transmitted to the bridge structure through the track. In studying the lateral and vertical vibrations of the train-bridge system, the bridge is usually analyzed with spatial FEM, using the following assumptions:

(1) There is no relative displacement between track and bridge deck, and the elastic effect of the track system is also neglected.
(2) The modal analysis is conducted for the bridge as a whole. The mode-shape displacements at beam nodes are consistent with those of the track. The value of mode-shape between any two nodes is determined using the interpolation function.
(3) The deformation of cross section in vibration is neglected for the beam with solid sections. For hollow structures, such as box-beams and trussed beams, the deformation of cross section can be taken into account in FE modeling.

According to the above assumptions, the bridge structure can be discretized as a spatial FE model. The motion equations of the bridge subsystem can be expressed as

$$\mathbf{M}_{\mathrm{b}}\ddot{\mathbf{X}}_{\mathrm{b}} + \mathbf{C}_{\mathrm{b}}\dot{\mathbf{X}}_{\mathrm{b}} + \mathbf{K}_{\mathrm{b}}\mathbf{X}_{\mathrm{b}} = \mathbf{F}_{\mathrm{b}} \tag{5.1}$$

where $\mathbf{M}_{\mathrm{b}}$, $\mathbf{C}_{\mathrm{b}}$, and $\mathbf{K}_{\mathrm{b}}$ are, respectively, the global mass, damping, and stiffness matrices of the bridge; $\mathbf{X}_{\mathrm{b}}$ is the displacement vector of bridge nodes; $\mathbf{F}_{\mathrm{b}}$ is the vector of forces of the vehicle wheel-sets on the bridge deck, which will be introduced in Sect. 5.4 *Wheel-rail interaction* and Sect. 5.5 *Motion equations of train-bridge coupling system*; The damping matrix $\mathbf{C}_{\mathrm{b}}$ adopts the Rayleigh damping, expressed by combination of mass matrix and stiffness matrix as

$$\mathbf{C}_{\mathrm{b}} = \frac{2\xi\omega_1\omega_2}{\omega_1+\omega_2}\mathbf{M}_{\mathrm{b}} + \frac{2\xi}{\omega_1+\omega_2}\mathbf{K}_{\mathrm{b}} \tag{5.2}$$

where ξ is damping ratio of the bridge, taken as $0.5\% \sim 1.5\%$ for steel beam, $1.5\% \sim 2\%$ for steel-concrete composite beam, and $2\% \sim 3\%$ for concrete beam, or using the measured value when available; ω_1 and ω_2 are, respectively, the first- and second-order circular frequencies of the beam.

Although the original finite element model can be directly used to constitute the basic equations for the coupled train-bridge system, the direct integration of these equations in the time domain to find the dynamic responses of bridge and train is very cumbersome. In analyzing the running safety of train vehicles on a railway bridge, the deformation of the bridge can be approximately considered within the elastic range. Therefore, the modal decomposition technique is performed herein for modeling the bridge subsystem. First, the free vibration frequencies and modes of

the system are solved. Upon the orthogonality of the modes, the FEM equations coupled with each other can then be decoupled, which makes the bridge calculation model become the superposition of independent modal equations. Owing to the fact that the dynamic response of a structure is dominated by its several lowest modes, this approach has a great advantage that an adequate estimation of the dynamic response can be obtained by considering only a few modes of vibration, thus the computational efforts can be significantly reduced.

The motion equations of the bridge subsystem established by the modal decomposition method can be expressed as

$$\ddot{\mathbf{Q}}_{\mathrm{b}} + 2\boldsymbol{\xi}\boldsymbol{\omega}\dot{\mathbf{Q}}_{\mathrm{b}} + \boldsymbol{\omega}^2\mathbf{Q}_{\mathrm{b}} = \boldsymbol{\Phi}^{\mathrm{T}}\mathbf{F}_{\mathrm{b}} \tag{5.3}$$

where $\boldsymbol{\omega}$ and $\boldsymbol{\xi}$ are the diagonal matrices for circular frequency and damping ratio; $\boldsymbol{\Phi}$ is the normalized modal matrix with respect to the mass matrix of the bridge subsystem. If the first N_{q} modes of the bridge are considered, the above matrices are N_{q} order square matrix. $\mathbf{Q}_{\mathrm{b}}$ is the generalized displacement vector with N_{q} elements of the bridge subsystem

$$\mathbf{Q}_{\mathrm{b}} = \boldsymbol{\Phi}^{\mathrm{T}}\mathbf{X}_{\mathrm{b}} \tag{5.4}$$

where $\mathbf{X}_{\mathrm{b}}$ is the displacement vector of bridge nodes, and $\boldsymbol{\Phi}^{\mathrm{T}}$ is the transpose matrix of $\boldsymbol{\Phi}$.

The number of bridge modes taken into account in the computation should be large enough to include the effects of both the global deformation of the bridge and the local deformation of the structural elements supporting the track. This decision may be made through a convergent study on the effects of the mode numbers or through a comparison with the measured data. According to experience, to calculate the overall vibration of bridge, only several or dozens of vibration modes should be considered; while to calculate the local vibration of bridge members, dozens or even hundreds of vibration modes should be involved.

Both Eq. (5.1) established by direct stiffness method and Eq. (5.3) established by modal decomposition method for bridge can be used in dynamic analysis of train-bridge coupling system. One can choose any of them according to the characteristics of bridge model and the dynamic responses concerned. When the bridge model is large, the modal decomposition method is applicable, because the FE geometric model has large amount of DOFs, thus the direct stiffness method requires storage of dynamic matrix, long time consuming, and large computer memory in calculation. When the model of bridge is small or the local vibration of bridge is concerned, the direct stiffness method is preferred, because the calculation process of mode decomposition method is more complicated.

Note that the main modes in the θ-direction (torsional direction) of the bridge should be considered when adopting the modal decomposition method, because they will be used for calculating the wheel-rail contact force. In the two-dimensional model of bridge (such as simply-supported beam or continuous beam without piers), however, whether the bridge equation is expressed by the

direct stiffness method or the modal decomposition method, it is impossible to obtain the torsional vibration component, where the mass matrix is constituted by lumped mass elements with none moment of inertia. Therefore, to ensure the accuracy of calculation, the mass matrix of the bridge should be established by consistent mass method.

5.4 Wheel-Rail Interaction

Modeling of wheel-rail interaction is a key for dynamic analysis of train-bridge coupling system. The wheel-rail interaction model determines the relative movement and the interaction force between the wheel and the rail, which links the train subsystem and the bridge subsystem. There are various wheel-rail interaction models, which can be divided into the following two categories.

(1) Define the wheel-rail interaction force as the function of the relative movement between wheel and rail. This model category is based on the principle of elastic mechanics or contact mechanics, including the wheel-rail normal elastic force by the Hertz contact theory, the wheel-rail tangent creep force by the Kalker creep theory (Kalker 1967), and its simplified form amended by the Shen's theory (Shen et al. 1983).
(2) Define the wheel-set movement as the function of the rail movement, including the wheel-rail vertical correspondence contact assumption and the wheel-set hunting wave assumption.

The above five models of wheel-rail interaction in the two categories will be respectively introduced in Sects. 5.4.2–5.4.6 and will be summarized and compared in Sect. 5.4.7.

There are two sets of coordinates, the natural coordinates and the contact-spot coordinates, adopted to define the direction of wheel-rail force and the relative displacement between wheel and rail. The natural coordinates is herein introduced first, and the contact-spot coordinates and its conversion relation with the natural coordinates will be introduced in Sect. 5.4.1 *Wheel-rail contact geometry*.

For convenience, the deformation of track structure is not considered in the five models of wheel-rail interaction, thus the rail movement is the sum of the deck motion and the track irregularity. In the following description, the movement of wheel-set, track, and deck in swing (lateral), floating (vertical), rolling (torsional), and yawing (rotational about z-axis) directions are expressed, respectively, as y, z, θ, and ψ; r is the wheel rolling radius; g_0 is the distance between the left and right wheel-rail contact points, being 1.493 m; subscript "w" stands for the center of the wheel-set, subscript "wo" the wheel-rail contact point on the rim, subscript "r" the center between the left and right rail, subscript "ro" the wheel-rail contact point on the rail, and subscript "d" the deck location under the track center. The locations of

Table 5.1 Definitions for movements of wheel-set, track and deck in various directions

Position	x-direction	y-direction	z-direction	θ-direction	ψ-direction
Center of wheel-set	–	y_w	z_w	θ_w	ψ_w
Wheel-rail contact point on the rim	x_{wo}	$y_{wo} = y_w - r\theta_w$	$z_{wo} = z_w \pm g_0\theta_w/2$	$\theta_{wo} = \theta_w$	ψ_{wo}
Wheel-rail contact point on the rail	x_{ro}	$y_{ro} = y_r$	$z_{ro} = z_r \pm g_0\theta_r/2$	–	–
Center between left and right rails	–	$y_r = y_d + y_i$	$z_r = z_d + z_i$	$\theta_r = \theta_d + \theta_i$	–
Deck location under track center	–	y_d	z_d	θ_d	–

Note The sign in the formulas: for right wheel, use "+", and for the left wheel, use "−", with respect to the moving direction of train

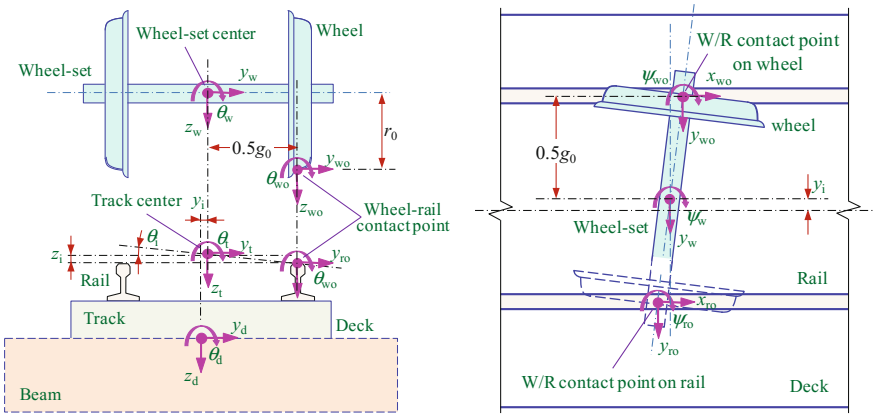

Fig. 5.5 Movements of wheel-set, track and bridge deck

various above points and the relations between them can be seen in Table 5.1 and Fig. 5.5.

5.4.1 Wheel-Rail Contact Geometry

When a train runs on the track, with wheel-set rolling forward on the rails, there exist various small relative movements between the wheel and the rail in lateral

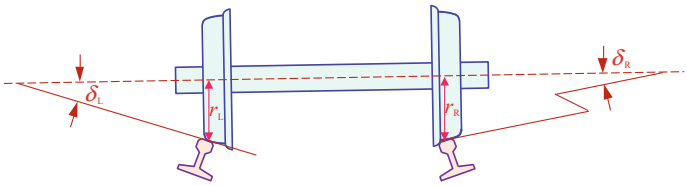

Fig. 5.6 Geometry relationship of wheel-rail contact

swing (y), vertical floating (z), rolling (θ), and yawing (ψ) directions. Under different wheel-rail relative displacement conditions, the wheel-rail contact points at the left and the right sides are different, and correspondingly, the wheel-rail contact parameters at these points vary, which are necessary in railway vehicle dynamics.

Note that the rail is infinitely long, the wheel is round, and on the macro, the elastic compression between wheel and rail can be neglected and the embedding between them cannot be considered; the wheel-rail contact geometry parameters have nothing to do with the wheel-rail relative motions in x-, φ-, z-, and θ-directions. Therefore, the wheel-rail contact geometry parameters are only decided by the wheel-rail relative motion in directions of lateral swing (y) and yawing (ψ), as illustrated in Fig. 5.6, which contain: (1) the left and the right wheel-rail contact angles, namely the angle between the wheel-rail contact surface and the wheel-set axis, with $\delta_L < 0$ and $\delta_R > 0$; (2) the actual left and right wheel rolling radii, r_L and r_R; (3) the curvature radii of wheel tread surface and rail head at wheel-rail contact point.

Different wheel-rail contact geometry relationship and geometric parameters are coordinated with different wheel and rail profiles fit. Usually, the profiles of wheel and rail cannot be expressed by simple analytical formulas, while can be described by the coordinates measured on wheel or rail surface at a series of points, especially for the contour profile of the worn wheel or rail. In early research, the analytical methods were proposed to determine the wheel-rail contact geometry parameters for conical tread with single circular rail section. However, for the worn wheel tread with circular rail section more commonly appeared in railway engineering, the wheel-rail contact geometry parameters cannot be calculated by the analytical methods (Li et al. 2007; Zhai 2007; Wu et al. 2007). Currently, there are two methods to determine the wheel-rail contact geometry parameters, the iteration method by left and right wheel-rail equal intervals and the trace line method. By the trace line method, the iteration process is avoided and all concerned wheel-rail contact geometry parameters can be obtained via once calculation; therefore, it is introduced in this chapter.

The trace line method determines the wheel-rail contact geometry parameters by analyzing the spatial characteristics of the wheel-rail contact geometry. For the straight track, the rail is a cylinder perpendicular to the yoz plane, while the wheel tread is a revolution surface around the wheel-set axis, so the common normal of the rail surface and the wheel tread must intersects with the wheel-set axis and be parallel to the yoz plane, as shown in Fig. 5.7.

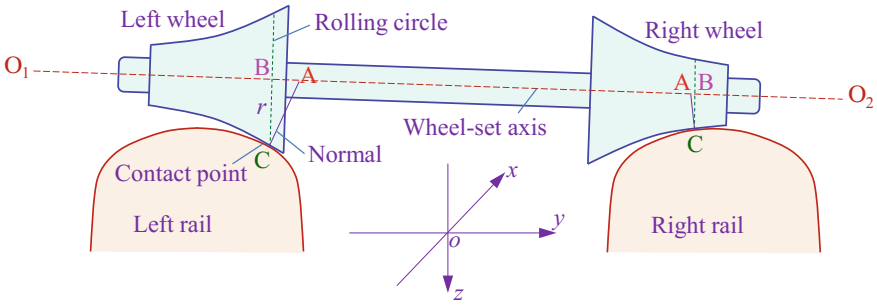

Fig. 5.7 Calculation principle of the trace line method

In the figure, O_1O_2 is the wheel-set axis, C is the wheel-rail contact point, and B is the center of the rolling circle. According to the characteristic of common normal, the common normal of rail surface and wheel tread should intersect with the wheel-set axis at A. Because the line AC is perpendicular to the wheel-rail interface and the line BC is perpendicular to the wheel-set axis O_1O_2, we have $\angle ACB = \delta$, where the subscript L or R of δ is omitted, because the expression is applicable to both the left and right wheels. It is agreed that $\delta > 0$ for the left wheel and $\delta < 0$ for the right wheel.

Assume the rolling angel of wheel-set is θ_w, and the yawing angel is ψ_w. Because the plane in which the wheel-set rolls is perpendicular to the wheel-set axis, the directional cosines l_x, l_y, and l_z of the wheel-set axis O_1O_2 can be obtained by rotating the wheel-set by a θ_w angle around the x-axis and then by a ψ_w angle around the z-axis. When the left wheel is in the octant VIII and the right wheel is in the octant II, the directional cosine vector of O_1O_2 is

$$\begin{aligned}\begin{bmatrix} l_x \\ l_y \\ l_z \end{bmatrix} &= \begin{bmatrix} \cos\psi_w & -\sin\psi_w & 0 \\ \sin\psi_w & \cos\psi_w & 0 \\ 0 & 0 & 1 \end{bmatrix} \begin{bmatrix} 1 & 0 & 0 \\ 0 & \cos\theta_w & -\sin\theta_w \\ 0 & \sin\theta_w & \cos\theta_w \end{bmatrix} \begin{bmatrix} 0 \\ 1 \\ 0 \end{bmatrix} \\ &= \begin{bmatrix} -\cos\theta_w \sin\psi_w \\ \cos\theta_w \cos\psi_w \\ \sin\theta_w \end{bmatrix} \end{aligned} \tag{5.5}$$

The rolling center B is a point on the plane of the wheel rolling circle, so the equation for the plane can be expressed as

$$l_x(x - x_B) + l_y(y - y_B) + l_z(z - z_B) = 0 \tag{5.6}$$

When the center B of the wheel rolling circle is determined, and the radius r of the circle is known, the wheel-rail contact point C is on the surface of a sphere with B as the center and r as the radius, expressed as

$$(x - x_B)^2 + (y - y_B)^2 + (z - z_B)^2 = r^2 \tag{5.7}$$

Because the plane AO_1C is parallel to the yoz plane, the wheel-rail contact point C should be on the AO_1C plane, thus we have

$$x = x_C = x_A = x_B + l_x r \tan\delta \tag{5.8}$$

The wheel-rail contact point C should be simultaneously on the plane defined by Eq. (5.6), the sphere by Eq. (5.7) and the plane by Eq. (5.8). By considering Eqs. (5.6)–(5.8) simultaneously, note that the directional cosine meets the formula $l_x^2 + l_y^2 + l_z^2 = 1$ and z_B is smaller than z_C according to Fig. 5.7, the coordinates of the wheel-rail contact point C can be obtained as

$$\begin{cases} x_C = x_B + l_x r \tan\delta \\ y_C = y_B - \frac{r}{1-l_x^2}(l_x^2 l_y \tan\delta + l_z m) \\ z_C = z_B + \frac{r}{1-l_x^2}(-l_x^2 l_z \tan\delta + l_y m) \end{cases} \tag{5.9}$$

where $m = \sqrt{1 - l_x^2(1 + \tan^2\delta)}$; x_B, y_B, and z_B are the coordinates at center B of the wheel rolling circle.

In Fig. 5.7, BC is perpendicular to O_1O_2, namely the center of the given wheel rolling circle. When the wheel rolling circle center is B, the curvature radius δ of the rim and the rolling circle radius r of the wheel in Eq. (5.9) are determined. The x, y, and z coordinates of each possible wheel-rail contact point can be calculated, by changing the wheel rolling circle center B.

The procedures for calculating the wheel-rail contact geometry parameters are as follows:

(1) Determine the coordinates of the wheel rolling circle center B in the vehicle coordinates according to the lateral swing (y) and yawing (ψ) displacements of the wheel-set. Then, calculate the coordinates of corresponding wheel-rail contact point by Eq. (5.9).
(2) Utilizing the relative geometric relationship in x- and y-directions between the vehicle coordinates and the bridge coordinates, to calculate the x- and y-coordinates in the bridge coordinates for the corresponding wheel-rail contact point on the rail.
(3) Calculate the z-coordinate of corresponding wheel-rail contact point in the bridge coordinates, according to the rail surface profile and the factors of track irregularity and rail base slope.
(4) Calculate the difference Δz of z-coordinate between the vehicle's coordinates and the bridge's coordinates at the wheel-rail contact point.
(5) Change the position of the wheel rolling circle center B in turn to calculate the corresponding Δz at each position. The minimum Δz is the real wheel-rail contact point.

(6) When the wheel-rail contact point C is determined, the vector from the wheel-set center to the wheel-rail contact point can be decided; the contact angle of the left and right wheel is ∠ACB shown in Fig. 5.7; the actual wheel rolling circle radius is the length of BC; and the curvature radii of the wheel and the rail at the wheel-rail contact point can be directly calculated by differentials of the respective profile data near the wheel-rail contact point.

The creep exists when two rigid-bodies compress and roll on each other, and a contact region is formed around the contact point. The contact region is an ellipse, called contact-spot. The contact-spot coordinates are established, respectively, at the left and the right wheel-rail contact points, expressed as $o^*x^*y^*z^*$. The origin o^* of contact-spot coordinates is at the center of the contact-spot ellipse, and the axis direction is determined by rotating the overall coordinates oxyz first by $\theta_w + \delta$ around the x-axis and then by ψ_w around the z-axis. The directional cosines of x^*-axis of the left and right contact-spot coordinates in the vehicle or bridge coordinates are expressed as

$$\begin{Bmatrix} l^*_{x-x} \\ l^*_{y-x} \\ l^*_{z-x} \end{Bmatrix} = \begin{bmatrix} \cos\psi_w & -\sin\psi_w & 0 \\ \sin\psi_w & \cos\psi_w & 0 \\ 0 & 0 & 1 \end{bmatrix} \begin{bmatrix} 1 & 0 & 0 \\ 0 & \cos(\theta_w+\delta) & -\sin(\theta_w+\delta) \\ 0 & \sin(\theta_w+\delta) & \cos(\theta_w+\delta) \end{bmatrix} \begin{Bmatrix} 1 \\ 0 \\ 0 \end{Bmatrix} \tag{5.10}$$

The directional cosines of y^*-axis of the left and right contact-spot coordinates in the vehicle or bridge coordinates are expressed as

$$\begin{Bmatrix} l^*_{x-y} \\ l^*_{y-y} \\ l^*_{z-y} \end{Bmatrix} = \begin{bmatrix} \cos\psi_w & -\sin\psi_w & 0 \\ \sin\psi_w & \cos\psi_w & 0 \\ 0 & 0 & 1 \end{bmatrix} \begin{bmatrix} 1 & 0 & 0 \\ 0 & \cos(\theta_w+\delta) & -\sin(\theta_w+\delta) \\ 0 & \sin(\theta_w+\delta) & \cos(\theta_w+\delta) \end{bmatrix} \begin{Bmatrix} 0 \\ 1 \\ 0 \end{Bmatrix} \tag{5.11}$$

The directional cosines of z^*-axis of the left and right contact-spot coordinates in the vehicle or bridge coordinates are expressed as

$$\begin{Bmatrix} l^*_{x-z} \\ l^*_{y-z} \\ l^*_{z-z} \end{Bmatrix} = \begin{bmatrix} \cos\psi_w & -\sin\psi_w & 0 \\ \psi\sin w_w & \cos\psi_w & 0 \\ 0 & 0 & 1 \end{bmatrix} \begin{bmatrix} 1 & 0 & 0 \\ 0 & \cos(\theta_w+\delta) & -\sin(\theta_w+\delta) \\ 0 & \sin(\theta_w+\delta) & \cos(\theta_w+\delta) \end{bmatrix} \begin{Bmatrix} 0 \\ 0 \\ 1 \end{Bmatrix} \tag{5.12}$$

5.4.2 Normal Hertz Contact Theory

The Hertz contact theory was originally published in 1882. It proposed the hypothesis of elliptic contact-spot, assuming that the distribution shape of pressure

on elastic contact-spot is half axiolitic, and the normal elastic deformation is paraboloidal. The Hertz contact theory assumes that the contact surface is smooth, without friction effect, and it only transfers the normal force. To calculate the local deformation, some simplifications are made, including the contact body is regarded as an elastic half space, the contact force only acts on a small ellipse area of a flat surface, and the stress distribution near the contact zone is highly centralized and is related to the geometry size near the contact zone. The Hertz contact theory has been verified for more than a hundred years, laying a foundation for the contact and rolling contact theory (Dinh Van et al. 2009).

It should be noticed that in the wheel-rail normal Hertz contact theory, the normal direction is perpendicular to the wheel-rail contact surface, namely the z^*-axis direction of contact-spot coordinates, which is not the same as that defined in the vertical wheel-rail relationship.

In the $y^* o^* z^*$ plane of the left and right contact-spot coordinates, the normal contact force is determined by the normal compression between the wheel and the rail, which is calculated by the Hertz nonlinear contact theory, and expressed as

$$N = \left[\frac{1}{G_{\mathrm{w-r}}}(z_{\mathrm{wo}} - z_{\mathrm{ro}})\right]^{3/2} \tag{5.13}$$

where N is the wheel-rail normal contact force; $G_{\mathrm{w\text{-}r}}$ is the wheel-rail contact constant, and $G_{\mathrm{w\text{-}r}} = 3.86r^{-0.115} \times 10^{-8}$ $(\mathrm{m/N})^{2/3}$ for the worn tread wheel; $z_{\mathrm{wo}} - z_{\mathrm{ro}}$ (m) is the instantaneous elastic relative compression between the wheel and the rail, equal to the relative displacement of the wheel and the rail at the contact point in the z^*-direction of the contact-spot coordinates, and the compression from the static wheel load is included. In particular, when $z_{\mathrm{wo}} - z_{\mathrm{ro}} < 0$, it means that the wheel and the rail have been detached from each other, and correspondingly, the wheel-rail force N is zero.

5.4.3 Vertical Wheel-Rail Correspondence Assumption

The wheel-rail correspondence model assumes no relative movement between the wheel and the rail in the z-direction of vehicle coordinates, meaning that the wheel movement corresponds to the rail movement, thus the vertical wheel-rail force is determined by the relative movement between the wheel and the rail in the z-direction.

Under the correspondence assumption, the wheel-set and the rail have the same dynamic displacement, as well as the same velocity and acceleration in the z- and θ-directions. The velocity and acceleration of wheel-set induced by the track displacement can be calculated, for example in the z-direction, by the differential form

$$\dot{z}_r = \lim_{t\to 0}\frac{\Delta z_r}{\Delta t} = \lim_{t\to 0}\frac{\Delta z_r}{\Delta x/V} = V\cdot\lim_{t\to 0}\frac{\Delta z_r}{\Delta x} = V\cdot\frac{\partial z_r}{\partial x} \tag{5.14}$$

$$\ddot{z}_r = \lim_{t\to 0}\frac{\Delta \dot{z}_r}{\Delta t} = \lim_{t\to 0}\frac{\Delta \dot{z}_r}{\Delta x/V} = V\cdot\lim_{t\to 0}\frac{\Delta \dot{z}_r}{\Delta x} = V^2\cdot\frac{\partial^2 z_r}{\partial x^2} \tag{5.15}$$

where V means the train speed.

The forces of vehicle element acting on the bridge subsystem include the spring force and the damping force from primary suspension system, the inertia force of the wheel-set, and the static axle load of the vehicle. While for the vehicle element, these forces also apply but the static axle load, because the z-direction of the vehicle element is in the gravity balance position. Since the wheel-set movements in the z- and θ-directions correspond to the rail movement, they are not independent DOFs, so it is not necessary to consider the inertia force of wheel-set in the vehicle element; thus, the forces from the bridge applied to the vehicle element are only those through the primary suspension.

The wheel-rail interaction forces act on the left and the right wheel-rail contact points. Shown in Fig. 5.8 are the vertical interaction forces between rail and wheel and between wheel and bogie.

According to this figure, the vertical displacements $z_1 \sim z_4$ at positions ① ~ ④ can be expressed as

$$\begin{cases} z_1 = z_t + \eta\cdot d_1\cdot\varphi_t - b_1\cdot\theta_t \\ z_2 = z_t + \eta\cdot d_1\cdot\varphi_t + b_1\cdot\theta_t \\ z_3 = z_r - b_1\cdot\theta_r \\ z_4 = z_r + b_1\cdot\theta_r \end{cases} \tag{5.16}$$

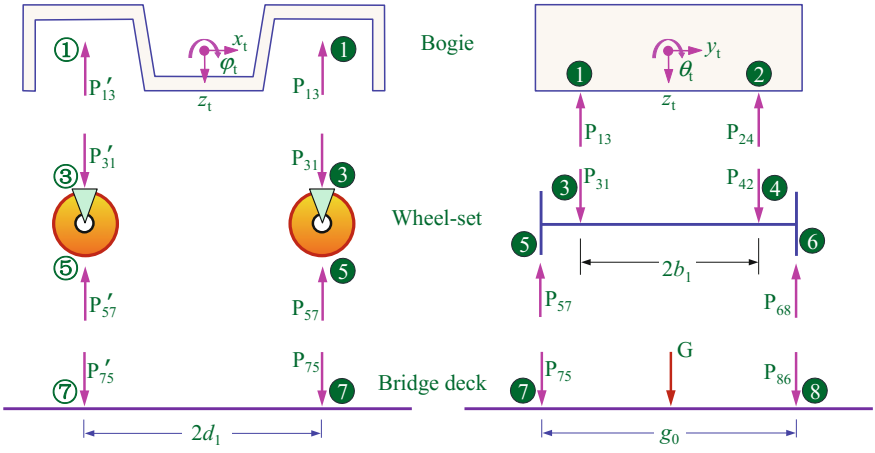

Fig. 5.8 Vertical interaction forces between bogie, wheel and rail

where z_t, θ_t, and φ_t are the bogie displacement in z-, θ-, and φ-directions; $2b_1$ is the lateral distance between the two primary springs/damper sets; $2d_1$ is the longitudinal distance between the two bogies; η is the sign function, $\eta = 1$ for the front wheel of the bogie and $\eta = -1$ for the rear. The displacement in the z-direction at point ① and ② is $z_t + d_1\varphi_t$, when the wheel-set is at the front of the bogie, and $z_t - d_1\varphi_t$ when the wheel-set is at the rear.

Then, the vertical interaction forces between the bogie and the wheel-set are expressed as

$$\begin{cases} P_{13} = P_{31} = k_{z1}(z_1 - z_3) + c_{z1}(\dot{z}_1 - \dot{z}_3) \\ P_{24} = P_{42} = k_{z1}(z_2 - z_4) + c_{z1}(\dot{z}_2 - \dot{z}_4) \end{cases} \tag{5.17}$$

where k_{z1} and c_{z1} are, respectively, the vertical stiffness and damping coefficients between the bogie and the wheel-set.

The forces between the vehicle element and the bridge include the vertical interaction forces between the bogie and the wheel-set, the inertia force of the wheel-set, and the static axle load. The vertical wheel-rail interaction forces are expressed as.

$$\begin{cases} P_{75} = P_{57} + \frac{G}{2} = \frac{G}{2} - \frac{m_w \ddot{z}_r}{2} + \frac{I_{xw}\ddot{\theta}_r}{g_0} + \left(\frac{1}{2} + \frac{b_1}{g_0}\right)P_{13} + \left(\frac{1}{2} - \frac{b_1}{g_0}\right)P_{24} \\ P_{86} = P_{68} + \frac{G}{2} = \frac{G}{2} - \frac{m_w \ddot{z}_r}{2} - \frac{I_{xw}\ddot{\theta}_r}{g_0} + \left(\frac{1}{2} - \frac{b_1}{g_0}\right)P_{13} + \left(\frac{1}{2} + \frac{b_1}{g_0}\right)P_{24} \end{cases} \tag{5.18}$$

where m_w and I_{xw} are the mass and the x-inertia of the wheel-set, respectively; G is the static axle load.

Owing to the vertical correspondence assumption of wheel-rail contact, the wheel-set movement in the z-direction is not independent, thus it is not necessary to apply its inertia force to the vehicle element, The forces from the left and right wheels on the vehicle element are calculated by Eq. (5.17) and those on the bridge by Eq. (5.18).

5.4.4 *The Kalker's Linear Creep Theory and the Shen's Correction*

The famous linear creep theory was proposed by Kalker in 1967, which solved the problem of the three-dimensional steady rolling contact in the elliptical contact zone. This theory has been widely adopted to simulate the lateral wheel-rail relationship (Wang 1994; Gao 2002).

In the wheel-rail tangential Kalker's linear creep theory, the tangential direction is the y^*-axis direction of the contact-spot coordinates. In calculation by this theory, the results are usually amended by the Shen's theory (Shen et al. 1983).

Generally, the circumferential speeds of two rolling bodies on the contact surface are not equal. In the contact-spot coordinates, the speed difference between two bodies in pure rolling state is used to define the creep rate expressed as

$$\begin{cases} \xi_{\mathrm{x}} = \frac{\dot{x}_{\mathrm{wo}} - \dot{x}_{\mathrm{ro}}}{V_{\mathrm{n}}} \\ \xi_{\mathrm{y}} = \frac{\dot{y}_{\mathrm{wo}} - \dot{y}_{\mathrm{ro}}}{V_{\mathrm{n}}} \\ \xi_{\psi} = \frac{\dot{\psi}_{\mathrm{wo}} - \dot{\psi}_{\mathrm{ro}}}{V_{\mathrm{n}}} \end{cases} \tag{5.19}$$

where V_{n} is the nominal forward speed of the left or right wheel on the rail expressed as

$$V_{\mathrm{n}} = \frac{1}{2}\left(V + \frac{r}{r_{\mathrm{n}}} V \cos\psi_{\mathrm{w}}\right) \tag{5.20}$$

where r is the actual radius of rolling circle, namely the length of BC in Fig. 5.7; r_{n} is the nominal radius of rolling circle, namely the radius of wheel-set measured at 70 mm inside the rim.

The speed of the wheel-set or the rail refers to that at the wheel-rail contact point in the contact-spot coordinates. x_{wo} and x_{ro} are, respectively, the displacements of the wheel and the rail in the x-direction at the wheel-rail contact point. The ξ_{x} in Eq. (5.19) has nothing to do with the lateral wheel-rail interaction model, so it is not discussed herein. ψ_{ro} is the displacement of the rail in the ψ-direction at the wheel-rail contact point and it is usually ignored.

In the contact-spot coordinates, the wheel-rail creep force can be expressed as follows by the Kalker's linear creep theory, when the coupled relationship between the y^*-axis and the z^*-axis directions is ignored.

$$\begin{cases} F_{\mathrm{x}} = -f_{11}\xi_{\mathrm{x}} \\ F_{\mathrm{y}} = -f_{22}\xi_{\mathrm{y}} \\ F_{\psi} = -f_{33}\xi_{\psi} \end{cases} \tag{5.21}$$

where F_{x} and F_{y} are, respectively, the creep forces in x^*- and y^*-directions; F_{ψ} is the creep moment around z^*-direction; f_{11} and f_{22} are, respectively, the creep coefficients in x^*- and y^*- directions; f_{33} is the creep coefficients around z^*-direction. The creep coefficients in Eq. (5.21) are expressed as

$$\begin{cases} f_{11} = C_{11}Eab \\ f_{22} = C_{22}Eab \\ f_{33} = C_{33}E(ab)^2 \end{cases} \tag{5.22}$$

where E is the elastic modulus of steel wheel and rail; a and b are, respectively, the long half-axis and short half-axis of the contact ellipse; C_{11}, C_{22}, and C_{33} are the Kalker coefficients, which are the functions of Poisson's ratio v and the ratio a/b.

The parameter ρ/r is introduced, which can be calculated by

$$\frac{1}{\rho}=\frac{1}{4}\left[\frac{1}{r}+\left(\frac{1}{r_{\mathrm{wo}}}+\frac{1}{r_{\mathrm{ro}}}\right)\right] \tag{5.23}$$

where r_{wo} and r_{ro} are, respectively, the curvature radii of the wheel tread and the rail surface at the wheel-rail contact point, which are determined by Wang (1994); a/b is the function of the parameter ρ/r, so all the Kalker coefficients are functions of the parameter ρ/r.

The long half-axis a and the short half-axis b of the contact ellipse in Eq. (5.22) can be further expressed as

$$\begin{cases} a=a_{\mathrm{e}}(Nr)^{1/3} \\ b=b_{\mathrm{e}}(Nr)^{1/3} \\ ab=a_{\mathrm{e}}b_{\mathrm{e}}(Nr)^{2/3} \end{cases} \tag{5.24}$$

where N is the normal wheel-rail force; a_{e} and b_{e} are only related to the parameter ρ/r.

By substituting Eqs. (5.24), (5.22) becomes

$$\begin{cases} f_{11}=C_{11}Ea_{\mathrm{e}}b_{\mathrm{e}}(Nr)^{2/3}=S_{11}(Nr)^{2/3} \\ f_{22}=C_{22}Ea_{\mathrm{e}}b_{\mathrm{e}}(Nr)^{2/3}=S_{22}(Nr)^{2/3} \\ f_{33}=C_{33}E(a_{\mathrm{e}}b_{\mathrm{e}})^{2}(Nr)^{4/3}=S_{33}(Nr)^{4/3} \end{cases} \tag{5.25}$$

Obviously, S_{11}, S_{22}, and S_{33} in the equation are only the functions of parameter ρ/r, which are called creep geometric parameters. For the steel wheel and rail, the Poisson ratio v = 0.3, the elastic modulus E = 200 GPa, and the creep geometric parameters are listed in Table 5.2. The unit for S_{11} and S_{22} is $\mathrm{N}^{1/3}\cdot\mathrm{m}^{-2/3}$ and for S_{33} is $\mathrm{N}^{-1/3}\cdot\mathrm{m}^{2/3}$.

Thus, the relationship between the wheel-rail contact geometric parameters and the creep coefficients is established, and then, the wheel-rail creep forces can be calculated by Eq. (5.21).

The Kalker's linear creep theory in Eq. (5.19) is only applicable to the situations with small creep rate or small spin, where the wheel-rail interface is mainly controlled by the stick friction zone. For those situations with large creep rate, large spin or even completely sliding, where the wheel-rail interface is mainly controlled by the sliding area, the linear relationship of creep force will be broken, the further increase of creep rate cannot raise the creep force by the same proportion, and finally, tends to the saturation limit of the Coulomb (slide) friction. To this end, the Shen's theory is usually adopted for correction as follows.

The longitudinal creep force F_{x} and the lateral creep force F_{y} are combined to form the resultant force. The ratio of the resultant force to the wheel-rail friction is defined as

Table 5.2 Creep geometric parameters

ρ/r	S_{11}	S_{22}	S_{33}	ρ/r	S_{11}	S_{22}	S_{33}
0.108	7590	8498	2491	1.500	10948	9974	67441
0.120	7541	8342	2865	1.600	11126	10018	76466
0.140	7775	8524	3462	1.700	11373	10076	85343
0.160	7852	8548	3971	1.800	11589	10148	94937
0.180	7914	8571	4463	1.900	11652	10293	107506
0.200	7903	8517	4943	2.000	11552	10325	119374
0.225	8116	8717	5636	2.100	12013	10566	136003
0.250	8083	8646	6094	2.200	12262	10548	147841
0.275	8250	8786	6907	2.300	12548	10591	166384
0.300	8236	8724	7587	2.400	12810	10716	186335
0.350	8509	8946	9114	2.500	13146	10941	211390
0.400	8685	9051	10725	2.600	13373	11036	234430
0.450	8823	9112	12354	2.700	13654	11142	265136
0.500	8845	9043	13833	2.800	13944	11302	301508
0.550	9058	9172	15911	2.900	14410	11625	350963
0.600	9176	9203	17784	3.000	14796	11802	403533
0.650	9263	9210	19570	3.050	15000	11861	434036
0.700	9333	9197	21518	3.100	15230	11934	468394
0.750	9416	9209	23580	3.150	15428	11988	503164
0.800	9503	9245	25424	3.200	15581	12010	541460
0.850	9625	9319	27650	3.250	15952	12226	600862
0.900	9793	9441	30278	3.300	16180	12355	652719
0.950	9879	9482	32529	3.350	16444	12518	720488
1.000	9971	9526	34904	3.400	16827	12777	803680
1.100	10215	9648	40841	3.450	17127	12963	888867
1.200	10300	9610	46139	3.500	17379	13101	976640
1.300	10466	9664	52743	3.550	17872	13397	1122252
1.400	10715	9825	60059	3.600	18458	13757	1304721

$$\beta = \frac{\sqrt{F_{\mathrm{x}}^2 + F_{\mathrm{y}}^2}}{f \cdot N} \tag{5.26}$$

where f is the wheel-rail friction coefficient, with an acceptable value being $f = 0.25$.

By introducing the correction coefficient

$$\varepsilon = \begin{cases} 1 - \frac{\beta}{3} + \frac{\beta^2}{27} & (\beta \leq 3) \\ \frac{1}{\beta} & (\beta > 3) \end{cases} \tag{5.27}$$

the corrected creep force and creep moment are obtained and expressed as

$$\begin{cases} F_{\mathrm{x}}^{'} = \varepsilon \cdot F_{\mathrm{x}} \\ F_{\mathrm{y}}^{'} = \varepsilon \cdot F_{\mathrm{y}} \\ F_{\psi}^{'} = \varepsilon \cdot F_{\psi} \end{cases} \tag{5.28}$$

The corrected creep forces by the Shen's theory apply to the situation with any creep rate or spin, which is convenient to calculate various wheel-rail interactions.

5.4.5 The Simplified Kalker Linear Creep Theory

In some situations of simplified calculation, keeping approximate linear relationship between the wheel-rail lateral (or tangential) movement and the corresponding force is important for establishment and solution of the coupled train-bridge equations. To this end, usually only the wheel-rail creep force in y^*-direction is considered, while that in x^*-direction or around z^*-direction is ignored. When the y^*-direction of contact-spot coordinates is approximately regarded as the y-direction of the vehicle's coordinates, the yawing displacement ψ_{w} of wheel-set is ignored, and the nominal forward speed V_{n} of wheel on the rail is replaced with the train speed V, thus the lateral wheel-rail creep force can be calculated as

$$F_{\mathrm{y}} = -f_{22}\xi_{\mathrm{y}} = -\frac{f_{22}}{V}(\dot{y}_{\mathrm{w}} - \dot{y}_{\mathrm{r}}) = -\frac{S_{22}r^{2/3}}{V}N^{2/3}(\dot{y}_{\mathrm{w}} - \dot{y}_{\mathrm{r}}) \tag{5.29}$$

The ideal wheel-rail contact point is defined when neither relative lateral displacement nor relative yawing angle exists between the wheel and the rail. In normal operation state of train, the distance between the actual wheel-rail contact point and the ideal contact point is less than 20 mm. For the LM wheel tread, there are two circular arcs with 100 mm and 500 mm radii in the area from 29 mm inside to 20 mm outside the ideal contact point, and for the 60-kg/m standard rail surface, there are three circular arcs with 80 mm, 300 mm, and 80 mm radii in the area from 25 mm inside to 25 mm outside the ideal contact point. Considering the wheel radii of Chinese railway vehicles are 420 mm for freight car, 430 mm for high-speed car, 457.5 mm for common passenger car, and 625 mm for locomotive, the parameter $S_{22}r^{2/3}$ can be calculated with the above curvature radii of the wheel-rail contact points, as listed in Table 5.3.

In Eq. (5.29), if $S_{22}r^{2/3}$ adopts the average value given by Table 5.3, the maximum error is only 4.43%, the wheel-rail normal connect force can be approximated as the static axle load G, for a certain train speed V, the lateral wheel-rail creep force is proportional to the lateral wheel-rail relative velocity, which can meet the requirement of engineering accuracy in general.

Table 5.3 Parameter $S_{22}r^{2/3}$

r (mm)	r_w (mm)	r_{tr} (mm)	ρ (mm)	ρ/r	$S_{22}r^{2/3}$		
					Calculation	Average	Max. error (%)
420 (Freight car)	100	80	160.8	0.383	5065	5194	2.47
	500	80	237.0	0.564	5157		0.71
	100	300	254.5	0.606	5162		0.61
	500	300	518.5	1.235	5390		3.79
430 (HSR car)	100	80	161.1	0.375	5127	5268	2.68
	500	80	237.7	0.553	5226		0.79
	100	300	255.4	0.594	5241		0.52
	500	300	522.3	1.215	5479		4.01
457.5 (Passenger car)	100	80	162.0	0.354	5323	5475	2.76
	500	80	239.7	0.524	5399		1.38
	100	300	257.7	0.563	5459		0.29
	500	300	532.0	1.163	5717		4.43
625 (Locomotive)	100	80	166.0	0.266	6384	6643	3.90
	500	80	248.4	0.398	6614		0.43
	100	300	267.9	0.429	6651		0.13
	500	300	576.9	0.923	6921		4.19

$$F_y = -\frac{S_{22}r^{2/3}}{V}N^{2/3}(\dot{y}_w - \dot{y}_r) = -C_{w-r}(\dot{y}_h - \dot{y}_r) \tag{5.30}$$

where $C_{w\text{-}r}$ is regarded as the additional damping induced by the wheel-rail lateral creep.

5.4.6 Hunting Assumption

In dynamic analysis of train-bridge system, as introduced in Chap. 3, the wheel-set hunting movement can be defined as a given relative motion between wheel-set and track. In the lateral y-direction, the resultant of wheel-set hunting and track irregularity is the relative displacement between the vehicle wheel-set and the bridge at the wheel-set position, or in other words, the wheel-set hunting is the relative displacement between the wheel-set and the wheel-rail contact point, which can be expressed as

$$y_w(x) = y_r(x) + y_h(x) \tag{5.31}$$

where y_w is the relative displacement between the vehicle wheel-set and the bridge at the wheel-set position; y_r is the track irregularity; y_h is the wheel-set hunting.

According to the hunting assumption, the lateral relative displacement between the wheel and the rail is a sinusoidal curve with the given wavelength and amplitude expressed as

$$y_{\mathrm{h}}(x) = A_{\mathrm{h}} \sin\left(\frac{2\pi x}{L_{\mathrm{h}}} + \varphi_{\mathrm{h}}\right) \tag{5.32}$$

where x is the geometry coordinate representing the position of wheel-set; A_{h}, L_{h}, and φ_{h} are, respectively, the amplitude, wavelength, and phase angle of the hunting. The phase angle φ_{h} of the hunting is the random variable uniformly distributed in $[0, 2\pi]$. The amplitude A_{h} and the wavelength L_{h} of the hunting are different for various wheel-sets, which obey some certain probability distribution as shown in Sect. 3.2 of this book.

Once the hunting parameters of the wheel-set are known, the lateral wheel-rail interaction force can be determined by the following method. As shown in Fig. 5.9, the displacement in the y-direction at points ① and ② is $y_{\mathrm{t}} + d_1\psi_{\mathrm{t}}$ for the front wheel-set on the bogie and is $y_{\mathrm{t}} - d_1\psi_{\mathrm{t}}$ for the rear. Thus, the lateral displacements at points ① ~ ④ in the figure are defined as

$$\begin{cases} y_1 = y_2 = y_{\mathrm{t}} + \eta \cdot d_1 \cdot \psi_{\mathrm{t}} - h_3\theta_{\mathrm{t}} \\ y_3 = y_4 = y_{\mathrm{w}} = y_{\mathrm{r}} + y_{\mathrm{h}} \end{cases} \tag{5.33}$$

where ψ_{t} is the bogie yawing displacement; h_3 is the vertical distance between the bogie center and the upper connection point of the primary suspension. The lateral interaction forces between the bogie and the wheel-set are expressed as

$$\begin{cases} Q_{13} = Q_{31} = k_{\mathrm{y1}}(y_1 - y_3) + c_{\mathrm{y1}}(\dot{y}_1 - \dot{y}_3) \\ Q_{24} = Q_{42} = k_{\mathrm{y1}}(y_2 - y_4) + c_{\mathrm{y1}}(\dot{y}_2 - \dot{y}_4) \end{cases} \tag{5.34}$$

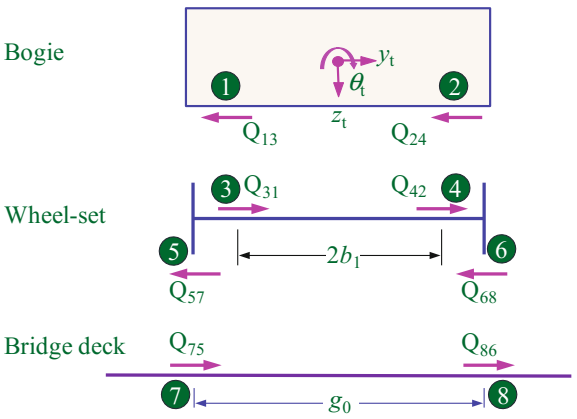

Fig. 5.9 Lateral wheel-rail interaction relationship

where k_{y1} and c_{y1} are the lateral stiffness and damping coefficients between the bogie and the wheel-set, respectively.

According to the equilibrium of the forces on the wheel-set, we have

$$Q_{57} + Q_{68} = Q_{31} + Q_{42} - m_w \ddot{y}_w = Q_{13} + Q_{24} - m_w(\ddot{y}_r + \ddot{y}_h) \tag{5.35}$$

The second derivative of y_h to time in the above equation can be calculated with reference to Eq. (5.15).

When using Eq. (5.19) to calculate the wheel-rail creep rate, if the train speed $V \to 0$, the denominator will be zero, which may cause an unreasonable creep rate result. Therefore, the hunting assumption can be an alternative to replace the Kalker's Creep Theory at the low train speeds, e.g., under braking condition. For the high-speed train, the above two lateral wheel-rail relationships can be selected, respectively, according to situations of high or low train speed, with their results coordinated by adjusting the phase angle φ_h of the hunting.

According to the current study, the actual hunting wavelength is consistent with the theoretical geometric hunting wavelength when the train speed is not very high, while for the high-speed train, the hunting movement is much more complicated, which needs further special research.

5.4.7 *Comparison of Various Wheel-Rail Relationship Models*

The above five wheel-rail interaction models in train-bridge coupling analysis have different characteristics, mainly in coordinates, wheel-rail contact assumptions, wheel-rail relative motion relationships, and wheel-rail contact parameters required in solution, which are summarized in Table 5.4.

Table 5.4 Summary of wheel-rail interaction calculation methods

Wheel-rail relationship model	Coordinate system	Type of w-r model	Feature of w-r relationship	W-r contact parameter
W-r correspondence contact	Natural coordinates	Wheel movement versus rail movement	Linear	No need
Hertz contact	Contact-spot coordinates	W-r force versus w-r relative movement	Nonlinear	Need
Kalker's creep with Shen's correction	Contact-spot coordinates	W-r force versus w-r relative movement	Nonlinear	Need
Simplified Kalker linear creep	Natural coordinates	W-r force versus w-r relative movement	Linear	No need
Hunting wave	Natural coordinates	Wheel movement versus rail movement	Linear	No need

These wheel-rail interaction models have their respective advantages, and all have been applied to the train-bridge coupling dynamic analysis. When local details of the wheel-rail contact state need to be calculated, e.g., in analysis of derailment process, it is applicable to adopt the Normal Hertz Contact Theory and Tangential Kaller Creep Theory with the Shen's Correction. If only the overall response of the train-bridge system is concerned, it is more reasonable to use the vertical wheel-rail correspondence assumption and lateral simplified Kalker linear creep theory or and lateral hunting assumption, because they can provide sufficient calculation accuracy while do not need wheel-rail contact parameters, with higher calculation efficiency by avoiding the complicated analysis of wheel-rail contact geometry.

5.5 Establishment of Train-Bridge System Motion Equations

In the vehicle modeling in this chapter, in terms of wheel-rail interaction, the wheel-rail correspondence contact assumption is adopted in the vertical direction and the simplified Kalker creep assumption in the lateral direction. The motion equations for the train-bridge coupling dynamic system can be established when the wheel-rail interaction model is determined.

5.5.1 Motion Equation of Vehicle Element

Firstly, the motion equation of a vehicle element is established, which can be expressed as

$$\mathbf{M}_{\mathrm{e}}\ddot{\mathbf{X}}_{\mathrm{e}} + \mathbf{C}_{\mathrm{e}}\dot{\mathbf{X}}_{\mathrm{e}} + \mathbf{K}_{\mathrm{e}}\mathbf{X}_{\mathrm{e}} = \mathbf{F}_{\mathrm{e}} \tag{5.36}$$

where subscript e denotes the vehicle element; $\mathbf{M}_{\mathrm{e}}$, $\mathbf{C}_{\mathrm{e}}$, and $\mathbf{K}_{\mathrm{e}}$ are, respectively, the mass, damping, and stiffness matrices; $\mathbf{F}_{\mathrm{e}}$ is the load vector; $\mathbf{X}_{\mathrm{e}}$ is the displacement vector, with each overhead dot representing a derivative with respect to the time t, resulting in the velocity vector $\dot{\mathbf{X}}_{\mathrm{e}}$ and acceleration vector $\ddot{\mathbf{X}}_{\mathrm{e}}$. The displacement vector is sequenced according to the DOFs as

$$\mathbf{X}_{\mathrm{e}} = \left\{ \mathbf{X}_{\mathrm{c}} \quad \mathbf{X}_{\mathrm{t1}} \quad \mathbf{X}_{\mathrm{t2}} \quad \mathbf{X}_{\mathrm{w1}} \quad \mathbf{X}_{\mathrm{w2}} \quad \mathbf{X}_{\mathrm{w3}} \quad \mathbf{X}_{\mathrm{w4}} \right\}^{\mathrm{T}} \tag{5.37}$$

where subscript c refers to car-body; subscripts t_1 and t_2 refer to the front and rear bogie, w_1 and w_2 to the wheel-sets associated with the front bogie, and w_3 and w_4 to the wheel-sets associated with the rear bogie, respectively.

In the vehicle element, five DOFs, namely lateral swing y, vertical floating z, rolling θ, yawing ψ, and pitching φ, are considered, respectively, for each car-body

or bogie. According to the wheel-rail vertical correspondence contact assumption and the lateral Kalker creep assumption, the motions in the y-, z-, and θ-directions are considered for each wheel-set. Therefore, the subvectors in Eq. (5.37) can be expressed as

$$\begin{cases} \mathbf{X}_{\mathrm{c}}=\{\, y_{\mathrm{c}} \quad z_{\mathrm{c}} \quad \theta_{\mathrm{c}} \quad \varphi_{\mathrm{c}} \quad \psi_{\mathrm{c}} \,\}, \\ \mathbf{X}_{\mathrm{t}j}=\{\, y_{\mathrm{t}j} \quad z_{\mathrm{t}j} \quad \theta_{\mathrm{t}j} \quad \varphi_{\mathrm{t}j} \quad \psi_{\mathrm{t}j} \,\}, & (j=1,2) \\ \mathbf{X}_{\mathrm{w}k}=\{\, y_{\mathrm{w}k} \quad z_{\mathrm{w}k} \quad \theta_{\mathrm{w}k} \,\}, & (k=1,2,3,4) \end{cases} \tag{5.38}$$

For the car-body and the bogie of the vehicle element, with subscript c representing the car-body and t the bogie, m denotes the mass, I_{x}, I_{y}, and I_{z} denote the moment of inertia around the x-, y-, and z-axes, respectively; d_2 is half the distance between bogies, b_2 is half lateral span of the secondary suspension; h_1 is the vertical distance from the center of the car-body to the upper connection point of secondary suspension; h_2 is the vertical distance from the lower connection point of secondary suspension to the center of bogie, as shown in Fig. 5.4.

For the car-body, the motion equations with respect to the five DOFs of lateral swing y, vertical floating z, rolling θ, yawing ψ, and pitching φ are established and expressed as

$$\begin{aligned} &2k_{\mathrm{y}2}\left[\sum_{j=1}^{2}\left(y_{\mathrm{t}j}+\theta_{\mathrm{t}j}h_2\right)-2y_{\mathrm{c}}+2\theta_{\mathrm{c}}h_1\right]+2c_{\mathrm{y}2}\left\{\sum_{j=1}^{2}\left(\dot{y}_{\mathrm{t}j}+\dot{\theta}_{\mathrm{t}j}h_2\right)-2\dot{y}_{\mathrm{c}}+2\dot{\theta}_{\mathrm{c}}h_1\right\} \\ &\quad=m_{\mathrm{c}}\ddot{y}_{\mathrm{c}} \end{aligned} \tag{5.39}$$

$$2k_{\mathrm{z}2}\left(\sum_{j=1}^{2}z_{\mathrm{t}j}-2z_{\mathrm{c}}\right)+2c_{\mathrm{z}2}\left(\sum_{j=1}^{2}\dot{z}_{\mathrm{t}j}-2\dot{z}_{\mathrm{c}}\right)=m_{\mathrm{c}}\ddot{z}_{\mathrm{c}} \tag{5.40}$$

$$\begin{aligned} &2k_{\mathrm{y}2}h_1\left(-\sum_{j=1}^{2}\left(y_{\mathrm{t}j}+\theta_{\mathrm{t}j}h_2\right)+2y_{\mathrm{c}}-2\theta_{\mathrm{c}}h_1\right)+2k_{\mathrm{z}2}b_2^2\left(\sum_{j=1}^{2}\theta_{\mathrm{t}j}-2\theta_{\mathrm{c}}\right) \\ &\quad+2c_{\mathrm{y}2}h_1\left(-\sum_{j=1}^{2}\left(\dot{y}_{\mathrm{t}j}+\dot{\theta}_{\mathrm{t}j}h_2\right)+2\dot{y}_{\mathrm{c}}-2\dot{\theta}_{\mathrm{c}}h_1\right)+2c_{\mathrm{z}2}b_2^2\left(\sum_{j=1}^{2}\dot{\theta}_{\mathrm{t}j}-2\dot{\theta}_{\mathrm{c}}\right)=I_{\mathrm{xc}}\ddot{\theta}_{\mathrm{c}} \end{aligned} \tag{5.41}$$

$$\begin{aligned} &2k_{\mathrm{x}2}h_1\left(-\sum_{j=1}^{2}\varphi_{\mathrm{t}j}h_2-2\varphi_{\mathrm{c}}h_1\right)+2k_{\mathrm{z}2}d_2\left(\sum_{j=1}^{2}\zeta_j z_{\mathrm{t}j_{\mathrm{c}}}-2\varphi_{\mathrm{c}}d_2\right) \\ &\quad+2c_{\mathrm{x}2}h_1\left(-\sum_{j=1}^{2}\dot{\varphi}_{\mathrm{t}j}h_2-2\dot{\varphi}_{\mathrm{c}}h_1\right)+2c_{\mathrm{z}2}d_2\left(\sum_{j=1}^{2}\zeta_j\dot{z}_{\mathrm{t}j}-2\dot{\varphi}_{\mathrm{c}}d_2\right)=I_{\mathrm{yc}}\ddot{\varphi}_{\mathrm{c}} \end{aligned} \tag{5.42}$$

$$2k_{x2}b_2^2\left(\sum_{j=1}^{2}\psi_{tj}-2\psi_c\right)+2k_{y2}d_2\left(\sum_{j=1}^{2}\zeta_j\left(y_{tj}+\theta_{tj}h_2\right)-2\psi_c d_2\right)$$
$$+2c_{x2}b_2^2\left(\sum_{j=1}^{2}\dot{\psi}_{tj}-2\dot{\psi}_c\right)+2c_{y2}d_2\left(\sum_{j=1}^{2}\zeta_j\left(\dot{y}_{tj}+\dot{\theta}_{tj}h_2\right)-2\dot{\psi}_c d_2\right)=I_{zc}\ddot{\psi}_c \tag{5.43}$$

where ζ_j is the sign function; $\zeta_1 = 1$ for front bogie, $\zeta_2 = -1$ for rear bogie.

For the bogie, define front bogie $j = 1$ and rear bogie $j = 2$, the motion equations with respect to the five DOFs of lateral swing y, vertical floating z, rolling θ, yawing ψ, and pitching φ are expressed as

$$2k_{y1}\left(-2y_{tj}+2\theta_{tj}h_3+\sum_{k=2j-1}^{2j}y_{wk}\right)+2k_{y2}\left(y_c-\theta_c h_1+\zeta_j\psi_c d_2-y_{tj}-\theta_{tj}h_2\right)$$
$$+2c_{y1}\left(-2\dot{y}_{ti}+2\dot{\theta}_{ti}h_3+\sum_{k=2j-1}^{2j}\dot{y}_{wk}\right)+2c_{y2}\left(\dot{y}_c-\dot{\theta}_c h_1+\zeta_j\dot{\psi}_c d_2-\dot{y}_{tj}-\dot{\theta}_{tj}h_2\right)=m_t\ddot{y}_{tj} \tag{5.44}$$

$$2k_{z1}\left(\sum_{k=2j-2}^{2j}z_{wk}-2z_{ti}\right)+2k_{z2}\left(z_c+\zeta\varphi_c d_2-z_{tj}\right)+2c_{z1}\left(\sum_{k=2j-2}^{2j}\dot{z}_{wk}-2\dot{z}_{ti}\right)$$
$$+2c_{z2}\left(\dot{z}_c+\zeta\dot{\varphi}_c d_2-\dot{z}_{tj}\right)=m_t\ddot{z}_{tj} \tag{5.45}$$

$$2k_{y1}h_3\left(2y_{tj}-2\theta_{tj}h_3-\sum_{k=2j-1}^{2j}y_{wk}\right)+2k_{z1}b_1^2\left(-2\theta_{tj}+\sum_{k=2j-1}^{2j}\theta_{wk}\right)$$
$$+2k_{y2}h_2\left(y_{tj}+\theta_{tj}h_2-y_c+\theta_c h_1-\zeta_j\psi_c d_2\right)+2k_{z2}b_2^2\left(\theta_c-\theta_{tj}\right)$$
$$+2c_{y1}h_3\left(2\dot{y}_{tj}-2\dot{\theta}_{tj}h_3-\sum_{k=2j-1}^{2j}\dot{y}_{wk}\right)+2c_{z1}b_1^2\left(-2\dot{\theta}_{tj}+\sum_{k=2j-1}^{2j}\dot{\theta}_{wk}\right)$$
$$+2c_{y2}h_2\left(\dot{y}_{tj}+\dot{\theta}_{tj}h_2-\dot{y}_c+\dot{\theta}_c h_1-\zeta_j\dot{\psi}_c d_2\right)+2c_{z2}b_2^2\left(\dot{\theta}_c-\dot{\theta}_{tj}\right)=I_{xt}\ddot{\theta}_{tj} \tag{5.46}$$

$$-4k_{x1}h_3^2\varphi_{tj}+2k_{z1}d_1\left(-2\varphi_{ti}d_1+\sum_{k=2j-1}^{2j}\eta_k z_{wk}\right)+2k_{x2}h_2\left(-\varphi_c h_1-\varphi_{tj}h_2\right)$$
$$-4c_{x1}h_3^2\dot{\varphi}_{tj}+2c_{z1}d_1\left(-2\dot{\varphi}_{ti}d_1+\sum_{k=2j-1}^{2j}\eta_k\dot{z}_{wk}\right)+2c_{x2}h_2\left(-\dot{\varphi}_c h_1-\dot{\varphi}_{tj}h_2\right)=I_{yt}\ddot{\varphi}_{ti} \tag{5.47}$$

$$-4k_{x1}b_1^2\psi_{tj}+2k_{y1}d_1\left(-2\psi_{tj}d_1+\sum_{k=2j-1}^{2j}\eta_k y_{wk}\right)+2k_{x2}b_2^2\left(\psi_c-\psi_{tj}\right)$$
$$-4c_{x1}b_2^2\dot{\psi}_{tj}+2c_{y1}d_1\left(-2\dot{\psi}_{tj}d_1+\sum_{k=2j-1}^{2j}\eta_k\dot{y}_{wk}\right)+2c_{x2}b_2^2\left(\dot{\psi}_c-\dot{\psi}_{tj}\right)=I_{zt}\ddot{\psi}_{tj} \tag{5.48}$$

where η_k is sign function; $\eta_1 = \eta_3 = 1$ for the wheel-sets at the front of the bogie; $\eta_2 = \eta_4 = -1$ for the wheel-sets at the rear of the bogie.

For the kth wheel-set connected to the jth bogie, the motion equations with respect to the three DOFs of lateral swing y, vertical floating z, and rolling θ are expressed as

$$2k_{y1}\left(y_{tj}-\theta_{tj}h_3+\eta_{jk}\psi_{tj}d_1-y_{wk}\right)+2c_{y1}\left(\dot{y}_{tj}-\dot{\theta}_{tj}h_3+\eta_{jk}\dot{\psi}_{tj}d_1-\dot{y}_{wk}\right)=m_w\ddot{y}_{wk} \tag{5.49}$$

$$2k_{z1}\left(z_{tj}+\eta_k\varphi_{tj}d_1-z_{wk}\right)+2c_{z1}\left(\dot{z}_{tj}+\eta_k\dot{\varphi}_{tj}d_1-\dot{z}_{wk}\right)=m_w\ddot{z}_{wk} \tag{5.50}$$

$$2k_{z1}b_1^2\left(\theta_{tj}-\theta_{wk}\right)+2c_{z1}b_1^2\left(\dot{\theta}_{tj}-\dot{\theta}_{wk}\right)=I_{xw}\ddot{\theta}_{wk} \tag{5.51}$$

In Eq. (5.36), $\mathbf{F}_e$ is the load vector of vehicle element. According to the wheel-rail interaction model adopted, the excitation to the vehicle element consists of two parts:

(1) The y-direction forces from wheel-sets $w_1 \sim w_4$ determined by the simplified Kalker Creep Theory, the excitation of this part is expressed as the right side vector of the equation, because the element of the DOF where the right side vector ($\mathbf{F}_e$) of Eq. (5.36) corresponds to the direction of wheel-set is not zero.
(2) The z-direction and θ-direction forces determined by the wheel-set displacements $z_{w1} \sim z_{w4}$ and $\theta_{w1} \sim \theta_{w4}$, according to the vertical wheel-rail correspondence. This part of excitation is expressed by the forced movement of wheel-sets. To introduce the forced movement of wheel-sets, it is necessary to simultaneously solve the bridge equation and the vehicle equation. In other words, $z_{w1} \sim z_{w4}$ and $\theta_{w1} \sim \theta_{w4}$ are dependent on the motion state of the bridge and the track irregularity. These factors are the known external boundary conditions of vehicle element, which should be moved to the right side of the equation, and the related DOFs in the equation be eliminated.

Based on the above treatment, the motion equation of the vehicle element is defined. In other words, adopting the wheel-rail correspondence assumption means to provide a set of given time-varying boundary conditions for the vehicle element, thus the movements corresponding to wheel-sets in vectors $\mathbf{X}_e$, $\dot{\mathbf{X}}_e$ and $\ddot{\mathbf{X}}_e$ of

Eq. (5.36) are known. For the vehicle element, this is similar to the common seismic time history analysis of structures.

In Eq. (5.36), the mass, damping, and stiffness matrices $\mathbf{M}_e$, $\mathbf{C}_e$, and $\mathbf{K}_e$ of vehicle element are all constant matrices, which can be obtained from Eqs. (5.39)–(5.51).

Equation (5.36) is the motion equation of the vehicle element without considering the boundary conditions. After rearrangement, it can be separated into dependent DOFs and independent DOFs and expressed as

$$\begin{bmatrix} \mathbf{M}_{ff} & \mathbf{0} \\ \mathbf{0} & \mathbf{M}_{ss} \end{bmatrix} \begin{Bmatrix} \ddot{\mathbf{X}}_f \\ \ddot{\mathbf{X}}_s \end{Bmatrix} + \begin{bmatrix} \mathbf{C}_{ff} & \mathbf{C}_{fs} \\ \mathbf{C}_{sf} & \mathbf{C}_{ss} \end{bmatrix} \begin{Bmatrix} \dot{\mathbf{X}}_f \\ \dot{\mathbf{X}}_s \end{Bmatrix} + \begin{bmatrix} \mathbf{K}_{ff} & \mathbf{K}_{fs} \\ \mathbf{K}_{sf} & \mathbf{K}_{ss} \end{bmatrix} \begin{Bmatrix} \mathbf{X}_f \\ \mathbf{X}_s \end{Bmatrix} = \begin{Bmatrix} \mathbf{F}_f \\ \mathbf{0} \end{Bmatrix} \tag{5.52}$$

where $\mathbf{X}_f$ is the displacement vector of free (independent) DOFs, and $\mathbf{X}_s$ is the displacement vector of supported (dependent) DOFs, respectively, expressed as

$$\mathbf{X}_f = \{ \mathbf{X}_c \quad \mathbf{X}_{t1} \quad \mathbf{X}_{t2} \quad y_{w1} \quad y_{w2} \quad y_{w3} \quad y_{w4} \}^T \tag{5.53}$$

$$\mathbf{X}_s = \{ z_{w1} \quad \theta_{w1} \quad z_{w2} \quad \theta_{w2} \quad z_{w3} \quad \theta_{w3} \quad z_{w4} \quad \theta_{w4} \}^T \tag{5.54}$$

By eliminating the dependent DOFs ($\mathbf{X}_s$), the motion equations corresponding to the independent DOFs can be obtained as

$$\mathbf{M}_{ff}\ddot{\mathbf{X}}_f + \mathbf{C}_{ff}\dot{\mathbf{X}}_f + \mathbf{K}_{ff}\mathbf{X}_f = \mathbf{F}_f - \mathbf{C}_{fs}\dot{\mathbf{X}}_s - \mathbf{K}_{fs}\mathbf{X}_s \tag{5.55}$$

The wheel-rail lateral creep forces acting on four wheel-sets of the vehicle element are reflected in the corresponding DOFs of wheel-set in the right side term $\mathbf{F}_e$ of Eq. (5.36), thus

$$\mathbf{F}_f = \frac{2f_{22}}{V} \begin{Bmatrix} \mathbf{0}_{15\times1} \\ \dot{y}_{r1} - \dot{y}_{w1} \\ \dot{y}_{r2} - \dot{y}_{w2} \\ \dot{y}_{r3} - \dot{y}_{w3} \\ \dot{y}_{r4} - \dot{y}_{w4} \end{Bmatrix} = \frac{2f_{22}}{V} \begin{Bmatrix} \mathbf{0}_{15\times1} \\ \dot{y}_{r1} \\ \dot{y}_{r2} \\ \dot{y}_{r3} \\ \dot{y}_{r4} \end{Bmatrix} - \frac{2f_{22}}{V} \begin{Bmatrix} \mathbf{0}_{15\times1} \\ \dot{y}_{w1} \\ \dot{y}_{w2} \\ \dot{y}_{w3} \\ \dot{y}_{w4} \end{Bmatrix} \tag{5.56}$$

By defining

$$\mathbf{F}_{fr} = \frac{2f_{22}}{V} \{ \mathbf{0}_{1\times15} \quad \dot{y}_{r1} \quad \dot{y}_{r2} \quad \dot{y}_{r3} \quad \dot{y}_{r4} \}^T \tag{5.57}$$

$$\mathbf{C}_c = \frac{2f_{22}}{V} \begin{bmatrix} \mathbf{0}_{15\times15} & \\ & \mathbf{I}_{4\times4} \end{bmatrix} \tag{5.58}$$

$$\dot{\mathbf{X}}_{\mathrm{f}} = \{\, \mathbf{0}_{1\times 15} \quad \dot{y}_{\mathrm{w1}} \quad \dot{y}_{\mathrm{w2}} \quad \dot{y}_{\mathrm{w3}} \quad \dot{y}_{\mathrm{w4}} \,\}^{\mathrm{T}}, \tag{5.59}$$

Equation (5.56) can be rewritten as

$$\mathbf{F}_{\mathrm{f}} = \mathbf{F}_{\mathrm{fr}} - \mathbf{C}_{\mathrm{c}}\dot{\mathbf{X}}_{\mathrm{f}} \tag{5.60}$$

With the vehicle motion terms moved to the left side of the equation, the right side of the equation only includes the terms related to bridge motion, track irregularity at the wheel position, and its additional velocity, thus the motion equation of vehicle element can be rewritten as

$$\mathbf{M}_{\mathrm{ff}}\ddot{\mathbf{X}}_{\mathrm{f}} + (\mathbf{C}_{\mathrm{ff}} + \mathbf{C}_{\mathrm{c}})\dot{\mathbf{X}}_{\mathrm{f}} + \mathbf{K}_{\mathrm{ff}}\mathbf{X}_{\mathrm{f}} = \mathbf{F}_{\mathrm{fr}} - \mathbf{C}_{\mathrm{fs}}\dot{\mathbf{X}}_{\mathrm{s}} - \mathbf{K}_{\mathrm{fs}}\mathbf{X}_{\mathrm{s}} = \mathbf{F}_{\mathrm{fe}} \tag{5.61}$$

where

$$\mathbf{M}_{\mathrm{ff}} = \mathrm{diag}[\,\mathbf{M}_{\mathrm{c}} \quad \mathbf{M}_{\mathrm{t1}} \quad \mathbf{M}_{\mathrm{t2}} \quad \mathbf{M}_{\mathrm{w}}\,] \tag{5.62}$$

$$\mathbf{K}_{\mathrm{ff}} = \begin{bmatrix} \mathbf{K}_{\mathrm{cc}} & & & & \text{sym.} \\ \mathbf{K}_{\mathrm{tc}}(1) & \mathbf{K}_{\mathrm{tt1}} + \mathbf{K}_{\mathrm{tt2}} & & & \\ \mathbf{K}_{\mathrm{tc}}(-1) & \mathbf{0} & \mathbf{K}_{\mathrm{tt1}} + \mathbf{K}_{\mathrm{tt2}} & & \\ \mathbf{0} & \mathbf{K}_{\mathrm{wt}} & \mathbf{0} & \mathbf{K}_{\mathrm{ww}} & \\ \mathbf{0} & \mathbf{0} & \mathbf{K}_{\mathrm{wt}} & \mathbf{0} & \mathbf{K}_{\mathrm{ww}} \end{bmatrix} \tag{5.63}$$

$$\mathbf{M}_{\mathrm{c}} = \mathrm{diag}[\,m_{\mathrm{c}} \quad m_{\mathrm{c}} \quad I_{\mathrm{xc}} \quad I_{\mathrm{yc}} \quad I_{\mathrm{zc}}\,] \tag{5.64}$$

$$\mathbf{M}_{\mathrm{t1}} = \mathbf{M}_{\mathrm{t2}} = \mathrm{diag}[\,m_{\mathrm{t}} \quad m_{\mathrm{t}} \quad I_{\mathrm{xt}} \quad I_{\mathrm{yt}} \quad I_{\mathrm{zt}}\,] \tag{5.65}$$

$$\mathbf{M}_{\mathrm{w}} = \mathrm{diag}[\,m_{\mathrm{w}} \quad m_{\mathrm{w}} \quad m_{\mathrm{w}} \quad m_{\mathrm{w}}\,] \tag{5.66}$$

$$\mathbf{K}_{\mathrm{cc}} = 4\begin{bmatrix} k_{\mathrm{y2}} & & & & \text{sym.} \\ 0 & k_{\mathrm{z2}} & & & \\ -k_{\mathrm{y2}}h_1 & 0 & k_{\mathrm{y2}}h_1^2 + k_{\mathrm{z2}}b_2^2 & & \\ 0 & 0 & 0 & k_{\mathrm{x2}}h_1^2 + k_{\mathrm{z2}}d_2^2 & \\ 0 & 0 & 0 & 0 & k_{\mathrm{x2}}b_2^2 + k_{\mathrm{y2}}d_2^2 \end{bmatrix} \tag{5.67}$$

$$\mathbf{K}_{\mathrm{tt1}} = 4\begin{bmatrix} k_{\mathrm{y1}} & & & & \text{sym.} \\ 0 & k_{\mathrm{z1}} & & & \\ -k_{\mathrm{y1}}h_3 & 0 & k_{\mathrm{y1}}h_3^2 + k_{\mathrm{z1}}b_1^2 & & \\ 0 & 0 & 0 & k_{\mathrm{x1}}h_3^2 + k_{\mathrm{z1}}d_1^2 & \\ 0 & 0 & 0 & 0 & k_{\mathrm{x1}}b_1^2 + k_{\mathrm{y1}}d_1^2 \end{bmatrix} \tag{5.68}$$

$$\mathbf{K}_{\mathrm{tt2}} = 2\begin{bmatrix} k_{\mathrm{y2}} & & & & \text{sym.} \\ 0 & k_{\mathrm{z2}} & & & \\ k_{\mathrm{y2}}h_2 & 0 & k_{\mathrm{y2}}h_2^2 + k_{\mathrm{z2}}b_2^2 & & \\ 0 & 0 & 0 & k_{\mathrm{x2}}h_2^2 & \\ 0 & 0 & 0 & 0 & k_{\mathrm{x2}}b_2^2 \end{bmatrix} \tag{5.69}$$

$$\mathbf{K}_{\mathrm{ww}} = 2\begin{bmatrix} k_{\mathrm{y1}} & \text{sym.} \\ 0 & k_{\mathrm{y1}} \end{bmatrix} \tag{5.70}$$

$$\mathbf{K}_{\mathrm{tc}}(i) = 2\begin{bmatrix} -k_{\mathrm{y2}} & 0 & k_{\mathrm{y2}}h_1 & 0 & -ik_{\mathrm{y2}}d_2 \\ 0 & -k_{\mathrm{z2}} & 0 & -ik_{\mathrm{z2}}d_2 & 0 \\ -k_{\mathrm{y2}}h_2 & 0 & k_{\mathrm{y2}}h_1h_2 - k_{\mathrm{z2}}b_2^2 & 0 & -ik_{\mathrm{y2}}d_2h_2 \\ 0 & 0 & 0 & k_{\mathrm{x2}}h_1h_2 & 0 \\ 0 & 0 & 0 & 0 & -k_{\mathrm{x2}}b_2^2 \end{bmatrix} \tag{5.71}$$

$$\mathbf{K}_{\mathrm{wt}} = 2\begin{bmatrix} -k_{\mathrm{y1}} & 0 & k_{\mathrm{y1}}h_3 & 0 & -k_{\mathrm{y1}}d_1 \\ -k_{\mathrm{y1}} & 0 & k_{\mathrm{y1}}h_3 & 0 & k_{\mathrm{y1}}d_1 \end{bmatrix} \tag{5.72}$$

Note that the same arrangement of spring assembly and dashpots in the vehicle model, the expression form of damping matrix $\mathbf{C}_{\mathrm{ff}}$ is similar to the stiffness matrix $\mathbf{K}_{\mathrm{ff}}$, thus $\mathbf{C}_{\mathrm{ff}}$ can be obtained simply by replacing the spring coefficients in stiffness matrix $\mathbf{K}_{\mathrm{ff}}$ with the corresponding damping coefficients.

Defining $y_{\mathrm{r}k}$, $z_{\mathrm{r}k}$, and $\theta_{\mathrm{r}k}$ as the rail displacements in the y-, z-, and θ-directions at the position of the kth wheel-set, respectively, and F_i as the ith nonzero element of $\mathbf{F}_{\mathrm{fe}}$ in Eq. (5.61), we have

$$\begin{Bmatrix} F_7 \\ F_8 \\ F_9 \end{Bmatrix} = 2k_{\mathrm{z1}}\begin{Bmatrix} z_{\mathrm{r1}} + z_{\mathrm{r2}} \\ b_1^2(\theta_{\mathrm{r1}} + \theta_{\mathrm{r2}}) \\ d_1(z_{\mathrm{r1}} - z_{\mathrm{r2}}) \end{Bmatrix} + 2c_{\mathrm{z1}}\begin{Bmatrix} \dot{z}_{\mathrm{r1}} + \dot{z}_{\mathrm{r2}} \\ b_1^2\left(\dot{\theta}_{\mathrm{r1}} + \dot{\theta}_{\mathrm{r2}}\right) \\ d_1(\dot{z}_{\mathrm{r1}} - \dot{z}_{\mathrm{r2}}) \end{Bmatrix} \tag{5.73}$$

$$\begin{Bmatrix} F_{12} \\ F_{13} \\ F_{14} \end{Bmatrix} = 2k_{\mathrm{z1}}\begin{Bmatrix} z_{\mathrm{r3}} + z_{\mathrm{r4}} \\ b_1^2(\theta_{\mathrm{r3}} + \theta_{\mathrm{r4}}) \\ d_1(z_{\mathrm{r3}} - z_{\mathrm{r4}}) \end{Bmatrix} + 2c_{\mathrm{z1}}\begin{Bmatrix} \dot{z}_{\mathrm{r3}} + \dot{z}_{\mathrm{r4}} \\ b_1^2\left(\dot{\theta}_{\mathrm{r3}} + \dot{\theta}_{\mathrm{r4}}\right) \\ d_1(\dot{z}_{\mathrm{r3}} - \dot{z}_{\mathrm{r4}}) \end{Bmatrix} \tag{5.74}$$

$$\begin{Bmatrix} F_{16} \\ F_{17} \\ F_{18} \\ F_{19} \end{Bmatrix} = \frac{2f_{22}}{V}\begin{Bmatrix} \dot{y}_{\mathrm{r1}} \\ \dot{y}_{\mathrm{r2}} \\ \dot{y}_{\mathrm{r3}} \\ \dot{y}_{\mathrm{r4}} \end{Bmatrix} \tag{5.75}$$

As shown in Fig. 5.10, the forces from the kth wheel-set acting on the bridge in the y-, z-, and θ-direction are

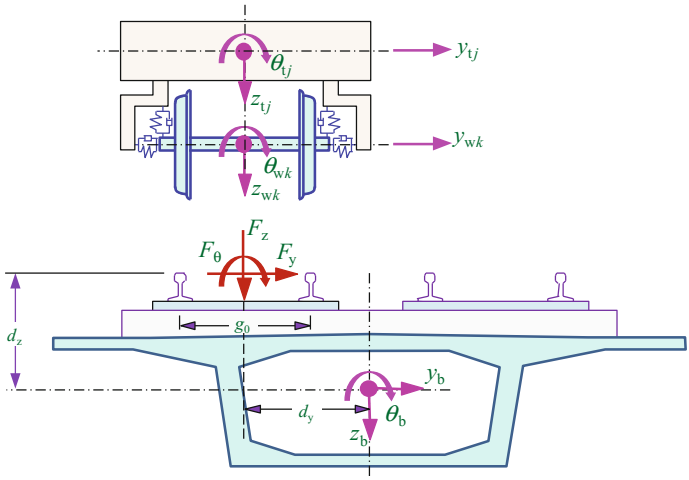

Fig. 5.10 Force vector ($\mathbf{F}_d$) acting on the bridge

$$F_y = \frac{2f_{22}}{V}(\dot{y}_{wk} - \dot{y}_{rk}) \tag{5.76}$$

$$F_\theta = 2k_{z1}b_1^2(\theta_{tj} - \theta_{rk}) + 2c_{z1}b_1^2\left(\dot{\theta}_{tj} - \dot{\theta}_{rk}\right) - I_{xw}\ddot{\theta}_{rk} \tag{5.77}$$

$$F_z = 2k_{z1}\left(z_{tj} + \eta_k d_1 \varphi_{tj} - z_{rk}\right) + 2c_{z1}\left(\dot{z}_{tj} + \eta_k d_1 \dot{\varphi}_{tj} - \dot{z}_{rk}\right) + G - m_w\ddot{z}_{rk} \tag{5.78}$$

where z_{tj}, θ_{tj} and φ_{tj} are, respectively, the displacements of the jth bogie where the kth wheel-set locates in the z-, θ-, and φ-directions.

In the current train-bridge coupling dynamic analysis, the linkage between vehicle elements is usually neglected (Cao 1991; Zeng and Guo 1999; Li 2000; Xia and Zhang 2005a, b; Zhang et al. 2008; Pan and Gao 2008; Xia et al. 2012), namely, the vehicles are mutually independent. Consequently, for a train composed of N_v vehicles, the total mass, damping, and stiffness matrices and the total displacement and force vectors can be, respectively, expressed as

$$\mathbf{M}_v = \mathrm{diag}\{\,\mathbf{M}_{ff1} \quad \mathbf{M}_{ff2} \quad \mathbf{M}_{ff3} \quad \cdots \quad \mathbf{M}_{ffN_v}\,\}^T \tag{5.79}$$

$$\mathbf{C}_v = \mathrm{diag}\{\,\mathbf{C}_{ff1} + \mathbf{C}_{c1} \quad \mathbf{C}_{ff2} + \mathbf{C}_{c2} \quad \mathbf{C}_{ff3} + \mathbf{C}_{c3} \quad \cdots \quad \mathbf{C}_{ffN_v} + \mathbf{C}_{cN_v}\,\}^T \tag{5.80}$$

$$\mathbf{K}_v = \mathrm{diag}\{\,\mathbf{K}_{ff1} \quad \mathbf{K}_{ff2} \quad \mathbf{K}_{ff3} \quad \cdots \quad \mathbf{K}_{ffN_v}\,\}^T \tag{5.81}$$

$$\mathbf{X}_v = \{\,\mathbf{X}_{f1} \quad \mathbf{X}_{f2} \quad \mathbf{X}_{f3} \quad \cdots \quad \mathbf{X}_{fN_v}\,\}^T \tag{5.82}$$

$$\mathbf{F}_{\mathrm{v}} = \{\, \mathbf{F}_{\mathrm{fe1}} \quad \mathbf{F}_{\mathrm{fe2}} \quad \mathbf{F}_{\mathrm{fe3}} \quad \cdots \quad \mathbf{F}_{\mathrm{fe}N_{\mathrm{v}}} \,\}^{\mathrm{T}} \tag{5.83}$$

Thus, the motion equation for the train subsystem can be expressed as

$$\mathbf{M}_{\mathrm{v}}\ddot{\mathbf{X}}_{\mathrm{v}} + \mathbf{C}_{\mathrm{v}}\dot{\mathbf{X}}_{\mathrm{v}} + \mathbf{K}_{\mathrm{v}}\mathbf{X}_{\mathrm{v}} = \mathbf{F}_{\mathrm{v}} \tag{5.84}$$

5.5.2 *Motion Equation of Train-Bridge Coupling System*

The motion equations for the train-bridge coupling system can be obtained by combining Eq. (5.84) with Eqs. (5.1) or (5.3), and by superposition of all wheel-set forces from Eqs. (5.76)–(5.78), to form the force vector $\mathbf{F}_{\mathrm{b}}$ of bridge subsystem.

When the bridge subsystem model is established by the direct stiffness method, the motion equation for the train-bridge system is

$$\begin{cases} \mathbf{M}_{\mathrm{v}}\ddot{\mathbf{X}}_{\mathrm{v}} + \mathbf{C}_{\mathrm{v}}\dot{\mathbf{X}}_{\mathrm{v}} + \mathbf{K}_{\mathrm{v}}\mathbf{X}_{\mathrm{v}} = \mathbf{F}_{\mathrm{v}} \\ \mathbf{M}_{\mathrm{b}}\ddot{\mathbf{X}}_{\mathrm{b}} + \mathbf{C}_{\mathrm{b}}\dot{\mathbf{X}}_{\mathrm{b}} + \mathbf{K}_{\mathrm{b}}\mathbf{X}_{\mathrm{b}} = \mathbf{F}_{\mathrm{b}} \end{cases} \tag{5.85}$$

When the modal decomposition method is adopted, the motion equation for the train-bridge system is

$$\begin{cases} \mathbf{M}_{\mathrm{v}}\ddot{\mathbf{X}}_{\mathrm{v}} + \mathbf{C}_{\mathrm{v}}\dot{\mathbf{X}}_{\mathrm{v}} + \mathbf{K}_{\mathrm{v}}\mathbf{X}_{\mathrm{v}} = \mathbf{F}_{\mathrm{v}} \\ \ddot{\mathbf{Q}}_{\mathrm{b}} + 2\boldsymbol{\xi}\boldsymbol{\omega}\dot{\mathbf{Q}}_{\mathrm{b}} + \boldsymbol{\omega}^2\mathbf{Q}_{\mathrm{b}} = \boldsymbol{\Phi}^{\mathrm{T}}\mathbf{F}_{\mathrm{b}} \end{cases} \tag{5.86}$$

In the above two equations, the force factors at the right side of the equation are the wheel-rail forces on the train and the bridge, as well as the gravity of bridge structure. When the external loads $\mathbf{F}_{\mathrm{v}}^{\mathrm{e}}$ and $\mathbf{F}_{\mathrm{b}}^{\mathrm{e}}$ are considered, the above equations are extended to

$$\begin{cases} \mathbf{M}_{\mathrm{v}}\ddot{\mathbf{X}}_{\mathrm{v}} + \mathbf{C}_{\mathrm{v}}\dot{\mathbf{X}}_{\mathrm{v}} + \mathbf{K}_{\mathrm{v}}\mathbf{X}_{\mathrm{v}} = \mathbf{F}_{\mathrm{v}} + \mathbf{F}_{\mathrm{v}}^{\mathrm{e}} \\ \mathbf{M}_{\mathrm{b}}\ddot{\mathbf{X}}_{\mathrm{b}} + \mathbf{C}_{\mathrm{b}}\dot{\mathbf{X}}_{\mathrm{b}} + \mathbf{K}_{\mathrm{b}}\mathbf{X}_{\mathrm{b}} = \mathbf{F}_{\mathrm{b}} + \mathbf{F}_{\mathrm{b}}^{\mathrm{e}} \end{cases} \tag{5.87}$$

or

$$\begin{cases} \mathbf{M}_{\mathrm{v}}\ddot{\mathbf{X}}_{\mathrm{v}} + \mathbf{C}_{\mathrm{v}}\dot{\mathbf{X}}_{\mathrm{v}} + \mathbf{K}_{\mathrm{v}}\mathbf{X}_{\mathrm{v}} = \mathbf{F}_{\mathrm{v}} + \mathbf{F}_{v}^{\mathrm{e}} \\ \ddot{\mathbf{Q}}_{\mathrm{b}} + 2\boldsymbol{\xi}\boldsymbol{\omega}\dot{\mathbf{Q}}_{\mathrm{b}} + \boldsymbol{\omega}^2\mathbf{Q}_{\mathrm{b}} = \boldsymbol{\Phi}^{\mathrm{T}}\left(\mathbf{F}_{\mathrm{b}} + \mathbf{F}_{\mathrm{b}}^{\mathrm{e}}\right) \end{cases} \tag{5.88}$$

The dynamic analyses of the train-bridge system under external loads will be discussed in the subsequent chapters of this book. In the following sections of this chapter, only the case without external loads is studied

In Eqs. (5.73)–(5.75), the motion states of the track at wheel-set positions are $y_{\mathrm{r}1} \sim y_{\mathrm{r}4}$, $z_{\mathrm{r}1} \sim z_{\mathrm{r}4}$ and $\theta_{\mathrm{r}1} \sim \theta_{\mathrm{r}4}$, which are all motion state of bridge subsystem, and in Eqs. (5.76)–(5.78), $y_{\mathrm{w}k}$, $z_{\mathrm{t}j}$, $\theta_{\mathrm{t}j}$ and $\varphi_{\mathrm{t}j}$ (k = 1, 2, 3, 4; j = 1, 2) refer to the

motion state of the vehicle element. It can be seen that the two equations in Eqs. (5.85) or (5.86) are coupled, and iteration should be used for solving them.

What need to be noticed is that the wheel-rail forces on the vehicle element and the bridge are acting and reacting relationship between each other, but the load vector $\mathbf{F}_b$ of bridge subsystem and the load vector $\mathbf{F}_v$ of train subsystem are not. This is because that in Eq. (5.84), the terms related to the motion state of vehicles have been moved to the left side of the equation, thus $\mathbf{F}_v$ is only a part of wheel-rail forces, while in Eqs. (5.1) or (5.3), $\mathbf{F}_b$ contains all wheel-rail forces.

Moreover, the motion state of vehicle wheel-set in the z- and θ-direction is determined by that of bridge; thus, the wheel-set is essentially a part of the bridge subsystem, and its inertial forces in the z- and θ-direction should be applied to the bridge. In addition, the zero-coordinate of vehicle element locates at the gravity balance position, so the gravity action need not be considered in modeling the vehicle element, while it should be applied on the bridge. In short, the load vector $\mathbf{F}_b$ acting on the bridge should include the inertial force of wheel-set and the gravity of the vehicle while the load vector $\mathbf{F}_v$ on train subsystem need not.

5.6 Solution Methods for Train-Bridge Coupling System

There are various methods for solving the motion equation of train-bridge coupling system. Due to the time-varying feature of train-bridge system, at present, all the methods are based upon the time history integral technique, such as the Newmark-β integration and Wilson-θ integration. In terms of solution in the time domain, the major difference in various methods lies in how to handle the coupling relationship between the train subsystem and the bridge subsystem, or how to find a set of wheel-rail interaction force and motion state to meet the two subsystems simultaneously. In this section, three main methods for solving train-bridge coupling system are introduced, namely the direct coupling iteration method, the in-time-step iteration method, and the intersystem iteration method (Zhang et al. 2010; Zhang and Xia 2013).

It should be pointed out that the three methods are only different in mathematical form but are equivalent in the physical sense.

5.6.1 The Direct Coupling Iteration Method

In this method, the train movement and the bridge movement are coupled by wheel-rail interaction, thus the motion equations for the train subsystem and the bridge subsystem can be established as a unified system equation, if the wheel-rail relationship meets the linear condition. Obviously, the preconditions for adopting the direct coupling iteration method are that the train subsystem and the bridge subsystem should be linear systems, and also the wheel-rail relationship be linear

(Zhang 2002; Xu et al. 2004). In this section, the direct coupling iteration method is introduced based on the wheel-rail vertical correspondence assumption and lateral simplified Kalker Creep Theory adopted in Sect. 5.5.

For a wheel-set, define the force vector acting on it and the bogie connected to it as $\mathbf{F}_a$, and that of the wheel-set on the deck as $\mathbf{F}_d$.

$$\mathbf{F}_a = [F_{tz} \quad F_{t\theta} \quad F_{t\varphi} \quad F_{wy}]^T \tag{5.89}$$

$$\mathbf{F}_d = [F_{dy} \quad F_{dz} \quad F_{d\theta}]^T \tag{5.90}$$

where F_{tz}, $F_{t\theta}$, and $F_{t\varphi}$ refer to the acting force and moments of the bogie, respectively, in z-, θ-, and φ-direction, and F_{wy} refers to the acting force of wheel-set in the y-direction, defined by Eqs. (5.73)–(5.75); F_{dy}, F_{dz}, and $F_{d\theta}$ refer to the acting force or moments on the bridge deck at wheel-set position, respectively, in the y-, z-, and θ-directions, defined by Eqs. (5.76)–(5.78).

As defined in Table 5.1, the displacements of bogie are z_t, θ_t, and φ_t, respectively, in z-, θ-, and φ-directions; the displacement of wheel-set center is y_w in y-direction; the displacement of bridge at the wheel-set position is y_d, z_d, and θ_d, respectively, in y-, z-, and θ-directions.

Define $\eta = 1$ for the front wheel-set, and $\eta = -1$ for the rear on a same bogie, by Eqs. (5.73)–(5.78), the force vectors $\mathbf{F}_a$ and $\mathbf{F}_d$ can be expressed as

$$\begin{Bmatrix} \mathbf{F}_a \\ \mathbf{F}_d \end{Bmatrix} = \begin{Bmatrix} \mathbf{0} & \mathbf{0} & \mathrm{K}_{aa} & \mathbf{C}_{aa} & \mathbf{0} & \mathrm{K}_{ai} & \mathbf{C}_{ai} & \mathbf{0} \\ \mathrm{K}_{da} & \mathbf{C}_{da} & \mathrm{K}_{dd} & \mathbf{C}_{dd} & \mathbf{M}_{dd} & \mathrm{K}_{di} & \mathbf{C}_{di} & \mathbf{M}_{di} \end{Bmatrix} \begin{Bmatrix} \mathbf{S}_a \\ \dot{\mathbf{S}}_a \\ \mathbf{S}_d \\ \dot{\mathbf{S}}_d \\ \ddot{\mathbf{S}}_d \\ \mathbf{S}_i \\ \dot{\mathbf{S}}_i \\ \ddot{\mathbf{S}}_i \end{Bmatrix} + \begin{Bmatrix} \mathbf{0} \\ \mathbf{F}_g \end{Bmatrix} \tag{5.91}$$

where

$$\mathbf{S}_a = [z_t \quad \theta_t \quad \varphi_t \quad y_w]^T \tag{5.92}$$

$$\mathbf{S}_d = [y_d \quad z_d \quad \theta_d]^T \tag{5.93}$$

$$\mathbf{S}_i = [y_i \quad z_i \quad \theta_i]^T \tag{5.94}$$

$$\mathbf{F}_g = [0 \quad G \quad 0]^T \tag{5.95}$$

$$\mathbf{K}_{aa} = \mathbf{K}_{ai} = \mathbf{K}_{da}^{T} = \begin{bmatrix} 0 & 2k_{z1} & 0 \\ 0 & 0 & 2k_{z1}b_1^2 \\ 0 & 2\eta k_{z1}d_1 & 0 \\ 0 & 0 & 0 \end{bmatrix} \tag{5.96}$$

$$\mathbf{C}_{aa} = \mathbf{C}_{ai} = \mathbf{C}_{da}^{T} = \begin{bmatrix} 0 & 2c_{z1} & 0 \\ 0 & 0 & 2c_{z1}b_1^2 \\ 0 & 2\eta c_{z1}d_1 & 0 \\ \frac{2f_{22}}{V} & 0 & 0 \end{bmatrix} \tag{5.97}$$

$$\mathbf{K}_{dd} = \mathbf{K}_{di} = -2\mathrm{diag}\{\, 0 \quad k_{z1} \quad k_{z1}b_1^2 \,\} \tag{5.98}$$

$$\mathbf{C}_{dd} = \mathbf{C}_{di} = -2\mathrm{diag}\{\, f_{22}/V \quad c_{z1} \quad c_{z1}b_1^2 \,\} \tag{5.99}$$

$$\mathbf{M}_{dd} = \mathbf{M}_{di} = -\mathrm{diag}\{\, 0 \quad m_w \quad I_{xw} \,\} \tag{5.100}$$

The following relationships exist between the force vector $\mathbf{F}_a$ and the term $\mathbf{F}_v$ in the right side of train subsystem equation, as well as between the displacement vector $\mathbf{S}_a$ and the term $\mathbf{X}_v$ in the right side of train subsystem equation

$$\begin{cases} \mathbf{F}_v = \sum\limits_{N} \mathbf{T}_{av}\mathbf{F}_a \\ \mathbf{S}_a = \mathbf{T}_{va}\mathbf{X}_v \end{cases} \tag{5.101}$$

where Σ indicates $\mathbf{F}_v$ is the superposition of all wheel-set forces, and N is the number of wheel-sets. It is easy to give the transformation matrices in the above equations as

$$\mathbf{T}_{va} = \mathbf{T}_{av}^{T} = \begin{bmatrix} 0 & \mathbf{I}_3 & 0 & 0 & 0 \\ 0 & 0 & 0 & \mathbf{I}_1 & 0 \end{bmatrix} \tag{5.102}$$

In the equation, the nonzero submatrices locate at the corresponding position between the DOFs in the z-, θ- and φ-directions of the bogie connecting to the wheel-set, and that in the y-direction of the wheel-set concerned.

The following relationships exist between the force vector $\mathbf{F}_d$ and the term $\mathbf{F}_b$ in the right side of train subsystem equation, as well as between the displacement vector $\mathbf{S}_d$ and the term $\mathbf{X}_b$ in the right side of train subsystem equation

$$\begin{cases} \mathbf{F}_b = \sum\limits_{N} \mathbf{T}_{db}\mathbf{F}_d \\ \mathbf{S}_d = \mathbf{T}_{bd}\mathbf{X}_b \end{cases} \tag{5.103}$$

Similarly, Σ indicates $\mathbf{F}_b$ is the superposition of all wheel-set reaction forces. The transformation matrices in the equations are

$$\mathbf{T}_{\mathrm{db}}=\begin{bmatrix}\mathbf{0}\\ \frac{d_{\mathrm{x2}}}{d_{\mathrm{x1}}+d_{\mathrm{x2}}}\mathbf{I}_3\\ \mathbf{0}\\ \frac{d_{\mathrm{x1}}}{d_{\mathrm{x1}}+d_{\mathrm{x2}}}\mathbf{I}_3\\ \mathbf{0}\end{bmatrix}\begin{bmatrix}1 & 0 & 0\\ 0 & 1 & 0\\ -d_{\mathrm{z}} & d_{\mathrm{y}} & 1\end{bmatrix}=\mathbf{T}_{\mathrm{bd}}^{\mathrm{T}} \tag{5.104}$$

where d_{y} and d_{z} are, respectively, the directional vectors of the bride nodes to the bridge deck at the wheel-set position in the y- and z-directions; d_{x1} and d_{x2} are, respectively, the distances between the wheel-set and the two adjacent bridge nodes in the x-direction.

Thus, $\mathbf{F}_{\mathrm{v}}$ in Eq. (5.85) and $\mathbf{F}_{\mathrm{b}}$ in Eq. (5.86) can be expressed as

$$\begin{aligned}\mathbf{F}_{\mathrm{v}}&=\sum_N\mathbf{T}_{\mathrm{av}}\mathbf{F}_{\mathrm{a}}=\sum_N\mathbf{T}_{\mathrm{av}}\left(\mathbf{K}_{\mathrm{ad}}\mathbf{S}_{\mathrm{d}}+\mathbf{C}_{\mathrm{ad}}\dot{\mathbf{S}}_{\mathrm{d}}+\mathbf{K}_{\mathrm{ai}}\mathbf{S}_{\mathrm{i}}+\mathbf{C}_{\mathrm{ai}}\dot{\mathbf{S}}_{\mathrm{i}}\right)\\&=\sum_N\mathbf{T}_{\mathrm{av}}\left(\mathbf{K}_{\mathrm{ad}}\mathbf{T}_{\mathrm{bd}}\mathbf{X}_{\mathrm{b}}+\mathbf{C}_{\mathrm{ad}}\mathbf{T}_{\mathrm{bd}}\dot{\mathbf{X}}_{\mathrm{b}}\right)+\sum_N\mathbf{T}_{\mathrm{av}}\left(\mathbf{K}_{\mathrm{ai}}\mathbf{S}_{\mathrm{i}}+\mathbf{C}_{\mathrm{ai}}\dot{\mathbf{S}}_{\mathrm{i}}\right)\end{aligned} \tag{5.105}$$

$$\begin{aligned}\mathbf{F}_{\mathrm{b}}&=\sum_N\mathbf{T}_{\mathrm{db}}\mathbf{F}_{\mathrm{d}}=\sum_N\mathbf{T}_{\mathrm{db}}\left(\mathbf{K}_{\mathrm{da}}\mathbf{S}_{\mathrm{a}}+\mathbf{C}_{\mathrm{da}}\dot{\mathbf{S}}_{\mathrm{a}}+\mathbf{K}_{\mathrm{dd}}\mathbf{S}_{\mathrm{d}}+\mathbf{C}_{\mathrm{dd}}\dot{\mathbf{S}}_{\mathrm{d}}+\mathbf{M}_{\mathrm{dd}}\ddot{\mathbf{S}}_{\mathrm{d}}\right)\\&\quad+\sum_N\mathbf{T}_{\mathrm{db}}\left(\mathbf{K}_{\mathrm{di}}\mathbf{S}_{\mathrm{i}}+\mathbf{C}_{\mathrm{di}}\dot{\mathbf{S}}_{\mathrm{i}}+\mathbf{M}_{\mathrm{di}}\ddot{\mathbf{S}}_{\mathrm{i}}+\mathbf{F}_{\mathrm{g}}\right)\\&=\sum_N\mathbf{T}_{\mathrm{db}}\left(\mathbf{K}_{\mathrm{da}}\mathbf{T}_{\mathrm{va}}\mathbf{X}_{\mathrm{v}}+\mathbf{C}_{\mathrm{da}}\mathbf{T}_{\mathrm{va}}\dot{\mathbf{X}}_{\mathrm{v}}+\mathbf{K}_{\mathrm{dd}}\mathbf{T}_{\mathrm{bd}}\mathbf{X}_{\mathrm{b}}+\mathbf{C}_{\mathrm{dd}}\mathbf{T}_{\mathrm{bd}}\dot{\mathbf{X}}_{\mathrm{b}}+\mathbf{M}_{\mathrm{dd}}\mathbf{T}_{\mathrm{bd}}\ddot{\mathbf{X}}_{\mathrm{b}}\right)\\&\quad+\sum_N\mathbf{T}_{\mathrm{db}}\left(\mathbf{K}_{\mathrm{di}}\mathbf{S}_{\mathrm{i}}+\mathbf{C}_{\mathrm{di}}\dot{\mathbf{S}}_{\mathrm{i}}+\mathbf{M}_{\mathrm{di}}\ddot{\mathbf{S}}_{\mathrm{i}}+\mathbf{F}_{\mathrm{g}}\right)\end{aligned} \tag{5.106}$$

When the bridge subsystem is modeled by the direct stiffness method, the train-bridge coupling equations can be obtained by moving the terms concerning $\mathbf{X}_{\mathrm{v}}$ and $\mathbf{X}_{\mathrm{b}}$ in Eq. (5.85) to the left side, thus the coupled motion equations of the train-bridge system are formed as

$$\begin{bmatrix}\mathbf{M}_{\mathrm{vv}} & \mathbf{0}\\ \mathbf{0} & \mathbf{M}_{\mathrm{bb}}\end{bmatrix}\begin{Bmatrix}\ddot{\mathbf{X}}_{\mathrm{v}}\\ \ddot{\mathbf{X}}_{\mathrm{b}}\end{Bmatrix}+\begin{bmatrix}\mathbf{C}_{\mathrm{vv}}+\mathbf{C}_{\mathrm{c}} & \mathbf{C}_{\mathrm{vb}}\\ \mathbf{C}_{\mathrm{bv}} & \mathbf{C}_{\mathrm{bb}}\end{bmatrix}\begin{Bmatrix}\dot{\mathbf{X}}_{\mathrm{v}}\\ \dot{\mathbf{X}}_{\mathrm{b}}\end{Bmatrix}+\begin{bmatrix}\mathbf{K}_{\mathrm{vv}} & \mathbf{K}_{\mathrm{vb}}\\ \mathbf{K}_{\mathrm{bv}} & \mathbf{K}_{\mathrm{bb}}\end{bmatrix}\begin{Bmatrix}\mathbf{X}_{\mathrm{v}}\\ \mathbf{X}_{\mathrm{b}}\end{Bmatrix}=\begin{Bmatrix}\mathbf{P}_{\mathrm{v}}\\ \mathbf{P}_{\mathrm{b}}\end{Bmatrix} \tag{5.107}$$

where

$$\mathbf{M}_{\mathrm{vv}}=\mathbf{M}_{\mathrm{v}} \tag{5.108}$$

$$\mathbf{M}_{\mathrm{bb}}=\mathbf{M}_{\mathrm{b}}-\sum_N\mathbf{T}_{\mathrm{db}}\mathbf{M}_{\mathrm{dd}}\mathbf{T}_{\mathrm{bd}} \tag{5.109}$$

$$\mathbf{C}_{vv} = \mathbf{C}_v \tag{5.110}$$

$$\mathbf{C}_{vb} = -\sum_N \mathbf{T}_{av}\mathbf{C}_{ad}\mathbf{T}_{bd} = \mathbf{C}_{bv}^{T} \tag{5.111}$$

$$\mathbf{C}_{bb} = \mathbf{C}_b - \sum_N \mathbf{T}_{db}\mathbf{C}_{dd}\mathbf{T}_{bd} \tag{5.112}$$

$$\mathbf{K}_{vv} = \mathbf{K}_v \tag{5.113}$$

$$\mathbf{K}_{vb} = -\sum_N \mathbf{T}_{av}\mathbf{K}_{ad}\mathbf{T}_{bd} = \mathbf{K}_{bv}^{T} \tag{5.114}$$

$$\mathbf{K}_{bb} = \mathbf{K}_b - \sum_N \mathbf{T}_{db}\mathbf{K}_{dd}\mathbf{T}_{bd} \tag{5.115}$$

$$\mathbf{P}_v = \sum_N \mathbf{T}_{av}\left(\mathbf{K}_{ai}\mathbf{S}_i + \mathbf{C}_{ai}\dot{\mathbf{S}}_i\right) \tag{5.116}$$

$$\mathbf{P}_b = \sum_N \mathbf{T}_{db}\left(\mathbf{K}_{di}\mathbf{S}_i + \mathbf{C}_{di}\dot{\mathbf{S}}_i + \mathbf{M}_{di}\ddot{\mathbf{S}}_i + \mathbf{F}_g\right) \tag{5.117}$$

When the bridge subsystem is modeled by the modal decomposition method, the similar coupled motion equations of the train-bridge system can also be obtained by moving the terms concerning $\mathbf{X}_v$ and $\mathbf{X}_b$ in Eq. (5.86) to the left side.

5.6.2 The In-Time-Step Iteration Method

When the motion Eqs. (5.85) and (5.86) of train-bridge coupling system are solved by the numerical time history integration method, $\mathbf{F}_v$ and $\mathbf{F}_b$ on the right side of the equations are respectively the functions of the train and bridge motion states. Therefore, the solution applicable to both the motion state and the acting force relationship can be obtained through iteration between two subsystems within each time step. This is the in-time-step iteration method, whose calculation procedures are shown in Fig. 5.11.

In convergence judgment, it requires that the train and bridge subsystems, respectively, meet the convergence conditions, namely, the difference between the motion state of the nth iteration step within the given period of time and that of the $(n + 1)$th step be small enough. Note that the wheel-rail interaction force reflects the response states and coupling relationship of both train and bridge subsystems, it is taken as the index for convergence judgment in the iteration calculation. The convergence error is determined by the computational requirements, and in most previous calculations, satisfactory accuracy was obtained by adopting error 10 N for wheel-rail interaction force and 10 N·m for the moment.

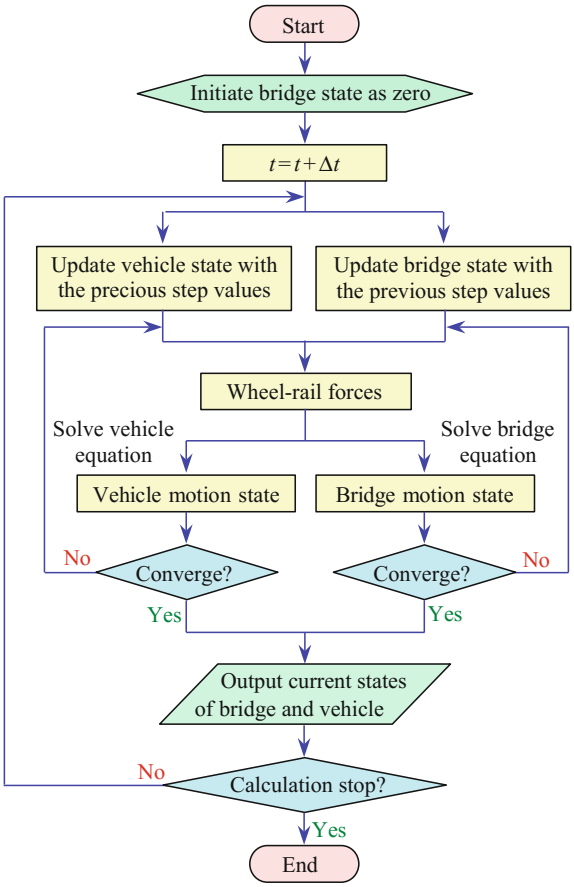

Fig. 5.11 Iteration procedures of the in-time-step iteration method

5.6.3 *The Intersystem Iteration Method*

The intersystem iteration method, also called as the Whole-process Iteration method, is a newly developed method to solve Eqs. (5.85) and (5.86). In this method, firstly, the vehicle motion and wheel-rail force time histories can be calculated through solution of independent train equations under the assumption that the bridge subsystem is rigid, then the time histories of calculated wheel-rail forces are applied to the bridge, thus the motion state of the bridge can be calculated through solution of independent bridge equations. The next iteration is carried out by superposition of the calculated deck motion time histories with the track irregularities as an updated train subsystem excitation. In this method, the wheel-rail interaction force can also be adopted as the index for convergence judgment.

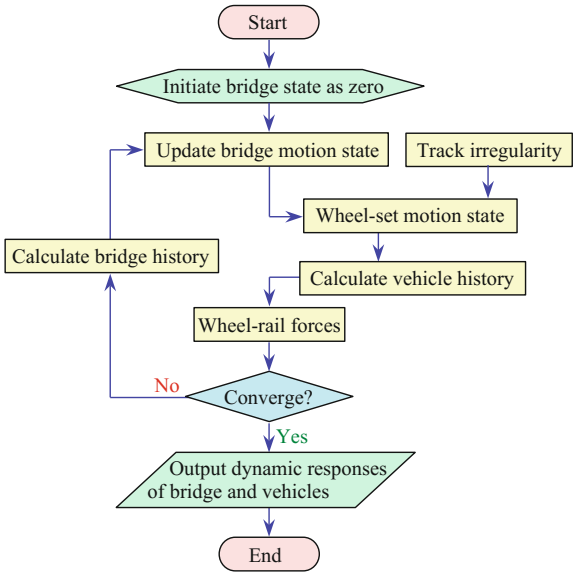

Fig. 5.12 Iteration procedures of the intersystem iteration method

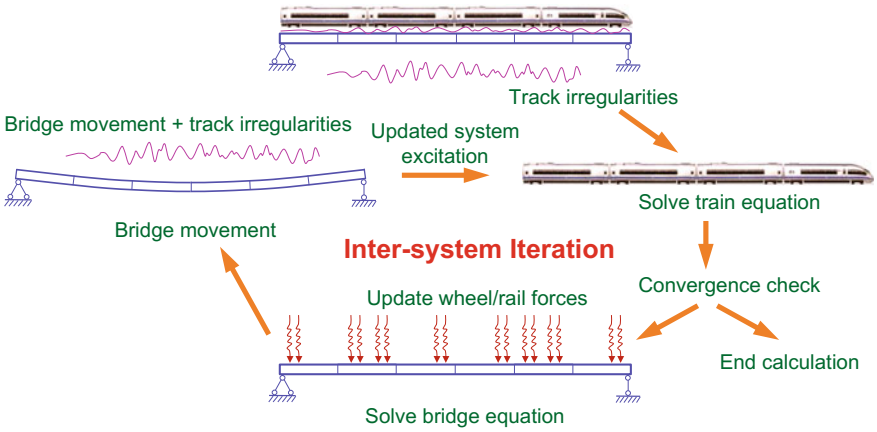

Fig. 5.13 Execution flowchart of the intersystem iteration method

The procedures for the intersystem iteration method are shown in Figs. 5.12 and 5.13, and described as follows:

Step 1: Solve the train subsystem by assuming the bridge subsystem rigid, setting the bridge motion to zero, and using the track irregularities as the excitation, to obtain the time histories of wheel-rail forces/moments for all wheel-sets;

Step 2: Solve the bridge subsystem by applying the wheel-rail interaction force histories obtained in the previous iteration loop (or Step 1) on bridge deck, to obtain the updated time histories of bridge deck movement at all nodes;

Step 3: Solve the train subsystem by combining the updated bridge deck movements obtained in Step 2 with the track irregularities as the updated system excitation, to obtain the updated time histories of wheel-rail forces/moments for all wheel-sets;

Step 4: Calculate the errors between the updated wheel-rail interaction force histories of all wheel-sets obtained in Step 3 and those in the previous iteration loop (or Step 1) for the convergence check. If the maximum instantaneous absolute differences for all wheel-sets in the whole integral time satisfy the given threshold, the convergence check is OK, meaning the calculation is completed. Otherwise, return to Step 2 to start a next iteration loop.

By comparing Fig. 5.11 with Figs. 5.12 and 5.13, one can understand the main difference between the intersystem iteration method and the in-time-step iteration method. In the intersystem iteration method, each iteration is for full time history calculation, where the train subsystem and the bridge subsystem are solved separately to obtain their dynamic response time histories, and the convergence is judged according to the whole time histories in an iteration loop. While in the in-time-step iteration method, each iteration is carried out within a time step, where the train subsystem and the bridge subsystem are solved simultaneously at a certain moment, and the convergence is judged according to the responses within the time step. When the two iteration methods are used to solve the same equation, although using different iteration procedures and convergence principles, there is no essential difference between the analyzed results.

As a numerical method for time integration of multi-system, especially compared with the in-time-step iteration method, the intersystem iteration method has the following features:

(1) For both the train subsystem and the bridge subsystem, the intersystem iteration method can ensure their respective convergence in each calculation loop, as long as adopting non-conditionally converged integral scheme. Although the intersystem iteration between the two subsystems is not unconditionally converged, where may appear gradual increase of calculated amplitudes, since the system response time histories can be obtained in each iteration loop, it is easy to get the final convergence by controlling the calculation process. This will be described in Sect. 5.7 of this book by an illustrative example.

(2) The in-time-step iteration method needs to establish the overall dynamic matrix of the train, thus the more vehicles the train has, the larger the internal memory is required and the longer the calculation time consumed. In the intersystem iteration method, however, the excitation source of the train subsystem is the given time-varying irregularity, namely the resultant displacement of track irregularity and bridge motion; thus, in any iteration loop, the excitation

condition of a vehicle will not be affected due to the changed motion state of the bridge caused by the other vehicles. Therefore, the intersystem iteration method can separately solve the dynamic response of each vehicle element, without the need to calculate the dynamic matrix of the whole train, which helps to improve the computational efficiency and reduce internal memory consumption.

(3) In the in-time-step iteration method, it is imperative to use the explicit expressions of the mass, damping, and stiffness matrices of bridge subsystem and requires special analysis software for solution. For large or complex bridges, it is difficult. In the intersystem iteration method, however, it can calculate the dynamic response of the bridge under the given external-load time histories by using general finite element software, being convenient and highly efficient.

5.7 A Case Study

A simply-supported HSR bridge with box-girders and the China-made "Pioneer" EMU are considered as an illustrating case study. The dynamic responses of the bridge and the train vehicle are analyzed by the train-bridge coupling analysis model, and the solution method is proposed in this chapter. The accuracy of the proposed method is verified by comparing the calculated results with the experimental data. The convergence and its control of the Intersystem Iterative Method for solving the train-bridge dynamic coupling equations are discussed.

5.7.1 Introduction to the Bridge

The Gouhe Bridge is situated in the test section of the Qin-Shen (Qinhuangdao-Shenyang) HSR line constructed in Northeast China. The length of the line is 404.64 km, and the design train speed is 200 km/h, with infrastructure reserved speed is 250 km/h.

The bridge consists of successively twenty-eight simply-supported 24 m-span double-track PC box-girders, as shown in Fig. 5.14. The length of each box-girder is 24.6 m, the width of the girder is 12.4 m at the top and 6.125 m at the bottom, and the height is 2.2 m. The cross section and the main dimensions of the girder are shown in Fig. 5.15.

The substructure of the bridge influences the plate piers with rounded-end section and the height of 8 ~ 10 m, friction piles, embedded piles, and open-cut foundations. Along the direction from Qinhuangdao, the piers are numbered from 1 to 27 (with abutments 0 and 28), and the corresponding girders are from 1 to 28. Each girder is supported with four QSPZ-VI 4000 kN pot rubber bearings, and the

Fig. 5.14 View of the Gouhe Bridge on the Qin-Shen HSR line

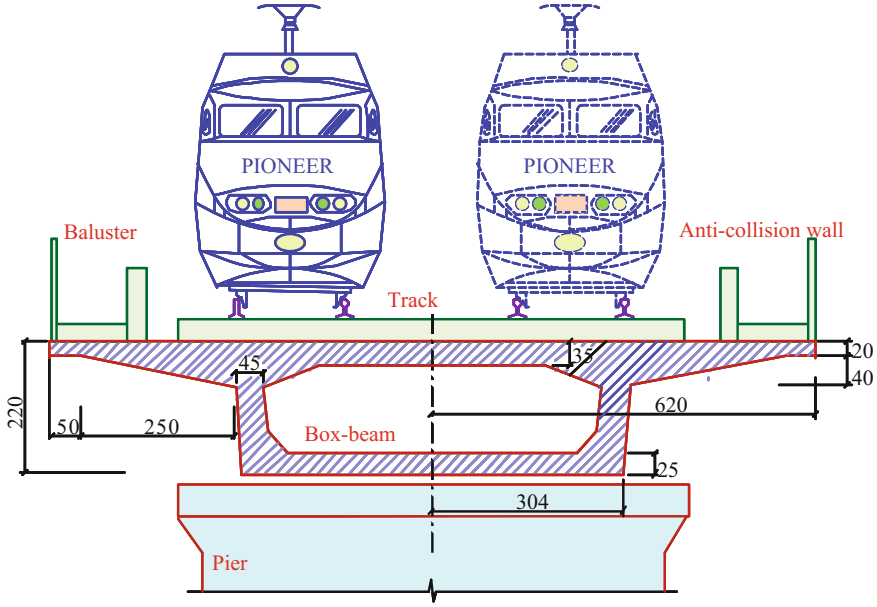

Fig. 5.15 Cross section of the 24 m-span PC box-beam (Unit: cm)

lateral center-to-center distance between bearings is 5.7 m. The bridge are laid with ballastless slab tracks.

5.7.2 *Field Experiment*

The Qin-Shen HSR line started construction in August 1998, and opened to operation on October 12, 2003. The field experiments on the bridge were organized by the Ministry of Railways of PRC from September to December 2002. On 27

Fig. 5.16 Pioneer train passing on the Gouhe Bridge

November, the China-made "Pioneer" EMU and "China-star" train, respectively, ran the highest test speeds of 292.8 and 321.5 km/h, bringing China to the "HSR Era." Shown in Fig. 5.16 is the Pioneer EMU passing on the Gouhe Bridge. The experimental data proved the good dynamic performance of bridges on the Qin-Shen HSR line and verified the validity of the dynamic simulation method for train-bridge system in China.

To investigate the dynamic behaviors of the bridge under high-speed trains and to verify the analytical model, the in situ experiment on the bridge was carried out in September 2002. The vibrations of the 22nd and 23rd girders and the 22nd and 23rd piers under the Pioneer EMU were measured in the experiment.

The arrangement of measuring points in the experiment is shown in Fig. 5.17, in which A stands for bridge acceleration, D for displacement, the figures represent the number of measuring points, and the subscripts x, y, and z refer to the vertical, lateral, and vertical directions, respectively.

In the experiment, there were 36 measuring points, including 4 for dynamic deflection, 12 for amplitude, 9 for acceleration, 4 for wheel/rail force, and 7 for concrete strain. Detailed measuring point arrangements are as follows:

(1) For vertical dynamic deflections, 4 measuring points (D10z, D11z, D15z, D16z) were set at the bottoms of the two test girder mid-spans below the track centers.
(2) For vertical and lateral dynamic amplitudes and accelerations, 18 measuring points (DA1yz, DA2yz, DA5z, DA6y, DA7y, DA8z, DA9y) were set on the beam flanges of the two girders, and 2 measuring points (D17xy, D18y) at the two pier-tops.

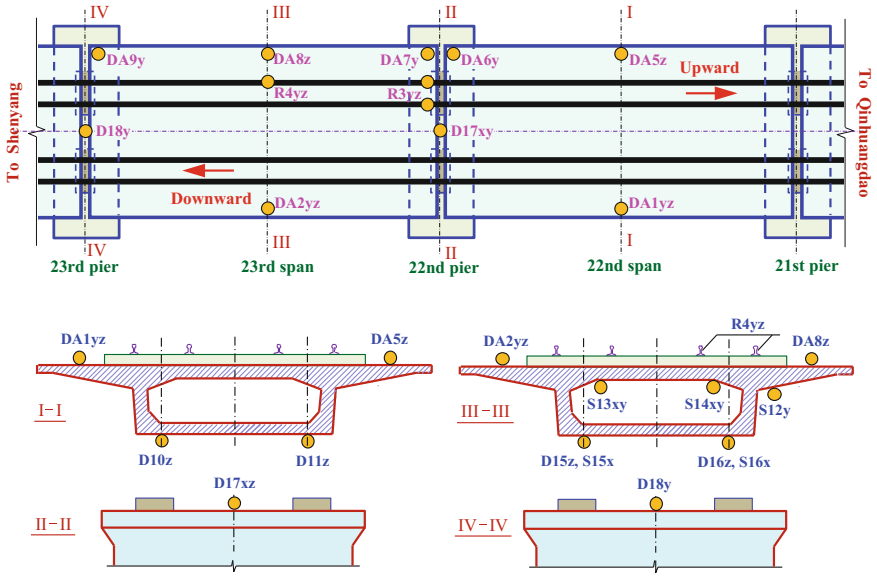

Fig. 5.17 Schematic diagram of measuring points

(3) For concrete strains, 7 measuring points (S12y, S13xy, S14xy, S15x, S16x) were set on the upper and lower concrete plates at mid-span of the 23rd girder span.
(4) For lateral and vertical wheel/rail forces, 4 measuring points (R3yz, R4yz) were set on the rail at the mid-span and the end of the 23rd span.

In the measurement, the sampling frequency of all signal channels was set to 2048 Hz.

Because the pier vibration and the concrete strains are very small, the signal-to-noise ratios of the amplitudes and accelerations measured at pier-tops and beam-ends, and the strains measured at concrete plates, are not ideal for verifying the calculated results. In the experiment, the wheel/rail force was measured at the fixed position of the rail where the stain gauges were stuck, and the force was excited by a series of wheels. However, in the numerical analysis, the wheel/rail force is calculated at the given wheel, and the force history varies with the wheel position on the rail. Therefore, they are not comparable and not used to check the calculation results.

The vertical dynamic deflections at mid-spans (D10z, D11z, D15z, D16z) were measured by the LVDT (Linear Variable Differential Transformer) installed on the fixed support. The amplitudes and accelerations at mid-spans (DA1yz, DA2yz, DA5z, DA8z) were measured by the China-made 891-4 sensors and the associated signal acquisition system. The instrument parameters of the 891-4 sensors are shown in Table 5.5. The data measured at these measuring points are adopted to check the calculation results.

Table 5.5 Instrument parameters of 891-4 sensors

Technical index	Parameters	Acceleration	Small velocity	Medium velocity	Large velocity
Sensitivity		0.13 m/s^2/V	8 m/s/V	30 m/s/V	1.5 m/s/V
Maximum range	Displacement (mm, p-p)		15	50	200
	Velocity (m/s, p-p)		0.5	1.0	1.2
	Acceleration (m/s^2, p-p)	20			
Frequency band	Horizontal	1 ~ 30 Hz		1 ~ 30 Hz	0.5 ~ 30 Hz
	Vertical		2 ~ 30 Hz		0.8 ~ 30 Hz

In the experiment, the dynamic response of the bridge was measured under 24 train passages, with the speed ranging from 182 to 279 km/h. Under the train excitation, the forced vibration of the bridge is composed of transient response and steady-state response.

(1) **Transient response.** The transient vibration frequency denotes the natural frequency of the bridge. Because the loading time of the train through the bridge is very short, the transient response components cannot be ignored. By analyzing the free vibration responses of the bridge after the train left, the natural frequencies of the bridge were obtained, including 8.15 Hz of the first vertical bending mode, 11.60 Hz of the first torsional mode, and 19.40 Hz of the first lateral bending mode.

(2) **Steady-state response.** The steady-state response includes the following 6 period components:

(a) The period of the whole process of a train passing through the bridge, corresponding to the time interval between the moments of the first wheel-set enters the bridge and the last one leaves. For the Pioneer EMU composed of six cars, the distance between the first wheel-set and the last one is 148 m. With respect to the train speed from 182 to 279 km/h, this period excites vertical vibration of the bridge with frequencies from 0.34 to 0.52 Hz.

(b) The period is the time interval between two adjacent cars passing through the bridge. The full length of each Pioneer car is 25.5 m, thus producing vertical excitation on the bridge with frequencies from 1.98 to 3.04 Hz.

(c) The period is the time interval between the front and rear bogie passing through one position of the bridge. The distance between two bogies of the Pioneer car is 18 m, thus producing vertical excitation on the bridge with frequencies from 2.81 to 4.31 Hz.

(d) The period is the time interval between the rear bogie of the previous car and the front bogie of the following car passing through one position of the bridge. The distance between the rear bogie of the previous car and the front bogie of

the following car is 7.5 m, thus producing vertical excitation on the bridge with frequencies from 6.74 to 10.33 Hz.

(e) The period is the time interval between two wheel-sets on the same bogie passing through one position of the bridge. The wheelbase of Pioneer car is 2.5 m, thus producing vertical excitation on the bridge with frequencies from 20.22 to 31.00 Hz.

(f) The period is the time interval when the train passes through a wave length of track irregularly. For the track irregularity, wavelength ranges from 2 to 40 m considered in the analysis, this period produces excitations on the train-bridge system with frequencies from 1.26 to 38.75 Hz.

According to the sensor parameters in Table 5.5, the excitation frequency by case (a) is lower than the sensitivity limit 1 Hz of 891-4 sensors, therefore, the vertical displacement measured at DA1z, DA2z, DA5z, and DA8z cannot be used to compare with the dynamic analysis results. On the other hand, when the train passes on one-side track, the vertical and the lateral movements of the girder are coupled due to the torsional effect, thus the measured lateral displacement also contains the corresponding low frequency components. Limited by the frequency sensitivity, the sensors at D1y and D2y cannot measure the low frequency components less than 1 Hz. Therefore, in the numerical analysis, the measured results by LVDT at the girder bottom are used to verify the vertical displacement, and the measured results by 891-4 sensors at mid-span of the girders are used to verify the lateral amplitudes, and vertical and lateral accelerations.

In summary, the measuring points used for verification of numerical results and their position parameters are as follows:

(1) Vertical dynamic displacements at mid-span: D10z, D11z, D15z, D16z, below the track with 2.5 m lateral eccentricity to the longitudinal axis of the girder.
(2) Lateral amplitudes at mid-span: D1y, D2y, on the bridge deck 1.0 m above the section centroid of the girder.
(3) Vertical accelerations at mid-span: A1z, A2z, A5z, A8z, on the bridge deck with 3.5 m lateral eccentricity to the longitudinal axis of the girder.
(4) Lateral accelerations at mid-span: A1y, A2y, on the bridge deck 1.0 m above the section centroid of the girder.

5.7.3 Calculation Parameters of the Bridge

Due to very large stiffness, the piers of this bridge have little influence on the train-bridge dynamic response, so for simplicity, a single span simply-supported 24 m girder model is established in the analysis. The full length of the girder is 24.6 m, with design span of 24.0 m and two 0.3 m extended ends. The finite element model consists of 82 spatial beam elements, with each element being 0.3 m. The cross section of the bridge is shown in Fig. 5.15. Because the difference

between sections along the girder is small, uniform material parameters and section geometries are adopted for all elements.

According to the design parameters, the vertical, torsional, and lateral fundamental natural frequencies of the bridge are, respectively, 6.02 Hz, 17.17 Hz, and 23.10 Hz, while the measured results are 8.15 Hz, 11.60 Hz, and 19.40 Hz. Because the concrete plate of the ballastless track can provide certain vertical bending stiffness, the measured vertical frequency higher than the calculation one is reasonable. The lateral and the torsional frequencies are lower than the calculated ones, probably because the lateral and torsional deformations of the bridge may not strictly conform to the plane section assumption. To take into account the above influences, the finite element model of the bridge is modified by parameter updating, namely by adjusting vertical bending, lateral bending, and torsional moments of inertia, while keeping other parameters unchanged, to make the calculated frequencies of the model consistent with the measured ones, as shown in Table 5.6. It can be seen that after model updating, the vertical bending moment of inertia is increased by 84%, while the lateral is reduced by 29%, and the torsional reduced by 51%.

Table 5.6 Natural frequencies and cross section parameters of the bridge

Parameter		Unit	Measured value	Design parameter	Updated parameter for dynamic analysis
Section parameter	Area	m^2	–	7.482	7.482
	Material density	kg/m^3	–	2500	2500
	Material bending elastic modulus	GPa	–	35.5	35.5
	Poisson ratio	–	–	0.1667	0.1667
	Secondary dead load	kN/m	–	160	160
	Vertical bending moment of inertia	m^4	–	4.758	8.731
	Torsion moment of inertia	m^4	–	11.217	5.499
	Lateral bending moment of inertia	m^4	–	70.158	49.465
Frequency	First-order vertical frequency	Hz	8.15	6.02	8.15
	First-order torsion frequency	Hz	11.60	14.60	11.60
	First-order lateral frequency	Hz	19.40	23.10	19.40

The damping ratios for the bridge were also measured, which were 2.61% for the 22nd span and 2.57% for the 23rd span (Xia and Zhang 2005b). In the analysis, an identical damping ratio 2.6% is adopted.

5.7.4 Calculation Parameters of Vehicle

The train concerned in the case study is the Pioneer EMU composed of six cars, in which the 1st, 3rd, 4th, and 6th are motor-cars and the 2nd and 5th are trailer-cars. The composition of the first three cars is shown in Fig. 5.18. The vehicle parameters used in the calculation are listed in Table 5.7. The average static axle loads for motor-car and trailer-car are 139.3 kN and 137.8 kN, respectively, and the total length of each car is 25.5 m.

Using the mass matrix and stiffness matrix of the vehicle, and by restraining the y-direction movement of the wheel-sets, the natural frequencies and the vibration modes of the motor-car and trailer-car are calculated, as shown in Table 5.8. The first-order natural frequencies of the vehicle in various directions are between 0.45 to 1.60 Hz, which is much lower than the natural frequencies of the bridge listed in Table 5.6. Therefore, there is no possibility of coupling resonance between the bridge and the vehicle. In addition, it can be found that the yawing and rolling motions of the vehicle vibration modes are coupled, which form the lower-center rolling-and-swing and upper-center rolling-and-swing modes described in Fig. 5.3.

5.7.5 Dynamic Responses of Bridge and Experimental Verification

Taking the track irregularities measured on the Qin-Shen HSR mentioned in Chap. 3 as the excitation, the whole histories of the Pioneer EMU running through the bridge are simulated, at each 10 km/h of train speed from 180 km/h to 300 km/h, by which the dynamic responses of the bridge and the train vehicles are obtained. In the iterative process, the upper bounds of convergence errors are, respectively, 100 N for lateral and vertical wheel-rail forces, and 100 N•m for wheel-rail rolling force moment. In order to better compare the calculated results with the measured data, the integration time step is taken as 1/2048 s, just the value of the sampling interval in the experiment.

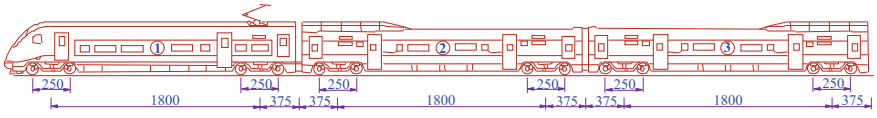

Fig. 5.18 Composition of the Pioneer train (Unit: cm)

Table 5.7 Vehicle parameters of Pioneer EMU train

Parameter	Unit	Motors-car	Trailer-car
Distance of wheel-sets, $2d_1$	m	2.50	2.50
Distance of bogies, $2d_2$	m	18.0	18.0
Transverse span of primary suspension, $2b_1$	m	2.05	2.05
Transverse span of secondary suspension, $2b_2$	m	2.05	2.05
Car-body to secondary suspension, h_1	m	0.36	0.83
Secondary suspension to bogie, h_2	m	0.24	0.15
Bogie to wheel-set, h_3	m	0.33	0.34
Wheel radius, r_w	m	0.4575	0.4575
Wheel-set mass m_w	t	1.9	2.2
Wheel-set X-inertia, I_{xw}	t-m^2	1.067	1.63
Bogie mass, m_t	t	3.4	1.7
Bogie X-inertia, I_{xt}	t-m^2	3.2	1.6
Bogie X-inertia, I_{yt}	t-m^2	7.2	1.7
Bogie X-inertia, I_{zt}	t-m^2	6.8	1.7
Car-body mass, m_c	t	42.4	44
Car-body, x-inerita, I_{xc}	t-m^2	101.5	74
Car-body, y-inerita, I_{yc}	t-m^2	1064.4	1370
Car-body, z-inerita, I_{zc}	t-m^2	867.2	1370
Primary suspension x-damp/side, c_{x1}	kN-s/m	0	0
Primary suspension y-damp/side, c_{y1}	kN-s/m	0	0
Primary suspension z-damp/side, c_{z1}	kN-s/m	30	38
Secondary suspension x-damp/side, c_{x2}	kN-s/m	120	150
Secondary suspension y-damp/side, c_{y2}	kN-s/m	30	15
Secondary suspension z-damp/side c_{z2}	kN-s/m	33	40
Primary suspension x-spring/side, k_{x1}	kN/m	960	960
Primary suspension y-spring/side, k_{y1}	kN/m	960	960
Primary suspension z-spring/side, k_{z1}	kN/m	1040	700
Secondary suspension x-spring/side, k_{x2}	kN/m	240	210
Secondary suspension y-spring/side, k_{y2}	kN/m	240	210
Secondary suspension z-spring/side, k_{z2}	kN/m	400	350

Shown in Figs. 5.19, 5.20, 5.21, and 5.22 are, respectively, the calculated and measured time histories of vertical displacement, lateral amplitude, and vertical and lateral accelerations of the bridge at mid-span, under the train speed of 270 km/h. In order to compare with the measured curves, the calculated lateral displacement history shown in Fig. 5.20 was high-pass filtered by 1 Hz, meaning there is no frequency component lower than 1 Hz in it.

It can be seen from the figures that there appear seven peaks in the displacement and acceleration histories, in both the measured and the calculated ones. The whole process of the Pioneer EMU passing through the bridge can be clearly reflected by these peaks: the 1st peak is from the first front bogie and the 7th from the last rear

Table 5.8 Natural frequencies and modes of the Pioneer EMU vehicles

Order number	Motor-car		Trailer-car	
	Frequency (Hz)	Mode description	Frequency (Hz)	Mode description
1	0.5394	Lower-center rolling-and-swing	0.4506	Lower-center rolling-and-swing
2	0.7734	Upper-center rolling-and-swing	0.8017	Car-body floating, first order
3	0.8935	Car-body floating, first order	0.9175	Upper-center rolling-and-swing
4	1.4041	Car-body yawing, first order	1.0577	Car-body yawing, first order
5	1.5977	Car-body pitching, first order	1.2939	Car-body pitching, first order

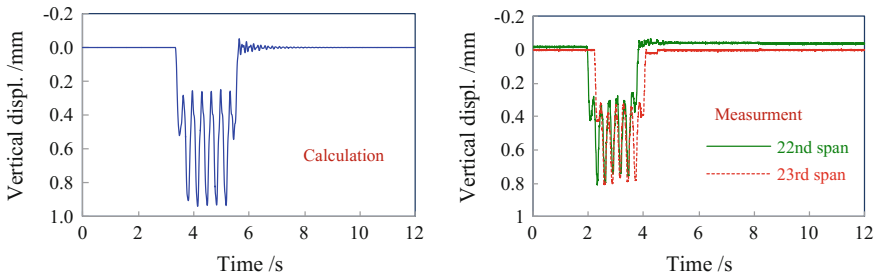

Fig. 5.19 Vertical displacement histories of girder at mid-span (V = 270 km/h)

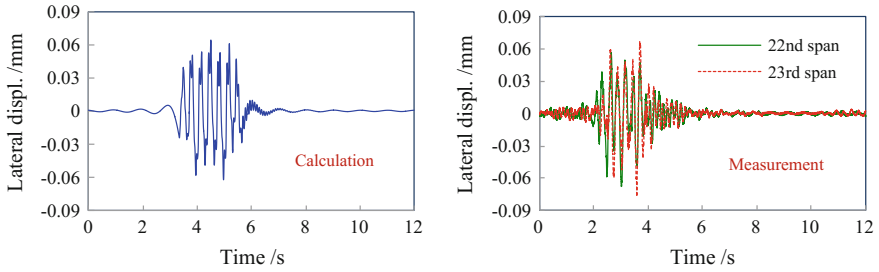

Fig. 5.20 Lateral displacement histories of girder at mid-span (V = 270 km/h)

bogie; and the nth peak is from the rear bogie of the (n-1)th car and the front bogie of the nth car, where n = 2, 3, 4, 5, and 6.

Shown in Fig. 5.23 are the calculated frequency spectra of vertical displacement and lateral amplitude, and those measured at the 22nd span. The spectrum curve of vertical displacement is almost the same as the measured curve, in which the peaks appear at zero frequency and 3.0 Hz. The zero frequency relates to the quasi-static

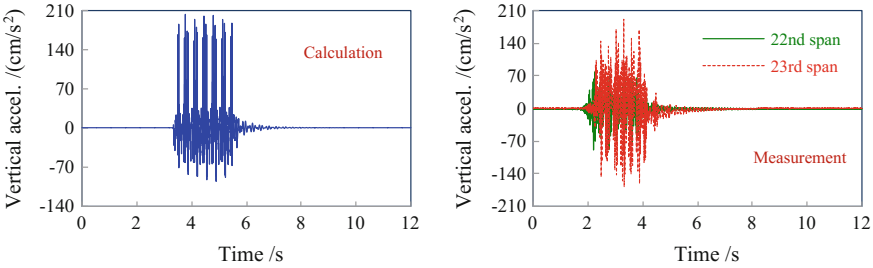

Fig. 5.21 Vertical acceleration histories of girder at mid-span (V = 270 km/h)

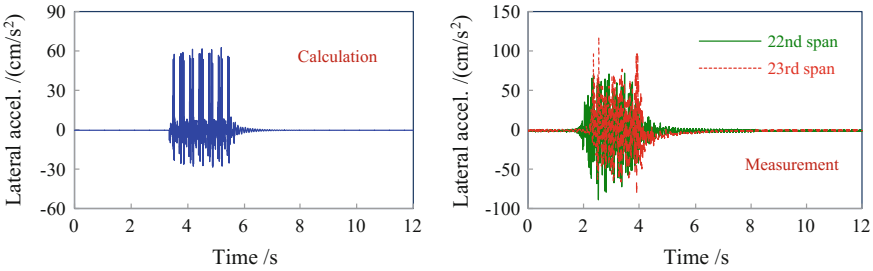

Fig. 5.22 Lateral acceleration histories of girder at mid-span (V = 270 km/h)

component of the vertical displacement caused by the whole train passing through the bridge, while 3.0 Hz approaches to frequency 2.81 Hz by a length of a vehicle. For the lateral amplitudes, the calculated spectrum curve is close to the measured one when the frequency is below 5 Hz, without component of zero frequency, but the peaks appearing at 1.1 Hz and 3.0 Hz. The difference is greater when the frequency is higher than 5 Hz. In the calculated spectrum higher than 5 Hz, two peaks appear at 8.8 Hz and 11.8 Hz, with the 8.8 Hz close to the vertical natural frequency 8.15 Hz, and 11.8 Hz to the torsional frequency 11.6 Hz of the bridge, while the measured spectrum curve is complex and no obvious peak appears.

Shown in Fig. 5.24 are the calculated vertical and lateral acceleration spectrum curves, and those measured at the 22nd span. In the vertical acceleration spectrum curves, there again appear peaks at 3.0 Hz, 8.8 Hz, and 11.8 Hz, in which 3.0 Hz approaches to the loading frequency 2.81 Hz by a length of a vehicle, 8.8 Hz close to the vertical natural frequency 8.15 Hz, and 11.8 Hz close to the torsional natural frequency 11.6 Hz of the bridge. Note that these frequency components can also be found in the lateral acceleration spectrum curves, because the measuring points are not at the section center of the girder, thus the lateral and vertical vibrations of the bridge are coupled. Besides, another peak appears in the measured spectrum at 20.5 Hz, which is close to the lateral natural frequency 19.40 Hz of the bridge.

The calculated curves were very close to the measured results in waveform, amplitude, and spectral components, indicating that the calculation model and the

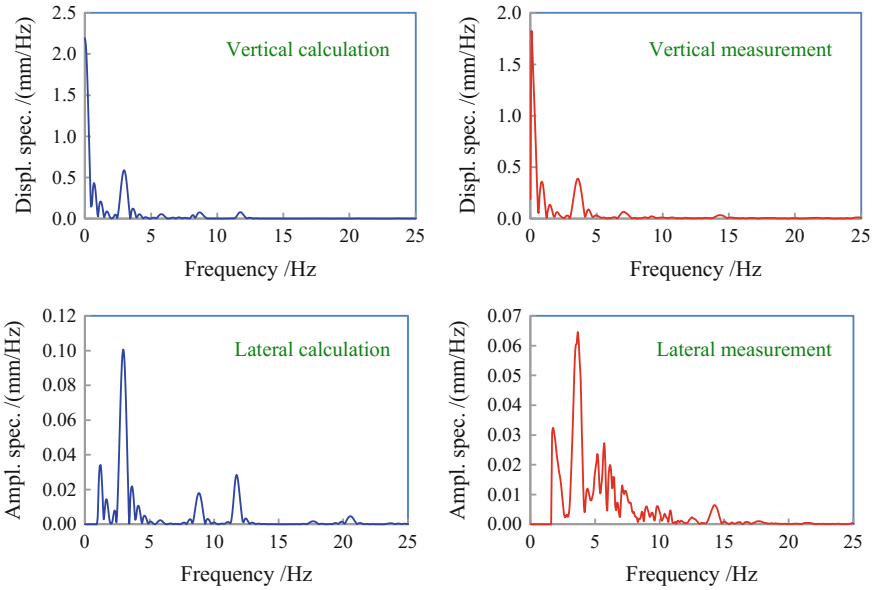

Fig. 5.23 Frequency spectra of vertical displacement and lateral amplitude of the bridge (V = 270 km/h)

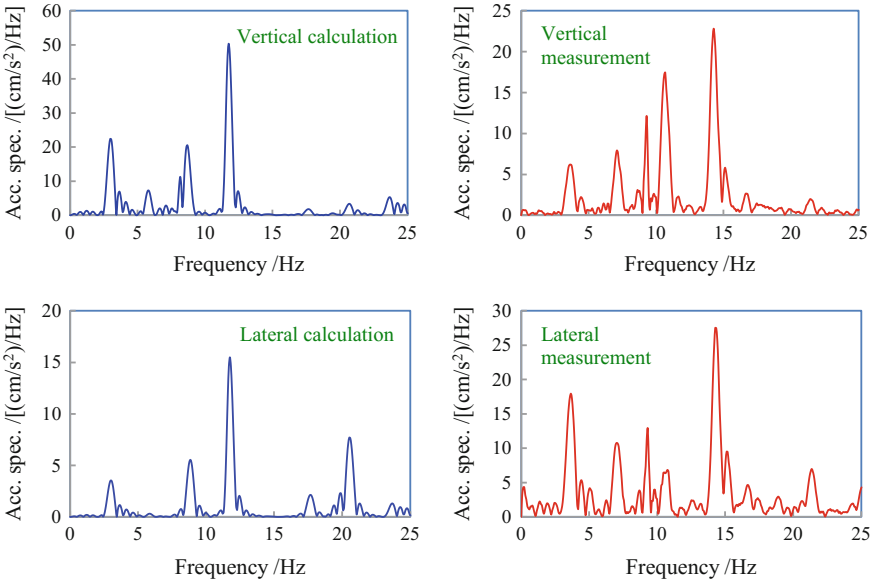

Fig. 5.24 Frequency spectra of vertical and lateral accelerations of the bridge (V = 270 km/h)

analysis method established in this chapter have sufficient accuracy, and they can be used for train-bridge coupling dynamic analysis. The errors between the calculated and measured results originate from but not limited to the following aspects:

(1) Difference exists between the input and the real track irregularities.
(2) In the calculation, the vehicle is regarded as a linear system, while the nonlinear characteristics of its components in vibration are not considered.
(3) The elastic deformation of the track structure is neglected in the calculation model.
(4) The track structure is continuously across the beam joint, which links the adjacent spans, so the dynamic behavior of the calculated girder is affected by the adjacent spans.
(5) The displacement was measured by steel string LVDT, which may produce error by elastic elongation and local deformation of the steel wire.

Shown in Figs. 5.25 and 5.26 are the distributions of maximum displacements and accelerations of the bridge under the train speed of 180–300 km/h, with the solid curves representing the calculated results, and the discrete points the measured data. Since the structures of the 22nd and 23rd spans are identical, the measured data of the two spans are plotted in the same diagrams, but expressed by different symbols.

In Fig. 5.25, the peak of vertical displacement appears at the train speed of 250 km/h. The pioneer EMU is regarded as a moving load series with 25.5 m interval (length of each vehicle), producing 2.94 Hz loading frquency on the bridge when it runs at 250 km/h, which is roughly equivalent to 1/3 of the bridge natural frequency 8.15 Hz. This phenomenon corresponds to the first resonance condition of simply-supported beam proposed in Sect. 2.4 of this book, viz the resonance of $i = 3$ appears at the train speed of 250 km/h. As seen from the figure, the lateral amplitudes of the bridge are small, and they increase with the train speed in the speed range of 180–300 km/h, indicating no significant transverse resonance phenomenon appears.

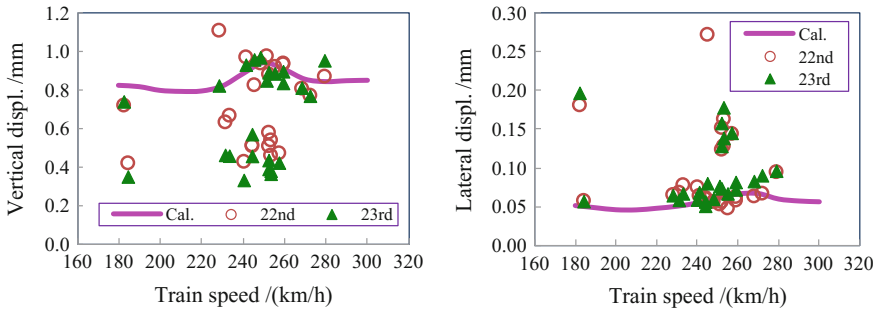

Fig. 5.25 Distributions of maximum displacements of the bridge at mid-span versus train speed

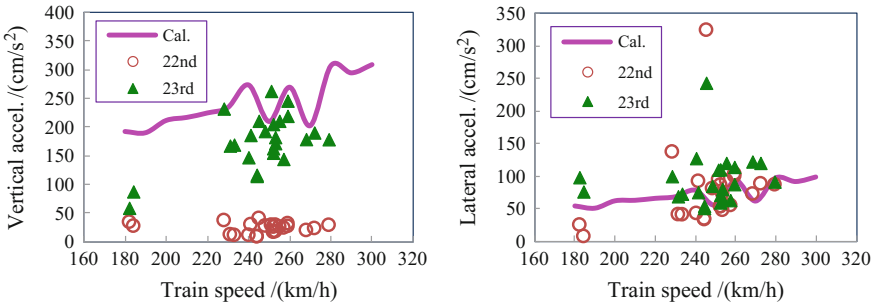

Fig. 5.26 Distributions of maximum accelerations of the bridge at mid-span versus train speed

In Fig. 5.26, the accelerations of the bridge increase with the train speed, while there is no significant lateral resonance phenomenon appeared in the speed range from 180 km/h to 300 km/h. However, the distribution curve of maximum lateral amplitudes exhibits a certain fluctuation, owing to the randomness of the track irregularity excitation.

As shown in Figs. 5.25 and 5.26, the measured data are discretely distributed. To better compare the calculated results with them, the vertical displacement, lateral amplitude, vertical, and lateral accelerations measured in 11 train passages at 250–270 km/h were analyzed statistically, as shown in Table 5.9. It can be seen that all calculation values are within 2 times of the standard deviations from the averages of the measured data.

From Table 5.9 and Figs. 5.25 and 5.26, one can see that the calculated results are quite consistent with the measured data, not only in dynamic response amplitudes and waveforms, but also in distributions of their maximums with train speed. It can be concluded that the analysis model and the solution method proposed in this chapter are applicable to simulating the dynamic responses of train-bridge coupling system.

5.7.6 Dynamic Responses of Vehicle

Shown in Fig. 5.27 are the vertical and lateral wheel-rail force time histories of the first wheel-set of the train at 270 km/h, in which from 3.33 to 3.66 s is the time duration of the wheel-set running on the bridge. It can be seen that the whole waveforms are rather steady, without significant difference when the wheel-set runs on and outside the bridge.

Shown in Fig. 5.28 are the car-body acceleration time histories of the first car at the train speed of 270 km/h, in which from 3.33 to 3.93 s is the time duration from the first wheel-set of the car running onto the bridge to the fourth one leaving out.

In the figure, there is no significant change in the car-body acceleration time histories during the car passing on the bridge, while large oscillations appear,

Table 5.9 Comparison between the measured statistics and the calculated results of the bridge

Item	Calculated result			250–270 km/h, measured statistics			
	250 km/h	260 km/h	270 km/h	Maximum	Minimum	Average	Standard deviation
Vertical displacement of bridge at loading side (mm)	0.938	0.904	0.856	0.976	0.364	0.689	0.227
Vertical displacement of bridge at non-loading side (mm)	0.605	0.570	0.537	1.009	0.433	0.698	0.193
Lateral amplitude of bridge at loading side (mm)	0.062	0.067	0.068	0.178	0.048	0.102	0.043
Vertical acceleration of bridge at loading side (cm/s^2)	209.6	269.4	202.3	263.0	17.2	109.5	90.9
Vertical acceleration of bridge at non-loading side (cm/s^2)	61.8	75.9	48.2	236.9	47.8	134.0	62.9
Lateral acceleration of bridge at loading side (cm/s^2)	56.2	94.1	62.5	121.9	47.8	83.2	23.6

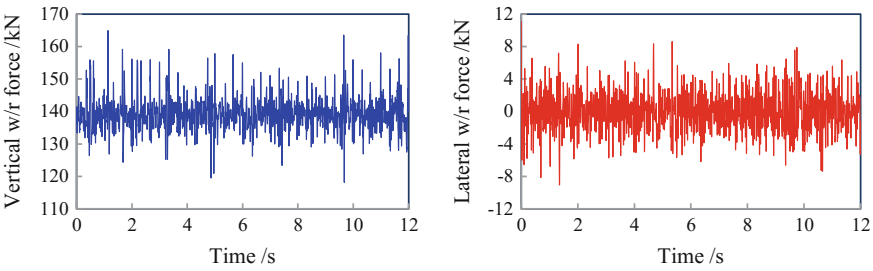

Fig. 5.27 Time histories of vertical and lateral wheel-rail forces of the first wheel-set (V = 270 km/h)

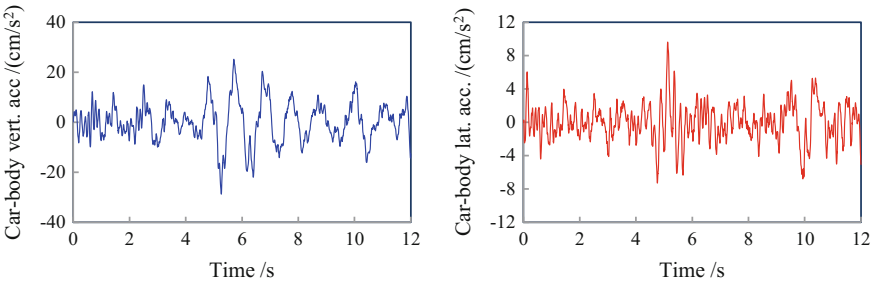

Fig. 5.28 Time histories of vertical and lateral car-body accelerations of the first car (V = 270 km/h)

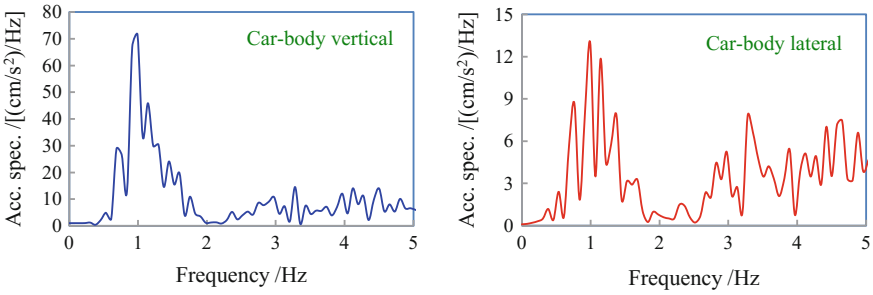

Fig. 5.29 Frequency spectra of vertical and lateral car-body accelerations of the first car (V = 270 km/h)

respectively, at 1.6 s (vertical) and 1.5 s (lateral) after it leaves. It is analyzed that these oscillation waves are caused by track irregularities: the vertical irregularity has a peak at 91 m out of the bridge, while the alignment at 81 m, and correspondingly, the oscillation waves appear just at 0.4 s after the car passed the irregularity peak positions.

Shown in Fig. 5.29 are the frequency spectrum curves for car-body accelerations of the first car. There appear a peak at 1 Hz in vertical acceleration, and two peaks at 0.8 Hz and 1.3 Hz in lateral, which correspond to the car-body floating frequency 0.89 Hz, the rolling-and-swing frequency 0.77 Hz, and the yawing frequency 1.40 Hz, respectively.

By comprehensive comparison on the bridge response and the vehicle response in this case study, one can find that the bridge deformation has less influence on the wheel-rail forces and car-body accelerations than the track irregularity does.

Shown in Figs. 5.30, 5.31, and 5.32 are distributions of maximum derailment factors, offload factors, vertical and lateral wheel-rail forces, and car-body accelerations versus train speed from 180 to 300 km/h, which are drawn either from all the wheel-sets or from all the cars in the whole process of the train running on the

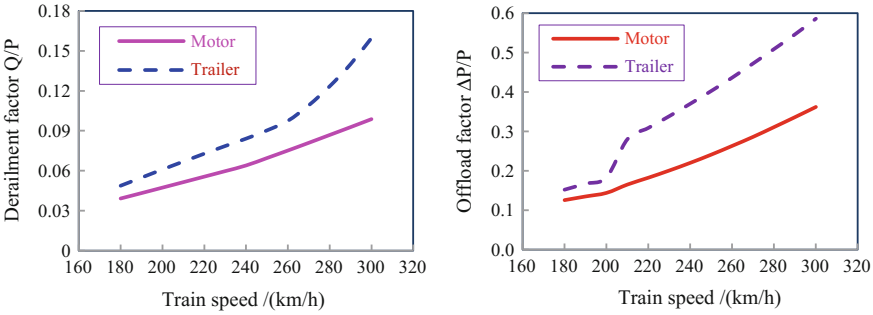

Fig. 5.30 Distributions of maximum vehicle derailment factors and offload factors versus train speed

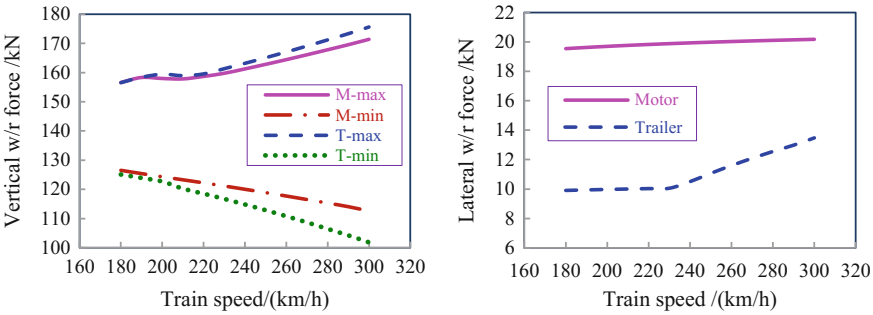

Fig. 5.31 Distributions of maximum vertical and lateral wheel-rail forces versus train speed

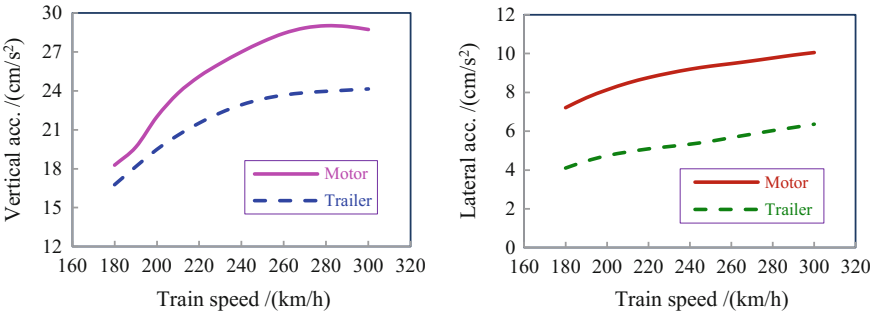

Fig. 5.32 Distributions of maximum vertical and lateral car-body accelerations versus train speed

bridge, and the maximum car-body accelerations refer to the values at the center of the car-body.

It can be seen that with the increase of train speed and the intensification of train-bridge vibration, the running safety and stability of the train tend to be worsened. In train speeds ranging from 180 km/h to 300 km/h, the variations of maximum and minimum vertical wheel-rail forces, maximum lateral wheel-rail forces, and vertical and lateral car-body accelerations are very small, but the derailment factors and the offload factors increase significantly with the train speed. When the train speed increases from 180 km/h to 300 km/h, the derailment factors and offload factors of motor-car approximately increase by 3 times, and trailer-car by 4 times. When the train speed is 300 km/h, the maximum offload factor of trailer-car reaches to 0.586, approaching to the running safety limit 0.6 of this index.

5.7.7 *Discussion on Iteration Convergence*

The intersystem iteration method is used for simulation calculation in this example, with the vertical wheel-rail force, lateral wheel-rail force, and wheel-rail rolling force moment as the convergence control indices. Shown in Fig. 5.33 are the convergence processes of the control indices, when the train speed is 270 km/h. For comparison, the convergence processes of convergence indices of mid-span displacements of the bridge and car-body accelerations of the vehicle, although they are not governed ones, are also given, as shown in Fig. 5.34.

It is found that the indices converge very fast in the iteration processes, with their error limits satisfied in only 6 iteration loops, indicating the method has a good convergence. The monotonousness of wheel-rail force and force moment in convergence process is better than that of bridge displacement and car-body acceleration, so they are more suitable to be used as convergence control index.

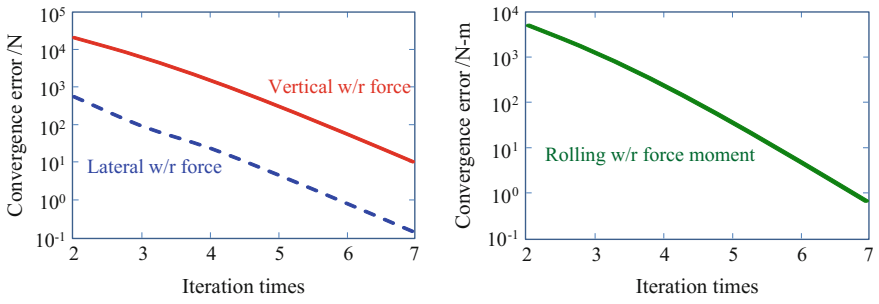

Fig. 5.33 Convergence processes of wheel-rail forces

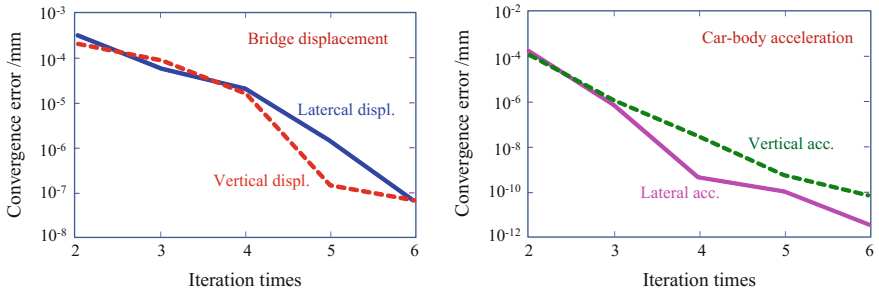

Fig. 5.34 Convergence processes of bridge displacements and car-body accelerations

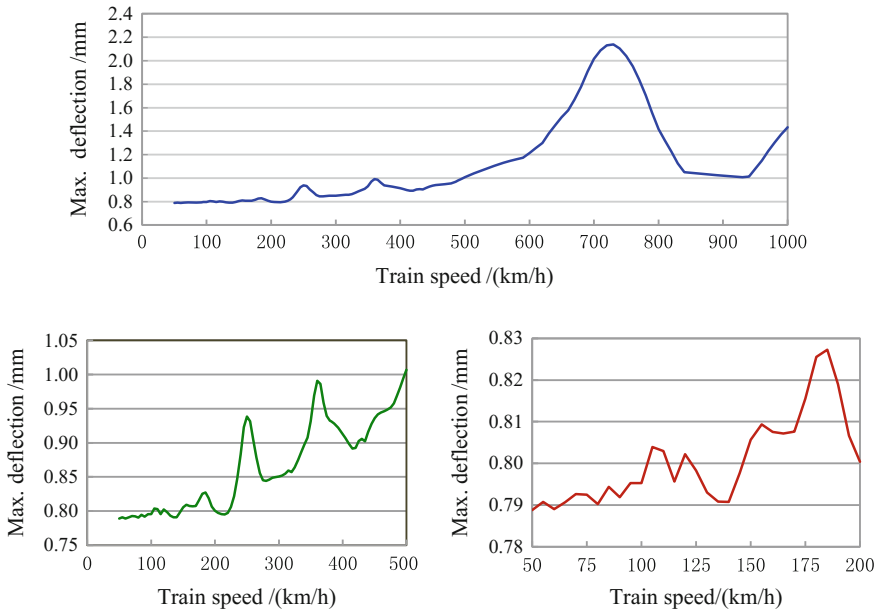

Fig. 5.35 Distributions of maximum vertical displacements of bridge versus train speed

5.7.8 *Vertical Resonance Analysis of Bridge Subsystem*

To study the resonance of bridge subsystem, a further calculation is performed by extending the train speed range to 50–1000 km/h, at each 5 km/h between train speed 50–500 km/h, and each 10 km/h between 510 and 1000 km/h. Shown in Fig. 5.35 are the distributions of maximum vertical displacement of the bridge versus the train speed.

In Fig. 5.35, the distribution curves of bridge deflection exhibit peaks with different levels at the train speeds of 120, 155, 185, 250, 360, and 730 km/h. Note

that for this bridge, the vertical fundamental frequency is f_b = 8.15 Hz, thus the loading frequencies of these peaks with respect to the vehicle length 25.5 m can be estimated as

$$f_{L1} = \frac{730/3.6}{25.5} = 7.95\,\text{Hz} \approx f_b \tag{5.118a}$$

$$f_{L2} = \frac{360/3.6}{25.5} = 3.92\,\text{Hz} \approx \frac{f_b}{2} \tag{5.118b}$$

$$f_{L3} = \frac{250/3.6}{25.5} = 2.72\,\text{Hz} \approx \frac{f_b}{3} \tag{5.118c}$$

$$f_{L4} = \frac{185/3.6}{25.5} = 2.02\,\text{Hz} \approx \frac{f_b}{4} \tag{5.118d}$$

$$f_{L5} = \frac{155/3.6}{25.5} = 1.69\,\text{Hz} \approx \frac{f_b}{5} \tag{5.118e}$$

$$f_{L6} = \frac{120/3.6}{25.5} = 1.31\,\text{Hz} \approx \frac{f_b}{6} \tag{5.118f}$$

These results correspond to the first resonance condition of simply-supported beam proposed in Sect. 2.4 of this book, namely when the loading frequency is equal to $1/i$ times the bridge natural frequency, the bridge vibration will be significantly magnified, indicating the resonance occurs, and the smaller the resonance order i, the larger the response amplitude.

Although a variety of excitation frequencies are given in Sect. 5.7.2, this example shows the effect of loading period by vehicle length is the most significant on the bridge resonance.

Compared in Fig. 5.36 are the vertical displacement time histories of bridge mid-span at two resonance train speeds of 250 and 360 km/h and their adjacent speeds.

The amplification mechanism of bridge dynamic response when resonance occurs is clearly illustrated by the curves in the figure. At the resonance train speed of 250 km/h, the vertical amplitude of bridge increases continuously, thus the dynamic deflection is significantly magnified, showing the typical characteristic of the damped resonance waveform, which is obviously different from the curves at adjacent lower and higher non-resonance speeds (230 and 270 km/h). The same difference can be seen between the curves at resonance speed 360 km/h and its adjacent non-resonance speeds 320 and 400 km/h.

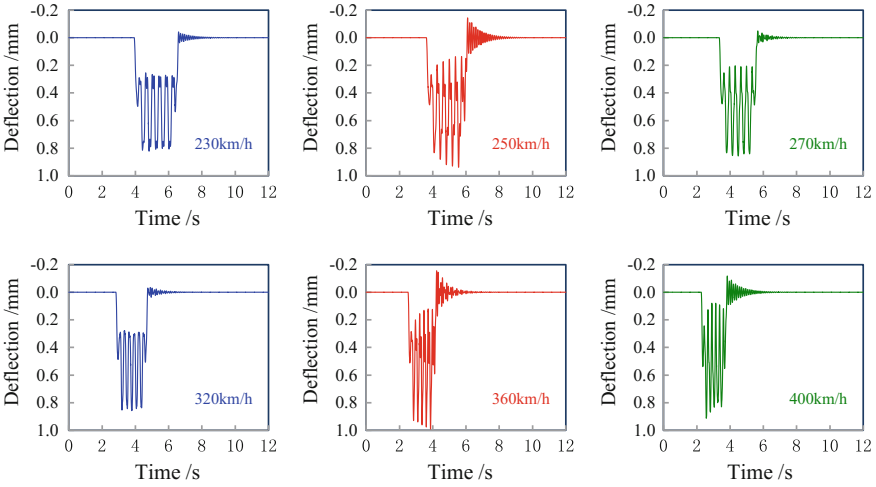

Fig. 5.36 Dynamic deflection time histories of bridge at mid-span under different train speeds

References

Cao XQ (1991) Lateral vibrations of steel trussed bridge [M]. The China Railway Publishing House, Beijing (in Chinese)

Dinh Van N, Kim KD, Warnitchai P (2009) Dynamic analysis of three-dimensional bridge-high-speed train interactions using a wheel-rail contact model [J]. Eng Struct 31:3090–3106

Gao MM (2002) Dynamic analysis of train-track-bridge coupling system and train running properties in high-speed railway [D]. China Academy of Railway Sciences, Beijing (in Chinese)

Kalker JJ (1967) On the rolling contact of two elastic bodies in the presence of dry friction [D]. Delft University of Technology, Netherlands

Li Q, Wu DJ, Li J (2007) Vibration analysis of train-bridge coupling system for mix-loaded freight trains and small-and-medium span bridges [J]. J Tongji Univ 35(2):171–175 (in Chinese)

Li XZ (2000) Theory and application of coupling vibrations of train-bridge system in high-speed railway [D]. Southwest Jiaotong University, Chengdu (in Chinese)

Pan JY, Gao MM (2008) Dynamic analysis of railway vehicle-track-bridge system [M]. The China Railway Publishing House, Beijing (in Chinese)

Shen ZY, Hedrick JK, Elkins JA (1983) A comparison of alternative creep force models for rail vehicle dynamic analysis [J]. Veh Syst Dyn Int J Veh Mech Mobil 12(1/2/3):79–83

Wang FT (1994) Dynamics of vehicle system [M]. The China Railway Publishing House, Beijing (in Chinese)

Wu DJ, Li Q, Chen AR (2007) The problem of numerical stability of iterative solution of vehicle-bridge coupling vibration [J]. Chin Q Mech 28(3):405–411 (in Chinese)

Xia H, Zhang N et al (2003) Dynamic analysis of high-speed railway bridge under articulated trains [J]. Comput Struct 81:2467–2478

Xia H, Zhang N (2005a) Dynamic interaction of vehicles and structures [M]. Science Press, Beijing (in Chinese)

Xia H, Zhang N (2005b) Experimental analysis of railway bridge under high-speed trains [J]. J Sound Vib 282(2):517–528

Xia H, De Roeck G, Goicolea JM (2012) Bridge vibration and controls: new research [M]. Nova Science Publishers Inc, New York

Xu YL, Zhang N, Xia H (2004) Vibration of coupled train and cable-stayed bridge system in cross wind [J]. Eng Struct 26:1389–1406

Zeng QY, Guo XR (1999) Theory and application of train-bridge time-varying vibration system [M]. The China Railway Publishing House, Beijing (in Chinese)

Zhai WM (2007) Vehicle-track coupling dynamics [M]. Science Press, Beijing (in Chinese)

Zhang N (2002) Theoretical analysis and experimental study on dynamic interaction of high-speed railway bridge and articulated trains [D]. Beijing Jiaotong University, Beijing (in Chinese)

Zhang N, Xia H, Guo WW (2008) Vehicle-bridge interaction analysis under high-speed trains [J]. J Sound Vib 309(3–5):407–425

Zhang N, Xia H, Guo WW, De Roeck G (2010) A vehicle-bridge linear interacted model and its validation [J]. Int J Struct Stab Dyn 10(2):335–361

Zhang N, Xia H (2013) Dynamic analysis of coupled vehicle–bridge system based on inter-system iteration method [J]. Comput Struct 114–115:26–34

Chapter 6
Dynamic Analysis of Train-Bridge System Subjected to Crosswinds

In this chapter, the dynamic responses of train-bridge system subjected to crosswinds are analyzed. Several simulation methods of stochastic wind forces are introduced. Based on fluid dynamics, the influences of wind barriers on the wind velocity field around bridge structures and the aerodynamic behaviors of train vehicles are analyzed, in which the structure forms, hole shapes, and arrangement patterns are discussed. A spatial dynamic analysis model of coupled train-bridge system subjected to crosswinds is established. As an example, the dynamic responses of the Tsing Ma Suspension Bridge in Hong Kong are calculated and some results are compared with the data measured during the Typhoon York, recorded by the Wind and Structural Health Monitoring System (WASHMS) installed on the bridge. The threshold curve of train speed and wind velocity for ensuring the running safety of the train on the bridge is proposed. Taking a simply-supported PC girder bridge located in the wind area on the Lanzhou-Xinjiang high-speed railway as another case study, the dynamic analysis on the wind-train-bridge interaction system is performed considering the aerodynamic effect of wind barriers, based on which the windbreak effect of different wind barrier structures is evaluated.

6.1 Numerical Simulation of Wind Loads

Bridges located in the strong wind areas vibrate intensively when subjected to the wind excitation, which not only affects the vibration performance of the train running on the bridge, but also increases significantly the lateral loads on the bridge owing to the wind pressures from the bridge itself and from train vehicles. Meanwhile, when a high-speed train suffers from strong lateral wind pressures, the original vibration properties of the train are changed by the aerodynamic forces and moments acting on it, which greatly increases the derailment or overturn risk of the train. In addition, while the wind generates loads on the bridge and the train, it is

H. Xia et al., *Dynamic Interaction of Train-Bridge Systems in High-Speed Railways*, Advances in High-speed Rail Technology, https://doi.org/10.1007/978-3-662-54871-4_6

also influenced by the motion state of them in turn. The wind-train-bridge dynamic interaction system is thus constituted by considering the coupling effects of all these factors. In wind-resistant design of high-speed railway bridges, therefore, it is important in theory as well as in engineering practice to perform a comprehensive research on the dynamic responses of train-bridge system under strong wind, so as to analyze and evaluate the dynamic performance of the bridge and the running safety of the train, and to ensure the service reliability in various operation conditions (Suzuki et al. 2003; Sanquer et al. 2004; Cai and Chen 2004; Li et al. 2005, 2014; Tian 2007; Guo et al. 2015).

In studying the train-bridge time-varying system under wind loads, the usual method is to establish a dynamic analysis model for the train-bridge system (Yang and Yau 1997; Zeng and Guo 1999; Xia et al. 2000; Lou 2005; Zhai 2007), to input the time series of turbulent wind velocity to the system, and then to solve this system in the time domain by adopting numerical simulation methods. When lack of measured data, the artificial wind velocity time series is often adopted as the input. In order to ensure the rationality of calculation results, the simulated artificial turbulent wind velocity series should be as much as possible to satisfy the natural wind properties. There are various methods available to simulate a stochastic wind velocity field, and introduced hereinbelow are four commonly used numerical methods.

6.1.1 Spectral Representation Method

The spectral representation method (SRM) regards the wind velocity field as a series of harmonic waves (sine or cosine waves) constituted by FFT (Fast Fourier Transform) techniques. The digital random wind velocity field can be generated by superposing the series of harmonic waves. This method is clear and simple, by which the unconditionally stable and highly accurate simulation results can be obtained. In this section, two spectral representation methods are introduced.

6.1.1.1 SRM Based on Proper Orthogonal Decomposition

Suppose the wind velocity vector at N space points can be expressed as an N-variate stochastic series vector $\mathbf{V}(t) = [\,v_1(t) \quad v_2(t) \quad \cdots \quad v_N(t)\,]^{\mathrm{T}}$ which consists of N partially correlated zero-mean stationary process $v_j(t)$ ($j = 1, 2, \ldots, N$). The power spectral matrix $\mathbf{S}_{\mathrm{VV}}(\omega)$ of $\mathbf{V}(t)$ is expressed as

$$\mathbf{S}_{\mathrm{VV}}(\omega) = \begin{bmatrix} S_{11}(\omega) & \cdots & S_{1N}(\omega) \\ \vdots & \ddots & \vdots \\ S_{N1}(\omega) & \cdots & S_{NN}(\omega) \end{bmatrix} \tag{6.1}$$

$$S_{ij}(\omega) = S_{v_i v_j}(\omega) = \sqrt{S_{v_i}(\omega) S_{v_j}(\omega)} \cdot \gamma(i,j;\omega) \tag{6.2}$$

where $\gamma(i,j;\omega)$ is the coherency function between v_i and v_j; $\mathbf{S}_{VV}(\omega)$ is a positive semi-definite matrix for the fluctuating wind velocity time history with N different eigenvalues $\eta_1(\omega)$, $\eta_2(\omega)$, …, $\eta_N(\omega)$, which are all positive real numbers, and the corresponding N eigenvectors $\varphi_1(\omega)$, $\varphi_2(\omega)$, …, $\varphi_N(\omega)$ are all composed of real numbers.

Assuming the eigenvectors satisfy the orthogonal conditions with respect to the spectrum matrix $\mathbf{S}_{VV}(\omega)$, i.e.,

$$\boldsymbol{\varphi}_i^{\mathrm{T}}(\omega)\boldsymbol{\varphi}_j(\omega) = \delta_{ij} \tag{6.3}$$

$$\boldsymbol{\varphi}_i^{\mathrm{T}}(\omega)\mathbf{S}_{VV}(\omega)\boldsymbol{\varphi}_j(\omega) = \delta_{ij}\eta_j(\omega) \tag{6.4}$$

The decomposition of $\mathbf{S}_{VV}(\omega)$ can be written as

$$\mathbf{S}_{VV}(\omega) = \sum_{i=1}^{N} \boldsymbol{\varphi}_i(\omega)\eta_i(\omega)\boldsymbol{\varphi}_i^{\mathrm{T}}(\omega) = \boldsymbol{\Phi}(\omega)\boldsymbol{\Lambda}(\omega)\boldsymbol{\Phi}^{\mathrm{T}}(\omega) \tag{6.5}$$

where $\boldsymbol{\Phi}(\omega) = [\,\varphi_1(\omega) \quad \varphi_2(\omega) \quad \cdots \quad \varphi_N(\omega)\,]$ is the vibration mode shape matrix of $\mathbf{S}_{VV}(\omega)$, and $\boldsymbol{\Lambda}(\omega) = \mathrm{diag}[\,\eta_1(\omega) \quad \eta_2(\omega) \quad \cdots \quad \eta_N(\omega)\,]$ is the eigenvalue matrix.

Assuming $\mathbf{Y}(t)$ is an N-variate unrelated random vector process, $y_j(t)$ is the component (j = 1, 2, …, N), and $\mathbf{Y}(\omega)$ is the corresponding Fourier transform, the power spectral matrix of $\mathbf{Y}(t)$ is expressed as

$$\mathbf{S}_{YY}(\omega) = \boldsymbol{\Lambda}(\omega) \tag{6.6}$$

Substituting Eq. (6.6) into Eq. (6.5), the spectrum matrix becomes

$$\mathbf{S}_{VV}(\omega) = \boldsymbol{\Phi}(\omega)\mathbf{S}_{YY}(\omega)\boldsymbol{\Phi}^{\mathrm{T}}(\omega) \tag{6.7}$$

So the Fourier transform $\mathbf{V}(\omega)$ of the stochastic series vector $\mathbf{V}(t)$ can be written as

$$\mathbf{V}(\omega) = \boldsymbol{\Phi}(\omega)\mathbf{Y}(\omega) = \sum_{i=1}^{N} \boldsymbol{\varphi}_i(\omega)\mathbf{Y}(\omega) \tag{6.8}$$

This formula is the strong form of proper orthogonal decomposition of the stationary stochastic vector process $\mathbf{V}(t)$. In fact, Eq. (6.8) is based on the eigenvalue decomposition of the symmetrical matrix $\mathbf{S}_{VV}(\omega)$, which expresses $\mathbf{V}(t)$, in the frequency domain, into the sum of all vibration modes weighted with the principal coordinates of their spectra.

The eigenvalues of spectral proper transform represent the vibration energies in the corresponding modes. By sequencing the vibration modes in descending order of the eigenvalues, the following eigenpairs are obtained

$$[\eta_k(\omega);\ \varphi_k(\omega)] \quad (k = 1, 2, \ldots, N;\ \eta_1 \geq \eta_2 \geq \cdots \geq \eta_N) \tag{6.9}$$

The modal truncation technique, which is similar to the modal decomposition method in structure dynamics, can be incorporated into the spectral proper transform; that is, $\mathbf{S}_{\mathrm{VV}}(\omega)$ can be approximated by a limited order N_{s} with enough precision if the first N_{s} modes of vibration contain enough energies, thus

$$\mathbf{S}_{\mathrm{VV}}(\omega) = \sum_{k=1}^{N_{\mathrm{s}}} \boldsymbol{\varphi}_k(\omega)\eta_k(\omega)\boldsymbol{\varphi}_k^{\mathrm{T}}(\omega) \tag{6.10}$$

Accordingly, $\mathbf{V}(\omega)$ can be expressed as

$$\mathbf{V}(\omega) = \sum_{k=1}^{N_{\mathrm{s}}} \boldsymbol{\varphi}_k(\omega)\mathbf{Y}(\omega) \tag{6.11}$$

The number of vibration modes N_{s} is selected according to actual conditions, and when $N_{\mathrm{s}} \ll N$ (sometimes $N_{\mathrm{s}} = 1$), the calculation of Eq. (6.11) will be very simple.

By combining the proper orthogonal decomposition and the spectral representation method, and dividing the frequency interval $[\omega_0, \omega_u]$ into M sections with $\Delta\omega = (\omega_u - \omega_0)/M$, the simulation formula based on proper orthogonal decomposition can be expressed as

$$\mathbf{V}(t) = \sum_{k=1}^{N_{\mathrm{s}}} \sum_{l=1}^{M} 2\sqrt{\Delta\omega}\sqrt{\eta_k(\omega_l)}\varphi_k(\omega_l)\cos(\omega_l t + \theta_{kl}) \tag{6.12}$$

where θ_{kl} is the independent random phase angle, distributed uniformly in [0, 2π], and $\omega_l = (l-1) \cdot \Delta\omega$.

When the FFT technique is applied, the computational efficiency can be dramatically improved.

6.1.1.2 SRM Based on Explicit Cholesky Decomposition

A fast spectrum analysis method based on explicit Cholesky decomposition was proposed by Cao et al. (2000), which is successfully used to decompose the spectral density matrix of the target stochastic process into a deterministic algebraic formula, then calculate them with the IFFT (Inverse Fast Fourier Transform) technique. This method can greatly reduce the computational effort, because no iteration is required in it.

According to the Cholesky decomposition method, the power spectral density matrix of Eq. (6.1) can be decomposed as

$$\mathbf{S}(\omega) = \mathbf{H}(\omega)\mathbf{H}^{\mathrm{T}}(\omega) \tag{6.13}$$

$$\mathbf{H}(\omega) = \begin{bmatrix} H_{11}(\omega) & 0 & \cdots & 0 \\ H_{21}(\omega) & H_{22}(\omega) & \cdots & 0 \\ \vdots & \vdots & \ddots & \vdots \\ H_{n1}(\omega) & H_{n2}(\omega) & \cdots & H_{nn}(\omega) \end{bmatrix} \tag{6.14}$$

where the matrix $\mathbf{H}(\omega)$ is the Cholesky decomposition formula of the auto-power spectrum density matrix $\mathbf{S}(\omega)$, and $H_{jm}(\omega)$ is a typical element in $\mathbf{H}(\omega)$.

When simulating the wind loads acting on the bridge, the wind velocity series on each node can be regarded as one-dimensional Gauss stochastic process $f_j(t)$, expressed as

$$f_j(t) = \Omega \sum_{m=1}^{j} \sum_{k=1}^{N_\mathrm{f}} \left|H_{jm}(\omega_{mk})\right| \cos(\omega_{mk}t - \theta_{jm}(\omega_{mk}) + \varphi_{mk}), \quad (j = 1, 2, \ldots, n_1) \tag{6.15}$$

where $\Omega = \sqrt{2(\Delta\omega)}$; N_f is the total number of frequency interval $\Delta\omega$ in the spectrum; n_1 is the total number of wind velocity simulation points; φ_{mk} is a random variable uniformly distributed between 0 and 2π.

Through mathematical operation for auto-power spectral density matrix, Eq. (6.14) can be simplified as

$$\mathbf{H}(\omega) = \sqrt{\mathbf{S}(\omega)}\mathbf{G}(\omega) \tag{6.16}$$

where $\mathbf{G}(\omega)$ is the correlation matrix between different wind velocity points, which can be expressed as

$$\mathbf{G}(\omega) = \begin{bmatrix} 1 & 0 & 0 & 0 & \cdots & 0 \\ C & \sqrt{1-C^2} & 0 & 0 & \cdots & 0 \\ C^2 & C\sqrt{1-C^2} & \sqrt{1-C^2} & 0 & \cdots & 0 \\ C^3 & C^2\sqrt{1-C^2} & C\sqrt{1-C^2} & \sqrt{1-C^2} & \cdots & 0 \\ \vdots & \vdots & \vdots & \vdots & \ddots & \vdots \\ C^{n-1} & C^{n-2}\sqrt{1-C^2} & C^{n-3}\sqrt{1-C^2} & C^{n-4}\sqrt{1-C^2} & \cdots & \sqrt{1-C^2} \end{bmatrix} \tag{6.17}$$

$\mathbf{G}(\omega)$ can be also written with explicit algebraic expressions as

$$G_{jm}(\omega) = \begin{cases} 0, & 1 \le j < m \le n_1 \\ C^{|j-m|}, & m = 1,\ m \le j \le n_1 \\ C^{|j-m|}\sqrt{1-C^2}, & 2 \le m \le j \le n_1 \end{cases} \tag{6.18}$$

where

$$C = \exp\left(-\frac{\lambda \omega_{mk} d}{2\pi \bar{U}(z)}\right) \tag{6.19}$$

$$\omega_{mk} = (k-1)\Delta\omega + \frac{m}{N}\Delta\omega, \quad (k = 1, 2, \ldots, M) \tag{6.20}$$

where M is a sufficiently large number; λ is a dimensionless attenuation factor between 7 and 10, $\overline{U}(z)$ is the mean wind velocity at the elevation of the bridge deck, and d is the horizontal distance between the adjacent wind simulation points, so the horizontal spatial distance from j-point to m-point is $\Delta_{jm} = d|j-m|$.

By substituting Eq. (6.16) into Eq. (6.15), we obtain

$$f_j(t) = \Omega \sum_{m=1}^{j} \sum_{k=1}^{N_t} \sqrt{S_u(\omega_{mk})} G_{jm}(\omega_{mk}) \cos(\omega_{mk} t + \varphi_{mk}), \quad (j = 1, 2, \ldots, n_1) \tag{6.21}$$

According to the above equation, the time histories of wind velocity components $u_j(t)$ and $w_j(t)$, acting on the jth point in horizontal direction and vertical direction, respectively, and both perpendicular to the main deck of the bridge, can then be generated by the following equations

$$u_j(t) = \sqrt{2\Delta\omega} \sum_{m=1}^{j} \sum_{k=1}^{N} \sqrt{S_{\mathrm{u}}(\omega_{mk})} G_{jm}(\omega_{mk}) \cos(\omega_{mk} t + \varphi_{mk}) \tag{6.22a}$$

$$w_j(t) = \sqrt{2\Delta\omega} \sum_{m=1}^{j} \sum_{k=1}^{N} \sqrt{S_{\mathrm{w}}(\omega_{mk})} G_{jm}(\omega_{mk}) \cos(\omega_{mk} t + \varphi_{mk}) \tag{6.22b}$$

In order to utilize the FFT technique and the simulation formulas of wind velocity histories, taking the horizontal wind for example, Eq. (6.22a) can be rewritten as

$$u_j(p\Delta t) = \mathrm{Re}\left\{ \sum_{m=1}^{j} h_{jm}(q\Delta t) \exp\left[\mathrm{i}\left(\frac{m\Delta\omega}{n}\right) p\Delta t \right] \right\} \tag{6.23}$$

where $p = 0, 1, \ldots, 2N \times n - 1$; $q = 0, 1, \ldots, 2N - 1$; $M \ge 2N$; $j = 1, 2, \ldots, n$; and $h_{jm}(q\Delta t)$ is given by

$$h_{jm}(q\Delta t) = \sum_{k=0}^{2N-1} B_{jm}(k\Delta\omega)\exp[\mathrm{i}(k\Delta\omega)(q\Delta t)] \tag{6.24}$$

$$B_{jm}(k\Delta\omega) = \begin{cases} \sqrt{2\Delta\omega S_{\mathrm{u}}(\omega)}G_{jm}\left(k\Delta\omega + \frac{m\Delta\omega}{n}\right)\exp(\mathrm{i}\varphi_{mk}) & (0 \le k < N) \\ 0 & (N \le k < 2N-1) \end{cases} \tag{6.25}$$

It can be seen that $h_{jm}(q\Delta t)$ is the inverse Fourier transform of $B_{jm}(k\Delta\omega)$.

6.1.2 Linear Filtering Method

The linear filtering method (LFM) is used to artificially generate random series, by inputting a zero-mean white noise series and outputting a Gaussian random process with the specified spectral characteristics through a filter. As two typical LFMs, the auto-regressive moving average model (ARMA) and the auto-regressive model (AR) are used to describe the stationary random process, and good results can be obtained. In this section, the AR model is introduced.

Under satisfying calculation accuracy in engineering practice, the following assumptions can be made in simulating wind velocity histories:

(1) The average wind velocity at any point keeps unchanged with time;
(2) The fluctuating wind velocity history is an ergodic and stationary stochastic process with zero-mean value;
(3) The wind velocity histories at all the points are spatially correlated;
(4) The fluctuating wind velocities at different heights have the same phase, that is, their cross-correlation matrix is even symmetric.

A wind velocity history is in nature a stochastic time series. A multi-variate AR model can be used to simulate the wind velocity field for a bridge as a large-scale linear spatial structure. Supposing there are m wind velocity simulation points, the related turbulent wind histories $\mathbf{v}(\mathbf{X}, \mathbf{Y}, \mathbf{Z}, t) = [v_1(x_1, y_1, z_1, t), v_2(x_2, y_2, z_2, t), \ldots, v_m(x_m, y_m, z_m, t)]$ can be generated by

$$\mathbf{v}(\mathbf{X},\mathbf{Y},\mathbf{Z},t) = -\sum_{k=1}^{p} \boldsymbol{\varphi}_k \cdot \mathbf{v}(\mathbf{X},\mathbf{Y},\mathbf{Z},t-k\cdot\Delta t) + \mathbf{N}(t) \tag{6.26}$$

where $\mathbf{X} = [x_1, x_2, \ldots, x_m]^{\mathrm{T}}$, $\mathbf{Y} = [y_1, y_2, \ldots, y_m]^{\mathrm{T}}$, $\mathbf{Z} = [z_1, z_2, \ldots, z_m]^{\mathrm{T}}$, and (x_i, y_i, z_i) is the coordinate of the ith point; p is the order of the AR model; Δt is the time interval for wind field simulation; $\boldsymbol{\varphi}_k$ is the $m \times m$ auto-regressive coefficient matrix of the AR model, $k = 1, 2, \ldots, p$; and $\mathbf{N}(t)$ is a zero-mean independent stochastic process with a given variance.

For convenience, $\mathbf{v}(\mathbf{X}, \mathbf{Y}, \mathbf{Z}, t)$ is abbreviated as $\mathbf{v}(t)$, and Eq. (6.26) is post-multiplied by $\mathbf{v}^{\mathrm{T}}(t - j \cdot \Delta t)$ on both sides, so we obtain

$$\mathbf{v}(t) \cdot \mathbf{v}^{\mathrm{T}}(t - j \cdot \Delta t) = -\sum_{k=1}^{p} \boldsymbol{\varphi}_k \cdot \mathbf{v}(t - k \cdot \Delta t) \cdot \mathbf{v}^{\mathrm{T}}(t - j \cdot \Delta t) + \mathbf{N}(t) \cdot \mathbf{v}^{\mathrm{T}}(t - j \cdot \Delta t) \tag{6.27}$$

where $j = 0, 1, 2, \ldots, p$.

Note that $\mathbf{N}(t)$ with zero mean is independent of random process $\mathbf{v}(t)$, by taking mathematical expectation on both sides of Eq. (6.27) and utilizing the properties of auto-correlation functions, the relationship between the correlation function $\mathbf{R}(j \cdot \Delta t)$ and the auto-regression coefficient $\boldsymbol{\varphi}_k$ is derived via mathematical transformation, expressed as

$$\mathbf{R}(j \cdot \Delta t) = -\sum_{k=1}^{p} \boldsymbol{\varphi}_k \cdot \mathbf{R}[(j - k) \cdot \Delta t], \quad (j = 1, 2, \ldots, p) \tag{6.28}$$

$$\mathbf{R}(0) = -\sum_{k=1}^{p} \boldsymbol{\varphi}_k \cdot \mathbf{R}(k \cdot \Delta t) + \mathbf{R}_N \tag{6.29}$$

They can further be written in matrix form as

$$\mathbf{R} \cdot \boldsymbol{\varphi} = \begin{bmatrix} \mathbf{R}_N \\ \mathbf{O}_p \end{bmatrix} \tag{6.30}$$

where $\boldsymbol{\varphi}_{(p+1)m \times m} = [\,\mathbf{I} \quad \boldsymbol{\varphi}_1 \quad \boldsymbol{\varphi}_2 \quad \cdots \quad \boldsymbol{\varphi}_p\,]^{\mathrm{T}}$; $\mathbf{I}$ is an $m \times m$ unit matrix; $\mathbf{R}_N$ is the $m \times m$ covariance matrix; $\mathbf{O}_p$ is a $pm \times m$ null matrix; and $\mathbf{R}$ is the $(p + 1)$ $m \times (p + 1)m$ auto-correlation Toeplitz matrix, which can be expressed by partitioned matrix as

$$\mathbf{R} = \begin{bmatrix} \mathbf{R}_{11}(0) & \mathbf{R}_{12}(\Delta t) & \mathbf{R}_{13}(2\Delta t) & \cdots & \mathbf{R}_{1(p+1)}(p\Delta t) \\ \mathbf{R}_{21}(\Delta t) & \mathbf{R}_{22}(0) & \mathbf{R}_{23}(\Delta t) & \cdots & \mathbf{R}_{2(p+1)}[(p-1)\Delta t] \\ \mathbf{R}_{31}(2\Delta t) & \mathbf{R}_{32}(\Delta t) & \mathbf{R}_{33}(0) & \cdots & \mathbf{R}_{3(p+1)}[(p-2)\Delta t] \\ \vdots & \vdots & \vdots & \ddots & \vdots \\ \mathbf{R}_{(p+1)1}(p\Delta t) & \mathbf{R}_{(p+1)2}[(p-1)\Delta t] & \mathbf{R}_{(p+1)3}[(p-2)\Delta t] & \cdots & \mathbf{R}_{(p+1)(p+1)}(0) \end{bmatrix} \tag{6.31}$$

where $\mathbf{R}_{st}(j\Delta t)$ is an $m \times m$ square matrix; $s = 1, 2, \ldots, p + 1$; $t = 1, 2, \ldots, p + 1$; $j = 0, 1, 2, \ldots, p$.

The element in matrix $\mathbf{R}_{st}(j\Delta t)$ can be determined by the Wiener–Khintchine formula

$$R_{ih}(\tau) = \int_0^\infty S_{ih}(f)\cos(2\pi f \cdot \tau)\mathrm{d}f \tag{6.32}$$

where f is the frequency of fluctuating wind velocity (Hz); $S_{ih}(f)$ is the auto-spectrum density function of fluctuating wind velocities when $i = h$, and it is the cross-spectrum density function when $i \neq h$ that can be calculated by the auto-spectrum density function $S_{ii}(f)$ and the correlation function $r_{ih}(f)$ of the wind velocities; $i = 1, 2, 3, \ldots, m$; $h = 1, 2, 3, \ldots, m$.

The cross-power spectrum $S_{ih}(f)$ of wind velocities at various points in a wind field can be expressed as

$$S_{ih}(f) = \sqrt{S_{ii}(f)S_{hh}(f)} \cdot r_{ih}(f) \cdot \exp[\mathrm{i}\theta(f)] \tag{6.33}$$

where $\theta(f)$ is the phase angle related to different frequency f, herein $\theta(f) = 0$ according to the assumptions for wind velocity simulation.

For a structure with great longitudinal and vertical sizes, such as a bridge with high piers, the spatial correlation coefficient $r(f)$ suggested by Davenport (1961) is

$$r_{ih}(f) = \exp\left[-\frac{2f\sqrt{C_z^2(z_i - z_h)^2 + C_x^2(x_i - x_h)^2}}{\bar{v}(z_i) + \bar{v}(z_h)}\right] \tag{6.34}$$

where $\bar{v}(z_i)$ and $\bar{v}(z_h)$ denote the average wind velocities at the ith and the hth points, and (x_i, z_i) and (x_h, z_h) are the coordinates of the ith and the hth points, respectively; C_x and C_z are, respectively, the decay factors between any two points along the x- and the z-directions, which are usually determined by experiments, and the values suggested by Simiu and Scanlan (1996) are $C_x = 16$ and $C_z = 10$.

The independent stochastic process vector $\mathbf{N}(t)$ can be written as

$$\mathbf{N}(t) = \mathbf{L} \cdot \mathbf{n}(t) \tag{6.35}$$

where $\mathbf{n}(t) = [\, n_1(t) \quad n_2(t) \quad \cdots \quad n_m(t) \,]^{\mathrm{T}}$, $n_i(t)$ is an independent normal random process with zero mean and variance 1, $i = 1, 2, 3, \ldots, m$. $\mathbf{L}$ is a lower triangular matrix with m orders, which can be obtained by Cholesky decomposition on the $m \times m$ covariance matrix $\mathbf{R}_N$.

$$\mathbf{R}_N = \mathbf{L} \cdot \mathbf{L}^{\mathrm{T}} \tag{6.36}$$

The order p of auto-regression model is an important parameter. Generally, a low-order AR model can simulate random fluctuating wind velocity time history quite well.

There are several methods to determine the AR model order, such as the singular value decomposition method (SVD), the final prediction error criterion method (FPE), the Akaike information theoretic criterion method (AIC), the minimum

description length criterion method (MDL), and the criterion for auto-regressive transfer functions (CAT), in which the AIC method and the FPE method are widely used. Taking the AIC method for example, this criterion is acquired by applying the maximum likelihood principle to statistical hypothesis test of time series. The AIC is the function of order p, and its expression is

$$\mathrm{AIC}(p) = \lg(\hat{\sigma}_p^2) + \frac{2p}{t} \tag{6.37}$$

The optimal order p is selected by minimizing Eq. (6.37), that is, it should build p models from AR (1) to AR (p), and calculate the AIC values for all models, then compare the AIC values between two adjacent models. If the AIC of AR (p) changes little compared with that of AR (p − 1), i.e., the difference between them is less than a given threshold, the optimal order can be determined as p.

6.1.3 Wavelet Simulation

The wavelet analysis method has a nice local characteristic in both time domain and frequency domain, which can consider the local similarity of a random wind field, so it is especially applicable for local solution of random samples. Different from the Fourier transform with single frequency domain analysis, the wavelet bases for wavelet analysis in the time domain can use any linear combination of functions associated with real signals.

Set $f(t)$ as a square-integrable function, i.e., $f(t) \in L^2(\mathbf{R})$, $L^2(\mathbf{R})$ is a square and integrable space, $\psi(t) \in L^2(\mathbf{R})$, and $\psi(\omega)$ is the Fourier transform of $\psi(t)$, if $\psi(\omega)$ satisfies the condition

$$\int_{\mathbf{R}} \frac{|\psi(\omega)|^2}{\omega} \mathrm{d}\omega < \infty \tag{6.38}$$

$\psi(t)$ is called the basic wavelet or mother wavelet. Define $w_\mathrm{f}(a, b)$ as the continuous wavelet transform of $f(t)$, expressed as

$$w_\mathrm{f}(a,b) = |a|^{-1/2} \int_{\mathbf{R}} f(t)\psi\left(\frac{t-b}{a}\right)\mathrm{d}t = \langle f(t), \psi_{a,b}(t)\rangle \tag{6.39}$$

in which a is the scale factor, b is the translation factor; $a, b \in \mathbf{R}$, $a \neq 0$, $\langle x, y\rangle$ represents the inner product; $\psi_{a,b}(t)$ is a continuous wavelet base function expressed as

$$\psi_{a,b}(t) = |a|^{-1/2}\psi\left(\frac{t-b}{a}\right) \tag{6.40}$$

This is a set of function series obtained by the same mother wavelet $\psi(t)$ after scaling and translating.

Because the wind speed time histories are discrete functions, the wavelet should be discretized. The binary sampling grids are most commonly used for numerical discretization, and the wavelet with scale 2^j and translation $2^j k$ corresponding to each grid point is called dyadic wavelet, namely

$$\psi_{j,k}(t) = 2^{-j/2}\psi(2^{-j}t - k), \quad (j,k \in \mathbf{Z}) \tag{6.41}$$

where $\psi(t)$ is the mother wavelet function on the interval $[0, 2M-1]$.

In wavelet transform, there are two important functions, namely the wavelet function $\psi(t)$ and the scaling function $\phi(t)$ (also known as the paternal wavelet), and the relationship between them is

$$\begin{cases} \psi(t) = \sqrt{2}\sum\limits_{k=0}^{2M-1} g_{k+1}\phi(2t-k) \\ \phi(t) = \sqrt{2}\sum\limits_{k=0}^{2M-1} h_{k+1}\phi(2t-k) \end{cases} \tag{6.42}$$

The above formulas are called two-scale equation, in which g_k and h_k are suitable constants. So the complete wavelet expansion of $f(t)$ defined by the wavelet function and the scaling function can be obtained as

$$f(t) = \sum_{k=-\infty}^{\infty} c_{k,J}\phi_{J,k}(t) + \sum_{j=-\infty}^{J}\sum_{k=-\infty}^{\infty} d_{k,j}\psi_{j,k}(t) \tag{6.43}$$

where $c_{k,J} = \int_{-\infty}^{\infty} f(t)\phi_{J,k}(t)\mathrm{d}t$ is the scale coefficient, and $d_{k,j} = \int_{-\infty}^{\infty} f(t)\psi_{j,k}(t)\mathrm{d}t$ is the wavelet coefficient of $f(t)$.

The simulation procedures of random fluctuating wind fields using the wavelet method are as follows:

(1) Calculate the auto-correlation function $R_f(t)$ by applying Inverse Fourier Transform on the given PSD function;
(2) Select the wavelet base. For most projects, the Daubechies wavelet with vanishing moment 3 (db3) can meet the requirement of $R_f(t)$;
(3) According to the sample data quantity required for wind velocity simulation, initially determine the number of levels for decomposition and the data quantity of auto-correlation function, and calculate the related parameters on various scales;
(4) Calculate the estimated scale coefficient $c_{k,J}$ on the largest scale;

(5) Calculate the wavelet coefficient $d_{k,j}$ on the corresponding scale;
(6) Utilizing the obtained scaling coefficient and wavelet coefficient, calculate the estimated scale coefficient $c_{k,J-1}$ on more accurate scale by the reconstruction algorithm;
(7) Repeat steps (5) and (6), to reconstruct the coefficients until most accurate scale is acquired, and validate the obtained wind velocity samples.

6.1.4 Wind Field Simulation Based on Observed Records

Assume $X_0(t)$ is an original observed record in time interval T_0, and $X_0(\omega)$ is the Fourier transform of $X_0(t)$, namely

$$X_0(t) = \frac{1}{2\pi}\int_{-\infty}^{\infty} X_0(\omega)\exp(\mathrm{i}\omega t)\mathrm{d}\omega \tag{6.44}$$

$$X_0(\omega) = \int_{-\infty}^{\infty} X_0(t)\exp(-\mathrm{i}\omega t)\mathrm{d}t \tag{6.45}$$

When $\mathrm{Re}[X_0(\omega)] \neq 0$, the phase angle $\zeta_0(\omega)$ of $X_0(\omega)$ can be expressed as

$$\zeta_0(\omega) = -\zeta_0(-\omega) = \arctan\{\mathrm{Im}[X_0(\omega)]/\mathrm{Re}[X_0(\omega)]\} \tag{6.46}$$

where $\mathrm{Re}[X_0(\omega)] = \mathrm{Re}[X_0(-\omega)]$ is the real part of $X_0(\omega)$, and $\mathrm{Im}[X_0(\omega)] = \mathrm{Im}[X_0(-\omega)]$ is the imaginary part.

When $\mathrm{Re}[X_0(\omega)] = 0$, the phase angle $\zeta_0(\omega)$ of $X_0(\omega)$ can be expressed as

$$\zeta_0(\omega) = \pm\pi/2 + 2k\pi \quad (k = 0, \pm1, \pm2, \ldots) \tag{6.47}$$

$X_0(\omega)$ and $X_0(t)$ can be written as

$$X_0(\omega) = |X_0(\omega)|\exp[\mathrm{i}\zeta_0(\omega)] \tag{6.48}$$

$$X_0(t) = \frac{1}{2\pi}\int_{-\infty}^{\infty} |X_0(\omega)|\exp\{\mathrm{i}[\omega t + \zeta_0(\omega)]\}\mathrm{d}\omega \tag{6.49}$$

where $|X_0(\omega)| = |X_0(-\omega)|$ is the Fourier spectrum of $X_0(t)$.

Based on the observed record $X_0(t)$, a non-stationary stochastic process can be established as follows

$$X(t) = \frac{1}{2\pi}\int_{-\infty}^{\infty} |X_0(\omega)|\exp\{\mathrm{i}[\omega t + \zeta_0(\omega) + \varphi(\omega)]\}\mathrm{d}\omega \tag{6.50}$$

It is written in a sample function form

$$X^{(k)}(t) = \frac{1}{2\pi}\int_{-\infty}^{\infty} |X_0(\omega)| \exp\left\{\mathrm{i}[\omega t + \zeta_0(\omega) + \varphi^{(k)}(\omega)]\right\}\mathrm{d}\omega \tag{6.51}$$

where $\varphi^{(k)}(\omega)$ is the kth sample function of stochastic process $\varphi(\omega)$ with respect to ω.

According to Eqs. (6.48)–(6.51), the phase angle $\zeta^{(k)}(\omega)$ of $X^{(k)}(t)$ can be expressed as

$$\zeta^{(k)}(\omega) = \zeta_0(\omega) + \varphi^{(k)}(\omega) \tag{6.52}$$

The stochastic process $\varphi(\omega)$ is defined by

$$\varphi(\omega) = \Phi \cdot \mathrm{sgn}(\omega) \tag{6.53}$$

where $\mathrm{sgn}(\omega)$ is a sign function, and Φ is a stochastic variable, whose sample function $\varphi^{(k)}(\omega)$ can be given by:

$$\varphi^{(k)}(\omega) = \Phi^{(k)} \cdot \mathrm{sgn}(\omega) \tag{6.54}$$

in which $\varphi^{(k)}$ is a sample of Φ.

According to Eq. (6.50), the inverse Fourier transform of $X(t)$ is given by

$$X(\omega) = |X_0(\omega)| \exp\{\mathrm{i}[\zeta_0(\omega) + \varphi(\omega)]\} = X_0(\omega)\exp[\mathrm{i}\varphi(\omega)] \tag{6.55}$$

Assuming φ obeys uniform distribution, the probability density function of φ is

$$f_\varphi(x) = \begin{cases} 1/2a & (\mu - a \le x \le \mu + a) \\ 0 & (\text{Other}) \end{cases} \tag{6.56}$$

where μ is the expectation value, and $2a$ is the distribution width.

Equation (6.50) can be rewritten as

$$X(t) \approx \sqrt{2}\sum_{k=1}^{n} \sqrt{S_1(\omega_k)\Delta\omega}\cos[\omega_k t + \varphi(\omega_k)] \tag{6.57}$$

where $S_1(\omega)$ is the single-sided power spectral density, $S_1(\omega) = 2S_0(\omega)$; $\omega_k = k\Delta\omega$, and ω_n is the upper limit of cutoff frequency, $\omega_n = n\Delta\omega$.

Because $\zeta_0(\omega) + \varphi(\omega)$ is an odd function of ω, Eq. (6.50) can be rewritten as

$$X(t) = \frac{1}{\pi}\int_0^{\infty} |X_0(\omega)| \cos[\omega t + \zeta_0(\omega) + \Phi]\mathrm{d}\omega \tag{6.58}$$

or as an equivalent form

$$X(t) = X_0(t)\cos\Phi - \hat{X}_0(t)\sin\Phi \tag{6.59}$$

in which

$$X_0(t) = \frac{1}{\pi}\int_0^\infty |X_0(\omega)|\cos[\omega t + \zeta_0(\omega)]\mathrm{d}\omega \tag{6.60}$$

$$\hat{X}_0(t) = \frac{1}{\pi}\int_0^\infty |X_0(\omega)|\sin[\omega t + \zeta_0(\omega)]\mathrm{d}\omega \tag{6.61}$$

where $X_0(t)$ is an observed record, and $\hat{X}_0(t)$ is the Hilbert transform of $X_0(t)$.

6.2 Effect of Wind Barriers on Wind Flow Field Around Bridge

There are two approaches to increase the traffic capacity of the bridge in strong wind areas and to guarantee running safety of the train (Fujii et al. 1999). One is to optimize the structural parameters of the bridge to improve its wind resistance performance. The other is to install wind barriers on the bridge to decrease the wind loads on the train or to eliminate sudden change of wind loads (Dierickx et al. 2001; Strukelj et al. 2005; Procino et al. 2008; Kim et al. 2011; Kwon et al. 2011; Li et al. 2013; Zhang et al. 2013; Guo et al. 2014, 2015). According to the experiences from Japan's Shinkansen, setting wind barriers is an effective measure, which can decrease the railway outage times, raise train speed, and greatly reduce the overturn risk of running trains (Noguchi and Fujii 2000).

When a train passes through the bridge, the wind load on the train depends not only on the wind velocity, but also on the structural types of the bridge, the train vehicles, and the wind barriers. Correct calculation of wind loads on the train-bridge system is important for the design of bridge structure and the running safety of trains. However, the wind loads given in the Chinese code are separately for the bridge and for the train (JTG/T D60-01-2004 2004; TB 10621-2009 2010), without considering the influence of the train-bridge as a combination on their respective aerodynamic characteristics. Studies have shown that the aerodynamic coefficients of the bridge and the train may increase when they exist as a combination system (Cai and Chen 2004; Xu et al. 2004; Li et al. 2005, 2014; Xu and Ding 2006; Guo et al. 2010). In addition, setting wind barriers on the bridge will also affect the wind field and increase the turbulence, which makes the wind field around the bridge structure more complex.

This section will introduce several types of wind barriers on the bridge, then based on the theory of computational fluid dynamics and the FLUENT software platform, study the attenuation characteristics of wind field when the natural wind

flows through wind barriers, evaluate the protection effect of wind barriers, and analyze the aerodynamic performance of train-bridge system and the effects of wind barriers under crosswinds.

6.2.1 Types of Wind Barriers

There are several types of wind barriers on bridges in China and abroad:

(1) Wind barriers separate from bridge. The windshields are installed separately from the main bridge structure. The superstructure of the barrier consists of steel load-bearing beams and steel windshields with holes, which is strengthened on sides by cables anchored on the ground. This type of wind barriers are simple in structure, reasonable in stress, and clear in function of different parts, which have been successfully adopted for windproof design of bridges on the Southern Xinjiang Railway and the Lanzhou-Xinjiang HSR.
(2) Fence-type wind barriers connected with the main beam. The windproof structure consists of fan-shaped steel windshields. The fan-shaped windshields are installed on the bridge deck at equal distance along the track, with their upper parts longitudinally connected to improve the co-working integrity of the wind barriers.
(3) Grille-type wind barriers connected with the main beam. This type is often used for long-span bridges, classified as curved and standing types from the side view, and also as fixed and movable types. This wind barrier has the characteristics of beautiful appearance, good perspective, convenient processing, construction, and maintenance. It can also work as sidewalk railings to reduce the space occupied on the bridge deck, thereby greatly improving the aerodynamic performance of the bridge. This design is used on the Millau Viaduct in France, as shown in Fig. 6.1.

Fig. 6.1 Grille wind barriers on the Millau Viaduct in France (*left*, highestbridges 2004) and plate wind barriers on a bridge of the Lan-Xin HSR (*right*)

(4) Plate-type wind barriers connected with the main beam through stand columns (Fig. 6.1). The windshields are installed on the upwind side of the bridge, and on this side, no sidewalk railing is needed. The windshield is made of corrugated steel plate with holes, which can not only change the direction of the part incoming wind, but also decay the kinetic energy of the wind flow and reduce the wind velocity, so as to protect the train against winds.

6.2.2 *Aerodynamic Optimization of Wind Barriers Based on CFD Theory*

Due to the characteristics of natural winds, the complexity of bridge section, and the uncertainty of wind field behind the windshield, it is difficult to describe exactly the effect of wind on the bridge with direct analytical method. Therefore, the general method is to measure, by a wind tunnel test, the surface wind pressure coefficients and the tri-component forces for the well-scaled section model of a bridge. However, the wind tunnel test has the disadvantages of high cost, long test cycle, complex equipment, and weak repeatability. As a new research method, the computational fluid dynamics (CFD) has been developed since 1960s, and become a new tool instead of wind tunnel test (Versteeg and Malalasekera 1995; Wang 2004; Teitel 2010). By the CFD method, the aerodynamic optimization for bridge wind barriers can be performed following the flowchart, as shown in Fig. 6.2.

6.2.2.1 Theory of Computational Fluid Dynamics

CFD is a technology to analyze the system including the relevant physical phenomena such as fluid flow and heat transfer by numerical computation and image display. In CFD analysis, an original continuous physical field in the time domain and the space domain, such as a velocity field or a pressure field, is replaced by a series of variables at a finite number of discrete points, then the algebraic equations are established by certain principles and ways based on the relationship between these field variables at discrete points, and finally, the approximations of these field variables are obtained by solving the algebraic equations (Launder and Spalding 1974; Hagen et al. 1981; Wilson 1985; Heisler and Dewalle 1988; Baetke and Werner 1990; Bekele and Hangan 2002).

There are various numerical methods in CFD, and in general, they can be divided into three categories: the finite difference method (FDM), the finite element method (FEM), and the finite volume method (FVM), while the FVM is the most widely used one. The FVM divides the calculation region into a series of control volumes, and derives the discrete equations by integrating the differential equations for all control volumes, based on an assumption for the distribution of the demanded functions and their derivatives on the interface.

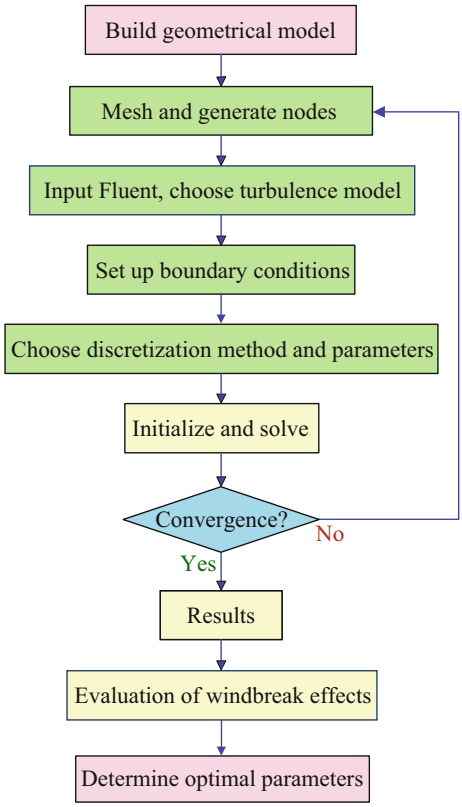

Fig. 6.2 Flowchart for aerodynamic optimization of wind barriers

The fluid flow is dominated by such physical conservation laws as the mass conservation law, the momentum conservation law, and the energy conservation law, and for the turbulent flow, the system is also subjected to additional turbulence transport equations.

(1) The mass conservation law

Any flow issues must satisfy the mass conservation law, i.e., the increased mass in a fluid infinitesimal element in unit time equals to the net mass flowing into this element during the same time interval, and the mathematical expression for this law is

$$\frac{\partial \rho}{\partial t} + \frac{\partial (\rho u)}{\partial x} + \frac{\partial (\rho v)}{\partial y} + \frac{\partial (\rho w)}{\partial z} = 0 \tag{6.62}$$

Introduce a vector symbol $\mathrm{div}(\mathbf{a}) = \partial a_x/\partial x + \partial a_y/\partial y + \partial a_z/\partial z$, or represent the divergence with ∇, i.e., $\nabla \cdot \mathbf{a} = \mathrm{div}(\mathbf{a})$, the above equation can be rewritten as

$$\frac{\partial \rho}{\partial t} + \mathrm{div}(\rho \mathbf{u}) = 0 \quad \text{or} \quad \frac{\partial \rho}{\partial t} + \nabla \cdot (\rho \mathbf{u}) = 0 \tag{6.63}$$

where ρ is the fluid density; t is time; $\mathbf{u}$ is the velocity vector; u, v, and w are the components of $\mathbf{u}$ along the x-, y-, and z-directions, respectively.

(2) The momentum conservation law

Fluid should also follow the momentum conservation law, i.e., the variation rate with respect to time of the momentum in a fluid infinitesimal element equals to the sum of external forces on this element. Its mathematical expression is the momentum conservation equation, also known as the motion equation, or the N-S (Navier-Stokes) equations. For the Newtonian fluid, the fluid viscous force is proportional to the rate of deformation, so the differential form of the N-S equations is expressed as follows

$$\begin{cases} \frac{\partial(\rho u)}{\partial t} + \mathrm{div}(\rho u \mathbf{u}) = \mathrm{div}[\mu \cdot \mathrm{grad}(u)] - \frac{\partial p}{\partial x} + S_u \\ \frac{\partial(\rho v)}{\partial t} + \mathrm{div}(\rho v \mathbf{u}) = \mathrm{div}[\mu \cdot \mathrm{grad}(v)] - \frac{\partial p}{\partial y} + S_v \\ \frac{\partial(\rho w)}{\partial t} + \mathrm{div}(\rho w \mathbf{u}) = \mathrm{div}[\mu \cdot \mathrm{grad}(w)] - \frac{\partial p}{\partial z} + S_w \end{cases} \tag{6.64}$$

where $\mathrm{grad}(u) = \partial u/\partial x + \partial u/\partial y + \partial u/\partial z$; $S_u = s_x + F_x$, $S_v = s_y + F_y$ and $S_w = s_z + F_z$ are the broad source terms, respectively, in which the specific expressions of s_x, s_y, and s_z are

$$\begin{aligned} s_x &= \frac{\partial}{\partial x}\left(\mu \frac{\partial u}{\partial x}\right) + \frac{\partial}{\partial y}\left(\mu \frac{\partial v}{\partial x}\right) + \frac{\partial}{\partial z}\left(\mu \frac{\partial w}{\partial x}\right) + \frac{\partial}{\partial x}[\lambda \cdot \mathrm{div}(\mathbf{u})] \\ s_y &= \frac{\partial}{\partial x}\left(\mu \frac{\partial u}{\partial y}\right) + \frac{\partial}{\partial y}\left(\mu \frac{\partial v}{\partial y}\right) + \frac{\partial}{\partial z}\left(\mu \frac{\partial w}{\partial y}\right) + \frac{\partial}{\partial y}[\lambda \cdot \mathrm{div}(\mathbf{u})] \\ s_z &= \frac{\partial}{\partial x}\left(\mu \frac{\partial u}{\partial z}\right) + \frac{\partial}{\partial y}\left(\mu \frac{\partial v}{\partial z}\right) + \frac{\partial}{\partial z}\left(\mu \frac{\partial w}{\partial z}\right) + \frac{\partial}{\partial z}[\lambda \cdot \mathrm{div}(\mathbf{u})] \end{aligned} \tag{6.65}$$

Generally, s_x, s_y, and s_z are small values, and $s_x = s_y = s_z = 0$ for the incompressible fluids with constant viscosity.

(3) The energy conservation law

In the energy conservation law, it is described that the increased energy in a fluid infinitesimal element in unit time equals to the sum of net heat into this element during the time interval and the work done by surface forces to this element. The energy conservation equation can be expressed as

$$\frac{\partial(\rho T)}{\partial t} + \mathrm{div}(\rho \mathbf{u} T) = \mathrm{div}\left[\frac{k}{c_\mathrm{p}} \cdot \mathrm{grad}(T)\right] + S_\mathrm{T} \tag{6.66}$$

where T is the temperature; k is a heat transfer coefficient of fluid; S_T is the internal heat sources of fluid and the heat energy converted by mechanical energy due to viscosity, sometimes also called a viscous dissipation term; c_p is the specific heat capacity.

The relationship among the temperature T, density ρ, and pressure p is given by

$$p = p(\rho, T) \tag{6.67}$$

For an ideal case, $p = \rho RT$, where R is the molar gas constant.

It should be noted that the energy conservation equation can be ignored for an incompressible fluid if the heat exchange is negligibly small. The external turbulent flow of a bridge is generally considered to be incompressible, so the energy equation is usually neglected in numerical analysis.

(4) The turbulence transport equations

Turbulence is a highly complex three-dimensional non-stationary irregular flow with rotation. In a turbulent flow, the physical parameters of fluid such as speed, pressure, and temperature vary randomly with time and space. There are three numerical methods for simulation of turbulence flow, as classified in Fig. 6.3.

The first is the direct numerical simulation method (DNS), which performs a direct numerical simulation for turbulence flow by the three-dimensional unsteady Navier-Stokes equations. In direct numerical calculation for highly complex turbulent flow, however, this method needs very small time step and very tiny space grids to distinguish the detailed spatial structure and the dramatically changed time characteristics of the turbulence.

The second is the large eddy simulation method (LES). This approach aims to use the unsteady Navier-Stokes equations to direct simulation on large-scale

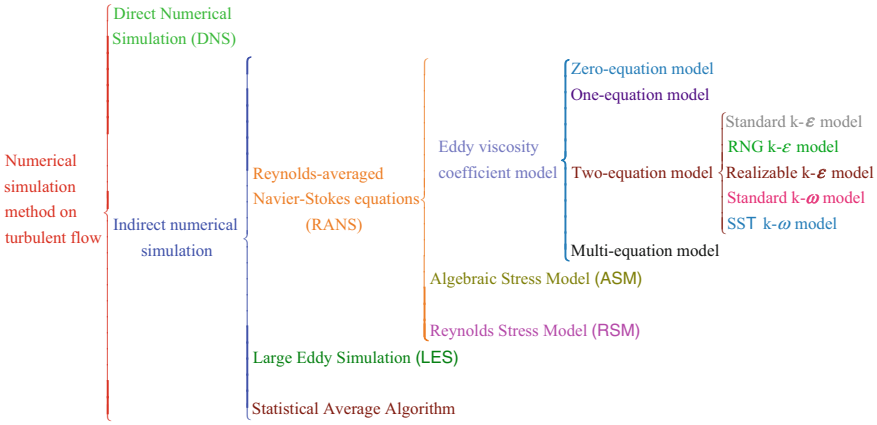

Fig. 6.3 Classification of numerical simulation methods on turbulent flow

Table 6.1 Features of the commonly used two-equation turbulence model

Principle	Feature description
Standard k-ε	Solve k and ε based on two transport equations; the default model coefficients are given by the system, and only valid for high Reynolds number turbulence; including options of viscous heat, buoyancy, compressibility
RNG k-ε	Modification of standard k-ε model, with the equations and coefficient from analytical solution; the ability to simulate high strain flow is improved in ε equation; to predict moderate-intensity swirl flow and low Reynolds number flow
Realizable k-ε	Modification of standard k-ε model; the performance is improved by mathematic restrictions; to predict moderate-intensity swirl flow
Standard k-ω	Solve k and ω based on two transport equations; good performance for low Reynolds number flow and bounded wall, especially for the flow around structures; include options of transition, free shear and compressibility
SST k-ω	Modification of standard k-ω model; combination of standard k-ε model and standard k-ω model with mixed function, including options of transition and shear flow

vortices, but not on small-scale vortices, and the effect of small vortices on large eddy is considered by the approximate model.

The third is the simulation method applying Reynolds-averaging equation. In this method, the non-stationary control equations are averaged over time; thus, the governing equations about the time-averaged physical quantities contain the unknowns such as the time-averaging values of the fluctuation product, so the number of equations obtained is less than that of unknowns, and the equations cannot be closed by a further time-averaging process. To have a closed equation, some assumptions are required, that is, a model should be established, which treats the unknown time-average quantities of higher orders as a function of determinable quantities from the lower order calculation.

The simulation methods using Reynolds-averaging equation are widely used for turbulence calculation in engineering practice, which include the eddy viscosity coefficient model, the algebraic stress model, and the Reynolds stress model. The eddy viscosity coefficient model can be further divided into zero-equation, one-equation, two-equation, and multi-equation models according to the number of differential equations, in which the two-equation model is the most commonly used. The features of the two-equation turbulence model with various principles are described in Table 6.1.

6.2.2.2 Determination of Hole Forms and Array Patterns of Wind Barriers

There are various forms of holes for wind barriers. The numerical simulation methods are different for wind barriers with different forms of holes. Xiang et al. (2014) studied the effect of hole forms on the windproof performance of wind

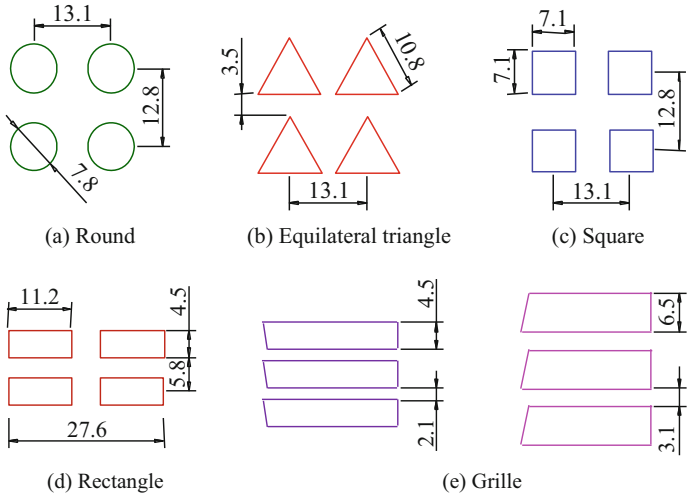

Fig. 6.4 Various hole forms for wind barriers (unit: mm)

barriers by a wind tunnel test, and compared the aerodynamic performances of a bridge with wind barriers of round, triangle, square, rectangular, and grille holes (Fig. 6.4).

The forms of wind barrier holes have a certain influence on the drag coefficient and lift coefficient of a windward vehicle, while little effect on the tri-component coefficients of a leeward vehicle. Protected by a wind barrier with rectangular or grille holes, the drag coefficient of the windward vehicle is smaller than that by a barrier with other forms of holes.

The array pattern of the holes is an important factor affecting the flow field distribution behind the wind barrier. There are various hole arraying patterns for wind barriers, such as uniform distribution, upper sparse and lower dense distribution, or the opposite, and other irregular distribution patterns. The drag coefficient of a windshield with non-uniform hole arrays is slightly smaller than that with uniform arrays (Li 2012). To reduce the computation effort, wind barriers with uniform hole arrays are usually used in CFD numerical simulation.

There are three methods for numerical simulation of wind barriers:

(1) Direct simulation method. Directly establish the wind barrier model with/without holes, applicable to wind barriers without holes or with simple forms of holes.
(2) Additional momentum source term method. Add the momentum source term in the standard momentum equation, to achieve air flow control when the wind passes through the holes by UDF in Fluent software.
(3) Porous medium model and porous jump model. In the Fluent software, there are two models. The porous jump model is the two-dimensional simplification of the porous medium model, which is relatively simple in setting, much easier in

use, and converges easily in calculation. However, in numerical calculation, the porous jump model cannot consider the volume blocking effect of wind barriers for airflow, while the additional momentum source term method relies on the pressure drop factor obtained by experiments, so it is hardly chosen when lack of experimental data.

6.2.2.3 Parameter Selection for CFD Simulation

In establishing the flow field model, the following assumptions are made: (1) the flow field is steady, i.e., the air flow and the physical parameters do not change over time; (2) the fluid is incompressible; (3) the turbulence is analyzed by the two-equation k-ε model.

The geometric model can be established by CAD, Pro/E, CATIA, SolidWorks, and other drawing softwares, also by meshing software such as Gambit or ICEM.

In CFD analysis, a reasonable calculation region is required for accurately simulating the flow field while not wasting computing resources due to oversizing the region. To ensure the simulation accuracy, the calculation region should be selected with the blocking rate less than 3%. In the two-dimensional calculation, the blocking rate is defined as the ratio of the model height to the height of the computational region. Qu and Liu (2007) suggested that for a model with streamlined section, when the calculation region is 20 times larger than the size of the model, it can be avoided that the separation vortex behind the structure reflects back after hitting the outer boundary, and the distribution of flow field parameters near the boundary is better compatible with the proposed boundary conditions, so as to make the solution have a good convergence. In a similar CFD flow field simulation by Zhu et al. (2007), the structure model was a thin plate with width of 0.45 m and width/thickness ratio of 22.5:1, and the distances from the top/bottom boundary and the inlet/outlet of the calculation region to the section center of the model are more than 15 times the width of the thin plate.

It can be seen that the height and width of the calculation region are related to the shape and size of the model at the windward side. Therefore, a rough estimate should be made for setting the calculation region: For a streamline section, the width of the region should be about 20 times the model width, and the height should be 30 times greater than the model height; for an elongated blunt section such as a thin plate, both width and height of the region should be 10 times greater than the sectional width of the model; for a blunt section without large width/height ratio, the calculation region should be set similar to a streamlined section, but an appropriately larger region is better. For bridge models in a wind field, the size of the calculation region can be determined by step-by-step trial, and by referencing the existing research results. Shown in Fig. 6.5 is a diagrammatic sketch of the calculation region for CFD simulation of a bridge.

As mentioned above, the low Reynolds number k-ε model and the wall function method are often used to simulate turbulent flow in Fluent software. In the wall

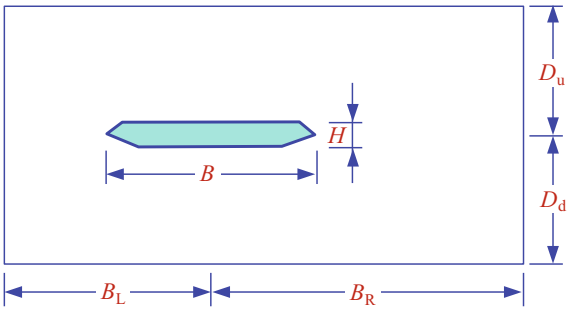

Fig. 6.5 Size setting sketch of a calculation region

area, the fluid motion is obviously influenced by wall flow conditions. Experimental studies indicated that the wall area can be divided into three sublayers, namely the viscous sublayer, the transition layer, and the logarithmic law layer, as shown in Fig. 6.6, where $y^* = yu_\tau\rho/\mu$, $u^* = u/u_\tau$, $u_\tau = \sqrt{\tau_w/\rho}$, u^*, and y^* are, respectively, the dimensionless parameters of velocity and distance, y represents the distance to the wall, u_τ the wall friction velocity, τ_w the wall shear stress, μ the dynamic viscosity of the fluid, and ρ the fluid density.

In the figure, the region corresponding to $y^* < 5$ is the viscous sublayer, where the velocity is linearly distributed along the normal direction of wall, and $u^* = y^*$. When $60 < y^* < 300$, the flow is in the logarithmic law layer, in which the velocity is expressed as

$$u^* = \frac{1}{\kappa}\ln y^* + B = \frac{1}{\kappa}\ln(Ey^*) \tag{6.68}$$

where κ is the Karman constant; B and E are constants related to the surface roughness. For a smooth wall, $\kappa = 0.42$, $B = 5.45$, $E = 9.8$. B will reduce with the wall roughness.

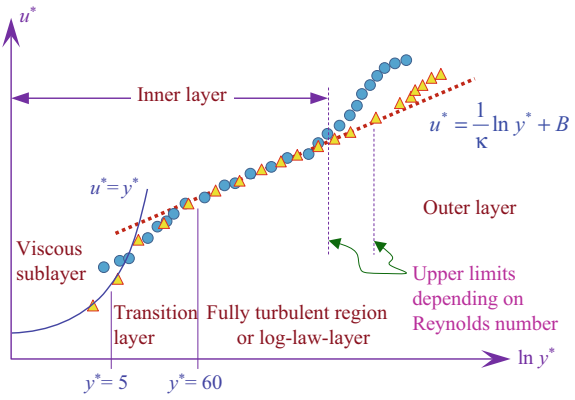

Fig. 6.6 Dimensionless velocity profile near the wall

The cutoff values for sublayers given above are only approximations. For example, in the study of Procino et al. (2008), $30 < y^* < 300$ corresponds to the logarithmic law layer, and $y^* = 11.63$ is recommended as the cutoff value between the viscous sublayer and the transition layer.

When using the low Re number (Reynolds number) model to calculate the near wall region flow, the mesh near the wall needs to be refined. There should be at least ten grids in the region affected by the viscosity ($Re < 200$) in an ideal meshing, in order to calculate the average velocity and turbulence in the region. The height of the first layer grid should be properly controlled, the most ideal manner is to set the first layer grid at $y^* = 1$.

In order to reduce the mesh number and to save calculation time, the wall function method is herein used to simulate the flow near the wall, and the RNG (renormalization group) $k-\varepsilon$ model is adopted to solve the flow in the turbulence core area, while on the wall region, the semiempirical formula is directly used to relate the physical parameters on the wall with the solved variables in the turbulence core area. Using this method, the mesh nodes in the first layer are arranged in the fully developed turbulence region, while the grid near the wall region need not be refined. For rational use of wall function, the y^* value of model section should be controlled, in general requirement, to $30 \leq y^* \leq 60$ (Versteeg and Malalasekera 1995).

When using the wall function method, as mentioned above, the mesh size near the wall is closely related to y^*. When y^* satisfies the control value, and if $y^* = 60$, the normal distance Δy_p from the wall element center to the wall achieves the maximum value. According to Launder and Spalding (1974), y^* is calculated as follows

$$y^* = \Delta y_p \rho (C_\mu^{1/4} k^{1/2})/\mu \tag{6.69}$$

where $\rho = 1.225\ \text{kg/m}^3$; k is the turbulent kinetic energy at the wall element center; $\mu = 1.7894 \times 10^{-5}\ \text{N} \cdot \text{s/m}^2$; C_μ is a constant related to the turbulence model adopted, for the RNG k-ε model, $C_\mu = 0.0845$, and for the standard k-ε model, $C_\mu = 0.09$.

Thus, Δy_p can be derived as

$$\Delta y_p = y^* \mu/(\rho C_\mu^{1/4} k^{1/2}) \tag{6.70}$$

There are three categories for CFD mesh: structured mesh, unstructured mesh, and hybrid structured mesh. Structured mesh has fast generation speed, good mesh quality, and simple data structure, which applies to simple structures. Unstructured mesh adopts a random data structure, which can easily control the mesh density in key areas as required, and facilitates the adaptability of the mesh, but it cannot handle the viscous issue very well, and the mesh number is much larger than that of the structured mesh, which leads to a lot of computing resources and long calculation time. Hybrid structured mesh retains the advantages of unstructured mesh,

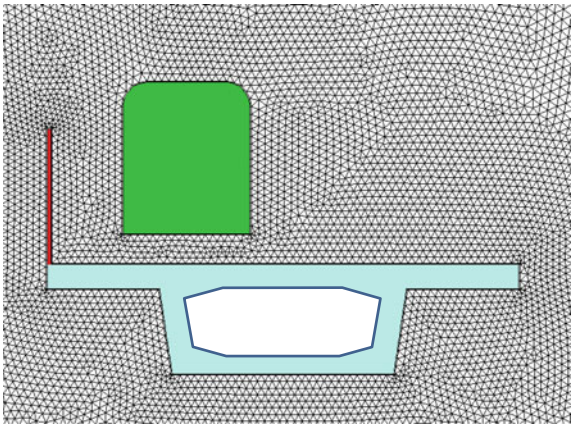

Fig. 6.7 Grid sketch near the vehicle-bridge system

which not only has a good adaptability to discretize the complex calculation region, but also saves computer resources to improve computational efficiency. A schematic sketch of meshing around the vehicle-bridge system is shown in Fig. 6.7. In the figure, the unstructured mesh is used in certain range (three times height and width of bridge along its height and width directions) to obtain better mesh around the vehicle-bridge system, while structured mesh is used for the other areas in the calculation region, to optimize the mesh and save computing resources.

The Chinese code *Wind-resistant Design Specification for Highway Bridges* (JTG/T D60-01-2004 2004) provides the mean wind velocity at the inlet as follows

$$V = V_{10}(z/10)^{\alpha} \tag{6.71}$$

where V_{10} is the 10 min average annual maximum wind speed at the height of 10 m above the ground or water surface for 100-year return period (m/s); z is the reference height of the structure (m); α is the ground surface roughness factor, which varies in 0.12–0.3 according to the surface categories A, B, C, D. For high-pier bridges, the wind field at bridge deck is less affected by surface roughness, so the inlet boundary condition adopts velocity inlet with the mean wind velocity, and the turbulent kinetic energy and the dissipation rate do not change with height. The outlet boundary condition adopts pressure outlet, and the surfaces at the top/bottom of calculation region and the structure adopt no-slip wall conditions.

The wall has influence on the flow field. When using the Fluent software in numerical calculation, the non-equilibrium wall function is adopted, by modifying the RNG model, to simulate the complex flow phenomena near the wall. When using the finite volume method to discretize the governing equations, the second-order upwind scheme is adopted to discretize the convection term, the second-order central difference scheme to discretize the diffusion term, and then the SIMPLE algorithm to solve the pressure-velocity coupling equations.

6.2.2.4 Windbreak Effect Evaluation of Wind Barriers

Based on the Fluent software platform and using the CFD method, the windbreak effect of wind barriers with different heights and porosity rates on the wind velocity field of bridges is studied by the parameter sensitivity analysis of wind barriers.

(1) Engineering background

The Lan-Xin high-speed railway, from Lanzhou to Urumqi (Capital of Xinjiang Uygur Autonomous Region), started its construction on November 4, 2009, and opened to service on December 26, 2014, with a total length of 1777 km and the design speed of 250 km/h. This railway is the longest HSR line of one-time construction in the world, and is honored as modern "Steel Silk Road" crossing the East and the West. The Lan-Xin HSR passes through five major wind zones: the Anxi wind zone, the Yandun wind zone, the 100-km wind zone, the 30-km wind zone, and the Dabancheng wind zone, with the total length of about 420 km, which is one of the worst regions of railway wind disaster in China and even in the world, where occurred frequent serious accidents including railway outages and even train overturns. In order to ensure the safety of high-speed trains running through these zones, the design required that wind barriers be set on the bridges.

During the design, three types of wind barriers were schemed for the common-span simply-supported bridges in the wind zones, as illustrated in Fig. 6.8, in which single-side, closed, and semi-closed barriers are, respectively, for box-beams, T-beams, and U-shaped beams.

In order to analyze the influence of the height and porosity rate on the windbreak effect of wind barriers, various cases were considered by considering different parameters, as listed in Table 6.2, and the wind attack angle is zero for all cases.

(2) Evaluation criteria of windbreak effect

Due to the influence of the main beam and the wind barriers, a boundary layer with a certain thickness would form when lateral wind flows through the bridge deck, so the wind velocity varies with the height above the bridge deck. To evaluate the windbreak effect of wind barriers, the equivalent wind velocity U_{eq} at bridge

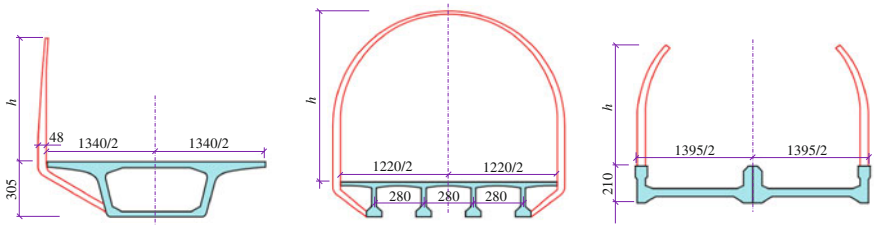

(a) Single-side for box-beam (b) Closed for T-beam (c) Semi-closed for U-shaped beam

Fig. 6.8 Schemed wind barriers for box-beam, T-beam, and U-shaped beam (unit: cm)

Table 6.2 Parameters of wind barriers in various cases

Bridge type	Barrier height h (m)	Location	Porosity rate β (%)	Remark
Box-beam	3.0	Windward side	0 10 20 30 40 50 60 70	–
	4.0	Windward side	0 10 20 30 40 50 60 70	–
	7.0	Windward side	0 10 20 30 40 50 60 70	–
T-beam	4.0	Windward side	0 10 20 30 40 50 60 70	–
	7.0	Windward side	0 10 20 30 40 50 60 70	–
	7.0	Semi-closed both sides	20	Frame closed, top hollow
	9.76	Totally closed	20	–
U-shaped beam	7.0	Semi-closed both sides	20	Frame closed, top hollow
	9.25	Totally closed both sides	20	–

deck is defined according to the equivalent principle of aerodynamic forces within a certain height, namely

$$U_{\mathrm{eq}} = \sqrt{\frac{1}{z_{\mathrm{r}}}\int_0^{z_{\mathrm{r}}} u^2(z)\mathrm{d}z} \tag{6.72}$$

where z_{r} is the equivalent height range, which is the height range of lateral wind affecting the vehicles on the bridge deck. For four common vehicles such as passenger cars, box cars, tank wagons, and open wagons, the heights from the top of car-body to the surface of track are 4.063 m, 4.029 m, 4.433 m, and 3.082 m, respectively, while in analysis, z_{r} is safely taken as 5 m for passenger cars, boxcars, and tank wagons, and as 4 m for open wagons.

The windbreak effect of wind barriers can be evaluated by the ratio of the equivalent wind velocity at bridge deck to the incoming wind velocity, i.e., the local wind velocity reduction factor λ as follows

$$\lambda = U_{\mathrm{eq}}/U \tag{6.73}$$

where U is the incoming wind velocity at the altitude of bridge deck.

(3) Effect of different wind barriers on wind flow field around vehicle-bridge system

The flow field analysis is based on the Fluent software, using the finite volume method to solve the conservation equations, the hybrid grids to discretize the

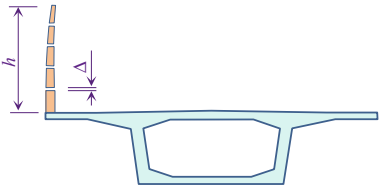

Fig. 6.9 Simulation of porosity rate for a box-beam

calculation region, and the unstructured grids to refine the interested region around the structure, so as to realize accurate simulation of the target. The structured grids are used for the other parts of the calculation region to improve the computation speed and accuracy. The RNG k-ε turbulence model is used to simulate the flow field.

In the two-dimensional model, the porosity rates are simulated by adjusting the gaps between the barrier's segments, as shown in Fig. 6.9. The thickness of the segment is taken as that of the barrier at the corresponding position, and the overall length $\Sigma\Delta$ of the block is the height h of the barrier. The length of each segment is determined by the barrier height h and the porosity rate β.

The incoming wind velocity is taken as 10 m/s, the velocity boundary condition as inlet, the pressure boundary condition as outlet, and the surfaces of the structure and the top/bottom of the calculation region are walls without slipping.

Shown in Fig. 6.10 are the wind velocity profiles versus the height above the tracks on the box-beam with wind barriers. As can be seen, the wind velocities at bridge deck are efficiently reduced. The windbreak effect is affected by the porosity rate of the barriers, which is presented by the increase of wind velocities with the porosity rate in the protection area. In general, wind velocities at the left track (windward side) are greater than those at the right track (leeward side), and the formers present obvious fluctuation, because the left track is closer to the barrier and thus suffers more influence of the holes, and the higher the porosity rate, the more significant the fluctuation. The windbreak effect is also affected by the height of wind barriers: For the 3 m barrier, even if its porosity rate is very low, the wind velocity above 3 m increases dramatically, while for the 4 m and the 7 m barriers,

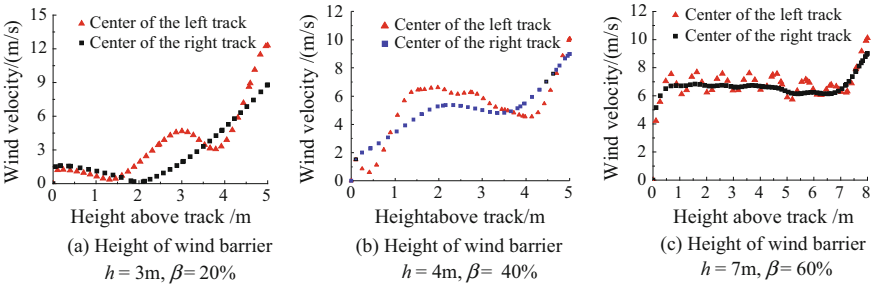

(a) Height of wind barrier $h = 3$m, $\beta = 20\%$

(b) Height of wind barrier $h = 4$m, $\beta = 40\%$

(c) Height of wind barrier $h = 7$m, $\beta = 60\%$

Fig. 6.10 Wind velocity profiles versus height above tracks on the box-beam with wind barriers

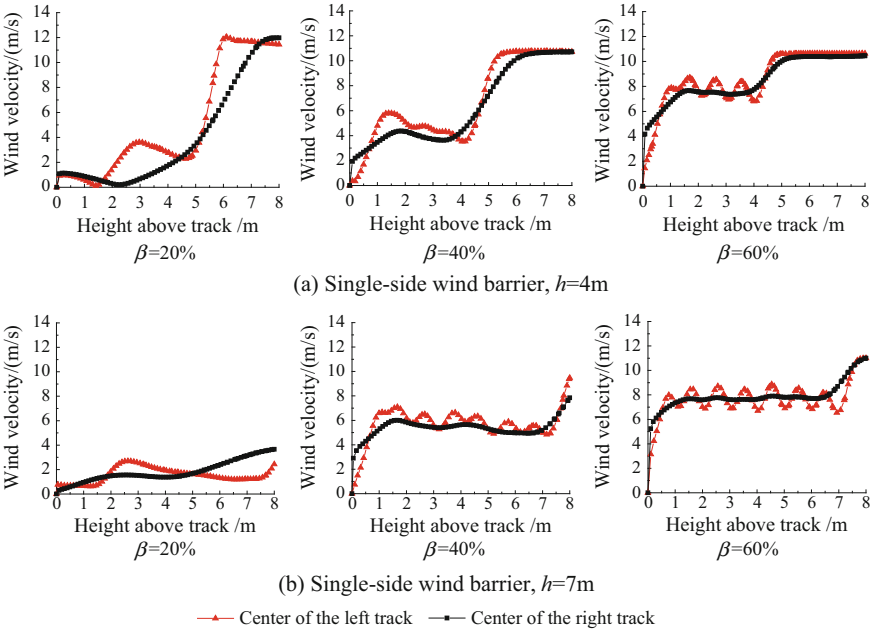

Fig. 6.11 Wind velocity profiles versus height above tracks on the T-beam with wind barriers

respectively, with large porosity rates of 40% and 60%, wind velocities approach to constant values within a certain height range.

Shown in Fig. 6.11 are the wind velocity profiles versus the height above the tracks on the T-beam with wind barriers, from which similar regularities to those at the box-beam can be obtained.

In order to compare the influence of wind barriers on wind velocities at the same position, the wind velocity profiles versus the height above the left track on the beam with different wind barriers are plotted in Fig. 6.12, where an identical porosity rate β = 20% is adopted for all barriers.

As shown in Fig. 6.12a, for the box-beam, in a certain range of height above the track, the wind velocities behind the 7 m barrier are greater than those behind the 4 m barrier with the same porosity rate. In general, for a protection height of 5 m, the windbreak effects of 4 m and 7 m barriers have little difference, while when the 3 m wind barrier is adopted, the wind velocity increases significantly in the range higher than 3 m above the track.

As shown in Fig. 6.12b, for the T-beam, in the height range of 5 m above the track, the wind velocities behind the 4 and 7 m barriers have little difference, but in the higher range of 5–8 m, the wind velocities behind the 4 m barrier become much greater.

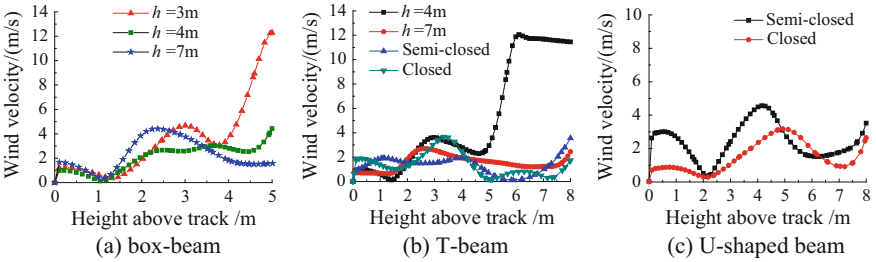

Fig. 6.12 Wind velocity profiles versus height above the left track on the beam with different wind barriers

As compared between Fig. 6.12b, c, the difference of wind velocities is not obvious for the semi-closed and closed wind barriers in the height range of 8 m above the track.

In order to quantitatively evaluate the windbreak effect of different wind barriers, keeping the equivalent height as 5 m, the local reduction factors of wind velocities are calculated above the left tracks on the box-beam and T-beam with wind barriers of different porosity rates, as shown in Fig. 6.13.

As shown in Fig. 6.13, when the protection height is 5 m, the windbreak effect of the 7 m barrier is not obviously higher than the 4 m barrier with the same porosity rate, and even lower for a certain porosity rate, while the effect of the 4 m barrier is significantly higher than the 3 m barrier. So the design height of barriers should be as possible as close to the given protection height. When the barrier height is determined, the windbreak effect mainly depends on the porosity rate; therefore, the wind velocity reduction coefficient, namely the wind velocity, increases with the porosity rate.

For the box-beam adopting single-side wind barriers with the porosity rate of 20% and 40%, the equivalent wind velocities are reduced by about 80% and 45% for the 4 m barrier, and by about 80% and 50% for the 7 m barrier, respectively.

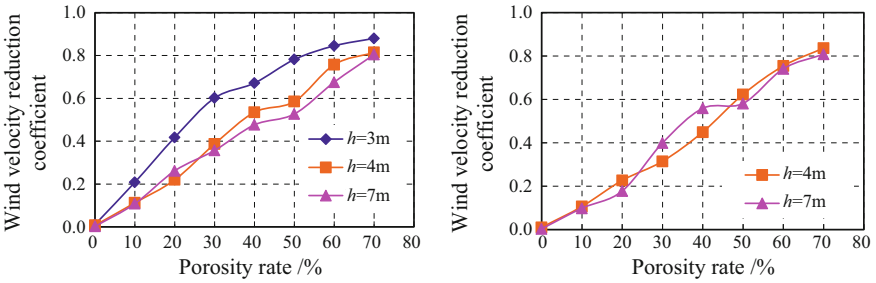

Fig. 6.13 Local reduction coefficients of wind velocities above tracks on box-beam (*left*) and T-beam (*right*)

Table 6.3 Wind velocity reduction coefficients without wind barriers

Bridge type		Box-beam	T-beam	U-shaped beam
Equivalent wind velocity (m/s)	Left track	10.8	10.6	9.15
	Right track	10.4	10.01	8.56
Reduction coefficient of wind velocity	Left track	1.08	1.06	0.92
	Right track	1.04	1.001	0.86

For the T-beam adopting semi-closed wind barriers with the porosity rate of 20% and 40%, the equivalent wind velocity is reduced by about 77% and 55% for the 4 m barrier, and by about 82% and 45% for the 7 m barrier, respectively.

For better comparison, the wind velocity reduction factors of box-beam, T-beam, and U-shaped beam without wind barriers are also calculated, and the results are listed in Table 6.3.

As can be seen, the wind velocity reduction factors of box-beam and T-beam without wind barriers are greater than 1.0, indicating the increase of wind velocity in the region, while the factors of U-shaped beam are smaller than 1.0 because of the windproof effect of its side web plates.

The wind velocity reduction factors for T-beam and U-shaped beam with semi-closed and closed wind barriers are calculated, using the porosity rate 20%, and the results are listed in Table 6.4.

As can be seen, the equivalent wind velocities are greatly reduced for T-beam and U-shaped beam with closed wind barriers. In reality, however, when a bridge is only subjected to the unidirectional wind, it is not necessary to use semi-closed or closed wind barriers, while single-side wind barriers with suitable height can achieve the required windproof effect.

Table 6.4 Wind velocity reduction coefficient of T-beam and U-shaped beam with enclosed barriers

Bridge type		T-beam		U-shaped beam	
Wind barrier type		Semi-closed	Closed	Semi-closed	Closed
Equivalent wind velocity (m/s)	Left track	2.09	1.58	2.89	1.53
	Right track	1.23	1.13	2.50	1.12
Reduction coefficient of wind velocity	Left track	0.21	0.16	0.29	0.15
	Right track	0.12	0.11	0.25	0.11

6.2.3 *Aerodynamic Performance of Train-Bridge System Under Crosswinds and Windproof Effect of Wind Barriers*

When a train runs on a bridge, the lateral wind loads applied to the train and bridge not only depend on the wind velocity, but are also related to the profiles of the bridge and the train vehicles, and the wind forces on the bridge are also affected by the train. Therefore, it is essential to correctly determine the wind loads for running safety of train and bridge design. As indicated by studies, the coexistence of train and bridge increases their respective aerodynamic coefficients, which should be paid more attention in the design.

In order to analyze the dynamic responses of the bridge and the train under wind loads, the aerodynamic coefficients of train-bridge coupling system need to be determined to calculate the wind forces acting on the bridge and the train vehicles. Based on the Fluent software, the computation model is established, as shown in Fig. 6.14, where the bridge section comes from a 32 m simply-supported box-beam, and the vehicle profile from a German ICE high-speed train. In the analysis, the wind attack angle varying from −5° to +5°, and two cases of the vehicle running on the windward side and the leeward side, are considered, respectively.

When the wind barrier is considered, the vehicle-bridge system model is established, as shown in Fig. 6.15, in which the height of wind barriers is 4 m. In order to compare the effects of wind barriers with different porosity rates on the aerodynamic performance of the vehicle and the bridge, six porosity rates with 0, 10, 20, 30, 40, and 50% are taken into account, the wind attack angle is taken as zero, and the incoming wind velocity as 15 m/s.

6.2.3.1 Calculation Model

In a lateral wind field, the vehicle and the box-beam can be approximated with a two-dimensional model. Because the incoming wind velocity is much lower than 0.3 times the sound speed, the flow field can be regarded as incompressible. The

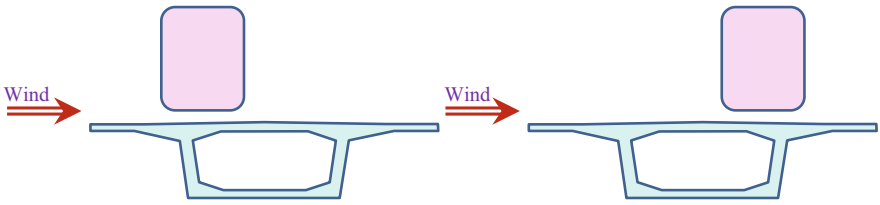

Fig. 6.14 Model of a German ICE train vehicle on the bridge

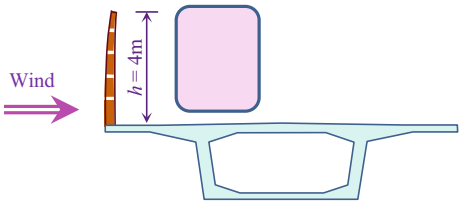

Fig. 6.15 Vehicle-bridge model with a wind barrier

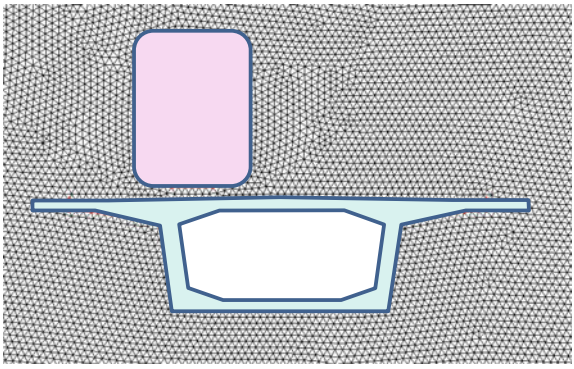

Fig. 6.16 Sketch of mesh generation for the vehicle-bridge model

static calculation is considered as a steady process, temperature as unchanged, the standard k-ε model as turbulence model, and the SIMPLE algorithm as pressure and velocity coupling.

To ensure the accuracy of calculation, a reasonable calculation region should be chosen, considering both the computation capacity and efficiency. According to Li (2012) and Sect. 6.2.2, the distance from the inflow boundary to the structure center is taken as 20 times the width of bridge section, that from the outflow boundary is 25 times, and the distances from the upper and lower boundaries to the section center are larger than 20 times the height of bridge section. The model is discretized by triangular unstructured grids, and refined in the walls of the structure and the vehicle. A schematic diagram of the mesh generation is shown in Fig. 6.16.

Assuming that the vehicle and the bridge are static, three cases are considered, namely a vehicle, a bridge, and a vehicle-bridge combination. The inlet boundary is velocity condition, the upper and lower boundaries are given by no-slip wall conditions, the outlet boundary is the pressure condition, and the surfaces of the bridge and the vehicle are the wall condition.

6.2.3.2 Aerodynamic Characteristics of Vehicle-Bridge System

The aerodynamic coefficients per unit length of a bridge and a vehicle can be defined as

$$\begin{cases} C_{\mathrm{D}}(\alpha) = D_{\mathrm{st}}/(0.5\rho\bar{U}^2 H) \\ C_{\mathrm{L}}(\alpha) = L_{\mathrm{st}}/(0.5\rho\bar{U}^2 B) \\ C_{\mathrm{M}}(\alpha) = M_{\mathrm{st}}/(0.5\rho\bar{U}^2 B^2) \end{cases} \tag{6.74}$$

where ρ is the air density; $\bar{U}$ is the mean wind velocity; D_{st}, L_{st}, and M_{st} are aerodynamic drag, lift, and moment of the structure, respectively; $C_{\mathrm{D}}(\alpha)$, $C_{\mathrm{L}}(\alpha)$, and $C_{\mathrm{M}}(\alpha)$ are dimensionless aerodynamic coefficients determined by structure section and airflow direction, which vary with the attack angle α of airflow.

In Eq. (6.74), H is the structure height (including railings and other ancillary structures), and B is the width of the structure. For the bridge with wind barriers, H is the total height of the bridge and the wind barrier, and B is the bridge width. For the vehicle, H is the height of vehicle, B is the width of vehicle, the directions of the aerodynamic forces are determined by the body-axis coordinate system, and the positive direction of the moment is defined by clockwise rotation of the vehicle around its symmetric axis.

The vehicle model, the bridge model, and the vehicle-bridge combination model are calculated, respectively, to obtain the aerodynamic coefficients and pressure field characteristics of the vehicle and the bridge in each model under different wind attack angles. The calculated rolling moment aerodynamic coefficients of the vehicle are listed in Table 6.5. It can be seen that for all attack angles, the rolling moment coefficients of vehicle on the bridge are significantly greater than the vehicle alone, and those for the vehicle on the windward side of the bridge are greater than those on the leeward side.

The calculated aerodynamic drag coefficients of bridge and vehicle versus wind attack angles are shown in Fig. 6.17. It can be seen that for all attack angles, the drag coefficients of bridge and vehicle in the vehicle-bridge combination are larger than those as an individual bridge or vehicle, and when the vehicle is on the bridge, the drag coefficient of the bridge increases monotonously with the attack angle from −5° to +5°, while that of the vehicle decreases monotonically.

The calculated aerodynamic lifts of bridge and vehicle versus wind attack angle are shown in Fig. 6.18. It can be seen that for all attack angles, the absolute values of the vehicle lift coefficients in the vehicle-bridge combination are larger significantly than those as an individual bridge or vehicle, and the lift coefficients of the bridge for the vehicle on the windward side are much greater than those on the leeward side.

Table 6.5 Calculated results of moment coefficient C_{M} of vehicle

Attack angle	−5°	−2°	0°	2°	5°
Vehicle alone	0.0062	0.0067	0.0065	0.0067	0.0072
Vehicle on the windward side	0.2334	0.2640	0.2811	0.2987	0.3856
Vehicle on the leeward side	0.0572	0.0557	0.0582	0.0590	0.0373

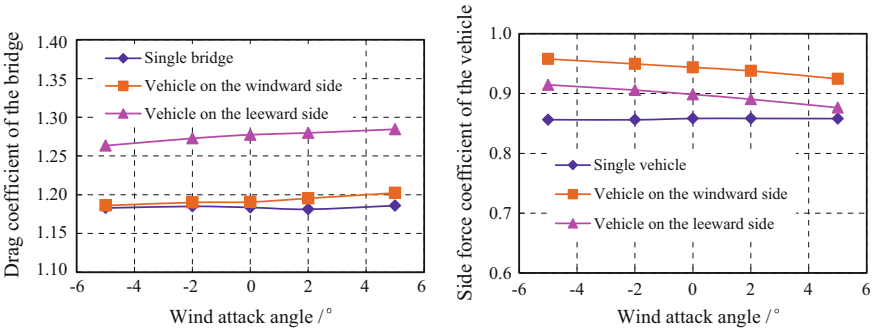

Fig. 6.17 Distributions of drag coefficients of bridge (*left*) and vehicle (*right*) versus attack angle

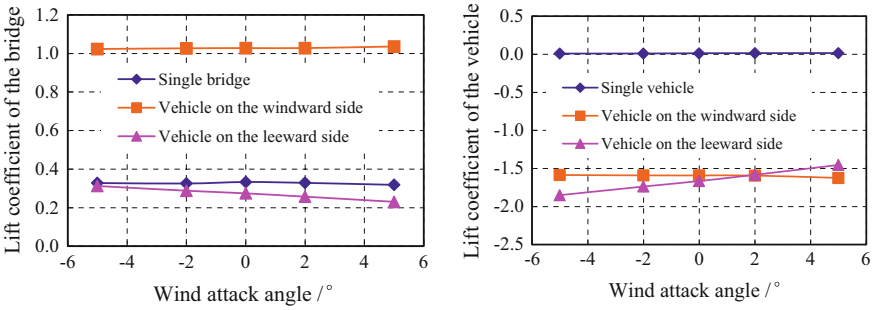

Fig. 6.18 Distributions of lift coefficients of bridge (*left*) and vehicle (*right*) versus attack angle

6.2.3.3 Effect of Porosity Rate of Wind Barrier on Aerodynamic Performance of Vehicle-Bridge System

To study the effect of wind barrier porosity rate, the aerodynamic coefficients of the bridge and the vehicle are calculated, by keeping other parameters of the wind barrier remain unchanged, considering six cases with porosity rates of 0, 10, 20, 30, 40, 50, in which the wind attack angle is taken as zero and the wind velocity as 15 m/s.

Shown in Table 6.6 are the calculated aerodynamic coefficients for the bridge and the vehicle under different porosity rates, when the vehicle is on the windward side of the bridge. As can be seen, the drag and moment coefficients of the bridge decrease with the porosity rate, and the drag coefficient more dramatically, because the higher the porosity rate, the more the airflow through the barrier, and the reduction of wind action area decreases the surface pressure difference before and after the bridge. The lift coefficient of the bridge changes from negative to positive, monotonically increasing with the porosity rate.

Table 6.6 Calculated aerodynamic coefficients of vehicle and bridge with wind barriers

Porosity rate		0	10%	20%	30%	40%	50%
C_D	Bridge	1.863	1.668	1.528	1.279	1.161	0.966
	Vehicle	−0.084	−0.002	0.042	0.205	0.307	0.443
C_L	Bridge	−0.448	−0.166	−0.028	0.191	0.328	0.645
	Vehicle	−0.053	−0.079	−0.197	−0.320	−0.365	−0.561
C_M	Bridge	−0.190	−0.229	−0.254	−0.273	−0.280	−0.3150
	Vehicle	−0.150	−0.110	0.040	0.240	0.291	0.353

Different from the bridge, the drag, lift, and moment coefficients of the vehicle change from negative to positive and increase monotonically with the porosity rate, because the higher the porosity rates, the more the airflow through the barrier, and the stronger the wind load acting on the vehicle. By comparing Tables 6.5 and 6.6, it can be found that for the porosity rates 40 and 50%, the moment coefficients of the vehicle are larger than those without wind barriers. Therefore, the porosity rate should be less than 40% to ensure the protection effectiveness of wind barriers in order to prevent the vehicle from overturn.

6.3 Dynamic Model of Train-Bridge System Subjected to Crosswinds

The train-bridge interaction system in wind field is composed of two subsystems, the moving vehicle subsystem and the bridge subsystem, as shown in Fig. 6.19, in which, each vehicle with four axles adopts 27 degrees-of-freedom multi-rigid-body model, the bridge is modeled with the modal comprehension analysis technique to reduce the computation DOFs, taking into account the effect of wind barriers. The two subsystems interact with each other through the contact forces between the wheels and the rail.

In this study, the wheel/rail contact forces are obtained by assuming rigid contacts in both lateral and vertical directions, and track irregularities and wheel hunting are taken as the system input that controls the relative displacement between wheels and rails. Wind forces on the train-bridge system consist of three components of drag F_D, lift F_L, and rolling moment F_M. Each component includes the steady-state force due to the mean wind, the buffeting force due to the wind turbulence, and the self-exciting force due to the interaction between the wind and the bridge/vehicle motion.

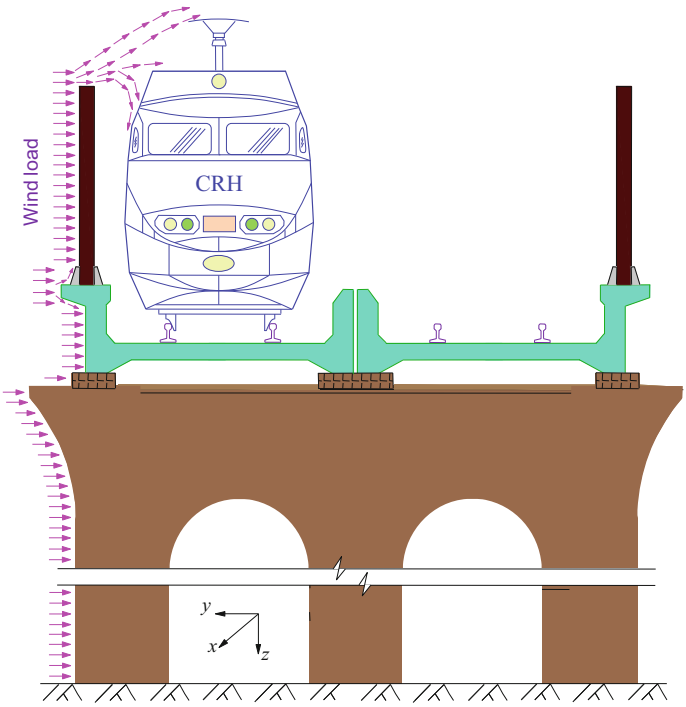

Fig. 6.19 Dynamic model of train-bridge (with barrier) system subjected to crosswinds

6.3.1 Wind Forces on Vehicle-Bridge System

6.3.1.1 Wind Forces on Bridge Structure

As shown in Fig. 6.20, the three components—drag, lift, and moment—of wind loads acting on the bridge can be written as

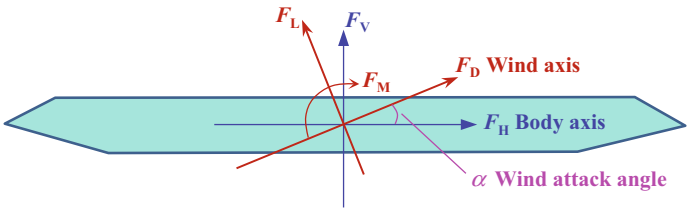

Fig. 6.20 Wind forces on the bridge

$$\begin{cases} F_{\mathrm{D}} = F_{\mathrm{D}}^{\mathrm{st}} + F_{\mathrm{D}}^{\mathrm{bf}} + F_{\mathrm{D}}^{\mathrm{se}} \\ F_{\mathrm{L}} = F_{\mathrm{L}}^{\mathrm{st}} + F_{\mathrm{L}}^{\mathrm{bf}} + F_{\mathrm{L}}^{\mathrm{se}} \\ F_{\mathrm{M}} = F_{\mathrm{M}}^{\mathrm{st}} + F_{\mathrm{M}}^{\mathrm{bf}} + F_{\mathrm{M}}^{\mathrm{se}} \end{cases} \tag{6.75}$$

where the superscripts st, bf, and se represent the static, buffeting, and self-exciting forces, respectively.

According to the classical airfoil theory (Davenport 1961), the steady wind forces per unit deck length can be expressed as

$$\mathbf{F}_{\mathrm{b}}^{\mathrm{st}} = \begin{Bmatrix} f_{\mathrm{D}}^{\mathrm{st}} \\ f_{\mathrm{L}}^{\mathrm{st}} \\ f_{\mathrm{M}}^{\mathrm{st}} \end{Bmatrix} = \frac{1}{2}\rho \bar{U}^2 \begin{Bmatrix} C_{\mathrm{D}} H \\ C_{\mathrm{L}} B \\ C_{\mathrm{M}} B^2 \end{Bmatrix} \tag{6.76}$$

where $f_{\mathrm{D}}^{\mathrm{st}}, f_{\mathrm{L}}^{\mathrm{st}}$, and $F_{\mathrm{M}}^{\mathrm{st}}$ are the static drag, lift, and moment, respectively; ρ is the air density; $\bar{U}$ is the mean wind velocity; C_{D}, C_{L}, and C_{M} are, respectively, the static coefficients of drag, lift, and moment; B and H are the width and height of the deck, respectively.

The buffeting forces per unit deck length can be expressed as

$$\mathbf{F}_{\mathrm{b}}^{\mathrm{bf}} = \mathbf{A}^{\mathrm{bf}} \boldsymbol{\eta} \tag{6.77}$$

in which,

$$\mathbf{F}_{\mathrm{b}}^{\mathrm{bf}} = \begin{Bmatrix} f_{\mathrm{D}}^{\mathrm{bf}} \\ f_{\mathrm{L}}^{\mathrm{bf}} \\ f_{\mathrm{M}}^{\mathrm{bf}} \end{Bmatrix}; \quad \boldsymbol{\eta} = \begin{Bmatrix} u(t) \\ w(t) \end{Bmatrix}; \quad \mathbf{A}^{\mathrm{bf}} = \frac{1}{2}\rho \bar{U}^2 B \begin{bmatrix} \frac{2C_{\mathrm{D}}(\alpha)}{\bar{U}} & \frac{C'_{\mathrm{D}}}{\bar{U}} \\ \frac{2C_{\mathrm{L}}(\alpha)}{\bar{U}} & \frac{C'_{\mathrm{L}} + C_{\mathrm{D}}(\alpha)}{\bar{U}} \\ \frac{2C_{\mathrm{M}}(\alpha)}{\bar{U}} B & \frac{C'_{\mathrm{M}}}{\bar{U}} B \end{bmatrix} \tag{6.78}$$

where $f_{\mathrm{D}}^{\mathrm{bf}}$, $f_{\mathrm{M}}^{\mathrm{bf}}$, $f_{\mathrm{L}}^{\mathrm{bf}}$ are the buffeting drag, moment, and lift, respectively; C'_{D}, C'_{L}, and C'_{M} are the first derivatives of the drag, lift, and moment coefficients with respect to zero wind angle, respectively; $C'_{\mathrm{D}} = \mathrm{d}C_{\mathrm{D}}(\alpha)/\mathrm{d}\alpha$, $C'_{\mathrm{L}} = \mathrm{d}C_{\mathrm{L}}(\alpha)/\mathrm{d}\alpha$, $C'_{\mathrm{M}} = \mathrm{d}C_{\mathrm{M}}(\alpha)/\mathrm{d}\alpha$; α is the wind attack angle with respect to the horizontal plane of the deck; $u(t)$ and $w(t)$ are the along-wind and vertical turbulent wind component, respectively.

The self-exciting forces can be expressed by the convolution integrals of bridge deck motion and impulse response function. The impulse response functions can be obtained by the flutter derivatives of the bridge deck from the wind tunnel test, and also by the rational function approximation approach (Chen et al. 2000). The vector

of self-excited forces per unit deck length can be expressed as (Xia et al. 2008, 2012)

$$\mathbf{F}_{\mathrm{b}}^{\mathrm{se}} = \begin{Bmatrix} f_{\mathrm{D}}^{\mathrm{se}} \\ f_{\mathrm{L}}^{\mathrm{se}} \\ f_{\mathrm{M}}^{\mathrm{se}} \end{Bmatrix} \tag{6.79}$$

where $f_{\mathrm{D}}^{\mathrm{se}}$, $f_{\mathrm{L}}^{\mathrm{se}}$, and $f_{\mathrm{M}}^{\mathrm{se}}$ are the self-exciting drag, lift, and moment, respectively, which can be deduced as

$$\begin{aligned} f_{\mathrm{D}}^{\mathrm{se}}(t) = \frac{1}{2}\rho\bar{U}^2 B\Bigg\{ & A_{\mathrm{D}\alpha 1}\alpha(t) + A_{\mathrm{D}\alpha 2}\left(\frac{B}{\bar{U}}\right)\dot{\alpha}(t) + A_{\mathrm{D}\alpha 3}\left(\frac{B}{\bar{U}}\right)^2\ddot{\alpha}(t) \\ & + \sum_{k=1}^{m} A_{\mathrm{D}\alpha k+3}\int_{-\infty}^{t}\dot{\alpha}(\tau)\exp[-\frac{d_{\mathrm{D}\alpha k}}{B}(t-\tau)]\mathrm{d}\tau\Bigg\} + \frac{1}{2}\rho\bar{U}^2\{A_{\mathrm{Dh}1}h(t) \\ & + A_{\mathrm{Dh}2}\left(\frac{B}{\bar{U}}\right)\dot{h}(t) + A_{\mathrm{Dh}3}\left(\frac{B_i}{\bar{U}}\right)^2\ddot{h}(t) + \sum_{k=1}^{m} A_{\mathrm{Dh}k+3}\int_{-\infty}^{t}\dot{h}(\tau)\exp\left[-\frac{d_{\mathrm{Dh}k}}{B}(t-\tau)\right]\mathrm{d}\tau\Bigg\} \\ & + \frac{1}{2}\rho\bar{U}^2\Bigg\{ A_{\mathrm{Dp}1}p(t) + A_{\mathrm{Dp}2}\left(\frac{B}{\bar{U}}\right)\dot{p}(t) + A_{\mathrm{Dp}3}\left(\frac{B}{\bar{U}}\right)^2\ddot{p}(t) \\ & + \sum_{k=1}^{m} A_{\mathrm{Dp}k+3}\int_{-\infty}^{t}\dot{p}(\tau)\exp[-\frac{d_{\mathrm{Dp}k}}{B}(t-\tau)]\mathrm{d}\tau\Bigg\} \end{aligned} \tag{6.80}$$

$$\begin{aligned} f_{\mathrm{L}}^{\mathrm{se}}(t) = \frac{1}{2}\rho\bar{U}^2 B\Bigg\{ & A_{\mathrm{L}\alpha 1}\alpha(t) + A_{\mathrm{L}\alpha 2}\left(\frac{B}{\bar{U}}\right)\dot{\alpha}(t) + A_{\mathrm{L}\alpha 3}\left(\frac{B}{\bar{U}}\right)^2\ddot{\alpha}(t) \\ & + \sum_{k=1}^{m} A_{\mathrm{L}\alpha k+3}\int_{-\infty}^{t}\dot{\alpha}(\tau)\exp\left[-\frac{d_{\mathrm{L}\alpha k}}{B}(t-\tau)\right]\mathrm{d}\tau\Bigg\} + \frac{1}{2}\rho\bar{U}^2\{A_{\mathrm{Lh}1}h(t) \\ & + A_{\mathrm{Lh}2}\left(\frac{B}{\bar{U}}\right)\dot{h}(t) + A_{\mathrm{Lh}3}\left(\frac{B}{\bar{U}}\right)^2\ddot{h}(t) + \sum_{k=1}^{m} A_{\mathrm{Lh}k+3}\int_{-\infty}^{t}\dot{h}(\tau)\exp\left[-\frac{d_{\mathrm{Lh}k}}{B}(t-\tau)\right]\mathrm{d}\tau\Bigg\} \\ & + \frac{1}{2}\rho\bar{U}^2\{A_{\mathrm{Lp}1}p(t) + A_{\mathrm{Lp}2}\left(\frac{B}{\bar{U}}\right)\dot{p}(t) + A_{\mathrm{Lp}3}\left(\frac{B}{\bar{U}}\right)^2\ddot{p}(t) \\ & + \sum_{k=1}^{m} A_{\mathrm{Lp}k+3}\int_{-\infty}^{t}\dot{p}(\tau)\exp\left[-\frac{d_{\mathrm{Lp}k}}{B}(t-\tau)\right]\mathrm{d}\tau\Bigg\} \end{aligned} \tag{6.81}$$

$$
\begin{aligned}
f_{\mathrm{M}}^{\mathrm{se}}(t) = {} & \frac{1}{2}\rho\bar{U}^2B^2\left\{A_{\mathrm{M}\alpha 1}\alpha(t) + A_{\mathrm{M}\alpha 2}\left(\frac{B}{\bar{U}}\right)\dot{\alpha}(t) + A_{\mathrm{M}\alpha 3}\left(\frac{B}{\bar{U}}\right)^2\ddot{\alpha}(t)\right. \\
& \left. + \sum_{k=1}^{m} A_{\mathrm{M}\alpha k+3}\int_{-\infty}^{t}\dot{\alpha}(\tau)\exp\left[-\frac{d_{\mathrm{M}\alpha k}}{B}(t-\tau)\right]\mathrm{d}\tau\right\} + \frac{1}{2}\rho\bar{U}^2B\{A_{\mathrm{Mh}1}h(t) \\
& + A_{\mathrm{Mh}2}\left(\frac{B}{\bar{U}}\right)\dot{h}(t) + A_{\mathrm{Mh}3}\left(\frac{B}{\bar{U}}\right)^2\ddot{h}(t) + \sum_{k=1}^{m} A_{\mathrm{Mh}k+3}\int_{-\infty}^{t}\dot{h}(\tau)\exp\left[-\frac{d_{\mathrm{Mh}k}}{B}(t-\tau)\right]\mathrm{d}\tau\Bigg\} \\
& + \frac{1}{2}\rho\bar{U}^2B\left\{A_{\mathrm{Mp}1}p(t) + A_{\mathrm{Mp}2}\left(\frac{B}{\bar{U}}\right)\dot{p}(t) + A_{\mathrm{Mp}3}\left(\frac{B}{\bar{U}}\right)^2\ddot{p}(t)\right. \\
& \left. + \sum_{k=1}^{m} A_{\mathrm{Mp}k+3}\int_{-\infty}^{t}\dot{p}(\tau)\exp\left[-\frac{d_{\mathrm{Mp}k}}{B}(t-\tau)\right]\mathrm{d}\tau\right\}
\end{aligned}
\tag{6.82}
$$

where $p(t)$, $\alpha(t)$, and $h(t)$ are the lateral, torsional, and vertical displacement, respectively; $A_{\mathrm{L}\alpha j}$, $A_{\mathrm{L}pj}$, $A_{\mathrm{L}hj}$, $A_{\mathrm{D}\alpha j}$, $A_{\mathrm{D}pj}$, $A_{\mathrm{D}hj}$, $A_{\mathrm{M}\alpha j}$, $A_{\mathrm{M}pj}$, $A_{\mathrm{M}hj}$ (j = 1, 2, …, 3 + m) and $d_{\mathrm{L}ak}$, $d_{\mathrm{L}pk}$, $d_{\mathrm{L}hk}$, $d_{\mathrm{D}ak}$, $d_{\mathrm{D}pk}$, $d_{\mathrm{D}hk}$, $d_{\mathrm{M}ak}$, $d_{\mathrm{M}pj}$, $d_{\mathrm{M}hk}$ (k = 1, 2, …, m) are the frequency-independent coefficients of rational functions, which can be determined by the linear and nonlinear least squares methods using the measured flutter derivatives at different reduced frequencies (Nikitas et al. 2011; Salvatori and Spinelli 2006; Zhang et al. 2011; Zhang 2011). In practice, the coefficients $A_{\mathrm{L}\alpha 3}$, $A_{\mathrm{L}p3}$, $A_{\mathrm{L}h3}$, $A_{\mathrm{D}\alpha 3}$, $A_{\mathrm{D}p3}$, $A_{\mathrm{D}h3}$, $A_{\mathrm{M}\alpha 3}$, $A_{\mathrm{M}p3}$, $A_{\mathrm{M}h3}$ related to the additional aerodynamic masses are often neglected, and the value of m is usually taken as 2. The convolution integral in Eqs. (6.80) to (6.82) can be calculated using the recursive algorithm.

6.3.1.2 Wind Forces on Vehicle

When a train runs on a bridge at a certain speed, the train vehicles with lateral wind pressure may form a lateral moving load series, which may be transferred through vehicle wheels to the bridge deck. In this case, the static wind forces due to the mean wind may also induce dynamic responses of the bridge. Moreover, the static wind on car-bodies may directly affect the anti-overturn stability of the train (Cooper 1981, 1984; Ahmed et al. 1985; Howell 1986; Baker 1991a, b; Baker and Reynolds 1992; Cheli et al. 2003; Andersson et al. 2004; Carrarini 2007; Diedrichs et al. 2007; Chen et al. 2010; Diedrichs 2010; Han et al. 2010). The above-mentioned two issues on the vibrating bridge may form a most disadvantageous state, and should be well considered (Xu and Guo 2004; Li et al. 2005; Xia et al. 2008). Since the windward areas of bogies and wheel-sets are very small compared with the car-body, the wind forces acting on the bogies and wheel-sets can be neglected.

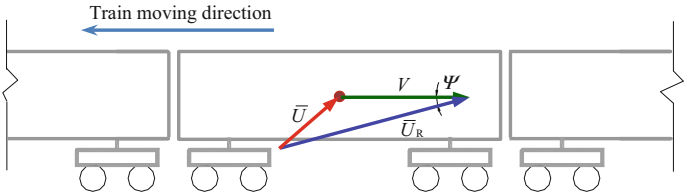

Fig. 6.21 Resultant wind velocity related to lateral mean wind velocity and train speed

When a train moves on the bridge at the speed of V, the lateral mean wind velocity $\bar{U}$ is perpendicular to the longitudinal axis of the train; thus, the resultant mean wind velocity on the car-body can be expressed as (Ref. Fig. 6.21)

$$\bar{U}_R = \sqrt{\bar{U}^2 + V^2} \tag{6.83}$$

The angle between the resultant wind velocity $\bar{U}_R$ and the moving direction of the train, which is known as the yaw angle Ψ, can be expressed as

$$\Psi = \arctan(\bar{U}/V) \tag{6.84}$$

The static wind forces on the ith vehicle can be expressed as

$$\mathbf{F}_v^{st} = \begin{Bmatrix} f_D^{st} \\ f_L^{st} \\ f_M^{st} \end{Bmatrix} = \frac{1}{2}\rho A \bar{U}_R^2 \begin{Bmatrix} C_D(\Psi) \\ C_L(\Psi) \\ HC_M(\Psi) \end{Bmatrix} \tag{6.85}$$

where f_D^{st}, f_L^{st}, and f_M^{st} are, respectively, the drag, lift, and moment on the car-body induced by static winds; A is the windward area of the vehicle; H is the height from the bridge deck to the center of the car-body; C_D, C_L, and C_M are, respectively, the drag, lift, and moment coefficients which are the function of the yaw angle Ψ.

Owing to the unstable feature of the wind, a vehicle is also acted on by buffeting wind forces. In this study, the buffeting wind forces induced by turbulent winds are calculated in the following way. First, the buffeting wind forces at different points along the bridge are simulated, with some of them at the bridge nodes and some at the points out of the bridge. Second, when a vehicle is between two adjacent points, its buffeting wind force can be obtained by the numerical interpolation of those at the two points, by assuming the same spatial correlation between the turbulent winds along the bridge and those along the train.

The buffeting wind forces acting on the car-body can be expressed as

$$\mathbf{F}_v^{bf} = \begin{Bmatrix} f_D^{bf} \\ f_L^{bf} \\ f_M^{bf} \end{Bmatrix} \tag{6.86}$$

where $f_{\mathrm{D}}^{\mathrm{bf}}$, $f_{\mathrm{L}}^{\mathrm{bf}}$, and $f_{\mathrm{M}}^{\mathrm{bf}}$ are, respectively, the drag, lift, and moment on the car-body induced by turbulent winds.

The self-exciting wind forces acting on the car-body can be expressed as

$$\mathbf{F}_{\mathrm{v}}^{\mathrm{se}} = \begin{Bmatrix} f_{\mathrm{D}}^{\mathrm{se}} \\ f_{\mathrm{L}}^{\mathrm{se}} \\ f_{\mathrm{M}}^{\mathrm{se}} \end{Bmatrix} \tag{6.87}$$

where $f_{\mathrm{D}}^{\mathrm{se}}$, $f_{\mathrm{L}}^{\mathrm{se}}$, and $f_{\mathrm{M}}^{\mathrm{se}}$ are, respectively, the drag, lift, and moment on the car-body due to the interaction between the bridge motion and the wind.

For the sake of brevity, the self-exciting forces can usually be neglected in the dynamic analysis of train-bridge system.

6.3.2 *Motion Equations of Coupled Train-Bridge System Subjected to Crosswinds*

The motion equations of train-bridge system subjected to crosswinds can be expressed as (Xia and Zhang 2005)

$$\begin{cases} \mathbf{M}_{\mathrm{v}}\ddot{\boldsymbol{\delta}}_{\mathrm{v}} + \mathbf{C}_{\mathrm{v}}\dot{\boldsymbol{\delta}}_{\mathrm{v}} + \mathbf{K}_{\mathrm{v}}\boldsymbol{\delta}_{\mathrm{v}} = \mathbf{F}_{\mathrm{vb}} + \mathbf{F}_{\mathrm{v}}^{\mathrm{st}} + \mathbf{F}_{\mathrm{v}}^{\mathrm{bf}} \\ \ddot{\mathbf{q}} + \boldsymbol{\Phi}^{\mathrm{T}}\mathbf{C}_{\mathrm{b}}\boldsymbol{\Phi}\dot{\mathbf{q}} + \boldsymbol{\Phi}^{\mathrm{T}}\mathbf{K}_{\mathrm{b}}\boldsymbol{\Phi}\mathbf{q} = \boldsymbol{\Phi}^{\mathrm{T}}\left(\mathbf{F}_{\mathrm{bv}} + \mathbf{F}_{\mathrm{b}}^{\mathrm{st}} + \mathbf{F}_{\mathrm{b}}^{\mathrm{bf}} + \mathbf{F}_{\mathrm{b}}^{\mathrm{se}}\right) \end{cases} \tag{6.88}$$

where the subscripts "b" and "v" represent the bridge and the train, respectively; $\mathbf{M}_{\mathrm{v}}$, $\mathbf{K}_{\mathrm{v}}$, and $\mathbf{C}_{\mathrm{v}}$ are the mass, stiffness, and damping matrices of the vehicle, respectively; $\mathbf{q}$, $\dot{\mathbf{q}}$, and $\ddot{\mathbf{q}}$ are, respectively, the displacement, velocity, and acceleration vectors of the bridge in the modal coordinates, and $\boldsymbol{\Phi}$ is the mode shape matrix; $\mathbf{C}_{\mathrm{b}}$ and $\mathbf{K}_{\mathrm{b}}$ are, respectively, the damping and stiffness matrices of the bridge; $\mathbf{F}_{\mathrm{vb}}$ and $\mathbf{F}_{\mathrm{bv}}$ are the force vectors due to the interaction on the wheel/rail interfaces; $\mathbf{F}^{\mathrm{st}}$, $\mathbf{F}^{\mathrm{bf}}$, and $\mathbf{F}^{\mathrm{se}}$ are, respectively, the steady-state force vector, buffeting force vector, and the self-exciting force vector, which can be calculated using the static tri-component coefficients of the vehicle and the bridge obtained from a wind tunnel test.

For the dynamic interaction system composed of wind, train, and bridge, the motion equations of the bridge and the train could be solved separately, and the geometric and mechanical coupling between the bridge and the train can be satisfied by separate iterations.

As shown in Fig. 6.22, the calculation procedures are as follows:

(1) For the time step t, take the displacements of the train and the bridge at the previous time step as the initial iteration values, and calculate the buffeting wind forces $F_{\mathrm{v}}^{\mathrm{bf}}$ and $F_{\mathrm{b}}^{\mathrm{bf}}$ on the train and the bridge of the current time by interpolating calculation;

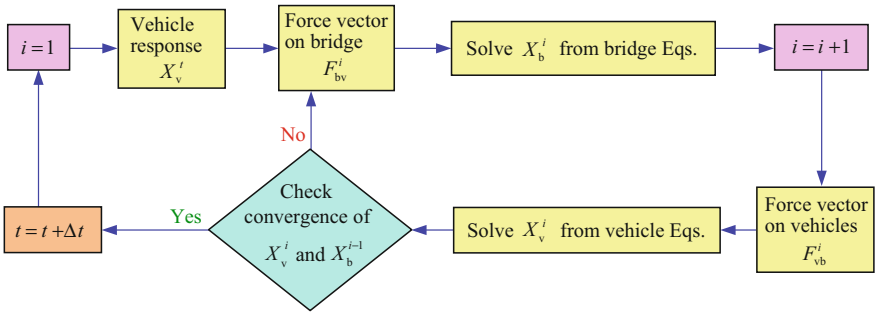

Fig. 6.22 Calculation procedure of wind-train-bridge system

(2) For the ith iteration, calculate the displacement parameters W^i of all wheel-sets, by interpolating the bridge vibration modes according to the wheel-set positions, and considering the irregularities of the track and the hunting movements;
(3) Calculate the force vector F_{vb}^i by the displacement parameters W^i, and generate the external forces acting on the train by $F_v^i = F_{vb}^i + F_v^{st} + F_v^{bf}$;
(4) Calculate the response parameters X_v^i of train vehicles at the moment of t by numerical integration;
(5) Calculate the forces acting on the bridge F_{bv}^i by the displacement parameters W^i of the wheel-sets and the response parameters X_v^i of the train vehicles, calculate the self-excited forces $(F_b^{se})^i$ by the bridge displacements from the previous iteration, and generate the external forces acting on the bridge by $F_b^i = F_{bv}^i + F_b^{st} + F_b^{bf} + (F_b^{se})^i$;
(6) Calculate the responses of the bridge X_b^i at time t by numerical integration;
(7) Compare the results between the ith and the $(i-1)$th iteration, repeat steps (2)–(6) until the iteration results meet the convergence conditions;
(8) Let $t = t + \Delta t$, repeat steps (1)–(7), calculate the system responses at the updated time step, until the train runs out of the bridge.

6.4 Dynamic Analysis of a Train and Long-Span Bridge System Under Crosswinds

6.4.1 Engineering Background

The Tsing Ma Bridge in Hong Kong is a suspension bridge crossing the strait between the Ma Wan Island and the Tsing Yi Island (Fig. 6.23). It was built in 1997, and is now the longest rail-cum-road bridge in the world, with an overall length of 2160 m, a main span of 1377 m, and the navigation clearance of 62 m.

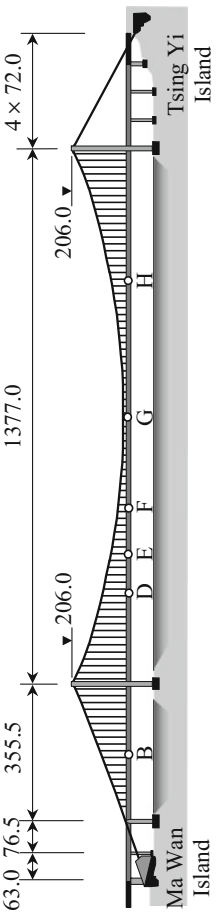

Fig. 6.23 Configuration of the Tsing Ma Bridge (unit: m)

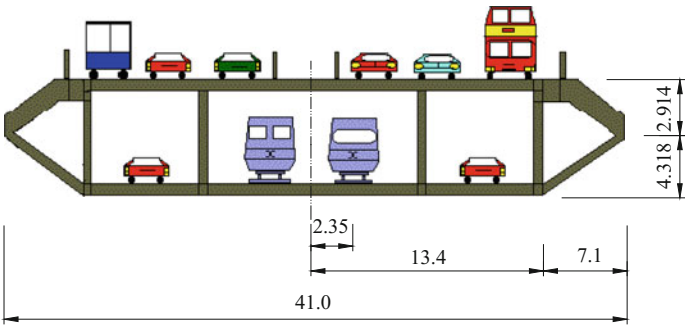

Fig. 6.24 Cross section of bridge decks (unit: m)

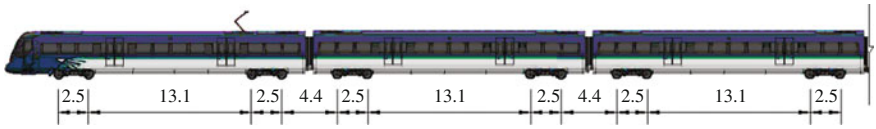

Fig. 6.25 Composition of the MTR train running on the Tsing Ma Bridge (unit: m)

The height of the two reinforced concrete towers is 206 m, measured from the base level to the tower saddle. The main span of the bridge is a hybrid steel structure consisting of Vierendeel cross-frames supported on two longitudinal trusses acting compositely with stiffened steel plates.

The upper deck of the bridge carries a dual three-lane highway, while the lower deck carries two railway tracks and two carriageways (Fig. 6.24). The bridge links the Hong Kong International Airport to the central commercial areas of Hong Kong Island and Kowloon.

The MTR train running on the bridge consists of eight passenger cars with a total length of 182 m. Each car has two identical bogies, and each bogie is supported by two wheel-sets. The composition of the train is shown in Fig. 6.25. The average static axle loads of the car are 10,144 kg (tare) and 13,250 kg (crush). The design train speed on the bridge is 135 km/h. Other parameters of the train have been given in detail in Xia and Zhang (2005).

6.4.2 Wind and Structural Health Monitoring System (WASHMS) on the Bridge

The Tsing Ma Bridge is located in one of the most active typhoon-prone regions in the world. To have an online monitoring of the performance and health status of the Tsing Ma Bridge, a Wind And Structural Health Monitoring System (WASHMS)

was installed on the bridge by the Highways Department of Hong Kong in 1997. The WASHMS is composed of the sensory system, the data acquisition system (DAS), the data processing and analysis system (DPAS), and the computer for system operation and control (CSOC). There are more than nine hundreds of sensors and related interface devices in the sensory system. The WASHMS continuously monitors the structural state of the bridge during 24 h per day, to provide a variety of data and parameters, including deck temperatures, structural stresses, wind velocities, dynamic/static displacements, and accelerations.

The operation guidelines adopted for the Tsing Ma Bridge during high wind period are as follows: (1) when the hourly mean wind speed recorded on-site is in excess of 40 km/h but does not exceed 65 km/h, all motor-bicycles and road vehicles with height exceeding 1.6 m will be prohibited from using the upper deck and diverted to the lower deck. (2) when the hourly mean wind speed is in excess of 65 km/h but does not exceed 165 km/h, the upper deck will be closed and all road vehicles will be diverted to the lower deck. (3) when the hourly mean wind speed is in excess of 165 km/h, both the upper and lower decks will be closed for all road vehicles except trains. The hourly mean wind speed used in the operation is referenced to the anemometer installed on the gantry rather than the bridge.

On September 12, 1999, the tropical cyclone Typhoon York developed on the Northwest Pacific at about 430 km from east of Manila, and intensified into a tropical storm on the next day over the South China Sea (Hong Kong Observatory 1999). During the passage of Typhoon York on September 16, the Hong Kong Observatory recorded a maximum hourly wind velocity of 42 m/s, and a maximum gust of 65 m/s at 75 m height on the Waglan Island. This gust is the highest one recorded at Waglan since the station there was established. On that day, all vehicles except trains were prohibited from running on the bridge for two and a half hours from 3:30 pm to 6:00 pm. This event provided a distinctive opportunity to examine the dynamic behavior of the Tsing Ma Bridge and the analytical models for predicting the dynamic responses of long suspension bridges subjected to strong winds and running trains.

6.4.3 Case Identification of Train Loads

According to the strain curves recorded by the strain gauge installed at Section H of the deck (Fig. 6.23), the numbers and positions of trains on the bridge and the approximate train speeds are identified by analysis of the waveforms, including four particular cases: (a) the bridge without any vehicles; (b) the bridge with one running train; (c) the bridge with two trains running in opposite directions; and (d) the bridge with three running trains, as shown in Fig. 6.26. The wind data in these four cases, such as mean wind velocities, directions, attack angles, and turbulent intensities, were simultaneously measured by the WASHMS, as listed in Table 6.7.

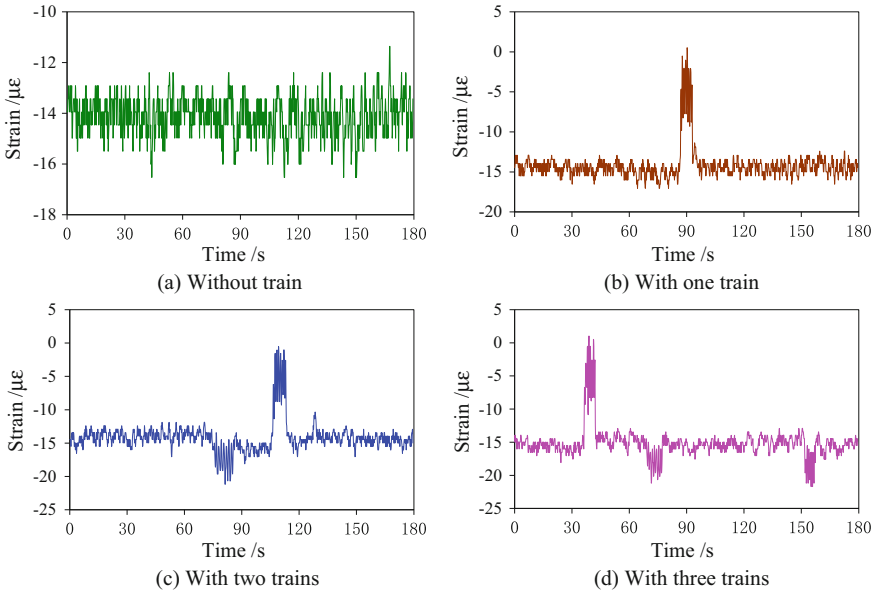

Fig. 6.26 Measured strain time histories in four cases

Table 6.7 Four cases of train loads and wind data identified during Typhoon York

Case	Wind				Train			
	Mean wind velocity (m/s)	Average attack angle (°)	Turbulent intensity		Tsing-Yi to Ma-Wan		Ma-Wan to Tsing-Yi	
			Along wind (%)	Upward (%)	Number	Speed (km/h)	Number	Speed (km/h)
Case a	18.8	−1.4	10.3	7.3	0	–	0	–
Case b	18.9	+10.6	14.9	7.9	0	–	1	99
Case c	19.9	+6.1	9.5	7.7	1	65	1	89
Case d	19.8	+13.2	12.7	8.5	2	78, 110	1	105

6.4.4 Numerical Simulation and Analysis

As the first step of wind-train-bridge dynamic analysis, the wind velocities along the bridge deck are generated. Shown in Fig. 6.27 are, for instance, the along-wind and upward components of fluctuating wind velocities in Case b.

A three-dimensional finite element model was established for the Tsing Ma suspension bridge by Xu et al. (1997). The numerical results show that the lowest natural frequency of 0.068 Hz of the bridge corresponds to the first lateral vibration mode with a very small vertical, torsional, or longitudinal movement. The first

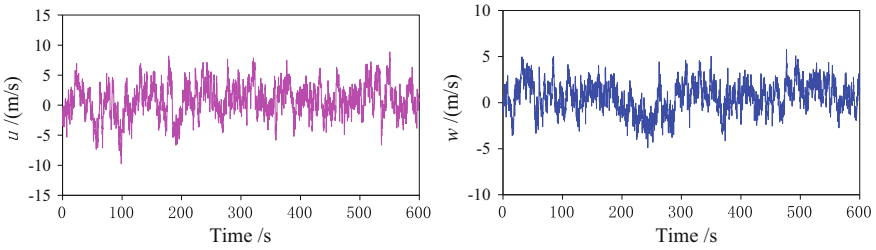

Fig. 6.27 Simulated time histories of fluctuating wind components at bridge mid-span in along-wind (*left*) and upward (*right*) directions

vertical mode of the bridge is almost antisymmetric in the main span at a natural frequency of 0.117 Hz, while the first torsional vibrational mode occurs at a natural frequency of 0.271 Hz. In the analysis, the first eighty vibration modes of the bridge up to a natural frequency of 1.2 Hz are taken into account, to include the effects of both the global deformation of the bridge and the local deformation of the structural components supporting the tracks. The average modal damping ratios estimated from the measured acceleration responses of the Tsing Ma suspension bridge (Guo et al. 2007, Xu 2013) are used, which are 1.0% for lateral and vertical directions, and 0.5% for torsional.

Illustrated in Fig. 6.28 are the measured and calculated time histories of vertical displacements of the bridge at Sections B, E, and G (see Fig. 6.23) for Case c when two trains running on the bridge. To match the cutoff frequency 0.05 Hz used in the measurement, the calculated results are correspondingly treated with a digital low-pass filter.

It can be seen that a fairly good agreement between the measured and calculated results for each section. As shown in Fig. 6.28a, there are two displacement peaks appearing in the time histories during the period of 50–75 s and 140–165 s, indicating two trains successively passing Section B with the time interval about 90 s. Similarly, as displayed in Fig. 6.28b, the two displacement peaks are closer to each other with the time interval of 46 s for the two trains successively passing Section E. From Fig. 6.28c, one can find only one displacement peak with very large amplitude appearing at Section G, which is formed by superposition of the two displacements due to the two trains meeting at the mid-span of the bridge.

From the figures, it can also be seen that the vertical dynamic displacements induced by moving trains are quite similar to the static influence lines, indicating that for such a long bridge, the vertical displacements are caused mainly by the moving gravity loading of the train.

Displayed in Fig. 6.29 are the calculated and measured maximum accelerations along the bridge deck in lateral and vertical directions for Case d. Because the highest modal frequency involved in the calculation is 1.2 Hz, the measured accelerations are correspondingly treated with a digital low-pass filter, to have a reasonable comparison between them. It is seen a fairly good agreement between the calculated curves and measured data.

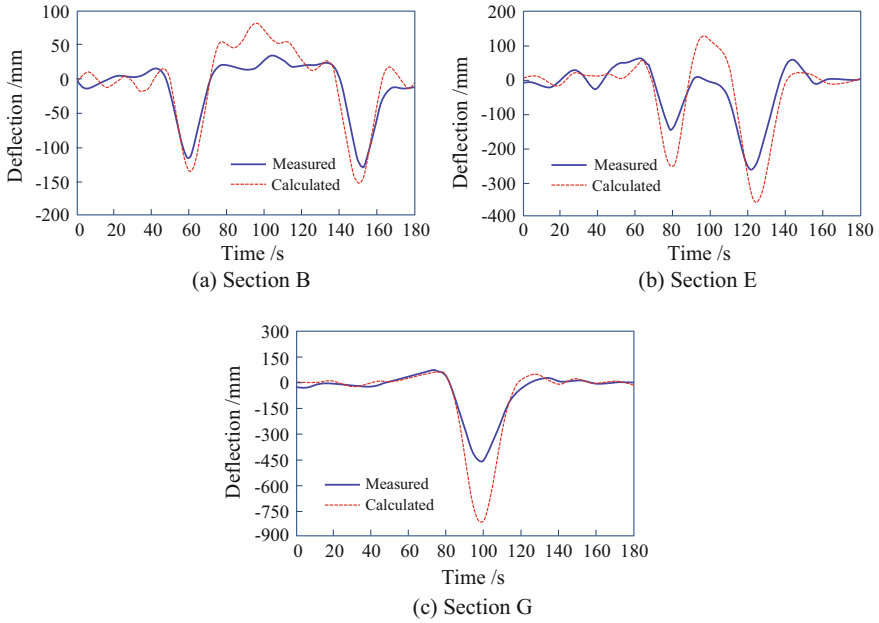

Fig. 6.28 Measured and calculated vertical displacement time histories of the bridge under two trains (Case c)

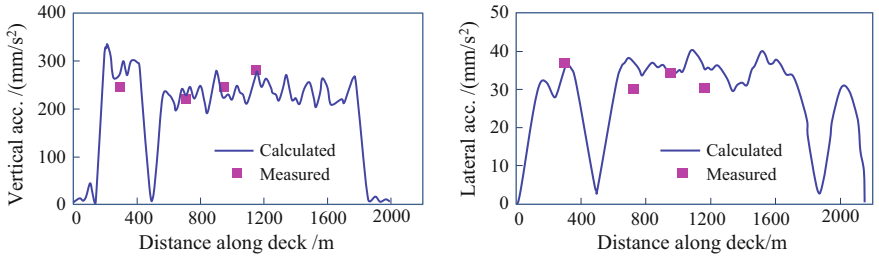

Fig. 6.29 Measured and calculated maximum accelerations of the bridge along the deck (Case d)

To analyze the running performance of the train on the bridge, the dynamic responses of the vehicles are calculated for Case b. Displayed in Fig. 6.30 are the distributions of the maximum derailment factors and offload factors of vehicles versus train speed, when the train runs on the bridge under several wind velocities. It can be noticed that the two running safety indices increase significantly with the mean wind velocity, whereas appear fluctuations with the train speed. When the mean wind velocity reaches 20 m/s and the train speed is higher than 120 km/h, the offload factor exceeds its limit (0.6), indicating the running safety of the train on the bridge cannot be guaranteed.

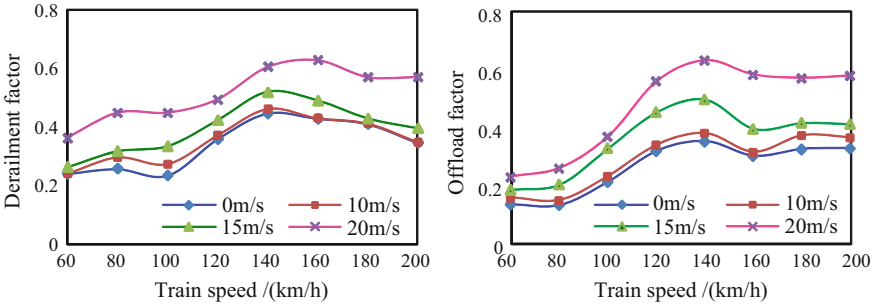

Fig. 6.30 Maximum derailment factor (*left*) and offload factor (*right*) versus train speed (Case b)

To ensure the running safety of the train on the bridge, it is necessary to strictly limit the train speed under various wind velocities. The threshold speed of a train traveling on the bridge under crosswinds can be determined in the following way.

(1) For a certain wind velocity, the running safety indices of the train, such as the derailment factor, offload factor, overturn factor, and lateral wheel/rail force, are calculated by gradually increasing the train speed, until any of the indices exceeds the allowance, and the critical train speed at this wind velocity is determined.
(2) In the concerned range of wind velocities, calculate the critical train speeds as described above for various wind velocities.
(3) Plot the calculated results in an identical coordinate system, with the abscissa representing the mean wind velocity and the ordinate the train speed, to obtain the threshold curve for critical train speeds at various wind velocities.

With the above procedures, the critical train speeds at various wind velocities are calculated for the MTR train on the Tsing Ma suspension bridge, and the proposed threshold curve is shown in Fig. 6.31. The curve shows the boundary between the safety area and the dangerous area. It can be seen that when the mean wind velocity $\bar{U}$ is higher than 15 m/s, the critical train speed decreases remarkably. When $\bar{U}$ reaches 25 m/s, the critical train speed drops to 50 km/h. When $\bar{U}$ reaches 30 m/s,

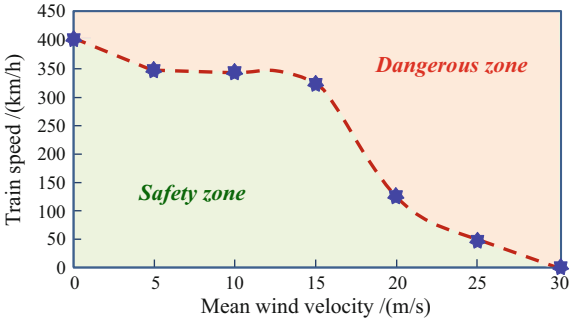

Fig. 6.31 Threshold curve of critical train speeds versus mean wind velocity

the critical train speed is only 2 km/h, indicating the rail traffic on the bridge should be closed to ensure the running safety of the train.

The present case study investigates the dynamic responses of the Tsing Ma Bridge under both running trains and turbulent winds, as well as the train running performance on the bridge. Some of the numerical results are compared with the measured data, showing the proposed analysis framework and the associated computer program can efficiently predict the dynamic responses of coupled train-bridge system in turbulent winds with reasonable computation efforts.

6.5 Dynamic Analysis of Wind-Train-Bridge System Considering Aerodynamic Effects of Wind Barriers

6.5.1 Engineering Background

In this section, a simply-supported bridge, composed of 32 m-span PC box-beams and 15 m height solid piers, located on the Lan-Xin HSR, is selected to perform the dynamic analysis of wind-train-bridge system, since it is the most important type of common-span bridges in the wind prone area in this railway.

Based on the aerodynamic selection and optimization, two types of barrier structures were designed for the bridge (Fig. 6.32). One is the single-side structure composed of steel columns and upright screens. The height of the column is 4.0 m, and the porosity rate of the screen is 30%. The other is the bilateral structure composed of steel columns and bilateral upright screens. The height of the screen is 5.0 m, whose lower 2.0 m part is solid while the upper 3.0 m part is holed with 30% porosity rate.

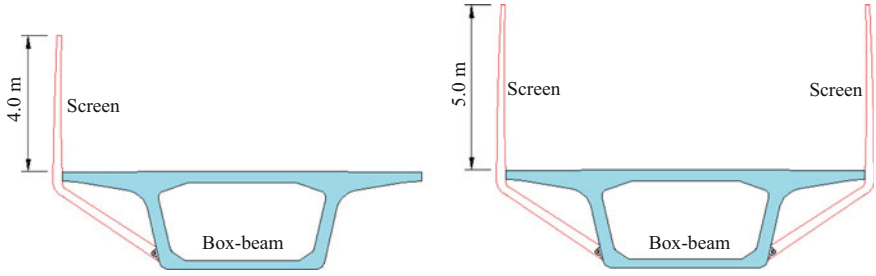

Fig. 6.32 Two types of wind barriers (unit: m)

6.5.2 Input Data

As the first step of dynamic analysis, a three-dimensional FE model is established with ten identical spans to consider the multi-span effect, as shown in Fig. 6.33. Because the stiffness of the wind barrier is much smaller than that of the bridge, and only the columns are connected with the beams directly, the barrier structures are not included in the bridge FE model.

By the FEM modal analysis, the vibration characteristics of the bridge including natural frequencies and mode shapes are obtained. The fundamental frequencies in longitudinal, lateral, and vertical directions are, respectively, 1.229 Hz, 3.274 Hz, and 4.436 Hz. To include the effects of the global deformation of the bridge, the first 60 modes up to a natural frequency of 27.224 Hz are taken into account for analysis of the wind-train-bridge system, with a uniform damping ratio 5% for all modes.

The train considered is a high-speed ICE3 train, with a composition of $4 \times (3\ \mathrm{M} + 1\mathrm{T})$, where M represents the motor-car and T the trailer-car, whose main wheelbase arrangements are shown in Fig. 6.34. The average static axle load is 156.96 kN for a motor-car and 143.23 kN for a trailer-car. Table 6.8 lists the main calculation parameters of the ICE3 vehicles.

Considering that wind barriers may affect the aerodynamic properties of the train-bridge system, a wind tunnel test was conducted to measure the drag, lift, and moment coefficients of the box-beam and the vehicle on the beam, as well as their first derivatives at the zero wind attack angle, as listed in Table 6.9. It can be seen that the wind barriers have a good windproof effect on the vehicle on the bridge. The drag force and the moment on the vehicle are greatly reduced when wind barriers are installed. However, the wind barriers have negative influence on the aerodynamic behavior of the bridge, because they increase the windward area of the

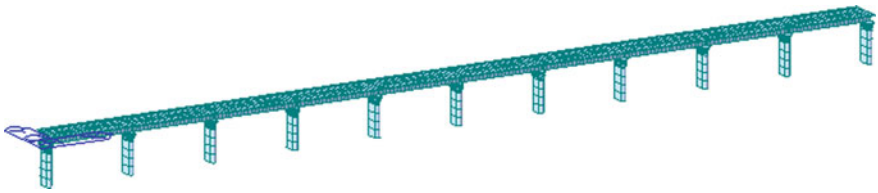

Fig. 6.33 Three-dimensional FE model for the simply-supported bridge with 10×32 m box-beams

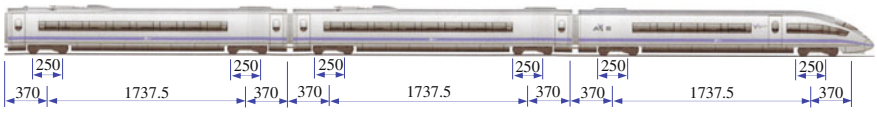

Fig. 6.34 Configuration of high-speed ICE3 train (unit: cm)

Table 6.8 Main calculation parameters of ICE3 vehicles

Item	Unit	Motor-car	Trailer-car
Distance between wheel-sets	m	2.50	2.50
Distance between bogies	m	17.375	17.375
Span of the primary suspension system	m	2.00	2.00
Span of the secondary suspension system	m	2.00	2.00
Distance between the car-body and the secondary suspension system	m	0.80	0.80
Distance between the secondary suspension system and the bogie	m	0.30	0.20
Distance between the bogie and the wheel-set	m	0.14	0.24
Radius of the wheel-set	m	0.46	0.46
Mass of the wheel-set m_w	t	2.4	2.4
Roll mass moment of the wheel-set I_x	t-m^2	1.2	1.1
Mass of the bogie m_t	t	3.2	2.4
Mass moment of inertia of the bogie around x-axis I_x	t-m^2	3.2	1.8
Mass moment of inertia of the bogie around y-axis I_y	t-m^2	7.2	2.2
Mass moment of inertia of the bogie around z-axis I_z	t-m^2	6.8	2.2
Mass of the car-body m_c	t	48.0	44.0
Mass moment of inertia of the car-body around x-axis I_x	t-m^2	115	100
Mass moment of inertia of the car-body around y-axis I_y	t-m^2	2700	2700
Mass moment of inertia of the car-body around z-axis I_z	t-m^2	2700	2700
Longitudinal damping of the primary suspension system c_{x1}	kN-s/m	0	0
Lateral damping of the primary suspension system c_{y1}	kN-s/m	0	0
Vertical damping of the primary suspension system c_{z1}	kN-s/m	40	40
Longitudinal damping of the secondary suspension system c_{x2}	kN-s/m	500	500
Lateral damping of the secondary suspension system c_{y2}	kN-s/m	30	25
Vertical damping of the secondary suspension system c_{z2}	kN-s/m	60	60
Longitudinal stiffness of the primary suspension system k_{x1}	kN/m	15000	15000
Lateral stiffness of the primary suspension system k_{y1}	kN/m	5000	5000
Vertical stiffness of the primary suspension system k_{z1}	kN/m	700	700
Longitudinal stiffness of the secondary suspension system k_{x2}	kN/m	240	280
Lateral stiffness of the secondary suspension system k_{y2}	kN/m	240	280
Vertical stiffness of the secondary suspension system k_{z2}	kN/m	400	300

structure. As a result, the drag force and the moment on the bridge are remarkably increased, and the increase of those on the bridge with bilateral barriers and higher upright screens is more remarkable.

The wind force time histories on the train-bridge system are calculated using the tri-component coefficients listed in Table 6.9, based on which the whole histories of

Table 6.9 Tri-component coefficients of the vehicle-bridge system

Cases	Box-beam						Vehicle		
	C_D	C_L	C_M	$C_D^{'}$	$C_L^{'}$	$C_M^{'}$	C_D	C_L	C_M
Without barrier	1.0903	0.4681	0.1483	−3.489	0.7391	−0.401	1.9114	−0.0012	1.1727
With single-side barriers	2.0302	−0.1334	0.2366	1.329	0.0573	0.1318	0.3290	0.0940	0.2120
With bilateral barriers	3.924	−0.051	0.2545	2.363	−1.344	0.1743	0.1882	0.0968	0.1055

the train travelling through the bridge subjected to the crosswinds are then simulated. The integration time step in calculation is taken as 0.005 s.

6.5.3 Bridge Responses

Compared in Fig. 6.35 are the calculated lateral and vertical displacements of the bridge at mid-span, when the train speed is 250 km/h and the instantaneous wind velocity is 30 m/s, which corresponds to an average wind velocity of about 22 m/s.

It can be seen that compared to the case without barriers, for the bridges with wind barriers, the calculated displacements are increased, and the increase of those with bilateral barriers and higher upright screens is more obvious, especially in lateral direction.

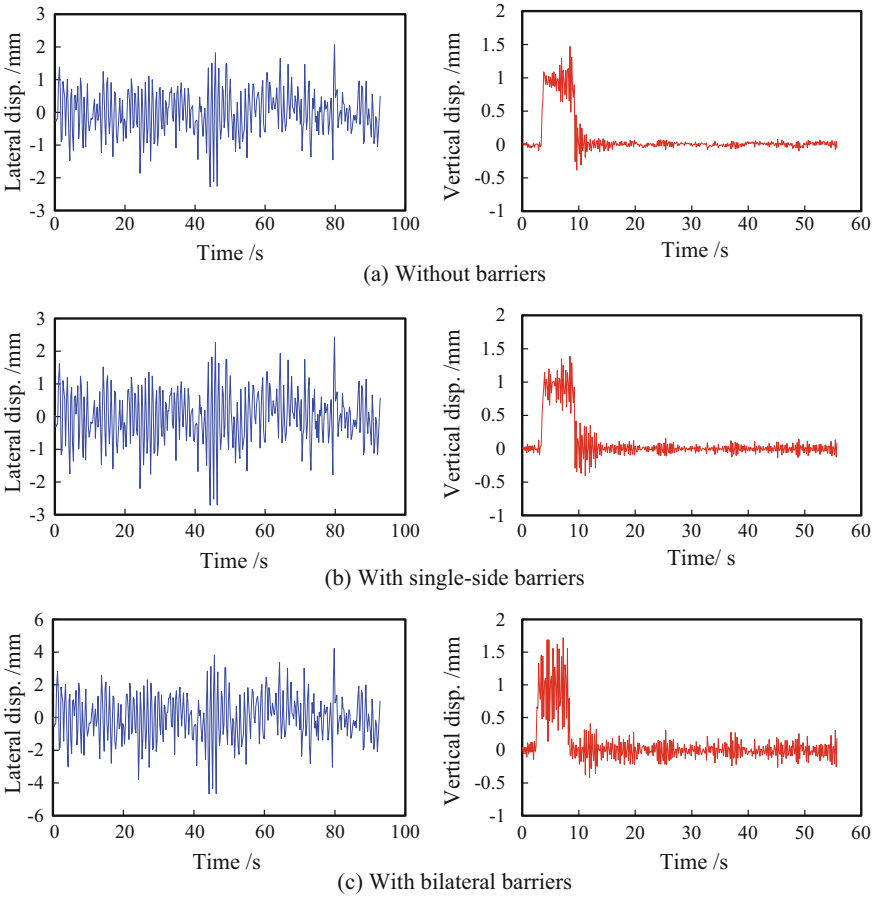

Fig. 6.35 Comparisons of bridge displacement time histories at mid-span

6.5.4 *Vehicle Responses*

Compared in Fig. 6.36 are the distribution curves of the maximum derailment factors, offload factors, and lateral wheel/rail forces of the train, when it runs at a constant speed of 250 km/h on the bridge under the crosswinds with instantaneous wind velocities varying from 0 m/s (without wind action) to 60 m/s.

It can be seen that all the running safety indices of the train are sensitive to the wind velocity. In the case without wind barrier, the indices increase remarkably with the wind velocity. According to the Chinese railway code, the allowable values for the derailment factor and the offload factor are 0.8 and 0.6, respectively. The allowable lateral wheel/rail forces for the motor-car and trailer-car are 52.97 kN and 49.08 kN, respectively. As the wind velocity reaches 45, 55 and 60 m/s, the lateral wheel/rail force of the trailer-car, the offload factor, and the derailment factor of the vehicle exceed, successively, their corresponding allowable limits.

In the cases with wind barriers, the running safety indices of the train are decreased obviously. With the single-side barriers, even when the wind velocity reaches 60 m/s, the maximum derailment factor and the offload factor are 0.35 and 0.30, and the lateral wheel/rail forces for the motor-car and trailer-car are 35.71 kN and 35.76 kN, respectively. With the bilateral barriers, the running safety indices of the train are further decreased compared with the single-side barriers, with the derailment factor and offload factor by 8.78% and 6.98%, and the lateral wheel/rail

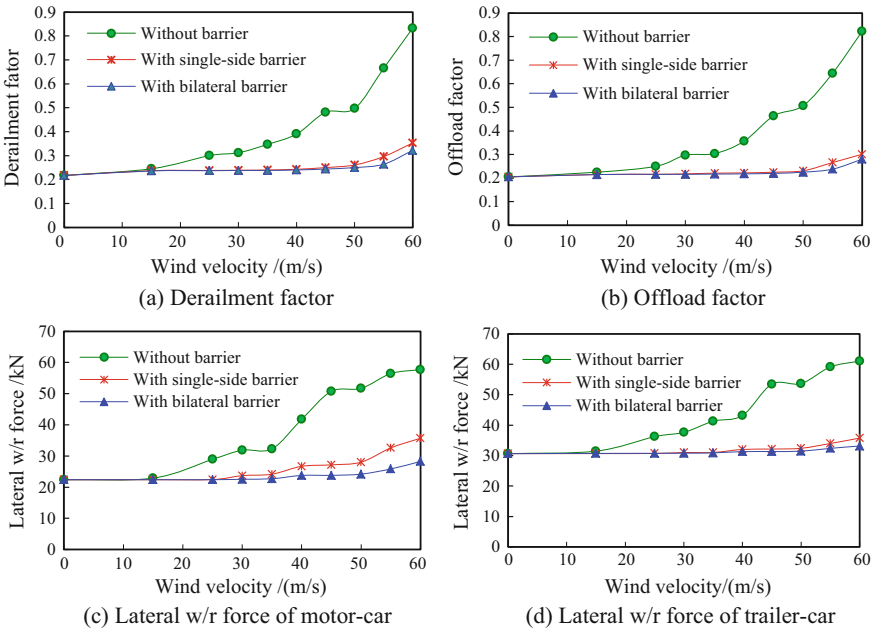

Fig. 6.36 Running safety indices of the train versus instantaneous wind velocity

forces for the motor-car and trailer-car by 20.88% and 7.28%, respectively. However, it should be noticed that with the bilateral barriers, the lateral displacement and acceleration of the bridge are increased by 73.02 and 91.13% due to the enlargement of their windward areas, producing an adverse effect on the vibration of the bridge.

In this case study, the dynamic responses of a multi-span simply-supported bridge with 32 m box-beams under both a high-speed train and crosswinds considering the aerodynamic effects of wind barriers are analyzed by numerical simulation. The results show that installing wind barriers on the bridge has dual effects, which may effectively improve the running safety of high-speed trains, but enlarge the responses of the bridge, especially in lateral direction. This should be noticed in design of wind barriers for HSR bridges. Therefore, further investigations on the relationship between the design details of wind barriers and the dynamic behaviors of train-bridge system are required before solid conclusions can be proposed.

References

Ahmed SR, Gawthorpe RG, Mackrodt PA (1985) Aerodynamics of road and rail vehicles. Veh Syst Dyn 14(4–6):319–392

Andersson E, Haggstro MJ, Sima M, Stichel S (2004) Assessment of train-overturning risk due to strong cross-winds. J Rail Rapid Transit 218(3):213–223

Baetke F, Werner H (1990) Numerical simulation of turbulent flow over surface-mounted obstacles with sharp edges and corners. J Wind Eng Ind Aerodyn 35:129–147

Baker CJ (1991a) Ground vehicles in high cross winds—part I: steady aerodynamic forces. J Fluids Struct 5(2):69–90

Baker CJ (1991b) Ground vehicles in high cross winds—part II: unsteady aerodynamic forces. J Fluids Struct 5(2):91–111

Baker CJ, Reynolds S (1992) Wind-induced accidents of road vehicles. Accid Anal Prev 24(6):559–575

Bekele SA, Hangan H (2002) A comparative investigation of the TTU pressure envelope-numerical versus laboratory and full scale results. Wind Struct 5(2–4):337–346

Cai CS, Chen SR (2004) Framework of vehicle-bridge-wind dynamic analysis. J Wind Eng Ind Aerodyn 92:579–607

Cao YH, Xiang HF, Zhou Y (2000) Simulation of stochastic wind velocity field on long-span bridges. Eng Mech, ASCE 126(1):1–6

Carrarini A (2007) Reliability based analysis of the crosswind stability of railway vehicles. J Wind Eng Ind Aerodyn 95(7):493–509

Cheli F, Corradi R, Diana G, Tomasini G (2003) A numerical-experimental approach to evaluate the aerodynamic effects on rail vehicle dynamics. Veh Syst Dyn 41:707–716

Chen RL, Zeng QY, Huang YQ et al (2010) Analysis theory of random energy of train derailment in wind. Sci China 53(4):751–757

Chen XZ, Matsumoto M, Kareem A (2000) Time domain flutter and buffeting response analysis of bridges. Eng Mech, ASCE 126(1):7–16

Cooper RK (1981) The effect of cross winds on trains. J Fluid Mech 103(1):170–178

Cooper RK (1984) Atmospheric turbulence with respect to moving ground vehicles. J Wind Eng Ind Aerodyn 17(2):215–238

Davenport AG (1961) The application of statistical concepts to the wind loading of structures. Proc Inst Civ Eng 19(2):449–472

Diedrichs B, Sima1 M, Orellano A, Tengstrand H (2007) Crosswind stability of a high-speed train on a high embankment. J Rail Rapid Transit 221(2):205–225
Diedrichs B (2010) Aerodynamic crosswind stability of a regional train model. J Rail Rapid Transit 224(F6):580–591
Dierickx W, Gabriels D, Cornelis WM (2001) Wind tunnel study on wind speed reduction through successive synthetic windscreens. J Agric Eng Res 79(1):117–123
Fujii T, Maeda T, Ishida H, Imai T, Tanemoto K, Suzuki M (1999) Wind-induced accidents of train/vehicles and their measures in Japan. Q Rep Railw Tech Res Inst 40(1):50–55
Guo WW, Xu YL, Xia H et al (2007) Dynamic response of suspension bridge to typhoon and trains II: numerical results. J Struct Eng, ASCE 133(1):12–21
Guo WW, Xia H, Xu YL (2010) Running safety analysis of a train on the Tsing Ma Bridge under turbulent winds. J Earthq Eng Eng Vib 9(3):307–318
Guo WW, Wang YJ, XIA H, Lu S (2014) Wind tunnel test on aerodynamic effect of wind barriers on train-bridge system. Sci China Technol Sci 57(12):1–7
Guo WW, Xia H, Karoumi R, Zhang T, Li XZ (2015) Aerodynamic effect of wind barriers and running safety of trains on high-speed railway bridges to cross winds. Wind Struct 20 (2):213–236
Hagen LJ, Skidmore EL, Miller PL, Kipp JE (1981) Simulation of effect of wind barriers on airflow. Trans ASAE 24(4):1002–1008
Han Y, Chen ZQ, Hua XG (2010) New estimation methodology of six complex aerodynamic admittance functions. Wind Struct 13(3):293–307
Heisler GM, Dewalle DR (1988) Effects of windbreak structure on wind flow. Agric Ecosyst Environ 22(23):41–69
highestbridges (2004). http://www.highestbridges.com/wiki/index.php?title=Millau_Viaduct
Hong Kong Observatory (1999). http://www.weather.gov.hk/informtc/90s/york/yorkrp.htm
Howell JP (1986) Aerodynamic response of maglev train models to a crosswind gust. J Wind Eng Ind Aerodyn 22(2–3):205–213
JTG/T D60-01-2004 (2004). Wind resistant design specification for highway bridges. Ministry of Communications of PRC, China Communications Press, Beijing (in Chinese)
Kim DH, Kwon SD, Lee IK, Jo BW (2011) Design criteria of wind barriers for traffic—part 2: decision making process. Wind Struct 14(1):71–80
Kwon SD, Kim DH, Lee SH, Song HS (2011) Design criteria of wind barriers for traffic—part 1: wind barrier performance. Wind Struct 14(1):55–70
Launder BE, Spalding DB (1974) The numerical computation of turbulent flows. Comput Methods Appl Mech Eng 3(2):269–289
Li YL, Qiang SZ, Liao HL, Xu YL (2005) Dynamics of wind-rail vehicle-bridge systems. J Wind Eng Ind Aerodyn 93(6):483–507
Li YL, Hu P, Cai CS, Qiang SZ (2013) Wind tunnel study of sudden change of vehicle wind loads due to windshield effects of bridge towers and passing vehicles. J Eng Mech 139(9):1249–1259
Li YL, Hu P, Xu YL, Zhang MJ, Liao HL (2014) Wind loads on a moving vehicle-bridge deck system by wind-tunnel model test. Wind Struct 19(2):145–167
Li ZY (2012) Experimental and numerical study on aerodynamic performance of windbreaks. Harbin Institute of Technology, Harbin (in Chinese)
Lou P (2005) Vehicle-track-bridge interaction element considering vehicle's pitching effect. Finite Elem Anal Des 41:397–427 (in Chinese)
Nikitas N, Macdonald JHG, Jakobsen JB (2011) Identification of flutter derivatives from full-scale ambient vibration measurements of the Clifton Suspension Bridge. Wind Struct 14(3):221–238
Noguchi T, Fujii T (2000) Minimizing the effect of natural disasters. Jpn Railw Transp Rev 23:52–59
Procino L, Kozma H, Bartoli G et al (2008) Wind barriers on bridges: the effect of wall porosity. In: Proceedings of 6th international colloquium on bluff bodies aerodynamics and applications, Milano, Italy, 20–24 July 2008
Qu WL, Liu LN (2007) CFD-based numerical research in the identifying of tri-component force coefficient of bridge. J Wuhan Univ Technol 29(7):85–88 (in Chinese)

Salvatori L, Spinelli P (2006) Effects of structural nonlinearity and along-span wind coherence on suspension bridge aerodynamics: Some numerical simulation results. J Wind Eng Ind Aerodyn 94:415–430

Sanquer S, Barre C, De Virel MD, Cleon LM (2004) Effect of cross winds on high-speed trains: development of a new experimental methodology. J Wind Eng Ind Aerodyn 92:535–545

Simiu E, Scanlan RH (1996) Wind effects on structures, 3rd edn. Wiley, New York

Strukelj A, Ciglaric I, Pipenbaher M (2005) Analysis of a bridge structure and its wind barrier under wind loads. Struct Eng Int 15(4):220–227

Suzuki M, Tanemoto K, Maeda T (2003) Aerodynamic characteristics of train/vehicles under cross winds. J Wind Eng Ind Aerodyn 91(1):209–218

TB 10621-2009 (2010) Code for design of high-speed railway. Ministry of Railways of PRC, China Railway Publishing House, Beijing

Teitel M (2010) Using computational fluid dynamics simulations to determine pressure drops on woven screens. Biosyst Eng 105(2):172–179

Tian HQ (2007) Train aerodynamics. China Railway Publishing House, Beijing (in Chinese)

Versteeg HK, Malalasekera W (1995) An introduction to computational fluid dynamics: the finite volume method. Wiley, New York

Wang FJ (2004) Theory and application of CFD software for computational fluid dynamics analysis. Tsinghua University Press, Beijing (in Chinese)

Wilson JD (1985) Numerical studies of flow through a windbreak. J Wind Eng Ind Aerodyn 21(2):119–154

Xia H, Xu YL, Chan THT (2000) Dynamic interaction of long suspension bridges with running trains. J Sound Vib 237(2):263–280

Xia H, Zhang N (2005) Dynamic interaction of vehicles and structures. Science Press, Beijing

Xia H, Guo WW, Zhang N et al (2008) Dynamic analysis of a train-bridge system under wind action. Comput Struct 86:1845–1855

Xia H, De Roeck G, Goicolea JM (2012) Bridge vibration and controls: new research. Nova Science Publishers, New York

Xiang HY, Li YL, Chen B, Liao HL (2014) Protection effect of railway wind barrier on running safety of train under cross winds. Adv Struct Eng 17(8):1177–1187

Xu YL (2013) Wind effects on cable-supported bridges. Wiley, America

Xu YL, Ko JM, Zhang WS (1997) Vibration studies of Tsing Ma suspension bridge. Bridge Eng, ASCE 3(4):149–156

Xu YL, Zhang N, Xia H (2004) Vibration of coupled train and cable-stayed bridge systems in crosswinds. Eng Struct 26(10):1389–1406

Xu YL, Guo WH (2004) Effects of bridge motion and crosswind on ride comfort of road vehicles. J Wind Eng Ind Aerodyn 92:641–662

Xu YL, Ding QS (2006) Interaction of railway vehicles with track in cross-winds. J Fluids Struct 22(3):295–314

Yang YB, Yau JD (1997) Vehicle-bridge interaction element for dynamic analysis. J Struct Eng 123(11):1512–1518

Zeng QY, Guo XR (1999) Analysis theory and application of vibration for train-bridge time varying system. China Railway Publishing House, Beijing (in Chinese)

Zhai WM (2007) Vehicle-track coupling dynamics, 3rd edn. Science Press, Beijing (in Chinese)

Zhang T, Xia H, Guo WW (2013) Analysis on running safety of train on bridge with wind barriers subjected to cross wind. Wind Struct 17(3):203–225

Zhang WM, Ge YJ, Levitan ML (2011) Aerodynamic flutter analysis of a new suspension bridge with double main spans. Wind Struct 14(3):187–208

Zhang XJ (2011) Investigation on the wind-induced instability of long-span suspension bridges with 3D cable system. Wind Struct 14(3):209–220

Zhu ZW, Gu M, Chen ZQ (2007) CFD system identification and flutter derivatives identification based on aerodynamic simulation model. In: Proceedings of 13th national conference on wind engineering structure, Dalian, China, October, pp 961–967

Chapter 7
Dynamic Analysis of Train-Bridge System Subjected to Earthquake Action

This chapter deals with the vibration of train-bridge system subjected to earthquake action. The spectrum-based simulation method for seismic ground motion considering spatial variation and the method for obtaining consistent earthquake record are summarized. Two kinds of input manners of seismic ground motion, namely the displacement input and the acceleration input, are compared in terms of their characteristics and applicability. The dynamic analysis models of a single WSM (wheel-spring/damper-sprung-mass) unit and a WSM unit series passing through a simply-supported beam and the MDOF train-bridge system subjected to earthquakes are established. The running safety criteria and evaluation process of train vehicles on bridge subjected to earthquakes are proposed. An ICE3 train passing through a steel trussed-arch bridge subjected to earthquake actions is taken as a case study, in which the influences of seismic characteristics and input manners on the dynamic responses of train-bridge system are investigated.

7.1 Introduction

If an earthquake occurs when a train is passing through a bridge, the seismic action will induce the pier vibration through soil and foundation and thus act on the running train via bearings and bridge superstructure, forming the train-bridge–subsoil interaction system during earthquakes. In traditional bridge aseismic design, how to ensure the safety of the structure is usually the main concern, which means the relative motion of the system is usually paid more attention, while the safety of the running train on bridge is guaranteed by restricting the displacements and deformation angles of the track. During earthquakes, however, the train-bridge system will produce more violent vibration than in the normal operating state. In this case, even if the displacements and deformation angles of the track can satisfy the requirements specified in codes, the intense vibration of the bridge may also lead to derailment or overturn of the moving train, which is related to the absolute

H. Xia et al., *Dynamic Interaction of Train-Bridge Systems in High-Speed Railways*, Advances in High-speed Rail Technology, https://doi.org/10.1007/978-3-662-54871-4_7

motion of the system. Besides, instantaneous separation may occur between the rail and the high-speed running wheel, which can only be reflected by nonlinear wheel–rail interaction relationship. Therefore, the dynamic analysis of train-bridge system during earthquakes cannot be a simple combination of bridge seismic design and train-bridge dynamic interaction calculation, but has its own characteristics (Xia et al. 2006, 2014; Yau and Frýba 2007; Zhang et al. 2010a, b; He et al. 2011; Konstantakopoulos et al. 2012; Ju 2013; Chen et al. 2014). The research on this issue has theoretical value as well as engineering significance in optimizing the basic theory of dynamic disaster research of large-span and long-extended bridges, improving the aseismic performance of bridges, ensuring the safety of running trains, and fully exerting the bridge functions.

7.2 Numerical Simulation of Seismic Ground Motion

The train-bridge coupling system subjected to earthquake action has distinct time-varying features, and its dynamic response is usually obtained by time history analysis method, which needs to input the seismic time histories at the bridge site in calculation. The ground motion at the bridge site is usually very complicated, owing to the influence of seismic magnitude, epicenter distance, and site conditions, showing prominent characteristics of spatial variation. Therefore, it is essential to obtain multi-point seismic time histories that can reflect the site characteristics and the spatial variation. The seismic ground motion used in the analysis can be obtained from strong seismic motion records, but they are usually rare and insufficient. Even if the strong seismic motion records analogous to the specified site conditions can be found out, their spatial variation is rarely reflected. Besides, in statistical analysis of train-bridge dynamic response during earthquakes, massive ground motion samples are required as systematic excitations. As a result, it is a good option to generate artificial ground motions using numerical simulation.

7.2.1 Spatial Variation of Seismic Ground Motion

During the propagation of seismic waves from epicenter to the ground through different strata, their amplitudes and phases may change in a large area, which present prominent difference in time histories. This kind of variation is called the spatial variation of seismic ground motion. As a linearly distributed engineering structure, a long-extended or a long-span bridge may experience dramatically distinct motions at its different supports during an earthquake. Therefore, the spatial variation of ground motion has a significant effect on the dynamic response of long-extended and large-span bridges.

In the *Eurocode 8—Design of Structures for Earthquake Resistance—Part 2: Bridge* (European Standard 2005), it is clearly indicated that the influence of spatial

variation on the dynamic response of bridge should be taken into consideration when: (1) the site conditions vary greatly, with 2 or more soil types at the supports; (2) the site conditions vary little, but the total length of bridge spans exceeds a certain threshold. In the *Code for Seismic Design of Railway Engineering* (GB 50111-2006 2009) in China, however, the spatial variation has not been taken into account.

From the viewpoint of bridge engineering, the spatial variation of seismic ground motion mainly involves the following aspects.

Wave Traveling Effect

When an earthquake wave propagates in strata in the form of a plane wave with a limited velocity, owing to the oblique incidence, the times of the wave arriving to the bridge supports on the ground surface may be different. This difference is usually represented as a deterministic time lag, which is called the wave traveling effect. As shown in Fig. 7.1, the earthquake wave travels from the wave front to Support 1 via Paths S_1 and $S_1^{'}$, and to Support 2 via Paths S_2 and $S_2^{'}$, respectively. Since the line connecting the two supports has an acute angle with the wave front, the distance from the wave front to Support 1 is shorter, thus the time of the wave arriving to Support 1 is earlier than that arriving to Support 2.

Incoherence Effect

As shown in Fig. 7.2a, the crack generated during earthquake develops along the extended fault. Due to different "vibration sources" from various points on the fault, the seismic ground motions propagate to Supports 1 and 2 via different paths, and then superimpose each other at the supports. The arrival time difference of these seismic ground motions may cause the change of the waveforms, which is called the extended source effect.

As shown in Fig. 7.2b, if the earthquake wave encounters a scattering object when it propagates in an inhomogeneous stratum, the propagation direction may change, thus the waveform will be different when it arrives at Supports 1 and 2. This effect leading to the variations of seismic ground motion between different supports is called the scattering effect.

Because both the extended source effect and the scattering effect reduce the correlation between earthquake waves at different supports, they are collectively called as the incoherence effect.

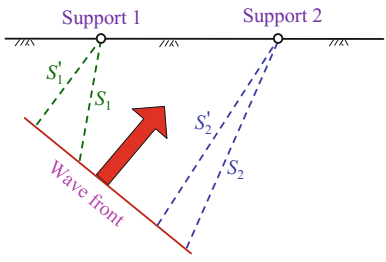

Fig. 7.1 Sketch of wave traveling effect

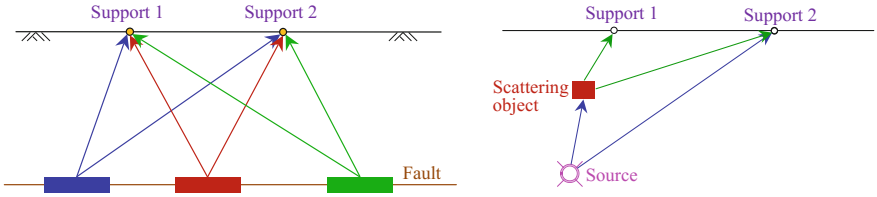

(a) Extended source effect (b) Scattering effect

Fig. 7.2 Incoherence effect of earthquake motion **a** Extended source effect **b** Scattering effect

Fig. 7.3 Attenuation effect

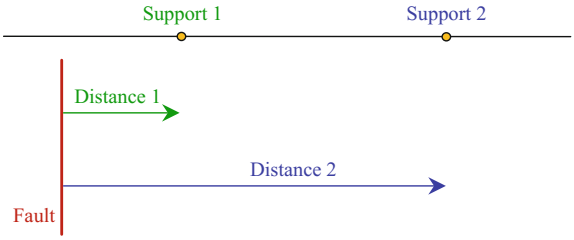

Local Site Effect

Usually, the geological conditions of local sites at various supports are different, which may directly lead to great change of the seismic wave in amplitude as well as in frequency component.

Attenuation Effect

The earthquake waves traveling from the epicenter will attenuate with the distance due to the damping and other factors. As shown in Fig. 7.3, compared with Support 1, the earthquake wave at Support 2 is smaller because it travels a longer distance. This is called the attenuation effect.

7.2.2 Simulation of Seismic Ground Motion Considering Spatial Variation

The seismic ground motion is a typical non-stationary process, and the motion samples considering spatial variation can be obtained by using the random field theory based on spectral method (Zerva 2002, 2009). There are two methods to simulate the random field of seismic ground motion (Shama and Armen 2010). One is based on the power spectral density (PSD) function (or response spectrum) and the complex coherence function, which is called the unconditional simulation. The other is based on the existing time histories of seismic ground motion and the complex coherence function, which is called the conditional simulation.

7.2.2.1 Unconditional Simulation

Both the PSD function and the response spectrum can reflect the field characteristics of the bridge site. Accordingly, the unconditional simulation can be classified into two kinds: one is based on the PSD function and the other is based on the response spectrum.

According to the theory of non-stationary random vector process, the non-stationary seismic ground motions at the bridge supports can be expressed by the product of a stationary random process and the time modulation function, in which the stationary motion can be simulated via the stationary PSD function and the spatial correlation between the supports.

(1) Unconditional simulation based on PSD function

The unconditional simulation method based on PSD function can be used to produce the time histories of completely non-stationary multi-support seismic accelerations. The basic procedure consists of the following steps:

(a) Select the time modulation function

The Bogdanoff–Goldberg–Bernard Model (Bogdanoff et al. 1961) can be taken as the time modulation function. It has a single exponential form expressed as

$$A(\omega, t) = A(t) = \alpha_1 t \exp(-\alpha_2 t) \tag{7.1}$$

where α_1 governs the amplitude of acceleration, and α_2 the shape of the function.

For different supports, the time lag due to wave traveling effect should be considered.

$$A_i(\omega, t) = A_i(t) = \begin{cases} 0, & \left(0 \le t < \frac{\lambda_{i1}^{\mathrm{P}}}{v_{\mathrm{app}}}\right) \\ \alpha_1\left(t - \frac{\lambda_{i1}^{\mathrm{P}}}{v_{\mathrm{app}}}\right) \exp\left[-\alpha_2\left(t - \frac{\lambda_{i1}^{\mathrm{P}}}{v_{\mathrm{app}}}\right)\right], & \left(t \ge \frac{\lambda_{i1}^{\mathrm{P}}}{v_{\mathrm{app}}}\right) \end{cases} \tag{7.2}$$

where v_{app} is the apparent seismic velocity; λ is the distance between the supports, with superscript P representing the projection of λ along the propagation direction of earthquake wave; subscript i is the number of the bridge support, and 1 represents the support at which the seismic wave arrives earliest; ω denotes the circular frequency.

(b) Determine the stationary PSD function

According to the site characteristics of bridge supports, the stationary PSD function can be determined with the Kanai–Tajimi acceleration spectrum modified by Clough and Penzien (1975).

$$s_i(\omega) = s_{0i}\left\{\frac{1+4\xi_{gi}^2(\omega/\omega_{gi})^2}{\left[1-(\omega/\omega_{gi})^2\right]^2+4\xi_{gi}^2(\omega/\omega_{gi})^2}\right\} \times \left\{\frac{(\omega/\omega_{fi})^4}{\left[1-(\omega/\omega_{fi})^2\right]^2+4\xi_{fi}^2(\omega/\omega_{fi})^2}\right\} \tag{7.3}$$

where the first term s_{0i} is a constant for determining the acceleration amplitude; the second term is the Kanai–Tajimi spectrum, in which ω_{gi} and ξ_{gi} represent the characteristic frequency and damping ratio of the site, respectively; the third term is a filter, in which ω_{fi} and ξ_{fi} correspond to the cutoff frequency and the peak value of the frequency response function, respectively.

(c) Select the complex coherence function

The complex coherence function model proposed in *Eurocode 8* (European Standard 2005) is adopted here, expressed as

$$\Gamma_{ij}(\omega) = \exp\left[-\left(\frac{\alpha\omega\lambda_{ij}}{v_s}\right)^2\right] \times \exp\left(-\mathrm{i}\frac{\omega\lambda_{ij}^P}{v_{app}}\right) \tag{7.4}$$

where the first term at the right side of equation corresponds to the incoherency effect; the second term is the phase variation due to wave traveling effect; α is a parameter reflecting the characteristics of the site soil, usually adopted in the range of [0, 0.5]; v_s is the shear velocity of the site soil; subscript j represents the bridge support.

(d) Form the evolutionary cross-PSD matrix

By discretization of the frequency and the time, the cross-PSD matrix corresponding to the discrete point (ω_l, t_r) can be calculated as

$$\mathbf{S}(\omega_l, t_r) = \begin{bmatrix} s_{11} & s_{21}^* & \cdots & s_{n1}^* \\ s_{21} & s_{22} & \cdots & s_{n2}^* \\ \cdots & \cdots & \cdots & \cdots \\ s_{n1} & s_{n2} & \cdots & s_{nn} \end{bmatrix} \tag{7.5}$$

where subscript n denotes the number of bridge supports; s_{ii} (ω_l) represents the auto-PSD of support i; $s_{ij}(\omega_l)$ represents the cross-PSD between supports i and j. The expressions of the above items are

$$s_{ii} = |A_i(\omega_l, t_r)|^2 s_i(\omega_l) \tag{7.6}$$

$$s_{ij} = A_i(\omega_l, t_r)A_j(\omega_l, t_r)\sqrt{s_i(\omega_l)s_j(\omega_l)} \cdot \Gamma_{ij}(\omega_l), \quad (i \neq j) \tag{7.7}$$

$$\begin{aligned} &\omega_l = l\Delta\omega, \quad \Delta\omega = \omega_{\mathrm{u}}/N, \quad (l = 1, 2, \cdots, N) \\ &t_r = r\Delta t, \quad (r = 1, 2, \cdots) \end{aligned} \tag{7.8}$$

where ω_{u} is the upper cutoff frequency in analysis; Δt is the time interval; N is the number of frequency divisions.

(e) Decompose the cross-PSD matrix

The Cholesky method is used to decompose the evolutionary cross-PSD matrix.

$$\mathbf{S}(\omega_l, t_r) = \mathbf{H}(\omega_l, t_r)(\mathbf{H}^*)^{\mathrm{T}}(\omega_l, t_r) \tag{7.9}$$

where, $\mathbf{H}(\omega_l, t_r)$ is a lower triangular matrix, and the superscript * denotes the complex conjugate calculation. The matrix $\mathbf{H}$ can be written as

$$\mathbf{H}(\omega_l, t_r) = \begin{bmatrix} H_{11}(\omega_l, t_r) & 0 & \cdots & 0 \\ H_{21}(\omega_l, t_r) & H_{22}(\omega_l, t_r) & 0 & 0 \\ \cdots & \cdots & \cdots & 0 \\ H_{n1}(\omega_l, t_r) & H_{n2}(\omega_l, t_r) & \cdots & H_{nn}(\omega_l, t_r) \end{bmatrix} \tag{7.10}$$

where $H_{ii}(\omega_l, t_r)$ (i = 1, 2, …n) are nonnegative real numbers, and $H_{ij}(\omega_l, t_r)$ (i = 2, 3,…n; j = 1, 2, …; $i \neq j$) are usually complex numbers.

(f) Constitute the seismic acceleration time histories at different supports

The acceleration time histories at different supports can be constituted by the following formulas

$$\ddot{X}_i(t_r) = 2\sum_{m=1}^{i}\sum_{l=1}^{N}\left\{|H_{im}(\omega_l, t_r)|\sqrt{\Delta\omega}\cdot \cos[\omega_l t_r - \theta_{im}(\omega_l, t_r) + \Phi_{ml}]\right\} \tag{7.11}$$

$$\theta_{im}(\omega_l, t_r) = \tan^{-1}\left\{\frac{\mathrm{Im}[H_{im}(\omega_l, t_r)]}{\mathrm{Re}[H_{im}(\omega_l, t_r)]}\right\} \tag{7.12}$$

where Φ_{ml} denotes the independent random phase angles uniformly distributed in [0, 2π]; the functions Im and Re represent to take the imaginary part and real part of a complex, respectively.

Note that the above algorithm degenerates to the trigonometric series simulation method when it is applied to simulate the single-point ground motion.

A (85+130+85) m continuous rigid-frame bridge is taken as a case study. According to the site conditions, the horizontally transverse seismic acceleration time histories are generated via unconditional simulation based on PSD function. In the simulation procedure, the seismic wave is assumed to propagate along the longitudinal direction from Support 1 to Support 4, and the modulation functions at all supports are the same. The parameters in simulation are listed in Table 7.1.

Table 7.1 Main parameters in seismic ground motion simulation

Parameter	Support 1	Support 2	Support 3	Support 4
Control parameter of acceleration amplitude, α_1	1.36	1.36	1.36	1.36
Control parameter of acceleration shape, α_2	0.5	0.5	0.5	0.5
Characteristic parameter of site soil, α	0.2	0.2	0.2	0.2
Shear velocity of soil, v_s (m/s)	300	300	300	300
Apparent seismic velocity of soil, v_{app} (m/s)	500	500	500	500
Constant of acceleration amplitude of support, s_{01-04} (cm^2/s^3)	30	30	30	30
Site characteristic frequency of support, ω_{g1}–ω_{g4} (rad/s)	8π	5π	2.4π	2.4π
Site characteristic damping ratio of support, ξ_{g1}–ξ_{g4}	0.60	0.60	0.85	0.85
Filter cutoff frequency of support, ω_{f1}–ω_{f4} (rad/s)	0.8π	0.5π	0.5π	0.5π
Filter peak parameter of support, ξ_{f1}–ξ_{f4}	0.60	0.60	0.85	0.85

Note In analysis, the upper cutoff frequency $\omega_u = 40\pi$; the time interval $\Delta t = 0.01$ s; the number of frequency divisions $N = 1000$

Shown in Fig. 7.4 are the simulated samples of seismic acceleration time histories at the four supports.

(2) Unconditional simulation based on response spectrum

In practice, the PSD functions reflecting the site characteristics are rarely presented in design specifications, instead, the response spectra are more common. By modifying the above unconditional simulation method based on PSD function, the seismic acceleration time histories at the bridge supports can be obtained (Deodatis 1996), which can satisfy both the response spectrum and the spatial correlation. The basic procedure consists of the following steps:

(a) Calculate the acceleration response spectra corresponding to the non-stationary seismic acceleration time histories at various supports, and compare them with the target response spectra.
(b) If the compared results cannot satisfy the specified error, adjust the stationary PSD function of all supports, and then repeat the above steps.

Shown in Fig. 7.5 are the procedures of unconditional simulation based on response spectrum.

It can be seen that the procedures of unconditional simulation based on response spectrum are the same as those based on PSD, but different formulations are adopted in the following three steps.

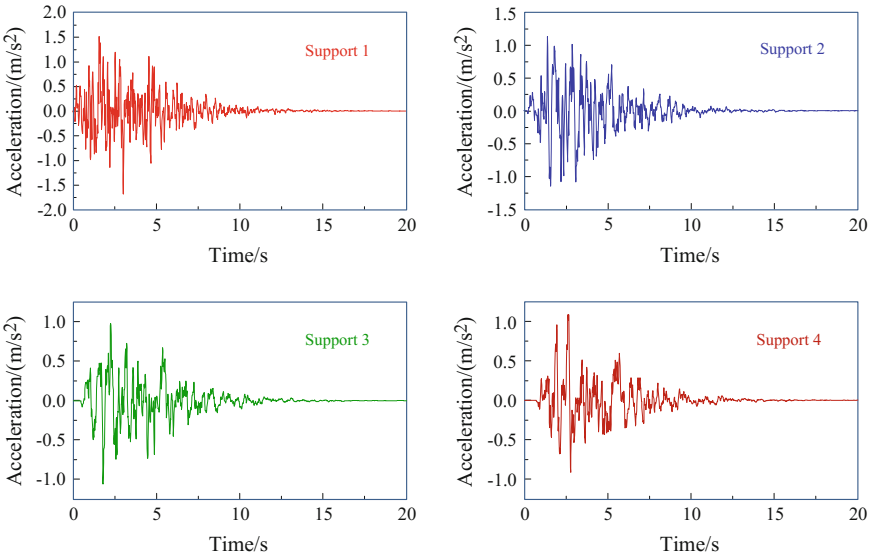

Fig. 7.4 Seismic acceleration time histories obtained by unconditional simulation based on PSD

(c) Determine the stationary PSD function

When determining the stationary PSD function, the PSD functions at various supports are modified by

$$s_i(\omega) \rightarrow s_i(\omega)\left(\frac{\mathrm{RSA}_i(\omega)}{\mathrm{RSA}^{\ddot{X}_i(t)}(\omega)}\right)^2 \tag{7.13}$$

where$\mathrm{RSA}_i(\omega)$ is the target response spectrum, and $\mathrm{RSA}^{\ddot{X}_i(t)}(\omega)$ is the calculated response spectrum of the ith support.

(d) Form the stationary cross-PSD matrix

In Eq. (7.5), the elements in the cross-PSD matrix are modified by

$$s_{ii}(\omega_l) = s_i(\omega_l) \tag{7.14}$$

$$s_{ij}(\omega_l) = \sqrt{s_i(\omega_l)s_j(\omega_l)} \cdot \Gamma_{ij}(\omega_l) \quad (i \neq j) \tag{7.15}$$

(f) Form the non-stationary seismic acceleration time histories at various supports

The acceleration time histories at various supports are modified by

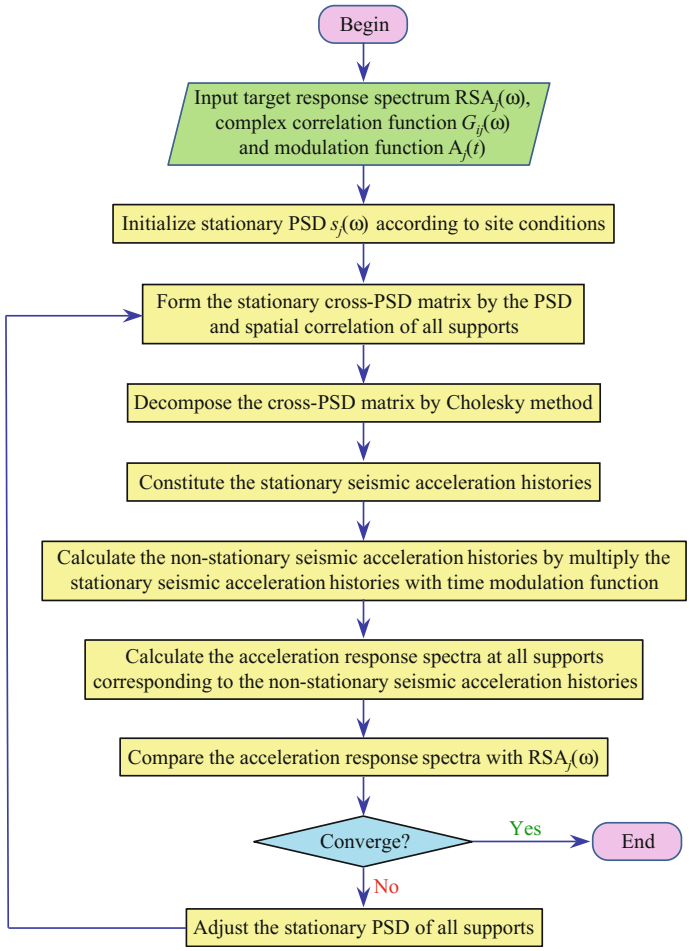

Fig. 7.5 Procedures of unconditional simulation based on response spectrum

$$\ddot{X}_i(t_r) = 2A_i(t_r)\sum_{m=1}^{i}\sum_{l=1}^{N}\left\{|H_{im}(\omega_l,t_r)|\sqrt{\Delta\omega}\times\cos[\omega_l t_r-\theta_{im}(\omega_l,t_r)+\Phi_{ml}]\right\} \tag{7.16}$$

For the (85 + 130 + 85) m continuous rigid-frame bridge, the time histories of horizontally transverse seismic accelerations are generated via unconditional simulation based on the response spectrum. In the simulation procedure, the earthquake wave is still assumed to propagate along the longitudinal direction from Support 1 to Support 4. The seismic intensity at the bridge site is the frequent 7°. The site category at Supports 1 and 2 is I_0 and that at Supports 3 and 4 is I_1. Other parameters have been listed in Table 7.1. Shown in Fig. 7.6 are the seismic

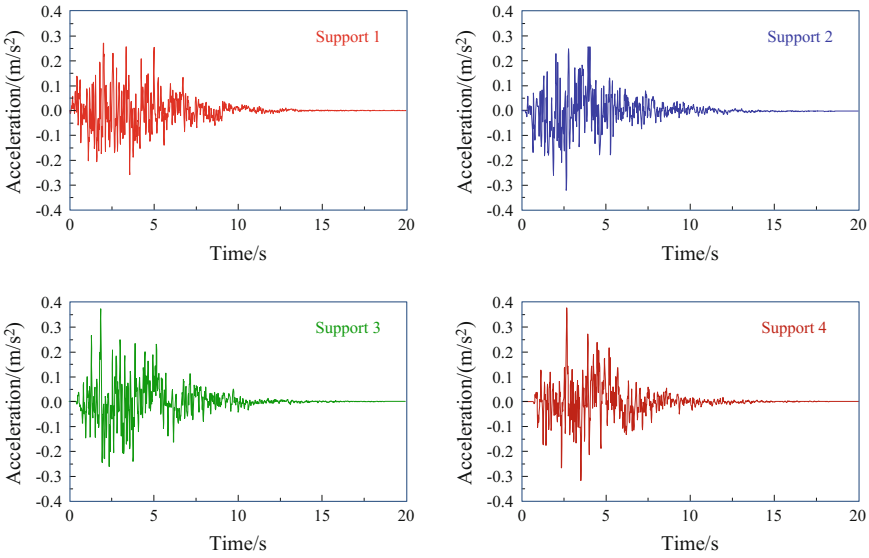

Fig. 7.6 Seismic acceleration time histories produced by unconditional simulation based on response spectrum

acceleration time histories at the four bridge supports, and in Fig. 7.7 are the comparisons between the simulated and the standard response spectra at the supports.

7.2.2.2 Conditional Simulation

The earthquake motion generated by unconditional simulation depends on the white noise time series, which actually contains only a part of the information derived from real seismic records. Different from the unconditional simulation, the conditional simulation uses one or more existing earthquake waves to generate seismic motions of spatial variation, which can better inherit the physical characteristics of the existing seismic waves, such as the non-stationary characteristics of amplitude and frequency, the characteristics of epicenter, the propagation path, and the local site conditions.

There are two kinds of conditional simulation methods mainly used recently. One is the multivariate linear prediction (MLP) method based on the traditional Krige technique proposed by Vanmarcke and Fenton (1991), in which the Fourier coefficients in the simulated time history are obtained by unbiased estimation. The other is the conditional probability density function (CPDF) method, in which the Fourier coefficients in the simulated time history are determined by the closed-form conditional probability functions. Even though the ways of obtaining Fourier coefficients are different, the above two methods are equivalent in the stochastic

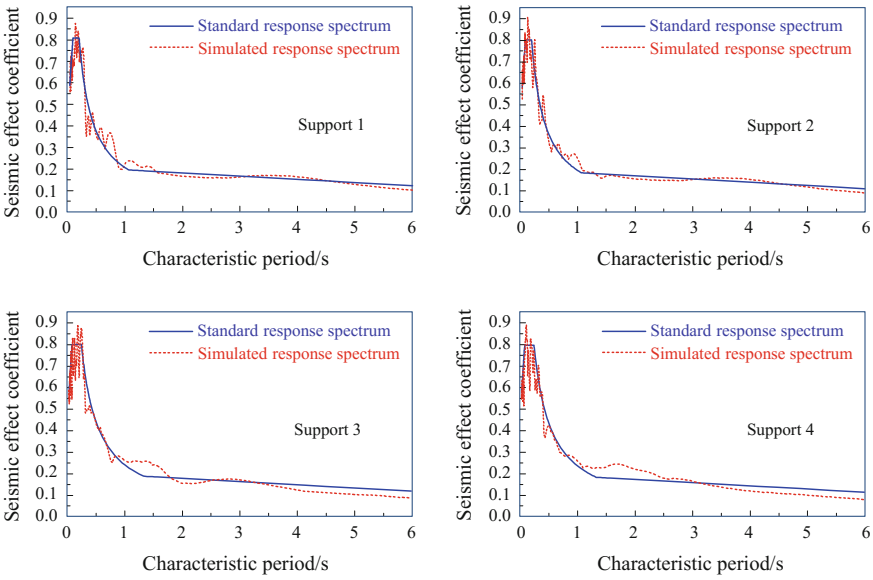

Fig. 7.7 Comparisons between the simulated and standard response spectra of seismic acceleration time histories

sense. Therefore, only the MLP method is introduced here, and its procedures are as follows:

(1) Divide the existing earthquake acceleration time history into continuous non-overlapping time history segments with different numbers of time step, by the time domain segment method.

Each time history segment in the existing seismic wave should be approximated as a stationary process, because the Fourier transform with inherent characteristics of stationarity is adopted in the subsequent procedures. In implementation, the amplitudes and the zero intersection points in various segments should be relatively similar, which can be done simply by observation.

(2) Simulate the unknown time history segments at the bridge supports, by taking the time history segments of existing earthquake waves as the reference time series.

All the time history segments at the bridge supports are homologous Gaussian stochastic processes with zero means, which can be expressed by the following Fourier series

$$\ddot{X}_i(t) = \sum_{l=1}^{n_f} \left[A_{i,l} \cos(\omega_l t) + B_{i,l} \sin(\omega_l t) \right], \quad (i = 1, 2, \ldots, n) \tag{7.17}$$

where n is the number of bridge supports; ω_l stands for the discretized frequency point, and n_f is the number of frequency discretization.

When the Fourier coefficients of earthquake time history segments, the spatial correlation model, and the site characteristics at the bridge supports are known, the Fourier coefficients of the unknown earthquake time history segments at the target (unknown) supports can be estimated via the MLP method, then the required time history segments can be obtained using the inverse Fourier transform. The procedures of this conditional simulation method are summarized as follows.

(a) Arrange the time history segments respectively at the known and the target supports as follows

$$\ddot{\mathbf{X}}_{\mathrm{kn}} = \left[\ddot{X}_1(t), \cdots, \ddot{X}_M(t)\right]^{\mathrm{T}} \tag{7.18a}$$

$$\ddot{\mathbf{X}}_{\mathrm{un}} = \left[\ddot{X}_{M+1}(t), \cdots, \ddot{X}_n(t)\right]^{\mathrm{T}} \tag{7.18b}$$

where subscripts kn and un denote known and unknown (target), respectively; M is the number of the known supports; superscript T denotes the transposition operation of vector.

(b) Define the vector $\mathbf{Z}$ corresponding to the Fourier coefficients of each time history segment at frequency discrete point

$$\begin{cases} \mathbf{Z} = (\mathbf{Z}_{\mathrm{kn}}^{\mathrm{T}}, \mathbf{Z}_{\mathrm{un}}^{\mathrm{T}})^{\mathrm{T}} \\ \mathbf{Z}_{\mathrm{kn}} = \left(A_{1,l}, B_{1,l}, \cdots, A_{M,l}, B_{M,l}\right)^{\mathrm{T}} \\ \mathbf{Z}_{\mathrm{un}} = \left(A_{M+1,l}, B_{M+1,l}, \cdots, A_{n,l}, B_{n,l}\right)^{\mathrm{T}} \end{cases} \tag{7.19}$$

and form the covariance matrix of $\mathbf{Z}$, expressed as

$$\mathbf{C}_l = \begin{bmatrix} \mathbf{C}_{\mathrm{kn,kn}} & \mathbf{C}_{\mathrm{kn,un}} \\ \mathbf{C}_{\mathrm{kn,un}}^{\mathrm{T}} & \mathbf{C}_{\mathrm{un,un}} \end{bmatrix} \tag{7.20}$$

where

$$\mathbf{C}_{\mathrm{kn,kn}} = \mathrm{COV}(\mathbf{Z}_{\mathrm{kn}}); \quad \mathbf{C}_{\mathrm{kn,un}} = \mathrm{COV}(\mathbf{Z}_{\mathrm{kn}}, \mathbf{Z}_{\mathrm{un}}); \quad \mathbf{C}_{\mathrm{un,un}} = \mathrm{COV}(\mathbf{Z}_{\mathrm{un}}) \tag{7.21}$$

The elements in $\mathbf{C}_l$ can be calculated based on the statistical correlations between the Fourier coefficients

$$\mathrm{E}[A_{i,l}A_{j,l}] = \mathrm{E}[B_{i,l}B_{j,l}] = \begin{cases} s_{ii}(\omega_l)\Delta\omega & (i = j) \\ \mathrm{Re}[s_{ij}(\omega_l)\Delta\omega] & (i \neq j) \end{cases} \tag{7.22a}$$

$$\mathrm{E}[A_{i,l}B_{j,l}] = -\mathrm{E}[B_{i,l}A_{j,l}] = \begin{cases} 0 & (i=j) \\ -\mathrm{Im}[s_{ij}(\omega_l)\Delta\omega] & (i\neq j) \end{cases} \tag{7.22b}$$

where E[·] denotes the mathematical expectation; $s_{ii}(\omega_l)$ denotes the auto-PSD of support i; $s_{ij}(\omega_l)$ denotes the cross-PSD between supports i and j, which can be obtained by

$$s_{ij}(\omega_l) = \sqrt{s_{ii}(\omega_l)s_{jj}(\omega_l)}\cdot\ \Gamma_{ij}(\omega_l) \quad (i\neq j) \tag{7.23}$$

where $\Gamma_{ij}(\omega_l)$ is the spatial complex coherence function between supports; other parameters are defined previously.

(c) Decompose the covariance matrix $\mathbf{C}_l$ by the Cholesky decomposition

$$\mathbf{C}_l = \mathbf{L}_l\cdot\ \mathbf{L}_l^{\mathrm{T}} \tag{7.24}$$

(d) Calculate the Fourier coefficients in unconditional simulation corresponding to Eq. (7.19),

$$\mathbf{Z}_{\mathrm{s}} = (\mathbf{Z}_{\mathrm{s,kn}}^{\mathrm{T}}, \mathbf{Z}_{\mathrm{s,un}}^{\mathrm{T}})^{\mathrm{T}} = \mathbf{L}_l\cdot\ \mathbf{Y}_l \tag{7.25}$$

where $\mathbf{Y}_l$ is a random vector whose elements obey independent standard normal distribution and subscript s stands for unconditional simulation.

(e) Calculate the multivariate linear predictive values by C_l and the known Fourier coefficients

$$\mathbf{Z}_{\mathrm{un}}^{*} = \mathbf{C}_{\mathrm{kn,un}}^{\mathrm{T}}\mathbf{C}_{\mathrm{kn,kn}}^{-1}\mathbf{Z}_{\mathrm{kn}} \tag{7.26}$$

(f) Similarly, calculate the multivariate linear predictive values corresponding to Fourier coefficients $Z_{\mathrm{s,kn}}$ in unconditional simulation

$$\mathbf{Z}_{\mathrm{s,un}}^{*} = \mathbf{C}_{\mathrm{kn,un}}^{\mathrm{T}}\mathbf{C}_{\mathrm{kn,kn}}^{-1}\mathbf{Z}_{\mathrm{s,kn}} \tag{7.27}$$

(g) Calculate the unknown Fourier coefficients in conditional simulation

$$\mathbf{Z}_{\mathrm{un}} = \mathbf{Z}_{\mathrm{un}}^{*} + \left(\mathbf{Z}_{\mathrm{s,un}} - \mathbf{Z}_{\mathrm{s,un}}^{*}\right) \tag{7.28}$$

(h) Repeat the above procedures for every frequency points, to obtain the corresponding time history segments using the inverse Fourier transform

(3) Connect the simulated time history segments at various supports by the linear weighted function, to extend the simulated earthquake motions from the stationary state to the non-stationary state.

(4) Add zeros to consider the time lags of earthquake waves arriving at different supports owing to the wave traveling effect, and finally obtain the spatial variably seismic acceleration time histories in the entire time domain.

For a (180+216+180) m continuous steel trussed-arch bridge, the time histories of horizontally transverse seismic accelerations are generated by the conditional simulation. In the simulation, the seismic wave propagates along the longitudinal direction from Support 1 to Support 4 with the speed of v_{app} = 500 m/s; the site characteristics at all supports are identical, and the PSD function is determined by the known seismic wave at Support 1; the shear velocity of the site soil is v_s = 300 m/s; the correlation coefficient in the complex coherence function is α = 0.25, and the time interval is Δt = 0.02 s. Shown in Fig. 7.8 are the simulated seismic accelerations at the four supports.

In the aseismic analysis of bridges, it is important to select a suitable seismic wave, because inputting different seismic waves may lead to great difference of structural response. The selected seismic waves can be the artificial waves for

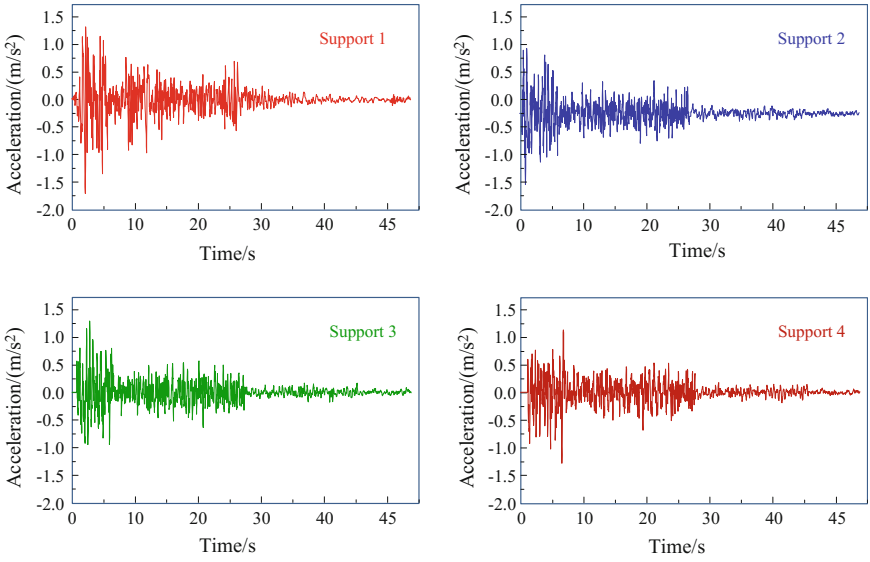

Fig. 7.8 Seismic accelerations at bridge supports obtained by the conditional simulation

earthquake hazard evaluation, as well as the recorded real earthquake waves. The seismic waves obtained by earthquake hazards evaluation can not only predict the vibration of bedrock at the bridge site, but also effectively take into account the influence of local site soil on the earthquake motion, but due to heavy calculation cost, they are usually used in aseismic design of important projects. Instead, as a feasible choice, the recorded real earthquake waves are more applicable, because they reflect the actual motion of the ground during earthquake, thus using them as input for seismic analysis can better estimate the dynamic performance of structures subjected to earthquake action.

The main factors governing the seismic waves include intensity, spectral characteristics, and duration of intense earthquake, which should be considered in selecting the real earthquake wave input.

The intensity of seismic waves is usually measured by the acceleration amplitude of the ground motion. If the amplitude of the selected earthquake wave is different from the design intensity at the bridge site, it can be modified by increasing or decreasing proportionally.

The spectral characteristics of seismic waves are usually represented by the predominant period, which are influenced by many factors, such as the characteristics of epicenter, the propagation distance of the wave, and the local site conditions. In selecting a real seismic wave, the site conditions should be as similar as possible, namely the main period of the selected seismic wave should be as close as possible to the predominant period of the bridge site.

The longer duration the seismic wave, the more energy it has, and the more intensive the structural response. In principle, therefore, earthquake waves with longer duration should be adopted in the analysis.

In the current aseismic design code for railway bridges in China, in terms of the types and properties of the rock and soil, as well as the range of the shear wave velocity, the site is classified into four groups: rock or hard soil, moderate hard soil, moderate soft soil, and soft soil. In dynamic analysis of train-bridge system subjected to earthquake action, the real seismic waves widely used in aseismic calculation can be adopted according to the site classification.

7.2.3 Consistency Treatment of Earthquake Record

For dynamic analysis of large-span or long-extended bridges subjected to multi-point and multi-dimensional seismic ground motion, it is indispensable to use the displacement time histories from a real earthquake wave or an artificial one, because the influence of quasi-static component of the ground motion on the structural response cannot be neglected, which relies on the time history of ground displacement. In fact, in analysis of bridge response under non-uniform earthquakes, the displacement time histories are usually required as the input excitation

at bridge supports by most of the commercial FE software. Moreover, as mentioned previously, different from the traditional aseismic analysis of the bridge which focuses on the relative motion, the dynamic analysis of train-bridge system during earthquakes should consider more the absolute motion of the system. If only acceleration time histories are input in the train-bridge system, the calculated dynamic response may lean to be unsafe. Therefore, it is essential to obtain reasonable seismic displacement time histories.

However, most of the measured earthquake records or artificial seismic waves are acceleration histories, and they often contain various noises and deviations, thus by direct integral of them to obtain the velocity and displacement time histories may result in error trend lines (Wilson 2002). Hence, it is necessary to modify the seismic acceleration time histories, to make the seismic velocities and displacements at the initial moment and the end moment in a reasonable state, namely, to ensure them satisfy the fundamental principle of physics. This modification is called the consistency treatment of earthquake record. Only after consistency treatment, can the earthquake acceleration, velocity and displacement time histories be used in dynamic analysis of train-bridge system.

The modification methods for seismic acceleration time history can be classified into two categories: one leads to a nonzero residual displacement, and the other leads to a zero value residual displacement (Chen et al. 1996). In the modification method with nonzero residual displacement, the seismic acceleration time history is directly integrated and the least square velocity method is used to adjust its zero line, or the seismic displacement and velocity are assumed to satisfy certain initial conditions to remove the error. The final displacement obtained in this way is usually nonzero, meaning that a large residual displacement occurs at the bridge support, which is acceptable for sites near the epicenter and prone to produce permanent deformation. However, in most aseismic analysis, the site is usually assumed to be far from the epicenter, where it is more reasonable that the seismic accelerations, velocities, and displacements at the initial moment and the end moment are all zero. Therefore, in this chapter, the modification method with zero residual displacement is introduced, which mainly involves the Wilson modification method and the time domain high-pass filtering method.

1. The Wilson modification method

During an earthquake, the deviation of an acceleration time history at the initial stage affects more the final displacement, while the deviation of the acceleration time history approaching to the end stage affects more the final velocity. With the earthquake acceleration records as a series of impulses, Wilson (2002) modified the acceleration time histories at the initial stage and the end stage by linear functions, and obtained the zero velocity and zero displacement at the end moment. The main steps of the Wilson modification can be summarized as follows:

(1) Add zeros before and after the seismic acceleration record;

(2) Calculate the displacement increment of the acceleration impulse series at the end

$$\Delta X = \sum_{i=1}^{I} (t_I - t_i)\ddot{X}_i \Delta t \tag{7.29}$$

where I is the total number and Δt is the time interval of the record.

The acceleration time history is modified by a linear function from $t = 0$ to $t = t_L$ (L is the corresponding series number)

$$\sum_{i=1}^{L} \alpha \frac{L-i}{L}(t_I - t_i)\ddot{X}_i \Delta t = \alpha_{\text{pos}} X_{\text{pos}} + \alpha_{\text{neg}} X_{\text{neg}} = -\Delta X \tag{7.30}$$

Assuming the corrections of positive and negative terms identical in the equation, then

$$\alpha_{\text{pos}} = \frac{X_{\text{pos}}}{-2\Delta X}; \quad \alpha_{\text{neg}} = \frac{X_{\text{neg}}}{-2\Delta X} \tag{7.31}$$

Thus, the modification formulas for the acceleration history satisfying displacement consistency are obtained as

$$\left.\begin{array}{ll} \ddot{X}_i = \left(1 + \alpha_{\text{pos}} \frac{L-i}{L}\right)\ddot{X}_i & \text{if } \ddot{X}_i > 0 \\ \ddot{X}_i = \left(1 + \alpha_{\text{neg}} \frac{L-i}{L}\right)\ddot{X}_i & \text{if } \ddot{X}_i < 0 \end{array}\right\}, \quad (i = 1, 2, \ldots, L) \tag{7.32}$$

(3) Calculate the velocity increment of acceleration impulse series at the end

$$\Delta \dot{X} = \sum_{i=1}^{I} \ddot{X}_i \Delta t \tag{7.33}$$

The acceleration time history is modified by a linear function from $t = t_m$ (m is the corresponding series number) to the end $t = t_I$

$$\sum_{i=I-m}^{I} \beta \frac{I-i}{m} \ddot{u}_i \Delta t = \beta_{\text{pos}} \dot{X}_{\text{pos}} + \beta_{\text{neg}} \dot{X}_{\text{neg}} = -\Delta \dot{X} \tag{7.34}$$

Similarly, assuming the corrections of positive and negative terms identical in Eq. (7.34), then

$$\beta_{\text{pos}} = \frac{\dot{X}_{\text{pos}}}{-2\Delta\dot{X}}; \quad \beta_{\text{neg}} = \frac{\dot{X}_{\text{neg}}}{-2\Delta\dot{X}} \tag{7.35}$$

Thus, the modification equations of acceleration satisfying velocity uniformity are obtained, expressed as

$$\left.\begin{array}{ll} \ddot{X}_i = \left(1+\beta_{\text{pos}}\frac{I-i}{M}\right)\ddot{X}_i & \text{if } \ddot{X}_i > 0 \\ \ddot{X}_i = \left(1+\beta_{\text{neg}}\frac{I-i}{M}\right)\ddot{X}_i & \text{if } \ddot{X}_i < 0 \end{array}\right\}, \quad (i = I-M,\ldots,I) \tag{7.36}$$

(4) Check the convergence, if not satisfied, repeat Steps (2) and (3).

The Wilson modification method can ensure most part of the seismic acceleration records unchanged, especially in the peak zones. Its disadvantage is that the durations of the two modification sections have to be determined completely by experience.

2. The time domain high-pass filtering method

In the time domain high-pass filtering method, the seismic acceleration time history is modified by a high-pass filter with the form of critical damping oscillator, to obtain the earthquake records satisfying the consistent requirements, which can be realized by solving the following differential equations

$$\ddot{\mathbf{u}}_{\text{b}}(t) + 2\omega_{\text{c}}\dot{\mathbf{u}}_{\text{b}}(t) + \omega_{\text{c}}^2\mathbf{u}_{\text{b}}(t) = \ddot{\mathbf{u}}_{\text{o}}(t) \tag{7.37a}$$

$$\ddot{\mathbf{u}}_{\text{o}}(t) = \begin{bmatrix} \ddot{X}_1 & \cdots & \ddot{X}_i & \cdots \end{bmatrix}^{\text{T}} \tag{7.37b}$$

where $\mathbf{u}$ represents the displacement vector; subscripts o and b stand for the ground motion at bridge supports before and after modification, respectively; ω_{c} is the angular frequency of the filter.

Equation (7.37a, 7.37b) can be solved either by analytical method or by numerical integration method. Here, the analytical method is introduced. Assuming that the seismic acceleration time history changes linearly within the time step $[t, t + \Delta t]$, expressed as

$$\ddot{\mathbf{u}}_{\text{b}}(t+\tau) = \ddot{\mathbf{u}}_{\text{b}}(t) + \frac{\ddot{\mathbf{u}}_{\text{b}}(t+\Delta t) - \ddot{\mathbf{u}}_{\text{b}}(t)}{\Delta t} \cdot \tau \tag{7.38}$$

where, $t + \tau$ is any moment within this time step, and $\tau \in [0, \Delta t]$.

The displacement solution of Eq. (7.37a, 7.37b) consists of two parts, namely

$$\mathbf{u}_{\text{b}}(t+\tau) = \mathbf{u}_{\text{b}}^{\text{G}}(t+\tau) + \mathbf{u}_{\text{b}}^{\text{S}}(t+\tau) \tag{7.39}$$

where superscript S denotes the particular solution and G denotes the general solution.

The characteristic equation of Eq. (7.37a, 7.37b) can be expressed as

$$r^2 + 2\omega_c r + \omega_c^2 = 0 \tag{7.40}$$

Its roots are two identical real numbers

$$r_1 = r_2 = -\omega_c \tag{7.41}$$

Therefore, the particular solution and the general solution can be, respectively, expressed in the following forms

$$\mathbf{u}_b^S(t+\tau) = \mathbf{A} \cdot \tau + \mathbf{B} \tag{7.42}$$

$$\mathbf{u}_b^G(t+\tau) = (\mathbf{c}_1 + \mathbf{c}_2 \cdot \tau) \cdot \exp(-\omega_c \tau) \tag{7.43}$$

where $\mathbf{A}$, $\mathbf{B}$, $\mathbf{c}_1$, and $\mathbf{c}_2$ are parameter vectors to be determined.

Substituting Eq. (7.42) into Eq. (7.37a) leads to the following solutions for vectors $\mathbf{A}$ and $\mathbf{B}$ as

$$\mathbf{A} = \frac{\ddot{\mathbf{u}}_b(t+\Delta t) - \ddot{\mathbf{u}}_b(t)}{\Delta t \omega_c^2}; \quad \mathbf{B} = \frac{\ddot{\mathbf{u}}_b(t)}{\omega_c^2} - 2\frac{(\ddot{\mathbf{u}}_b(t+\Delta t) - \ddot{\mathbf{u}}_b(t))}{\Delta t \omega_c^3} \tag{7.44}$$

Taking a derivative of Eq. (7.39) with respect to t leads to the following velocity solution

$$\dot{\mathbf{u}}_b(t+\tau) = [\mathbf{c}_2 - \omega_c \cdot (\mathbf{c}_1 + \mathbf{c}_2 \cdot \tau)] \cdot \exp(-\omega_c \tau) + \mathbf{A} \tag{7.45}$$

By setting the τ as zero in Eqs. (7.39) and (7.45), and introducing boundary conditions, we obtain

$$\mathbf{c}_1 = \mathbf{u}_b(t) - \mathbf{B}; \; \mathbf{c}_2 = \dot{\mathbf{u}}_b(t) + \omega_c \cdot (\dot{\mathbf{u}}_b(t) - \mathbf{B}) - \mathbf{A} \tag{7.46}$$

By substituting Eqs. (7.44) and (7.46) into Eqs. (7.39) and (7.45), and setting $\tau = \Delta t$, the following solutions are obtained

$$\begin{aligned} \mathbf{u}_b(t+\Delta t) = {} & [\mathbf{u}_b(t) \cdot (1 + \omega_c \Delta t) + \dot{\mathbf{u}}_b(t) \cdot \Delta t] \cdot \exp(-\omega_c \Delta t) \\ & - [\mathbf{B} \cdot (1 + \omega_c \Delta t) + \mathbf{A} \Delta t] \cdot \exp(-\omega_c \Delta t) + \mathbf{A} \cdot \Delta t + \mathbf{B} \end{aligned} \tag{7.47}$$

$$\begin{aligned} \dot{\mathbf{u}}_b(t+\Delta t) = {} & \left[\mathbf{u}_b(t) \cdot \left(-\omega_c^2 \Delta t\right) + \dot{\mathbf{u}}_b(t)(1 - \omega_c \Delta t)\right] \cdot \exp(-\omega_c \Delta t) \\ & + \left[\mathbf{B} \cdot \omega_c^2 \Delta t - \mathbf{A} \cdot (1 - \omega_c \Delta t)\right] \cdot \exp(-\omega_c \Delta t) + \mathbf{A} \end{aligned} \tag{7.48}$$

When the modified earthquake motion at time t is known, the displacement and velocity at time $t + \Delta t$ can be obtained by Eqs. (7.47) and (7.48), and then the acceleration can be obtained by Eq. (7.37a, 7.37b).

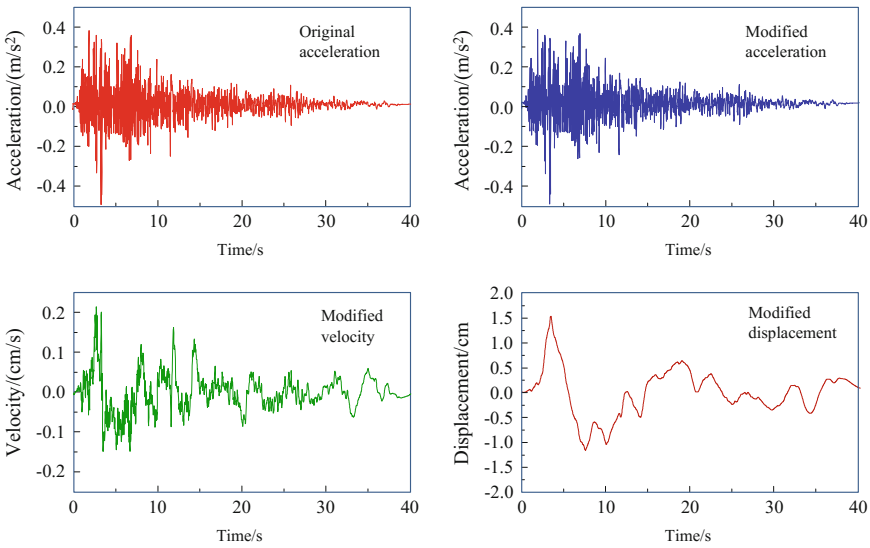

Fig. 7.9 Consistent treatment of seismic ground motion

An earthquake acceleration record is processed by the time domain high-pass filtering method by setting $\omega_c = 0.05$. Shown in Fig. 7.9 are the modified seismic acceleration, velocity, and displacement time histories, which illustrate that the velocity and displacement are approaching zeros at the end of the earthquake.

7.3 Dynamic Analysis of Structures Subjected to Seismic Ground Motion

Different from common structures, large-span and long-extended bridges are usually built across a large site; therefore, the seismic analysis should take into account the spatial variation of the excitation, namely the multi-point non-uniform ground motion. According to structural dynamics, the seismic response of bridge consists of dynamic component and pseudo-static component. The analysis model of bridge subjected to multi-point non-uniform seismic excitations may adopt either the acceleration input or displacement input. The solution method for the motion equations can be divided into two categories, the accurate solution method and the approximate solution method.

The accurate solution method includes the decomposition method and the direct solution method.

The decomposition method is based on the superposition principle, thus the linear response assumption is required for the structures. It usually adopts seismic ground acceleration input and neglects the pseudo-static component of the structure

because it has little influence. The dynamic component is solved by applying the seismic acceleration on the bridge through the influence matrix, and the motion equations of the system are established in the relative coordinate system.

The direct solution method does not need the assumption of linear structural response, and it usually adopts the seismic ground displacement input. The total response of the structure can be solved by applying the seismic ground displacement at the nodes close to the supports, and the motion equations are established in the absolute coordinate system.

In the approximate solution method, the seismic acceleration is usually applied by the large mass method, and the seismic displacement input by the large stiffness method, namely the seismic ground motion approximate to the reality is input onto the structure by setting large numbers in the mass matrix or the stiffness matrix.

In this section, the characteristics, implementation methods as well as applicability of acceleration input and displacement input in both the accurate solution method and the approximate solution method are discussed, based on the SDOF system and the MDOF system.

7.3.1 Single-Degree-of-Freedom Model (SDOF Model)

The analytical model of a SDOF system subjected to vertical ground motion $u_b(t)$ is shown in Fig. 7.10, and its motion equation is

$$m\ddot{u} + c(\dot{u} - \dot{u}_b) + k(u - u_b) = 0 \tag{7.49}$$

where m, c, and k are the mass, damping, and stiffness of the system, respectively; $u(t)$ denotes the system displacement.

When the circular frequency ω, damping ratio ξ, and relative motion w are defined as

$$\omega = \sqrt{k/m}; \quad \xi = c/2m\omega; \quad w = u - u_b \tag{7.50}$$

the motion equation of the SDOF system under the relative coordinates can be expressed as

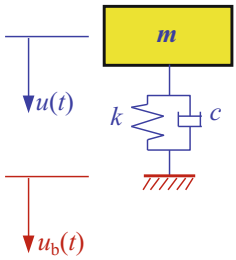

Fig. 7.10 The SDOF system

$$\ddot{w} + 2\xi\omega\dot{w} + \omega^2 w = -\ddot{u}_b \tag{7.51}$$

Obviously, Eq. (7.51) corresponds to the acceleration input. While under the absolute coordinates, the motion equation can be written as

$$\ddot{u} + 2\xi\omega\dot{u} + \omega^2 u = 2\xi\omega\dot{u}_b + \omega^2 u_b \tag{7.52}$$

If the damping term on the right side of the equation is neglected, the excitation input is only related to the seismic displacement. It is easy to see that when added with the ground motion, Eq. (7.51) is equivalent to Eq. (7.52).

7.3.2 Multi-Degree-of-Freedom Model (MDOF Model)

7.3.2.1 Finite Element Analytical Model

Under the absolute coordinates, the motion equations of bridge FE model during earthquakes can be expressed in matrix form as

$$\begin{bmatrix} \mathbf{M}_{ss} & \mathbf{M}_{sb} \\ \mathbf{M}_{bs} & \mathbf{M}_{bb} \end{bmatrix} \begin{Bmatrix} \ddot{\mathbf{u}}_s^t \\ \ddot{\mathbf{u}}_b^t \end{Bmatrix} + \begin{bmatrix} \mathbf{C}_{ss} & \mathbf{C}_{sb} \\ \mathbf{C}_{bs} & \mathbf{C}_{bb} \end{bmatrix} \begin{Bmatrix} \dot{\mathbf{u}}_s^t \\ \dot{\mathbf{u}}_b^t \end{Bmatrix} + \begin{bmatrix} \mathbf{K}_{ss} & \mathbf{K}_{sb} \\ \mathbf{K}_{bs} & \mathbf{K}_{bb} \end{bmatrix} \begin{Bmatrix} \mathbf{u}_s^t \\ \mathbf{u}_b^t \end{Bmatrix} = \begin{Bmatrix} \mathbf{0} \\ \mathbf{0} \end{Bmatrix} \tag{7.53}$$

where **M**, **C,** and **K** are the mass, damping, and stiffness matrices, respectively; subscript s denotes the superstructure and b for the bridge supports; superscript t denotes the total response of structure under the absolute coordinates.

(1) Accurate solution method

Direct solution method

The motion equation of bridge structure under the absolute coordinates can be obtained by expanding Eq. (7.53), expressed as

$$\mathbf{M}_{ss}\ddot{\mathbf{u}}_s^t + \mathbf{C}_{ss}\dot{\mathbf{u}}_s^t + \mathbf{K}_{ss}\mathbf{u}_s^t = -\mathbf{K}_{sb}\mathbf{u}_b^t - \mathbf{C}_{sb}\dot{\mathbf{u}}_b^t - \mathbf{M}_{sb}\ddot{\mathbf{u}}_b^t \tag{7.54a}$$

When the consistent mass matrix is used, the influence of the term with $\mathbf{M}_{sb}$ on the right side of the equation is significantly smaller than that with $\mathbf{K}_{sb}$, and when the lumped mass matrix is adopted, the term with $\mathbf{M}_{sb}$ equals to zero. As a result, the term with $\mathbf{M}_{sb}$ is usually neglected, thus Eq. (7.54a) becomes

$$\mathbf{M}_{ss}\ddot{\mathbf{u}}_s^t + \mathbf{C}_{ss}\dot{\mathbf{u}}_s^t + \mathbf{K}_{ss}\mathbf{u}_s^t = -\mathbf{K}_{sb}\mathbf{u}_b^t - \mathbf{C}_{sb}\dot{\mathbf{u}}_b^t \tag{7.54b}$$

Moreover, the influence of the term with $\mathbf{C}_{sb}$ is also small and difficult to be determined, so this term is usually not taken into account. Then the motion equation of the bridge based on displacement input can be obtained as

$$\mathbf{M}_{ss}\ddot{\mathbf{u}}_s^t + \mathbf{C}_{ss}\dot{\mathbf{u}}_s^t + \mathbf{K}_{ss}\mathbf{u}_s^t = -\mathbf{K}_{sb}\mathbf{u}_b^t \tag{7.54c}$$

Equation (7.54a, 7.54b, 7.54c) can be solved by numerical methods to obtain the total dynamic response of the bridge under earthquake action. This solving procedure is called the direct solution method.

Decomposition method

Assuming the structural response can be decomposed into the dynamic component and the pseudo-static component, expressed as

$$\begin{Bmatrix} \mathbf{u}_s^t \\ \mathbf{u}_b^t \end{Bmatrix} = \begin{Bmatrix} \mathbf{u}_s^s \\ \mathbf{u}_{bg} \end{Bmatrix} + \begin{Bmatrix} \mathbf{u}_s^d \\ \mathbf{0} \end{Bmatrix} \tag{7.55a}$$

$$\mathbf{u}_s^s = -\mathbf{K}_{ss}^{-1}\mathbf{K}_{sb}\mathbf{u}_b = \mathbf{R}\mathbf{u}_b \tag{7.55b}$$

where superscript s denotes the pseudo-static component and b the dynamic component; $\mathbf{R}$ is an influence matrix, which can be obtained by statics analysis. The physical meaning of each element in $\mathbf{R}$ can be expressed as "the displacements of other DOFs of the structure due to a unit forced displacement of the DOF of the structure at the support."

Suppose $\mathbf{C}_{sb} + \mathbf{C}_{ss}\mathbf{R} = \mathbf{0}$, the motion equation of the bridge based on acceleration input can be obtained by substituting Eq. (7.55a, 7.55b) into Eq. (7.54b), expressed as

$$\mathbf{M}_{ss}\ddot{\mathbf{u}}_s^d + \mathbf{C}_{ss}\dot{\mathbf{u}}_s^d + \mathbf{K}_{ss}\mathbf{u}_s^d = -\mathbf{M}_{ss}\mathbf{R}\ddot{\mathbf{u}}_b^t \tag{7.56}$$

Equation (7.56) can be solved by numerical methods, to obtain the dynamic component of the bridge response under earthquake action, and the total dynamic response can be obtained by superimposing the dynamic component with the pseudo-static component. This solving procedure is called the decomposition method.

Shown in Fig. 7.11 are two analysis models of a bridge pier subjected to horizontal seismic excitations, corresponding to the decomposition method based on acceleration input and the direct solution method based on displacement input, respectively. It is easy to see that for the acceleration input, the applied seismic loads are related to the mass distribution, while for the displacement input, the loads are applied directly on the node close to the support in forms of concentrated force and concentrated bending moment. Therefore, the acceleration input is more easily to excite low-frequency vibration of the structure, while the displacement input is more possible to motivate high-frequency vibration.

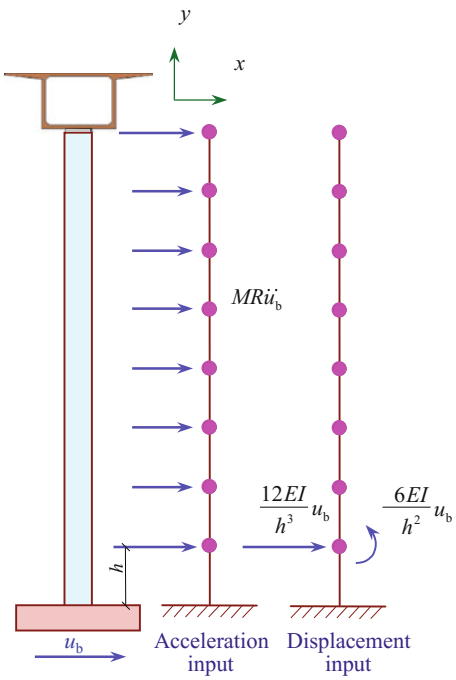

Fig. 7.11 Analysis models of a pier under two seismic input manners

When using the numerical integral method to solve the dynamic response of structures, to ensure the convergence, the time interval should satisfy the following requirement (Bathe 1982)

$$\Delta t \leq \frac{1}{\rho}\min(T_0, T) \tag{7.57}$$

where ρ is a constant; T_0 is the vibration period of the structure; T is the period of the load acting on the structure.

Based on the earthquake records, the displacement time history can be obtained by twice integrals of the acceleration time history, where the integral process is equivalent to low-pass filtering. Therefore, the period of load acting on the bridge based on acceleration input is smaller than that based on displacement input. For a complex MDOF bridge system, T_0 in Eq. (7.57) should be determined by the frequency of structure vibration due to external load. Compared with acceleration input, the displacement input increases the period of load, but makes T_0 decrease greatly because of its acting position (close to the support) and its acting form (as concentrated loads). As a result, the time interval Δt for convergence should be further smaller.

(2) Approximate solution method

In the approximate solution method, both the large mass method and the large stiffness method are dynamic approximate equivalent methods based on the matrices with predominant diagonal elements, which are different from the accurate solution method. In this method, the solution of Eq. (7.53) is realized by changing a constrained problem into an unconstrained one by introducing a proper penalty function into the objective function.

Large mass method

In the large mass method, in order to apply seismic acceleration to the bridge supports, large mass should be added on the diagonal elements corresponding to the supports in the mass matrix on the left side of the motion equation, and meanwhile, the external load should be applied to the elements corresponding to the supports in the force vector on the right side of the equation. The values of the external load are equal to the product of the given acceleration and the sum of the large mass and the diagonal elements. Thus, Eq. (7.53) can be written as

$$\begin{bmatrix} \mathbf{M}_{ss} & \mathbf{M}_{sb} \\ \mathbf{M}_{bs} & \mathbf{M}_{bb}+\mathbf{M}_{L} \end{bmatrix} \begin{Bmatrix} \ddot{\mathbf{u}}_{s}^{t} \\ \ddot{\mathbf{u}}_{b}^{t} \end{Bmatrix} + \begin{bmatrix} \mathbf{C}_{ss} & \mathbf{C}_{sb} \\ \mathbf{C}_{bs} & \mathbf{C}_{bb} \end{bmatrix} \begin{Bmatrix} \dot{\mathbf{u}}_{s}^{t} \\ \dot{\mathbf{u}}_{b}^{t} \end{Bmatrix} + \begin{bmatrix} \mathbf{K}_{ss} & \mathbf{K}_{sb} \\ \mathbf{K}_{bs} & \mathbf{K}_{bb} \end{bmatrix} \begin{Bmatrix} \mathbf{u}_{s}^{t} \\ \mathbf{u}_{b}^{t} \end{Bmatrix} = \begin{Bmatrix} \mathbf{0} \\ (\mathbf{M}_{bb}+\mathbf{M}_{L})\ddot{\mathbf{u}}_{b}^{t} \end{Bmatrix} \tag{7.58}$$

where $\mathbf{M}_{L}$ is the large mass, which is usually $10^{3} \sim 10^{6}$ times the total mass of the bridge.

Obviously, the internal force of the bridge structure calculated by Eq. (7.58) is consistent with the summation of the pseudo-static force component and the dynamic force component obtained by the decomposition method in the accurate solution method. What should be noticed is that the displacement response calculated by Eq. (7.58) does not include the part of rigid-body motion.

Large stiffness method

In the large stiffness method, in order to apply the seismic displacement to the bridge supports, large stiffness should be added on the diagonal elements corresponding to the supports in the stiffness matrix on the left side of the motion equation, and meanwhile, the external loads should be applied to the elements corresponding to supports in the force vector on the right side of the equation. The values of the external load are equal to the product of the given displacement and the sum of the large stiffness and the diagonal elements. Thus, Eq. (7.53) can be written as

$$\begin{bmatrix} \mathbf{M}_{ss} & \mathbf{M}_{sb} \\ \mathbf{M}_{bs} & \mathbf{M}_{bb} \end{bmatrix} \begin{Bmatrix} \ddot{\mathbf{u}}_{s}^{t} \\ \ddot{\mathbf{u}}_{b}^{t} \end{Bmatrix} + \begin{bmatrix} \mathbf{C}_{ss} & \mathbf{C}_{sb} \\ \mathbf{C}_{bs} & \mathbf{C}_{bb} \end{bmatrix} \begin{Bmatrix} \dot{\mathbf{u}}_{s}^{t} \\ \dot{\mathbf{u}}_{b}^{t} \end{Bmatrix} + \begin{bmatrix} \mathbf{K}_{ss} & \mathbf{K}_{sb} \\ \mathbf{K}_{bs} & \mathbf{K}_{bb}+\mathbf{K}_{L} \end{bmatrix} \begin{Bmatrix} \mathbf{u}_{s}^{t} \\ \mathbf{u}_{b}^{t} \end{Bmatrix} = \begin{Bmatrix} \mathbf{0} \\ (\mathbf{K}_{bb}+\mathbf{K}_{L})\mathbf{u}_{b}^{t} \end{Bmatrix} \tag{7.59}$$

where $\mathbf{K}_{\mathrm{L}}$ is the large stiffness, which is usually $10^3 \sim 10^6$ times the sum of element stiffness in the excitation direction.

Obviously, the structure internal force and displacement calculated by Eq. (7.59) are, respectively, consistent with the corresponding summation of the pseudo-static components and dynamic components obtained by the decomposition method in the accurate solution method.

The selection of large stiffness in the large stiffness method and the selection of large mass in the large mass method will directly influence the stability and accuracy of the numerical solution. In practical application, compared with the large stiffness method, the large mass method has better stability and higher accuracy, which is similar to the influence rule of displacement input and acceleration input in the accurate solution method (Zhang et al. 2010a, b).

7.3.2.2 Modal Analysis Model

The motion equation of the bridge can be decoupled by the modal decomposition method, if the damping matrix of the bridge is assumed to have the orthogonality. Suppose $\boldsymbol{\Phi} = [\varphi_1 \quad \varphi_2 \quad \ldots \quad \varphi_n]$ is the normalized modal matrix of the bridge, which satisfies

$$\begin{cases} \boldsymbol{\Phi}^{\mathrm{T}}\mathbf{M}_{\mathrm{ss}}\boldsymbol{\Phi} = \mathbf{I} \\ \boldsymbol{\Phi}^{\mathrm{T}}\mathbf{K}_{\mathrm{ss}}\boldsymbol{\Phi} = \boldsymbol{\Lambda} = \mathrm{diag}[\omega_1^2, \omega_2^2, \cdots, \omega_n^2] \\ \boldsymbol{\Phi}^{\mathrm{T}}\mathbf{C}_{\mathrm{ss}}\boldsymbol{\Phi} = \mathrm{diag}[2\xi_1\omega_1, 2\xi_2\omega_2, \cdots, 2\xi_n\omega_n] \end{cases} \tag{7.60}$$

When n modes are taken into consideration, the modal motion equations of the bridge based on the acceleration input can be expressed as

$$\ddot{q}_i + 2\xi_i\omega_i\dot{q}_i + \omega_i^2 q_i = -\varphi_i^{\mathrm{T}}\mathbf{M}_{\mathrm{ss}}R\ddot{\mathbf{u}}_{\mathrm{b}} \quad (i = 1, 2, \ldots, n) \tag{7.61}$$

where, superscript T denotes the transposition operation of matrix.

The modal motion equations of the bridge based on the displacement input can be expressed as

$$\ddot{q}_i + 2\xi_i\omega_i\dot{q}_i + \omega_i^2 q_i = -\varphi_i^{\mathrm{T}}\mathbf{K}_{\mathrm{sb}}\mathbf{u}_{\mathrm{b}} - \varphi_i^{\mathrm{T}}\mathbf{C}_{\mathrm{sb}}\dot{\mathbf{u}}_{\mathrm{b}} \quad (i = 1, 2, \ldots, n) \tag{7.62}$$

From Eq. (7.60), the following relation can be obtained

$$\boldsymbol{\Phi}^{\mathrm{T}}\mathbf{M}_{\mathrm{ss}} = \boldsymbol{\Lambda}^{-1}\boldsymbol{\Phi}^{\mathrm{T}}\mathbf{K}_{\mathrm{ss}} \tag{7.63}$$

As $\mathbf{R} = -\mathbf{K}_{\mathrm{ss}}^{-1}\mathbf{K}_{\mathrm{sb}}$ is known, we have

$$\boldsymbol{\Phi}^{\mathrm{T}}\mathbf{M}_{\mathrm{ss}}\mathbf{R} = -\boldsymbol{\Lambda}^{-1}\boldsymbol{\Phi}^{\mathrm{T}}\mathbf{K}_{\mathrm{sb}} \tag{7.64a}$$

namely

$$-\mathbf{\Phi}^{\mathrm{T}}\mathbf{K}_{\mathrm{sb}} = \Lambda\Phi^{\mathrm{T}}\mathbf{M}_{\mathrm{ss}}\mathbf{R} \tag{7.64b}$$

Suppose $\mathbf{C}_{\mathrm{sb}} + \mathbf{C}_{\mathrm{ss}}\mathbf{R} = \mathbf{0}$, the following equation can be obtained

$$\varphi_i^{\mathrm{T}}\mathbf{C}_{\mathrm{sb}} = -\varphi_i^{\mathrm{T}}\mathbf{C}_{\mathrm{ss}}\mathbf{R} = -\varphi_i^{\mathrm{T}}\mathbf{C}_{\mathrm{ss}}\sum_{i=1}^{N}\varphi_i\varphi_i^{\mathrm{T}}\mathbf{M}_{\mathrm{ss}}\mathbf{R} \tag{7.65}$$

At the same time

$$\varphi_i^{\mathrm{T}}\mathbf{C}_{\mathrm{ss}}\varphi_j = \begin{cases} 2\xi_i\omega_i\varphi_i^{\mathrm{T}}\mathbf{M}_{\mathrm{ss}}\varphi_i & (i=j) \\ 0 & (i\neq j) \end{cases} \tag{7.66}$$

Therefore, the following equation can be obtained

$$\varphi_i^{\mathrm{T}}\mathbf{C}_{\mathrm{sb}} = 2\xi_i\omega_i\varphi_i^{\mathrm{T}}\mathbf{M}_{\mathrm{ss}}\mathbf{R} \tag{7.67}$$

Substituting Eqs. (7.64b) and (7.67) into (7.62), a new series of modal motion equations can be acquired, namely

$$\ddot{q}_i + 2\xi_i\omega_i\dot{q}_i + \omega_i^2 q_i = \varphi_i^{\mathrm{T}}\mathbf{M}_{\mathrm{ss}}\mathbf{R}\omega_i^2\mathbf{u}_{\mathrm{b}} + 2\xi_i\omega_i\varphi_i^{\mathrm{T}}\mathbf{M}_{\mathrm{ss}}\mathbf{R}\dot{\mathbf{u}}_{\mathrm{b}} \quad (i=1,2,\ldots,n) \tag{7.68a}$$

When neglecting the damping term on the right side, a new series of modal motion equations of the bridge based on the displacement input can be obtained

$$\ddot{q}_i + 2\xi_i\omega_i\dot{q}_i + \omega_i^2 q_i = \varphi_i^{\mathrm{T}}\mathbf{M}_{\mathrm{ss}}\mathbf{R}(\omega_i^2\dot{\mathbf{u}}_{\mathrm{b}}) \quad (i=1,2,\ldots,n) \tag{7.68b}$$

It is well known that, for the vibration problem of a huge bridge structure, the first hundreds of modes or even dozens of modes are enough for analysis, which makes the numbers of equations to be solved decrease greatly when the modal decomposition method is used. The importance of any mode is controlled by two factors: one is the interaction between the mode-shape and the spatial distribution of external load, the other is the ratio of load frequency to the mode frequency. From Eqs. (7.62) and (7.68a, 7.68b), it can be seen that for each mode, the displacement input can be equivalent to the acceleration input, demonstrating that the interaction rule between the mode-shape and the spatial distribution of external load does not change due to the input manner selected. Under the same seismic excitation, the load frequency in the displacement input is smaller than that in the acceleration input, which reduces the ratio of load frequency to modal frequency and makes the

dynamic action on the high-frequency modes decrease more quickly. With combination of Eq. (7.57), it can be concluded that when modal analysis method is adopted for the bridge, if high-frequency modes are not involved, more accurate results can be obtained by the displacement input than by the acceleration input under the condition of the same mode number and the same time interval.

The natural frequencies and the mode-shapes of structures can be solved by the subspace iteration method, the Jacobi method, and the Raffarin method. However, the convergence criterion of these methods can only guarantee the accuracy of frequency and most part of mode-shape values, but cannot ensure the accuracy of mode-shapes close to the supports where they are usually small. Equation (7.62) is simple and the stiffness in the load term can be obtained by FE method, so it has a higher accuracy, but the product of the stiffness and the mode value close to the support may cause the inaccuracy of the load term. For huge and complex structures, this inaccuracy may definitely lead to unpredictable deviation. Equation (7.68a, 7.68b) is equivalent to Eq. (7.62), but it can diminish the deviation, thus it is more suitable in the calculation.

7.3.2.3 Comparison Between Acceleration Input and Displacement Input

According to the analysis above, the following conclusions can be drawn:

(1) When the FE model is adopted and solved by the accurate solution method, under the same integral time step, the acceleration input in the decomposition method has better accuracy than the displacement input in the direct method, because the displacement input may motivate higher modes of vibration while the minimum time step for convergence is controlled by the involved minimum period of structure. By the approximate solution, the large mass method which inputs acceleration time history shows better stability and higher accuracy than the large stiffness method.

(2) When the modal analysis model is adopted, the displacement input has better accuracy than the acceleration input, because the frequency of modal force generated by the displacement input is lower. Under the displacement input, the modal force equation involving stiffness is not suitable to be directly used in calculation; instead, it needs to be converted into the distributed load.

(3) The displacement input is more applicable, because its motion equation is based on the absolute coordinates, and the result involves the influence of pseudo-static response.

7.4 Dynamic Analysis Model of Train-Bridge System Subjected to Earthquake Action

In traditional bridge aseismic analysis, it is mainly concerned on the dynamic characteristics of bridges, such as internal force, strength, and stability, where more attention is paid to the relative motion of the structure, while the pseudo-static response is relatively small and neglected. In the dynamic analysis of train-bridge system during earthquakes, however, the running safety of trains becomes the research emphasis, which involves the absolute motion of the system, thus the influence of pseudo-static response cannot be neglected. Therefore, the input manner of seismic excitation in traditional bridge aseismic analysis cannot be simply adopted in dynamic analysis of train-bridge system. In this section, the dynamic analysis model of train-bridge system subjected to seismic ground motion is established, to study the characteristics, implementation methods, and applicability of different seismic excitation input manners.

7.4.1 Simplified Analysis Model

When a train runs on a bridge, its location is changing but the relative position between train and bridge at every moment is determinative. Therefore, the simplified train-bridge model is established at every discrete time point, which automatically takes into account the relative motion between the subsystems, as shown in Fig. 7.12. In the model, the train subsystem is simplified into a WSM unit composed of a moving wheel M_1 (unsprung-mass), a spring K_V (and dashpot C_V), and a sprung-mass M_2; the bridge is simplified into a SDOF model, the influence of track irregularities is ignored, and the wheel keeps contact with the bridge. In the

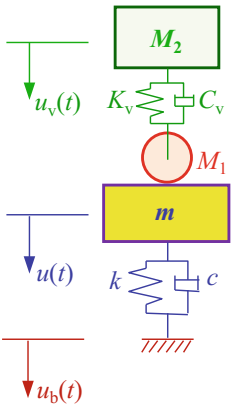

Fig. 7.12 The simplified WSM unit and bridge system

analysis, the interaction force between the wheel and the bridge is regarded as the virtual force.

Under the absolute coordinates, the motion equation of the bridge subsystem can be written as

$$\ddot{u} + 2\xi\omega\dot{u} + \omega^2 u = \frac{1}{m}[(M_1 + M_2)g - M_1\ddot{u} + K_v(u_v - u) + C_v(\dot{u}_v - \dot{u})] + 2\xi\omega\dot{u}_b + \omega^2 u_b \tag{7.69}$$

where u, ω, and ξ are the displacement, circular frequency, and damping ratio of the bridge, respectively; M, C, and K represent the mass, damping, and stiffness of the WSM unit, respectively; subscript v denotes the train subsystem, and subscripts 1 and 2 denote the unsprung and sprung-mass, respectively; u_b is the seismic ground displacement; the meanings of other symbols are the same as those in Fig. 7.10.

Compared with Eq. (7.52), Eq. (7.69) involves additional components related to the gravity and the dynamic interaction. Under the absolute coordinates, the motion equation of the sprung-mass can be expressed as

$$M_2\ddot{u}_v + C_v\dot{u}_v + K_v u_v = K_v u + C_v\dot{u} \tag{7.70}$$

If the relative coordinates are adopted, the motion equation of the bridge subsystem becomes

$$\begin{aligned}\ddot{w} + 2\xi\omega\dot{w} + \omega^2 w = {} & \frac{1}{m}[(M_1 + M_2)g - M_1\ddot{w} + K_v(u_v - w) + C_v(\dot{u}_v - \dot{w})] \\ & - \ddot{u}_b - \frac{1}{m}[M_1\ddot{u}_b + K_v u_b + C_v\dot{u}_b]\end{aligned} \tag{7.71}$$

Compared with Eq. (7.69), Eq. (7.71) involves the additional component related to the seismic acceleration, thus the motion equation of the sprung-mass can be written as

$$M_2\ddot{u}_v + C_v\dot{u}_v + K_v u_v = K_v w + C_v\dot{w} + K_v u_b + C_v\dot{u}_b \tag{7.72}$$

Compared with Eq. (7.70), Eq. (7.72) involves the additional components related to the seismic displacement and velocity.

By comparing Eqs. (7.69) and (7.70) with Eqs. (7.71) and (7.72), it is obvious that when the motion equation of bridge is established under the relative coordinates, both the seismic displacement, velocity, and acceleration histories should be input for the dynamic analysis, and the seismic load directly acting on the sprung-mass should be calculated. If the motion equation of the bridge is established under the absolute coordinates, only the seismic displacement and velocity inputs are needed and it is not necessary to calculate the seismic load acting on the sprung-mass. Therefore, the selection of coordinates in modeling may directly influence the complexity of programming.

7.4.2 Vibration Analysis of WSM Units Running on a Simply-Supported Beam Subjected to Multi-support Seismic Excitations

7.4.2.1 Analytical Model

In this section, the seismic response of a simply-supported beam under the action of a series of WSM units is discussed, as shown in Fig. 7.13. The seismic wave travels from Support A to Support B, and the two supports are subjected to different vertical seismic ground motions $a(t)$ and $b(t)$, respectively. A series of WSM units with unequal intervals represent the train, the dynamic deflection of the beam is $u(x,t)$, and the dynamic displacement of the sprung-mass M_2 is $Z(t)$. The unsprung-mass M_1 moves along the beam, and keeps contact with the beam, thus the displacement of M_1 can be obtained by combining the beam deflection and the track irregularity $Z_{IR}(x)$ at its location.

7.4.2.2 Motion Equations of the System

The simply-supported beam is simplified into a Bernoulli–Euler beam with Rayleigh damping, and the train runs on the beam at a constant speed of V. Shown in Fig. 7.14 is the force equilibrium diagram of the system. The forces acting on the beam include the inertia force of the wheel F_{I1}, the gravity of the moving mass $(M_1 + M_2)$ expressed as F_G, the elastic force of spring F_S, and the damping force F_D. The forces acting on the sprung-mass M_2 include the inertia force P_{I2}, the elastic force $P_S = F_S$, and the damping force $P_D = F_D$.

Suppose there are N vehicles (WSM units) on the bridge, the motion equations of the system subjected to multi-support seismic excitations can be expressed by the following two equations:

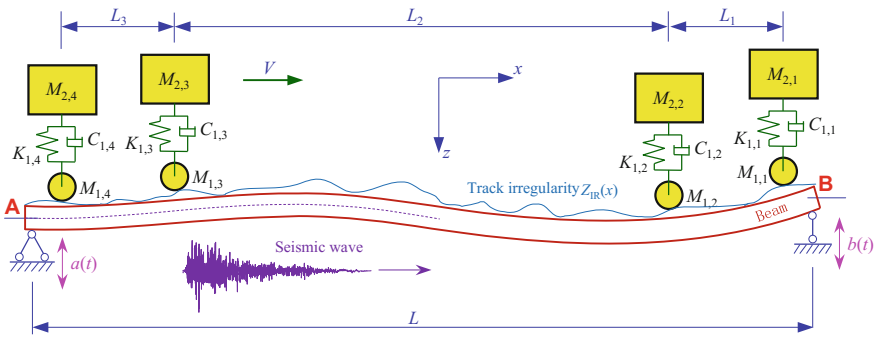

Fig. 7.13 Modeling of WSM units running on a simply-supported beam subjected to multi-support seismic excitations

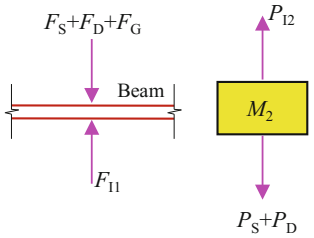

Fig. 7.14 Force equilibrium diagram

$$\begin{aligned}&\bar{m}\ddot{u}(x,t)+2\alpha\bar{m}\dot{u}(x,t)+\beta EI\dot{u}''''(x,t)+EIu''''(x,t)\\&=\sum_{i=1}^{N}\delta[x-V(t-t_i)]\cdot\left\{(M_{1,i}+M_{2,i})g-M_{1,i}\left[\frac{\mathrm{d}^2u(x,t)}{\mathrm{d}t}+\frac{\mathrm{d}^2Z_{\mathrm{IR}}}{\mathrm{d}t^2}\right]\right.\\&\left.+K_{1,i}\left[Z_{2,i}(t)-u(x,t)-Z_{\mathrm{IR}}\right]+C_{1,i}\left[\frac{\mathrm{d}Z_{2,i}(t)}{\mathrm{d}t}-\frac{\mathrm{d}u(x,t)}{\mathrm{d}t}-\frac{\mathrm{d}Z_{\mathrm{IR}}}{\mathrm{d}t}\right]\right\}\end{aligned}\tag{7.73}$$

$$\begin{aligned}&M_{2,i}\ddot{Z}_i(t)+C_{1,i}\dot{Z}_i(t)+K_{1,i}Z_i(t)=K_{1,i}\left[u(x,t)\big|_{x=V(t-t_i)}+Z_{\mathrm{IR}}\right]\\&+C_{1,i}\left[\frac{\mathrm{d}u(x,t)}{\mathrm{d}t}\big|_{x=V(t-t_i)}+\frac{\mathrm{d}Z_{\mathrm{IR}}}{\mathrm{d}t}\right]\end{aligned}\tag{7.74}$$

where

$$\frac{\mathrm{d}u(x,t)}{\mathrm{d}t}=\dot{u}(x,t)+u'(x,t)V\tag{7.75a}$$

$$\frac{\mathrm{d}^2u(x,t)}{\mathrm{d}t^2}=\ddot{u}(x,t)+2\dot{u}'(x,t)V+u''(x,t)V^2\tag{7.75b}$$

$$\frac{\mathrm{d}Z_{\mathrm{IR}}}{\mathrm{d}t}=V\cdot Z'_{\mathrm{IR}};\quad\frac{\mathrm{d}^2Z_{\mathrm{IR}}}{\mathrm{d}t^2}=V^2\cdot Z''_{\mathrm{IR}}\tag{7.75c}$$

where each head dot over u denotes a derivative of u with respect to time t, and each superscript $'$ represents a derivative of u with respect to distance x along the beam; EI, $\bar{m}$, and L are the stiffness, mass per unit length, and length of the beam, respectively; α and β are the coefficients of Rayleigh damping; Z_{IR} denotes track irregularity; t_i is the arrival time interval between the first unit and the ith unit.

In Eq. (7.75c), the derivative of the track irregularity $Z_{\mathrm{IR}}(x)$ with respect to time t can be calculated, because the speed V of the moving unit is a constant, and its moving distance x is the function of time t, namely $x = Vt$.

The boundary conditions of the simply-supported beam can be expressed as

$$u(0,t)=a(t);\quad u(L,t)=b(t)\quad u''(0,t)=u''(L,t)=0\tag{7.76}$$

The response of the beam is decomposed of the pseudo-static component u_s and the dynamic component u_d, namely

$$u(x,t) = u_s(x,t) + u_d(x,t) \tag{7.77}$$

and

$$u_d(x,t) = \sum_{n=1}^{\infty} q_n(t) \cdot \varphi_n(x); \quad \varphi_n(x) = \sin\left(\frac{n\pi x}{L}\right) \tag{7.78}$$

where $\varphi_n(x)$ is the natural mode-shape, and its contribution on the dynamic component is measured by generalized coordinate $q_n(t)$.

The pseudo-static component $u_s(x, t)$ satisfies

$$EI \cdot u_s''''(x,t) = 0 \tag{7.79}$$

and there exist the following boundary conditions

$$u_s(0,t) = a(t); \quad u_s(L,t) = b(t); \quad u_s''(0,t) = u_s''(L,t) = 0 \tag{7.80}$$

Thus, the solution of Eq. (7.79) can be written as

$$u_s(x,t) = a(t)\left(1 - \frac{x}{L}\right) + b(t)\left(\frac{x}{L}\right) \tag{7.81}$$

The first-order and second-order derivatives of $u(x,t)$ with respect to time t can be expressed as

$$\frac{\mathrm{d}u(x,t)}{\mathrm{d}t} = \dot{u}_d(x,t) + u_d'(x,t)V + \dot{a}(t)\left(1 - \frac{x}{L}\right) + \dot{b}(t)\frac{x}{L} + \left(\frac{b(t) - a(t)}{L}\right) \cdot V \tag{7.82}$$

$$\begin{aligned}\frac{\mathrm{d}^2u(x,t)}{\mathrm{d}t^2} = {} & \ddot{u}_d(x,t) + 2\dot{u}_d'(x,t)V + u_d''(x,t)V^2 + \ddot{a}(t) \cdot \left(1 - \frac{x}{L}\right) \\ & + \ddot{b}(t) \cdot \frac{x}{L} + 2V \cdot \left(\frac{\dot{b}(t) - \dot{a}(t)}{L}\right)\end{aligned} \tag{7.83}$$

Substituting Eqs. (7.82) and (7.83) into Eq. (7.73) leads to the following equation

$$\bar{m}\ddot{u}_d(x,t) + c\dot{u}_d(x,t) + EIu_d''''(x,t) = F^d + F^s \tag{7.84}$$

where F^{d} and F^{s} are the dynamic interaction force and the additional pseudo-static force acting on the beam, respectively, expressed as

$$\begin{aligned} F^{\mathrm{d}} = \sum_{i=1}^{N} \delta[x - V(t-t_i)] \cdot \{ & -M_{1,i} \cdot \left[\ddot{u}_{\mathrm{d}}(x,t) + 2\dot{u}'_{\mathrm{d}}(x,t)V + u''_{\mathrm{d}}(x,t)V^2\right] \\ & + K_{1,i}\left[Z_{2,i}(t) - u_{\mathrm{d}}(x,t)\right] + C_{1,i}\left[\dot{Z}_{2,i}(t) - \dot{u}_{\mathrm{d}}(x,t) - u'_{\mathrm{d}}(x,t)V\right]\} \end{aligned} \tag{7.85}$$

$$\begin{aligned} F^{\mathrm{s}} = \sum_{i=1}^{N} \delta[x - V(t-t_i)] \Bigg\{ & -M_{1,i}\left[\ddot{a}(t)\left(1-\frac{x}{L}\right) + \ddot{b}(t)\frac{x}{L} + \frac{2V(\dot{b}(t)-\dot{a}(t))}{L} + Z''_{\mathrm{IR}}V^2\right] \\ & - K_{1,i}[U(x,t) + Z_{\mathrm{IR}}] + (M_{1,i} + M_{2,i})g \\ & - C_{1,i}\left[\dot{a}(t)\left(1-\frac{x}{L}\right) + \dot{b}(t)\frac{x}{L} + \left(\frac{b(t)-a(t)}{L}\right)V + V \cdot Z'_{\mathrm{IR}}\right]\Bigg\} - \bar{m}\ddot{U}(x,t) - c\dot{U}(x,t) \end{aligned} \tag{7.86}$$

Similarly, Eq. (7.74) becomes

$$M_{2,i}\ddot{Z}_i(t) + C_{1,i} \cdot \dot{Z}_i(t) + K_{1,i} \cdot Z_i(t) = p^{\mathrm{d}} + p^{\mathrm{s}} \tag{7.87}$$

where p^{d} and p^{s} are the dynamic interaction force and the additional pseudo-static force acting on the sprung-mass, respectively, expressed as

$$p^{\mathrm{d}} = K_{1,i} \cdot u_{\mathrm{d}}(x,t)\big|_{x=V(t-t_i)} + C_{1,i} \cdot \left[\dot{u}_{\mathrm{d}}(x,t) + u'_{\mathrm{d}}(x,t)V\right]\big|_{x=V(t-t_i)} \tag{7.88}$$

$$\begin{aligned} p^{\mathrm{s}} = {} & K_{1,i}\left[U(x,t)\big|_{x=V(t-t_i)} + Z_{\mathrm{IR}}\right] \\ & + C_{1,i}\left\{\left[\dot{a}(t)\left(1-\frac{x}{L}\right) + \dot{b}(t)\frac{x}{L} + \left(\frac{b(t)-a(t)}{L}\right)V\right]\Big|_{x=V(t-t_i)} + Z'_{\mathrm{IR}}V\right\} \end{aligned} \tag{7.89}$$

The orthogonality of the bridge mode-shapes can be expressed by

$$\int_0^L \varphi_m(x) \cdot \varphi_n(x)\mathrm{d}x = \delta_{mn} \cdot \frac{L}{2} \quad (m,n = 1,2,\cdots) \tag{7.90}$$

By substituting Eq. (7.90) into the left side of Eq. (7.83), multiplying both sides of the equation by $u_m(x)$, integrating in the range of (0, L), and based on the orthogonality of modes, the following modal equations can be obtained

$$\ddot{q}_k(t) + 2\xi_k\omega_k\dot{q}_k(t) + \omega_k^2 q_k(t) = f_{\mathrm{M}}^{\mathrm{d}} + f_{\mathrm{M}}^{\mathrm{s}} \quad (k = 1,2,\cdots) \tag{7.91}$$

where: $\omega_k = \frac{k^2\pi^2}{L^2}\sqrt{\frac{EI}{\bar{m}}}$; $2\xi_k\omega_k = 2\alpha + \beta\omega_k^2$;

$$f_{\mathrm{M}}^{\mathrm{d}} = \sum_{i=1}^{N} \frac{2u_k(x)}{\bar{m}L} \Big\{ -M_{1,i} \cdot \left[\ddot{u}_{\mathrm{d}}(x,t) + 2\dot{u}_{\mathrm{d}}^{'}(x,t)V + u_{\mathrm{d}}^{''}(x,t)V^2 \right] + K_{1,i}\left[Z_{2,i}(t) - u_{\mathrm{d}}(x,t) \right] + C_{1,i}\left[\dot{Z}_{2,i}(t) - \dot{u}_{\mathrm{d}}(x,t) - u_{\mathrm{d}}^{'}(x,t)V \right] \Big\} \Big|_{x=V(t-t_i)} \tag{7.92}$$

$$f_{\mathrm{M}}^{\mathrm{s}} = \sum_{i=1}^{N} \frac{2u_k(x)}{\bar{m}L} \Big\{ (M_{1,i}+M_{2,i})g - M_{1,i}\left[\ddot{a}(t)\left(1-\frac{x}{L}\right) + \ddot{b}(t)\frac{x}{L} + \frac{2V(\dot{b}(t)-\dot{a}(t))}{L} + Z_{\mathrm{IR}}^{''}V^2 \right] - K_{1,i}[U(x,t)+Z_{\mathrm{IR}}] - C_{1,i}\left[\dot{a}(t)\left(1-\frac{x}{L}\right) + \dot{b}(t)\frac{x}{L} + \left(\frac{b(t)-a(t)}{L}\right)V + V \cdot Z_{\mathrm{IR}}^{'} \right] \Big\} \Big|_{x=V(t-t_i)} + \frac{2}{k\pi}\left[\ddot{b}(t)\cos(k\pi) - \ddot{a}(t) \right] + \frac{4\alpha}{k\pi}\left[\dot{b}(t)\cos(k\pi) - \dot{a}(t) \right] \tag{7.93}$$

where, the subscript M stands for the modal force.

If the seismic ground motion $a(t)$ at Support A and $b(t)$ at Support B are the same, namely under the uniform seismic excitations, the pseudo-static force acting on the sprung-mass becomes

$$p^{\mathrm{s}} = K_{1,i}[a(t)+Z_{\mathrm{IR}}] + C_{1,i}\left[\dot{a}(t) + Z_{\mathrm{IR}}^{'}V \right] \tag{7.94}$$

Meanwhile, the pseudo-static modal force acting on the beam becomes

$$f_{\mathrm{M}}^{\mathrm{s}} = \sum_{i=1}^{N} \frac{2u_k(x)}{\bar{m}L} \Big\{ (M_{1,i}+M_{2,i})g - M_{1,i}\left[\ddot{a}(t) + Z_{\mathrm{IR}}^{''}V^2 \right] - K_{1,i}[a(x)+Z_{\mathrm{IR}}] - C_{1,i}\left[\dot{a}(t) + V \cdot Z_{\mathrm{IR}}^{'} \right] \Big\} \Big|_{x=V(t-t_i)} + \frac{2\ddot{a}(t)}{k\pi}[\cos(k\pi)-1] + \frac{4\alpha\dot{a}(t)}{k\pi}[\cos(k\pi)-1] \tag{7.95}$$

When the seismic acceleration is zero, the corresponding seismic displacement and velocity may not necessarily equal to zero, which implies that the seismic load acting on the coupled system can still be generated through the spring and dashpot. Therefore, even if under uniform seismic excitations, the displacement, velocity, and acceleration time histories should still be input simultaneously to the system.

7.4.2.3 Numerical Solution

Equations (7.81), (7.87), and (7.91) constitute the motion equations of the coupled system, which can be solved using the numerical method, and the solution procedures are shown in Fig. 7.15.

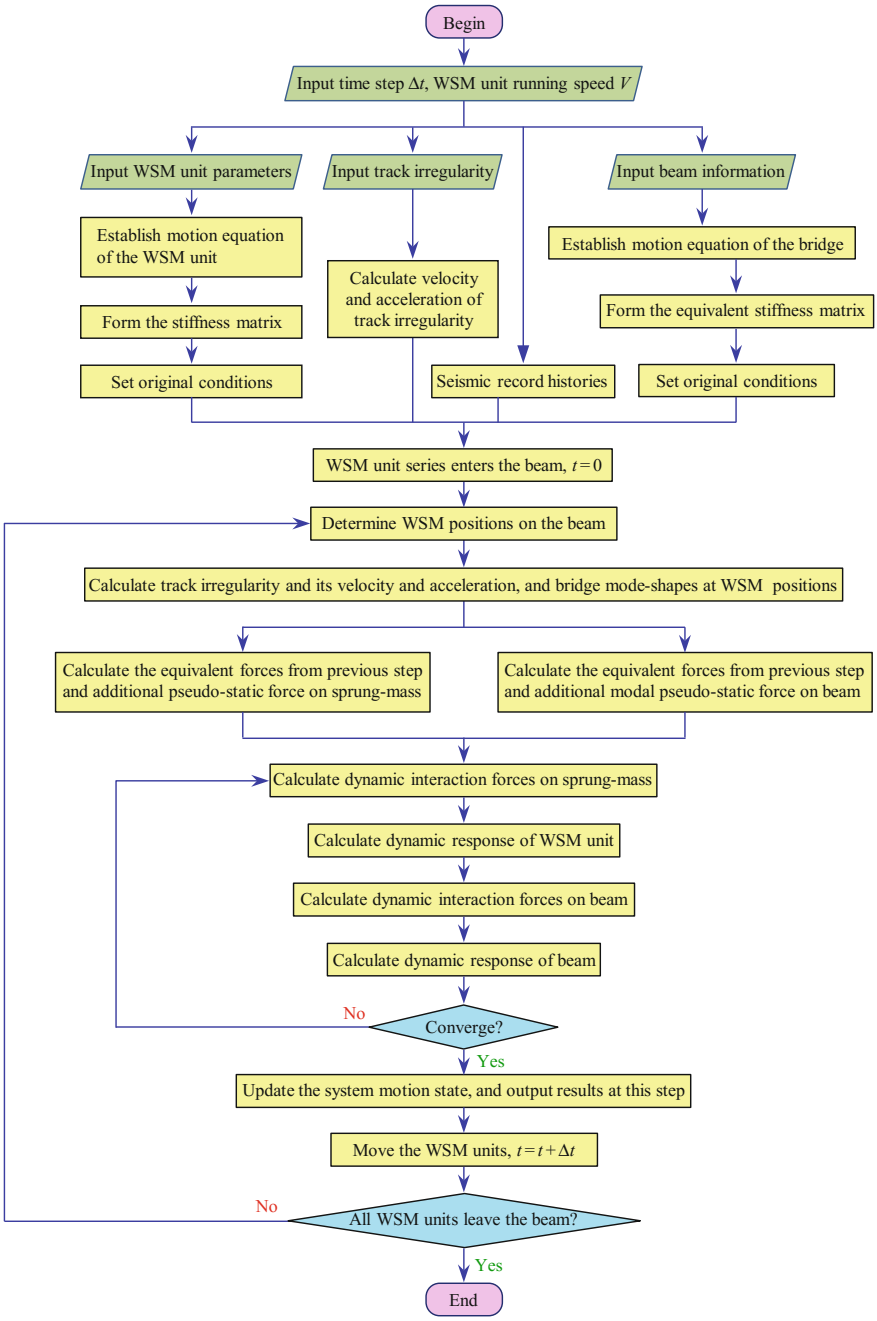

Fig. 7.15 Solution procedures

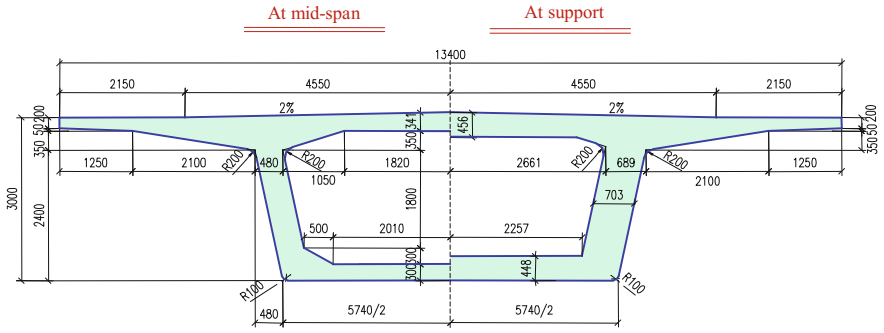

Fig. 7.16 Section of box-beam (unit: mm)

7.4.2.4 Case Study

A 32 m simply-supported double-track box-beam is taken as a case study, and its section is shown in Fig. 7.16. The fundamental frequency of the beam is 4.72 Hz, the mass per unit length is 28.14 t, and the Rayleigh damping coefficients are $\alpha = 0.138\ s^{-1}$ and $\beta = 0$ s. Only one vehicle is considered, which is simplified as a WSM unit. The sprung-mass and the unsprung-mass are 13.6 t and 2.4 t, respectively. The stiffness of the spring is 2.08 MN/m, and the damping coefficient of the dashpot is 100 kN/m·s^{-1}. The influence of track irregularity shown in Fig. 7.17 is taken into consideration in analysis. The speed V of the WSM unit ranges from 180 km/h to 324 km/h.

The seismic acceleration time history is processed using the high-pass filter in the time domain, and then the consistent seismic displacement, velocity, and acceleration time histories normalized in terms of peak acceleration 0.5 m/s^2 are obtained, as shown in Fig. 7.18. The earthquake wave is assumed to travel from Support A to Support B at the speed of 500 m/s (ref. Fig. 7.13).

A long railway bridge composed of multi-span simply-supported beams may extend thousands of meters, or even dozens of kilometers. The time of a WSM unit passing through a single beam is much less than the duration of an earthquake, whereas the total time of it passing through the whole bridge may be much more

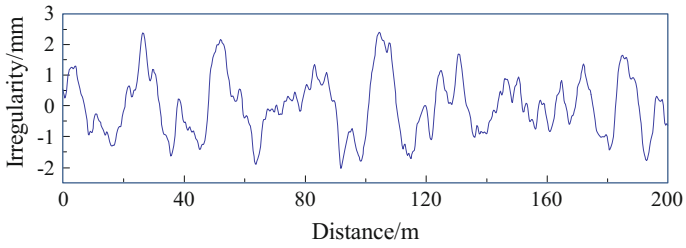

Fig. 7.17 Vertical track irregularity

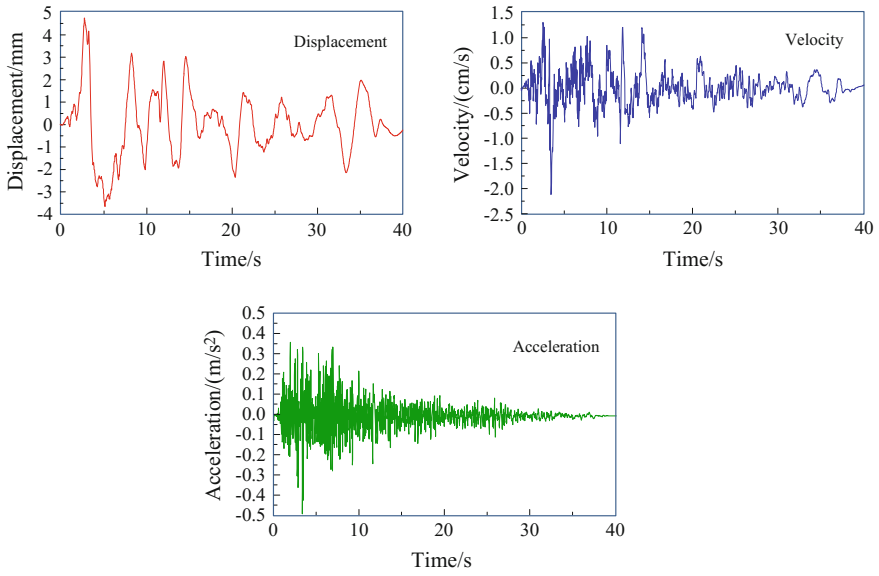

Fig. 7.18 Normalized consistent earthquake records

than the duration. The influence of the initial motion state of the beam on the system response can be considered by introducing the earthquake initial acting time, namely the time when the earthquake has already acted on the beam before the calculation.

Compared in Fig. 7.19 are the calculated displacement time histories of bridge mid-span and the acceleration time histories of the sprung-mass under seismic acceleration input and displacement input, considering the initial earthquake acting time of 5.5 s and the train speed of V = 324 km/h. It can be seen that the mid-span displacements of the bridge under two seismic input manners are almost the same, while the accelerations of the sprung-mass have obvious difference.

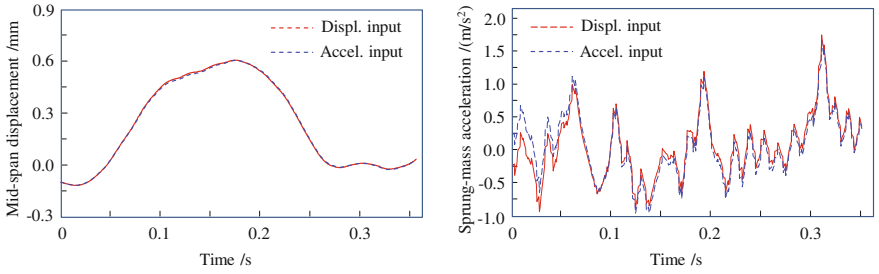

Fig. 7.19 Dynamic response time histories of bridge and sprung-mass under two seismic input manners

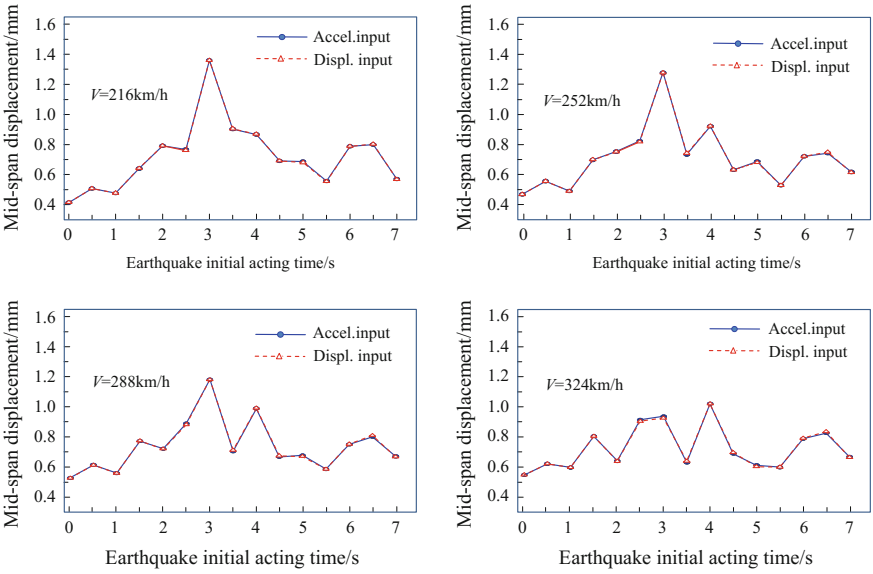

Fig. 7.20 Influence of earthquake initial acting time on the maximum displacements of bridge

Shown in Fig. 7.20 are the distributions of maximum displacement of bridge mid-span versus earthquake initial acting time, with the train speed of 216 km/h, 252 km/h, 288 km/h, and 324 km/h, respectively. It can be seen that, under the seismic displacement input and acceleration input, the distribution curves are almost the same; the displacements of the bridge reach their maximums when an earthquake starts to act at the time corresponding to the peak seismic displacement (ref. Fig. 7.18), demonstrating they are mainly affected by the earthquake while little by the earthquake input manner. Under different train speeds, the maximum mid-span displacements of bridge have obvious difference, which results from the change of train operation time passing through the bridge.

Displayed in Fig. 7.21 are the distributions of maximum accelerations of sprung-mass versus earthquake initial acting time, with the train speed of 216 km/h, 252 km/h, 288 km/h, and 324 km/h, respectively. It can be seen that under the two seismic displacement input manners, the accelerations of sprung-mass increase with the train speed and fluctuate with the earthquake initial acting time. The differences owing to input manners also vary with the earthquake initial acting time, demonstrating they are affected by earthquake action as well as train speed.

According to the above analysis, it can be concluded that the earthquake input manner has little influence on the bridge displacement but large influence on the sprung-mass acceleration, because the pseudo-static component of earthquake motion has little effect on the beam with large stiffness and mass, but has big effect on the sprung-mass with small stiffness and mass. Therefore, if the earthquake

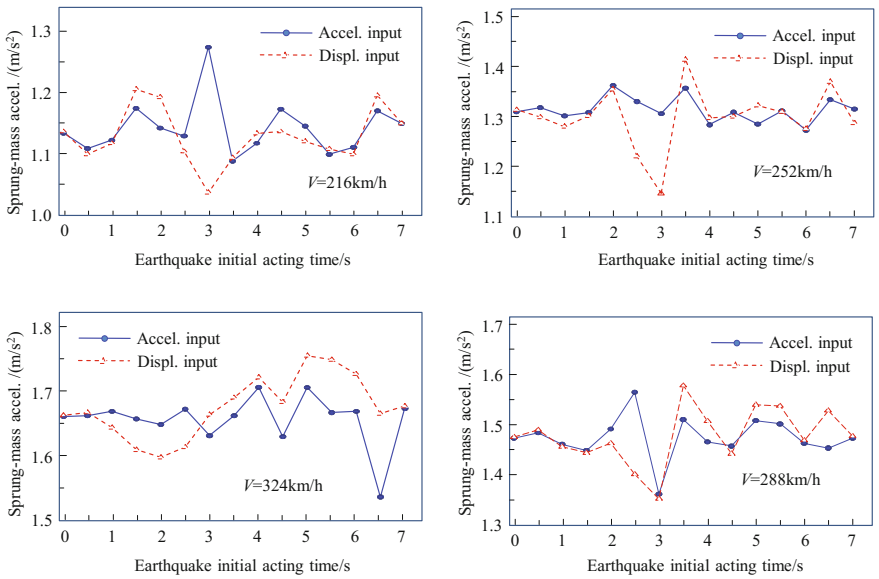

Fig. 7.21 Influence of earthquake initial acting time on the maximum acceleration of sprung-mass

acceleration input is adopted where the pseudo-static component is neglected, the response of the sprung-mass may be underestimated, especially at high train speed.

7.4.3 MDOF Train-Bridge Coupling Model

For a real bridge and a real train, the train-bridge coupling system subjected to non-uniform seismic ground motions consists of the bridge subsystem, the train subsystem, and the seismic excitations, as shown in Fig. 7.22.

7.4.3.1 FE Model of Train-Bridge System

When the FE model is used for describing the motion of train-bridge system, the absolute global coordinate system is adopted, in which the *x*-axis is defined as the

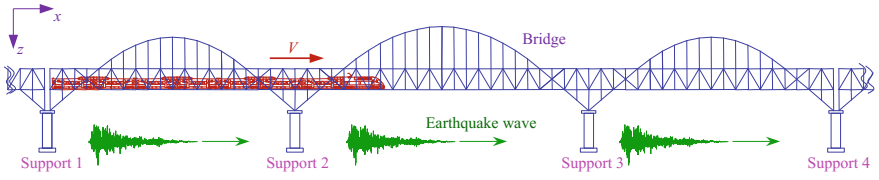

Fig. 7.22 Train-bridge system subjected to non-uniform seismic ground motion

longitudinal direction of the bridge, the *y*-axis the lateral direction, and the *z*-axis the vertical direction. The seismic ground motions at various supports of the bridge are considered to be non-uniform. The dynamic motion equations of the train subsystem and the bridge subsystem under the absolute coordinates can be expressed as

$$\mathbf{M}_{\mathrm{V}}\ddot{\mathbf{u}}_{\mathrm{V}} + \mathbf{C}_{\mathrm{V}}\dot{\mathbf{u}}_{\mathrm{V}} + \mathbf{K}_{\mathrm{V}}\mathbf{u}_{\mathrm{V}} = \mathbf{F}_{\mathrm{VB}} \tag{7.96}$$

$$\begin{bmatrix} \mathbf{M}_{\mathrm{ss}} & \mathbf{M}_{\mathrm{sb}} \\ \mathbf{M}_{\mathrm{bs}} & \mathbf{M}_{\mathrm{bb}} \end{bmatrix} \begin{Bmatrix} \ddot{\mathbf{u}}_{\mathrm{s}} \\ \ddot{\mathbf{u}}_{\mathrm{b}} \end{Bmatrix} + \begin{bmatrix} \mathbf{C}_{\mathrm{ss}} & \mathbf{C}_{\mathrm{sb}} \\ \mathbf{C}_{\mathrm{bs}} & \mathbf{C}_{\mathrm{bb}} \end{bmatrix} \begin{Bmatrix} \dot{\mathbf{u}}_{\mathrm{s}} \\ \dot{\mathbf{u}}_{\mathrm{b}} \end{Bmatrix} + \begin{bmatrix} \mathbf{K}_{\mathrm{ss}} & \mathbf{K}_{\mathrm{sb}} \\ \mathbf{K}_{\mathrm{bs}} & \mathbf{K}_{\mathrm{bb}} \end{bmatrix} \begin{Bmatrix} \mathbf{u}_{\mathrm{s}} \\ \mathbf{u}_{\mathrm{b}} \end{Bmatrix} = \begin{Bmatrix} \mathbf{F}_{\mathrm{BV}} \\ \mathbf{0} \end{Bmatrix} \tag{7.97}$$

where subscripts s and b denote the superstructure and supports, respectively; subscripts V and B denote the train subsystem and bridge subsystem, respectively; F_{VB} and F_{BV} are the interaction forces between the train and the bridge, respectively, which can be described by wheel–rail relationship.

Direct solution method

When Eq. (7.97) is solved using the direct solution method, the first term on the left side of the equation is expanded, and the motion equations of the bridge in the absolute coordinates can be written as

$$\mathbf{M}_{\mathrm{ss}}\ddot{\mathbf{u}}_{\mathrm{s}} + \mathbf{C}_{\mathrm{ss}}\dot{\mathbf{u}}_{\mathrm{s}} + \mathbf{K}_{\mathrm{ss}}\mathbf{u}_{\mathrm{s}} = -\mathbf{K}_{\mathrm{sb}}\mathbf{u}_{\mathrm{b}} - \mathbf{C}_{\mathrm{sb}}\dot{\mathbf{u}}_{\mathrm{b}} - \mathbf{M}_{\mathrm{sb}}\ddot{\mathbf{u}}_{\mathrm{b}} + \mathbf{F}_{\mathrm{BV}} \tag{7.98a}$$

Similar to traditional seismic analysis, the terms $\mathbf{M}_{\mathrm{sb}}$ and $\mathbf{M}_{\mathrm{bs}}$ in the equation are usually neglected, namely

$$\mathbf{M}_{\mathrm{ss}}\ddot{\mathbf{u}}_{\mathrm{s}} + \mathbf{C}_{\mathrm{ss}}\dot{\mathbf{u}}_{\mathrm{s}} + \mathbf{K}_{\mathrm{ss}}\mathbf{u}_{\mathrm{s}} = -\mathbf{K}_{\mathrm{sb}}\mathbf{u}_{\mathrm{b}} - \mathbf{C}_{\mathrm{sb}}\dot{\mathbf{u}}_{\mathrm{b}} + \mathbf{F}_{\mathrm{BV}} \tag{7.98b}$$

The damping terms $\mathbf{C}_{\mathrm{sb}}$ and $\mathbf{C}_{\mathrm{bs}}$ are also neglected because their influence is small and difficult to be determined. Then the motion equations of bridge related to the seismic displacement input can be obtained as

$$\mathbf{M}_{\mathrm{ss}}\ddot{\mathbf{u}}_{\mathrm{s}} + \mathbf{C}_{\mathrm{ss}}\dot{\mathbf{u}}_{\mathrm{s}} + \mathbf{K}_{\mathrm{ss}}\mathbf{u}_{\mathrm{s}} = -\mathbf{K}_{\mathrm{sb}}\mathbf{u}_{\mathrm{b}} + \mathbf{F}_{\mathrm{BV}} \tag{7.98c}$$

Equations (7.96) and (7.98c) constitute the motion equations of train-bridge system subjected to seismic ground motion.

Decomposition method

The wheel–rail relationship is related to the bridge motion and the vehicle motion. When the wheel–rail relationship is linear, similar to traditional seismic analysis, the dynamic response of the bridge is decomposed by introducing the pseudo-static displacement, expressed as

$$\begin{Bmatrix} \mathbf{u}_{\mathrm{s}} \\ \mathbf{u}_{\mathrm{b}} \end{Bmatrix} = \begin{Bmatrix} \mathbf{u}_{\mathrm{s}}^{\mathrm{s}} \\ \mathbf{u}_{\mathrm{b}} \end{Bmatrix} + \begin{Bmatrix} \mathbf{u}_{\mathrm{s}}^{\mathrm{d}} \\ \mathbf{0} \end{Bmatrix}; \quad \mathbf{u}_{\mathrm{s}}^{\mathrm{s}} = -\mathbf{K}_{\mathrm{ss}}^{-1}\mathbf{K}_{\mathrm{sb}}\mathbf{u}_{\mathrm{b}} = \mathbf{R}\mathbf{u}_{\mathrm{b}} \tag{7.99}$$

where superscripts d and s denote the pseudo-static term and the dynamic term, respectively.

By assuming $\mathbf{C}_{sb} + \mathbf{C}_{ss}\mathbf{R} = \mathbf{0}$, and substituting Eq. (7.99) into Eqs. (7.96) and (7.98c), the following equations can be obtained

$$\mathbf{M}_V\ddot{\mathbf{u}}_V + \mathbf{C}_V\dot{\mathbf{u}}_V + \mathbf{K}_V\mathbf{u}_V = \mathbf{F}_{VB}^D + \mathbf{F}_{VB}^S \tag{7.100}$$

$$\mathbf{M}_{ss}\ddot{\mathbf{u}}_s^d + \mathbf{C}_{ss}\dot{\mathbf{u}}_s^d + \mathbf{K}_{ss}\mathbf{u}_s^d = -\mathbf{M}_{ss}R\ddot{\mathbf{u}}_b + \mathbf{F}_{BV}^D + \mathbf{F}_{BV}^S \tag{7.101}$$

where, superscripts S and D represent, respectively, the component only related to the pseudo-static term and the component related to the dynamic term in train–bridge interaction.

The method for solving the dynamic interaction due to pseudo-static displacement of bridge is illustrated herein by reference of Xia et al. (2012). The displacement of wheel-set and rail due to pseudo-static displacement can be calculated by

$$\begin{Bmatrix} Y_{wijl}^s \\ \theta_{wijl}^s \\ Z_{wijl}^s \end{Bmatrix} = \begin{Bmatrix} Y_B^s(x_{ijl}) + h_{4i}\theta_B^s(x_{ijl}) \\ \theta_B^s(x_{ijl}) \\ Z_B^s(x_{ijl}) + e_i\theta_B^s(x_{ijl}) \end{Bmatrix} \tag{7.102}$$

where Y_B, Z_B, and θ_B are the lateral, vertical, and torsional displacements of bridge; Y_{wijl}, Z_{wijl}, and θ_{wijl} are the lateral, vertical, and rolling displacement of wheel-set; other parameters can be referred in the reference.

In the additional pseudo-static part, the force or moment acting on the bridge in lateral, vertical, and torsional directions can be expressed as

$$F_{hijl}^s = -m_{wijl}\ddot{Y}_{wijl}^s - c_{1ij}^h\dot{Y}_{wijl}^s - k_{1ij}^h Y_{wijl}^s \tag{7.103a}$$

$$F_{vijl}^s = -m_{wijl}\ddot{Z}_{wijl}^s - c_{1ij}^v\dot{Z}_{wijl}^s - k_{1ij}^v Z_{wijl}^s \tag{7.103b}$$

$$F_{\theta ijl}^s = -J_{wijl}\ddot{\theta}_{wijl}^s - a_i^2 c_{1ij}^v\dot{\theta}_{wijl}^s - a_i^2 k_{1ij}^v\theta_{wijl}^s + h_{4i}F_{hijl}^s + e_i F_{vijl}^s \tag{7.103c}$$

The force acting on the vehicle bogie in lateral, rolling, yawing, vertical, and pitching directions can be expressed as

$$\mathbf{F}_{tjwi}^s = \sum_{l=1}^{Nwi} \begin{Bmatrix} (k_{1ij}^h Y_{wijl}^s + c_{1ij}^h\dot{Y}_{wijl}^s) \\ a_i^2(k_{1ij}^v\theta_{wijl}^s + c_{1ij}^v\dot{\theta}_{wijl}^s) - h_{3i}(k_{1ij}^h Y_{wijl}^s + c_{1ij}^h\dot{Y}_{wijl}^s) \\ \eta_{jl}d_i(k_{1ij}^h Y_{wijl}^s + c_{1ij}^h\dot{Y}_{wijl}^s) \\ (k_{1ij}^v Z_{wijl}^s + c_{1ij}^v\dot{Z}_{wijl}^s) \\ \eta_{jl}d_i(k_{1ij}^v Z_{wijl}^s + c_{1ij}^v\dot{Z}_{wijl}^s) \end{Bmatrix} \tag{7.104}$$

When the wheel–rail relationship is nonlinear, $\mathbf{F}_{VB}$ and $\mathbf{F}_{BV}$ become the nonlinear functions of the motion states of train-bridge coupling system, therefore the

decomposition of dynamic and pseudo-static bridge response cannot be used, namely, Eq. (7.97) cannot be solved by the decomposition method.

Large stiffness method

Similar to traditional bridge aseismic analysis, Eq. (7.97) can be solved by the large stiffness method. In the equation, the large stiffness is added to the diagonal elements corresponding to bridge supports in the stiffness matrix, and external forces are input to the elements corresponding to bridge supports in the force vector. The values of the external forces are equal to the product of the given displacement and the sum of large stiffness and diagonal elements, so that the displacements of bridge supports are approximate to the given values. Then, the motion equations of the bridge subsystem can be expressed as

$$\begin{bmatrix} \mathbf{M}_{ss} & \mathbf{M}_{sb} \\ \mathbf{M}_{bs} & \mathbf{M}_{bb} \end{bmatrix} \begin{Bmatrix} \ddot{\mathbf{u}}_s \\ \ddot{\mathbf{u}}_b \end{Bmatrix} + \begin{bmatrix} \mathbf{C}_{ss} & \mathbf{C}_{sb} \\ \mathbf{C}_{bs} & \mathbf{C}_{bb} \end{bmatrix} \begin{Bmatrix} \dot{\mathbf{u}}_s \\ \dot{\mathbf{u}}_b \end{Bmatrix} + \begin{bmatrix} \mathbf{K}_{ss} & \mathbf{K}_{sb} \\ \mathbf{K}_{bs} & (\mathbf{K}_{bb} + \mathbf{K}_L) \end{bmatrix} \begin{Bmatrix} \mathbf{u}_s \\ \mathbf{u}_b \end{Bmatrix} = \begin{Bmatrix} \mathbf{F}_{BV} \\ (\mathbf{K}_{bb} + \mathbf{K}_L)\mathbf{u}_b \end{Bmatrix} \tag{7.105}$$

where $\mathbf{K}_L$ denotes the large stiffness.

As long as the value of large stiffness is reasonable, the dynamic response of train-bridge system subjected to earthquake action can be obtained by directly solving Eqs. (7.96) and (7.105).

Note that the large mass method is not suitable for dynamic analysis of train-bridge system subjected to earthquake action, because the accelerations at the bridge supports are the given values, thus the rigid motion component cannot be included in the calculated bridge displacement and velocity responses. While in reality, the wheel–track interaction forces F_{VB} and F_{BV} are functions of the system displacement, velocity, and acceleration. Even if the seismic acceleration is zero, the rigid motion of bridge due to seismic ground motion can still lead to the vibration of the train.

7.4.3.2 Modal Model of Train-Bridge System

If the modal decomposition method is adopted for the bridge subsystem, Eq. (7.98b) can be written as

$$\ddot{q}_i + 2\xi_i\omega_i\dot{q}_i + \omega_i^2 q_i = \varphi_i^{\mathrm{T}}\mathbf{M}_{ss}\mathbf{R}(2\xi_i\omega_i\dot{\mathbf{u}}_b) + \varphi_i^{\mathrm{T}}\mathbf{M}_{ss}\mathbf{R}(\omega_i^2\mathbf{u}_b) + \varphi_i^{\mathrm{T}}\mathbf{F}_{BV} \quad (i = 1, 2, \cdots, n) \tag{7.106a}$$

where φ_i, ξ_i, and ω_i are the ith normalized mode-shape, damping ratio, and circular frequency, respectively; n is the number of modes considered in the analysis.

When the damping term on the right side is neglected, Eq. (7.106a) becomes

$$\ddot{q}_i + 2\xi_i\omega_i\dot{q}_i + \omega_i^2 q_i = \varphi_i^{\mathrm{T}}\mathbf{M}_{\mathrm{ss}}\mathbf{R}(\omega_i^2\mathbf{u}_{\mathrm{b}}) + \varphi_i^{\mathrm{T}}\mathbf{F}_{\mathrm{BV}} \quad (i = 1, 2, \cdots, n) \qquad (7.106b)$$

and Eq. (7.101) becomes

$$\ddot{q}_i + 2\xi_i\omega_i\dot{q}_i + \omega_i^2 q_i = \varphi_i^{\mathrm{T}}(-\mathbf{M}_{\mathrm{ss}}R\ddot{\mathbf{u}}_{\mathrm{b}} + \mathbf{F}_{\mathrm{BV}}^{\mathrm{d}} + \mathbf{F}_{\mathrm{BV}}^{\mathrm{s}}) \quad (i = 1, 2, \cdots, n) \qquad (7.107)$$

Note that compared with Eq. (7.107), more modes should be taken into consideration when using Eq. (7.106a, 7.106b), because the pseudo-static component of bridge response is expressed in terms of mode composition.

From the above analysis, it is easy to see that:

When the direct solution method is adopted in the seismic analysis of train-bridge system, if the traditional displacement input is used and the damping part in force vector is neglected, only seismic displacement histories need to be input, and both the linear and nonlinear wheel–track relationships are applicable. While when the decomposition method is adopted, the bridge responses need to be decomposed into the pseudo-static part and the dynamic part, in which the influence of the pseudo-static part cannot be neglected, both the seismic displacement, velocity, and acceleration time histories need to be input, and only the linear wheel–track relationship is applicable.

In seismic analysis of train-bridge system by approximate method, the large stiffness method can be used to solve the motion equation with seismic displacement input, and both linear and nonlinear wheel–track relationships are applicable, while the large mass method cannot be used.

Therefore, when the analytical model of train-bridge system during earthquakes is established under the absolute coordinates, using the displacement input is more convenient for programming.

7.5 Running Safety of Train on Bridge During Earthquakes

7.5.1 Evaluation Indices for Running Safety of Train During Earthquakes

For running safety of train during earthquakes, the *Railway Structure Design Standards and Interpretation—Aseismatic Design* (RTRI 1999) in Japan proposed the limits for the relative displacement between piers and abutments as well as for the deformation fold angle of track on the bridge. However, the derailment of train results from the interaction between the train and the track, thus even if the train and the track satisfy their respective safety criteria, the coupling effect of them under some special conditions may also lead to the derailment (Nishimura et al. 2010).

The Nadal equation (Nadal 1896) based on static analysis of wheel derailment is widely used in the safety evaluation of trains. In UIC Code 518 (2003) and EN

14363 (2005), the safety limit for the derailment factor is $Q/P \leq 1.2$, and in the experimental standard for German ICE train, it is $Q/P \leq 0.8$ (Zhai and Chen 2001). In American standard (AAR 2011), the limits are separately set for a single axle and the whole axle (Wienstock limit), expressed as

$$Q/P \leq 1.0 \text{ (for a single axle)}; \sum Q/P \leq 1.5 \text{ (for the whole axle)} \tag{7.108}$$

In China, there is no special standard for evaluating the running safety of high-speed trains under earthquakes, so the general running safety indices are adopted, as given in Sect. 4.2.1.

What should be mentioned is when a train runs on the bridge during earthquakes, the derailment factor, offload factor, or lateral wheel–rail force may exceed the limits, and even occurs the separation between the wheel and the track, however, a safety index exceeding the limits in a very short time does not definitely mean the derailment, which has been verified by derailment test (Zhang et al. 2008).

The JNR (Japanese National Railways) standards (Ishida 1995) classified the train derailment into cases of gradual climbing-up rail and dynamic jumping-on rail, and proposed the evaluation standards for derailment considering the acting time of lateral wheel–rail force, expressed as

$$Q/P \leq \begin{cases} \lambda & t \geq 0.05\,\text{s} \\ \frac{0.05}{t}\lambda & t < 0.05\,\text{s} \end{cases} \tag{7.109}$$

where t is the acting duration of lateral wheel–rail force; λ is the target value of the derailment factor, with $\lambda = 0.8$ and $\lambda = 1.0$ corresponding to the dangerous limit and maximum tolerance limit, respectively.

In the JNR standard, the tolerant Q/P gets larger with smaller action time t, which is not strict enough and may lead to unsafe results. In this regard, the Japan Railway Technical Research Institute proposed a new criterion for evaluating derailment (Miyamoto 1996), namely the duration of Q/P exceeding 0.8 should not longer than 0.015 s. Besides, the JNR standard stipulates that the static limit for offload factor is 0.6 and the dynamic limit is 0.8.

There exists a dynamic geometrical restriction between wheel and rail, which ensures the normal running of the train on the track, while the break of this restriction leads to the derailment. Zhai and Chen (2001) simulated the process of climbing-up derailment and jumping-on derailment of a single wheel based on the train–track coupling dynamics theory and proposed the evaluation criteria for freight car derailment according to the geometric status of wheel–rail contact, expressed as

$$Q/P \leq \begin{cases} 1.0 & (t \geq t_0) \\ 1.0 \times \frac{t_0}{t} & (t < t_0) \end{cases}; \quad \begin{cases} \frac{\Delta P}{P} \leq 0.60 & (t \geq t_0) \\ \frac{\Delta P}{P} > 0.60 & (t < t_0) \end{cases} \tag{7.110}$$

where t is the sustaining duration of lateral wheel–rail force, or the time of offload factor exceeding the target value; $t_0 = 0.035$ s is the maximum tolerant time for derailment factor or offload factor exceeding the limit.

Compared with freight trains in normal running status, high-speed railway trains are greatly different in running speed, track irregularity standard, vehicle parameters, and many other aspects. As a result, the indices for freight trains cannot be directly used for the running safety evaluation of high-speed trains during earthquakes, which should be further studied.

7.5.2 Procedures of Train Running Safety Evaluation During Earthquakes

For a high-speed train on the bridge suffering from a sudden earthquake, the running safety of the train is affected by the running speed and vibration status of the train, the irregularities of the track, the dynamic performance and site features of the bridge, the characteristics of earthquake ground motion, and other factors, among which the most direct factors are ground motion intensity and train speed. The procedures of evaluating train running safety during earthquakes are as follows:

(1) Determine the evaluation indices and their limits for train running safety.
(2) Select the track irregularities.

The track irregularities measured on railway lines in real operation or with similar conditions can be selected as calculation parameters. When lack of measured one, the track irregularity samples can be generated based on the PSD function in terms of the grade of the railway line.

(3) Select the earthquake waves based on the site features of the bridge.

According to the aseismic design code of railway bridges, the selected earthquake waves should include three types: (a) artificial earthquake wave simulated based on the design response spectrum; (b) at least three earthquake waves resulting from earthquake disaster analysis; (c) recorded actual earthquake waves. Then the selected earthquake waves are processed to obtain the consistent seismic displacement, velocity, and acceleration time histories.

(4) Select one of the earthquake records and adjust increasingly its acceleration amplitude with an interval of 0.01 g. Then, calculate the dynamic response of train-bridge system and running safety indices under various ground motion intensities, by gradually increasing train speed. If any of the safety indices exceed the limit, the ground motion intensity is regarded as the safety limit under the corresponding train speed. With the ground motion intensity as horizontal axis and the train speed as vertical axis, the train running safety curve under given earthquake wave can be drawn.

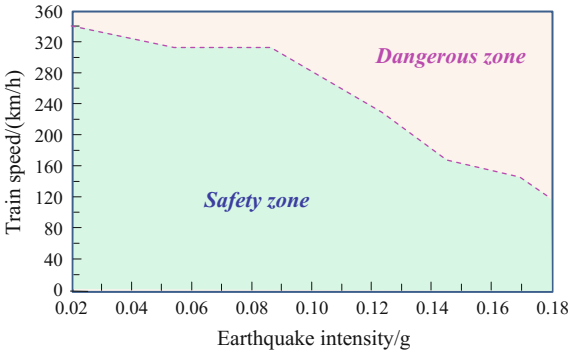

Fig. 7.23 Threshold diagram of earthquake intensity ensuring running safety of train during earthquakes

(5) Repeat Step (4) for the other earthquake waves in Step (3), to obtain the train running safety curves under all earthquake waves.
(6) Based on all the curves, the threshold diagram of earthquake intensity for ensuring the train running safety on bridge subjected to the selected earthquake actions can be drawn, as shown in Fig. 7.23.

7.6 Case Study

7.6.1 Calculation Parameters

A (180+216+180) m steel trussed-arch bridge is taken as a case study. The bridge carries two railway tracks on the lower deck and four-lane roadway on the upper. The finite element model is established with spatial beam elements, as shown in Fig. 7.24.

In the model, the connections between the truss ends and the pier-tops are simulated using the master-and-slave nodes, and the foundations of the four piers

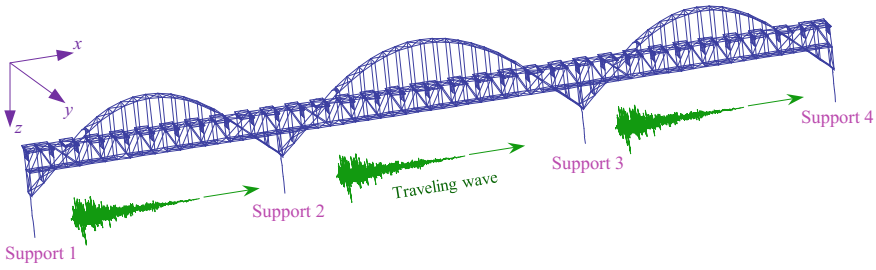

Fig. 7.24 Finite element model of the bridge

Table 7.2 Parameters for seismic ground motion simulation

Parameter	Value	Parameter	Value
Control parameter of acceleration amplitude α_1	1.359	Characteristic parameter of site soil α	0.1
Control parameter of acceleration shape α_2	0.5	Shear velocity of soil v_s (m/s)	300
Constant of acceleration amplitude s_0 (cm^2/s^3)	0.3	Apparent wave velocity v_{app} (m/s)	500
Characteristic frequency of site soil ω_g (rad/s)	5π	Characteristic damping ratio of Site soil ξ_g	0.6
Filter cutoff frequency ω_f (rad/s)	0.5π	Control parameter of filter peak value ξ_f	0.6
Angular frequency of high-pass filter ω_c (rad/s)	0.5π	Upper cutoff frequency in analysis ω_u (rad/s)	40π

Note In the analysis, the time interval Δt = 0.01 s, and the number of frequency divisions is N = 3000

are fixed on the ground. The modal characteristics of the bridge are analyzed, and the first 200 modes are used in the dynamic analysis. The lowest natural frequency of the bridge is 0.470 Hz, and the damping ratio of the bridge structure is assumed to be 2% for all interested modes. The integration time step is 10^{-5} s.

The site condition of the bridge is assumed to be medium clay, and the earthquake wave is assumed to travel from Support 1 to Support 4. The parameters for simulating ground motion are listed in Table 7.2. Based on the method in Sect. 7.2.3, the non-uniform seismic accelerations and displacements at the bridge supports can be obtained, as shown in Fig. 7.25.

The simulated earthquake waves are applied to the bridge supports as lateral earthquake actions, and half magnitude of them are as the vertical earthquake actions. It is assumed that the earthquake occurs when the train moves just onto the bridge.

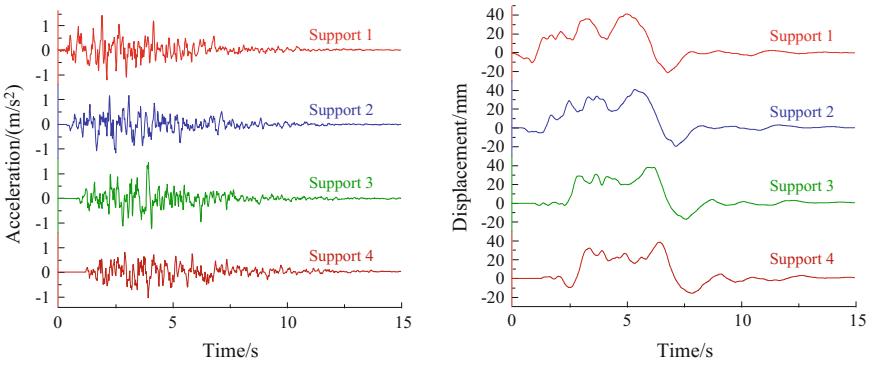

Fig. 7.25 Non-uniform seismic excitations at bridge supports

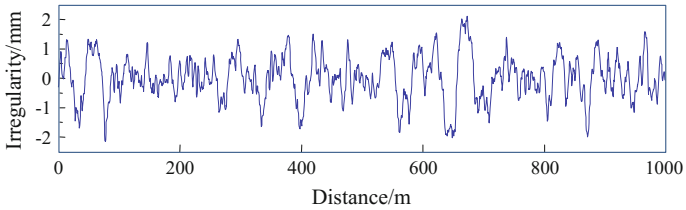

Fig. 7.26 Vertical track irregularity curve of left rail

The ICE3 high-speed train is used in the analysis, which consists of eight vehicles, with the first, third, fifth, and seventh vehicles being motor-cars, and the second, fourth, sixth, and eighth vehicles being trailer-cars. The train runs through the bridge at the speeds from 216 to 360 km/h, with an increment of 18 km/h. The rail irregularities measured from a real HSR line are used, and the vertical irregularity curve of the left rail is illustrated in Fig. 7.26.

The Hertz Contact Theory is adopted for nonlinear wheel–rail relationship in normal direction and the Kalker Creep Theory in tangential direction, which can well simulate the separation between wheel and rail during earthquakes (Du 2012; Du et al. 2012).

7.6.2 Calculation Results and Discussion

The dynamic responses of the train-bridge system are calculated using both seismic acceleration input and displacement input, but the pseudo-static response cannot be considered when using seismic acceleration input, due to the nonlinear wheel–rail relationship adopted. In addition to the completely non-uniform seismic excitations shown in Fig. 7.25, the seismic excitations only considering wave traveling effect and uniform seismic excitations are also adopted. When only considering the wave traveling effect, the ground motions at the 4 supports are the same as those at Support 1 in Fig. 7.25, but with the time lag arriving at different supports.

1. ***Comparison between displacement input and acceleration input***

Shown in Fig. 7.27 are the time histories of lateral and vertical mid-span displacements of the bridge at the central main span, and in Fig. 7.28 are the time histories of lateral and vertical car-body accelerations of the first vehicle, when the earthquake occurs and the train runs on the bridge at the speed of 288 km/h, by taking the displacement input and the acceleration input, respectively, and by considering wave traveling effect only.

Shown in Fig. 7.29 are the distributions of maximum mid-span displacements of the bridge versus train speed. It can be seen that in the train speed range of

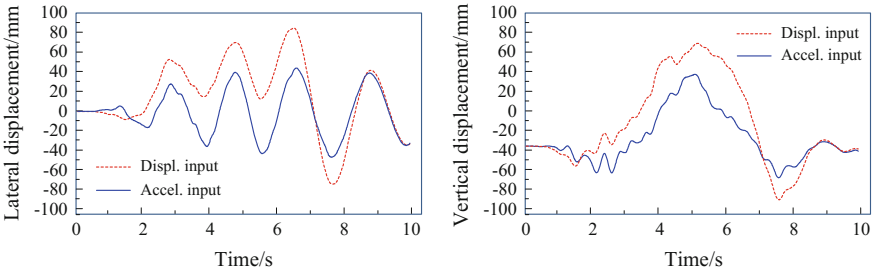

Fig. 7.27 Comparison of bridge displacement time histories between two seismic input manners (V = 288 km/h)

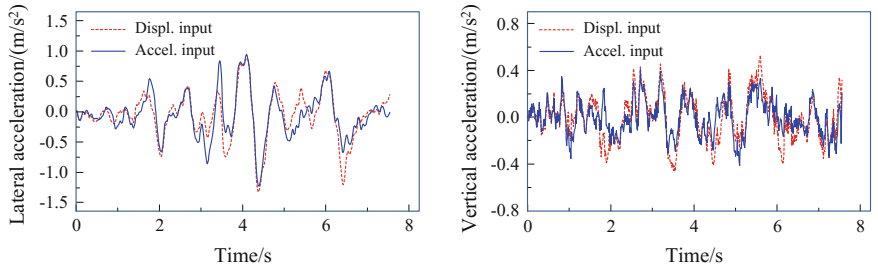

Fig. 7.28 Comparison of car-body acceleration time histories between two seismic input manners (V = 288 km/h)

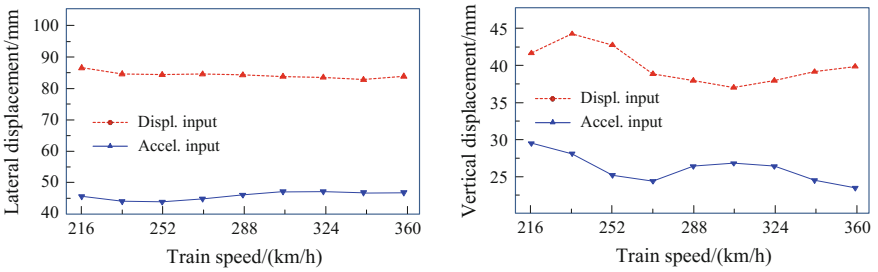

Fig. 7.29 Distribution of maximum bridge displacements versus train speed under two seismic input manners

216–360 km/h, the maximum bridge displacement by using seismic displacement input is all larger than those by acceleration input, with the maximum difference about 40 mm in lateral displacement and 18 mm in vertical.

Shown in Fig. 7.30 are the distributions of maximum car-body accelerations taken from all vehicles of the train versus train speed. In the main trend, the maximum car-body accelerations increase with the train speed, and the maximum car-body accelerations by using seismic displacement input are all greater than

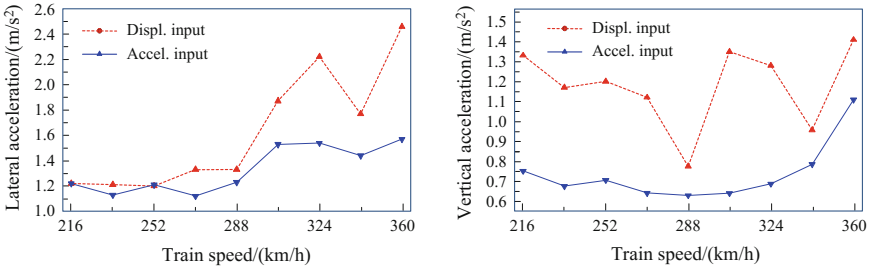

Fig. 7.30 Distribution of maximum car-body accelerations versus train speed under two seismic input manners

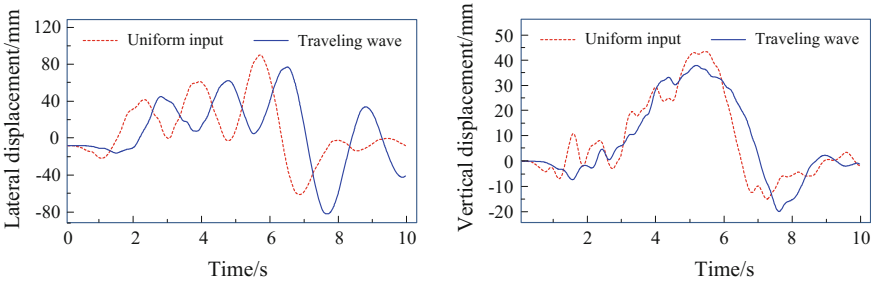

Fig. 7.31 Influence of wave traveling effect on bridge displacement time histories (V = 288 km/h)

those by seismic acceleration input, with the maximum difference about 0.9 m/s^2 in lateral acceleration and 0.6 m/s^2 in vertical.

2. ***Influence of wave traveling effect***

To analyze the influence of wave traveling effect, the seismic displacement input is adopted, and the ground motions with uniform and wave traveling effect are considered for the four bridge supports, respectively. Figure 7.31 displays the time histories of mid-span displacements of the bridge at the central main span, and Fig. 7.32 the time histories of car-body accelerations of the first vehicle at the train speed of 288 km/h. It can be seen that the seismic ground motions considering the wave traveling effect obviously change the magnitudes and appearance times of bridge displacement peaks as well as the car-body acceleration peaks.

Compared in Figs. 7.33 and 7.34 are the distributions of maximum mid-span displacements of the bridge and the maximum car-body accelerations of the vehicles versus train speed, under the uniform seismic input and seismic ground motion considering wave traveling effect, respectively.

It can be seen that the lateral mid-span displacements of the bridge change little with train speed, but they become much smaller when the wave traveling effect is considered. In general, the lateral car-body accelerations of the train increase with

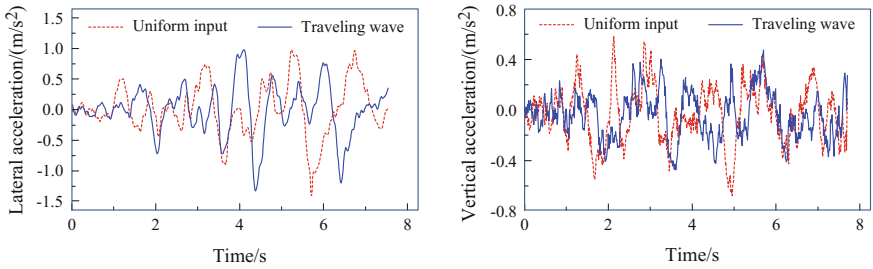

Fig. 7.32 Influence of wave traveling effect on car-body acceleration time histories (V = 288 km/h)

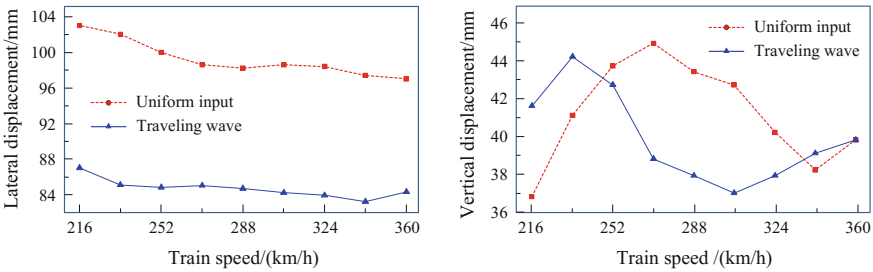

Fig. 7.33 Influence of wave traveling effect on the maximum bridge displacements

the train speed, except in the case of V = 288 km/h, and they become larger if the wave traveling effect is considered. The vertical displacements of bridge and the vertical accelerations of the train fluctuate as the train speed increases. Generally, the wave traveling affects the lateral vibration of the train-bridge system more than the vertical vibration, which is mainly because the gravities of the bridge and the train play a predominant role in the vertical vibration of the system.

3. ***Influence of seismic spatial incoherency effect***

As mentioned previously, the completely non-uniform seismic input should include the spatial incoherency effect, which is one of the factors affecting the spatial variation. The influence of seismic spatial incoherency effect is studied by using the seismic displacement input, considering both the completely non-uniform ground motions and the wave traveling effect only for the four bridge supports. Figure 7.35 shows the time histories of mid-span displacements of the bridge, and Fig. 7.36 the time histories of car-body accelerations of the first vehicle at the train speed of 288 km/h.

It can be seen that compared with considering wave traveling effect only, the seismic spatial incoherency effect changes not only the peak value but also the peak appearance time of the bridge displacements and car-body accelerations.

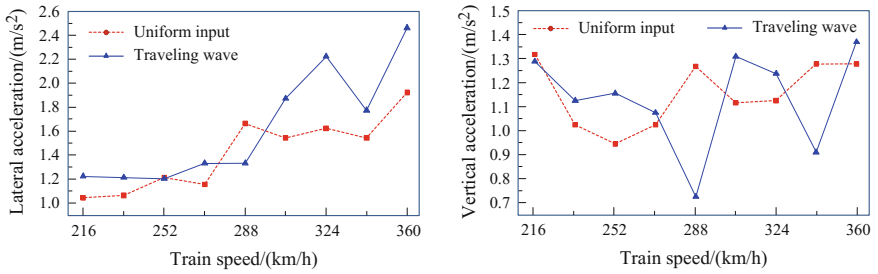

Fig. 7.34 Influence of wave traveling effect on the maximum car-body accelerations

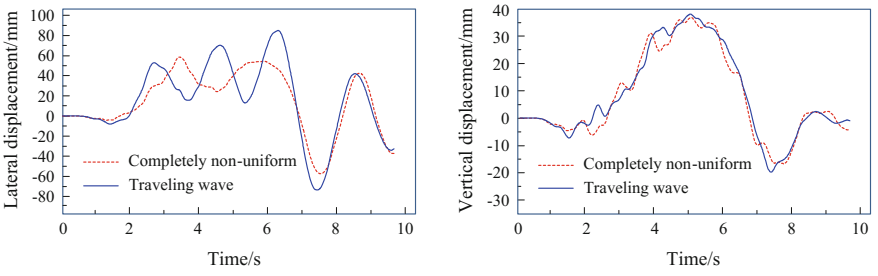

Fig. 7.35 Influence of seismic spatial coherence effect on bridge displacement time histories (V = 288 km/h)

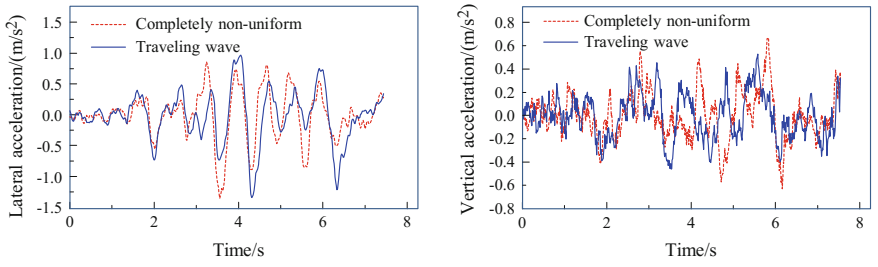

Fig. 7.36 Influence of seismic spatial coherence effect on car-body acceleration time histories (V = 288 km/h)

Compared in Figs. 7.37 and 7.38 are the distributions of maximum mid-span displacements of the bridge and the maximum car-body accelerations of the vehicles versus train speed, under the completely seismic non-uniform input and wave traveling effect only.

It can be seen that under different train speeds, the spatial incoherency effect in the completely non-uniform seismic ground motions yields much smaller lateral bridge displacements than only the wave traveling effect is considered, with about

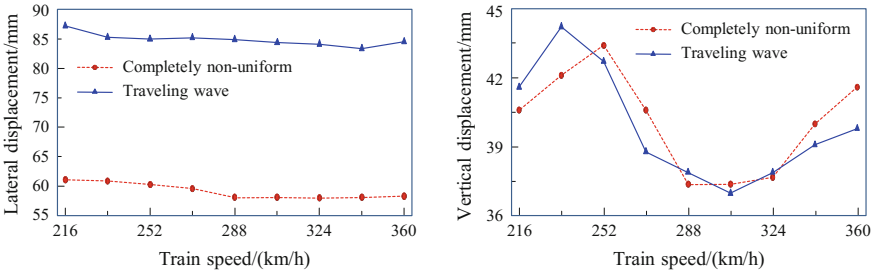

Fig. 7.37 Influence of seismic spatial coherence on the maximum bridge displacements

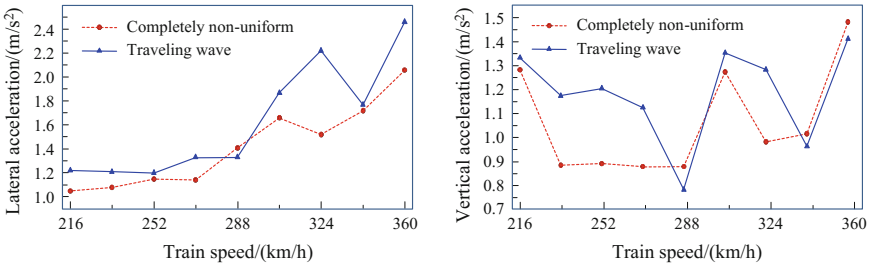

Fig. 7.38 Influence of seismic spatial coherence on the maximum car-body accelerations

35 mm difference between them. This is because in the completely non-uniform input, the seismic excitations at Supports 2 and 4 are smaller than those at Support 1 (ref. Fig. 7.25). As for the lateral car-body accelerations of vehicles, the difference under the two conditions fluctuates with the train speed, and except for $V = 324$ km/h, the results obtained by only considering wave traveling effect are all larger. The differences of vertical bridge displacements and car-body accelerations under the two input manners are slight.

4. ***Separation between wheel and rail***

When a train is running on the bridge while an earthquake occurs, the occurrence of separation between wheel and rail may have a higher probability. The wheel–rail relation adopted in train-bridge system analysis can simulate the wheel–rail separation phenomenon, and the results are summarized as follows.

The time duration of wheel–rail separation is calculated when the bridge is subjected to seismic displacement input with wave traveling effect and the train runs on the bridge at a speed of 324 km/h. Shown in Fig. 7.39 are the column diagram of occurrence times and the cumulative probability distribution of wheel–rail separation duration. It can be seen that most of the wheel–rail separation durations are less than 0.001 s. The exponential function is found to best fit the numerical results, as shown in Fig. 7.39b.

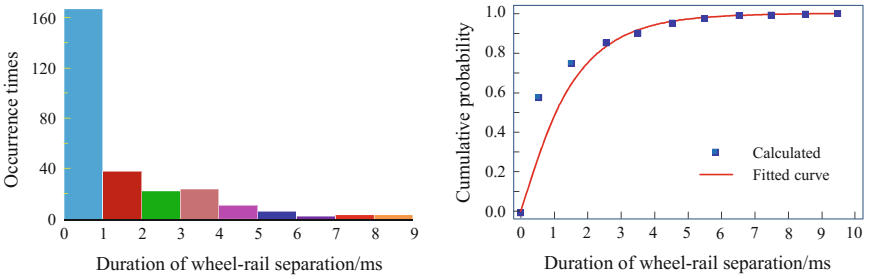

(a) Column diagram (b) Cumulative probability distribution

Fig. 7.39 Column diagram and cumulative probability distribution of wheel–rail separation duration **a** Column diagram **b** Cumulative probability distribution

A wheel–rail separation duration index, SDI, defined as the ratio of the total separation duration to the total period of the train running through the bridge, is used to estimate the probability of wheel–rail separation under earthquakes. Displayed in Fig. 7.40 are the distributions of SDIs versus train speed under several seismic input manners, in which the case without seismic input is also given for comparison.

The results show that the wheel–rail SDIs under various seismic input manners increase with train speed, especially for those at the speeds higher than 288 km/h. Under the completely non-uniform displacement input and traveling wave displacement input, the SDIs are much larger than those under acceleration input and without seismic input. For train speed higher than 306 km/h, the SDIs under traveling wave displacement input become greater than those under completely non-uniform displacement input.

Figure 7.41 shows the distributions of maximum wheel–rail separation durations versus train speed, under several seismic input manners. It can be seen that the maximum wheel–rail separation durations under seismic displacement input are

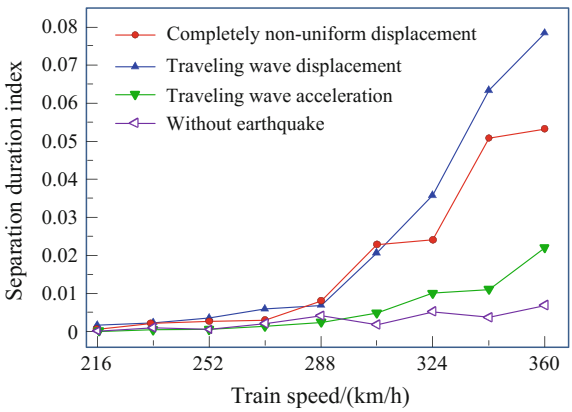

Fig. 7.40 Distribution of maximum wheel–rail separation time indices versus train speed

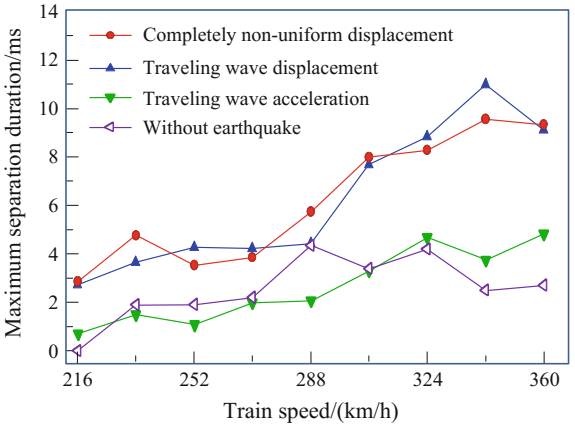

Fig. 7.41 Distributions of maximum separation duration versus train speed

greater than those under acceleration input, and this trend becomes larger with train speed. The difference between separation durations obtained by completely non-uniform seismic input and by considering wave traveling effect fluctuates with train speed.

7.6.3 Main Conclusions

According to the analysis results of this case study, some conclusions can be drawn:

(1) When the wheel–rail relationship is the nonlinear function of the train and bridge motions, only the seismic displacement input is applicable, because it can excite both dynamic and pseudo-static responses of the bridge, while the seismic acceleration input cannot be used, because it may lead to unsafe analytical results, especially for higher train speed.
(2) The lateral responses of train-bridge system are more sensitive to the earthquake.
(3) Train speed has large influence on the car-body acceleration of train, while has smaller influence on the displacement of bridge.
(4) The wave traveling effect plays an important role in dynamic analysis of train-bridge system. Neglecting this effect may lead to the underestimate of car-body vibration.
(5) The incoherency effect in the seismic spatial variation may change the dynamic response of train-bridge system, especially the car-body acceleration. Wave traveling effect is only one factor of seismic spatial variation, which cannot fully reflect the influence of seismic spatial variation on the dynamic response of train-bridge system, while the completely non-uniform seismic input can do so, which can ensure safer train response.

(6) When a high-speed train runs on a bridge, the possibility of wheel–rail separation increases greatly with train speed. Most of the wheel–rail separation durations are less than 0.01 s, and their distribution is close to the exponential curve. The wheel–rail separation index and maximum separation duration, as new running safety indexes, can be further studied.

References

AAR (2011) Manual of standards and recommended practices, Section A, Part I: safety and operations [S]. Association of American Railroads, N.W., Washington

Bathe KJ (1982) Finite element procedures in engineering analysis [M]. Prentice-Hall Inc, New Jersey

Bogdanoff JL, Goldberg JE, Bernard MC (1961) Response of a simple structure to a random earthquake-type disturbance [J]. Bull Seismol Soc Am 51:293–310

Chen JT, Hong HK, Yeh CS, Chyuan SW (1996) Integral representations and regularizations for a divergent series solution of a beam subjected to support motions [J]. Earthq Eng Struct Dyn 25:909–925

Chen LK, Jiang LZ, Guo WW et al (2014) The seismic response of high-speed railway bridges subjected to near-fault forward directivity ground motions using a vehicle-track-bridge element [J]. Shock Vibr Article ID985602

Clough RW, Penzien J (1975) Dynamics of structures [M]. McGraw-Hill Inc, New York

Deodatis G (1996) Non-stationary stochastic vector process: seismic ground motion applications [J]. Probab Eng Mech 11:149–168

Du XT (2012) Research on spatial dynamic effect of long-span bridge and running safety of train during strong earthquakes [D]. Beijing Jiaotong University, Beijing (in Chinese)

Du XT, Xu YL, Xia H (2012) Dynamic interaction of bridge-train system under non-uniform seismic ground motion [J]. Earthq Eng Struct Dyn 41(1):139–157

EN 14363 (2005) Railway applications—testing for the acceptance of running characteristics of railway vehicles [R]. Brussels, CEN

European Standard (2005) Eurocode 8—design of structures for earthquake resistance—part 2: bridge [S]. European Committee for Standardization, EN1998-2

GB 50111-2006 (2009) Code for seismic design of railway engineering [S]. Ministry of Construction of PRC, Planning Press, Beijing (in Chinese)

He XW, Kawatani MU, Hayashikawa TR, Matsumoto TS (2011) Numerical analysis on seismic response of Shinkansen bridge-train interaction system under moderate earthquakes [J]. Earthq Eng Eng Vibr 10:85–97

Ishida HA (1995) Research of stability evaluation indexes of the derailment [J]. Jpn Railway Tech Res Inst Rep 9(8):49–54

Ju SH (2013) Improvement of bridge structures to increase the safety of moving trains during earthquakes [J]. Eng Struct 56:501–508

Konstantakopoulos TG, Raftoyiannis IG, Michaltsos GT (2012) Suspended bridges subjected to earthquake and moving loads [J]. Eng Struct 45:223–237

Miyamoto MK (1996) Derailment mechanism of the train [J]. Jpn Railway Tech Res Inst Rep 10 (3):31–38

Nadal MJ (1896) Théorique de la stabilité des locomitives. Part2. Mouvement de Lacet [J]. Ann Min 10:232

Nishimura K, Terumichi Y et al (2010) Experimental study on the vehicle safety by earthquake track excitation with 1/10 scale vehicle and roller rig [J]. J Syst Des Dyn 4(1):226–237

RTRI (1999) Railway structure design stands and interpretation. Aseismatic design [S]. Japan Railway Technical Research Institute, Maruzen Co Ltd, Tokyo

Shama SR, Armen DK (2010) Simulation of synthetic ground motions for specified earthquake and site characteristics [J]. Earthq Eng Struct Dyn 39(10):1155–1180

UIC Code 518 (2003) Testing and approval of railway vehicles from the point of views of their dynamic behavior-safety-track fatigue-ride quality [S]. Paris, UIC

Vanmarcke EH, Fenton GA (1991) Conditioned simulation of local fields of earthquake ground motion [J]. Struct Saf 10:247–264

Wilson EL (2002) Three dimensional static and dynamic analysis of structures: a physical approach with emphasis on earthquake engineering [M]. Computers and Structures Inc, Berkley, California

Xia H, Han Y, Guo WW (2006) Dynamic analysis of train-bridge system subjected to non-uniform seismic excitations [J]. J Earthq Eng Struct Dyn 35:1563–1579

Xia H, De Roeck G, Goicolea JM (2012) Bridge vibration and controls: new research [M]. Nova Science Publishers Inc, New York

Xia H, Zhang N, Guo WW (2014) Coupling vibrations of train-bridge system [M]. Science Press, Beijing, pp 197–298 (in Chinese)

Yau JD, Frýba L (2007) Response of suspended beams due to moving loads and vertical seismic ground excitations [J]. Eng Struct 29:3255–3262

Zerva A (2002) Spatial variation of seismic ground motions: an overview [J]. Appl Mech Rev 55 (3):271–296

Zerva A (2009) Spatial variation of seismic ground motions: modeling and engineering application [M]. CRC Press, Boca Raton

Zhai WM, Chen G (2001) Method and criteria for evaluation of wheel derailment based on wheel vertical rise [J]. J China Railway Soc 32(2):17–26 (in Chinese)

Zhang SG, Kang X, Liu XB (2008) Characteristic analysis of the power spectral density (PSD) of track irregularity on Beijing-Tianjin inter-city railway [J]. China Railway Sci 29(5):25–30 (in Chinese)

Zhang N, Xia H, De Roeck G (2010a) Dynamic analysis of a train-bridge system under multi-support seismic excitations [J]. J Mech Sci Technol 24(11):2181–2188

Zhang ZC, Lin JH, Zhang YH et al (2010b) Non-stationary random vibration analysis for train-bridge systems subjected to horizontal earthquakes [J]. Eng Struct 32:3571–3582

Chapter 8
Dynamic Analysis of Train-Bridge System Subjected to Collision Loads

In this chapter, the characteristics of various collision loads on bridge are summarized. A dynamic analysis model is established for a coupled high-speed train and bridge system subjected to collision loads. A HSR double-track continuous bridge with (32+48+32) m PC box-girders is considered as an illustrative case study. The dynamic responses of the bridge and the running safety indices of the train on the bridge under three types of collision loads are analyzed. The results show large responses of the bridge induced by collision strongly threaten the running safety of trains. An assessment procedure is proposed for the running safety of high-speed trains on bridges subjected to collision loads, and related threshold curves for train speed versus collision intensity are proposed.

8.1 Collision Loads

When a collision load acts on a bridge pier, it may cause dislocation of bearings and girders, uneven deformation or fracture of expansion joints, and even collapse of girders, resulting in serious accidents, as studied by many researchers (Wuttrich et al. 2001; Larry and Olson 2005; Manuel et al. 2006; Xia et al. 2011; Sharma et al. 2012). For railway bridges, however, even if there is no collapse of girders, the vibrations and displacements induced by collision may deform the track and make it unstable, which may further threaten the running safety of the train on the bridge. When the collision is intense and the train speed is high, the running safety of the train may be seriously affected, and in the most serious case, the train may even derail from the track (Laigaard et al. 1996; Xuan and Zhang 2001; Xia et al. 2012a, b, 2013, 2014, 2015, 2016). As an important part of risk assessment on bridge operation safety, therefore, it is necessary to study the running safety of trains on the bridge subjected to vessel collisions.

Collision is a common physical phenomenon, which is formed by the fast intertouch between two moving objects. The kinetic energy of moving objects is

H. Xia et al., *Dynamic Interaction of Train-Bridge Systems in High-Speed Railways*, Advances in High-speed Rail Technology, https://doi.org/10.1007/978-3-662-54871-4_8

converted into deformation energy during the collision, which is a complex dynamic process. The interacting forces (i.e. the collision loads) formed during the collision process are influenced by many factors, including the mass and velocity of the moving object, the contact area, location and angle of collision, the deformation stiffness of the colliding object itself and the collided structure, and the boundary conditions.

Up to now, a lot of researches have been done toward the collision mechanism between colliding objects and collided bridge structures, based on which some practical design methods for bridge collisions have been proposed, and several related design codes are issued. However, most of the bridge codes adopt the equivalent static analysis method based on simplified static loads, in which the dynamic effects caused by the collision are usually taken into account by various impact coefficients, thus existing a risk of underestimate on the dynamic requirement of the bridge.

In order to study train-bridge coupling vibration and running safety of the train on the bridge subjected to collision loads, it is infeasible to simply use the equivalent static method prescribed in the design codes. However, due to the complexity of the problem, it is very difficult to simultaneously consider the coupling mechanism between the colliding object and the collided bridge structure. An applicable method is to use the time history of collision load as an input of the train-bridge system model to perform the analysis. In this section, some design specifications for bridge collision in Chinese and several foreign codes are introduced, some typical vessel, vehicle and ice-floe collision loads obtained by experiments and FE analysis are concluded, and the characteristics of various collision loads are summarized, which are used to determine the calculation method and to select the intense range of collision loads for the dynamic analysis model of train-bridge system subjected to collision loads in the following sections.

8.1.1 Collision by Vessels

The collision process between a vessel and a bridge structure is very complex, which is related to various factors, such as the circumstances during the collision (storm, climate and flow, and so on), the characteristics of the vessel (the type; size; velocity; loading status of the vessel; and the strength and stiffness of the bow, hull, and deck room), the structural characteristics (geometry, material strength, mass, damping, and stiffness) of the bridge, and the response time of the vessel pilot. Thus, it is very difficult to accurately determine the interacting force between the vessel and the bridge during collision. Over the years, researchers carried out many studies on the mechanism of vessel-structure collision, and according to different physical principles, proposed several practical design formulas for vessel collision loads, and have applied them in the design of bridge piers against vessel collision. These formulas mainly include the following three types.

(1) The design formula for colliding force based on the energy principle. According to the theorem of energy conservation, assuming the initial kinetic energy of the vessel is completely converted into the deformation potential energy after the collision, the maximum collision load can be calculated on account of the deformed stiffness, which is the basis of the Eurocode and the *Fundamental Code for Design on Railway Bridge and Culvert* (TB10002.1 2005) of China. The formula of collision force is established according to the conversion relationship between the kinetic energy and the deformation potential energy of the vessel, in which the factors such as energy loss during collision and colliding angle are considered, and the deformation stiffness is refined as two parts: the vessel stiffness and the bridge-pier stiffness.
(2) The design formula for colliding force based on the momentum principle. According to the momentum principle, knowing the initial momentum and the duration time of the vessel collision, the average collision load can be calculated. In the *General Code for Design of Highway Bridges and Culverts* (JTG D60 2015) of China, the design formula for average collision load adopts this principle, by which the maximum collision load is believed to be two times of the average collision load.
(3) The design formula for colliding force based on the experimental data and experiences. The vessel collision with a pier is a complex nonlinear dynamic process with a huge energy conversion in a very short time. In design codes, the empirical formulas based on simplified static load statistics are usually adopted, such as in AASHTO (1991, 2007), JTG D60 (2015), and TB10002.1 (2005). These empirical formulas, however, cannot take into account the duration time of the collision load, the interaction between vessel and pier, the structural behavior and elastic deformation of the bridge related to the loading rate of collision, etc.

Relatively, experiments are the best way to study the vessel-pier collision, but limited by the high cost and long performing time, full-scale field tests for vessel-pier collision are rarely conducted. Most researches are based on small-scale model tests or swing-hammer impact tests in laboratory, and then, the results are modified according to the accuracy and uncertainties of the test to estimate the actual-scale conditions (Consolazio et al. 2003).

After a half century's efforts, researchers in some countries have developed their respective practical calculation methods for vessel collision loads, and several technical regulations have been proposed in bridge design codes.

The 4th edition of *LRFD Bridge Design Specifications* issued by AASHTO in (2007) prescribes that the equivalent static vessel impact force on bridge pier can be calculated by the following formula

$$F_s = 1.2 \times 10^5 \cdot V_c \cdot \sqrt{\mathrm{DWT}} \tag{8.1}$$

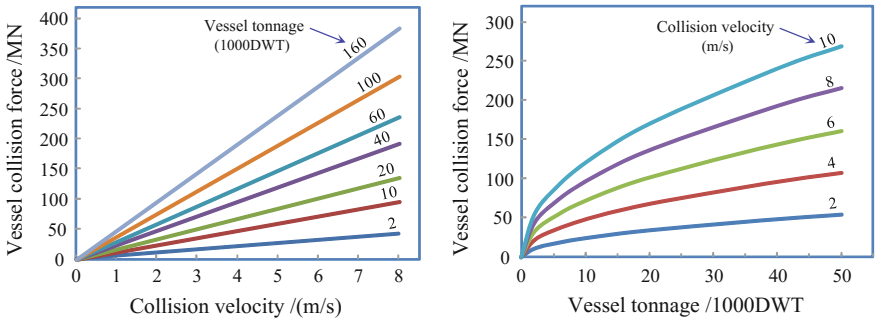

Fig. 8.1 Typical vessel impact forces (AASHTO LRFD)

where F_s is the equivalent static vessel impact force (N); DWT is the deadweight tonnage (Mg) of the vessel (including vessel body, goods, fuel, and water); and V_c is the impact velocity (m/s) of the vessel colliding on the bridge pier.

Shown in Fig. 8.1 are the typical vessel impact forces calculated by Eq. (8.1), with respect to various vessel tonnages and collision velocities

In the *Fundamental Code for Design on Railway Bridge and Culvert* (TB10002.1 2005) issued by the Ministry of Railways of PRC, it is stipulated that the design collision force of vessel to the pier and abutment can be calculated as

$$F = \gamma \cdot V_c \cdot \sin\alpha \sqrt{\frac{W}{C_1 + C_2}} \tag{8.2}$$

where F is collision force (kN); γ is the kinetic energy reduction factor ($s/m^{1/2}$), which can be taken as 0.2 for slanting vessel collision and 0.3 for forward collision; V_c is the vessel speed (m/s) when it collides the pier; α is the angle between the navigation direction of the vessel and the tangent at collision point with the pier; W is the weight of the vessel (kN); C_1 and C_2 are, respectively, elastic deformation coefficients of the vessel and the pier and can be assumed $C_1 + C_2 = 0.0005$ m/kN when lack of data.

The acting position of the vessel collision load should be determined according to the specific condition, and if no related data available, the height of navigable water level can be used.

In Eurocode EN 1991-1-7 and BS EN 1997-1-7 *Actions on Structures, Part 1–7: General Actions—Accidental Actions* (1991, 2006), the vessel collision loads in inland waterway and sea waterway are given for both static design and dynamic design. In this section, only the vessel collision load for dynamic calculation in the Eurocode is introduced.

According to the Eurocode, for the inland waterway vessel, when elastic deformation of the vessel is considered ($E_{def} \leq 0.21$ MN·m), the dynamic design impact force can be calculated by

$$F_{\mathrm{dyn,el}} = 10.95 \times \sqrt{E_{\mathrm{def}}}\,(\mathrm{MN}) \tag{8.3}$$

When the plastic deformation of the vessel is considered ($E_{\mathrm{def}} > 0.21$ MN·m), the dynamic design impact force can be calculated by

$$F_{\mathrm{dyn,pl}} = 5.0 \times \sqrt{1 + 0.128E_{\mathrm{def}}}\,(\mathrm{MN}) \tag{8.4}$$

where the deformation energy E_{def} (MN·m) is equal to the available total kinetic energy $E_{\mathrm{a}} = 0.5\ mV^2$ in case of frontal impact, while in case of lateral impact with $\alpha < 45°$, a sliding impact may be assumed and the deformation energy is taken as

$$E_{\mathrm{def}} = E_{\mathrm{a}}(1 - \cos\alpha) \tag{8.5}$$

In this case, it is recommended to use the average mass m for the relevant vessel type and the design velocity V equal to 3 m/s plus the water flow velocity.

In the dynamic structural analysis, the impact forces should be modeled, according to the response of the vessel, as a half-sine-wave pulse for $F_{\mathrm{dyn}} \leqq 5$ MN (elastic impact) and a trapezoidal pulse for $F_{\mathrm{dyn}} > 5$ MN (plastic impact), with the load durations and other details presented in Fig. 8.2.

For sea-going merchant vessels between 500 DWT and 300,000 DWT, the dynamic design impact force may be determined by

$$F = \begin{cases} F_0\bar{L}\left[\bar{E}_{\mathrm{imp}} + (5.0 - \bar{L})\bar{L}^{1.6}\right]^{0.5} & \left(\bar{E}_{\mathrm{imp}} \geq \bar{L}^{2.6}\right) \\ 2.24F_0\left[\bar{E}_{\mathrm{imp}}\bar{L}\right]^{0.5} & \left(\bar{E}_{\mathrm{imp}} < \bar{L}^{2.6}\right) \end{cases} \tag{8.6}$$

where F is the maximum bow collision force in MN; $\bar{L}$=$L_{\mathrm{pp}}/275$ (m); L_{pp} is the length of vessel in m; F_0 is the reference collision force equal to 210 MN; $\bar{E}_{\mathrm{imp}}$=$E_{\mathrm{imp}}/1425$ (MN · m), E_{imp} is the energy absorbed by plastic deformation, E_{imp}= $0.5\,mV_0^2$ where m is the mass of vessel (10^6 kg), and V_0 is the initial velocity of vessel, taken as 5 m/s.

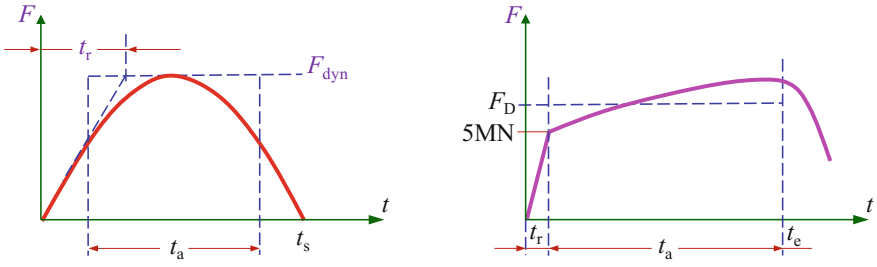

(a) Elastic impact ($F_{\mathrm{dyn}} \leqq 5$ MN) (b) Plastic impact ($F_{\mathrm{dyn}} > 5$ MN)

Fig. 8.2 Load-time functions for vessel collision

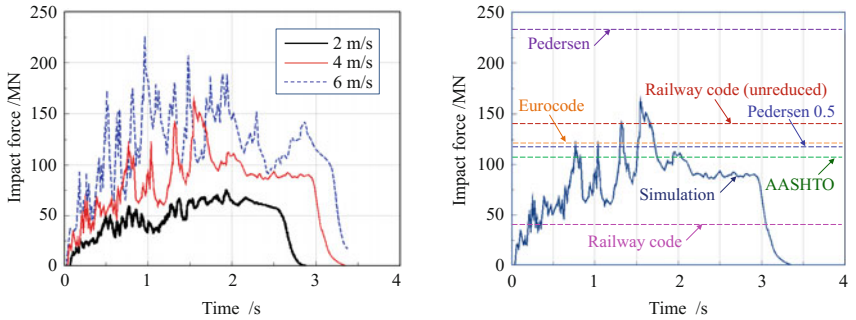

(a) Impact force curves of vessel collision at several velocities (b) Comparison of simplified formula and design codes

Fig. 8.3 Collision force curves of vessel and comparison of simplified formula and design codes

According to the wave propagation theory, the impact load is generated on the interface between the vessel and the bridge, forming a complex dynamic interaction process, which is related to the material and structural characteristics of the vessel and the bridge, and the involved boundary conditions. In this sense, the nonlinear dynamic numerical simulation is a good solution for this problem. With the progress of computer hardware and structural analysis software, the numerical simulation method has been favored by more and more researchers, such as Derucher (1984), Manen (2001), He (2004), Hu et al. (2005), Yan (2006), Wang et al. (2006, 2008), Wang and Chen (2007), Thilakarathna et al. (2010), Fan and Yuan (2012), and many results have been achieved.

Yan (2006) conducted FE simulation analysis on collision of a 50000DWT bulk carrier with several types of pier models, to study the influences of various factors, including vessel velocity (Fig. 8.3a), impact angle, vessel mass, bow stiffness, bow material strain rate and failure strain, and impact contact area and geometry, on the impact force peaks and their occurring time, and loading duration, of collision. By comparing the simulated results with the collision loads from simplified formula and design codes (Fig. 8.3b), he further studied the deficiency of the simplified formula and the applicable conditions of the design collision loads.

Chen (2006) carried out a systematical analysis on the vessel-bridge collision forces, concerning the mass and tonnage of vessel, the impact velocity and angle of collision, the geometry and size of piers and pile caps, and so on. He adopted the LS-DYNA software to simulate the vessel-bridge collision, and obtained several time histories of collision force. Shown in Fig. 8.4a, b are the simulated impact force time histories by collisions of a 5000-DWT bulk carrier with the pier of a (95+3×180+95) m continuous rigid-frame bridge at the speed of 4.0 m/s, and a 3000-DWT one at the speed of 3.0 m/s, respectively.

To better account for dynamic effect of bridge structure under vessel collisions, the equivalent static analysis procedure is employed in most of the design specifications for vessel-bridge collision, but it fails to avoid potentially underestimating the demand.

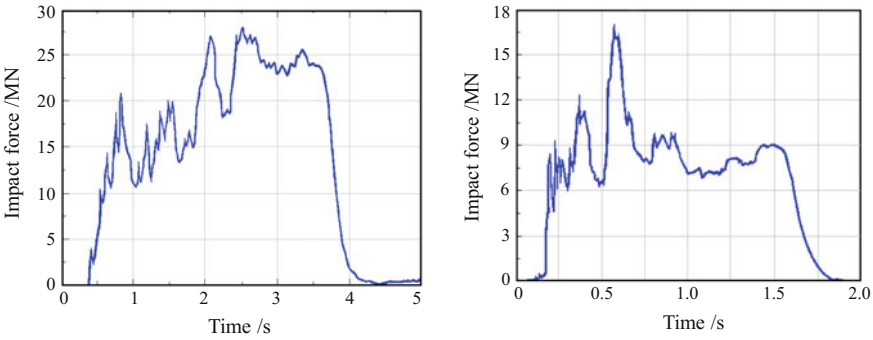

(a) 5000 DWT vessel, V_c=4.0m/s (b) 3000 DWT vessel, V_c=3.0m/s

Fig. 8.4 Collision force time histories of vessels with concrete piers

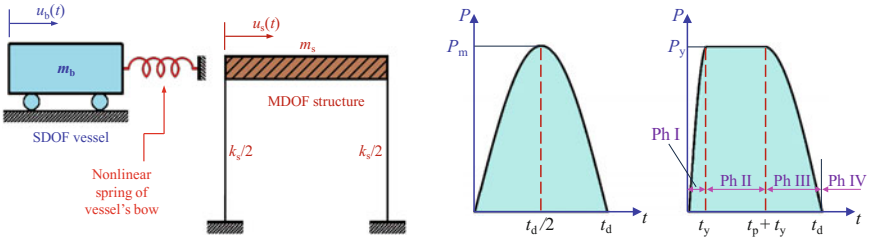

(a) Analysis models (b) Collision force curves

Fig. 8.5 Dynamic system for vessel-bridge collision and typical collision pulse forces

The shock spectrum analysis (SSA) approach was developed based on the theory of vessel-structure interaction in collision, which can efficiently determine the dynamic requirements of bridge structures under vessel collision. By the SSA approach, Fan and Yuan (2012) established a SDOF vessel model and a MDOF structure model, as shown in Fig. 8.5a. Using the models, he simulated the process of bridge subjected to vessel collision and proposed the vessel collision loads for bridge structure.

When the deformation of the bow is at elastic stage during the collision, the vessel-bridge collision force can be expressed as

$$P(t) = P_{\mathrm{m}} \sin(\pi t / t_{\mathrm{d}}) \tag{8.7}$$

where $P_{\mathrm{m}} = V_0 \cdot c_{\mathrm{P}}$ is the deformation energy of the bow; $t_{\mathrm{d}} = \pi m_{\mathrm{b}} V_0 / P_{\mathrm{m}}$ is the total duration time of the collision force; $c_{\mathrm{P}} = (k_{\mathrm{e}} \cdot m_{\mathrm{b}})^{1/2}$ is defined as the pseudo-damping coefficient; and k_{e} is the effective spring stiffness of the vessel-bridge collision.

When the deformation of the bow is at plastic stage during the collision, the vessel-bridge collision force can be expressed as

$$P(t) = \begin{cases} P_y \sin(\omega_y t) & (0 \le t < t_y) \\ P_y & (t_y \le t < t + t_y) \\ P_y \sin[\omega_u (t - t_d + 2t_u)] & (t_p + t_y \le t - t_d) \end{cases} \tag{8.8}$$

where $\omega_y = \pi/2t_y$, $\omega_u = \pi/2t_u$, and $t_u = \pi m_b/(2c_p)$.

Shown in Fig. 8.5b is the typical vessel collision force curve obtained by Eq. (8.8). It can be found that the collision load given in the figure is consistent with the dynamic analysis loads in EN 1991-1-7 of Eurocode and BS EN 1997-1-7 issued by the UK.

Chen et al. (2008) established a 3-D FE model to simulate and calculate the collision process between an oil tanker vessel with the weight of 1900 DWT and the tower platform of a long-span rail-cum-road cable-stayed bridge, by using the parallel computing technology based on the contact equilibrium, and obtained the time history of collision force, as shown in Fig. 8.6. It can be seen that during the collision, the collision force increases firstly, and reaches the maximum value of 11.2 MN at 0.63 s, then decreases gradually and reduces to zero at about 1.4 s when the vessel is rebound from the tower cap. The fluctuation of the collision force indicates several loading and unloading of the vessel structure during the collision process, and each unloading represents a failure or damage of a certain bow structure.

The anti-collision design is an important issue for bridge against vessel impact. He (2008) simulated the process of a 50000-DWT bulk carrier colliding on a bridge pier at velocity of 4.0 m/s and obtained the time histories of impact force considering the pier with and without anti-collision device, as shown in Fig. 8.7.

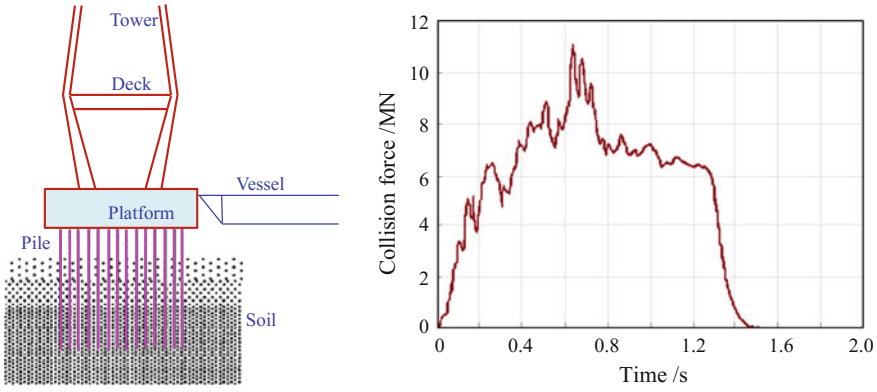

Fig. 8.6 Analysis model for vessel-tower-cap collision and impact force time history (1900DWT oil tanker vessel, V_c = 4.12 m/s)

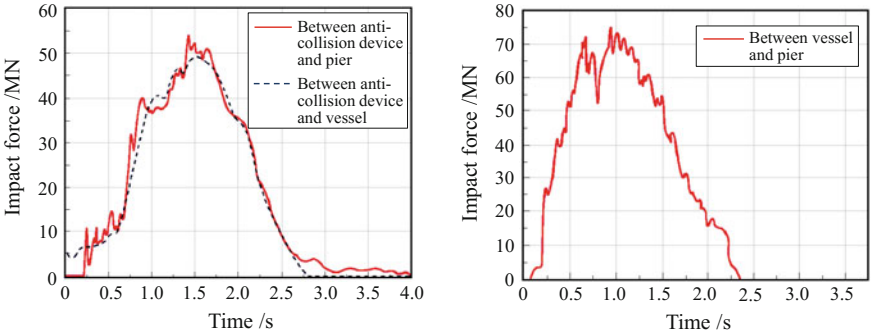

(a) With anti-collision device (b) Without anti-collision device

Fig. 8.7 Impact force time histories of a 50000DWT bulk carrier (V_c = 4.0 m/s)

According to the results, for the pier with anti-collision device, the vessel collision load shows a long duration of about 4.0 s, with the maximum impact force of 55 MN. While for the pier without anti-collision device, the collision load shows a shorter duration of about 2.5 s, but a greater maximum impact force of 75 MN, increased by 35% of the former.

The collision force curves exhibit jumped changes at several collision phases, indicating a strong nonlinear wave characteristic, which shows the anti-collision device effectively involved in the protection work, or reflect the failure or damage of structural components. This nonlinear wave characteristic is also found in other studies, such as those in Luo (2008) by simulation of a 1000 t vessel colliding on the pier with the anti-collision device at velocity 5 m/s, and in Li et al. (2006) by a 5000 t vessel colliding on the anti-collision device of the pier at 2 m/s.

The maximum impact force of vessel collision on pier is one of the most important factors for a bridge design. By means of nonlinear finite element simulation method, Hu et al. (2005) calculated the impact forces of collision between bow and rigid bridge pier for vessels of 5,000 ~ 60,000DWT and obtained the curves of maximum collision force versus vessel tonnage at several collision velocities, as shown in Fig. 8.8.

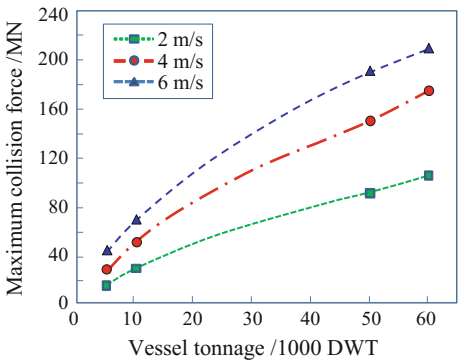

Fig. 8.8 Maximum collision forces of vessel with different DWTs

These research results show that the collision loads of vessel with pier are very complex. In general, the time histories of impact forces exhibit a characteristic of strong nonlinear waveform, with loading duration of about 3 $\sim$ 4 s; the heavier the vessel, and the faster the impact velocity, the greater the instant collision force, with the maximum being hundreds of MN.

8.1.2 Collision by Road Vehicles

Compared with the vessel and ice-floe collisions on bridge structures, the collision of road vehicle on bridge is more often. In a collision accident, with the vehicle crush, the bridge may be damaged or even collapsed due to the intense and sudden impact, bringing even more serious casualties and property losses. As indicated by researches and some related codes, vehicle-collision loads are very complicated, and the values of collision force are quite different for the various vehicle types under different conditions, such as the weight and velocity of vehicle, and the impact position and angle of collision.

In some countries, the vehicle collision is regarded as one of the most likely accidental loads for bridge structures, and related criteria for vehicle collision forces are set in design codes.

In the 4th edition of *LRFD Bridge Design Specifications* issued by AASHTO in (2007), it is prescribed that the bridge pier located within a distance of 9.0 m to the roadway edge or 15.0 m to the center line of a railway track shall be designed for an equivalent static force of 1,800 kN, which is assumed to act in any direction, in a horizontal plane at 1.2 m height above the ground.

In China, the design codes for roadway bridge (JTG D60 2015), railway bridge (TB10002.1 2005), and HSR bridge (TB10621-2014 2015) prescribe that: In case that pier columns are likely to be bumped by cars, if without protection works, the impact force shall be considered as 1,000 kN along the traffic direction, and 500 kN across the traffic direction, horizontally acting on the pier at 1.2 m above the road surface. The collision forces in two directions shall not be considered together.

In Eurocode EN 1991-1-7 and BS EN 1997-1-7 *Actions on Structures, Part 1–7: General Actions—Accidental Actions* (European Standard 1991, 2006), design values for actions due to impact on the columns of bridges adjacent to roads and railways are defined. The indicative equivalent static design forces due to vehicular impact are 1,000 kN in travel direction and 500 kN perpendicular to travel direction, horizontally acting at 0.50 m (cars) to 1.50 m (lorries) level above the surrounding ground surface or higher where certain types of protective barriers are provided. The indicative equivalent static design forces due to the impact of derailed train are 4,000 kN along the track direction and 1,500 kN perpendicular to the track direction, horizontally acting at 1.8 m above the track level. When the train speed is greater than 120 km/h, a risk analysis should be carried out by using refined methods such as dynamic analyses, nonlinear models, and interaction between the load and the structure. In the absence of a dynamic analysis, the

dynamic amplification factor for the elastic response may be assumed to be equal to 1.4.

The impact is characterized as either *hard impact*, where the energy is mainly dissipated by the impacting body, or *soft impact*, where the structure is designed to deform in order to absorb the impact energy.

For hard impact, it is assumed that the structure is rigid and immovable and that the colliding object deforms linearly during the impact phase. The maximum dynamic interaction force is given by expression

$$F = V_c\sqrt{k \cdot m} \tag{8.9}$$

where V_c is the velocity of the object when impacting; k is the equivalent elastic stiffness of the object (i.e., the ratio between force and total deformation); and m is the mass of the colliding object.

In this case, the force due to impact may be considered as a rectangular pulse on the surface of the structure, as shown in Fig. 8.9, and the duration of the pulse follows from

$$F\Delta t = mV_c \qquad \text{or} \qquad \Delta t = \sqrt{m/k} \tag{8.10}$$

in which $k = EA/L$ and $m = \rho AL$, when the colliding object is modeled as an equivalent impacting object of uniform cross section (see Fig. 8.9); L, A, E, and ρ are, respectively, the length, cross-sectional area, modulus of elasticity, and mass density of the colliding object.

If the structure is elastic and the colliding object is rigid, the collision energy is mainly absorbed by the deformation of the structure, and it can be regarded as "soft collision." Equations (8.9) and (8.10) are still applicable, while they should be used with k being the stiffness of the collided structure.

Generally, there are two ways to acquire the dynamic collision loads: on-site experiment and mathematic simulation. In studying truck collision with bridge pier, the full-scale test is very costly, because the expensive truck will be completely destroyed after impact, while the small-scale model test can hardly provide the required impact force curves, therefore, most investigations are based on finite element simulation (EL-Tawil et al. 2005; Buth 2009; NCAC 2010; Sharma et al. 2012). Buth (2009) established a FE model to simulate the complex process of a

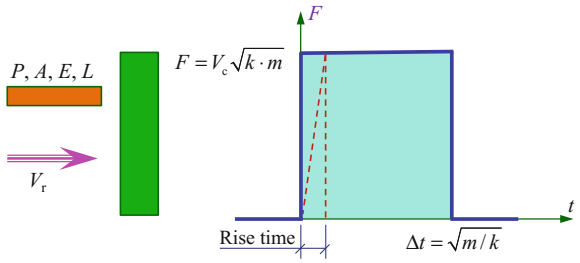

Fig. 8.9 Impact model (Eurocode)

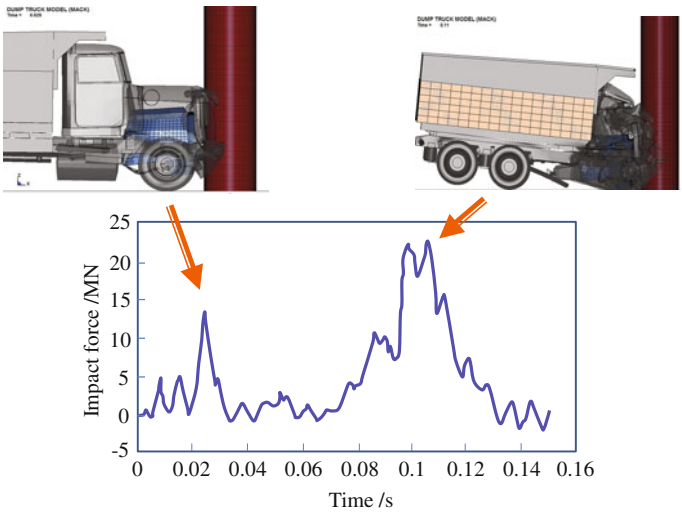

Fig. 8.10 Impact force time histories of a dump truck collision with pier

truck crash with an RC column of a bridge over the I-20 highway in Texas in the USA. He captured the time histories of collision force between the truck and the column and reported a general agreement between the simulated crack pattern and the actually observed failure mechanism of the column. The time history given in the Fig. 8.10 is the collision load of a 289-kN-weight dump truck colliding on the bridge pier with the velocity of 96.6 km/h, and the figure also shows that the states of truck and bridge pier after collision are related to the two peaks in the curve.

The impact force time history is formed by the interacting response of colliding truck and the collided pier. Owing to the structural and mass distribution characteristics of the truck, there appear two main peaks in the curve of Fig. 8.10. According to some researches, the durations of collision loads in various cases are basically the same.

The impact force by truck collision is usually measured by the "50 ms moving average" value. Shown in Fig. 8.11a are the impact force curves simulated with the 289-kN dump truck at two impact velocities (Buth 2009). It can be seen that the variation of the impact force curves is relatively less fluctuated. The maximum values of the impact force curves after "50 ms moving average" are often taken as the design load.

Similar results are presented by Yu and Zha (2011), who established a dynamic model to investigate the impact of a truck with a bridge pier. The truck had a weight of 77 kN, and the FE model of the truck was the one issued by NCAC (National Crash Analysis Center 2010) in the USA. Shown in Fig. 8.11b are the "50 ms

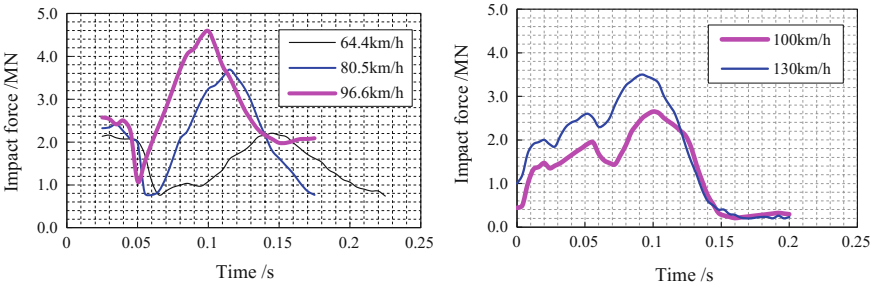

(a) 289 kN dump truck (b) 77kN truck

Fig. 8.11 Impact force time histories of truck collision with piers after "50 ms moving average"

moving" averaged collision force time histories of the truck acting on the pier at two impact velocities V_c = 100 km/h and V_c = 130 km/h, and the corresponding peak forces are 2.65 MN and 3.5 MN, respectively.

El-Tawil et al. (2005) used the inelastic transient finite element method to simulate the collision forces between truck and bridge pier. A 14 kN-Chevy truck and a 66 kN-Ford truck and two types of concrete piers were used in the simulation, and the impact velocities for the trucks were from 55 to 135 km/h. Shown in Fig. 8.12 are the impact force time histories of truck collision with pier.

These time histories of impact forces show a characteristic of narrow pulse load with very short loading duration of about 0.1 s and the pulse width of 0.003 s ~ 0.01 s; the faster the vehicle velocity, the earlier the peak appears, and the narrower the pulse width.

Regarding the collision intensity, El-Tawil et al. further studied the distributions of peak dynamic force (PDF) and equivalent static force (ESF, the static force necessary to produce the same displacement as that produced by the dynamic force) of the two trucks versus approach velocity, as shown in Fig. 8.13, where the design loads in AASHTO and Chinese code are also given for comparison.

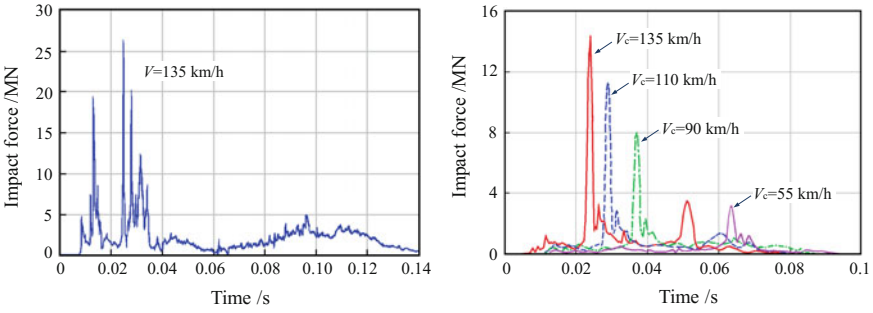

(a) 66 kN-Ford truck (b) 14 kN-Chevy truck

Fig. 8.12 Impact force time histories of truck collision with pier (El-Tawil et al. 2005)

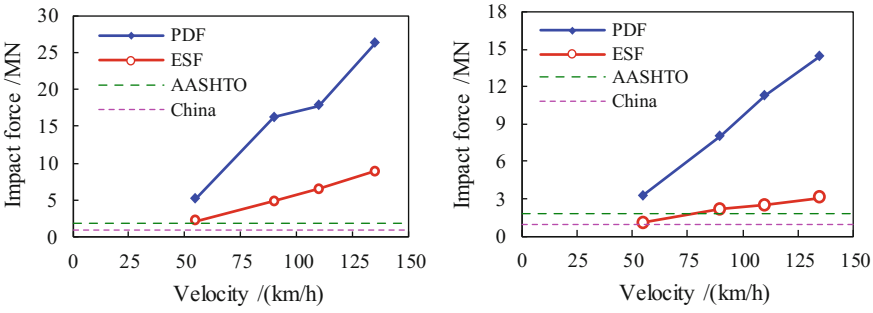

(a) 66 kN-Ford truck (b) 14 kN-Chevy truck

Fig. 8.13 Distributions of truck impact forces versus approach speed

The results showed that the collision forces appear to increase rapidly with the approach velocity of the truck. The maximum PDF is as high as 26.3 MN for the Ford truck and 14.4 MN for the Chevy, and the maximum ESF is 8.85 MN for the Ford and 3.07 MN for the Chevy, respectively. Even for the ESF, it turns out to be significantly higher than the design values (1.8 MN in AASHITO and 1.0 MN in Chinese code) when the truck velocity is high, indicating that the current collision design provisions could be severely insufficient and that there might be a number of bridge piers vulnerable to accidental impact of heavy trucks. Moreover, it should be mentioned that as the freight trucks are often overloaded and sometimes over-speeded in China, the actual collision forces might also be much greater than the one provided in the code.

Based on the refined nonlinear finite element analysis and the accident case investigation, Lu et al. (2011) studied the impact force and the structure damage mechanism of overheight truck colliding with bridge superstructures. Illustrated in Fig. 8.14a are the calculated impact force time histories of a 2-axle truck colliding with the T-beam of a bridge at several velocities. The curves show that the collision loads are greatly affected by the mass and the colliding velocity of truck, and both lateral and vertical impact impulses have linear relationship with the velocity of the truck, while they are little affected by the type of bridge structure (Fig. 8.14b).

Subsequently, further studies by Lu et al. (2011) and Xu et al. (2012, 2013) found that collision between overheight truck and bridge superstructure causes two types of failure modes, viz global damage and local damage, which are necessary to be incorporated into the bridge design. To reduce computation cost and facilitate engineering application, a simplified model for calculating the collision forces is proposed. The collision force histories by the simplified model and the FE method are compared in Fig. 8.15.

Sharma et al. (2012) developed a framework for estimating the dynamic shear force capacity of an RC column subjected to vehicle collision for different performance levels of the design. The method, as a more realistic representation of vehicle collision with structures, is an improvement over the existing static or

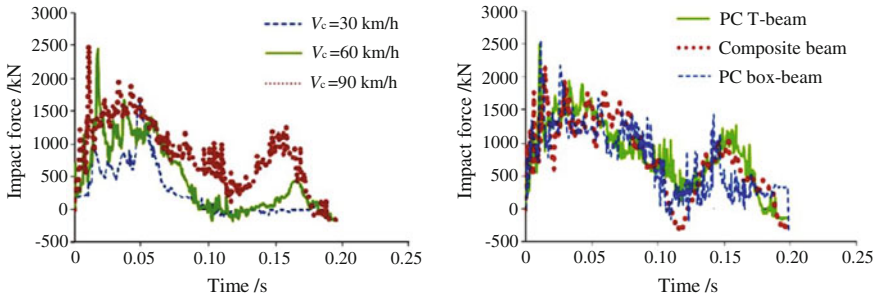

(a) By different truck velocities (b) For different bridge structural types

Fig. 8.14 Time histories of lateral impact forces by truck collision with bridge

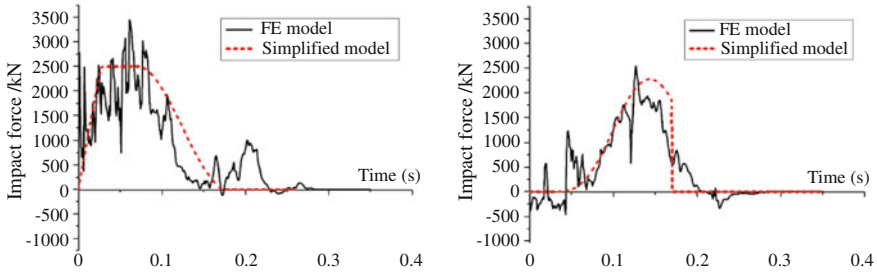

Fig. 8.15 Comparison of collision force histories by simplified model and FE method (V = 60 km/h)

quasi-static analysis to the dynamic analysis. The proposed procedure can be used for the design of RC columns to minimize damage and meet a set of performance objectives during different vehicle impact scenarios and can be extended to estimate the capacity of other members such as prestressed columns, steel columns, and beams and other hazards such as high-velocity impacts due to blasts or missiles. Shown in Fig. 8.16 are the failure modes of the column and two types of trucks after collision.

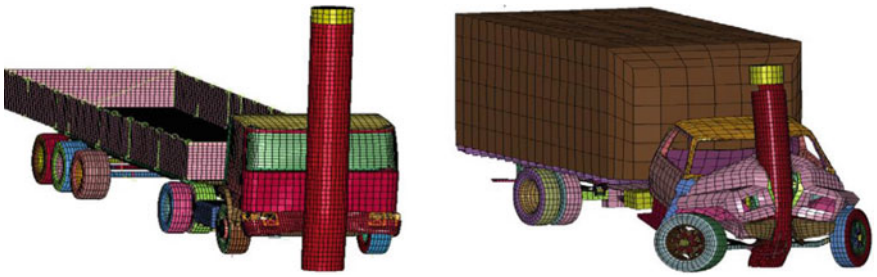

(a) 38-t truck, V_c = 18 m/s, no column failure. (b) 8-t truck, V_c = 32m/s, with column failure.

Fig. 8.16 FE simulation of an RC column collided by trucks

These research results show that in general, the time histories of impact force from vehicle collision with pier exhibit a characteristic of pulse waveform; the faster the vehicle velocity, the earlier the peak appears, and the narrower the pulse width, with very short loading duration usually less than 0.2 s. The heavier the vehicle, the faster the vehicle velocity, and the shorter the loading duration, the greater the instant collision force, with the maximum being dozens of MN.

8.1.3 Collision by Drifting-Floe

In addition to collisions by vessels and vehicles, the pier of a bridge crossing a river may be collided by drifting-floe or other floating objects. In particular, for the drifting-floe with large volume and huge impact energy, it may have a destructive impact on the structure; thus, the collision of ice-floe on bridge piers has been paid more attention by researchers.

There are two types of ice effects on structure: static ice load and dynamic ice load. The static ice load concerns the maximum static ice force on the structure, which is used to determine the static stiffness and strength of the structure, to ensure it against damage. The dynamic ice load concerns not only the maximum instant ice force, but also the variation of the force with time, which may induce the vibration of bridge. The dynamic ice load affects the structure response in its loading form, magnitude, and duration. Only by the characteristics of the dynamic ice load, can the structural response be exactly evaluated, so as to avoid structural damage caused by overlarge vibrations. However, the current bridge design codes only give the design formulas for static ice load, which are not applicable for dynamic analysis of bridges subjected to ice collision. With the occurrence of many ice-excited vibration accidents, this issue has been more and more noticed.

The dynamic ice load is complex, which is divided into three categories as periodic, random, and impact (Yu et al. 2009a, b; Guo 2010). Each category of dynamic ice load has its distinct feature in impact force magnitude, loading duration, and variation speed. In the three categories, the dynamic ice load caused by drifting-floe impact on a bridge pier is most concerned in train-bridge coupling dynamic analysis, so it is summarized as herein below.

There are two methods for studying ice-floe collision with pier, namely experiment, and numerical simulation.

The experimental study includes the in situ test and the laboratory test. The data measured at in situ test can well reflect the real ice-floe collision, but they are not easy to obtain, because under the difficult in situ test condition, the sensors always directly contact with the water and are often damaged by the impact of the huge ice-floe, and moreover, the free ice-floe drifting state cannot be controlled. The current studies are mainly concentrated on the fracture performance of ice-floes, while very few for direct measurement of their collision forces with bridge piers.

From the laboratory test, various factors affecting the ice-floe collision with piers can be accurately measured and quantitatively analyzed, by changing the

mechanical features, volumes, and drifting velocities of ice-floes and the structural parameters of the collided pier. However, due to the mechanical behavior of ice-floe that has a significant size effect, the scaled model test can hardly reflect the complicated conditions on the site.

With the development of numerical simulation techniques, the study on ice-structure collision based on various finite element models has achieved considerable progress. The ice loads, especially the dynamic ice loads, are rather complex, which depend not only on the mechanical characteristics of the ice and the type of the collided structure, but also on the dynamic interaction between the ice-floe and the structure. Because in-depth study of these issues is beyond the scope of this book, herein with the need of research in this chapter, several typical ice-collision loads obtained by experiments and finite element simulations are introduced.

Liu (2011) implemented the numerical simulations of interaction processes between sea ice and bridge foundation according to the condition of sea ice in Qingdao Gulf. The results showed that when the flow velocity is larger than 0.1 m/s, the ice crushing failure is formed, and during the crushing process it produces the dynamic force on the structure, as shown in Fig. 8.17a. In the case of the impact force curve, a strong impact pulse occurs very soon after the collision, with duration of about 0.5 s, and subsequently, with the process of impact, squeeze, and crushing the ice body suffered, there appears a series of smaller magnitude. This is in accordance with the model test result in Fig. 8.17b (Tuhkuri 1995).

Wu et al. (2008) conducted numerical simulations of bending failure processes between sea ice and conical structure, using the software LS-DYNA, and obtained the impact force time history of ice-floe, as shown in Fig. 8.17c. Zhang et al. (2002) analyzed the dynamic interaction between ice and structure by the DDA (discontinuous deformation analysis) approach, and with the inverse analysis on the structural response, a similar ice impact force acting on the structure is obtained, as shown in Fig. 8.17d.

Dong et al. (2012) conducted a series of tests of ice loads on cylindrical piles subjected to the impacts of drifting ice and obtained the ice impact force on the pier, as shown in Fig. 8.18a, which is similar to that from a field measurement by Guo (2010) shown in Fig. 8.18b. In these curves, the impact forces reach the peak within a very short time after the collision and then sharply decline, showing a typical pulse load. They then analyzed the relationship between ice kinetic energy and the impact force, finding that the design load on the piles can be determined with an envelope of logarithm curve.

Han (2000) conducted a field experiment on drifting-floe colliding with the No. 3 pier of the Harbin Songhua River Bridge. By installing five ice-pressure sensors on the ice guard, she measured the dynamic pressures of the floating floe on the pier and observed the crushing state of the floe when it collided with the guard body. Shown in Fig. 8.19 are two typical measured dynamic pressure signals under ice-floe collision, from which the maximum impact force was acquired, by scaling with the calibrated rate, as 507.6 kN.

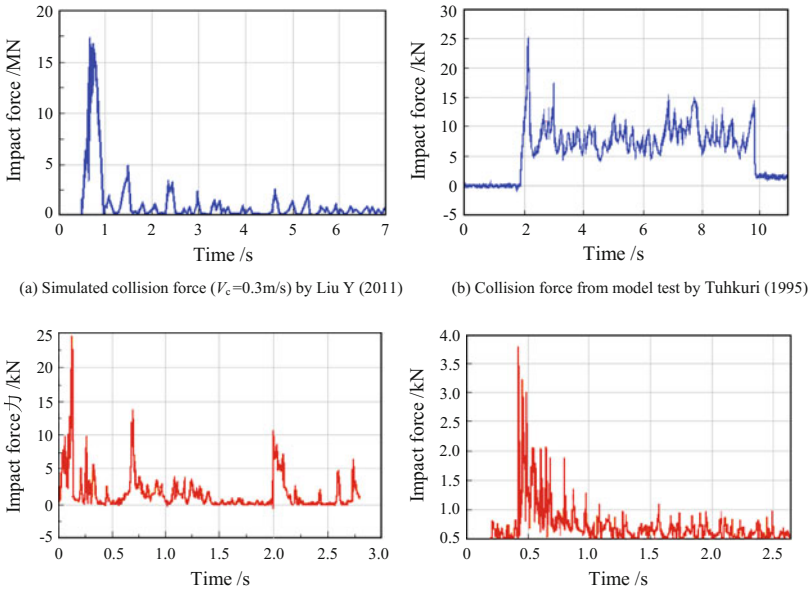

(a) Simulated collision force (V_c=0.3m/s) by Liu Y (2011)

(b) Collision force from model test by Tuhkuri (1995)

(c) Simulated collision force (V_c=1.0m/s) by Wu WH (2008)

(d) Simulated collision force (V_c=1.0m/s) by Zhang YL *et al*. (2002)

Fig. 8.17 Impact force time histories of ice-floe collision with structures

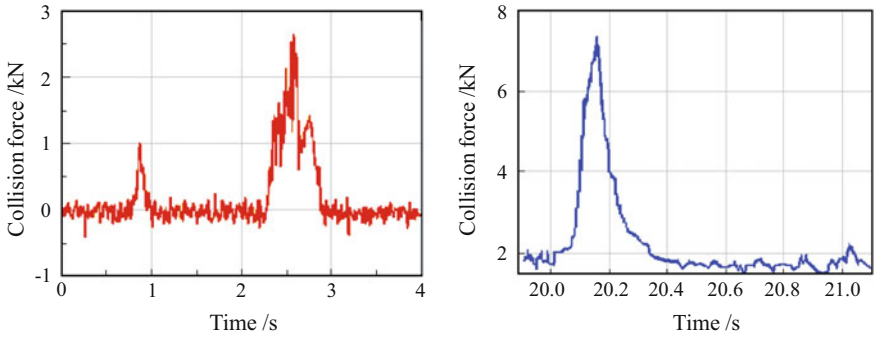

(a) Model test by Dong JW *et al*. (2012).

(b) Field experiment by Guo FW (2010).

Fig. 8.18 Impact force time histories of ice-floe collision by model test and field measurement

In the springs of 2008 ~ 2010, the author participated in the field experiments at several bridges suffering drifting-floe collision in the cold Northeast China (Yu et al. 2009; Xia et al. 2012a, b), measured the impact forces of the floes colliding with the piers, and recorded the statuses of the collisions. Shown in Fig. 8.20 are

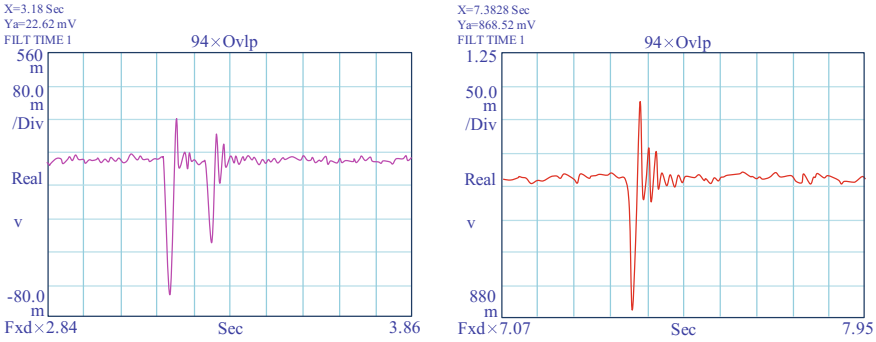

Fig. 8.19 Dynamic pressure signals under ice-floe collision measured at No. 3 pier of the Harbin Songhua River Bridge

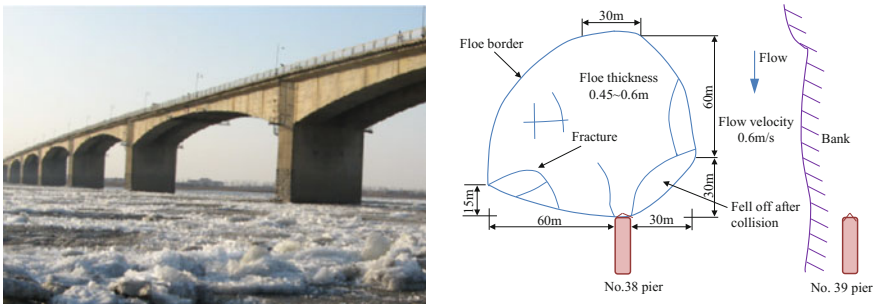

Fig. 8.20 Ice-floes drifting on the Tonghe Songhua River and a 90 m × 90 m floe colliding with the No. 38 pier of the bridge (maximum impact force 315.83 kN)

the scene of ice-floes drifting on the Tonghe Songhua River and the status of a 90 m × 90 m huge floe colliding the No. 38 pier of the bridge.

Summarized in Table 8.1 are maximum impact forces of ice-floe collision with piers measured at several bridges, with the respective geometries and flowing velocities of the floes.

In these experimental results, the maximum impact force of ice-floe collision was 2432.82 kN, measured at the No. 10 pier of the Jiamusi Songhua River Bridge, the area of the ice-floe was recorded as 80 × 60 m^2, and the flow velocity 1.35 ~ 1.45 m/s. Shown in Fig. 8.21a is the impact force time history of this collision. The impact load exhibits a typical repeated-impact feature, with the duration of about 4 s; the maximum force appeared at about 0.26 s and subsequently followed three peaks around 850 kN and one around 500 kN between 0.5 ~ 2.5 s; and afterward, at the end of this collision, appeared the second biggest peak of 1500 kN at about 3.7 s.

Table 8.1 Results of ice-floe collision with piers measured at bridge sites

No.	Bridge name	Pier No.	Floe size (m^2)	Floe velocity (m/s)	Max. impact force (kN)
1	Huma River Bridge	No. 1	60 × 80	0.85	1968.82
2	Xunbila River Bridge	No. 7	20 × 20	——	280
3	Jiamusi Songhua River Bridge	No. 10	80 × 60	1.35 ~ 1.45	2432.82
4	Tonghe Songhua River Bridge	No. 38	80 × 100	0.45 ~ 0.60	375.48
5	Harbin Songhua River Bridge	No. 3	60 × 100	——	387.1

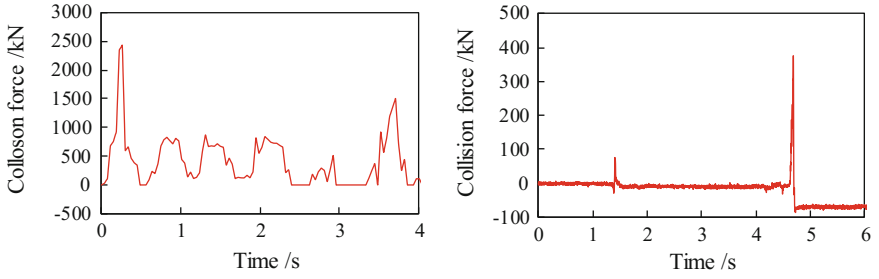

(a) No. 10 pier of Jiamusi Songhua River Bridge (b) No. 38 pier of Tonghe Songhua River Bridge

Fig. 8.21 Impact force time histories of ice-floe collision with piers measured at bridge sites

Shown in Fig. 8.21b is another typical impact force time history of ice-floe collision, which was measured at the No. 38 pier of the Tonghe Songhua River Bridge, the area of the ice-floe was recorded as 80 × 100 m^2, the thickness was 0.45 ~ 0.60 m, and the flow velocity was 0.6 m/s. There appeared two pulses in the impact force time history: The first small pulse was 75.34 kN with a short duration of about 0.02 s, and 3.3 s after it, the second pulse appeared, with a bigger peak of 375.48 kN and a longer duration of 0.16 s.

To study the collision intensity of ice-floe, Timco et al. (2003, 2011) summarized all available data related to ice-floe impacts on structures, including laboratory tests, forces on several bridge piers (Hondo, Pembina, Rideau), forces from small icebergs impacting dedicated test structures (Grappling Island, Newmans Cove), multi-year ice impacts on the offshore structure Molikpaq, and the Hans Island experiments. Based on statistical analysis, they found the impact force was best related to the kinetic energy of the floe at impact. This energy ranged over thirteen orders of magnitude in value, showing a good correlation of the impact force F with the energy E at impact with a function form $F = Ae^{0.532}$ where the coefficient A was determined to be 61.7 MN for the "likely" impact force and 388 MN for the

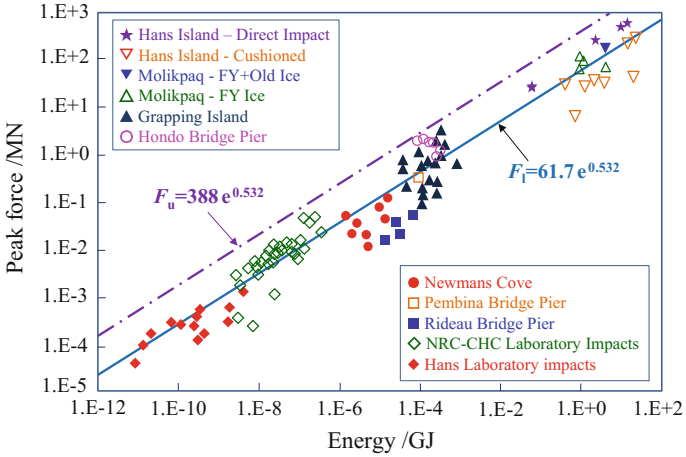

Fig. 8.22 Distribution of peak impact force versus the kinetic energy of ice-floe

upper-limit, as shown in Fig. 8.22. The figure shows that the maximum impact force of ice-floe can be hundreds of MN.

These research results show that in general, the time histories of ice-floe collision forces exhibit a characteristic of pulse waveform; the faster the flow velocity, the greater the instant force, and the shorter the impact action, being 0.05 $\sim$ 0.5 s, with wide duration range of 0.05 $\sim$ 4.0 s; the heavier the ice-floe, and the faster the flow velocity, the greater the instant collision force, with the maximum being hundreds of MN.

8.1.4 Characteristics of Bridge Collision Loads

The collision loads on bridge structure concerned in train-bridge coupling dynamic analysis mainly include vessel collision, vehicle collision, and ice-floe collision. These collision loads are very complicated, with their respective characteristics in impact force time histories, maximum impact forces, and acting positions, as summarized in Table 8.2.

Table 8.2 Characteristics of various bridge collision loads

Collision loads	Vessel collision	Vehicle collision	Drifting-floe collision
Impact force time history	Time history of impact force exhibits a characteristic of strong nonlinear waveform, with loading durations of 3 ~ 4 s	Time history of impact force exhibits a characteristic of pulse waveform. The faster the vehicle velocity, the earlier the peak appears, and the narrower the pulse width, with very short loading duration of usually less than 0.2 s	Time history of impact force exhibits a characteristic of pulse waveform. The faster the flow velocity, the greater the instant force, and the shorter the impact action, being 0.05 ~ 0.5 s, with wide duration range of 0.05 ~ 4.0 s
Maximum Impact force	The heavier the vessel, and the faster the impact velocity, the greater the instant collision force, with the maximum hundreds of MN	The heavier the vehicle, the faster the vehicle velocity, and the shorter the loading duration, the greater the instant collision force, with the maximum dozens of MN	The heavier the floe, and the faster the flow velocity, the greater the instant collision force, with the maximum hundreds of MN
Position of impact	Acting on pier at position varying with the navigation water level and colliding part of the vessel; sometimes on superstructure	Acting on pier usually at low position; sometimes on superstructure	Acting on pier at the flow surface, varying with the water level

8.2 Dynamic Analysis Model of Train-Bridge System Subjected to Collision Loads

When a bridge is collided by a vessel, a car or other colliding object, the analysis model of the train-bridge system can be regarded as a spatial dynamic system composed of three subsystems: the bridge subsystem, the train subsystem, and the colliding object subsystem, as shown in Fig. 8.23.

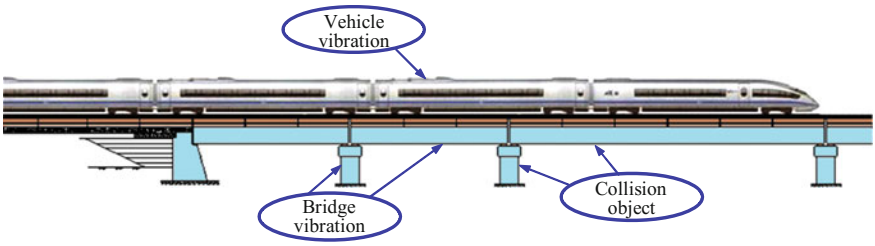

Fig. 8.23 A coupled train-bridge system subjected to a vessel collision

Theoretically, the motion equations for such a system can be expressed as

$$\begin{bmatrix} \mathbf{M}_{vv} & 0 & 0 \\ 0 & \mathbf{M}_{bb} & 0 \\ 0 & 0 & \mathbf{M}_{cc} \end{bmatrix} \begin{Bmatrix} \ddot{\mathbf{X}}_v \\ \ddot{\mathbf{X}}_b \\ \ddot{\mathbf{X}}_c \end{Bmatrix} + \begin{bmatrix} \mathbf{C}_{vv} & \mathbf{C}_{vb} & 0 \\ \mathbf{C}_{bv} & \mathbf{C}_{bb} & \mathbf{C}_{bc} \\ 0 & \mathbf{C}_{cb} & \mathbf{C}_{cc} \end{bmatrix} \begin{Bmatrix} \dot{\mathbf{X}}_v \\ \dot{\mathbf{X}}_b \\ \dot{\mathbf{X}}_c \end{Bmatrix} + \begin{bmatrix} \mathbf{K}_{vv} & \mathbf{K}_{vb} & 0 \\ \mathbf{K}_{bv} & \mathbf{K}_{bb} & \mathbf{K}_{bc} \\ 0 & \mathbf{K}_{cb} & \mathbf{K}_{cc} \end{bmatrix} \begin{Bmatrix} \mathbf{X}_v \\ \mathbf{X}_b \\ \mathbf{X}_c \end{Bmatrix} = \begin{Bmatrix} \mathbf{F}_{vb} \\ \mathbf{F}_{bv} + \mathbf{F}_{bc} \\ \mathbf{F}_{cb} \end{Bmatrix} \tag{8.11}$$

where the subscripts "v", "b", and "c" represent the train, bridge, and colliding objects, respectively; **M**, **C,** and **K** are the mass, damping, and stiffness matrices of the train-bridge system, respectively; **X**, $\dot{\mathbf{X}}$, and $\ddot{\mathbf{X}}$ are the displacement, velocity, and acceleration vectors, respectively; $\mathbf{F}_{vb}$ and $\mathbf{F}_{bv}$ are the interforce vectors of the bridge to the train and the train to the bridge; and $\mathbf{F}_{bc}$ and $\mathbf{F}_{cb}$ are the interforce vectors of the colliding object to the bridge and the bridge to the colliding object, respectively.

It should be noticed that the colliding object may produce plastic deformation during the collision, and the bridge may be damaged if the collision load is sufficiently large. In this case, the structural characteristics of the colliding object and the bridge may be changed, so the influence of nonlinear factors on the stiffness matrices $\mathbf{K}_{bb}$, $\mathbf{K}_{bc}$, $\mathbf{K}_{cb}$, and $\mathbf{K}_{cc}$ related to the colliding object and the bridge in Eq. (8.11) should be considered.

However, the coupling vibration of train-bridge system under collision loads is a complex problem. The complexity contains the following: (1) the characteristics of the collision load, whatever it is induced by vessel, vehicle, ice-floe, or other colliding objects, not only relate to the mass and motion speed of the colliding object, but also depend on the stiffness of the colliding object and the collided structure; (2) the stiffness of the colliding object that is related to its own material and structural characteristics, such as the material and the structure of the vessel bow and the anti-collision beam of the vehicle, and the hardness and shape of the ice-floe. The colliding object and the collided object with different stiffness have different deformation and energy absorption capacities, which directly influence the time histories of the collision load, such as the duration time and collision strength. Therefore, synchronously considering the interactions between train and bridge and between colliding object and collided structure makes the problem extremely complicated, which is almost unrealizable by the current analysis methods.

On the other hand, according to the existing researches, there are three methods to obtain the collision load: field test, model experiment, and numerical simulation. Whatever any method is used, the time history of the acquired collision load has included the influence of the stiffness and the deformation of the colliding object and the collided structure, and also the dynamic interaction between them. Therefore, with a known collision load, it is feasible to use a simplified method to analyze the dynamic responses of train-bridge system under collision load: By neglecting the interaction between the colliding object and the bridge structure, the time history of the collision load is directly taken as the input excitation on the train-bridge system, to solve the problem through simulation analysis.

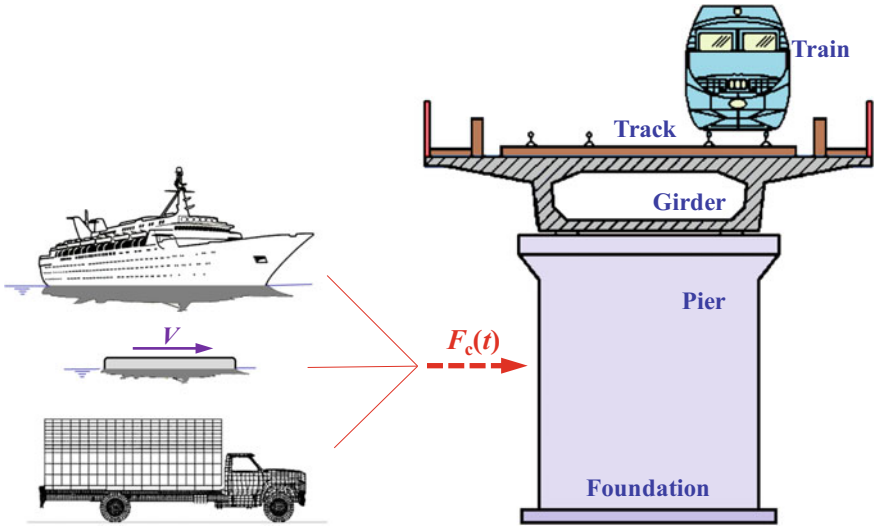

Fig. 8.24 Dynamic model for train-bridge system subjected to collision loads

The train-bridge dynamic interaction model established by this method is shown in Fig. 8.24, which consists of two subsystems, the train subsystem and the bridge subsystem, and the collision load is directly applied on the bridge structure as the external force $F_c(t)$.

In the analysis, the train subsystem model is established by rigid bodies with elastic connections, and the bridge subsystem model is established either by the FEM (Finite element method) or the MDM (modal decomposition method). The two subsystems are coupled by the wheel-rail interaction, and the track irregularity is regarded as the internal excitation of the two subsystems.

When the bridge subsystem is established by the FEM, the coupled motion equations for the train-bridge system subjected to collision loads can be expressed as

$$\begin{bmatrix} \mathbf{M}_{vv} & 0 \\ 0 & \mathbf{M}_{bb} \end{bmatrix} \begin{Bmatrix} \ddot{\mathbf{X}}_v \\ \ddot{\mathbf{X}}_b \end{Bmatrix} + \begin{bmatrix} \mathbf{C}_{vv} & \mathbf{C}_{vb} \\ \mathbf{C}_{bv} & \mathbf{C}_{bb} \end{bmatrix} \begin{Bmatrix} \dot{\mathbf{X}}_v \\ \dot{\mathbf{X}}_b \end{Bmatrix} + \begin{bmatrix} \mathbf{K}_{vv} & \mathbf{K}_{vb} \\ \mathbf{K}_{bv} & \mathbf{K}_{bb} \end{bmatrix} \begin{Bmatrix} \mathbf{X}_v \\ \mathbf{X}_b \end{Bmatrix} = \begin{Bmatrix} \mathbf{F}_{vb} \\ \mathbf{F}_{bv} \end{Bmatrix} + \begin{Bmatrix} 0 \\ \mathbf{F}_c \end{Bmatrix} \tag{8.12}$$

where the subscripts "v" and "b" represent the train and the bridge, respectively; **M**, **C**, and **K** are the mass, damping, and stiffness matrices, and **X**, $\dot{\mathbf{X}}$, and $\ddot{\mathbf{X}}$ are the displacement, velocity, and acceleration vectors, respectively; $\mathbf{F}_{vb}$ and $\mathbf{F}_{bv}$ are the interforce vectors of the bridge structure and the train vehicles, respectively. Details of these matrices and vectors can be found in Chap. 5 of this book.

When the bridge subsystem model is established by the MDM, the motion equation of the system can be expressed as

$$\begin{bmatrix} \mathbf{M}_{vv} & 0 \\ 0 & \mathbf{M}_{bb} \end{bmatrix} \begin{Bmatrix} \ddot{\mathbf{X}}_v \\ \ddot{\mathbf{Q}}_b \end{Bmatrix} + \begin{bmatrix} \mathbf{C}_{vv} & \mathbf{C}_{vb} \\ \mathbf{C}_{bv} & \mathbf{C}_{bb} \end{bmatrix} \begin{Bmatrix} \dot{\mathbf{X}}_v \\ \dot{\mathbf{Q}}_b \end{Bmatrix} + \begin{bmatrix} \mathbf{K}_{vv} & \mathbf{K}_{vb} \\ \mathbf{K}_{bv} & \mathbf{K}_{bb} \end{bmatrix} \begin{Bmatrix} \mathbf{X}_v \\ \mathbf{Q}_b \end{Bmatrix} = \begin{Bmatrix} \tilde{\mathbf{F}}_{vb} \\ \tilde{\mathbf{F}}_{bv} \end{Bmatrix} + \begin{Bmatrix} 0 \\ \tilde{\mathbf{F}}_c \end{Bmatrix} \tag{8.13}$$

where $\mathbf{Q}_b$, $\dot{\mathbf{Q}}_b$, and $\ddot{\mathbf{Q}}_b$ are the modal displacement, velocity, and acceleration vectors of the bridge subsystem, respectively; $\tilde{\mathbf{F}}_{vb}$ and $\tilde{\mathbf{F}}_{bv}$ are the interforce vectors of the train vehicle and the bridge subsystem with modal coordinates. The modal displacement $\mathbf{Q}_b$ can be acquired using the following transform formula:

$$\mathbf{Q}_b = [\, q_1 \quad q_2 \quad \cdots \quad q_n \quad \cdots \quad q_{N_b} \,] = \mathbf{\Phi}^T \mathbf{X}_b \tag{8.14a}$$

$$q_n = \sum_{k=1}^{N} \phi_n(k) X(k) \tag{8.14b}$$

where q_n is the nth modal coordinate of the bridge; $\mathbf{\Phi}$ is the mode-shape matrix of the bridge; $\phi_n(k)$ is the value of the nth modal function of the bridge at the kth node; N_b is the total number of the bridge modes concerned; $X(k)$ is the bridge displacement at the kth node; and N is the total number of bridge nodes.

According to the related design codes in China, for the bridge pier and abutment located in a navigable river or a river with floating objects, the collision by vessel or floating object should be considered in the design. For the bridge across a railway or highway, the collision on the pier and abutment by the vehicle should also be considered. In a general design, the collision load can be calculated by the related equations in the codes. In the present bridge code, however, the calculation method for the collision load is still at the static design stage, which cannot be used directly for calculating the dynamic response of the train-bridge system subjected to a collision load. Instead, the time history of the collision load is needed, which is input to the train-bridge system as an external excitation to carry out the simulation calculation.

When the bridge model is established by the FEM, the collision load on the bridge can be applied to the related structural nodes as the collision load vector $\mathbf{F}_c$. When the bridge model is established by the MDM, the generalized collision load vector $\tilde{\mathbf{F}}_c$ corresponding to the related modes can be expressed as

$$\tilde{\mathbf{F}}_c = \mathbf{\Phi}^T \mathbf{F}_c = [f_{c1}(t), f_{c2}(t), \cdots f_{cn}(t), \cdots f_{cN_b}(t)]^T \tag{8.15}$$

where f_{cn} is the generalized collision force acting on the bridge corresponding to the nth mode. Supposing the collision forces act horizontally on the pier, f_{cn} can be expressed as

$$f_{cn} = \sum_{k=1}^{N} \phi_n^{\mathrm{h}}(k) F_k(t) \tag{8.16}$$

where $\phi_n^{\mathrm{h}}(k)$ is the function value of the nth mode shape in horizontal direction of the bridge at the kth node; $F_k(t)$ is the collision force history of the vessel on the bridge at the kth node, which is only different from zero at the pier nodes affected by the collision.

When the collision load is known as an external load, the motion equations for the train-bridge interaction system subjected to a collision load can be solved by the software for dynamic analysis of train-bridge interaction system.

8.3 Dynamic Analysis of Train-Bridge System Subjected to Collision Loads

Using the established model, the whole process of a train passing through the bridge subjected to collision loads can be simulated, to calculate the dynamic responses of the bridge and the running safety indices of the on-bridge train, and further to analyze the characteristics of time histories and frequency spectra.

8.3.1 Bridge Description and Calculation Parameters

The case study concerns a double-track bridge situated on the Harbin-Dalian HSR line in Northeast China. The bridge is composed of (32+48+32) m continuous PC box-girders, with two 32 m simply-supported side spans added at both ends of the continuous span, as shown in Fig. 8.25.

The cross section and the main dimensions of the girder are shown in Figs. 8.26 and 8.27. The widths of top slab and bottom plate are 13.4 m and 5.74 m, respectively, and the depth of the girder is 3.0 m for the whole span length, while at the strengthened segments of 500 cm long (250 cm each side from the bearing

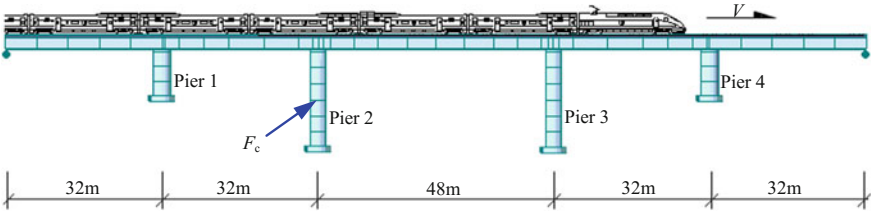

Fig. 8.25 Configuration of the (32 + 48 + 32) m continuous bridge with two 32 m side spans

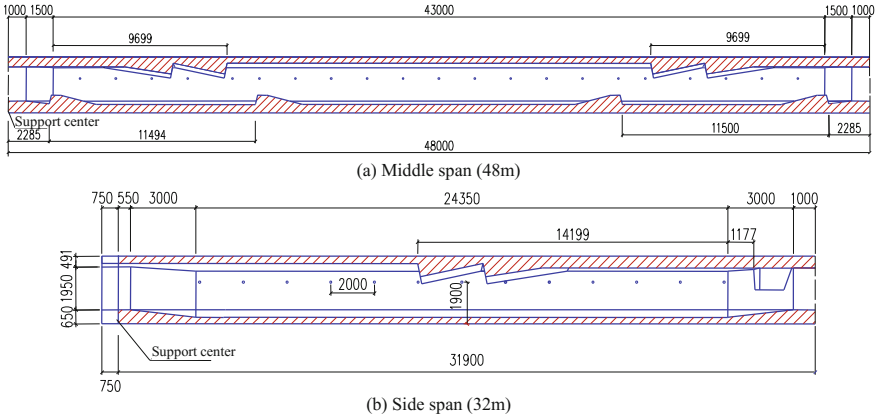

Fig. 8.26 Elevations of the (32+48+32) m continuous bridge (unit: mm)

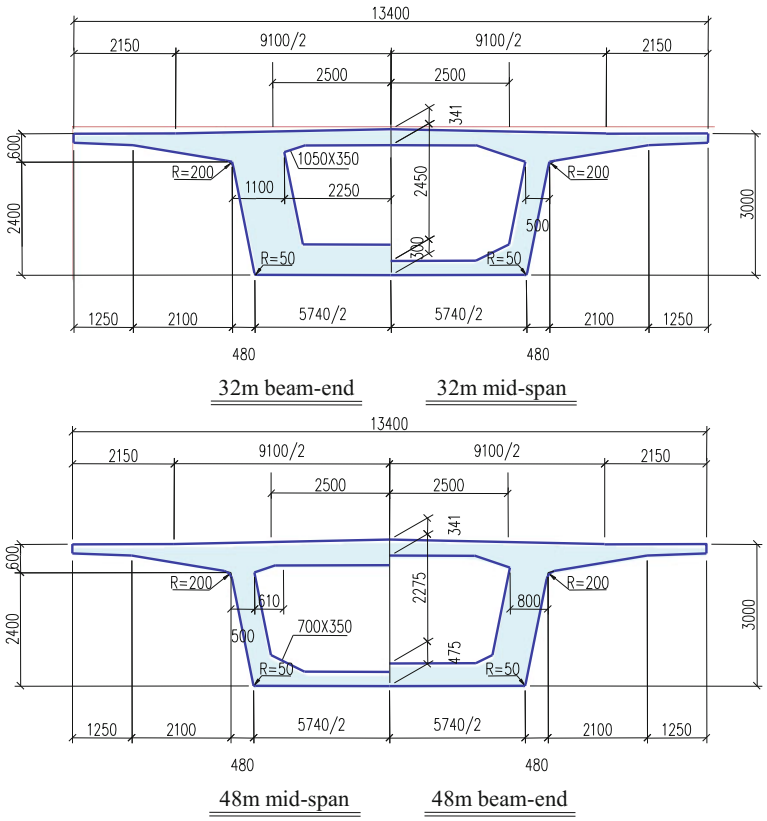

Fig. 8.27 Cross sections of the (32+48+32) m continuous bridge (unit: mm)

Table 8.3 Foundation stiffness of the (32+48+32) m continuous bridge piers

Pier		Section area (m^2)	Translational stiffness (MN/m)		Rotational stiffness (MN·m/rad)		
			R_x	R_y	R_z	M_x	M_y
Middle piers	Fixed bearing	7.75 × 4.45	1681.59	1681.59	13328.5	189480	189480
	Movable bearing	7.75 × 4.45	1683.91	1683.91	13906.7	197110	197110
Side piers		7.0 × 3.2	892.11	882.91	7725.1	83424	45567
Middle piers	Fixed bearing	7.75 × 4.45	13328.5	1681.59	189480	1681.59	189480
	Movable bearing	7.75 × 4.45	13906.7	1683.91	197110	1683.91	197110
Side piers		7.0 × 3.2	7725.1	892.11	45567	882.91	83424

center) above the Piers 2 and 3, the upper slab, bottom plate, and the webs are thickened. Laid on the bridge deck are the CRTS II ballastless double slab tracks, and the secondary phase dead load applied on the bridge model is 18.5 t/m.

The substructure of the bridge includes the concrete solid piers with round-ended sections and the concrete pile foundations. The height of two middle piers is 19.45 m, and the height of two side piers is 10.0 m. In the finite element model, the piers are modeled with beam elements and the support stiffness of pile foundations is considered, as listed in Table 8.3, in which R_x, R_y, and R_z are translational stiffness in longitudinal, transverse, and vertical directions, and M_x and M_y are rotational stiffness around the longitudinal and transverse axes of the bridge, respectively, provided by the designer.

For the (32+48+32) m continuous spans, mounted on the Pier 2 are fixed pot neoprene bearings, while the rest are sliding ones. In the analysis, the bearings are modeled according to the design. For the sliding bearing, the translational displacement in the longitudinal x-axis and the rotational angle about transverse y-axis of the girder end are free, while the other 2 translational displacements and 2 rotational angles are modeled as slave DOFs of the master DOFs at the pier-top. For the fixed bearing, the rotational angle about the transverse y-axis of the girder end is free, while the other 3 translational displacements and 2 rotational angles are connected through master-and-slave relation to the pier-top.

By a finite element modal analysis, the natural vibration characteristics including frequencies and mode shapes of the bridge are obtained. Shown in Table 8.4 are the first 10 modes with their characteristics in frequencies and mode shapes.

The high-speed train ICE3, which was used in China for the dynamic analysis of high-speed railway bridges, is adopted. The train is composed of (3 M + 1T) × 3 cars, with M representing the motor-car and T the trailer-car, respectively. The average axle loads are 156.96 kN for the motor-car and 143.23 kN for the trailer-car. Other parameters can be found in Table 6.8. Illustrated in Fig. 8.28 are the axle loads of a unit of ICE3 train with the main axle interval parameters.

Table 8.4 Dynamic properties of the (32+48+32) m continuous bridge on high-speed railway

Order of mode	Frequency (Hz)	Descriptions of vibration modes
1	3.351	Vertical symmetric bending
2	4.122	Lateral symmetric bending
3	4.994	Longitudinal bending with antisymmetric vertical bending
4	5.714	Longitudinal bending with antisymmetric vertical bending
5	6.347	Longitudinal bending with symmetric vertical bending
6	6.711	Lateral antisymmetric bending
7	7.785	Vertical antisymmetric bending
8	8.426	Vertical symmetric bending
9	9.231	Lateral symmetric bending
10	10.688	Vertical antisymmetric bending

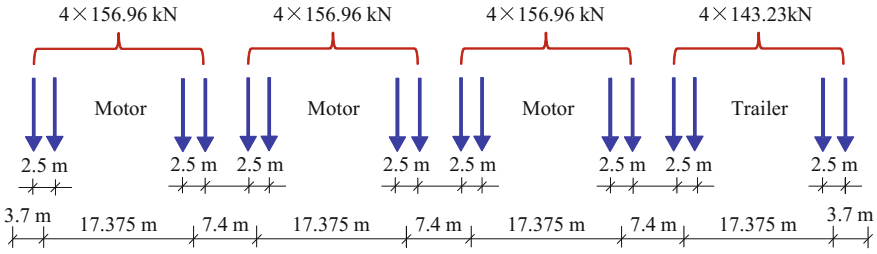

Fig. 8.28 Axle intervals and axle loads of a unit of ICE3 train

Three representative time histories and their spectra of collision loads are considered corresponding to ice-I load, ice-II load, and vessel load, as shown in Fig. 8.29.

It can be found that the time histories of collision loads are complicated during the collision with the piers:

For the ice-I load, it refers to the ice-floe collision load measured in the experiment on the Jiamusi Songhua River Bridge site in April 2009 (Xia et al. 2012a, b). It consists of six pulses acting repeatedly with an average width of 0.5 s and a total duration of 4 s.

The ice-II load was the ice-floe collision load measured in the experiment on the Tonghe Songhua River Bridge site in April 2010 (Xia et al. 2012a, b). It corresponds to a single pulse with a narrow pulse width of 0.06 s.

The vessel load is taken from the reference (Chen 2006) and represents the collision history by a ship, which is a wide continuous pulse with the total duration of 1.8 s.

In the analysis, the collision intensities (herein representing the maximum forces) of the three loads are normalized as 10 MN to compare the influence of different load histories, as shown in Fig. 8.29. As the three collision loads have different time evolutions, the dynamic responses of the bridge and the train will be different.

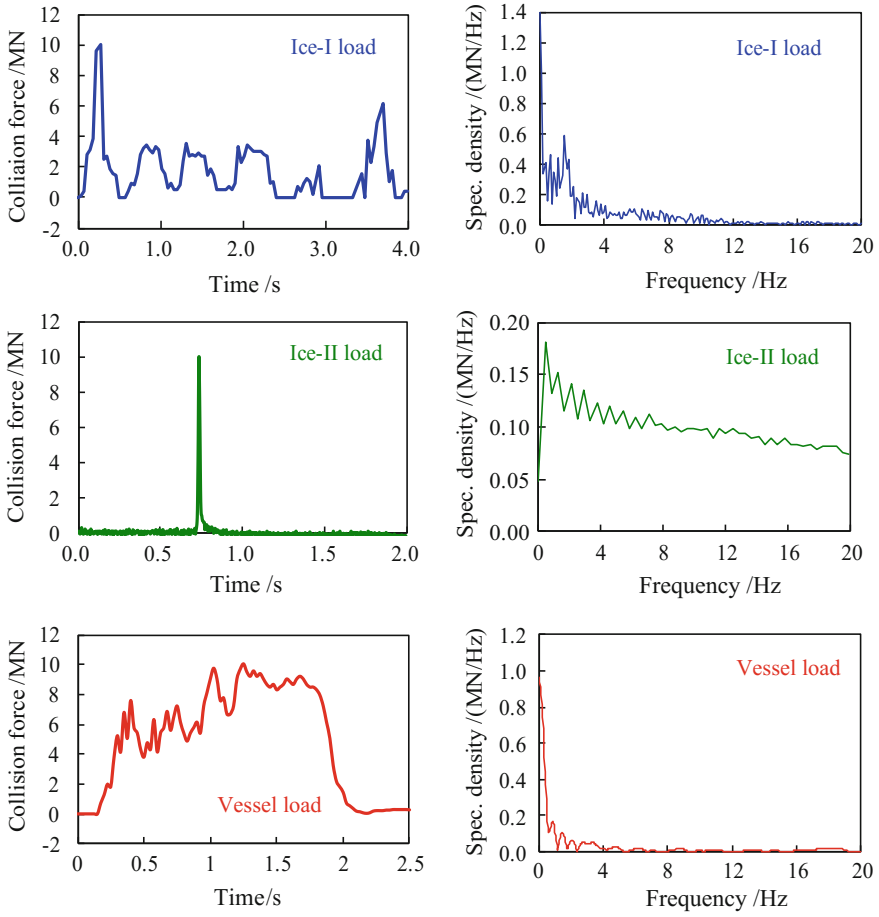

Fig. 8.29 Time histories and frequency spectra of collision loads

The three collision loads, in spite with identical intensity, have distinct features in impact velocity and duration, so they apply different effects on the dynamic responses of the bridge and the train vehicles, which will be analyzed hereinbelow.

The ICE3 train travelling on the bridge is simulated with and without collision. In the case with collision, the time history of the load is applied at level 10.2 m above the pile cap of the Pier 2, in the horizontal flow direction, as shown in Fig. 8.25. To better compare the results for different train speeds and different collision cases, each load is applied at the time when the train arrives at Pier 1, which ensures that some of the 12 cars of the train run on the first two continuous spans during the acting period of the collision load, in order to get the maximum vehicle responses.

The vertical, lateral, and rotational track irregularities are taken into consideration by using the data measured on the Qin-Shen HSR in China, as shown in Chap. 3. The damping ratio of bridge is 0.02, and the integration time step is 0.0005 s.

8.3.2 *Dynamic Responses of the Bridge*

Shown in Figs. 8.30 and 8.31 are the lateral displacement histories at the top of Pier 2 and at the mid-span (48 m middle span S4) of the bridge without collision and under three collision loads, when the ICE3 train travels on the bridge at the speed of V = 200 km/h.

From the figures, the effect of the collision is obvious:

(1) In the case without collision, the lateral displacements of the bridge are induced by the running train; therefore, the time history curves are steady with very small amplitudes, 0.063 mm for the pier-top and 0.066 mm for the mid-span. While under the collisions of ice-I load, ice-II load, and vessel load, the displacements are significantly amplified. The maximum displacements are 1.43 mm, 0.373 mm, and 1.24 mm for the pier-top, and 1.31 mm, 0.419 mm, and 1.09 mm for the mid-span, respectively.

(2) Loading rate and time duration of the collision loads have an obvious influence on the bridge displacements. For the ice-II load with the shortest pulse (0.06 s, much shorter than the first lateral period of the bridge), the most obvious impact effect in the displacement histories is induced, but the maximum peak value is relatively small. While for the ice-I and vessel loads with longer pulse widths (4 s and 1.8 s, respectively, both longer than the first lateral period of the bridge), the displacements at pier-top and mid-span are more than two times bigger than the ones induced by the ice-II load. This indicates that the load with longer duration time has a higher collision effect on the bridge displacement.

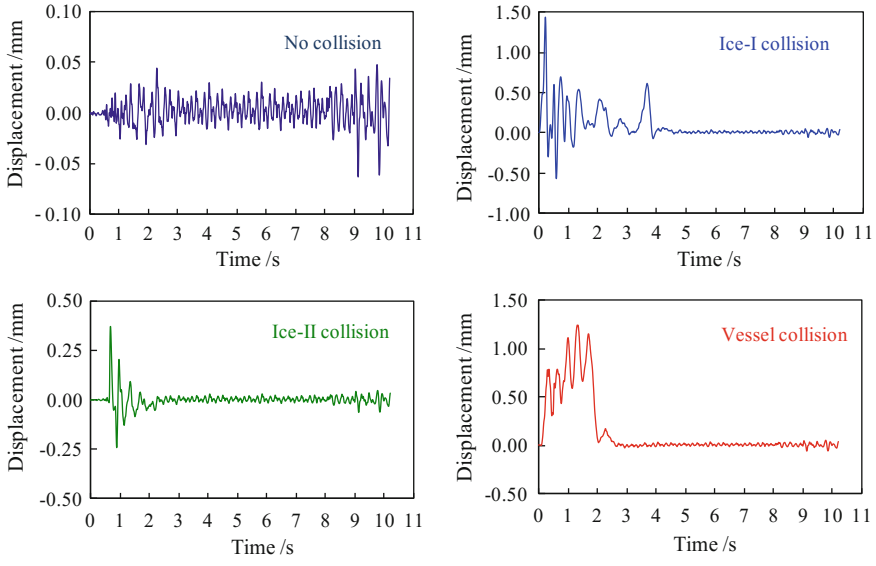

Fig. 8.30 Lateral displacements at the top of Pier 2 under V = 200 km/h

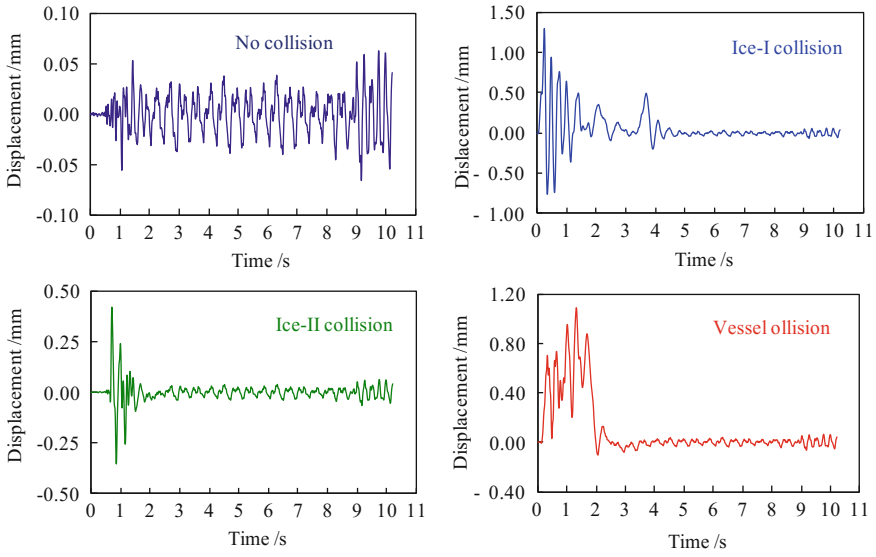

Fig. 8.31 Lateral mid-span displacements of the 48 m span under V = 200 km/h

(3) In the case with collision loads, the lateral displacement curves at the pier-top and mid-span of the bridge show clear impact characteristics. Owing to the damping action of the concrete pier and the girder, the vibrations attenuate fast, and the displacement curves return very soon to their steady state similar to the case without collision.

Shown in Figs. 8.32 and 8.33 are, respectively, the lateral acceleration histories at the top of Pier 2 and the mid-span (48 m middle span) of the bridge without collision and under the three collision loads, when the ICE3 train passes on the bridge at V = 200 km/h.

It can be observed from Figs. 8.32 and 8.33 that:

(1) In the case without collision, the time histories of the lateral accelerations are rather steady, with very small amplitudes of 23.0 cm/s^2 for the pier-top and 20.3 cm/s^2 for the mid-span. While under the collisions of ice-I load, ice-II load, and vessel load, the accelerations are greatly amplified, with the maximum values of 127 cm/s^2, 162 cm/s^2, and 73.5 cm/s^2 for the pier-top, and 135 cm/s^2, 100 cm/s^2, and 85.2 cm/s^2 for the mid-span, respectively.
(2) Owing to the damping action of the concrete pier and the girder, the accelerations attenuate fast, and the acceleration curves return very soon to their steady state similar to the case without collision.

The frequency contents of the bridge responses are shown in Figs. 8.34, 8.35, 8.36, and 8.37.

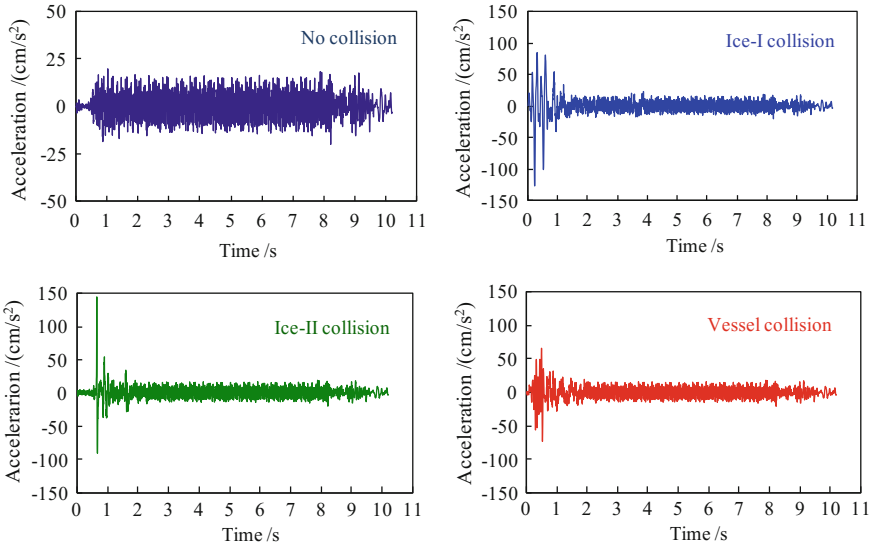

Fig. 8.32 Lateral accelerations at the top of Pier 2 under V = 200 km/h

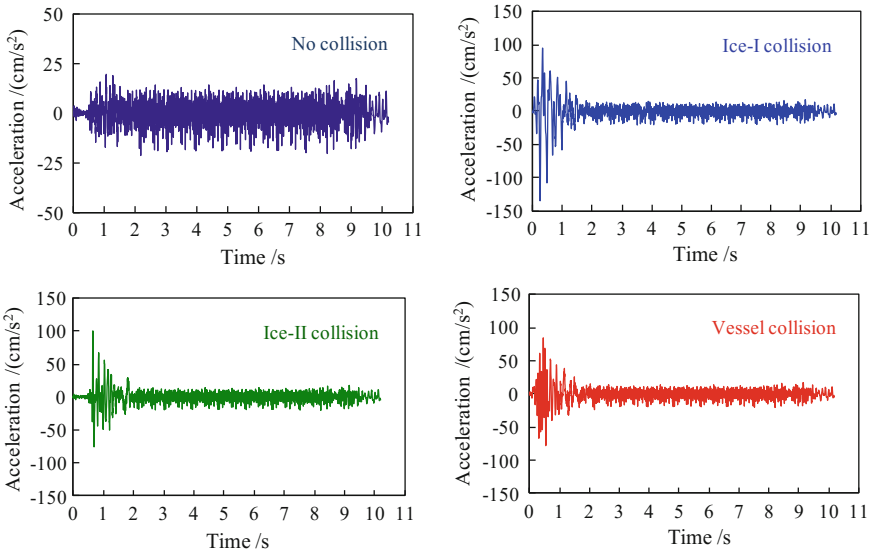

Fig. 8.33 Lateral mid-span accelerations of the 48 m span under V = 200 km/h

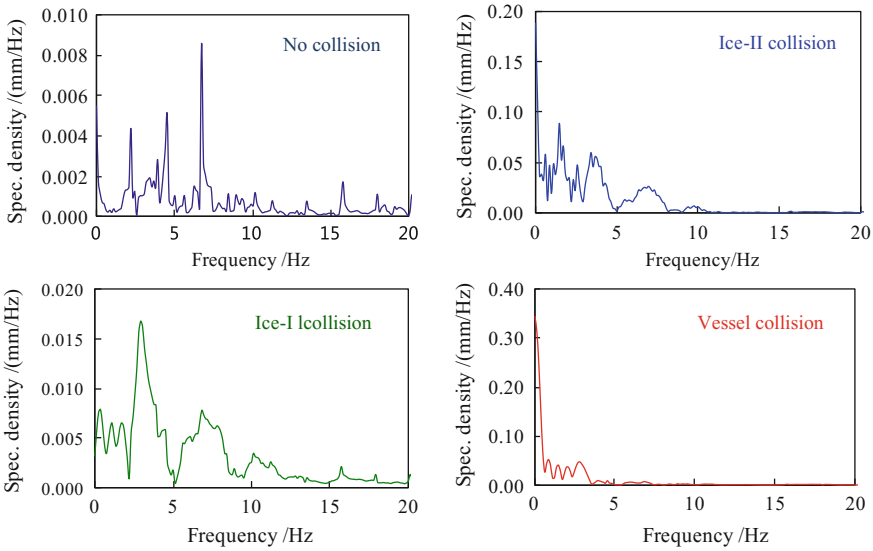

Fig. 8.34 Lateral displacement spectra at the top of Pier 2 under V = 200 km/h

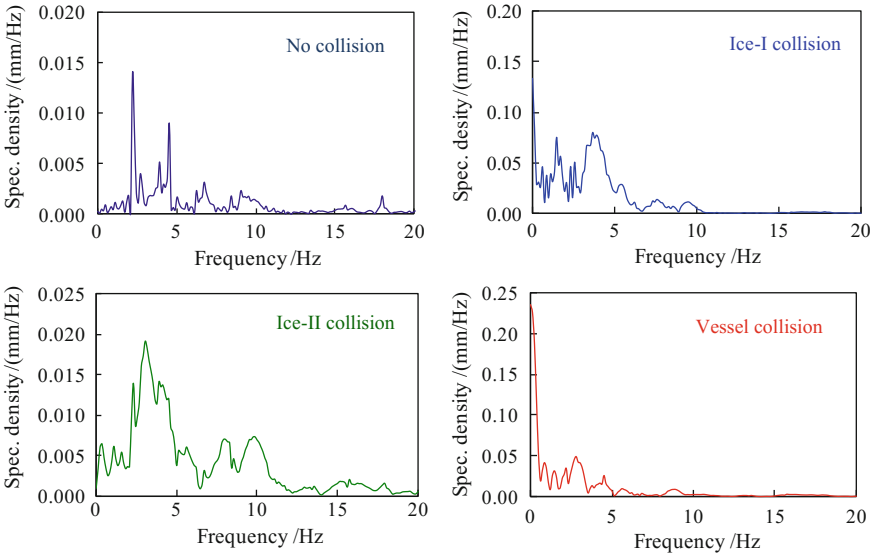

Fig. 8.35 Lateral displacement spectra of the 48 m mid-span under V = 200 km/h

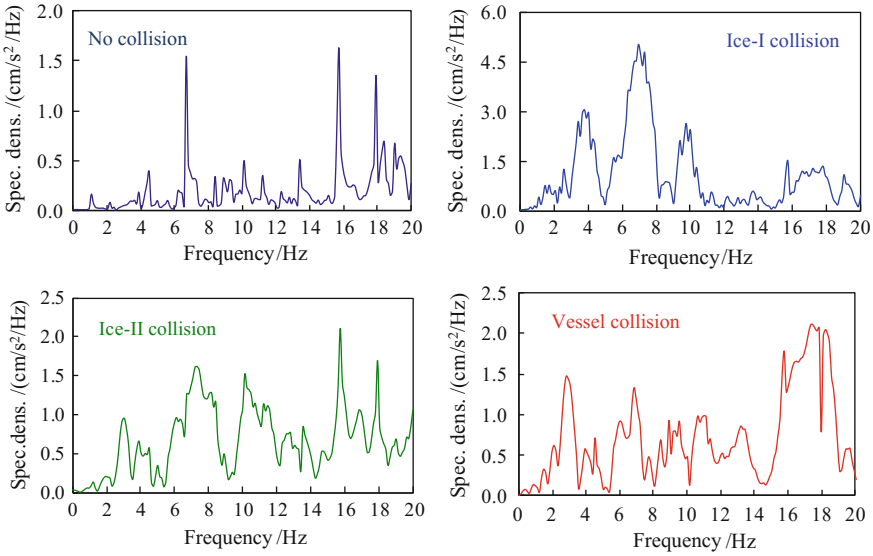

Fig. 8.36 Lateral acceleration spectra at the top of Pier 2 under V = 200 km/h

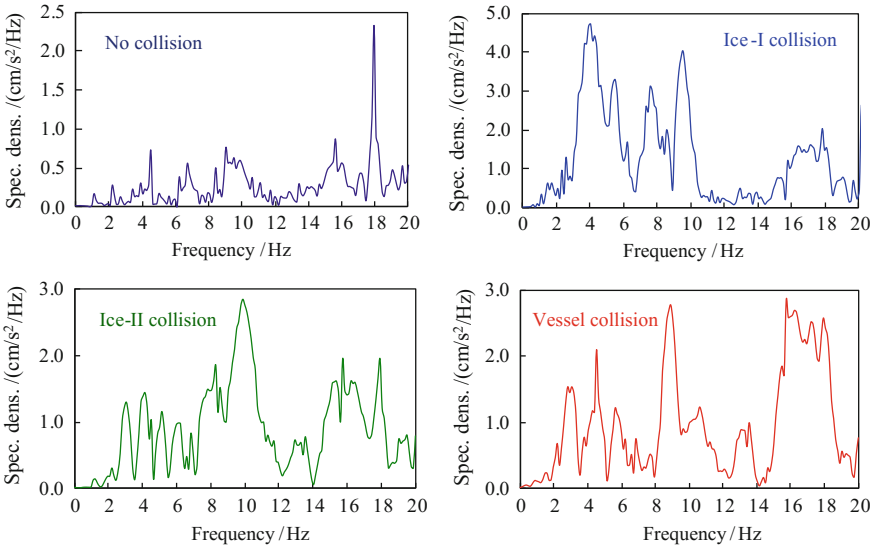

Fig. 8.37 Lateral acceleration spectra of the 48 m mid-span under V = 200 km/h

It can be observed from Figs. 8.34, 8.35, 8.36 and 8.37 that:

In the case without collision, the bridge is excited only by the train. For the lateral displacements, the dominant frequency components concentrate on 2.3 and 4.52 Hz (close to 4.12 Hz, the first lateral bending frequency of the bridge) and 6.71 Hz (exactly the second lateral bending frequency). These dominant frequency components are in the range of the natural frequencies, 0.139–7.394 Hz (see Table 8.6), of the ICE3 train vehicle. The spectra for the pier and the mid-span of girder are similar, except that the peak of 6.71 Hz disappeared in the girder's spectrum, as it corresponds to an antisymmetric mode for the girder.

In the case with a collision, a forced vibration occurs simultaneously induced by the train and collision loads. The three types of collision forces are impulsive loads with relatively short duration, so the acting time on the bridge is shorter than that of the train on bridge. During the collision, they excite much larger vibrations than the train, but owing to the damping, the transient vibration excited by the collision attenuates very fast after the collision.

When the collision finishes, it becomes a mixed response composed of the train-induced forced vibration and the free vibration after collision. Therefore, the frequency spectra for vibrations of the bridge simultaneously subjected to train and collision loads are rather complex. Under the ice-I load with several pulses, the dominant frequency of bridge displacement is 1.46 Hz, which is mainly the loading frequency (Fig. 8.29a). Under the ice-II load with shortest pulse and wide frequency band (Fig. 8.29b), the dominant frequency components of bridge displacement are 3.05 Hz (close to 3.35 Hz, the first vertical bending frequency of the bridge) and 6.96 Hz (close to 6.71 Hz, the second lateral bending frequency). This is because the train travels on one track of the bridge with double tracks, which induces a coupled lateral-vertical vibration when the bridge is acted on by a lateral collision. Under the vessel load with a wider continuous pulse, the vibration frequency spectrum shows clearly the quasi-static component, which is mainly due to the quasi-static component of the load (Fig. 8.29c).

For the lateral acceleration responses of the bridge, the frequency spectra are more complex. In the case without collision, the dominant frequencies appear at 2.3, 4.5, and 6.7 Hz for the pier, but again only 2.3 and 4.5 Hz for the girder. Under the collision loads, in addition to the dominant frequencies apparent in the displacement spectra, there appear many peaks at higher frequencies, such as 9.52 Hz for the ice-I load, 10.1 Hz for the ice-II load, and 8.91 Hz for the vessel load, which are close to 9.23 Hz, the third lateral bending frequency of the bridge. Different from the displacement spectra, there is no quasi-static component in any of the acceleration spectra.

To further compare the influence of different collision loads, the maximum lateral displacements and accelerations of the bridge under ice-I load, ice-II load, and vessel load with the collision intensities of 5 MN, 10 MN, and 15 MN are shown in Figs. 8.38, and 8.39, respectively.

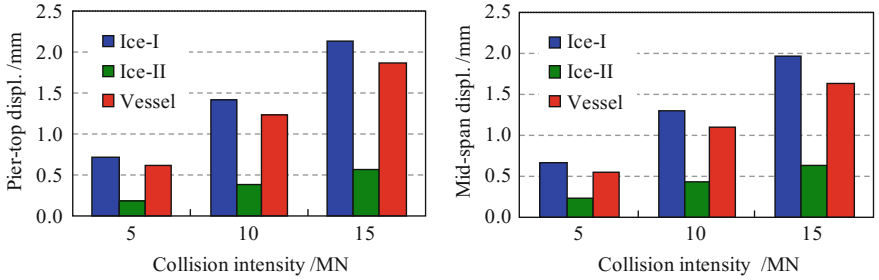

Fig. 8.38 Comparisons of maximum lateral displacements of the bridge at pier-top and mid-span under different collision loads (V = 200 km/h)

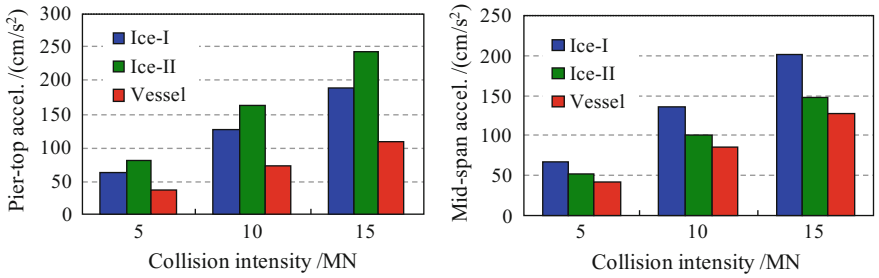

Fig. 8.39 Comparisons of maximum lateral accelerations of the bridge at pier-top and mid-span under different collision loads (V = 200 km/h)

It can be observed from the figures that:

(1) For the collision loads with the same intensity, the maximum displacement of a structure mainly depends on the duration lengths of the loads. From Fig. 8.38, it can be seen that the lateral displacements of the bridge induced by the ice-II load with the shortest duration is the smallest, while the displacements induced by the ice-I load with the longest duration and repeated impacts are bigger than those by the other two collision loads.

(2) The bridge accelerations are mainly influenced by the loading rate of the collision loads. For the three collision loads with the same intensity, the ice-II load with the shortest pulse width (0.06 s) produces the biggest pier-top acceleration and shows the most obvious impact effect. The ice-I load has an obvious peak at its first pulse, which induces a slightly smaller pier-top acceleration than that by the ice-II load. On the other hand, the ice-I load reveals the biggest mid-span acceleration. The accelerations caused by the vessel load, the smallest accelerations, have a relatively steady course, experience a relatively long time to reach their peak, which weakens the impact effect.

8.3.3 *Dynamic Responses of the Train*

Shown in Figs. 8.40, 8.41, and 8.42 are, respectively, the derailment factors, offload factors, and lateral wheel-rail forces of the first car, when the ICE3 train travels on the bridge at V = 200 km/h, without collision and under three collision loads.

It can be seen from the figures that the running safety indices of the train are strongly affected by the collision loads. When the ICE3 train travels on the (32+48+32) m continuous bridge under either of the three collision loads, the derailment factors, offload factors, and lateral wheel-rail forces exhibit obvious difference compared to those without collision. After the impact of collisions, there appear oscillations with large amplitude in the curves, and the peaks of the indices are greatly increased.

Shown in Table 8.5 for comparison are the maximum running safety indices of the train traveling on the bridge at the speed of 200 km/h without collision load and under the three collision loads.

The limits in the table are the criterion for train running safety adopted in the train-bridge coupling dynamic analysis and the joint debugging and commissioning test of Beijing-Shanghai HSR line, namely derailment $Q/P \leq 0.8$, offload factor $\Delta P/P \leq 0.6$, and lateral wheel-rail forces 52.97 kN and 49.08 kN for the motor-car and trailer-car of ICE3 train, corresponding to their static loads of 156.96 kN and 143.22 kN, respectively.

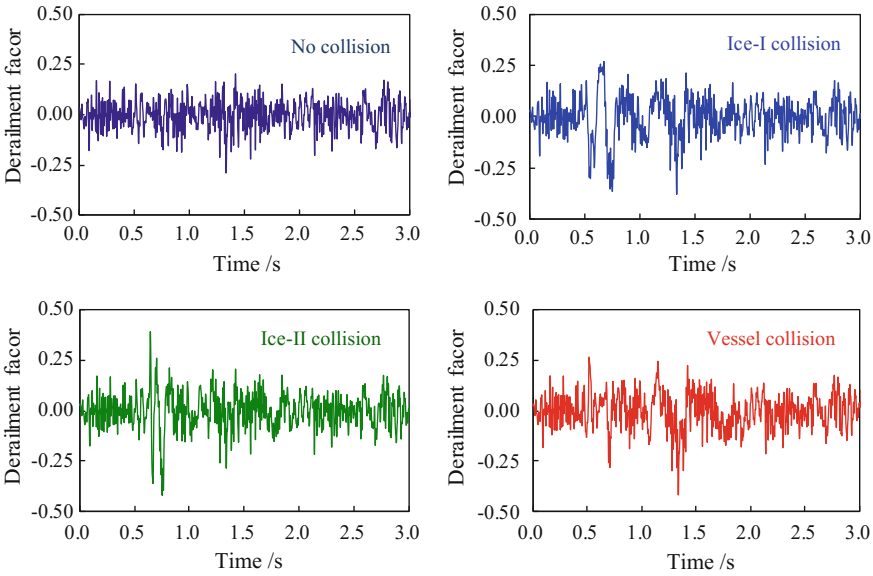

Fig. 8.40 Derailment factor histories of the first car under V = 200 km/h

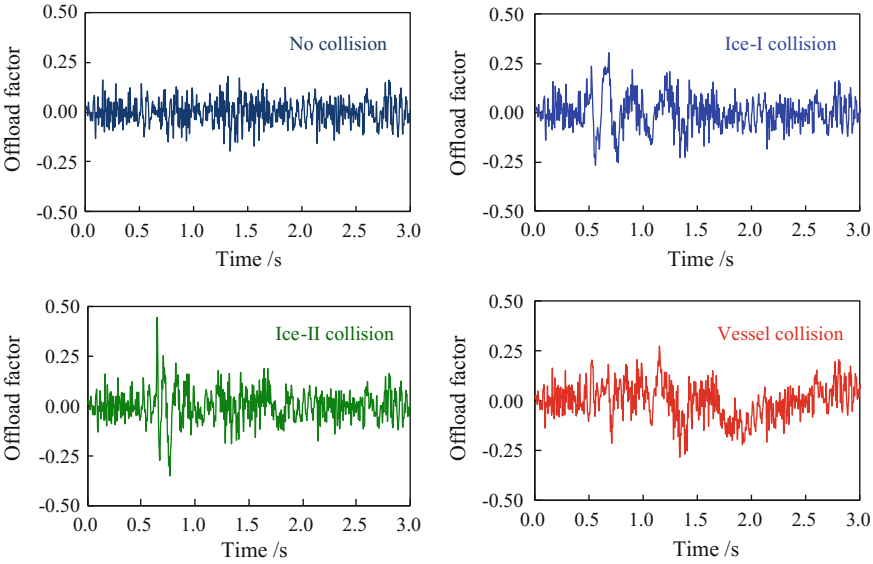

Fig. 8.41 Offload factor histories of the first car under V = 200 km/h

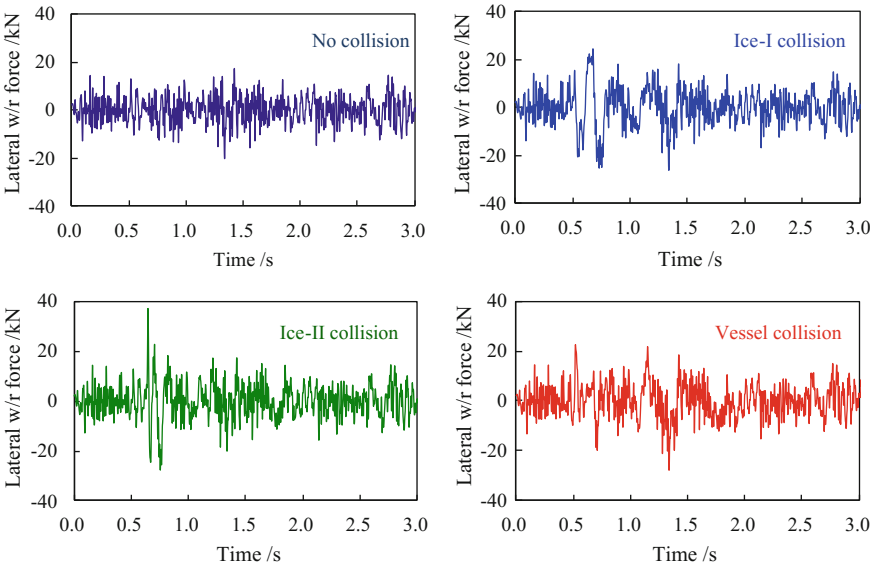

Fig. 8.42 Lateral wheel-rail force histories of the first car under V = 200 km/h

Table 8.5 Maximum running safety indices of ICE3 train on the bridge subjected to various collision loads (V = 200 km/h)

Running safety index		Without collision	With collision loads			Allowance
			Ice-I load	Ice-II load	Vessel load	
Derailment factor Q/P		0.292	0.381	0.424	0.422	0.8
Offload factor ΔP/P		0.196	0.306	0.461	0.293	0.6
Lateral wheel-rail force (kN)	Motor-car	20.535	26.393	37.430	28.110	52.97
	Trailer-car	19.247	20.945	20.046	20.756	49.08

It can be summarized from Figs. 8.40, 8.41, and 8.42, and Table 8.5 that:

(1) There appear strong shock waveforms in the time history curves of the derailment factor, offload factor, and lateral wheel-rail force when the collision load is applied on the bridge. The durations last about 1.5 s, which are shorter than those observed in the bridge responses. For these collision loads, the impact effect induced by the ice-II load is the most intense, indicating that the running safety indices are more influenced by a collision load with a short pulse.
(2) Under the collision loads, the maximum values for the running safety indices are greatly amplified: The derailment factors increase from 0.292 to 0.381 $\sim$ 0.424 by 30.5% $\sim$ 45.2%, the offload factors increase from 0.196 to 0.293 $\sim$ 0.461 by 49.5% $\sim$ 135.2%, and the lateral wheel-rail forces increase from 20.535 to 26.393 $\sim$ 37.43 by 28.5% $\sim$ 82.3%, respectively.
(3) When the bridge is excited by any of the three collision loads with maximum impact force 10 MN, the derailment factor, offload factor, and lateral wheel-rail force of the train running at V = 200 km/h are within the corresponding safety allowances in the Chinese code.

8.4 Influence of Collision Effect on Running Safety of High-Speed Train

The running safety of high-speed trains on railway bridges subjected to collision is an issue of concern in railway engineering. In this section, with the same bridge and track irregularity parameters given in Sect. 8.3.1, the effect of collision on the running safety of train is investigated by considering different train speeds, collision force intensities, and train types. The maximum values of running safety indices, which are taken from the corresponding time histories of all wheel-sets during passage of the train on the bridge, are used for comparison and are evaluated according to the safety evaluation indices.

8.4.1 Influence of Train Speed

While keeping the parameters of the bridge and the ICE3 train unchanged, the train speed is varied from 200 km/h to 320 km/h. The collision intensities are normalized as 5 MN. The curves of maximum derailment factors, offload factors, and lateral wheel-rail forces of motor-car and trailer-car versus train speed are shown in Fig. 8.43, in which the curves related to the "without collision" case have been also included. The horizontal dashed lines represent the related allowance values.

As shown in Fig. 8.43, the increasing tendency of the train running safety indices with the train speed is obvious. Generally, the higher the train speed, the bigger the running safety indices. When the train speed is 320 km/h, the derailment factor under ice-I load exceeds the allowable value, and when the train speed is 350 km/h, the offload factors and lateral wheel-rail forces of trailer-car under all collision loads exceed their related allowances.

8.4.2 Influence of Collision Load Intensity

Using the parameters of the bridge and the ICE3 train and keeping the load shapes and durations unchanged, the influence of collision intensity on the running safety indices is analyzed, by changing the collision intensities from 0 MN to 20 MN. The

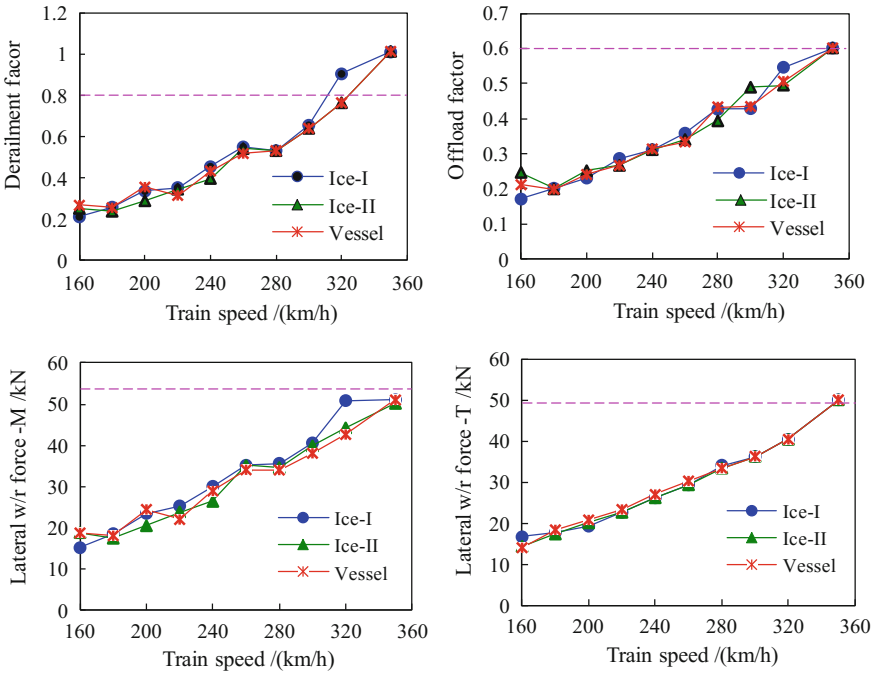

Fig. 8.43 Distributions of running safety indices versus train speed (F_c = 5 MN)

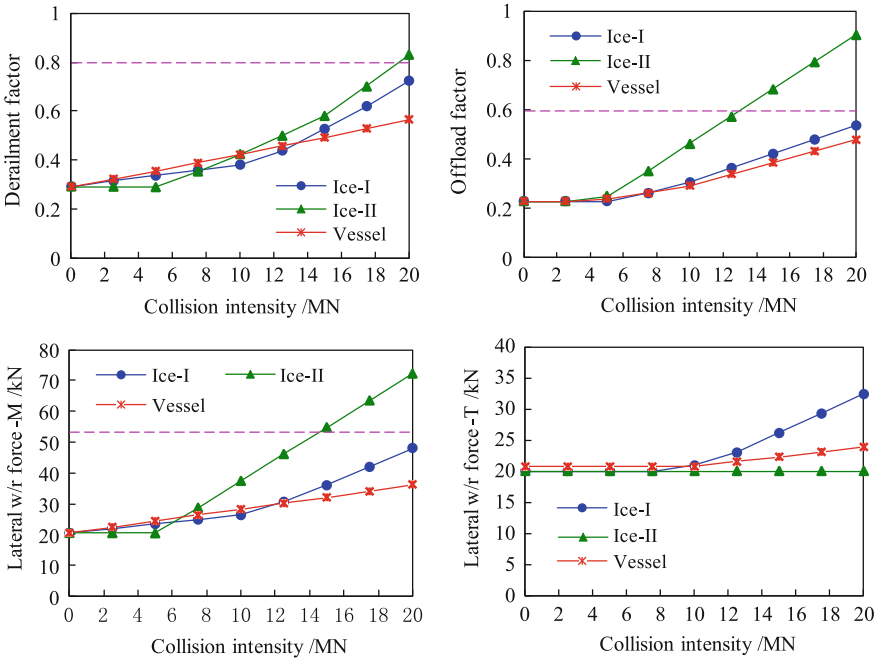

Fig. 8.44 Distributions of running safety indices versus collision intensity (V = 200 km/h)

train speed is 200 km/h. The distribution curves of maximum derailment factors, offload factors, and lateral wheel-rail forces versus collision intensities for the three collision loads are shown in Fig. 8.44, in which the horizontal dashed lines represent the related allowances.

Referring to these figures for the three collisions, the effect of collision intensity on the running safety of the train can be summarized as follows:

(1) The increase of vehicle running safety indices with collision intensity is obvious. Generally, the higher the collision intensity, the bigger the running safety indices, especially when the collision intensity is greater than 5 MN (for the derailment factor, offload factor, and lateral wheel-rail force of motor-car) or 10 MN (for the lateral wheel-rail force of trailer-car).
(2) The influence on the train running safety by the ice-II load with the shortest duration is the most obvious. The ice-I load has a minor influence and the vessel load the smallest.
(3) When the collision intensity of the ice-II load exceeds 15 MN, the offload factor and lateral wheel-rail force of trailer-car exceed the related allowances. For the ice-I load and the vessel load, when the collision intensity is less than 20 MN, the running safety of train can be ensured.

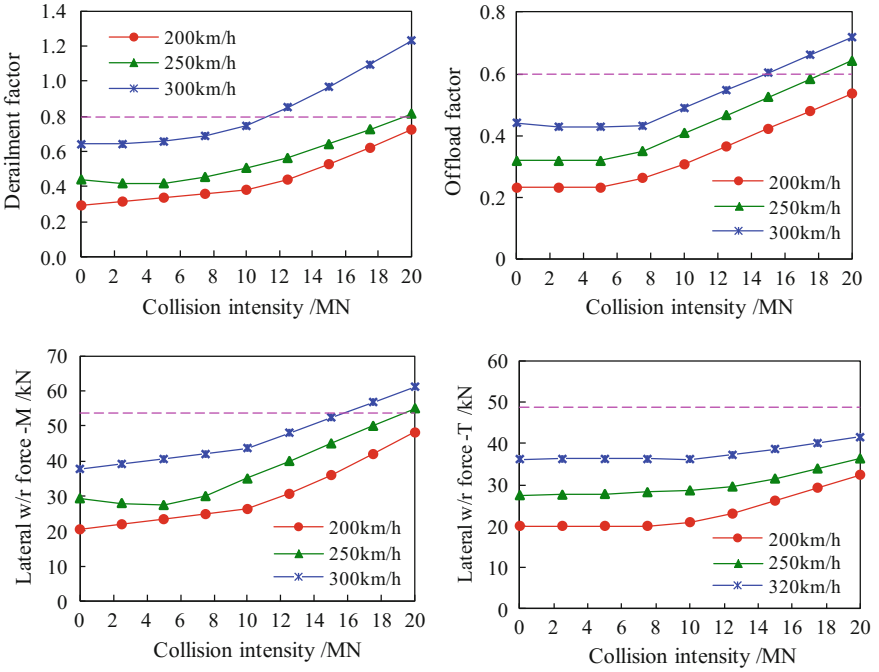

Fig. 8.45 Distributions of running safety indices of ICE3 train versus collision intensity of ice-I load

Shown in Fig. 8.45 are the distribution curves of maximum derailment factors, offload factors, and lateral wheel-rail forces versus collision intensity of the ice-I collision load, by considering three train speeds of 200, 250, and 300 km/h.

From the figures, it can be seen that the distribution curves under the three train speeds have the same tendency: All the train running safety indices increase obviously with the collision intensity. Under the train speed of V = 300 km/h, the derailment factor exceeds the allowance at collision intensity of 12.5 MN, and under V = 250 km/h, the derailment factor, offload factor, and motor-car lateral wheel-rail forces exceed the related allowances at collision intensity of 20 MN.

For better displaying the distributions of running safety indices versus train speed and collision intensity, Fig. 8.46 gives the 3-D graphs. The graphs clearly show how the indices increase with train speed and collision intensity and exceed their safety allowances under certain conditions, to form the respective dangerous zones.

8.4.3 Influence of Train Types

Three types of high-speed trains, Germany ICE3, Japan E500, and China CRH2 with the same composition of 4 × (3 motor-car +1 trailer-car), are considered to analyze the influence of train types on the running safety indices of train vehicles.

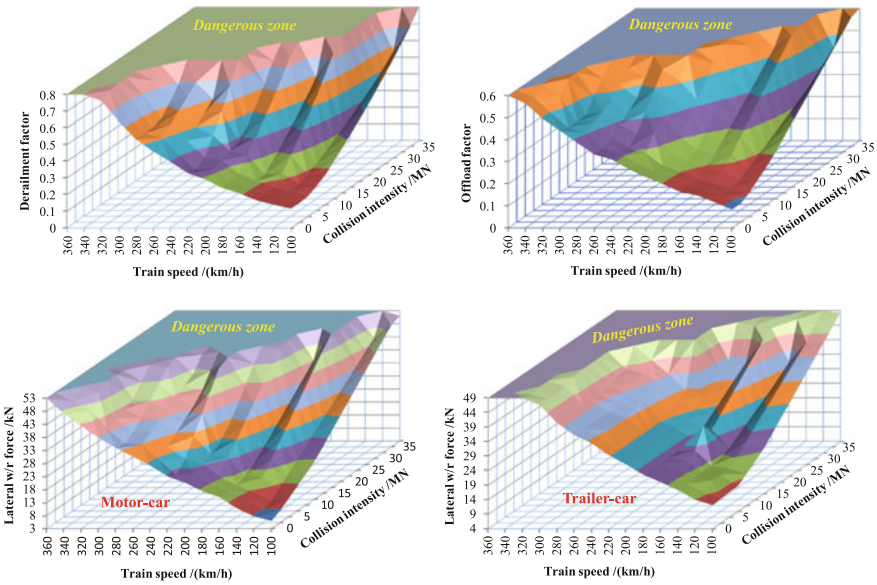

Fig. 8.46 Three-dimensional distribution graphs of train running safety indices versus train speed and collision intensity of ice-I load

For understanding the train-bridge interaction, it is useful to calculate the eigen-frequencies and eigen-modes of the vehicles. Summarized in Table 8.6 are the eigen-frequencies and the corresponding mode shape descriptions of the

Table 8.6 Calculated modal parameters of the train vehicles

Mode description	Frequency (Hz)					
	ICE3		E500		CRH2	
	Motor	Trailer	Motor	Trailer	Motor	Trailer
Vertical movement of car-body	0.588	0.527	0.691	0.730	0.652	0.699
Pitching movement of car-body	0.656	0.568	0.966	0.772	0.937	0.681
Yawing movement of car-body	0.561	0.601	1.126	0.751	0.703	0.704
Lateral-and-rolling movement of car-body, lateral and rolling swings in phase	0.195	0.139	0.437	0.369	0.321	0.381
Lateral-and-rolling movement of car-body, lateral and rolling swings out of phase	0.572	0.641	0.687	0.872	0.805	0.891
Lateral movement of bogie	6.961	7.394	12.765	12.467	10.667	11.834
Vertical movement of bogie	4.396	4.203	4.398	5.621	4.371	4.848

Table 8.7 Allowable values of lateral wheel-rail forces

Type of train	Car type	Static axle load P_{st} (kN)	Allowable lateral wheel-rail force (kN)
Germany ICE3 EMU	Motor	156.96	52.972
	Trailer	143.23	49.082
Japan E500 EMU	Motor	127.53	44.634
	Trailer	134.89	46.718
China CRH2 ENU	Motor	132.44	46.025
	Trailer	117.72	41.854

vehicle. One can find that the three trains have quite different frequencies for all the modes.

The running safety indices for the trains are calculated: For all train types, the allowance values for the derailment and the offload factor are, respectively, 0.8 and 0.6. Owing to the different axle loads of the considered trains, the allowance values for the lateral wheel-rail forces are separately given in Table 8.7.

The ice-I load is adopted with the collision intensities from 0 MN to 20 MN, and the train speed is 200 km/h. Shown in Fig. 8.47 are the curves of the running safety indices for different trains versus collision intensity, in which the dashed, dotted,

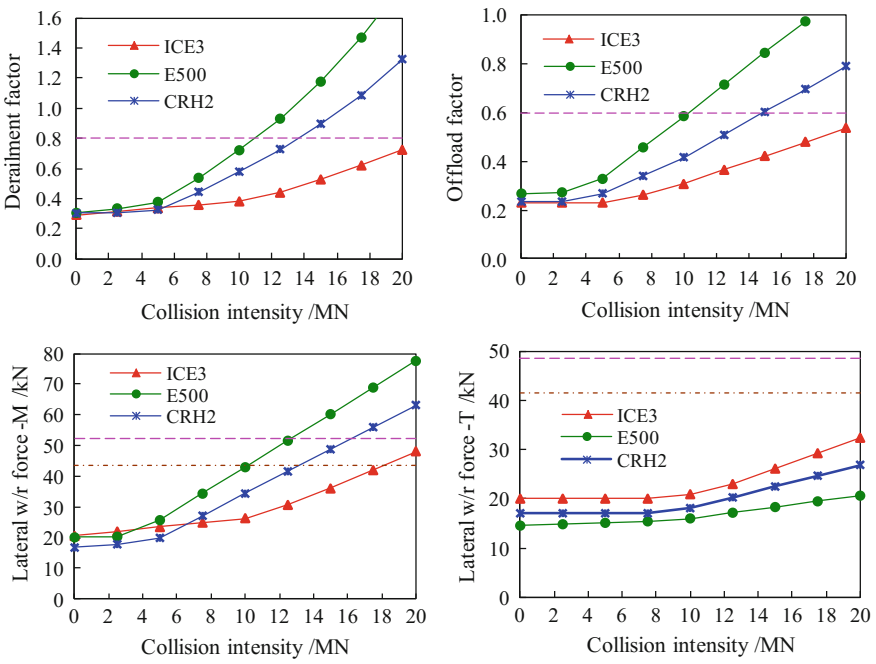

Fig. 8.47 Distributions of running safety indices of different trains versus collision intensity of ice-I load (V = 200 km/h)

and solid horizontal lines represent, respectively, the related allowable values for the ICE3, E500, and CRH2 trains.

Referring to these figures, the influence of train types on the train running safety indices can be summarized as follows:

(1) All the running safety indices of different trains increase with the collision intensity, especially for collision forces bigger than 5 MN.
(2) The influence of collision on the E500 train is the biggest, and the second is on the CRH2 train, while the influence on the ICE3 is the smallest. For the derailment factors, offload factors, and lateral wheel-rail forces, the E500 train exceeds the related allowances when the collision intensity reaches 12.5 MN, and so does the CRH2 train when the collision intensity reaches 15 MN.

Keeping the collision intensity of ice-I load as 5 MN, the running safety indices for ICE3, E500, and CRH2 trains at the speeds of 200 ∼ 350 km/h are calculated, as shown in Fig. 8.48.

As seen in the figures, when the ice-I load is 5 MN, the distributions of running safety indices of three types of trains versus train speed can be summarized as follows:

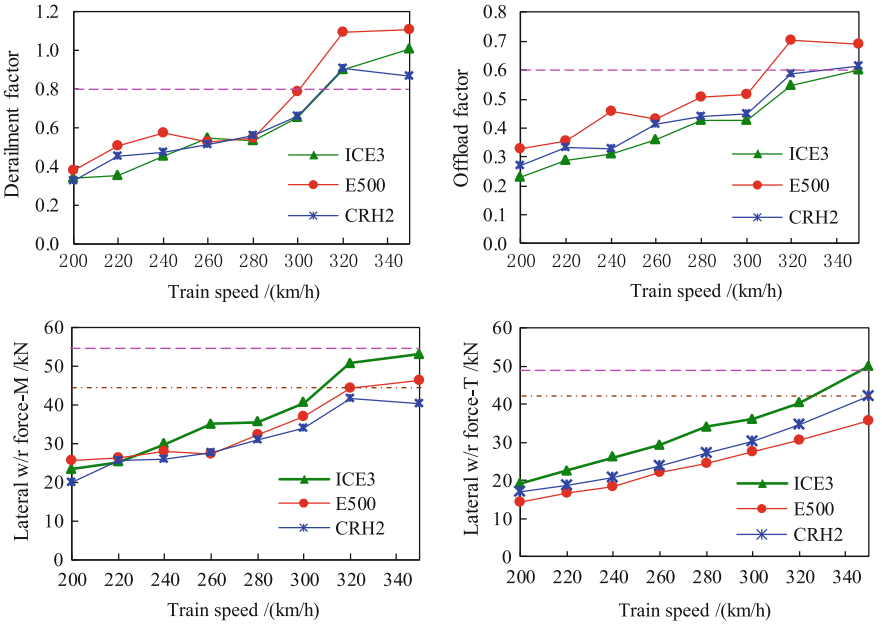

Fig. 8.48 Distributions of running safety indices of different trains versus train speed (ice-I load, F_{max} = 5 MN)

(1) In the main trend, all the indices increase with train speed.
(2) When the train speed reaches 320 km/h, the derailment factors of all the three trains exceed the allowance, and also the offload factor of E500 train. When train speed reaches 350 km/h, the offload factor of CRH2 train exceeds the allowance.
(3) For the train speeds ranged from 200 km/h to 320 km/h, the lateral wheel-rail forces of all the three trains satisfy the allowance. When the train speed reaches 350 km/h, the lateral wheel-rail forces of ICE3 train approaches to or slightly exceeds the allowance.

8.4.4 *Influence of Impulse Form and Duration of Collision Loads*

While keeping the parameters of the bridge and the ICE3 train unchanged, by changing the form and width of the collision load impulse, the derailment factors, offload factors, and lateral wheel-rail forces of ICE3 train are calculated to analyze the influence of impulse form and duration of collision loads on the train running safety. By comprehensively considering the specifications on collision loads in various codes, five types of impulse are adopted for analysis, which are triangular impulse, rectangular impulse, half-sinusoidal impulse, the first impulse of ice-I, and vessel load, as shown in Fig. 8.49. In the figures, F_c is the amplitude, T is the duration, and T_0 is the initial time of the impulse loads.

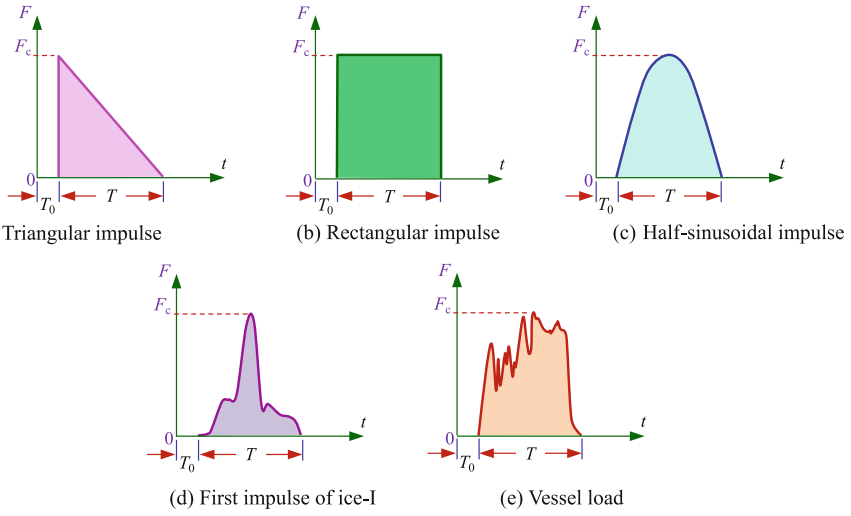

Fig. 8.49 Waveforms of various impulse loads

Keeping the train speed of 200 km/h and load intensity of 5 MN, the derailment factors, offload factors, and lateral wheel-rail forces of ICE3 train under various collision loads with impulse width 0.05 ~ 5 s are calculated, as shown in Figs. 8.50, 8.51 and 8.52.

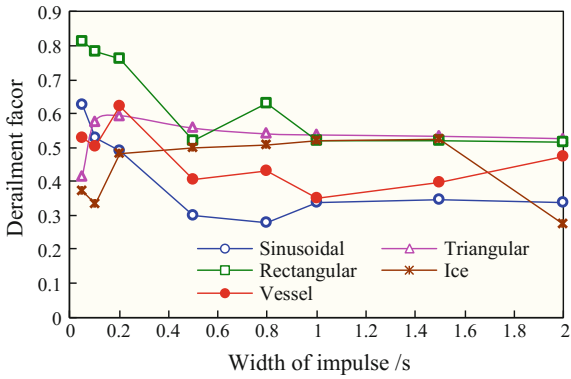

Fig. 8.50 Distributions of derailment factors versus impulse width under various collision loads

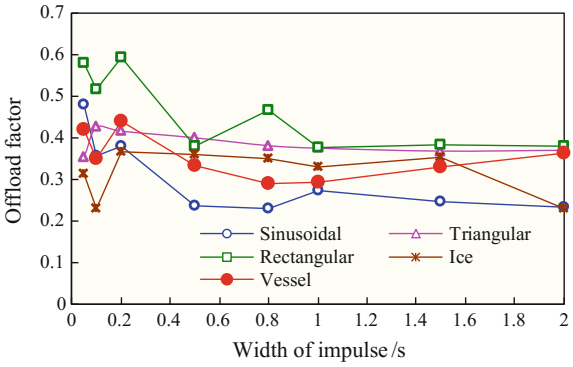

Fig. 8.51 Distributions of offload factors versus impulse width under various collision loads

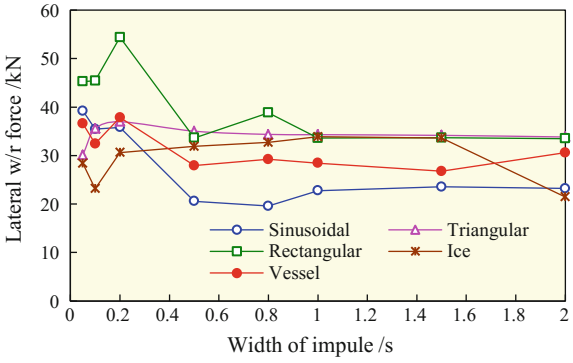

Fig. 8.52 Distributions of lateral wheel-rail forces of motor-car versus impulse width under various collision loads

Referring to these figures, the influence of impulse form and duration of collision loads on the running safety indices of the train can be summarized as follows:

(1) For collision loads with the same duration, the rectangular impulse affects the train running safety most, because it loads on and unloads from the pier as a step function with the most fast loading rate. For the triangular impulse, it loads on the pier as a step form but unloads gradually, so it has smaller effect.
(2) With the decrease of pulse width, the influence on train running safety is enlarged. For the rectangular impulse load less than 0.2 s (smaller than the fundamental natural period of the bridge, i.e., 0.24 s), the interval between loading and unloading is very short, so the impact effect is the most obvious, when the derailment factor, offload factor, and lateral wheel-rail force of ICE3 train approach to or exceed the allowances.
(3) In the five loads, the first impulse of ice-I load has the lowest loading rate, so when the impulse width is less than 0.2 s, its effect on train running safety is the smallest.
(4) In general, short impulsive loads (especially when $T < 0.2$ s) have more influence on the train running safety. When $T > 1.0$ s, the indices change little with impulse width.

8.5 A Framework for Running Safety Assessment of High-Speed Train on Bridge Subjected to Collision Loads

The previous analyses show that the running safety indices of the train are influenced by the types and intensities of the collision loads, and also the types and the speeds of the trains. To ensure the running safety of trains on bridges subjected to collision loads, a further simulation is performed to find out an assessment method and the corresponding thresholds.

8.5.1 Analysis Method

Collision intensity and train speed are the two main factors affecting the running safety of train. The threshold speed of trains can be determined according to the safety evaluation indices in the following way:

(1) Keeping the collision intensity as a constant at each stage, the dynamic responses of the train are calculated by changing the train speed from 100 km/h to 360 km/h with an increment of 20 km/h. The running safety indices (derailment factors, offload factors, and lateral wheel-rail forces) are calculated and compared with the related allowances. If any of these allowances is

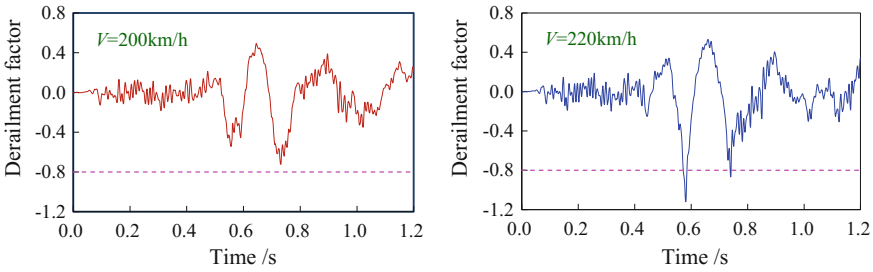

Fig. 8.53 Determination of the critical train speed for train running safety corresponding to a collision intensity of 20 MN

exceeded, the previous lower train speed is considered as the critical train speed for the corresponding collision intensity.

For example, as shown in Fig. 8.53, corresponding to the ice-I load with the intensity of 20 MN, the derailment factor of the train at V = 200 km/h is 0.724, which meets the allowance value of 0.8 (the dashed line in the figure). While at V = 220 km/h, the derailment factor increases to 1.119, which exceeds the allowance. At this time, no matter whether the offload factor and the lateral wheel-rail force exceed the related allowance values or not, V = 200 km/h is regarded as the critical train speed corresponding to the collision intensity of 20 MN.

(2) Then, the collision intensity is changed from 0 MN (no collision) with an increment of 2.5 MN. For each kind of collision intensity, the dynamic responses of the train vehicles are calculated at different train speeds. In this way, the critical train speeds related to all collision intensities considered are acquired.

Herein, the analysis is limited to the case where the bridge produces strong vibration but is not damaged when it is subjected to collision. Therefore, the collision intensity is limited to 40 MN for this bridge, to ensure the structure can still work in the elastic stage.

8.5.2 Threshold Curves for Running Safety of ICE3 Train on the Bridge Subjected to Ice-I Collision Load

The procedure to determine the threshold curves for train running safety is illustrated by using the continuous bridge, the ICE3 train, and the ice-I collision load as an example. The maximum values of running safety indices are calculated, in the case of the train travelling at different speeds on the bridge subjected to collision loads with different intensities. The results for the derailment factors are listed in Table 8.8.

Table 8.8 Maximum derailment factors with different train speeds and collision intensities

Train speed (km/h)	Collision intensity (MN)															
	0	2.5	5	7.5	10	12.5	15	17.5	20	22.5	25	27.5	30	32.5	35	37.5
100	0.116	0.116	0.121	0.148	0.176	0.222	0.269	0.318	0.369	0.422	0.478	0.536	0.596	0.659	0.726	*0.869*
120	0.140	0.144	0.152	0.16	0.18	0.211	0.243	0.277	0.313	0.349	0.387	0.427	0.467	0.517	0.569	
140	0.166	0.166	0.172	0.223	0.295	0.372	0.453	0.541	0.634	0.734	*0.841*	*0.956*	*1.079*	*1.213*	*1.357*	
160	0.208	0.210	0.211	0.216	0.270	0.327	0.387	0.450	0.517	0.589						
180	0.242	0.250	0.258	0.331	0.407	0.486	0.570	0.657	0.748	*0.856*						
200	0.292	0.314	0.336	0.358	0.381	0.439	0.527	0.620	0.724							
220	0.330	0.315	0.353	0.449	0.560	0.681	*0.813*	*0.959*	*1.119*							
240	0.398	0.407	0.454	0.501	0.550	0.600										
260	0.460	0.504	0.550	0.597	0.647	0.698										
280	0.532	0.532	0.532	0.553	0.618	0.686										
300	0.640	0.641	0.655	0.688	0.745	*0.852*										
320	0.764	0.793	*0.904*	*0.904*	*1.023*											
340	*0.895*	*0.895*														

It can be noticed that the maximum derailment factor increases with the train speed in general for each collision intensity, and it will exceed the allowance of 0.8 when the train speed reaches a certain value. The train speed at the previous lower level is regarded as the critical train speed corresponding to this collision intensity. Similar tables can be obtained for the offload factors and the lateral wheel-rail forces.

By plotting the calculated results in a coordinate system, with the abscissa representing the collision intensity and the ordinate the train speed, a group of relationship curves between the critical train speed and the collision intensity can be obtained, as shown in Fig. 8.54. The curves define the boundary of safety zones for the high-speed train on the bridge subjected to collision with various intensities, corresponding to the derailment factors, offload factor, and lateral wheel-rail forces of motor-car and trailer-car, respectively.

The curve in each figure divides the whole zone into two parts. In the lower left zone, the running safety index meets the related allowance given in Table 8.5, indicating that the running safety of the train can be ensured, while in the upper right zone, the index exceeds the related allowance, indicating that the running safety of the train cannot be guaranteed.

Furthermore, the lowest critical train speeds for different collision intensities are connected, forming an inscribed curve, as the thick line shown in Fig. 8.55. This inscribed curve divides the whole zone into two parts. In the lower left zone, all the running safety indices meet the related allowances, indicating that the running safety of the train is ensured, while in the upper right zone, at least one of the

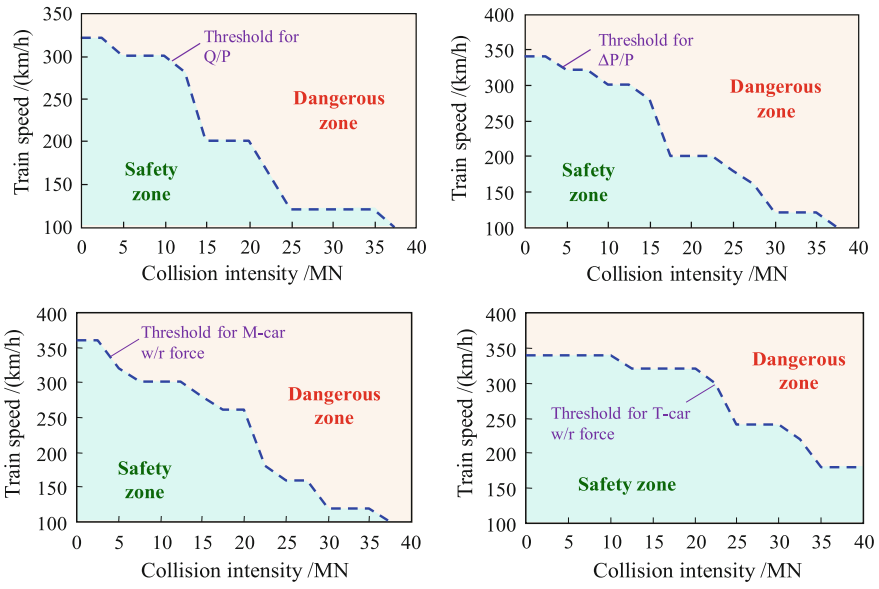

Fig. 8.54 Threshold curves of train speed versus impact intensity for running safety of ICE3

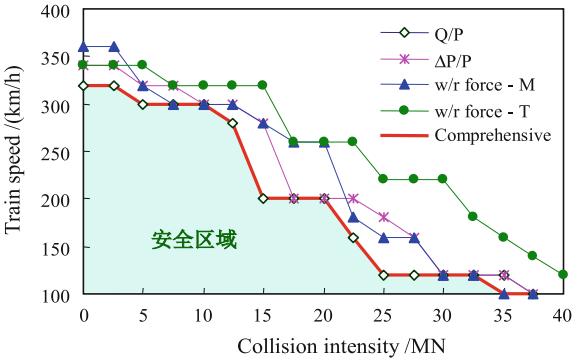

Fig. 8.55 Threshold curves of train speed versus impact intensity for running safety of ICE3 train considering ice-I collision loads

indices exceeds the related allowance, indicating that the running safety of the train cannot be guaranteed.

From the figure, it can be observed that the running safety indices of the train are influenced comprehensively by the collision intensity and the train speed.

(1) The greater the collision intensity, the lower the allowable train speed for running safety. In the case without collision load, all indices meet the related allowances for the train speed up to 320 km/h. With the increase of collision intensity, the train should gradually lower its speed to ensure the running safety. When the collision intensity reaches 35 MN, the train can only run safely at the speed of 100 km/h.

(2) The higher the train speed, the smaller the collision intensity that the train-bridge system can sustain. At V = 200 km/h, the train can run safely for a collision intensity up to 20 MN; at V = 250 km/h, the allowable collision intensity is lowered to less than 15 MN; while at V = 300 km/h, only 5 MN collision intensity is allowed to ensure the train running safety.

8.5.3 Comparison of Running Safety Thresholds for Different Collision Loads

Some bridges may suffer different types of collision loads. For example, for a bridge across a river that freezes in winter while it is open to navigation in summer, it may be collided by a vessel in summer as well as by ice-floes in early spring. Considering this case, the running safety threshold curves for the ice-II load and vessel load are also obtained in a similar way, and the three curves are plotted in a same figure, as shown in Fig. 8.56.

Because the different collisions do not happen at the same time, a comprehensive threshold curve for running safety of the ICE3 train is acquired, which is the inscribed curve that connects the lowest critical train speeds for each of the three collision loads, as the thick line shown in the figure.

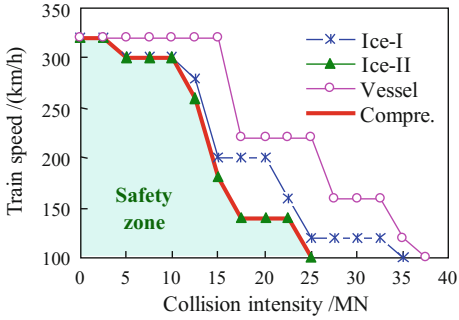

Fig. 8.56 Threshold curves of train speed versus impact intensity for running safety of ICE3 train under various collision loads

From all three collision loads, the ice-II load has the biggest influence on the running safety of the ICE3 train. For example, for the vessel load of 15 MN, the safety train speed is V = 320 km/h, for the ice-I load, it is lowered to 200 km/h, while for the ice-II load, the train can only run safely at 180 km/h. Thus, the boundary of safety zone is decided mainly by the ice-II load.

Comprehensively considering three types of loads, when the collision intensity F_c = 15 MN, the running safety of the ICE3 train at the speeds of 200 km/h and 250 km/h will be affected; while when F_c = 10 MN, the speed limit for ICE3 train will be 300 km/h.

8.5.4 *Comparison of Running Safety Thresholds for Different Trains*

Similar to Fig. 8.56 for the ICE3 train, the threshold curves can be obtained for the E500 and CRH2 trains, as shown in Fig. 8.57, to study the effects of collision on different types of high-speed trains.

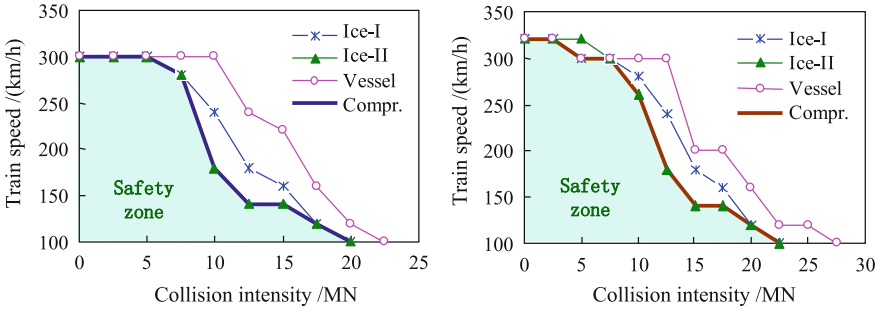

Fig. 8.57 Threshold curves of train speed versus impact intensity for running safety of E500 and CRH2 trains under various collision loads

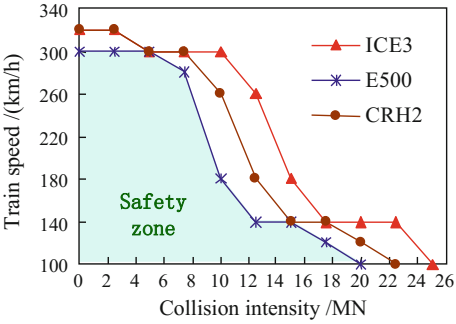

Fig. 8.58 Comparison of running safety threshold curves for different trains

It is observed from Figs. 8.56 and 8.57 that obvious differences exist between the threshold curves for different trains. Comparatively for the three trains, the ice-II load has the biggest influence on the running safety of the trains. This is especially true for the ICE3 and E500 trains where the threshold curves are completely determined by the ice-II load.

The comprehensive threshold curves for the three trains (the inscribed curves in Figs. 8.56 and 8.57) are resumed in Fig. 8.58.

Referring to the figure, the influence of train types on the running safety of trains can be summarized as follows:

(1) With the increase of collision intensity, the train has to lower its speed to ensure the running safety. For example, the safety train speed for E500 is 300 km/h for the collision intensity up to 5 MN, and it is 280 km/h for the collision intensity of 7.5 MN, while it can only run at a speed lower than 200 km/h when the collision intensity is 10 MN.

(2) Considering all three collision loads, the running safety threshold curves for the three trains show the same tendency: E500 is the most sensitive to collision, CRH2 is the second, and ICE3 is the less sensitive. For example, the E500 can run safely at 300 km/h when no collision is applied on the bridge. When the collision intensity reaches to 20 MN, the safe train speed of E500 is lowered to 100 km/h, while under the same intensity, CRH2 can run at 120 m/h and ICE3 at 140 km/h. Only when the collision intensities reach to 22.5 MN and 25 MN, the safe running speeds of CRH2 and ICE3 trains reduce to 100 km/h.

(3) From the above analysis and referring to Tables 8.7 and 8.8, one can notice that for the three types of trains, E500 has the lightest axle load and the highest natural frequencies (especially those of the bogies), while ICE3 has the heaviest axle load and the lowest natural frequencies. For a train vehicle, higher frequency of the bogie usually means larger suspension stiffness between the bogie and the wheel-sets, so it can be concluded that the running safety of the train with smaller axle load and larger suspension stiffness is more easily influenced when the bridge is collided.

8.6 Conclusions

The following conclusions can be drawn from the case study:

(1) A collision load has an obvious effect on the dynamic responses of the bridge. The lateral displacement and acceleration responses of the bridge subjected to a collision are much greater than the ones without collision. The lateral displacement of the bridge is more influenced by a collision load with a long pulse related to the natural period of the bridge, while the acceleration is more influenced by a load with a short pulse and a fast loading rate.
(2) Vibrations induced by collision loads have a great effect on the dynamic responses of high-speed trains. The running safety of the train is affected by both the type and intensity of the collision load acting on the bridge, and the type and running speed of the train. Strong collision may threaten the running safety of high-speed trains. Generally, the greater the collision intensity and the higher the train speed, the bigger the influence of collision on the running safety of the train. The running safety of the train can be evaluated by the threshold curve between train speeds and collision intensities.
(3) For the high-speed train on the bridge, the running safety indices are mainly influenced by the peak value and the width of the pulse of the collision load. The pulse with short duration time and fast loading rate has a bigger influence than the pulse with long duration time and slow loading rate.
(4) The sensitivities of the running safety indices to a collision are dependent on train type. The running safety of the train with lighter axle loads and larger suspension stiffness is more easily affected when the bridge is collided.
(5) The proposed methodology may provide a reference for the dynamic design of railway bridges.

Dynamic analysis of coupled train-bridge systems subjected to collision loads is a rather complex problem, which is related to the running speed of the train, the structural form of the bridge, the intensity, and acting position of the collision load, and many other factors. In this paper, only a preliminary study is performed and illustrated by a case study. The proposed analysis framework and the calculation results may provide a reference for the dynamic design of high-speed railway bridges subjected to vessel collision.

Moreover, in this study, only the case was considered where the bridge produced strong vibration but not damaged when it was subjected to a collision. When the structure is damaged by the collision, the structure may produce plastic deformation, which may not only change the structural properties of the bridge, but also seriously influence the profile of the track on the bridge, inducing a direct derailment risk of the train. This situation is much more complicated and will be considered in the future study.

References

AASHTO (1991) Guide specifications and commentary for vessel collision design of highway bridges (GVCB-2-2009) [S]. American Association of State Highway and Transportation Officials, Washington, D.C

AASHTO (2007) LRFD bridge design specifications [S]. American Association of State Highway and Transportation Officials, Washington, D.C

British Standard (2006) BS EN1991-1-7: Eurocode 1—actions on structures general action: accidental actions [S]

Buth CE (2009) Guidelines for designing bridge piers and abutments for vehicle collisions-semi annual report [S]. Texas Transportation Institute, College Station, TX, USA

Chen C (2006) Simulation research on design ship collision force and damage state of bridge [D]. Yongji University, Shanghai (in Chinese)

Chen XD, Jin XL, Du XG (2008) Simulation analysis of ship-bridge collision based on parallel algorithm [J]. J Vib Shock 27(9):82–86

Consolazio GR, Chung JH, Gurley KR (2003) Impact simulation and full-scale crash testing of a low profile concrete work zone barrier [J]. Comput Struct 81(13):1359–1374

Derucher KN (1984) Bridge pile damage upon vessel impact [J]. Comput Struct 18(5):931–935

Dong JW, Li ZJ, Lu P et al (2012) Design ice load for piles subjected to ice impact [J]. Cold Reg Sci Technol 71(2):34–43

EL-Tawil S, Severino E, Fonseca P (2005) Vehicle collision with bridge piers [J]. J Bridge Eng 10 (3):345–353

European Standard (1991) Eurocode EN1991-1-7: Actions Sur les Structures Partie 1-7: Actions Générales - Actions Accidentelles [S]. Comité Européen de Normalisation

Fan W, Yuan WC (2012) Shock spectrum analysis method for dynamic demand of bridge structures subjected to barge collisions [J]. Comput Struct 90–91:1–12

Guo FW (2010) Analysis of squeezing ice load of vertical structure based on experimental data [D]. Dalian University of Science and Technology, Dalian (in Chinese)

Han Y (2000) Study on calculation method of river ice to bridge pier structure [D]. Harbin University of Civil Engineering and Architecture, Harbin (in Chinese)

He HQ (2004) Finite element simulation of vessel-bridge collision [D]. Yongji University, Shanghai (in Chinese)

He ZX (2008) Study on some mechanical problems in the damage and destruction of road and bridge [D]. Taiyuan University of Science and Technology, Taiyuan (in Chinese)

Hu ZQ, Gu YN, Gao Z, Li YN (2005) Fast evaluation of ship-bridge collision force based on nonlinear numerical simulation [J]. Eng Mech 22(3):235–240 (in Chinese)

JTG D60 (2015) General specifications for design of highway bridges and culverts [S]. Ministry of communications of PRC. People's Communications Press, Beijing (in Chinese)

Laigaard JJ, Svensson E, Ennemark E (1996) Ship-induced derailment on a railway bridge [J]. Struct Eng Int 6(2):107–112

Li SY, Wang SG, Liu WQ et al (2006) Numerical simulations of ship collision with protective devices of bridge pier [J]. J Nat Disasters 15(5):100–106 (in Chinese)

Liu Y (2011) Numerical simulation of dynamic ice action on cross-sea bridge foundation [C]. In: 2nd international conference on mechanic automation and control engineering, MACE, pp 6625–6628

Lu XZ, He YT, Huang SN (2011) Collision between over-height vehicles and bridge superstructures: failure mechanism, design methodology and protective measures [M]. China Architecture and Building Press, Beijing (in Chinese)

Luo L (2008) Study on vessel-bridge collision theory and performance of anti-collision device on the liede bridge [D]. Changsha University of Science and Technology, Changsha (in Chinese)

Larry D, Olson PE (2005) Dynamic bridge substructure evaluation and monitoring [R]. Report No. FHWA-RD-03-089, US Federal Highway Administration

Manen SE (2001) Ship collision due to the presence of bridges [S]. Technical Report, PIANC General Secretariat, Brussels

Manuel L, Kallivokas LF, Williamson EB et al (2006) A probabilistic analysis of the frequency of bridge collapses due to vessel impact [R]. CTR Technical Report: 0-4650-1

NCAC (2010) Finite element model archive [OL]. http://www.ncac.gwu.edu/vml/models.html

Sharma H, Hurlebaus S, Gardoni P (2012) Performance-based response evaluation of reinforced concrete columns subject to vehicle impact [J]. Int J Impact Eng 43(5):52–62

TB10002.1 (2005) Fundamental code for design on railway bridge and culvert [S]. China Railway Press, Beijing

TB10621-2014 (2015) Code for design of high-speed railway [S]. China Railway Press, Beijing

Thilakarathna HMI, Thambiratnam DP, Dhanasekar M, Perera N (2010) Numerical simulation of axially loaded concrete columns under transverse impact and vulnerability assessment [J]. Int J Impact Eng 37(11):1100–1112

Timco GW, Johnston M (2003) Ice loads on the Molikpaq in the Canadian Beaufort Sea [J]. Cold Reg Sci Technol 37(2):51–68

Timco GW (2011) Isolated ice floe impacts [J]. Cold Reg Sci Technol 68(2):35–48

Tuhkuri J (1995) Experimental observations of the brittle failure process of ice and ice-structure contact [J]. Cold Reg Sci Technol 23:265–278

Wang JJ, Chen C (2007) Simulation of damage for bridge pier subjected to ship impact [J]. Eng Mech 24(7):156–160 (in Chinese)

Wang JJ, Yan HQ, Qian Y (2006) Comparisons of design formula of ship collision for bridges based on FEM simulations [J]. J Highw Transp Res Dev 23(2):68–73

Wang LL, Yang LM, Huang DJ, Zhang ZW, Chen GY (2008) An impact dynamics analysis on a new crashworthy device against ship–bridge collision [J]. Int J Impact Eng 35(8):895–904

Wuttrich R, Wekezer J, Yazdani N, Wilson C (2001) Performance evaluation of existing bridge fenders for ship impact [J]. J Perform Constr Facil ASCE 15(1):17–23

Wu WH, Yu BJ, Xu N, Yue QJ (2008) Numerical simulation of dynamic ice action on conical structure [J]. Eng Mech 25(11):192–196 (in Chinese)

Xia CY (2012a) Dynamic responses of train-bridge system subjected to collision loads and running safety evaluation of high-speed trains [D]. Beijing Jiaotong University, Beijing (in Chinese)

Xia CY, Lei JQ, Zhang N et al (2012b) Dynamic analysis of a coupled high-speed train and bridge system subjected to collision load [J]. J Sound Vib 331(10):2334–2347

Xia CY, Xia H, Zhang N et al (2013) Effect of truck collision on the dynamic response of train-bridge systems and running safety of high-speed trains [J]. Int J Struct Stab Dyn 13(3):1–18

Xia CY, Xia H, De Roeck G (2014) Dynamic response of a train-bridge system under collision loads and running safety evaluation of high-speed trains [J]. Comput Struct 140:23–28

Xia CY, Ma J, Xia H (2015) Dynamic analysis of a train-bridge system to vessel collision and running safety of high-speed trains [J]. Vibroengineering PROCEDIA 5:509–514

Xia CY, Zhang N, Xia H, Ma Q, Wu X (2016) A framework for carrying out train safety evaluation and vibration analysis of a trussed-arch bridge subjected to vessel collision [J]. Struct Eng Mech 59(4):683–701

Xia H, De Roeck G, Goicolea JM (2011) Bridge vibration and controls: new research [M]. Nova Science Publishers, New York

Xu LJ, Lu XZ, Smith ST et al (2012) Scaled model test for collision between over-height truck and bridge superstructure [J]. Int J Impact Eng 49:31–42

Xu LJ, Lu XZ, Guan H, Zhang YS (2013) Finite element and simplified models for collision simulation between over-height trucks and bridge superstructures [J]. J Bridge Eng ASCE 18 (11):1140–1151

Xuan Y, Zhang D (2001) Derailment of train caused by collision between ships and railway bridge pier [J]. Foreign Bridges 4:60–64 (in Chinese)

Yan HQ (2006) Simulation of damage and impact forces for bridge piers subjected to ship collision [D]. Tongji University, Shanghai (in Chinese)

Yu M, Zha XX (2011) Behavior of solid and hollow concrete filled steel tube columns under vehicle impact [J]. Prog Steel Build Struct 13(1):57–64

Yu TL, Yuan ZG, Huang ML (2009a) Experiment research on mechanical behavior of river ice [C]. In: Proceedings of the 19th international symposium on ice, Vancouver, pp 519–530

Yue QJ, Guo FW, Kärnä T (2009b) Dynamic ice forces of slender vertical structures due to ice crushing [J]. Cold Reg Sci Technol 56(2–3):77–83

Zhang YL, Lin G, Li ZJ et al (2002) Application of DDA approach to simulate ice-breaking process and evaluate ice force exerting on the structure [J]. China Ocean Eng 16(3):273–282 (in Chinese)

Chapter 9
Dynamic Analysis of Train-Bridge System Under Differential Settlement and Scouring Effect of Foundations

In this chapter, the influence of differential settlement and scouring effect of pier foundations on the dynamic responses of train-bridge system is studied. The influence factors of differential settlement and the mechanism of stream scouring effect of pier foundations are summarized. A prediction method for cumulative settlement of bridge foundations caused by cyclic train loading is proposed, and the differential settlement of existing bridge foundations induced by the construction of nearby bridge is studied by numerical simulation. Based on an engineering case, the influence of differential settlement of bridge foundations on the dynamic responses of train-bridge system is studied, and the train speed-settlement threshold curves for running safety and riding comfort of train are proposed. The calculation formulae of scouring depth are given, and the stiffness of a single pile and the equivalent stiffness of group-piles are studied, based on which the scouring effects on the stiffness of bridge foundations and the dynamic responses of train-bridge system are investigated.

9.1 Differential Settlement of Bridge Foundations

With the large-scale construction and operation of HSRs in China, there occurred some remarkable differential settlements of bridge foundations in several lines, which have been noticed by engineers and researchers in design, construction, operation management, and maintenance of bridges. The differential settlement of adjacent pier foundations may cause the distortion and deformation of bridge superstructure, resulting in the redistribution of structural internal forces. When the differential settlement is large, it may lead to the cracking of track-slab base, deterioration of material durability, worsen the smoothness state of the track, and thus influence the safety of bridge structures as well as the riding comfort of high-speed trains.

H. Xia et al., *Dynamic Interaction of Train-Bridge Systems in High-Speed Railways*, Advances in High-speed Rail Technology, https://doi.org/10.1007/978-3-662-54871-4_9

The main factors affecting the differential settlement of foundations are as follows:

(1) The cumulative deformation of subsoil

The cumulative deformations of subsoil include the static subsidence caused by the dead loads of the bridge structure and the layers themselves, and the dynamic settlement by the cyclic train loading. For years, the ground subsidence in the eastern plains of China has been growing, forming several subsidence zones. Before the construction of Beijing-Shanghai HSR, the ground subsidence between Beijing and Dezhou had been monitored for many years, and the data showed that the cumulative subsidence of subsoil in this area reached 300–1500 mm, with the annual average subsidence more than 20 mm. Especially in some sections between Tianjin and Cangzhou, the annual average subsidence was up to 50–90 mm, far more than the limit for post-construction settlement of HSR bridges (Li et al. 2008; Qi 2009). Due to the characteristics of long operation time and high operation density of HSR trains, the bridges are subjected to frequent loading and unloading, which can produce great vertical dynamic loads on the foundation. Acted on by the dynamic loads, and coupled with the dead loads of girder, bearing, track, pier, and foundation, the large ground subsidence around the bridge foundation can be caused.

On the Beijing-Tianjin HSR, also occurred the ground subsidence with different degrees during its operation, in which the most significant is the Yizhuang subsidence zone where the largest subsidence reached 690 mm (Song et al. 2010). Among the 7 continuous bridges and many 32 m or 24 m simply-supported bridges in the Yizhuang subsidence zone, large differential settlements were measured at two continuous bridges and five simply-supported bridges. The differential settlement between the No. 283 and No. 284 piers of the continuous bridge across the Fifth Ring Road of Beijing reached up to 60 mm. The CARS (China Academy of Railway Sciences) established a survey network to observe the subsidence in the Wuqing section of Beijing-Tianjin HSR, and the measured subsidence curves in the section of K82+968 ∼ K86+786 are shown in Fig. 9.1 (Zhai et al. 2014). As can be

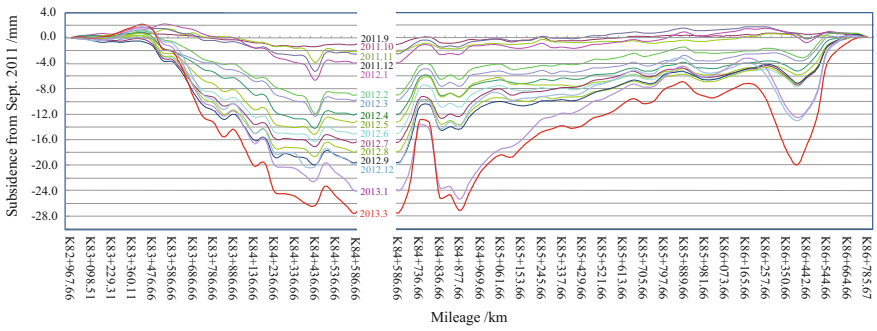

Fig. 9.1 Ground subsidence curves of Beijing-Tianjin HSR from K82+968 to K86+786 (Sept. 2011 ∼ March 2013)

seen, from September 2011 to March 2013, the maximum subsidence in this section was 27.5 mm, while only from December 2012 to March 2013, occurred the most significant subsidence in the section of K84+836 ~ K84+970, with its maximum exceeded 12 mm.

(2) Stacking loads around bridge foundations

From the investigation of several bridges with large settlement on the Beijing-Tianjin HSR, it was found that a mass of sands, stones, stone products, or semi-finished products were stacked, and some post-construction built parking lots and buildings, etc. appeared on the open sites around bridge piers (Cao 2014). These increased loads after the construction of bridges may produce great additional stresses in the surrounding subsoil of bridge foundations, leading to the local differential settlement.

In the K1309 section of the Beijing-Shanghai HSR, several bridge piers were found displaced due to the stacking loads of a dump yard, with the maximum side-shift of 94 mm and the maximum vertical settlement of 92 mm, which used to have the train speed reduced to 160 km/h for a time.

(3) Construction near the existing HSR bridges

In recent years, with the continuous increase of HSR lines and the densification of railway network, more foundation constructions need to be conducted with new bridges and other buildings crossing (Fig. 9.2) or very close to (Fig. 9.3) the existing bridges.

On 25 April, 2012, a serious vehicle vibration happened in the D2281 high-speed train when it was running through the K1008+800 section of the Beijing-Shanghai HSR. Careful examinations showed that the geometric profile of the track in that section was obviously beyond the prescribed limits. The later survey found that the incident was caused by the construction of a bridge foundation nearby, where a new subway line was constructing in parallel, and the bridge foundation was built very close to the foundation platform of the HSR bridge, while no safety precaution was done. According to the statistics by the Shanghai Railway Bureau, within the scope of its management, only in 2009, there happened more

Fig. 9.2 Construction of a new bridge crossing the existing railway (City8 2015)

Fig. 9.3 Construction of a new bridge parallel to the existing railway (Taken on Datong-Xi'an HSR line construction site)

than 20 incidents inducing the instability of existing bridge foundations, leading to vehicles swaying or even traffic accidents due to adjacent constructions.

The HSR has strict requirement on the deformation, smoothness, and stability of bridges and tracks, so it is important to study the differential settlement of bridge foundations and its influence on the running performance of the high-speed trains.

9.2 Prediction of Cumulative Settlement of Bridge Foundation Under Cyclic Train Loading

Due to the complexity of predicting the cumulative settlement of subsoils under traffic loads, the related theoretical and experimental studies started rather late. In this section, by the layered summation method, the cumulative plastic deformation model and the cumulative pore pressure model are derived based on the critical state theory (Li 2005; Huang et al. 2006; Liu et al. 2006), to predict the cumulative settlement of bridge foundation induced by cyclic train loading. For each layer of subsoil with different depths under foundation, the calculation procedures can be summarized as the following three steps:

(1) Calculate the static stress of subsoils induced by the deadweight of the structure and the dynamic stress by the train load, respectively, based on the quasi-static method.
(2) Calculate the cumulative plastic deformation of subsoils by the cyclic cumulative deformation model and the cumulative pore pressure deformation by the cumulative pore pressure model, respectively, with taking into account the stress level of subsoils and the cyclic train loading times.
(3) Calculate the subsoil settlement of each layer caused by the undrained cumulative plastic deformation and the consolidation settlement by the undrained cumulative pore pressure dissipation, respectively, and summarize the two kinds of settlements to obtain the accumulation deformation of the layer.

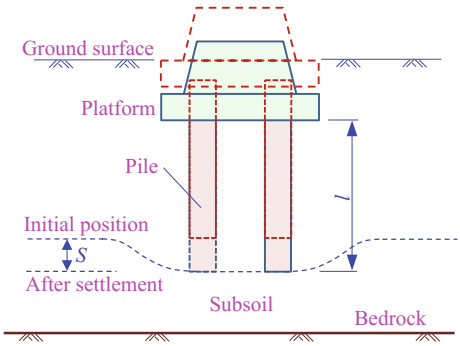

Fig. 9.4 Calculating model for cumulative settlement of a bridge pile foundation

Finally, the total cumulative settlement of the pier foundation can be obtained by superimposing the cumulative deformations of all subsoil layers.

To simplify the solution process, the following assumptions are introduced:

(1) Since the foundation settlement is much smaller than the bridge dimension, its influence on the dynamic performance of train-bridge system is neglected.
(2) The influence of adjacent bridges on the cumulative settlement of pier foundation is neglected, because the stress of the semi-infinite subsoil induced by the uniformly distributed local loads decays quickly in the horizontal direction.
(3) The cumulative settlement of bridge foundation is consistent with the subsoil subsidence under the foundation bottom.
(4) The bottom of subsoil is located on the bedrock, namely the vertical displacement at the model bottom is none.

Based on the above assumptions, the calculation model for the cumulative settlement of bridge pile foundation induced by cyclic train loading is established, as shown in Fig. 9.4.

9.2.1 Determination of Stress State in the Subsoil

To accurately predict the additional settlement of the pier foundation under cyclic train loading, the 3-dimensional FE model corresponding to the real site condition is established. Firstly, the stress state of subsoil, namely the average effective consolidation pressure of the subsoil under their own deadweights, is calculated. Then, the initial static deviator stress caused by the post-construction deadweights of subsoil, bridge structure and accessory facilities, and the dynamic deviator stress caused by train loading, are determined.

(1) Average effective consolidation pressure of the subsoil (p_c)

It is generally believed that the average effective consolidation pressure of subsoil is caused by the deadweights of layers, which can be calculated by

assuming the soil in a consolidation state. Firstly, the vertical stress σ_g of the subsoil at a calculation depth is calculated using the deadweights of all subsoil layers above the depth. Next, the constraints on the vertical stress from the lateral stress of surrounding subsoils are considered by the lateral confining coefficient K_0 of subsoil. The average effective consolidation pressure p_c of subsoil at any depth can be calculated by

$$p_c = \frac{1+2K_0}{3}\sigma_g = \frac{1+2K_0}{3}\sum_{i=1}^{n}\gamma_i h_i \tag{9.1}$$

$$K_0 = \frac{v}{1-v} \tag{9.2}$$

where v represents the Poisson ratio of the subsoil at the calculation depth; n denotes the layer numbers of subsoils above the calculation depth; γ_i and h_i are the effective bulk density and the thickness of the ith layer of subsoil above the calculation depth, respectively.

(2) Initial static deviator stress of the subsoil (q_s)

Assuming the initial static deviator stress in the subsoil is only caused by the deadweights of the bridge structure and the subsoil, the 3-dimensional bridge foundation-layered subsoil FE model is established, in which the foundation-subsoil interface is simulated by the contact elements. By applying the deadweights of bridge pier and superstructure onto the top of the pile platform, the six stress components, σ_x, σ_y, σ_z, $\tau_{xy} = \tau_{yx}$, $\tau_{yz} = \tau_{zy}$, and $\tau_{xz} = \tau_{zx}$, of subsoil elements at different depths can be solved. Then, the initial static deviator stress of subsoil can be obtained by

$$q_s = \sqrt{\frac{1}{2}\left[(\sigma_x-\sigma_y)^2+(\sigma_y-\sigma_z)^2+(\sigma_x-\sigma_z)^2+6\left(\tau_{xy}^2+\tau_{yz}^2+\tau_{xz}^2\right)\right]} \tag{9.3}$$

(3) Dynamic deviator stress of the subsoil caused by train load (q_d)

The single cycle of the train running through the bridge is simulated by FEM, to calculate the maximum dynamic deviator stress in subsoil. To simplify the solution, the quasi-static method is adopted: firstly, calculate the maximal additional dynamic load at the pier bottom caused by the running train using the train-bridge system analysis model, and then, apply the load onto the platform top, to solve the six stress components σ_x, σ_y, σ_z, $\tau_{xy} = \tau_{yx}$, $\tau_{yz} = \tau_{zy}$, and $\tau_{xz} = \tau_{zx}$ of subsoil elements at different layers using the 3-dimensional FE model of the bridge foundation-layered subsoil system. Thus, the dynamic deviator stress q_d can be achieved by

$$q_d = \sqrt{\frac{1}{2}\left[(\sigma_x-\sigma_y)^2+(\sigma_y-\sigma_z)^2+(\sigma_x-\sigma_z)^2+6\left(\tau_{xy}^2+\tau_{yz}^2+\tau_{xz}^2\right)\right]} \tag{9.4}$$

(4) Relative deviator stress level (D^*)

The relative deviator stress level, denoted by D^*, is introduced to consider the combined influence of static deviator stress and dynamic deviator stress. For the subsoil at a certain depth below the bottom of bridge foundation, D^* is defined by

$$D^* = \frac{q_\mathrm{p} - q_\mathrm{s}}{q_\mathrm{ult} - q_\mathrm{s}} \tag{9.5}$$

where q_s and q_p are, respectively, the initial static deviator stress and the peak deviator stress of subsoil at the calculation depth; q_ult is the undrained ultimate strength of the subsoil, which can be determined by Liu et al. (2006)

$$q_\mathrm{ult} = (0.5)^{1-\frac{\kappa}{\lambda}} M p_\mathrm{c} \tag{9.6}$$

where λ and κ are, respectively, the slopes of normal consolidation and rebound lines in the e-ln$p$ space; M is the slope of critical state line in the modified Cambridge model; p_c is the average effective consolidation pressure of subsoil at the calculation depth.

Note that the peak deviator stress q_p is used in Eq. (9.5), which is the superimposition of dynamic deviator stress q_d and static deviator stress q_s. When the train passes through, the additional load at the pier bottom caused by the deadweight of bridge superstructure always exists, so q_d and q_s are simultaneously applied onto the platform top, to solve the six stress components of the subsoil. Thus q_p can be calculated by

$$q_\mathrm{p} = \sqrt{\frac{1}{2}\left[(\sigma_x - \sigma_y)^2 + (\sigma_y - \sigma_z)^2 + (\sigma_x - \sigma_z)^2 + 6\left(\tau_{xy}^2 + \tau_{yz}^2 + \tau_{xz}^2\right)\right]} \tag{9.7}$$

9.2.2 Calculation of Cumulative Pore Pressure

The dynamic triaxial test shows that the cumulative pore pressure of soft clay under undrained condition is related to the initial static stress, the dynamic stress generated by a single loading, the times of cyclic loading, and other factors. Based on the calculated average effective consolidation pressure p_c and the relative deviator stress level D^*, the cumulative pore pressure u of subsoil at different depths caused by the cyclic train loading can be solved by the fitting formula proposed by Huang et al. (2006)

$$u = \zeta D^{*n} N^{\beta} p_\mathrm{c} \tag{9.8}$$

which: β is the parameter characterizing the type, physical state and stress state of subsoil; ζ and n are constants, which can be acquired from experiments; N is the times of cyclic loading.

9.2.3 Calculation of Additional Settlement of Bridge Foundation Under Train Loads

It is generally believed that the additional settlement of bridge foundation caused by cyclic train loading is equal to the undrained cumulative deformation S of subsoil under the foundation bottom. The additional settlement consists of two components: the subsidence S_s caused by undrained cumulative deformation and the consolidation subsidence S_v caused by cumulative pore pressure dissipation. The two components can be calculated by the layered summation method, where each layer should be modeled with small thickness, generally taking as 1–2 m, to guarantee the accuracy of solution.

(1) The subsidence S_s caused by undrained cumulative deformation

The subsoil with a certain thickness under the bridge foundation bottom is taken as the compression soil for calculation, which is then divided into several thin layers. Based on the previously calculated stresses of subsoil at different depths under the foundation bottom, the undrained cumulative plastic strain ε^p at the center of each subsoil layer can be determined. Next, ε^p is taken as the average value of the undrained cumulative plastic strain of this layer, to calculate S_s by the layered summation method, expressed as

$$S_s = \sum_{i=1}^{n} \varepsilon_i^p h_i = \sum_{i=1}^{n} aD_i^{*m} N^{\beta} h_i \tag{9.9}$$

where $\varepsilon^p = aD^{*m}N^{\beta}$ is the cumulative plastic strain of the ith subsoil layer, and h_i is its depth; n is the numbers of compression layers of subsoil; a and m are the experimental parameters, which can be obtained by the triaxial test of soil.

(2) The consolidation subsidence S_v caused by undrained cumulative pore pressure dissipation under train loads

Using Eq. (9.8) and the stress of subsoil at different depths under the foundation bottom, to calculate the cumulative pore pressure u at the center of the layer, and then let it be the average value of cumulative pore pressure of the layer. Based on the Terzaghi one-dimensional consolidation theory, the consolidation deformations of subsoil at various layers can be calculated, and the consolidation subsidence S_v can be obtained by the layered summation method, expressed as

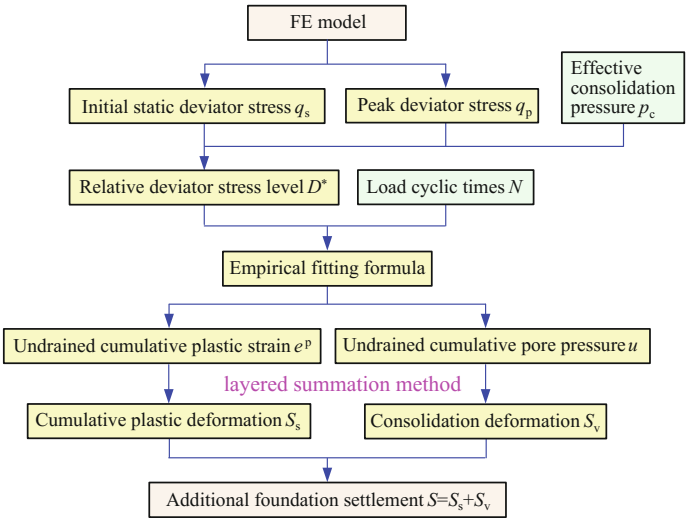

Fig. 9.5 Procedures for calculating cumulative settlement of bridge foundation under train loads

$$S_v = \sum_{i=1}^{n} m_{vi} h_i u_i U_i \tag{9.10}$$

where n is the numbers of compression subsoil layers; for the ith layer, h_i, u_i, m_{vi} and U_i are the thickness, undrained cumulative pore pressure, bulk compressibility coefficient and consolidation degree of subsoil, respectively. The undrained cumulative pore pressure may not quickly dissipate, but in terms of long-term effect, it has completely gone away when in calculation, that is, U_i = 100%, which is rather conservative in the engineering.

The additional settlement S of bridge foundation induced by cyclic train loading can be obtained by superimposition of S_s and S_v. In accordance with the ideas illustrated above, the detail calculation procedures are shown in Fig. 9.5.

9.2.4 Case Study

The additional settlement of bridge foundation induced by train loads is analyzed by the following case study.

1. ***Calculation parameters***

Main parameters of the train: The Germany ICE3 high-speed train composed of 8 vehicles: (3 motor-cars + 1 trailer cars) × 2, whose wheelbase arrangement and main parameters can be found in Fig. 6.36 and Table 6.8 of Chap. 6, respectively. The establishment of train model can be seen in Chap. 5.

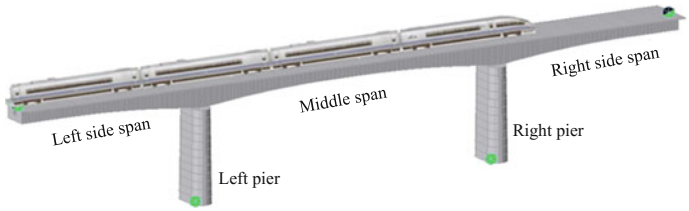

Fig. 9.6 The (48+80+48) m continuous PC box-beam bridge model

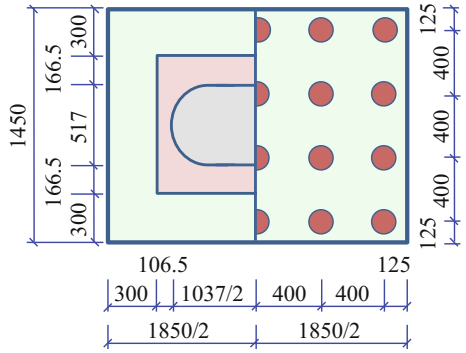

Fig. 9.7 Layout of pile foundation platform of the bridge (Unit: cm)

Main parameters of the bridge: A HSR (48+80+48) m continuous PC box-beam bridge as shown in Fig. 9.6; two hollow piers with round-ended section and 24 m-height; two pile foundations with the platform of 18.5 m × 14.5 m × 4 m (length × width × height), and each foundation platform supported by 20ϕ1.5 m piles with 57 m-length, as shown in Fig. 9.7. In the train-bridge interaction model, the boundary at the bottom of bridge pier is regarded to be fixed.

The soil parameters in the pile foundation-subsoil model are taken from Huang et al. (2006). There are four layers of subsoil: filled earth, gray silty clay, gray sludge clay, and dark green silty clay (from top to bottom in turn), and the basic parameters are listed in Table 9.1.

The required parameters in the empirical formula of cumulative deformation of subsoil can be fitted from the triaxial test data of soil samples, and the values of them are different with subsoil types. The parameters used in this section are taken from Li (2005), as listed in Table 9.2.

The coupling vibration analysis of train-bridge system is carried out by using the above parameters, the damping ratio of bridge structures is 0.03, the train speed is 160–360 km/h, and the integration time step is 0.001 s.

2. ***Additional loads at the pier bottom caused by a train***

When a train runs through the bridge, an additional load is generated at the pier bottom (namely the platform top). Shown in Fig. 9.8 are the time histories of

Table 9.1 Subsoil parameters

Layer	1	2	3	4
Subsoil type	Filled earth	Gray silty clay	Gray sludge clay	Dark green silty clay
Thickness (m)	15.6	5.10	8.30	51.0
Compression modulus (MPa)	7.00	11.5	6.00	20.0
Density (g/cm^3)	1.80	1.90	1.93	2.00
Inner friction angle φ_{cu} for undrained consolidation (°)	17.8	7.80	20.0	23.0
Cohesion c_{cu} for undrained consolidation (kPa)	13.0	10.0	6.50	26.0
Poisson ratio	0.29	0.30	0.37	0.37

Table 9.2 Parameters in the model

a	b	m	Ξ	n	β	κ	λ	M
0.34	0.39	2.68	0.0023	2.19	0.66	0.03	0.13	1.49

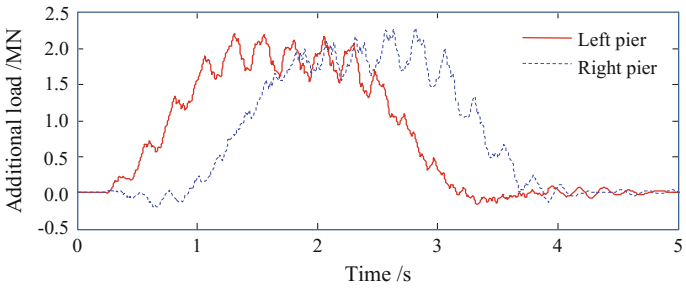

Fig. 9.8 Time histories of additional loads at the pier bottom by a running train

additional loads at the pier bottom when the train passes through the bridge at the speed of 360 km/h.

As can be seen from Fig. 9.8, each additional load time history curve is dominated by the quasi-static component induced by moving axle loads, in which a series of dynamic peaks appear with respect to the passages of bogies, but their amplitudes are far smaller than the quasi-static component. Based on this characteristics, the additional loads can be simplified to an equivalent half-sine load, that is, the times N of cyclic loading is equal to the numbers of train passage through the bridge.

The track irregularity is taken into account in the dynamic analysis of train-bridge system. In view of the randomness of track irregularity, ten samples of

track irregularity are produced based on the Germany low interference spectrum. For each track irregularity sample, the additional load induced by a train is calculated, and then the average of the ten results is used to analyze the additional settlement of bridge foundation.

Shown in Fig. 9.9 are the distributions of maximum additional loads of the two piers versus train speed. It can be seen that they do not monotonically increase with the train speed, while appear peaks at several speeds. The variation of additional loads among different train speeds is small, for example, the maximum additional load at train speed of 360 km/h is only 3.8% greater than that at 160 km/h. It is because that for such a long-span bridge, the influence line of the pier reaction is up to 128 m according to two-span lengths, leading to very small impact coefficient. There is a difference between the additional loads of the two piers, but the difference is no greater than 3.2%. Therefore, herein only the additional load of the left pier is taken as an example to study the additional settlement of bridge foundation induced by cyclic train loads.

3. ***Stress state of subsoil***

Considering the symmetry of the bridge foundation-subsoil system, a 1/4 pile-subsoil interaction FE model is established by ANSYS, as shown in Fig. 9.10. The dimensions of the model are 60 m in both x- and y-directions, and 100 m in z-direction. For the boundary conditions, the symmetrical constraints are applied on the two boundaries at $x = 0$ and $y = 0$; the displacements along x-direction and y-direction are restrained on the two boundaries at $x = 60$ m and $y = 60$ m; the displacements at the upper surface ($z = 0$) are free, while at the bottom ($z = -100$ m) are all restrained. In accordance with the foundation sizes and the subsoil parameters, the DP-plastic model and the isotropic-elastic model are adopted to simulate the subsoil and the pile foundation, respectively, both by the solid45 elements; the contact pairs produced by the targe170 and conta173 elements are used to simulate the interaction between pile foundation and subsoil. In total, there are 45,562 nodes and 42,742 elements in the model.

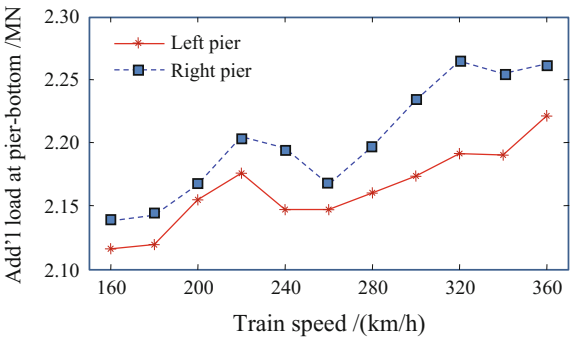

Fig. 9.9 Distribution of maximum additional loads versus train speed

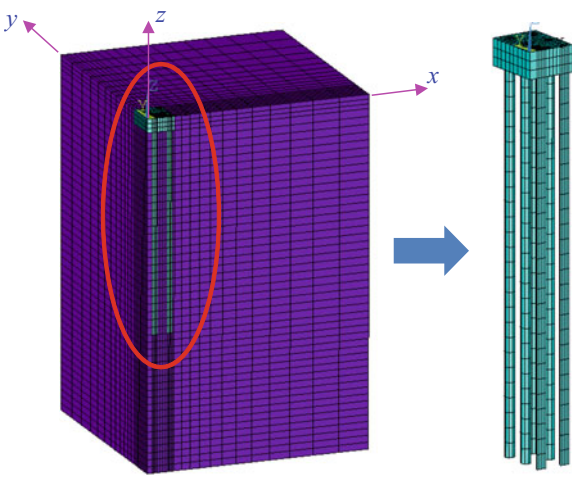

Fig. 9.10 The 1/4 pile foundation-subsoil FE model

The subsoil is assumed in the state of normal consolidation, to solve the initial static deviator stress q_s caused by the deadweight of bridge and the dynamic deviator stress q_d by the train loads.

Firstly, the subsoil model without pile foundation is established, with the same model dimensions and grid divisions as the above pile-subsoil FE model, to solve the stress state of subsoil under the deadweight, which is applied as the initial stress to the pile-subsoil FE model. After the construction of bridge, the stress field in subsoil may change due to bridge deadweight and train loading, and the difference between the concerned stress field and the initial stress field is called the additional stress field.

Shown in Fig. 9.11 are the calculated additional stress fields of subsoil when the train runs through the bridge at the speed of 360 km/h. There appear obvious stress concentrations around the platform bottom and pile-bottom, but the stress concentration zones are very small due to the plastic effect of soft clay. The additional stress field induced by train loading is obvious in z-direction, and the concentration zone is larger than those either in x- or in y- direction. The additional stress mainly concentrates in the subsoil of a certain depth close to the pile-bottom. The additional shear stresses in xz- and yz-directions are obvious, due to the frictional resistances on the pile-subsoil contact interface, which allows the vertical displacement of pile foundation to make the subsoil around piles produce large shear deformation.

The distributions of additional stresses in subsoil induced by the deadweight of bridge are similar with those induced by the train load (Fig. 9.11), and they also mainly concentrate in the subsoil at a certain depth close to the pile-bottom. As shown in Fig. 9.12, the additional stresses quickly attenuate with the distance from the pile-bottom. For example, at the depth of 10 m from the pile-bottom, the additional stresses of subsoil in three directions reduce to 11.9%, 14.5%, and 41.9% of those at the pile-bottom, respectively.

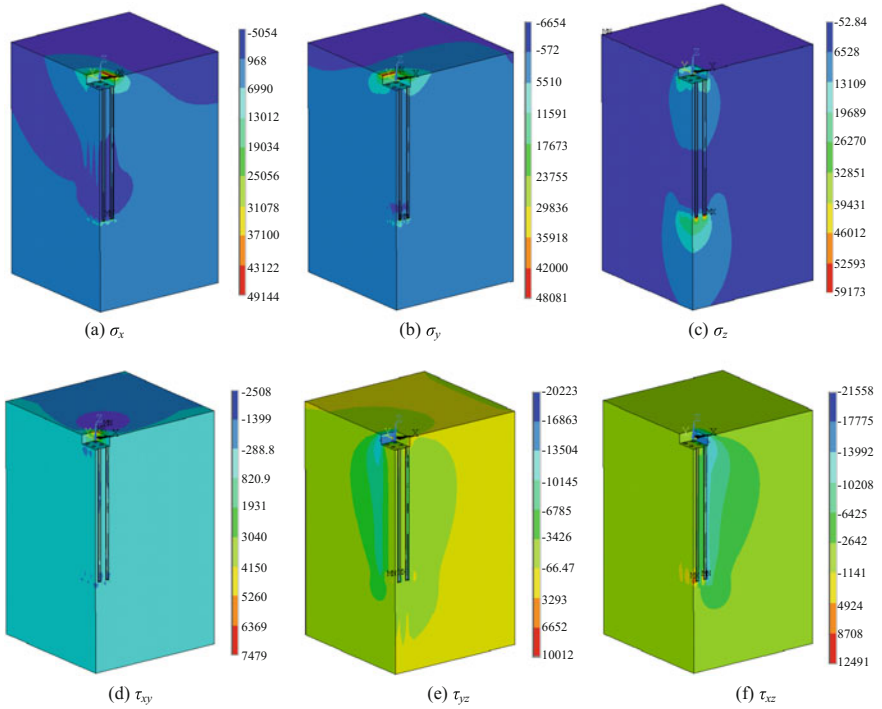

Fig. 9.11 Additional stress fields of subsoil induced by train loading (Unit: Pa)

Fig. 9.12 Distributions of bridge deadweight-induced additional stresses of subsoil at different depths

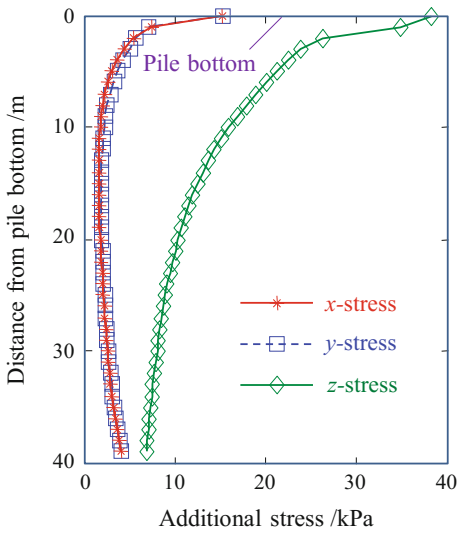

Shown in Fig. 9.13 are the displacement nephograms of subsoil induced by the deadweight of bridge. It is clear that the subsoil around the piles moves downward with the pile foundation due to the subsoil deformation under the platform bottom and the friction on the pile-subsoil interface, and the subsoil under the pile-bottom produces certain amount of transverse displacement, indicating the subsoil there is squeezed outward by the downward movement of the piles.

According to the above analysis, there exist stress concentration zones in some positions at certain distances from the pile-bottom, and the stress distribution is uneven, which may cause calculation error if only a single point at the pile-bottom is taken for analysis. Therefore, the static deviator stress q_s caused by bridge deadweight and the dynamic deviator stress q_d by train loads are solved, based on the average value of the samples from 11 points illustrated in Fig. 9.14.

4. ***Influence of cyclic loading times on additional settlement of foundation***

As previously mentioned, in the analysis, the cyclic loading times N is assumed equal to the numbers of train passages through the bridge, and the inverse effect of

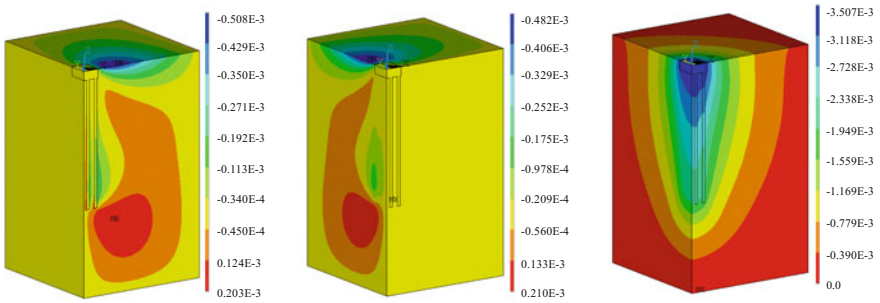

Fig. 9.13 Displacement nephograms of subsoil induced by bridge deadweight

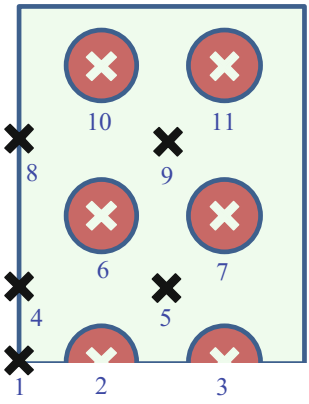

Fig. 9.14 Arrangement of sampling points on the platform for subsoil stress analysis

additional settlement of pile foundation on the additional force at the pier-top is neglected, namely the dynamic loads of the bridge in the N cycles of train passages are identical. It can be seen from Figs. 9.11 and 9.12 that the cumulative plastic deformation of subsoil mainly focuses on the subsoil at a certain depth close to the pile-bottom, and the deformation sharply decreases with the distance from the pile-bottom. Therefore, the compression layer of subsoil is taken as 30 m, which is sufficient in calculating the additional settlement of pile foundation induced by cyclic loading.

Shown in Fig. 9.15 are the relationship curves of additional settlements of pile foundation with cyclic loading times N under two train speeds. It can be seen that the additional settlements increase exponentially. At the beginning of operation, the additional settlement develops rapidly, and then, the developing rate tends to slow down gradually with the cyclic loading times.

Shown in Fig. 9.16 is the variation of additional settlement of pile foundation after 2×10^6 cycles of train loading at various train speeds. In the main trend, the additional settlement increases with train speed, but appears a peak at 220 km/h, which accords with the distributions of additional loads at pier bottom versus train speed shown in Fig. 9.9. However, the variation of additional settlement at various train speeds is very small, which is due to the small variation of additional loads with train speed, and also because the pile is long and the undrained shear strength of subsoil is high, resulting in small relative deviator stress level D^* and small cumulative deformation of subsoil solved by Eq. (9.9).

If the train interval of HSR is 5 min (in two direction), the annual cyclic train loading times on the bridge is about 1×10^5. By considering different operation periods and various train speeds, the additional settlements of bridge pile foundation caused by cyclic train loading are calculated, as listed in Table 9.3. The results show that at various train speeds, the additional settlements of bridge foundation develop rapidly in the early period of operation, and in the first three months, reach 16.8% of those after 20 years of operation.

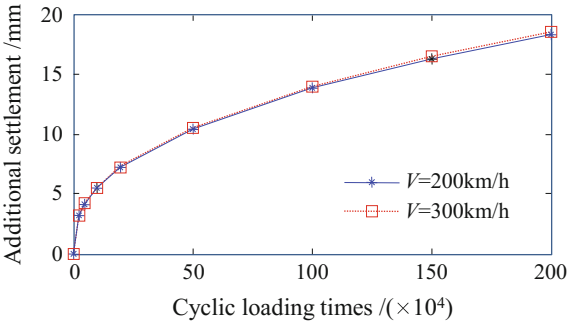

Fig. 9.15 Additional settlements of pile foundation versus cyclic loading times

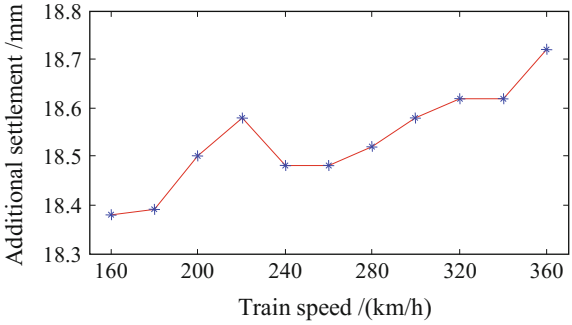

Fig. 9.16 Variation of additional settlement of pile foundation versus train speed

Table 9.3 Additional settlements of the bridge pile foundation (Unit: mm)

Train speed (km/h)	Three months	Six months	One year	Two years	Five years	Ten years	Fifteen years	Twenty years
200	3.1	4.1	5.4	7.2	10.4	13.8	16.3	18.4
220	3.1	4.1	5.4	7.2	10.4	13.8	16.3	18.4
240	3.1	4.1	5.5	7.2	10.5	13.9	16.4	18.5
260	3.1	4.1	5.5	7.2	10.5	14.0	16.5	18.6
280	3.1	4.1	5.4	7.2	10.4	13.9	16.4	18.5
300	3.1	4.1	5.4	7.2	10.4	13.9	16.4	18.5
320	3.1	4.1	5.5	7.2	10.5	13.9	16.4	18.5
340	3.1	4.1	5.5	7.2	10.5	14.0	16.5	18.6
360	3.2	4.2	5.5	7.3	10.5	14.0	16.5	18.6
380	3.2	4.2	5.5	7.3	10.5	14.0	16.5	18.6
400	3.2	4.2	5.5	7.3	10.6	14.1	16.6	18.7
420	3.1	4.1	5.4	7.2	10.4	13.8	16.3	18.4

9.3 Numerical Analysis of Differential Settlement of a Bridge Foundation Caused by Adjacent Foundation Construction

9.3.1 Engineering Background

The new bridge is to be built on the Datong-Xi'an HSR line located near Taiyuan City. The bridge adopts bored piles foundations, and the pile diameters are 1.0 m, 1.25 m and 1.5 m, corresponding to different subsoil conditions, span lengths, and

Fig. 9.17 In-situ locations of new bridge and existing bridge

pier heights. The new bridge is parallel with and adjacent to the No. 32–No. 194 piers of an existing bridge on the Shijiazhuang-Taiyuan HSR Line, as shown in Fig. 9.17.

To analyze the influence of pile foundation construction on the adjacent existing bridge piers, the most unfavorable case, namely the No. 166 pier of the existing bridge and No. 156 pier of the new bridge, where the clear distance between the platforms of them is only 5 m, are considered. A three-dimensional FE model is established by using the software ABAQUS, to simulate the construction process of the No. 156 pier (new pier) and its influence on the settlement of the No. 166 pier (existing pier).

9.3.2 Finite Element Modeling

According to the geotechnical conditions provided by the designer, the subsoil around the existing pier has two layers, and the parameters are listed in Table 9.4. In the model, only the concrete is considered in the piles, while the steel bars are neglected. Because the elastic modulus and the yield strength of concrete is much greater than those of soil, and plastic deformation will not occur in the whole analysis process, the elastic constitutive relation is adopted for the piles. For the subsoil, the elastic-plastic constitutive relation is used, with the Drucker-Prager constitutive model adopted for the plastic part.

The foundation platform-piles model of the existing bridge is shown in Fig. 9.18, in which the steps connecting the platform and pier are neglected. The dimensions of the platform are 12.8 m × 5.8 m × 4.2 m; the pile diameter is 1.25 m, and the length is 46 m. In the model, the pier-platform and platform-pile

Table 9.4 Subsoil parameters around the existing pier

Subsoil	Thickness (m)	Density (g/cm^3)	Poisson ratio	Elastic modulus (MPa)	Inner friction angle (°)	Dilation angle (°)	Yield strength (kPa)
1st layer	0–40	2.01	0.3	35	19.39	0	150
2nd layer	40–70	2.07	0.3	35	20.54	0	150

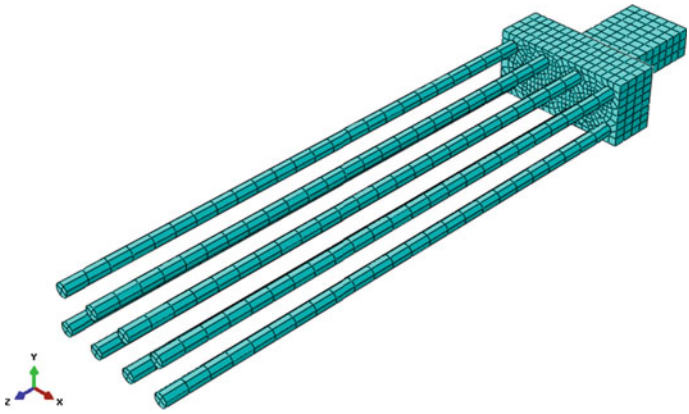

Fig. 9.18 Pier-platform-piles model of the existing bridge

connections adopt binding constraints; the piles have friction contact with the surrounding subsoil, and binding connection with the bottom soil.

The platform-piles model of the new bridge is shown in Fig. 9.19, in which the dimensions of the platform are 10.4 m × 7 m × 2.2 m; the pile diameter is 1 m, and the length is 47 m. The piles and the platform are connected by binding constraints, and the friction contact is set up between piles and soil. Before the construction of piles, the material is soil with tangential frictional coefficient of $\tan\varphi = 0.36$ (φ is the inner frictional angle of soil), and after the construction, the soil at the position of piles is replaced by C30 concrete with frictional coefficient of $\tan 0.75\varphi = 0.268$.

The 3-dimensional FE model of the pier-platform-piles-layered subsoil system is established, as shown in Fig. 9.20. The dimensions of the model are 95 m in x-direction, 60 m in y-direction, and 70 m on the new bridge part and 72 m on the existing bridge part in z-direction. In order to guarantee the calculation accuracy with less computational cost, the grid division of soil elements is densified in the areas around the piles and becomes sparser gradually far away. The 8-node linear reduced integral elements (C3D8R) are adopted in the model for subsoil, piles, platform, and pier, which can satisfy the calculation accuracy and improve the computational efficiency.

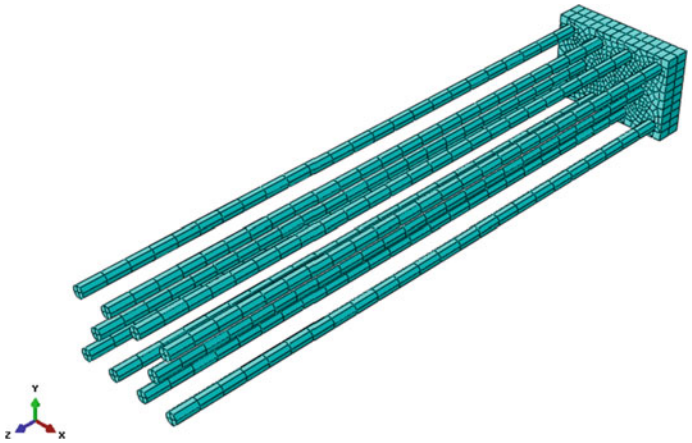

Fig. 9.19 Platform-piles model of the new bridge

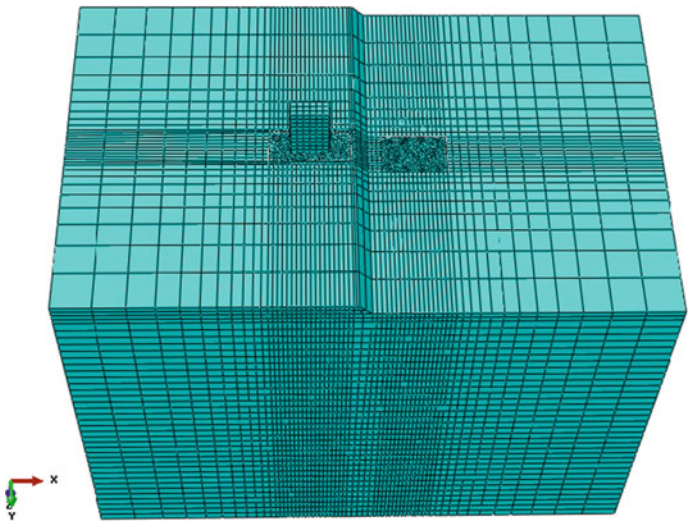

Fig. 9.20 Three-dimensional FE model for pier-platform-piles-layered subsoil system

The boundary conditions of the model include (1) free at top surface; (2) fixed at bottom, namely all DOFs of them are restrained; (3) normal constraints on side boundaries, namely the displacements of x-direction are restrained on the side planes of $x = \pm 47.5$ m, while those of y-direction restrained on the planes of $y = \pm 30$ m; (4) friction contact at pile-subsoil perimeter interface; (5) binding connection between the pile-bottom and the soil below.

The face-to-face contact is adopted in the pile-subsoil perimeter interface, with the stiffer pile as primary face and the softer subsoil as slave face. The normal

contact is set up as "hard contact" (Fen and Zhang 2009), namely the pile-subsoil contact can transfer normal compressive stress, while the pile-subsoil non-contact cannot transfer stress. The tangential contact adopts the penalty function to set the friction coefficient. In the model, the inner friction angle of the subsoil is φ = 19.39°–20.54°, the pile-subsoil friction angle is $\varphi_1 = 0.75\varphi$, and the friction coefficient is 0.268.

9.3.3 Division of Construction Stages

In the numerical simulation, the construction process of the new pier is divided into several stages according to the actual situation, as shown in Table 9.5. The platform and pile layouts of the new bridge and the existing bridge are shown in Fig. 9.21. For each construction stage of the new pier, the displacement of piles, the settlement of surrounding subsoil, and the spatial displacements of pier-top and platform of the existing pier are analyzed.

Construction stage 1: Before new bridge construction. The existing pier sustains the loads transferred from the superstructure, including the beam deadweight, secondary load, and static live-load. According to the design data, the beam deadweight is 4080 kN, the secondary load is 2980 kN, and the static live-load is 3790 kN; thus, the total load is 4080 + 2980 + 3790 = 10850 kN, which is applied as uniformly distributed load on the top surface of the pier. The calculated displacements and settlements of the existing bridge in this stage are regarded as the initial values before construction of the new pier, and those produced in the following stages should be the relative values with respect to the initial values.

Construction stages 2–5: According to the construction sequence in Table 9.5 and the pile number sequence on the new bridge platform in Fig. 9.21, the

Table 9.5 Division of construction stages

Construction stage	Construction works
Stage 1	Soil stress is in equilibrium, the existing pier bears the superstructure loads
Stage 2	Construction of pile-1 in the first row on the platform of the new bridge, including bore drilling, concrete pouring and hardening
Stage 3	Construction of piles-2, 3, 4 in the first row on the platform of the new bridge
Stage 4	Construction of piles-5, 6 in the second row on the platform of the new bridge
Stage 5	Construction of piles-7, 8, 9, 10 in the third row on the platform of the new bridge
Stage 6	Excavation of platform of the new bridge
Stage 7	Casting of platform concrete of the new bridge
Stage 8	Completion of platform construction of the new bridge, and the uniformly distributed load is applied on the top surface of platform

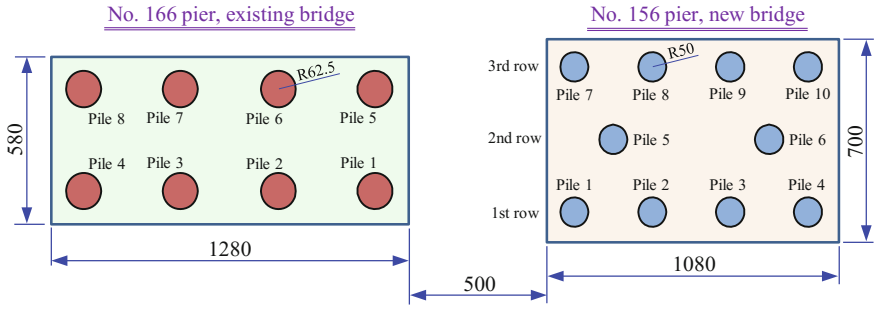

Fig. 9.21 Layout of platforms and piles of new bridge and existing bridge (Unit: cm)

construction influences of a single pile and each row of piles on the existing bridge foundation and pier are analyzed. In these stages, the pile holing and the concrete casting are realized by the birth-death elements, and the change of material parameters in concrete hardening process is realized by field variables. In simulating the slurry-supported pile holing, the density of slurry is $\rho_2 = 1200$ kg/m^3 (Wang 2015), and its effect on the surrounding subsoil is simplified as the hydrostatic pressure applied on the hole-wall and the pile-bottom.

Construction stage 6: The platform pit with the size of 10.7 m × 7 m × 2.2 m is excavated.

Construction stage 7: The platform concrete is cast, and it is integrated with the piles, thus the displacements of platform and piles are restrained by binding.

Construction stage 8: Completion of construction, the new platform bears the deadweights of pier, beams and tracks, and the live-load of train, which are as uniformly distributed load (149 kN/m^2) applied on the top surface of the platform.

In the next section, the displacement variations of the existing pile foundation and pier are analyzed, considering several construction stages of the new bridge foundation, such as group-piles construction, platform pit excavation, platform concrete casting, pier construction, and application of superstructures loads.

9.3.4 Displacements of Existing Piles After the Construction of New Group-Piles

Shown in Fig. 9.22 are the displacement nephograms of the existing pile foundation, calculated at the stage when the new group-piles construction is completed, in which the positive values indicate the displacements toward the construction site, while the negative ones away from the construction, with respect to the initial values in stage 1.

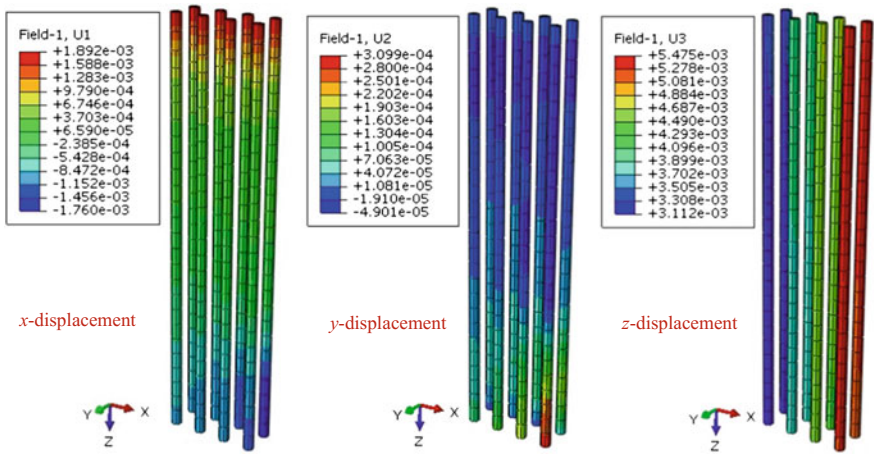

Fig. 9.22 Displacement nephograms of existing piles caused by adjacent group-piles construction

The figures show that:

(1) After the construction of group-piles, the maximum displacement of existing piles in *x*-direction (perpendicular to the railway line) is 1.89 mm, appearing at the pile-tops, and the maximum negative displacement is −1.76 mm, appearing at the bottoms of two piles close to the construction side.

(2) The displacements of existing piles in *y*-direction (parallel with the railway line) are small, with an order of magnitude less than those in *x*- and *z*-directions; the maximum is 0.3 mm, appearing at the bottom of the piles close to the construction side.

(3) The maximum vertical displacement of existing piles is 5.5 mm, appearing at two piles close to the construction side, and the displacement decreases progressively from the near construction side to the far side, with the minimum of 3.1 mm.

(4) Since the elastic modulus of concrete is much larger than that of subsoil, the vertical displacements at various nodes on each single pile are basically the same. At the top of the piles, the vertical displacements of each row of piles vary linearly, indicating that the existing platform produces not only overall vertical displacement, but also rotational displacement due to the construction of the new group-piles.

(5) Since the group-piles is bound together with the foundation platform at pile-tops, the displacements of all piles at top are identical with those of platform, the maximum lateral displacement in *x*-direction being 1.89 mm toward the construction, while at the lower parts of the piles, the lateral displacements in *x*-direction present difference with the distance from the construction side.

9.3.5 *Displacements of Existing Pile Foundation After the Pit Excavation of New Platform*

Shown in Fig. 9.23 are the displacement distribution curves of Piles 1–4 of the existing bridge foundation, at the stage after the platform pit of the new bridge foundation is excavated. In the figure, the lateral direction means that perpendicular to the railway line, and the longitudinal means that parallel with the line.

It can be observed from Fig. 9.23 that:

(1) When the platform pit excavation of the new bridge is completed, the maximum lateral displacement at the top of existing piles is 0.36 mm, which is 1.53 mm smaller than that before the excavation, indicating the incline of the piles rebounds a bit but is still toward the construction side. The lateral maximum displacement at the pile-bottom is −0.8 mm, slightly decreased after the excavation.
(2) The maximum longitudinal displacement of the existing piles is −0.05 mm at the pile-top, and 0.27 mm at the pile-bottom (Pile 4).
(3) The maximum vertical displacement is 0.55 m at Pile 1, and the minimum is 0.24 mm at Pile 4, both decreased in this stage, due to the uplift of subsoil by the unloading of soil after excavation.

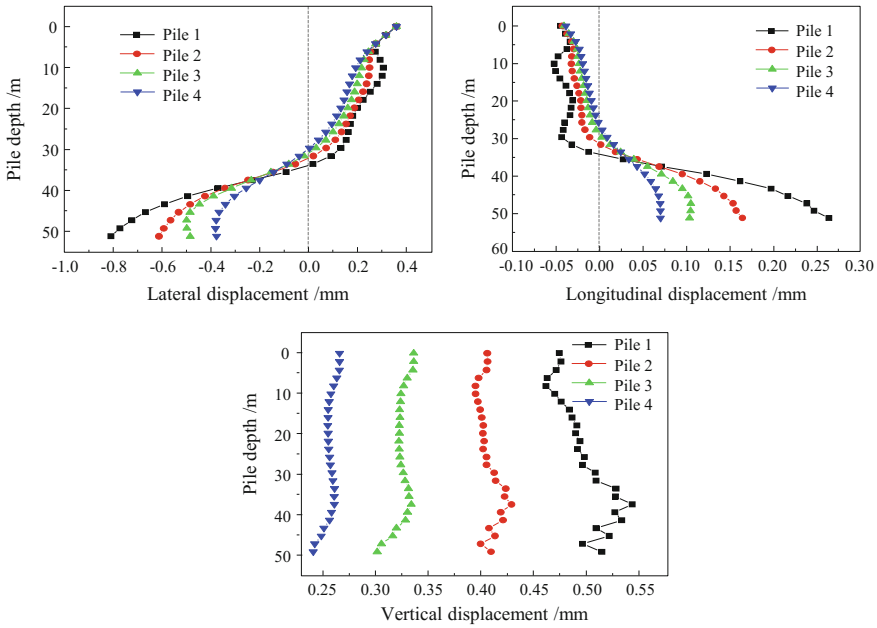

Fig. 9.23 Displacement distributions of existing piles induced by adjacent platform pit excavation

9.3.6 Displacements of Existing Pile Foundation After the Concrete Cast of New Platform

Shown in Fig. 9.24 are the lateral, longitudinal, and vertical displacement distributions of Piles 1–4 of the existing foundation after the concrete of new platform is cast.

By comparing Figs. 9.24 and 9.23, it can be seen that the existing piles continue to incline toward the construction side after the concrete cast of platform: the maximum lateral displacement at pile-top is 0.7 mm, increased by 0.34 mm from the previous stage; the maximum lateral displacement at pile-bottom is −0.9 mm, with very small change of −0.1 mm. The longitudinal displacements change little in this stage. The vertical displacements increase significantly, from 0.55 to 1.3 mm for Pile 1, and from 0.25 to 0.7 mm for Pile 4, due to the increase of subsoil deformation close to the construction side under the loading of new platform concrete.

9.3.7 Displacements of Existing Pier and Platform When the New Bridge Pier Is Loaded by Superstructure Loads

When the construction of the new pile foundation and platform is completed, the uniformly distributed load analyzed in Sect. 9.3.3 is applied on the platform to

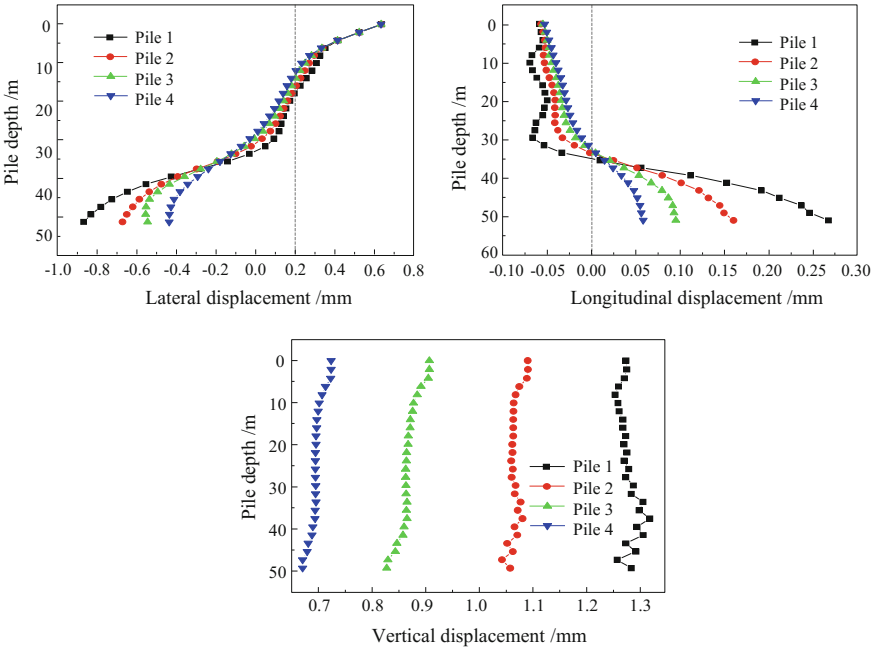

Fig. 9.24 Displacement distributions of existing piles after the new platform concrete is cast

simulate the effect of superstructure. Because the elastic modulus of concrete is much greater than that of soil, and the integrated stiffness of pier and platform as a whole is large, the lateral and vertical displacements of existing pier and platform are mainly caused by their overall translation or rotation. Therefore, in this section, the pier and the platform are analyzed as a whole, and the displacement coordination between them is achieved through binding constraints.

Shown in Fig. 9.25 are the pier-platform displacement nephograms of the existing bridge when the construction of the new pier is completed and the superstructure load is applied.

The displacements of existing pier-platform have the following characteristics:

(1) The maximum lateral displacement is 3.72 mm at the pier-top, the minimum is 1.06 mm at the platform bottom, and both of them are positive, indicating the platform shifts with an incline toward the construction side.
(2) The maximum longitudinal displacement is only 0.048 mm, appearing at the platform top, which is much smaller than the lateral and vertical displacements.
(3) The maximum vertical displacement is 5.56 mm appearing at the platform close to the construction side, the minimum is 3.02 mm appearing at the platform away from the construction side, and both of them are positive, indicating both pier and platform settle downward with an incline toward the construction side.

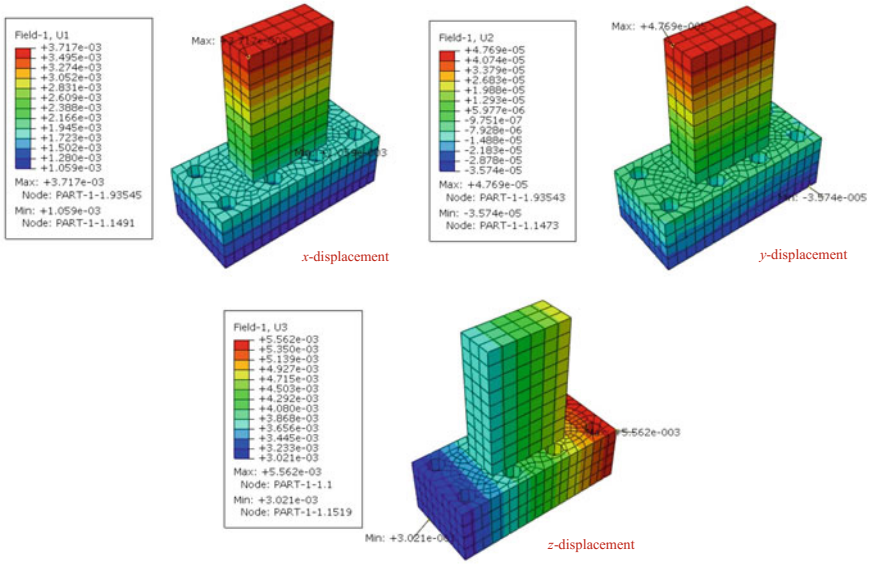

Fig. 9.25 Displacement nephograms of pier-platform of existing bridge

Table 9.6 Maximum displacements of existing pier and platform in various construction stages

Construction stages of new pier foundation	Maximum lateral displ. (mm)		Maximum vertical displ. (mm)	
	Existing platform	Existing pier	Existing platform	Existing pier
Before construction	0	0	0	0
Construction completion of Pile 1	0.02	0.05	0.06	0.05
Construction completion of the 1st row piles	0.13	0.25	0.28	0.28
Construction completion of the 2nd row piles	0.27	0.53	0.68	0.57
Construction completion of the 3rd row piles	0.54	1.07	1.35	1.16
After foundation pit excavation of platform	0.36	0.55	0.50	0.43
After concrete cast of platform	0.64	1.13	1.31	1.13
Application of superstructure load	1.89	3.72	5.56	4.88

In order to analyze in detail the vertical differential settlement of pier-platform of existing bridge caused by the foundation construction of the new bridge, Table 9.6 lists the maximum displacements of pier and platform at various construction stages. It can be seen that except in the stage of platform pit excavation, both the lateral and vertical displacements increase with the construction process, especially in the stage when the superstructure load is applied. The differential settlement of bridge foundation has a cumulative effect, and mainly occurs at positions close to the construction side. In various construction stages, the lateral displacements at the existing pier-top are greater than those of the platform, while the maximum vertical displacement occurs at the platform.

9.4 Influence of Differential Settlement of Bridge Foundation on Dynamic Responses of Train-Bridge System

According to the analysis above, the foundation construction may cause vertical differential settlements and lateral displacements at foundations and piers of nearby existing bridge.

In this section, the German ICE3 high-speed train passing through a (48+80+48) m continuous PC beam bridge is taken as an example, to study the influence of additional track deformation induced by the differential settlement of bridge foundation on the dynamic responses of train-bridge system.

9.4.1 Simulation of Additional Track Unevenness Induced by Differential Settlement of Bridge Foundation

When the differential settlement of bridge foundation occurs, the track on bridge may produce a vertical deformation. For the train-bridge vibration system, such deformation is equivalent to an additional long-wave unevenness superimposed to the original track irregularity, whose half wavelength is equal to the total span length of the beams supported by the subsided bridge pier.

In order to analyze the additional track unevenness, a FE model of three-span continuous bridge is established, as shown in Fig. 9.26, on which the double-block ballastless track is laid, and both ends of the track are stretched out by 20 m to simulate the beam-end-subgrade transition section. In the model, the bridge and track structures are simulated by beam elements, the fasteners connecting the track with the beam and the subgrade are simulated by spring elements with stiffness of 35 kN/mm, and the elastic deformation of the subgrade is neglected.

When there is a settlement of 10 mm at the left pier, the induced additional track unevenness curve is shown in Fig. 9.27. It can be seen that the curve is relatively gentle on the beam, but shows large local variation at the beam-ends. However, the local variation is smooth and continuous due to the continuity of the track, rather than a simple break angle. The maximum of the curve appears at the middle span near the left pier, and the unevenness in the left and middle spans is more obvious than that in the right span. In the following analysis, it is assumed that the additional track unevenness keeps its curve shape invariant but changes its amplitude with the settlement amount of the left pier.

Shown in Fig. 9.28 are the combined deformation curve by superimposing the additional unevenness induced by a 40 mm pier settlement with the original vertical track irregularity and the corresponding additional acceleration curve.

It can be seen that the baseline of the combined curve has a deviation when superimposed by the additional track unevenness, and the additional acceleration at the left beam-end shows an impact waveform, while almost unchanged in other part of the beam. This reflects that the additional track unevenness curve caused by the pier settlement varies intensely at the beam-end, while smoothly in the other part of the bridge.

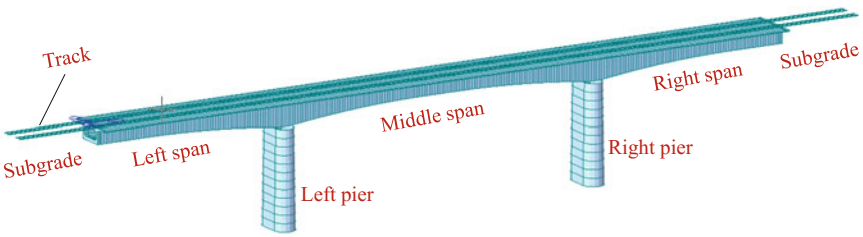

Fig. 9.26 FE model of bridge and track

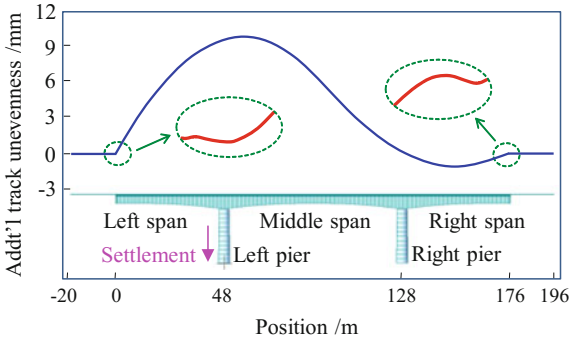

Fig. 9.27 Sketch of additional track unevenness caused by pier settlement

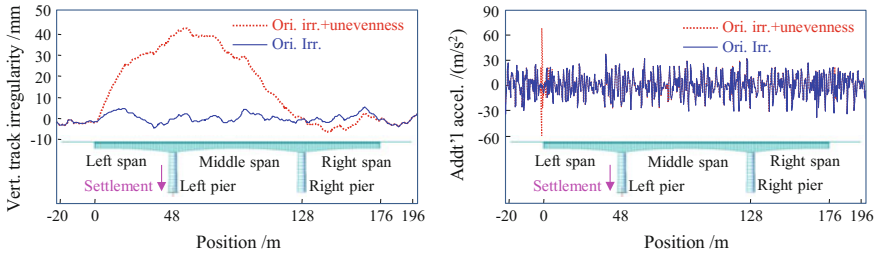

(a) Track irregularity (b) Additional acceleration

Fig. 9.28 Influence of pier settlement on track irregularity

The spatial spectra of the combined deformation curve and the original irregularity of the track are calculated, as shown in Fig. 9.29. In the spectrum curve of the combined deformation, there exists an obvious peak at the frequency of 0.004 m^{-1}. This peak represents a 250 m long-wave component, whose half wavelength is approximately equal to the sum of left span and middle span (128 m), while it does

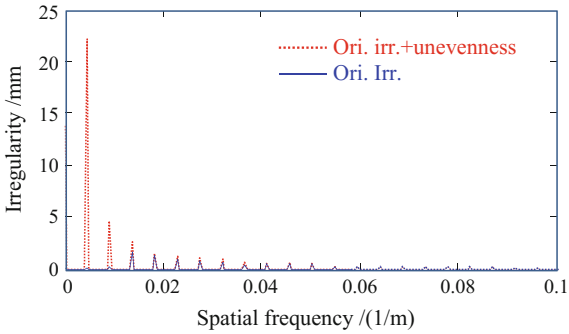

Fig. 9.29 Comparison of track irregularity spectra

not appear in the spectrum curve of the original track irregularity. Since the local deformation at beam-end is very small, the corresponding spectrum is not obvious.

9.4.2 Dynamic Response Analysis of the Train

In order to study the influence of differential settlement of bridge foundation on the running performance of high-speed trains, the settlement of the left pier is set to be 0–40 mm at every 5 mm, and the train speed to be 160–360 km/h at every 20 km/h, in the numerical analysis. Considering the randomness of track irregularity, ten samples of track irregularity are used in the analysis, and the average values of the calculated results are adopted to study the laws.

1. ***Car-body accelerations***

Shown in Fig. 9.30 are the car-body acceleration curves when the train passes through the bridge at the speed of 360 km/h, under the 40 mm settlement of the left pier, in which the position of the train is defined by its first wheel-set on the bridge.

It can be observed that when the train passes on the bridge with pier settlement, the car-body acceleration becomes much greater; when the train runs to the left end of the bridge, the car-body acceleration begins to increase and reaches the maximum at the position of the settled pier.

Shown in Fig. 9.31 are the spatial distributions and contour graphs of maximum car-body acceleration (the average of ten groups of results, the same as follows) versus train speed and pier settlement amount. It can be seen that the car-body acceleration increases with the settlement, and the higher the train speed, the more obvious the increasing trend. The maximum car-body acceleration reaches 0.7 m/s^2 at the train speed of 240 km/h under 35 mm settlement, while the same acceleration can be achieved at the train speed of 280 km/h under 25 mm settlement, and at 320 km/h under 13 mm, respectively.

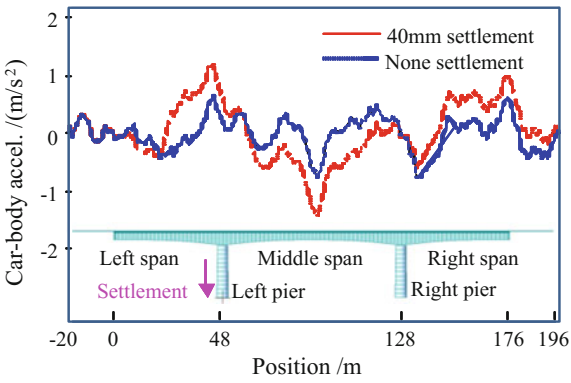

Fig. 9.30 Acceleration curves of car-body

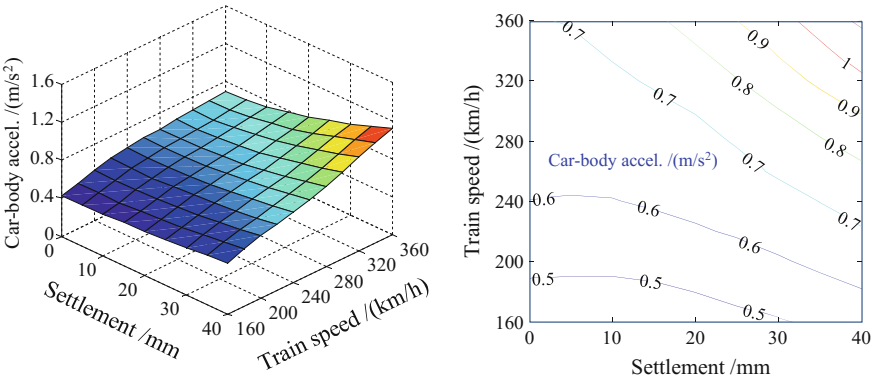

Fig. 9.31 Distributions of maximum car-body acceleration versus train speed and pier settlement

2. *Offload factor*

Compared in Fig. 9.32a are the variation curves of offload factors, when the train runs through the bridge with a 40 mm settlement and none settlement, at the speed of 360 km/h. In the case of 40 mm settlement, the offload factor changes dramatically when the train passes through the left beam-end, where the vertical wheel-rail interaction force increases a lot excited by the large local additional track unevenness due to the pier settlement.

To better describe the variations of vertical wheel-rail forces, Fig. 9.32b shows the variation curve of the dynamic wheel-rail force variation rate, defined as the ratio of dynamic wheel-rail force difference (between the values under settled and unsettled conditions) to static axle load. It can be seen that the wheel-rail force difference is very great when the train passes through the beam-end, while the variation curve is quite moderate in other sections. Because the long-wave unevenness caused by the pier settlement induces a low-frequency component on the vertical wheel-rail force, in the main trend, the wheel-rail force difference exhibits a decrease-increase-decrease variation curve when the first wheel-set of train passes successively on the left, middle and right spans.

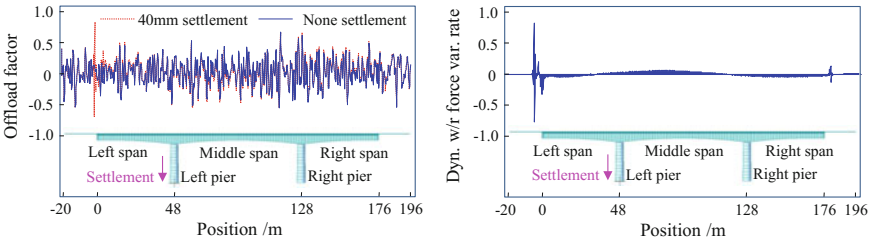

(a) Variation curves of offload factor (b) Curve of dynamic w-r force variation rate

Fig. 9.32 Variation curves of offload factor and dynamic w-r force variation rate

Shown in Fig. 9.33 are the spatial distributions and contour graphs of the maximum offload factors versus train speed and pier settlement, when the train passes through the beam-end and non-beam-end sections of the bridge.

It can be seen that when the train passes through the beam-end, the offload factor increases rapidly with both train speed and settlement, while on the other sections of the bridge, it only increases with train speed but changes little with pier settlement. For the settlement amount of 27 mm, 32 mm and 39 mm, the offload factors exceed the allowable value of 0.6, when the train passes through the beam-end at the speed of 360 km/h, 330 km/h and 300 km/h, respectively.

3. ***Derailment factor***

Compared in Fig. 9.34 are the variation curves of the derailment factors, when the train passes through the bridge with a 40 mm settlement and none settlement, at the speed of 360 km/h. It can be observed that the derailment factor changes sharply when the train passes through the beam-end due to the additional local track unevenness caused by the pier settlement.

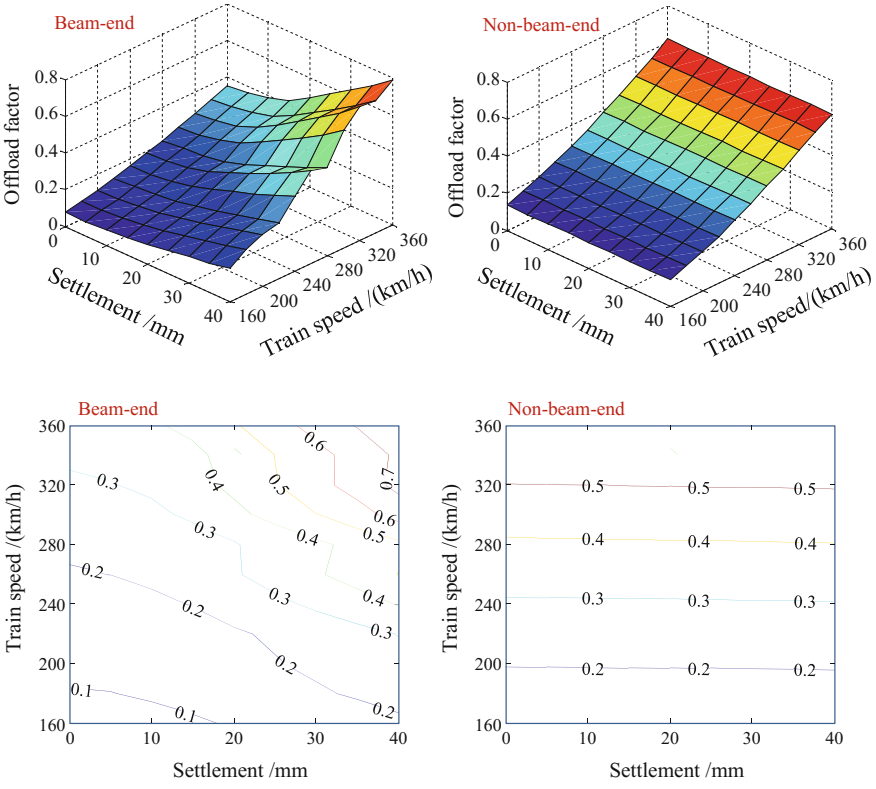

Fig. 9.33 Distributions of offload factors versus train speed and settlement amount

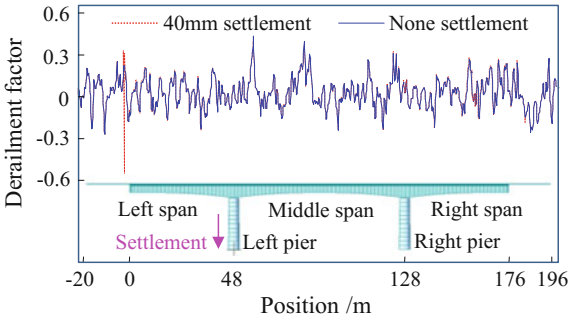

Fig. 9.34 Variation curves of derailment factors

Compared in Fig. 9.35 are the spatial distributions and contour graphs of maximum derailment factors versus train speed and pier settlement, when the train passing through the beam-end and non-beam-end sections of the bridge. It can be

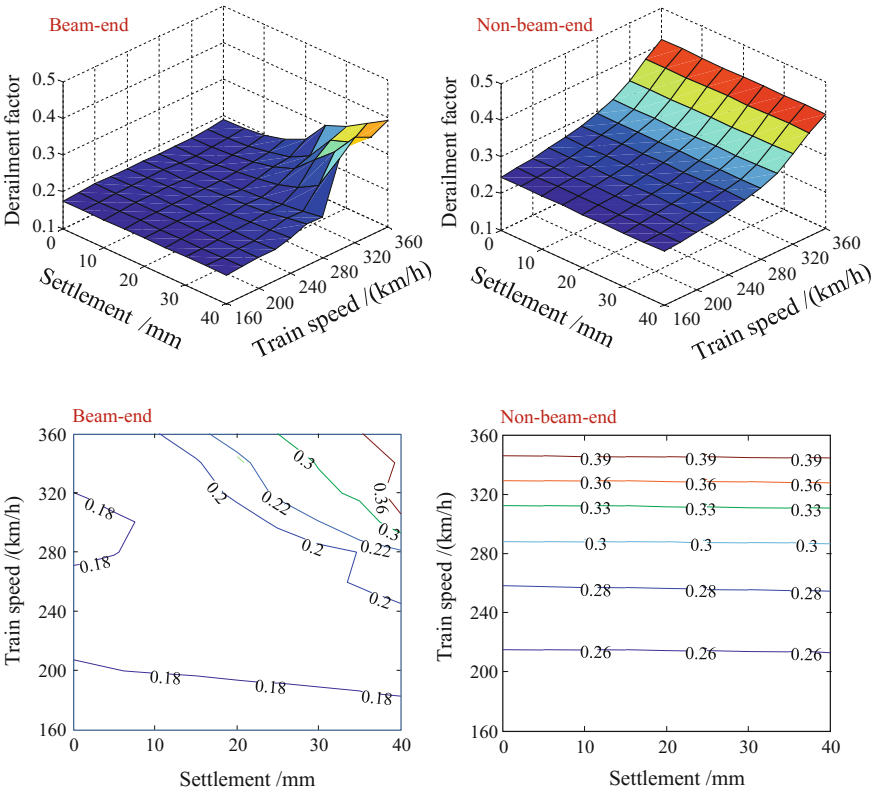

Fig. 9.35 Distributions of derailment factors versus train speed and settlement amount

seen that the distributions are similar to those of offload factors, namely the derailment factors increase with the train speed and the settlement; the settlement has greater impact on the derailment factors at the beam-end than in other sections; the higher the train speed, the faster the derailment factors increase; in this case study, no derailment factor exceeds the limit value of 0.8 in the considered ranges of settlement amount and train speed.

4. ***Evaluation threshold for running safety and riding comfort of trains***

The high-speed railway has strict requirements on running safety and riding comfort of trains. In the *Code for Design of High Speed Railway* (TB 10621 2014), some evaluation indices and their corresponding limits are regulated, such as offload factor, derailment factor, lateral wheel-rail force, and car-body acceleration.

In the previous analysis, the running indices of the train were discussed by using the averages of the results under ten track irregularity samples. This method can well reflect the influence of pier settlement on the running performance of trains, but there exists a problem, namely the acquired safety factors are insufficient when the maximums of the average values are directly used to determine the threshold of train speeds with respect to different settlement amounts to ensure the running safety and riding comfort of trains. Therefore, a more reasonable method, namely the probability-based method, is used in the following analysis.

In the analysis, the dynamic responses of the train under different track irregularity samples are assumed to obey the normal distribution, which indicates the running safety and riding comfort indices of the train have a 50% probability of exceeding the threshold based on the mean values.

Considering a 40 mm settlement at the left pier, the car-body accelerations, the offload factors, and the derailment factors under ten track irregularity samples when the train passes the bridge at different speeds are calculated, and the distributions of their maximums are illustrated in Fig. 9.36.

One can see that for the car-body accelerations, the influence of train speed on sample-1 is the most, while for the offload factors and derailment factors, the increase with train speeds under sample-6 is more obvious. At lower train speeds, the discreteness of running indices calculated from different samples is small, but it increases obviously with train speed. When the train speed is higher than 250 km/h, the offload factor and the derailment factor greatly increase, especially under sample-6, both of their maximums exceed 1.0 at the train speed of 360 km/h, much greater than the average values (0.789 and 0.390, respectively) calculated by the ten samples.

According to the probability theory, for a variable X obeying normal distribution, if the true standard deviation σ of X is unknown, when there are n random samples, the upper limit value $X_{(1-a)}$ with confidence (1-a) can be obtained by

$$X_{(1-a)} = \bar{X} + \frac{S}{\sqrt{n}} t_a(n-1) \tag{9.11}$$

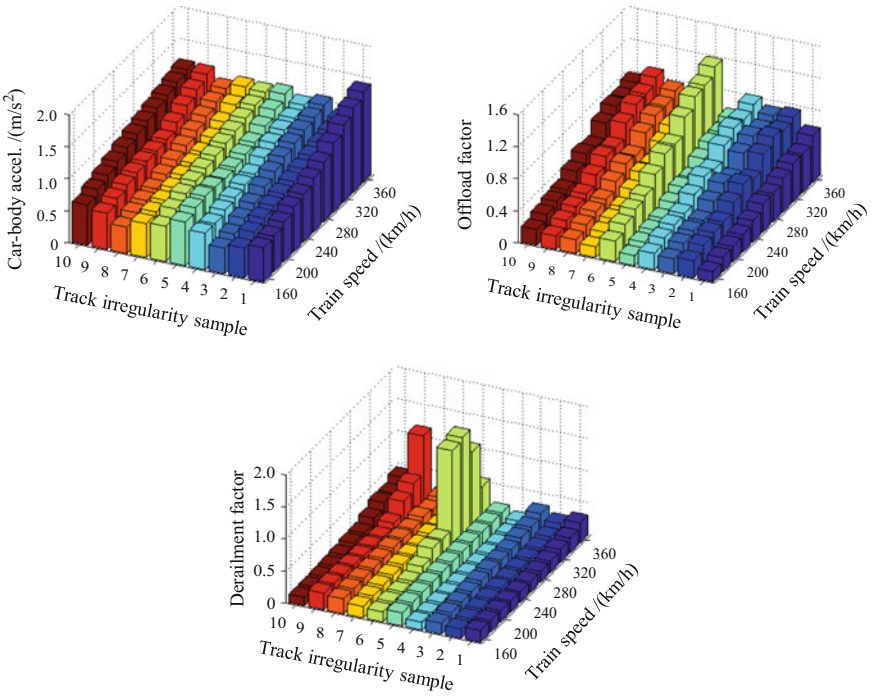

Fig. 9.36 Distributions of maximum running indices under ten track irregularity samples

where $\bar{X}$ is the average of n samples; S is the standard deviation of n samples; $t_a(n-1)$ is the upper limit value corresponding to confidence $(1-a)$ in t-distribution of the $(n-1)$ samples. When $a = 0.05$ and $n = 10$, $t_{0.05}(9) = 1.8331$ can be obtained from the mathematical manual.

When the train passes through the (48+80+48) m continuous bridge under the ten track irregularity samples and various settlement amounts, the dynamic responses of the train are calculated, based on which the safety and comfort thresholds with 95% confidence are proposed according to Eq. (9.11).

Taking the offload factor as an example, the threshold curves of running safety are shown in Fig. 9.37, in which the dash-dotted line denotes the safety boundary with confidence 95%, and the dashed line denotes the boundary with confidence 50% (obtained by using the average values). It can be seen that for the train speed of 280 km/h, the allowable differential settlement of piers can be 40 mm, while for the train speed of 360 km/h, it is reduced to 25 mm; the threshold boundary with confidence 95% lies within the boundary obtained from the average values, indicating a higher safety probability.

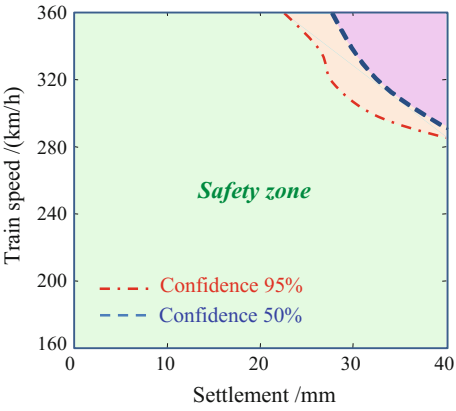

Fig. 9.37 Threshold diagram for running safety of train

9.4.3 Dynamic Response Analysis of the Bridge

Shown in Fig. 9.38 are the time histories of bridge mid-span displacement under the 40 mm settlement and none settlement, when the train passes through the bridge at the speed of 360 km/h. In the curves, several typical positions of the train on the bridge are located by the wheels. As can be seen, when the train runs through the three spans of the bridge with pier settlement, the mid-span displacement curves of them are similar to those without settlement, being slightly bigger at the middle span and a bit smaller at the two side spans. Owing to the large span lengths, the curves exhibit obvious characteristics of the quasi-static deflection curve produced by the axle load series of the train moving at lower speeds.

Shown in Fig. 9.39 are the distributions of maximum mid-span accelerations and displacements of the three spans versus train speed, respectively, under none, 20 and 40 mm settlement amounts.

It can be seen that in the main trend, the maximum accelerations of bridge increase monotonically with train speed, while for the displacement, the distributions are complex, with several peaks appearing at certain train speeds, indicating the vibrations of the bridge are amplified at these speeds. Under none, 20 and 40 mm settlement conditions, the difference of the maximum bridge displacements is very large, while the difference of maximum accelerations is quite small. The reason is that the foundation settlement produces great local additional track unevenness only at the beam-end, which has little influence on the mid-span accelerations. The maximum displacements of the middle span are more significantly influenced by foundation settlement amounts than the side spans, especially when the train speed is higher than 240 km/h.

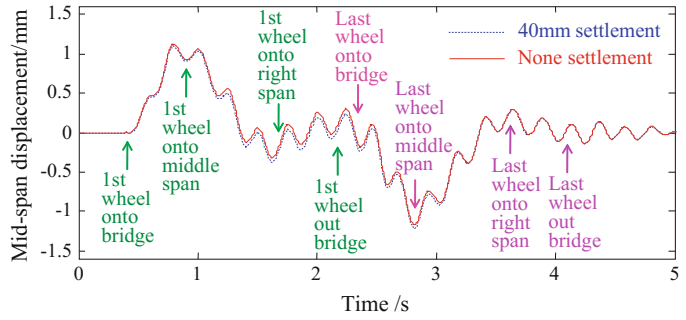

(a) Left side span

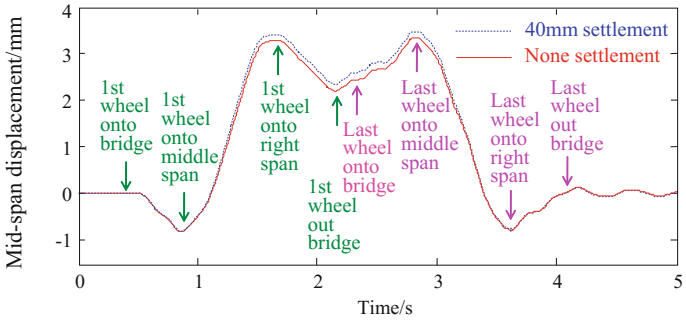

(b) Middle span

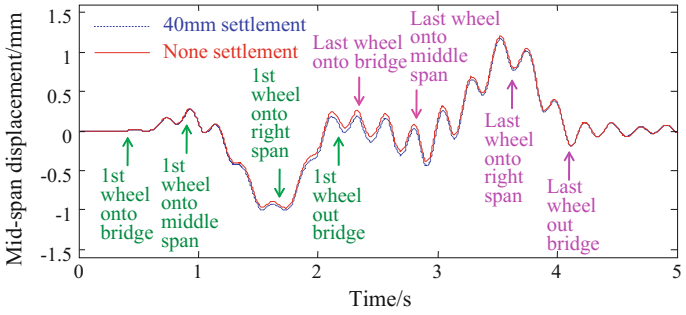

(c) Right side span

Fig. 9.38 Time histories of bridge mid-span displacement

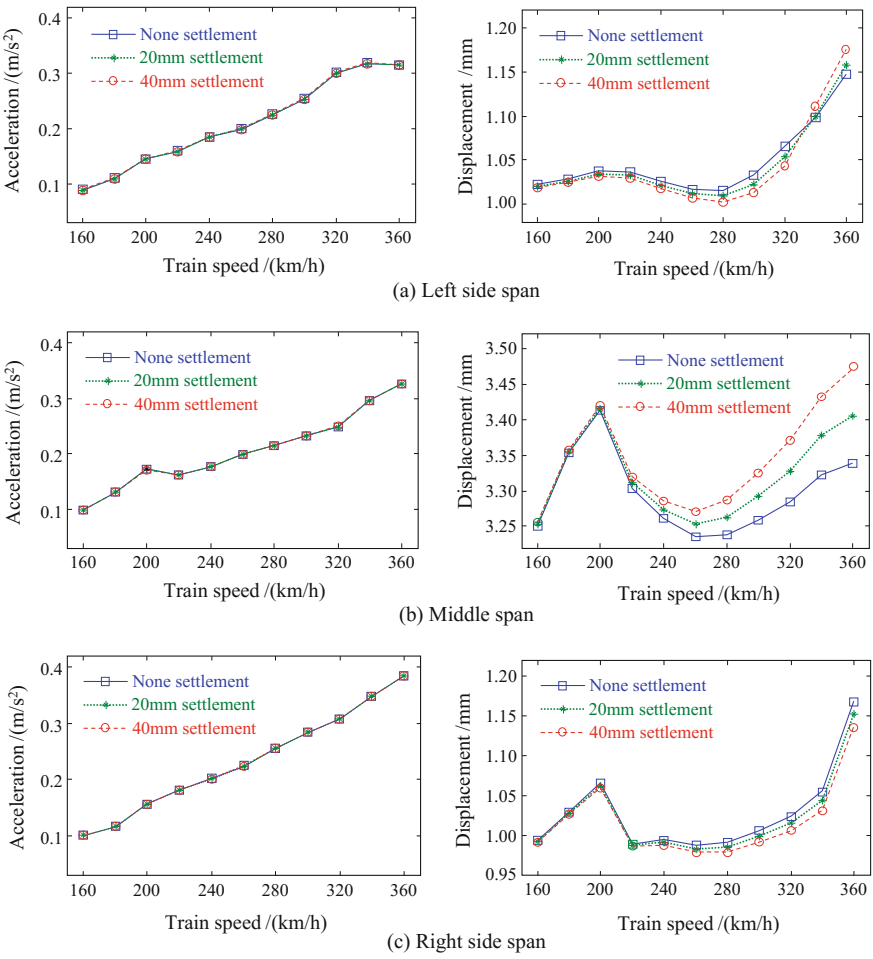

Fig. 9.39 Distributions of maximum mid-span accelerations and displacements of the bridge versus train speed

9.5 Influence of Pier Foundation Scouring on Running Safety of High-Speed Trains

9.5.1 Outline of Pier Foundation Scouring

For bridges in a water environment, the water scouring on pier foundations often leads to the decrease of their stiffness, insufficient bearing capacity, and even instability failure of piers (Fang 2013; Kong and Cai 2016). In China, there have been many bridge accidents caused by water scouring. For example, in 1956, after a flood peak, a pier of the Zhengzhou Yellow River Bridge was scoured by 14 m,

leading it badly leaned, and two years later, the bridge was destroyed by an extraordinary flood (Chen 2013). On 4 August, 2001, due to the over sand-excavation in the riverbed and a sudden heavy rainstorm, the Dongquan River Bridge was seriously scoured, causing two piers to become shallow foundations and tilt off the line, as seen in Fig. 9.40a, which made the bridge scraped and the traffic interrupted for 4 months (Ma et al. 2008). On November 14, 2009, a brick-arch bridge on Feltham Railway in England collapsed because of the water scouring to its foundations (Liu 2009), as shown in Fig. 9.40b. On June 4, 2015, the Huangkou Bridge on Yougang River collapsed, as shown in Fig. 9.40c, because the riverbed was scoured by flood and thus the pier foundations were hollowed out (Zeng 2015). According to the investigation statistics, among the 215 events of bridge flood accidents, more than 96 were caused by scouring to pier foundations (Chen 2013).

According to the *Report on Scouring and Calculation of American Bridges in 2001* (Lagasse and Richardson 2001), in more than 496,000 existing overwater bridges in the USA, there were 26,000 facing the threat of or suffering from the scouring to piers and waterbeds. Thirty years before, there had been about 1000 bridges destroyed in the USA, in which 60% of accidents were caused by serious scouring to pier foundations.

For high-speed railway bridges, once the foundation is scoured, even if there is no direct destruction of the girder or the pier, the stiffness of foundation will be

(a) the Dongquan River Bridge

(b) the brick-arch bridge on Feltham Railway (England)

(c) the Huangkou Bridge on Yougang River

Fig. 9.40 Bridges destroyed by scouring to pier foundations

reduced, thus resulting in large deformation and vibration of the bridge under the loads, which may change the smoothness and stability of the track, affecting the running safety and riding comfort of the train on bridge. Therefore, it is necessary to study the scouring effect on the dynamic characteristics of bridge foundations.

9.5.2 *Scouring Mechanism*

The influence factors of scouring effect on pier foundations can be divided into two categories. The first is related to the flow and sediment, including the flow velocity, water depth, sediment particle size and gradation, and bed sand viscosity. The second is related to the bridge pier, including its structural shape, upstream face width and length, and the angle with the flow direction. In the bridge hydrology, the scouring problem is studied in three patterns: natural evolution scour, general scour, and local scour, as shown in Fig. 9.41.

Before the bridge construction, the water at the pier site is in equilibrium state. After the bridge is constructed, the pier and the foundation lie in wave current. Due to the resistance effect of the pier, the water in upstream rises, while the flow of two sides contract and speed up, which makes the water kinetic energy increase and the water surface fall, thus the water in downstream becomes instability. Affected by the friction resistance of the riverbed, the velocity gradient occurs along the vertical direction, namely the water flows faster at the surface while slow close to the riverbed, forming the pressure gradient. Meanwhile, a high water head is formed over the foundation, which flows downward rapidly along the foundation surface when it encounters an obstacle, forming a clockwise whirlpool in the transverse direction. When it joins to the longitudinal flow near the bottom, a horseshoe vortex winding around the foundation forms, which is the main dynamic cause of

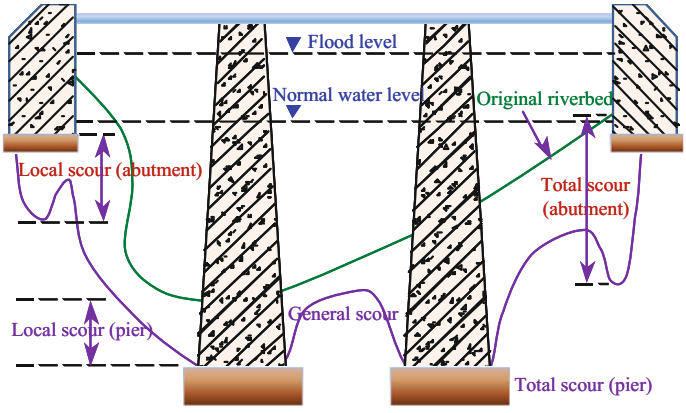

Fig. 9.41 Schematic diagram of bridge foundation scouring

foundation scouring. Since the negative pressure of the vortex center produces adsorption force to the sediments on the riverbed, the sediments begin to move if the gravity or the cohesive force between sediment particles cannot resist this adsorption. Next, the streaming occurs around the two sides of foundation, and the flow velocity increases, which makes the moving sediment particles in the state of suspension. Since the flow pressure gradient behind the foundation is contrary to that in the front zones, the rip current of water occurs, producing the wake flow moving toward the water surface, which carries the sediment particles away from the scouring pits. In the scouring equilibrium state, namely when the amount of sediment washed away from the pit is equal to that input from the outside, the depth of the scour pit reaches the maximum (Jing 1993).

The scouring to bridges is a complex process that involves in the continuous interaction of water with riverbed, pier, or abutment. In the past decades, the research on the scouring mechanism was mainly based on numerical analysis and experiments (Melville and Raudkivi 1977; Young et al. 1998; Kassem et al. 2003; Sheppard and Miller 2006). In recent years, people started to study the influence of stream scouring on bridge foundation by analyzing the variation of vibration characteristics of the bridge. The study of Samizo et al. (2007) showed that the natural frequencies of bridge piers decrease with the foundation scouring depth. Loh et al. (2011) carried out a series of model tests in hydraulic laboratory and studied the changes of dynamic characteristics of bridges in the process of scouring. Chen et al. (2014) proposed an evaluation method for pier scouring, based on the measured data from the ambient vibration survey on the superstructures of a cable-stayed bridge.

9.5.3 Calculation of Scouring Depth

Generally, the scouring depth is calculated by two steps: firstly the general scouring depth is calculated, then the local scouring depth is calculated according to the flow conditions after general scouring, and the sum of the two depths is the total scouring depth.

For the general scouring depth, both the *Code for Survey and Design on Hydrology of Railway Engineering* (TB10017 1999) and the *Code for Survey and Design on Hydrology of Highway Engineering* (JTG C30 2015) recommend the formulae derived by the principle of stopping velocity.

The stopping velocity refers to the average vertical flow velocity when the general scouring under the bridge stops, denoted by v_z (m/s). In the course of general scouring, when the flow velocity across the sections under the bridge is less than the stopping velocity, meaning the end of the scouring, the water depth at this time is considered to be the maximum water depth after general scouring. According to the principles of hydraulics, the formula for calculating the maximum scouring depth h_p is as follows:

$$h_{\mathrm{p}} = \frac{q_{\max}}{v_z} \tag{9.12}$$

where $v_z = Ed_j^{1/6}h_{\mathrm{p}}$, E is the parameter of sediment content in the flow, d_j is the average particle size of sediment; $q_{\max}$ is the largest flow per unit width under the bridge (m^3/s), expressed as

$$q_{\max} = \frac{Q_{\mathrm{s}}}{\mu L_j}\left(\frac{h_{\max}}{h_j}\right)^{\frac{5}{3}} \tag{9.13}$$

where Q_{s} is the design flow (m^3/s); L_j is the minimum clearance length under the bridge (m); $h_{\max}$ is the maximum water depth of design section near the bridge (m); h_j is the average water depth near the bridge (m); μ is the compression coefficient of the flow.

According to the concept of stopping velocity and the above formulae, the general scouring depth for the riverbed under the bridge can be calculated as

$$h_{\mathrm{p}} = \left(\frac{A\frac{Q_{\mathrm{s}}}{\mu L_j}\left(\frac{h_{\max}}{h_j}\right)^{\frac{5}{3}}}{Ed_j^{1/6}}\right)^{\frac{3}{5}} \tag{9.14}$$

where $A = \left(\sqrt{B}/H\right)^{0.15}$ is the concentration factor of flow per unit width, in which B is the riverbed width (m), and H is the average water depth of riverbed at the designed flood level (m).

The local scouring depth h_{b} of pier is related to the pier-ahead flow velocity, pier width, pier shape, water depth, particle size of sediments, and other factors. On the basis of some model test results and the long-term observation data for 52 bridges, the highway/railway administrations of China issued the calculation formulae of local scouring depth for bridge foundations. In the *Code for Survey and Design on Hydrology of Railway Engineering* (TB10017 1999), the local scouring depth of bridge piers on the riverbed with non-cohesive soil can be calculated by the following formulae

$$\begin{cases} h_{\mathrm{b}} = K_\xi K_\eta B_1^{0.6}(v - v_0') & (v \le v_0) \\ h_{\mathrm{b}} = K_\xi K_\eta B_1^{0.6}(v_0 - v_0')\left(\dfrac{v - v_0'}{v_0 - v_0'}\right)^n & (v > v_0) \end{cases} \tag{9.15}$$

where: K_ξ and K_η are the shape coefficient of pier and the particle coefficient of riverbed sediment, respectively; B_1 is the calculation width of pier; v is the approaching flow velocity ahead of the pier after general scouring (m/s); v_0 is the incipient velocity of riverbed sediment (m/s); v_0' is the initial flow velocity ahead of pier (m/s); n is the exponent. All the parameters can be valued from Clause 3.6.6 and Appendix G in the code.

For the group-piles foundation, when the relative height h_ϕ/h of platform bottom lies in [0, 1.0], the local scouring depth h_b of the pier can be calculated by

$$h_b = \left(K'_\xi K_{m\phi} K_{h\phi} \Phi^{0.6} + 0.85 K_{\xi 1} K_{h2} B_1^{0.6}\right) K_\eta (v_0 - v'_0) \left(\frac{v - v'_0}{v_0 - v'_0}\right)^n \tag{9.16}$$

where: K'_ξ is the shape coefficient of single pile; h_ϕ is the distance from platform bottom to riverbed (m); h is the distance from water level to riverbed (m); $K_{h\phi} = 1.0 - \frac{0.001}{(h_\phi/h + 0.1)^3}$ is the reduction coefficient due to piles submerged; $K_{m\phi} = 1 + 5\left[\frac{(m-1)\Phi}{B_m}\right]$ is the group-piles coefficient, in which m is the row number of piles perpendicular to the flow direction, Φ is the pile diameter (m), B_m is the distributed width of group-piles perpendicular to the flow direction (m); $K_{\xi 1}$ is the pier shape coefficient related to h_ϕ/h, which is calculated considering that the platform bottom is located on the general scouring line; K_{h2} is the reduction coefficient of pier-body and platform.

9.5.4 *Effect of Scouring on Equivalent Stiffness of Group-Piles*

In this section, the scouring process of subsoil is simulated by regarding it as the excavating process of subsoil, to analyze the equivalent stiffness variations of group-piles before and after scouring.

1. **Distribution of elastic resistance of subsoil**

The pile foundation may produce translational and rotational displacements when subjected to loads (including axial load, transverse load, and moment) and thus squeeze the subsoil around piles, while the subsoil inevitably generates resistance, called the elastic resistance of soil, to resist the external forces and keep the pile foundation stable. There are various factors affecting soil resistance, including the properties of soil, the stiffness, buried depth, section shape, spacing and loads of piles, and others.

The elastic resistance of soil can be calculated by the subsoil coefficient method, using subsoil coefficient C to represents the force required to produce the unit deformation for the soil per unit area within elastic limit (unit: kN/m^3). The foundation coefficient C is related to the categories and properties of subsoil, and also varies with the depth, which can be obtained by the inverse calculation method based on measuring the piles in different layers at different depths. There are various methods to determine the foundation coefficient, such as the typical m-method, K-method, C-method, and Zhang's method. In these methods, the distributions of subsoil coefficient C with depth are different, as shown in Fig. 9.42 and Table 9.7,

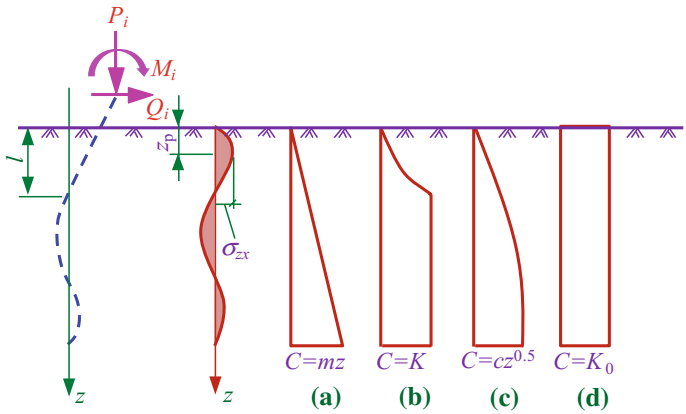

Fig. 9.42 Distribution curves of subsoil coefficient with depth

Table 9.7 Several typical subsoil coefficient methods

Method	Figure	Distribution with depth	Coefficient C	Remarks
m-method	9.42a	Proportional to depth	$C = mz$	m is the scale coefficient of soil horizontal resistance
K-method	9.42b	Parabolic varying with depth above the first zero point of pile deflection, and unchanged below	$C = K$	K is constant
C-method	9.42c	Varying parabolically with depth	$C = cz^{0.5}$	c is the proportionality coefficient of soil
Zhang's method	9.42d	Uniformly distributed with depth	$C = K_0$	K_0 is constant

in which z is the soil depth, and z_p is the soil depth corresponding to the peak stress. In the following sections, the m-method is used to consider the elastic resistance of subsoil.

2. **Calculation of equivalent stiffness of group-piles by the m-method**

(1) Scale coefficient m of horizontal subsoil resistance

The scale coefficient m of horizontal resistance of subsoil is generally determined by the horizontal static load test of piles. When no test is applicable, the m value can be selected from the empirical values shown in Table 9.8.

Table 9.8 Scale coefficients m of non-rock soils

No.	Soil type	m or m_0 (MN/m^4)
1	Fluid plastic clay soil with IL > 1, sludge	3–5
2	Soft plastic clay soil with 1 > IL > 0.5, silty sand	5–10
3	Hard plastic clay soil with 0.5 > IL > 0, fine sand, medium sand	10–20
4	Hard and half-hard clay soil with IL < 0, coarse sand	20–30
5	Gravel sand, rubble, pebbles, aggregates, cobbles	30–80
6	Dense coarse sand with cobbles, dense floated cobbles	80–120

Note (1) for the scale coefficient at the bottom of foundation, the formula is $C_0 = m_0 \cdot h$, in which m_0 is the scale coefficient of vertical resistance at the bottom of foundation, h is the buried depth of foundation; (2) IL means the liquidity index of the soil

When the subsoil is layered around the piles, the m values of various layers within the dominated influence depth h_m should be calculated, in which the depth starts from the ground surface or the local scouring line.

When there exist two subsoil layers in the depth of h_m, the m within the entire depth can be calculated by

$$m = \frac{m_1 h_1^2 + m_2(2h_1 + h_2)h_2}{h_m^2} \tag{9.17}$$

When there exist three subsoil layers in the depth of h_m, the m within the entire depth can be calculated:

$$m = \frac{m_1 h_1^2 + m_2(2h_1 + h_2)h_2 + m_3(2h_1 + 2h_2 + h_3)h_3}{h_m^2} \tag{9.18}$$

where $h_m = 2(d + 1)$, and d is the diameter of the piles (unit: m).

It can be seen from Tables 9.7 and 9.8 that the horizontal resistance coefficient of subsoil around piles is $C_n = m \cdot h_m$, and the vertical resistance coefficient at the bottom of pile foundation is $C_0 = m_0 \cdot h$ (when $h < 10$ m, $C_0 = 10 \times m_0$).

(2) The m-method for a single pile

If the pile-top is leveled with the ground surface ($z = 0$) and is subjected to the horizontal load Q_0 and the bending moment M_0, the pile will produce elastic deflection, and thus, the soil around the pile will generate lateral resistance σ_{zx}. The differential equation of pile deflection can be written as

$$EI\frac{d^4x}{dz^4} = -\sigma_{zx} \cdot b_1 \tag{9.19}$$

where E and I are elastic modulus and sectional moment of inertia of the pile, respectively; $\sigma_{zx} = Cx_z = mzx_z$ is resistance of soil around the pile; x_z is lateral displacement (namely lateral deflection) of the pile at depth z; b_1 is effective width of the pile.

Equation (9.19) can be rewritten as

$$\frac{\mathrm{d}^4 x}{\mathrm{d}z^4} + \alpha^5 z x_z = 0 \tag{9.20}$$

where $\alpha = \sqrt[5]{mb_1/EI}$ is deformation coefficient, or called the eigenvalue, of the pile (1/m).

It is easy to see that the lateral displacement of the pile is related to the calculation depth, the stiffness of the pile (reflected by pile material and section size), and the properties of the surrounding subsoil.

The lateral displacement x_z of the pile at any depth can be expressed as

$$x_z = x_0 A_1 + \frac{\phi_0}{\alpha} B_1 + \frac{M_0}{EI\alpha^2} C_1 + \frac{Q_0}{\alpha^3 EI} D_1 \tag{9.21}$$

where x_0, ϕ_0, M_0, and Q_0 are, respectively, the horizontal displacement, rotation angle, bending moment, and shear force of the pile on the ground surface ($z = 0$).

Then, the rotation angle ϕ_z, bending moment M_z, and shear force Q_z of the pile at any depth can be obtain by differentiating x_z, expressed as

$$\frac{\phi_z}{\alpha} = x_0 A_2 + \frac{\phi_0}{\alpha} B_2 + \frac{M_0}{\alpha^2 EI} C_2 + \frac{Q_0}{\alpha^3 EI} D_2 \tag{9.22}$$

$$\frac{M_z}{\alpha^2 EI} = x_0 A_3 + \frac{\phi_0}{\alpha} B_3 + \frac{M_0}{\alpha^2 EI} C_3 + \frac{Q_0}{\alpha^3 EI} D_3 \tag{9.23}$$

$$\frac{Q_z}{\alpha^3 EI} = x_0 A_4 + \frac{\phi_0}{\alpha} B_4 + \frac{M_0}{\alpha^2 EI} C_4 + \frac{Q_0}{\alpha^3 EI} D_4 \tag{9.24}$$

According to the basic assumption of soil resistance $\sigma_{zx} = mzx_z$, the resistance of the surrounding subsoil can be expressed as

$$\sigma_{zx} = mzx_z = mz\left(x_0 A_1 + \frac{\phi_0}{\alpha} B_1 + \frac{M_0}{EI\alpha^2} C_1 + \frac{Q_0}{\alpha^3 EI} D_1\right) \tag{9.25}$$

where A_i, B_i, C_i, and D_i (i = 1–4) are 16 dimensionless coefficients, which have been tabulated according to different conversion depths $\bar{z} = \alpha z$ in relevant specifications; M_0 and Q_0 can be determined by the known forces on the pile-top; x_0 and ϕ_0 need to be confirmed by the boundary conditions at the bottom of pile (Ling and Yi 1997).

(3) Stiffness coefficient of a single pile and equivalent stiffness coefficient of group-piles

For a bridge foundation with group-piles, the loads transferred from the pier are applied to the foundation platform, as shown in Fig. 9.43. Since the pile-tops are

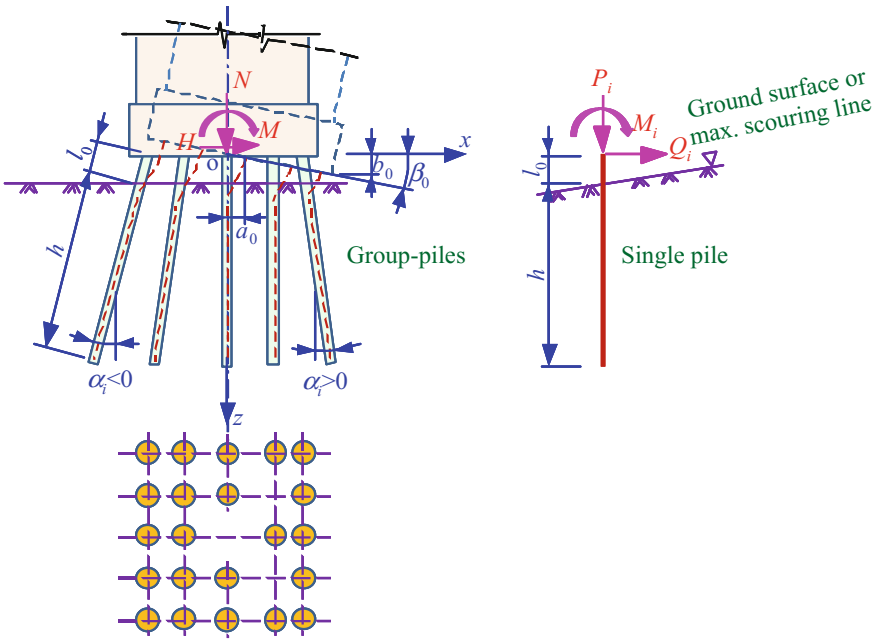

Fig. 9.43 Load-carrying diagrams of group-piles foundation and a single pile

embedded in the platform, the connection between the piles and the platform can be regarded to be rigid. In a group-piles, the relative position of each pile to the load is different, resulting in different displacements of the pile-tops under the external loads, and thus, the loads P_i, Q_i,and M_i distributed to each pile-top are different.

In the analysis model, the platform is assumed as a rigid body, the center o of the platform bottom surface is the representative point for the overall displacements of the platform, and the lateral displacement, vertical displacement, and rotation of point o produced by the external loads N, H, and M are denoted by a_0, b_0, and β_0, respectively.

Because the platform has large stiffness and is rigidly connected with the pile-tops, the relative positions between the pile-tops keep unchanged when the platform displaces under the external loads, and the rotation angle of each pile-top is equal to that of the platform. If the displacements of the ith row of piles in the x- and y-directions are a_i and b_i, and the rotation is β_i, respectively, then $a_i = a_0$, $b_i = b_0 + x_i\beta_0$ and $\beta_i = \beta_0$ are applicable, in which x_i is the horizontal distance from the axis of the ith row of piles to the platform center.

Furthermore, the relationship of pile-top displacements with the internal forces needs to be determined, to establish the displacement equation. So, the stiffness coefficient ρ_{AB} of a single pile-top is introduced, which means the internal force of pile-top in A-direction induced by a unit displacement on the pile-top in B-direction.

As shown in Fig. 9.43, when the axial force P_i, the horizontal force Q_i, and the bending moment M_i are applied on the ith pile-top, the stiffness coefficients of the pile-top are represented as follows:

(1) When a unit axial displacement ($b_i = 1$) occurs at the ith pile-top, the induced axial force there is ρ_{PP}, abbreviated as ρ_1;
(2) When a unit horizontal displacement ($a_i = 1$) occurs at the ith pile-top, the induced lateral force there is ρ_{QQ}, abbreviated as ρ_2; and the induced bending moment is ρ_{MQ}, abbreviated as ρ_3.
(3) When a unit rotation angle ($\beta_i = 1$) occurs at the ith pile-top, the induced lateral force there is ρ_{QM}, satisfying $\rho_{QM} = \rho_{MQ} = \rho_3$; and the induced bending moment there is ρ_{MM}, abbreviated as ρ_4.

The internal forces of the ith pile-top caused by the displacements of platform can be calculated as

$$\left.\begin{aligned} P_i &= \rho_1 b_i = \rho_1[a_0 \sin\alpha_i + (b_0 + x_i\beta_0)\cos\alpha_i] \\ Q_i &= \rho_2 a_i - \rho_3\beta_i = \rho_2[a_0\cos\alpha_i - (b_0 + x_i\beta_0)\sin\alpha_i] - \rho_3\beta_0 \\ M_i &= \rho_4\beta_i - \rho_3 a_i = \rho_4\beta_0 - \rho_3[a_0\cos\alpha_i - (b_0 + x_i\beta_0)\sin\alpha_i] \end{aligned}\right\} \tag{9.26}$$

Thus, as long as a_0, b_0, β_0 and ρ_1, ρ_2, ρ_3, ρ_4 are solved, P_i, Q_i, and M_i can be obtained by Eq. (9.26), and the internal forces of piles can be calculated by using the method for the single pile.

The axial displacement of the ith pile-top under the action of axial force P can be calculated by

$$b_i = \delta_c + \delta_k = \frac{P(l_0 + \xi h)}{AE} + \frac{P}{C_0 A_0} \tag{9.27}$$

where δ_c is the elastic compressive deformation of pile material; δ_k is the subsoil settlement at the pile-bottom.

The vertical stiffness ρ_1 of a single pile can be obtained by substituting $b_i = 1$ into Eq. (9.27) and the solved P is ρ_1, and similarly ρ_2–ρ_4, which are expressed as

$$\left.\begin{aligned} \rho_1 &= \frac{1}{\frac{l_0 + \xi h}{AE} + \frac{1}{C_0 A_0}} \\ \rho_2 &= \alpha^3 EIx_Q \\ \rho_3 &= \alpha^2 EIx_m \\ \rho_4 &= \alpha EI\varphi_m \end{aligned}\right\} \tag{9.28}$$

where ξ is the influence coefficient of surrounding friction resistance of subsoil on the pile deformation, which is related to the type of the pile, taken as 2/3 for driven piles and vibratory piles, 1/2 for drilling and excavating cast-in-place piles, and 1.0 for column piles; A is the cross-section area of a pile; E is the compressive elastic modulus of pile material; C_0 is the vertical subsoil coefficient at the pile-bottom, and $C_0 = m_0 h$; A_0 is the pressure distribution area at pile-bottom for a single pile.

For column piles (end bearing piles), A_0 is the base area $\pi d^2/4$ of a single pile; for friction piles, A_0 is the area spread to pile-bottom of pile friction resistance at $\varphi/4$ (φ is the weighted average of internal frictional angles of all soil layers), and it should be calculated by the following formula:

$$A_0 = \min\left[\pi\left(\frac{d}{2} + h\tan\frac{\varphi}{4}\right)^2, \frac{\pi}{4}S^2\right] \tag{9.29}$$

where d is the calculation diameter of a pile; S is the center-to-center space between piles; x_Q, x_m, and φ_m are dimensionless coefficients, functions of $\bar{h} = \alpha h$ and $\bar{l}_0 = \alpha l_0$, which can be picked up in design manuals. However, when the calculated A_0 is larger than that by the center-to-center space between piles at pile-bottom, the latter should be adopted.

The equivalent stiffness coefficient γ_{AB} of group-piles is defined as the force (or moment) in A-direction caused by a unit displacement (or rotation) in B-direction, which can be, respectively, calculated through the following formulae.

When the platform has a unit transverse displacement ($a_0 = 1$), the sum of vertical axial reactions (signed by γ_{ba}), the sum of transverse reactions (signed by γ_{aa}), and the sum of bending moments (signed by $\gamma_{\beta a}$) to the platform from all pile-tops can be calculated by

$$\left.\begin{aligned}
\gamma_{ba} &= \sum_{i=1}^{n}(\rho_1 - \rho_2)\sin\alpha_i\cos\alpha_i \\
\gamma_{aa} &= \sum_{i=1}^{n}(\rho_1\sin^2\alpha_i + \rho_2\cos^2\alpha_i) \\
\gamma_{\beta a} &= \sum_{i=1}^{n}[(\rho_1 - \rho_2)x_i\sin\alpha_i\cos\alpha_i - \rho_3\cos\alpha_i]
\end{aligned}\right\} \tag{9.30}$$

where n is the total number of piles.

When the platform has a unit transverse displacement ($b_0 = 1$), the sum of vertical axial reactions (signed by γ_{bb}), the sum of transverse reactions (signed by γ_{ab}), and the sum of bending moments (signed by $\gamma_{\beta b}$) to the platform from all pile-tops can be calculated by

$$\left.\begin{aligned}
\gamma_{bb} &= \sum_{i=1}^{n}(\rho_1\cos^2\alpha_i + \rho_2\sin^2\alpha_i) \\
\gamma_{ab} &= \gamma_{ba} \\
\gamma_{\beta b} &= \sum_{i=1}^{n}[(\rho_1\cos^2\alpha_i + \rho_2\sin^2\alpha_i)x_i + \rho_3\sin\alpha_i]
\end{aligned}\right\} \tag{9.31}$$

When the platform has a unit rotation angle ($\beta_0 = 1$), the sum of vertical axial reactions (signed by $\gamma_{b\beta}$), the sum of transverse reactions (signed by $\gamma_{a\beta}$), and the sum of bending moments (signed by $\gamma_{\beta\beta}$) to the platform from all pile-tops can be calculated by

$$\left.\begin{aligned}\gamma_{b\beta} &= \gamma_{\beta b}\\ \gamma_{a\beta} &= \gamma_{\beta a}\\ \gamma_{\beta\beta} &= \sum_{i=1}^{n}\left[(\rho_1\cos^2\alpha_i+\rho_2\sin^2\alpha_i)x_i^2+2x_i\rho_3\sin\alpha_i+\rho_4\right]\end{aligned}\right\} \tag{9.32}$$

The stiffness of group-piles foundation refers to the force required to make the center of platform bottom generate a unit displacement. From the above definition, one can know that: γ_{aa} is the lateral stiffness of group-piles, i.e., anti-pushing stiffness; γ_{bb} is the axial stiffness of group-piles, i.e., anti-compressive stiffness; $\gamma_{\beta\beta}$ is the rotating stiffness of group-piles, i.e., anti-bending stiffness; γ_{ab}, $\gamma_{a\beta}$ and $\gamma_{b\beta}$ are the stiffness influence coefficients of lateral-vertical, lateral-rotation and vertical-rotation displacements, respectively. When the piles are symmetrical about the center of platform, $\gamma_{ab} = \gamma_{ba} = 0$, meaning the lateral-vertical correlation stiffness is none, and also $\gamma_{\beta b} = \gamma_{b\beta} = 0$, meaning the vertical-rotation correlation stiffness is none.

9.5.5 *Dynamic Analysis Method for Train-Bridge System Considering Foundation Scouring Effect*

First, the equivalent stiffness of the group-piles subjected to scouring is calculated, and then, it is introduced into the train-bridge interaction model, to study the dynamic responses of train-bridge system subjected to scouring effect.

In the model, the spatial Cartesian coordinates is adopted, as shown in Fig. 9.44. When the group-piles is symmetrically arranged, the nodal displacement vector at center o of the platform is defined as $\delta = (\delta_1, \delta_2, \delta_3, \delta_4, \delta_5, \delta_6)$, in which δ_1, δ_2, and δ_3 are the platform center displacements along x-, y-, and z-direction, and δ_4, δ_5, and δ_6 are the rotation angles around x-, y-, and z-axis, respectively.

According to Sect. 9.5.4, when the piles are arranged symmetrically about the center of platform, the equivalent stiffness matrix of the group-piles foundation can be written as

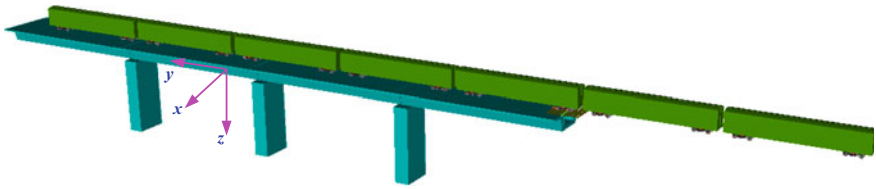

Fig. 9.44 Dynamic interaction model of train-bridge-pier-platform system

$$\mathbf{K}_{\text{piles}} = \begin{bmatrix} k_{11} & 0 & 0 & 0 & k_{15} & 0 \\ 0 & k_{22} & 0 & k_{24} & 0 & 0 \\ 0 & 0 & k_{33} & 0 & 0 & 0 \\ 0 & k_{42} & 0 & k_{44} & 0 & 0 \\ k_{51} & 0 & 0 & 0 & k_{55} & 0 \\ 0 & 0 & 0 & 0 & 0 & k_{66} \end{bmatrix} \tag{9.33}$$

where $\mathbf{K}_{\text{piles}}$ is the equivalent stiffness matrix, in which the diagonal elements are main stiffness with positive values, the non-diagonal elements represent interaction stiffness with negative values or zeros. If the group-piles structure is treated as the x-z plane model, then $k_{11} = \gamma_{\text{aa}}$, $k_{33} = \gamma_{\text{bb}}$, $k_{55} = \gamma_{\beta\beta}$, $k_{15} = \gamma_{\text{a}\beta}$, $k_{51} = \gamma_{\beta\text{a}}$, and other elements of $\mathbf{K}_{\text{piles}}$ are zeros; if it is treated as the spatial model, all the elements of $\mathbf{K}_{\text{piles}}$ can be obtained by the method of setting three beam elements combing the analysis in Sect. 9.5.4, which can be found in Li et al. (2010).

The motion equations of train-bridge-pier-platform-foundation system can be expressed as

$$\left.\begin{aligned} \hat{\mathbf{M}}_{\text{b}}\ddot{\mathbf{u}}_{\text{b}} + \hat{\mathbf{C}}_{\text{b}}\dot{\mathbf{u}}_{\text{b}} + \hat{\mathbf{K}}_{\text{b}}\mathbf{u}_{\text{b}} &= \mathbf{F}_{\text{bv}} \\ \mathbf{M}_{\text{v}}\ddot{\mathbf{u}}_{\text{v}} + \mathbf{C}_{\text{v}}\dot{\mathbf{u}}_{\text{v}} + \mathbf{K}_{\text{v}}\mathbf{u}_{\text{v}} &= \mathbf{F}_{\text{vb}} \end{aligned}\right\} \tag{9.34}$$

where the subscripts "b" and "v" represent bridge and train, respectively; $\mathbf{u}$, $\dot{\mathbf{u}}$, and $\ddot{\mathbf{u}}$ are displacement, velocity, and acceleration vectors, respectively; $\mathbf{F}_{\text{bv}}$ and $\mathbf{F}_{\text{vb}}$ are the interaction force vectors between train and bridge, respectively; $\mathbf{M}_{\text{v}}$, $\mathbf{K}_{\text{v}}$, and $\mathbf{C}_{\text{v}}$ are mass, stiffness, and damping matrices of train (see Chap. 5), while $\hat{\mathbf{M}}_{\text{b}}$, $\hat{\mathbf{K}}_{\text{b}}$, and $\hat{\mathbf{C}}_{\text{b}}$ are the mass, stiffness, and damping matrices of the bridge considering foundation scouring effect, respectively.

When the scouring effect is considered, $\hat{\mathbf{M}}_{\text{b}}$, $\hat{\mathbf{K}}_{\text{b}}$, and $\hat{\mathbf{C}}_{\text{b}}$ are divided into two parts, respectively, from the superstructure (i.e., beam span) and the bridge pier (including platform). For example, the expression of stiffness matrix can be written as

$$\hat{\mathbf{K}}_{\text{b}} = \begin{bmatrix} \mathbf{K}_{\text{b}} & \mathbf{K}_{\text{bp}} \\ \mathbf{K}_{\text{pb}} & \mathbf{K}_{\text{p}} \end{bmatrix} \tag{9.35}$$

where the subscripts "b" and "p" represent bridge superstructure and pier, respectively; $\mathbf{K}_{\text{bp}}$ and $\mathbf{K}_{\text{pb}}$ are interaction stiffness submatrices between bridge superstructure and pier, respectively; $\mathbf{K}_{\text{b}}$ is the stiffness submatrix of superstructure, whose details can be seen in Sect. 5.6.1; $\mathbf{K}_{\text{p}}$ is the stiffness submatrix of pier with the following form:

$$\mathbf{K}_{\text{p}} = \begin{bmatrix} \mathbf{K}_{\text{a}} & \mathbf{K}_{\text{oa}} \\ \mathbf{K}_{\text{oa}} & \mathbf{K}_{\text{o}} + \mathbf{K}_{\text{piles}} \end{bmatrix} \tag{9.36}$$

where $\mathbf{K}_o$ and $\mathbf{K}_a$ are the submatrices of pier stiffness matrix, corresponding to the displacements of center o of platform and those of other nodes on pier, respectively; $\mathbf{K}_{ao}$ and $\mathbf{K}_{oa}$ are interaction stiffness submatrices between the displacements of center o and other nodes, respectively; $\mathbf{K}_{piles}$ is the equivalent stiffness matrix of group-piles defined by Eq. (9.33).

By solving the motion Eq. (9.34) using the step-by-step integration method, the dynamic responses of the train-bridge system subjected to foundation scouring effect can be calculated, to study the influence of foundation scouring on the running safety and stability of high-speed trains.

9.5.6 *Effect of foundation scouring on equivalent stiffness of group-piles*

1. ***Engineering outline***

The Second Songhua River Bridge (Fig. 9.45) is located on the Harbin-Dalian HSR from K775+34.64 to K832+748.59, with the total length of 57.40 m. A group of 4×32 m simply-supported PC box-beams of the bridge is considered in the analysis, and their piers are built in the river channel, under the influence of water scouring. The piers are numbered as No. 926–No. 930. The hydrological data of the bridge site include design water level H = 7.48 m, river width 256 m, average water depth 6.13 m, maximum water depth 7.02 m, design flow Q = 8280 m^3/s, design flow velocity q = 2.34 m/s, and scouring coefficient 1.25. The subsoil of the bridge site consists of three layers: the surface layer is fine sand, silty clay, round gravel soil, etc.; the middle layer is medium sand, gravel, etc.; the lower layer is mudstone and sandstone interbedded, with the bearing strength of 44.5 MPa.

The No. 926–No. 930 piers adopt bored group-piles foundations, and the piles are symmetrically arranged about the center of the platform. Since these pier

Fig. 9.45 Second Songhua River Bridge on Harbin-Dalian HSR

foundations have similar dimensions, the same layout and sizes of group-piles are adopted in the analysis, as shown in Fig. 9.46.

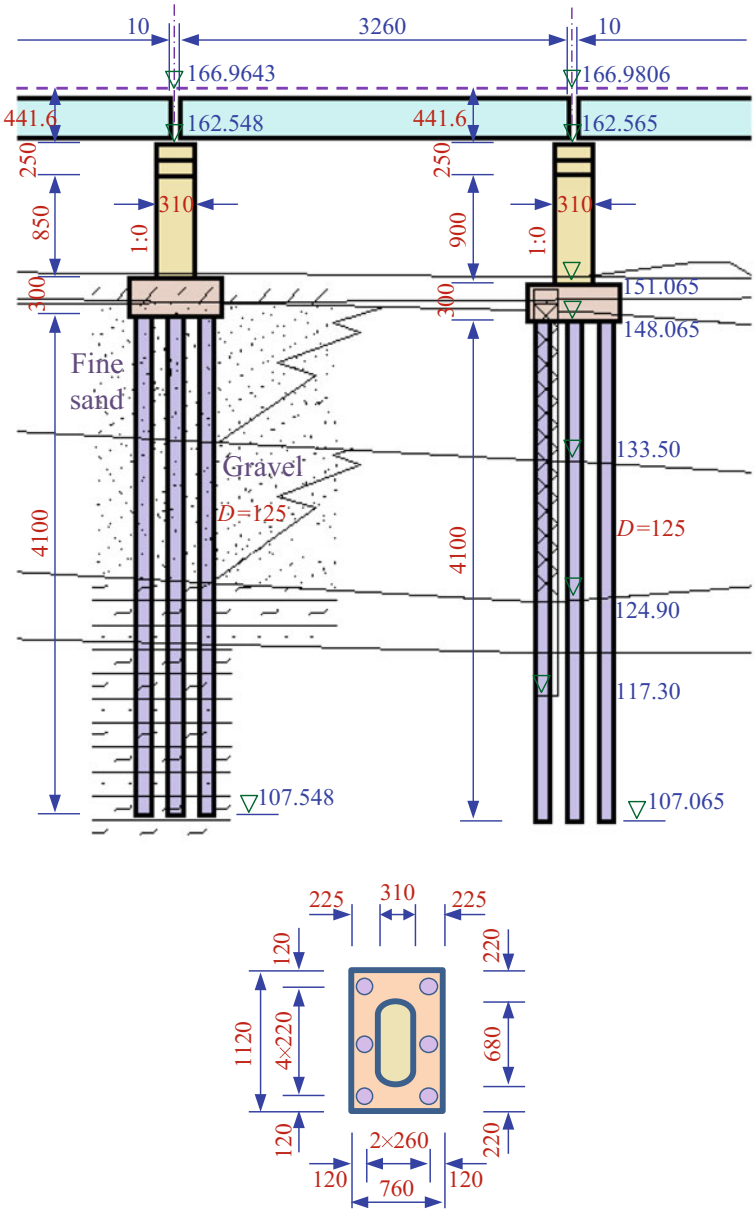

Fig. 9.46 Layout and dimensions of group-piles foundation (Unit of elevation: m; unit of size: cm)

2. ***Equivalent stiffness of group-piles before and after scouring***

In the analysis, all piles are modeled as column piles, i.e., the bottom nodes of piles are restrained in vertical direction; the elastic restraints of subsoil are applied on the platform at bottom and two sides, and around the pile-body. In accordance with the *Code for Design on Subsoil and Foundation of Railway Bridge and Culvert* (TB10002.5, 2005), the elastic effect of subsoil on the sides of platform and piles can be determined, and the foundation coefficients m and m_0 are listed in Table 9.9.

According to the method in Sect. 9.5.3, the maximum water depth h_p is about 1.0 m at the bridge site after general scouring. Considering h_p = 1.0 m is too small, to better study the effect of scouring on foundation stiffness, the scouring depth is artificially enlarged as 2 m, 4 m, 6 m, 8 m, and 10 m, respectively. Meanwhile, the equivalent stiffness of all piers is thought to be identical either before or after scouring.

The equivalent stiffness matrices of group-piles foundation under the effect of various scouring depths are calculated by using Eq. (9.33), considering the pile length variations before and after scouring, respectively, and the results are listed in Table 9.10.

Table 9.9 Foundation coefficients of No. 926–No. 930 piers

No of pier	Upper interface of subsoil layer (m)	Lower interface of subsoil layer (m)	Soil properties	m and m_0 (MPa/m^2)
926	0	9.15	Fine sand	10
	9.15	20.55	Medium sand	15
	20.55	Pile-bottom	Mudstone and sandstone interbedded	100
927	0	11.6	Fine sand	15
	11.6	23.2	Medium sand	55
	23.2	Pile-bottom	mudstones and sandstone interbedded	100
928	0	10.8	Fine sand	15
	10.8	18	Medium sand	55
	18	Pile-bottom	mudstones and sandstone interbedded	100
929	0	7.15	Fine sand	15
	7.15	19.95	Medium sand	55
	19.95	Pile-bottom	mudstones and sandstone interbedded	100
930	0	3.5	Fine sand	15
	3.5	21.9	Medium sand	55
	21.9	Pile-bottom	mudstones and sandstone interbedded	100

Table 9.10 Comparison of equivalent stiffness matrices of group-piles before and after scouring

Scouring Depth (m)	Before scouring	After scouring
2	$\begin{bmatrix} 18.32 & 0 & 0 & 0 & -25.43 & 0 \\ 0 & 19.74 & 0 & -21.29 & 0 & 0 \\ 0 & 0 & 96.34 & 0 & 0 & 0 \\ 0 & -21.29 & 0 & 193.8 & 0 & 0 \\ -25.43 & 0 & 0 & 0 & 216.8 & 0 \\ 0 & 0 & 0 & 0 & 0 & 38.47 \end{bmatrix}$	$\begin{bmatrix} 13.16 & 0 & 0 & 0 & -31.02 & 0 \\ 0 & 12.42 & 0 & -29.22 & 0 & 0 \\ 0 & 0 & 96.34 & 0 & 0 & 0 \\ 0 & -29.22 & 0 & 181.6 & 0 & 0 \\ -31.02 & 0 & 0 & 0 & 208.2 & 0 \\ 0 & 0 & 0 & 0 & 0 & 38.47 \end{bmatrix}$
4	$\begin{bmatrix} 18.32 & 0 & 0 & 0 & -25.43 & 0 \\ 0 & 19.74 & 0 & -21.29 & 0 & 0 \\ 0 & 0 & 96.34 & 0 & 0 & 0 \\ 0 & -21.29 & 0 & 193.8 & 0 & 0 \\ -25.43 & 0 & 0 & 0 & 216.8 & 0 \\ 0 & 0 & 0 & 0 & 0 & 38.47 \end{bmatrix}$	$\begin{bmatrix} 8.896 & 0 & 0 & 0 & -26.43 & 0 \\ 0 & 8.252 & 0 & -25.11 & 0 & 0 \\ 0 & 0 & 95.16 & 0 & 0 & 0 \\ 0 & -25.11 & 0 & 173.3 & 0 & 0 \\ -26.43 & 0 & 0 & 0 & 199.2 & 0 \\ 0 & 0 & 0 & 0 & 0 & 31.72 \end{bmatrix}$
6	$\begin{bmatrix} 18.32 & 0 & 0 & 0 & -25.43 & 0 \\ 0 & 19.74 & 0 & -21.29 & 0 & 0 \\ 0 & 0 & 96.34 & 0 & 0 & 0 \\ 0 & -21.29 & 0 & 193.8 & 0 & 0 \\ -25.43 & 0 & 0 & 0 & 216.8 & 0 \\ 0 & 0 & 0 & 0 & 0 & 38.47 \end{bmatrix}$	$\begin{bmatrix} 4.611 & 0 & 0 & 0 & -18.18 & 0 \\ 0 & 4.349 & 0 & -17.45 & 0 & 0 \\ 0 & 0 & 92.86 & 0 & 0 & 0 \\ 0 & -17.45 & 0 & 155.5 & 0 & 0 \\ -18.18 & 0 & 0 & 0 & 179.9 & 0 \\ 0 & 0 & 0 & 0 & 0 & 23.01 \end{bmatrix}$
8	$\begin{bmatrix} 18.32 & 0 & 0 & 0 & -25.43 & 0 \\ 0 & 19.74 & 0 & -21.29 & 0 & 0 \\ 0 & 0 & 96.34 & 0 & 0 & 0 \\ 0 & -21.29 & 0 & 193.8 & 0 & 0 \\ -25.43 & 0 & 0 & 0 & 216.8 & 0 \\ 0 & 0 & 0 & 0 & 0 & 38.47 \end{bmatrix}$	$\begin{bmatrix} 2.575 & 0 & 0 & 0 & -12.68 & 0 \\ 0 & 2.458 & 0 & -12.28 & 0 & 0 \\ 0 & 0 & 90.65 & 0 & 0 & 0 \\ 0 & -12.28 & 0 & 139.5 & 0 & 0 \\ -12.68 & 0 & 0 & 0 & 162.7 & 0 \\ 0 & 0 & 0 & 0 & 0 & 18.09 \end{bmatrix}$
10	$\begin{bmatrix} 18.32 & 0 & 0 & 0 & -25.43 & 0 \\ 0 & 19.74 & 0 & -21.29 & 0 & 0 \\ 0 & 0 & 96.34 & 0 & 0 & 0 \\ 0 & -21.29 & 0 & 193.8 & 0 & 0 \\ -25.43 & 0 & 0 & 0 & 216.8 & 0 \\ 0 & 0 & 0 & 0 & 0 & 38.47 \end{bmatrix}$	$\begin{bmatrix} 1.552 & 0 & 0 & 0 & -9.179 & 0 \\ 0 & 1.494 & 0 & -8.938 & 0 & 0 \\ 0 & 0 & 88.51 & 0 & 0 & 0 \\ 0 & -8.938 & 0 & 126.4 & 0 & 0 \\ -9.179 & 0 & 0 & 0 & 148.7 & 0 \\ 0 & 0 & 0 & 0 & 0 & 15.04 \end{bmatrix}$

By comparing the equivalent stiffness matrices of group-piles before and after scouring, the following conclusions can be drawn.

(1) There are obvious variations in equivalent stiffness matrices before and after scouring. For example, for the scouring depth of 4 m, the transverse stiffness of group-piles is reduced from 1832 MN/m before scouring to 889.6 MN/m after scouring, the longitudinal stiffness is from 1974 MN/m to 825.2 MN/m, and the vertical stiffness and the rotational stiffness also have different degrees of variations.
(2) In the main trend, the greater the scouring depth, the more the equivalent stiffness coefficients of group-piles decrease, i.e., the more obvious the effect of scouring depth on the equivalent stiffness, especially for the main stiffness coefficients.
(3) After scouring, the vertical equivalent stiffness coefficient of group-piles changes less than the horizontal stiffness coefficients, mainly because it is less affected by the embedded depth.
(4) When the scouring depth is small (2 m or 4 m), the correlation coefficients of lateral displacement-rotation and vertical displacement-rotation stiffness coefficients of group-piles increase after scouring, while when the scouring depth is larger (>4 m), the correlation coefficients show an obvious trend of decreasing, indicating the variation of stiffness correlation coefficient is related to the scouring depth.

9.5.7 Effect of foundation scouring on dynamic responses of train-bridge system

For high-speed railway bridges, once the foundation is scoured, the reduction of foundation stiffness may cause large deformation and vibration of the bridge under the train loads, which may change the smoothness and stability of the track, affecting the running safety of trains on the bridge. Next, an example is presented to further study the effect of foundation scouring on the dynamic responses of train-bridge system.

1. **Engineering outline**

The Mudanjiang River Bridge on the Changchun-Tumen line is shown in Fig. 9.47, which is orthogonal to the river. The bridge consists of (32+48+32) m continuous beams between piers P2–P5, 32 m simply-supported beams between P5–P9, and (40 + 64 + 40) m continuous beams between P9–P12, respectively. It adopts group-piles and platform foundations, and the pier heights are 7–12.1 m. The P4–P10 piers are located on the river and subjected to scouring. The riverbed width of bridge site is about 243 m, and the hydrological data include: design flow

Fig. 9.47 The river-crossing section of the Mudanjiang River Bridge

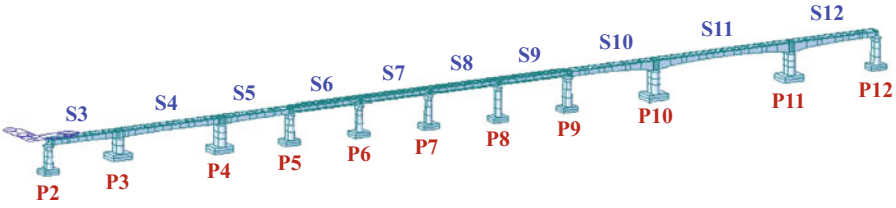

Fig. 9.48 The FE model of the Mudanjiang River Bridge

velocity Q_c = 5500 m^3/s, design water level H = 240.95 m, water width B_w = 256 m, average water depth h_c = 6.13 m, and maximum water depth h_{mc} = 7.02 m. According to the geological survey, the surface layer of bridge site is coarse sand and round gravel, underlying is the vesicular basalt with compressive strength of 44.5 MPa.

In the analysis, the software MIDAS is used to establish the FE model of the bridge section between piers P2–P12, with the corresponding beam spans numbered as S3–S12, as shown in Fig. 9.48. In the model, the spatial beam elements are utilized to simulate the beams, piers, platforms, and piles, the rigid links to simulate the connections between pier-bodies and pier-caps, the elastic links to simulate the connection between the platforms and pile-tops, the master-and-slave nodes to simulate the bearings, and the secondary dead loads of the tracks are applied to the beams by adjusting the material densities.

2. **Scouring depth and equivalent stiffness of foundations**

The general scouring depths are calculated by Eq. (9.14) on the basis of the hydrological data, as listed in Table 9.11. For the sake of more safety, the average

Table 9.11 Calculation parameters for general scouring and the calculated scouring depth

Parameters	A	Q_c (m^3)	B_c (m)	h_{mc} (m)	h_c (m)	E	d_c (mm)	h_p (m)
Value	1.15	5500	243.9	7.02	6.13	0.66	11	8.16

Table 9.12 Buried depths of platforms before general scouring and scouring depths of the piers

Pier No.	P5	P6	P7	P8	P9	P10	P11
Buried depth of platform before scouring (m)	3.86	1.89	1.94	1.65	1.94	1.93	3.42
Scouring depth (m)	5.01	4.81	4.44	4.65	4.5	4.86	5.34

depth of river way is increased by 2.03 m. Shown in Table 9.12 are the buried depths of platforms before general scouring and the scouring depths of the piers.

Since the platform bottoms of piers P5 and P11 are lower than the general scouring line, the local scouring depths of them are calculated with Eq. (9.15) by regarding the superstructure as solid body, while for other piers, the local scouring depths are calculated with Eq. (9.16). The calculated local scouring depths of the piers are listed in Table 9.12.

After local scouring, the platform bottoms of all piers are higher than the scouring line, and the piles are exposed to a considerable length. Shown in Fig. 9.49 are the foundation buried depths of pier P9 before and after scouring.

The bridge adopts the bored pile foundations, the pile ends are embedded in the moderate weathered basalt with certain depth. Shown in Fig. 9.50 are the group-piles arrangements for the piers, and in Table 9.13 are the equivalent stiffness values of the pier foundations before and after scouring. It can be seen that the equivalent stiffness of all pier foundations decreases after scouring, in which the changes of lateral translational stiffness and vertical torsional stiffness are the most obvious. Before scouring, the platform is resisted by the side soil, while after scouring, the whole platform is exposed to the water and only the piles in the soil are resisted transversely, so the stiffness decreases inevitably. On the other hand, since the bridge foundation adopts embedded piles, the vertical stiffness is mainly affected by the vertical bearing capacity of the base subsoil, thus the scouring only reduces the vertical resistance of subsoil under the platform and affects the vertical stiffness of the whole foundation less than the horizontal stiffness.

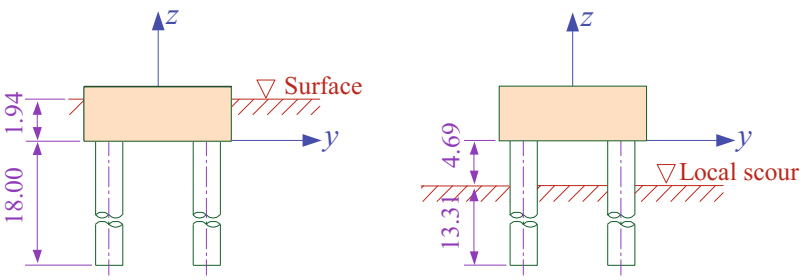

Fig. 9.49 Foundation buried depths of pier P9 before and after scouring (unit: m)

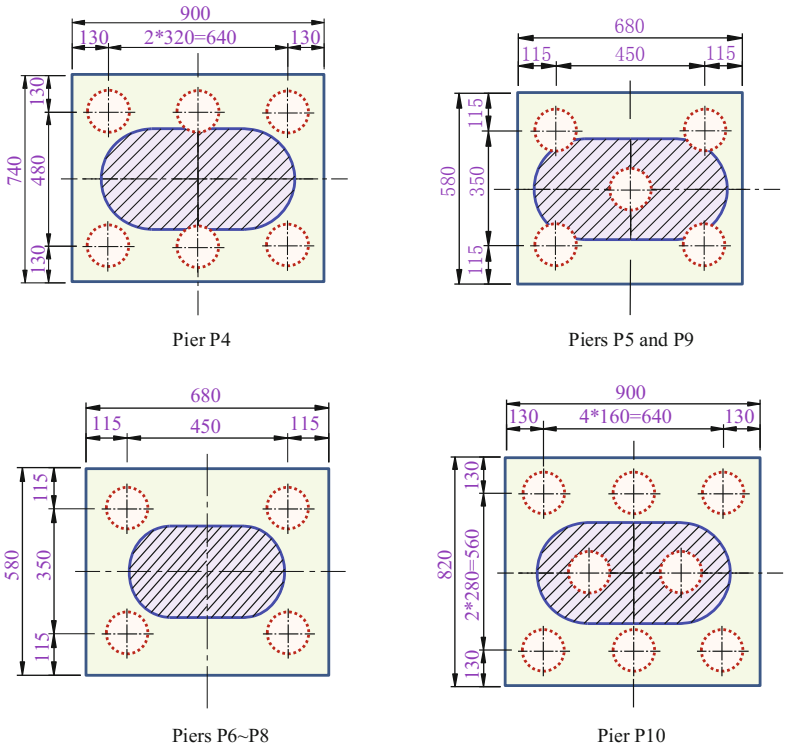

Fig. 9.50 Group-piles arrangements of bridge foundation

3. Natural frequencies and modes of the bridge

The natural frequencies and modes of the bridge are calculated before and after scouring, and the results are listed in Table 9.14. After scouring, the first natural frequency in vertical bending + longitudinal mode decreases from 1.757 to 1.364 Hz by 22.3%, and the first natural frequency in lateral bending mode of pier and beam decreases from 1.772 to 1.624 Hz by 8.4%. Obviously, the flow scouring makes the foundation stiffness decrease, especially for horizontal stiffness, thus the bridge structure becomes more flexible.

4. Dynamic responses of train-bridge system

The Mudanjiang River Bridge is on the railway for both passenger and freight trains. Because the freight train has heavier weight than the passenger train and has greater vibration effect on the bridge foundation and the surrounding site, for the sake of more safety, the freight train composed of fifty C70 cars with large axle loads is considered, and the dynamic responses of train-bridge system under train speed of 90 km/h are analyzed. In the analysis, the track irregularity samples are produced using the Germany low-interference track spectra, with the cutoff

Table 9.13 Equivalent stiffness values of pier foundations before and after scouring ($\times 10^9$)

Pier No.	δ_{aa1} (N/m)		δ_{aa2} (N/m)		δ_{aa3} (N/m)		δ_{cc1} (N.m/rad)		δ_{cc2} (N.m/rad)		δ_{cc3} (N.m/rad)	
	Before	After	Before	After	Before	After	Before	After	Before	After	Before	After
P5	3.6	1.07	3.46	0.93	40.82	35.59	258.2	222.8	301.0	260.1	32.23	15.57
P6	1.73	0.35	1.89	0.37	25.24	20.87	71.39	57.97	112.1	91.46	8.8	3.48
P7	1.73	0.38	1.90	0.40	25.84	20.87	87.49	69.95	139.4	111.8	10.5	4.21
P8	1.73	0.32	1.90	0.33	19.13	15.89	66.93	54.40	105.5	86.27	10.5	3.60
P9	1.73	0.37	1.90	0.39	16.01	13.96	57.37	48.76	89.66	76.78	10.5	4.10
P10	1.83	0.37	1.89	0.37	17.05	14.93	51.60	43.55	78.91	67.40	9.15	3.54
P11	3.94	0.96	3.56	0.84	52.98	44.18	340.2	282.7	332.3	276.3	32.89	13.90

Table 9.14 Natural frequencies and modes of bridge

Order	Before scouring		After scouring	
	Frequency (Hz)	Traits of modes	Frequency (Hz)	Traits of modes
1	1.576	S10–S12 vertical bending of main beam	1.364	S10–S12 vertical bending + longitudinal floating
2	1.757	S10– S12 vertical bending + longitudinal floating	1.600	S10–S12 vertical bending of main beam
3	1.772	S10–S12 lateral bending of pier and beam	1.624	S10–S12 lateral bending of pier and beam
4	2.084	S9–S10 lateral bending of pier and beam	1.708	S9–S10 lateral bending of pier and beam
5	2.375	S3–S5 vertical bending of main beam	2.092	S9 longitudinal floating of main beam
6	2.460	S9 longitudinal floating of main beam	2.116	S5–S6 lateral bending of pier and beam
7	2.742	S4–S9 lateral bending of pier and beam	2.196	S8 longitudinal floating of main beam
8	2.752	S8 longitudinal floating of main beam	2.319	S6–S9 lateral bending of pier and beam
9	2.782	S5–S9 lateral bending of pier and beam	2.366	S3–S5 vertical bending of pier and beam + S6 longitudinal floating of main beam
10	2.830	S3–S5 lateral bending of pier and beam + S6 longitudinal floating of main beam	2.411	S3–S5 vertical bending of pier and beam + S6 longitudinal floating of main beam

wavelength being 80 m; the time step of integration is 0.02 s; and the damping ratio is 0.02 for the bridge system.

(1) Dynamic responses of the bridge

Shown in Figs. 9.51 and 9.52 are the time histories of lateral displacements and accelerations of beam S9 (32 m simply-supported beam) at mid-span before and after scouring. It can be seen that after scouring of bridge foundation, the dynamic responses of the beam increase evidently, with the maximum lateral displacement increased from 0.92 mm to 2.24 mm by 144%, and the maximum acceleration from 0.32 m/s^2 to 0.59 m/s^2 by 84%. Because the train is longer than the bridge, when the first car moves into the bridge and the last car moves out of the bridge, the bridge is subjected to a suddenly applied load and a suddenly reduced load, respectively, and thus, there appears obvious impact effect on the history curves.

Listed in Table 9.15 are the maximum dynamic responses of beams S6–S10 at mid-span before and after bridge foundation scouring. It can be observed that the maximum lateral displacements and accelerations increase obviously when the

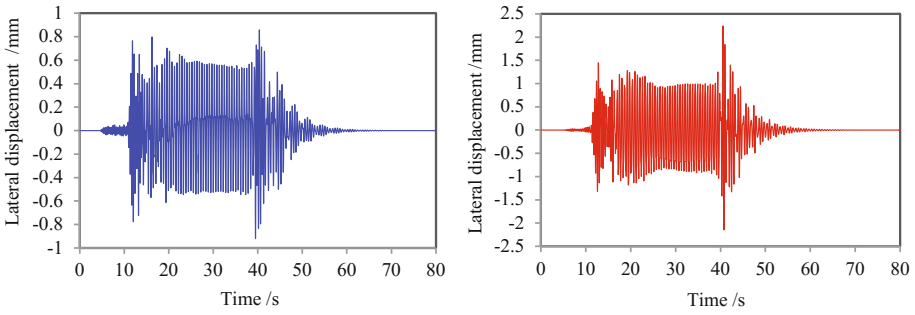

(a) Before scouring (b) After scouring

Fig. 9.51 Time histories of lateral displacements of beam S9 at mid-span before and after scouring

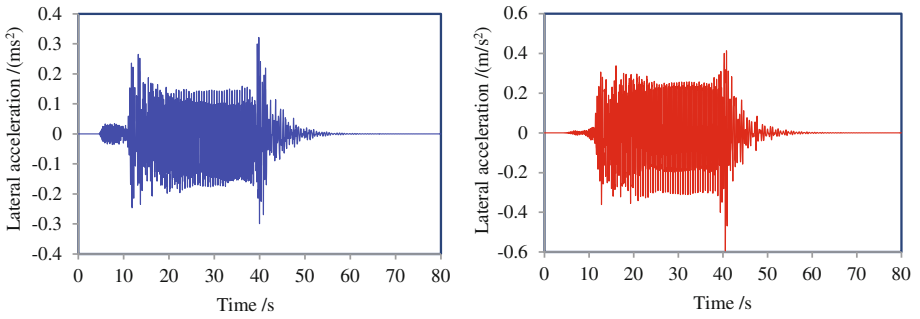

(a) Before scouring (b) After scouring

Fig. 9.52 Time histories of lateral accelerations of beam S9 at mid-span before and after scouring

Table 9.15 Maximum dynamic responses of the bridge beams

Beam No.	Displacements (mm)		Accelerations (m/s^2)	
	Before scouring	After scouring	Before scouring	After scouring
S6	0.45	0.65	0.19	0.27
S7	0.69	1.30	0.29	0.49
S8	1.45	2.56	0.39	0.57
S9	0.92	2.24	0.32	0.59
S10	0.7	1.73	0.13	0.23
Average	0.842	1.696	0.264	0.430

Table 9.16 Maximum dynamic responses of the train

Pier state	Derailment factors	Offload factors	Lateral wheel/rail forces (kN)	Car-body accelerations (m/s^2)		Sperling Index	
				Vertical	Lateral	Vertical	Lateral
Before scouring	0.30	0.59	48.77	3.7	1.52	3.5	2.51
After scouring	0.42	0.64	53.49	3.73	2.46	3.51	2.53

bridge foundations are scoured, with the average lateral displacement increased from 0.842 mm to 1.696 mm by 101% and the lateral acceleration increased from 0.264 cm/s^2 to 0.430 cm/s^2 by 62.9%, respectively.

(2) Dynamic responses of the train

The scouring of bridge foundation makes the lateral stiffness of bridge decrease and thus results in the increase of train-induced vibration. Table 9.16 lists the calculated maximum dynamic responses of the train before and after bridge foundation scouring. It can be seen that in both cases, the maximum derailment factors, lateral wheel/rail forces, and car-body accelerations are within their respective allowable values, and the vertical and lateral Sperling Indices reach excellent grades. When the bridge foundations are scoured, the dynamic responses of the train all increase, in which the maximum lateral car-body acceleration increases the most obviously, from 1.52 m/s^2 to 2.46 m/s^2 by about 64%. Before foundation scouring, the maximum offload factor is 0.59, very close to the allowable value, while after scouring, it is increased to 0.64, which exceeds the allowable value, affecting the running safety.

5 Concluding remarks

The following conclusions can be drawn from the calculation results:

(1) The decrease of buried depth of pile foundation induced by scouring is the main factor affecting the equivalent stiffness of the foundation. The longitudinal, lateral, rotational, and torsional equivalent stiffness values of group-piles decrease obviously after souring, while the vertical equivalent stiffness decreases very less.
(2) Because the lateral foundation stiffness decreases more obviously after scouring than the vertical stiffness, the lateral displacements and accelerations of pier-tops and beams increase evidently after scouring, while the vertical dynamic responses of the bridge have little variety.
(3) The flow scouring also affects the dynamic responses of the train. When the action of scouring is severe or the duration of scouring is long, the running safety and riding comfort of the train will be affected seriously, which should be paid more attention by the related administrations.

References

Cao FM (2014) The uneven settlement disease treatment application research of existing railway bridge. Urbanism and Architecture-Road and Bridge, 286–287

Chen CC, Wu WH, Shih F, Wang SW (2014) Scour evaluation for foundation of a cable-stayed bridge based on ambient vibration measurements of superstructure. NDT E Int 66:16–27

Chen W (2013) Study on the bearing capacity of existing bridge Piers with scouring of the river. Central South University, Changsha (in Chinese)

City8 (2015). http://www.city8.com/dituquantu/8683612.html. Accessed 24 Apr 2015

Fang XY (2013) The study of river scouring impact on railway running safety. Beijing Jiaotong University, Beijing (in Chinese)

Fen K, Zhang JW (2009) Application of ABAQUS in geotechnical engineering. China Waterpower Press, Beijing, pp 405–410 (in Chinese)

Huang MS, Li JJ, Li XZ (2006) Cumulative deformation behavior of soft clay in cyclic undrained tests. Chin J Geotech Eng 28(7):891–895 (in Chinese)

Jing TR (1993) Hydrology for bridge and culvert. Tongji University Press, Shanghai (in Chinese)

JTG C30 (2015) Code for survey and design on hydrology of highway engineering. Beijing: China Communication Press, Ministry of Communications of China (in Chinese)

Kassem A, Salaheldin TM, Imran J, Chaudhry MH (2003) Numerical modeling of scour around artificial rock island of Cooper river bridge. Trans Res Rec 1851:45–50

Kong X, Cai CS (2016) Scour effect on bridge and vehicle responses under bridge-vehicle-wave interaction. J Br Eng 21(4): 04015083: 1–16 (in Chinese)

Lagasse PF, Richardson EV (2001) ASCE compendium of stream stability and bridge scour papers. J Hydraul Eng 127(97):531–533

Li GH, Sun SL, Xu ZL et al (2008) The influence of land subsidence on the bridge of high-speed railway and its engineering countermeasure. J Railw Eng Soc 2008(4):37–41 (in Chinese)

Li JJ (2005) Analysis of long-term settlement of saturated soft clay under traffic loading. Tongji University, Shanghai (in Chinese)

Li YL, Zhao K, Cai XS (2010) Orthogonal three-beam model in FEM simulation of bridge foundation stiffness. Br Constr 6:17–21 (in Chinese)

Ling ZP, Yi JW (1997) Foundation engineering. China Communications Press, Beijing (in Chinese)

Liu M, Huang MS, Li JJ (2006) Long term settlement of saturated soft clay under subway loading. Chin J Undergr Space Eng 2(5):813–817 (in Chinese)

Liu XY (2009) Collapse and accidents of bridges in the world. http://liu-xiaoyao.blog.163.com/blog/static/ (in Chinese)

Loh CH, Wu FM, Chao SH (2011) In situ structural health monitoring for bridges under ambient stimulus: effect of scouring. The Engineering Mechanics Institute, Boston, USA, pp 2–4

Ma YL, Zheng LJ, Fu LL (2008) Analysis and countermeasures of scouring hazards of railway bridges. Shanxi Archit 18:315–316 (in Chinese)

Melville BW, Raudkivi AJ (1977) Flow characteristics in local scour at bridge piers. J Hydraul Res 15(4):373–380

Qi B (2009) The influence of surface subsidence on construction of jing-hu high-speed railway (Beijing-Ji'nan) and its analysis. Southwest Jiaotong University (in Chinese)

Samizo M, Watanabe S, Fuchiwaki A, Sugiyama T (2007) Evaluation of the structural integrity of bridge pier foundations using microtremors in flood conditions. QR RTRI 48(3):153–157

Sheppard DM, Miller W (2006) Live-bed local pier scour experiments. J Hydraul Eng 132(7):635–642

Song GH, Gao MM, Li GQ (2010) Vehicle-bridge vertical system coupled vibration analysis under the uneven settlement of bridge pier and abutment. Chin Railw Sci 31(2):29–33 (in Chinese)

TB10002.5 (2005). Code for design on subsoil and foundation of railway bridge and culvert. Ministry of Railways of PRC, Beijing: China Railway Publishing house

TB10017 (1999) Code for Survey and Design on Hydrology of Railway Engineering. China Railway Publishing house, Ministry of Railways of PRC, Beijing (in Chinese)

TB 10621 (2014) code for design on high-speed railway. China Railway Publishing house, Ministry of Railways of PRC, Beijing

Wang LZ (2015) Effect of cast-in-place piles of new high speed railway bridge on existing pier-pile foundation of nearby railway lines. Beijing Jiaotong University, Beijing (in Chinese)

Young GK, Dou X, Saffarinia K, Jones JS (1998) Testing abutment scour model. In: Proceedings of international water resources engineering conference, vol 1, Memphis, TN, USA, pp 180–185.

Zhai WM, Zhao CF, Xia H et al (2014) Basic scientific issues on dynamic performance evolution of the high-speed railway infrastructure and its service safety. Chin Sci 44(7):645–660

Zeng YH (2015) Collapse of a big bridge of S306 highway in Yueyang County. http://hn.rednet.cn/c/2015/06/04/3699628.htm (in Chinese)

Chapter 10
Dynamic Analysis of Train-Bridge System Under Beam Deformation Induced by Concrete Creep and Temperature Effect

In this chapter, the influence of PC beam deformation induced by creep camber and temperature effect on the dynamic responses and running safety of HSR train-bridge system is studied. In this chapter, the influence of PC beam deformation induced by creep camber and temperature effect on the dynamic responses and running safety of HSR train-bridge system is studied. The numerical simulation method for PC beam creep camber is introduced. The vibration responses of train-bridge system excited by creep camber deformation are analyzed, and the safety threshold curves of creep camber under different train speeds are proposed, to ensure the running safety and stability of train vehicles. By numerical simulation and field measurement, the characteristics of bridge sidewise bending and track slab warping deformation under non-uniform temperature field are studied, and their influences on the dynamic response and running safety of the train-bridge system are investigated.

10.1 Introduction

Bridges produce deformations under various factors, such as train loads, long-term creep camber due to prestress action, and temperature effect in non-uniform temperature field. Bridge deformations may change the track performance and deteriorate the track smoothness, which will intensify the vibrations of vehicles, increase the dynamic impact on bridge structures, influence the riding comfort of passengers, and even threaten the running safety of trains. For ballasted-track bridges, the additional track unevenness induced by bridge quasi-static deformation can be adjusted by regulating the ballast thickness and fasteners. While for the HSR bridges with ballastless track, the additional track unevenness can only be adjusted by fasteners, but the adjustment amount is limited. Therefore, the quasi-static deformations of the bridges during post-construction period, especially those induced by the creep camber and temperature effect, should be strictly controlled.

H. Xia et al., *Dynamic Interaction of Train-Bridge Systems in High-Speed Railways*, Advances in High-speed Rail Technology, https://doi.org/10.1007/978-3-662-54871-4_10

The elastic deformations of bridges induced by external loads may disappear quickly after the loads are removed, while the creep camber belongs to a kind of non-reversible quasi-static deformation with the characteristics of long-term growth (Bazant and Baweja 1995; Gardner and Lockman 2001; He 2003; Xia et al. 2011; Duan 2014). As one of the main structural forms, the precast simply-supported PC beams are widely used in HSR lines in China. The creep camber will produce periodic deformations of simply-supported bridges with successively arranged equi-span beams, which will change the geometric state of the track and is harmful to the running safety of train and riding comfort of passengers (Liu 2004; Liu 2005). For HSR bridges, the creep camber of PC beams should be limited (Zheng 2008; Xia 2010; Chai 2012), which is clearly defined in various bridge design codes (BS5400 1990; TB10002.1 2005; TB10002.3 2005; AASHTO 2012).

The quasi-static deformations of the bridge and track structure under the temperature effect may also change the track smoothness state, which will have a great impact on the normal operation of high-speed trains, and even exceed the effects of other loads to become the controlling design factor in some cases (Xia et al. 2006; Zhai 2007; Niu 2008; Zhang 2008; Sun 2013; Tian et al. 2015).

In this chapter, by using the standard 32 and 24 m simply-supported PC beam bridges as examples, the camber and lateral sidewise bending of PC beams and the slab warping deformation of ballastless tracks induced by the concrete creep and temperature effect are studied, and the influences of these deformations on the dynamic responses of train-bridge system and the running safety and stability of high-speed trains are analyzed.

10.2 Influence of PC Beam Creep Camber on Dynamic Responses of Train-Bridge System

10.2.1 Creep Camber of PC Beams

10.2.1.1 Concept of Creep Camber

The aging deformation of concrete materials consists of shrinkage and creep. The shrinkage and creep of concrete will continue to develop after the completion of bridge construction. Although the deformation rate gradually declines, the cumulative deformations increase with time, which will produce additional unevenness of the bridge deck, and further affect the running performance of high-speed trains on the bridges.

Concrete shrinkage is a physical–chemical phenomenon of volume reduction due to the evaporation of free water in cement gels of the concrete, which is not related to the external loads, but dependent on the time. There are mainly five forms of concrete shrinkage deformation: the condensation deformation in casting, the drying shrinkage deformation in hardening, the autogenous-shrinkage deformation,

the shrinkage deformation caused by temperature drop, and the carbonization shrinkage deformation. The shrinkage of concrete will change the internal forces and deformations of the bridge structure, thus alter the deck profiles.

The creep of concrete refers to the phenomenon that the deformation of concrete member increases with time under constant stress, which is related to the magnitude of stress it suffers from. Under the action of dead loads and prestressing forces, the axial compression and bending moment will occur on the beam section simultaneously, and the creep of the beam at the side with greater pressure is larger than that with smaller pressure. Under this action, the beam segment produces upward or downward convex deflection. The creep of concrete is described by creep coefficient, defined as the ratio of creep strain to elastic strain, which is related to the concrete age, loading time, member size, and working environment of the beam.

For a railway beam, the upward convex deflection induced by the concrete creep is called the creep camber. The large creep camber may change the geometric state of track on the beam, which is harmful to the running safety and riding comfort of high-speed trains, so it must be strictly limited.

The ultimate values for concrete shrinkage strain and creep coefficient are stipulated in the *Code for Design on RC and PC Structures of Railway Bridge and Culvert* (TB10002.3 2005), as shown in Table 10.1.

In addition to the causes of the structure itself, the creep deformation of concrete bridges is closely related to the environment and other factors, so it is very difficult to calculate the creep camber accurately. Ye and Liu (2009) measured the creep coefficients of a (85+135+85) m continuous PC beam bridge with ballastless tracks, and used them to simulate the whole process of construction and operation, and the variations of the deck profile with time were calculated, as shown in Fig. 10.1. In the figure, the curves represent the additional deflections after applying the secondary dead loads (laying tracks 90 days after casting the concrete).

Table 10.1 Ultimate values for concrete shrinkage strain and creep coefficient

Item		Ultimate concrete shrinkage strain ε_{co} ($\times 10^{-6}$)				Ultimate creep coefficient ϕ_{co}			
Theoretical thickness 2*A*/*u*/mm		100	200	300	≥ 600	100	200	300	≥ 600
Age of concrete when the prestress is exerted/d	3	250	200	170	110	3.00	2.50	2.30	2.00
	7	230	190	160	110	2.60	2.20	2.00	1.80
	10	217	186	160	110	2.40	2.10	1.90	1.70
	14	200	180	160	110	2.20	1.90	1.70	1.50
	28	170	160	150	110	1.80	1.50	1.40	1.20
	≥ 60	140	140	130	100	1.40	1.20	1.10	1.00

Note (1) For pretensioned structures, the concrete age when the prestress is exerted is generally 3–7 d; For post-tensioned structures, it is generally 7–28 d

(2) *A* is the area of concrete section in the calculation, *u* is the periphery contact length between the cross section and the atmosphere

(3) For concrete age and theoretical thickness between the values given in the table, the linearly interpolated values can be adopted

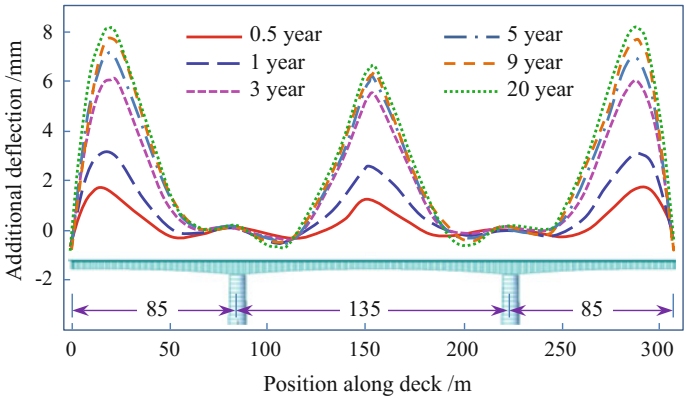

Fig. 10.1 Additional deflection curves of a (85+135+85) m continuous PC beam bridge in various periods

As shown in the figure, the camber and downward deformations of the girders caused by the joint action of concrete shrinkage, creep, and prestress loss increase with time. The additional deflection curves change quickly in the first few years after track laying, while the change gradually becomes slow in the later years.

10.2.1.2 Creep Mechanism and Influence Factors of Concrete

Since the early 1930s, the creep mechanism of concrete has been studied by scholars, and a variety of creep theories have been proposed based on various assumptions. The theories of concrete creep are generally based on the microstructure of the cement paste, such as the viscoelastic theory, the plastic flow theory, the viscous flow theory, the seepage theory, the microfracture theory, and the internal force equilibrium theory, while none of them can explain the creep phenomena satisfactorily. It is generally believed that the elastic deformation of aggregates and cement mortar (namely hydrate skeleton) and the microcracks constitute the initial deformation of the concrete member after loading; with the increase of time, the cement gel gradually produces plastic flows in the internal hydrates skeleton; the cement mortar-aggregate interface and the microcracks in the cement mortar continue to develop and thus cause the continuous and gradual deformation of the concrete member, namely the concrete creep. In addition, the evaporation of water inside concrete can also induce additional drying shrinkage creep of concrete.

The creep of concrete is influenced by various internal and external factors. The internal factors include cement type, concrete mixture ratio, water-cement ratio, size, and manufacturing and curing conditions of concrete members, which influence the microstructural or macrostructural characteristics of concrete. The external factors include the working environment (humidity and temperature), load level,

loading history, and duration of concrete members, which reflect the working characteristics of concrete.

10.2.1.3 Calculation Model of Concrete Creep

Concrete creep is usually described by creep coefficient $\varphi(t,\tau)$, which has two kinds of definition. Assuming $\sigma(\tau)$ the uniaxial constant stress acting on the concrete from time τ, and $\varepsilon_c(t,\tau)$ the generated creep strain at time t, the first definition of creep coefficient is based on the relationship between the creep coefficient and the elastic strain of concrete with 28 d age, expressed as

$$\varepsilon_c(t,\tau) = \frac{\sigma(\tau)}{E_{28}}\varphi(t,\tau) \tag{10.1}$$

where E_{28} is the elastic modulus of concrete with 28 d age.

This definition is adopted in the *Model Code for Concrete Structures* issued by the International Union of Concrete (CEB-FIP 2010), the *Fundamental Code for Railway Bridge and Culvert* issued by the Ministry of Railways of PRC (TB10002.1 2005), and several other codes.

The second definition of creep coefficient is based on the relationship between the creep coefficient and the instantaneous elastic strain of concrete, expressed as

$$\varepsilon_c(t,\tau) = \frac{\sigma(\tau)}{E(\tau)}\varphi(t,\tau) \tag{10.2}$$

where $E(\tau)$ is the elastic modulus of concrete at the moment τ.

This definition is proposed by the *American Concrete Institute Committee* (ACI209 1992), where τ is the standard loading age, which is 7 d for wet curing concrete and 1–3 d for steam curing concrete.

There are several theories to analyze the concrete creep, by considering various influence factors and adopting different calculation methods. In these theories, the mathematical expressions of the creep coefficients are divided into two categories. In the first category, the creep coefficient is expressed as the sum of several partial factors with different properties, such as that used in the early edition of *Code for Design of Highway RC and PC Bridges and Culverts* (JTJ023 1985) issued by the Ministry of Communications of PRC. In the second category, the creep coefficient is expressed as the product of a series of coefficients with different influences on the concrete creep, such as that adopted by the updated version of the *Code for Design of Highway RC and PC Bridges and Culverts* (JTG D62 2004).

In this chapter, the calculation method suggested in the Code JTG G62-2004 is adopted to analyze the creep of simply-supported PC beams. The concrete creep coefficient $\varphi(t, t_0)$ is expressed as

$$\varphi(t,t_0)=\varphi_0\cdot\beta_c(t,t_0) \tag{10.3}$$

$$\varphi_0=\left[1+\frac{1-\mathrm{RH}/\mathrm{RH}_0}{0.46(h/h_0)^{1/3}}\right]\cdot\frac{5.3}{(f_{cm}/f_{cm0})^{0.5}}\cdot\frac{1}{0.1+(t_0/t_1)^{0.2}} \tag{10.4}$$

$$\beta_c(t-t_0)=\left[\frac{(t-t_0)/t_1}{\beta_H+(t-t_0)/t_1}\right]^{0.3} \tag{10.5}$$

$$\beta_H=150\left[1+\left(1.2\frac{\mathrm{RH}}{\mathrm{RH}_0}\right)^{18}\right]\frac{h}{h_0}+250\le 1500 \tag{10.6}$$

where t_0 and t are, respectively, the concrete ages at the time of loading and calculation; φ_0 is the nominal creep coefficient; β_c is the development coefficient of creep after loading; f_{cm} is the average cubic compressive strength of C20–C50 concrete at the age of 28 d (MPa); β_c is a factor related to the average annual relative humidity RH (%), which applies to RH between 40% and 90%; h is the theoretical thickness of the member (mm); RH_0, h_0, t_1 and f_{cm0} are the given coefficients with the values of 100%, 100 mm, 1 d, and 10 MPa, respectively.

10.2.2 Experimental Investigation on PC Beam Creep Camber and Additional Track Unevenness

In the design codes for common railway bridges in China, neither the limit nor the explicit calculation method is proposed for the creep camber of PC beams. For early PC beams, because they were allowed to bear higher pressure stress in the service stage, and to speed up the equipment turnover, higher amount of cement was used and too sooner tensioning was conducted, and very big creep cambers emerged. For example, at the third 31.7 m simply-supported span of the K419 Bridge on the Tianjin–Pukou Railway Line, the maximum cambers of the four pieces of T-beams were measured as 135 mm, 118 mm, 113 mm, and 79 mm, respectively. Similarly, at the 38th span of the Shahe Bridge on the Tianjin-Qinhuangdao Railway Line, the maximum camber of the 31.7 m simply-supported PC T-beam reached 164 mm. According to the investigation, the average value of creep camber for the 32 m PC beams on common railways is about 60 mm. Due to the creep camber of beams, the ballast thickness of the track becomes insufficient and difficult to adjust, which causes the replacement of some beams and great economic losses.

In the *Code for Design of High Speed Railway* (TB10621 2014), the vertical residual creep and deformation of PC beams after track laying is restricted. For ballasted deck, the limit is 20 mm. For ballastless deck, when $L \le 50$ m, the limit

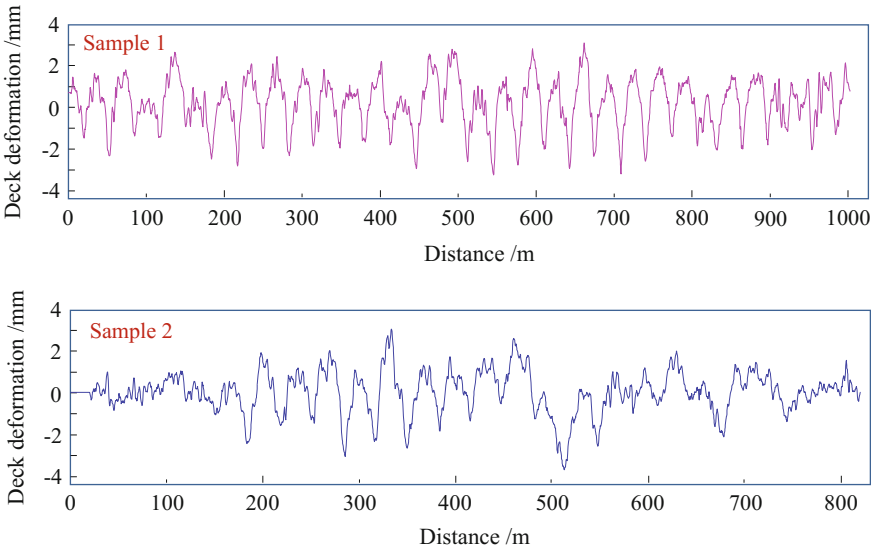

Fig. 10.2 Measured deformation curves caused by creep cambers of successively arranged PC beams

is 10 mm; when $L > 50$ m, the limit is $L/5000$, but not more than 20 mm, where L is the bridge span.

The CARS (China Academy of Railway Science) measured the creep cambers of 32 m simply-supported PC box-beams (43 spans in total) on the Beijing-Shanghai HSR line in 2013, which had served for more than two years by then. Shown in Fig. 10.2 are two typical samples of deformation curves measured at bridge decks, which reflect the joint influence of bridge cambers and uneven settlements. The curves exhibit obvious periodic waves. Analysis results show that they were mainly caused by the creep cambers of successively arranged 32 m PC beams (Li et al. 2014).

When the uneven settlements of piers are removed, the actual creep camber amplitudes of the beams are obtained and listed in Table 10.2.

The bridge deformation caused by the concrete creep produces the additional unevenness of the track on the bridge. For the simply-supported bridge with successive equi-span arrangement, the additional unevenness of the track structure is also periodic.

The CARS measured the track profiles on the Beijing-Shanghai HSR line and obtained the vertical and alignment irregularities of the left and right rails. Shown in Fig. 10.3 are the measured track irregularities of an 800 m section (from mileage K264.4 to K263.6) (Li et al. 2014).

Due to the successive arrangement of 32 m simply-supported PC beams, the amplitude of vertical track irregularity increases significantly with the obvious

Table 10.2 Distribution of creep camber amplitudes measured at the bridge

Creep camber amplitude (mm)	Number of spans	Percentage (%)
1.5–2.0	1	2.33
2.0–2.5	3	6.98
2.5–3.0	4	9.30
3.0–3.5	6	13.95
3.5–4.0	10	23.26
4.0–4.5	10	23.26
4.5–5.0	6	13.95
5.0–5.5	1	2.33
5.5–6.0	1	2.33
6.0–6.5	1	2.33

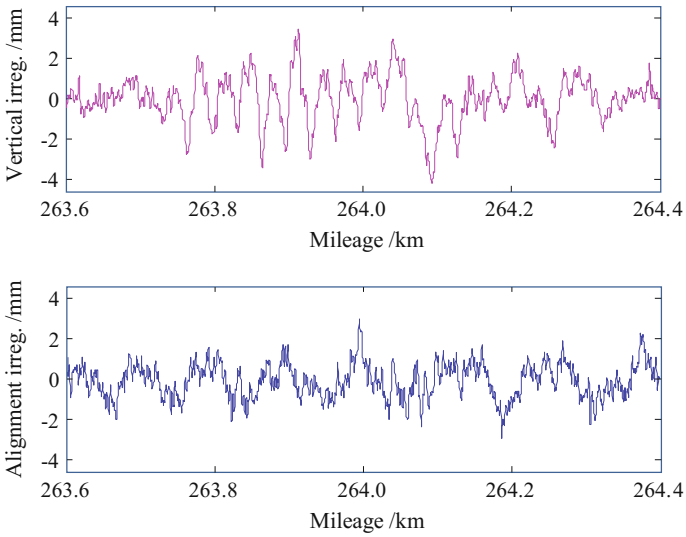

Fig. 10.3 Track irregularities measured on Beijing–Shanghai HSR line

periodic waves, which is consistent with the creep camber curve in Fig. 10.2. The spatial spectra of the track irregularities are analyzed and shown in Fig. 10.4.

It can be seen that in the spectrum of the vertical irregularity, there is a peak appearing near the 32 m wavelength (i.e., the spatial frequency 1/32 m^{-1}), while no peak at this frequency in the alignment irregularity. This shows that the periodic wavelength is mainly induced by the vertical deformations of the beams and the concrete creep is the main cause.

The experimental results prove that the concrete creep indeed affects the track profiles of the bridge. For the successively arranged simply-supported PC beams, the creep camber causes the additional periodic unevenness of the track. When a

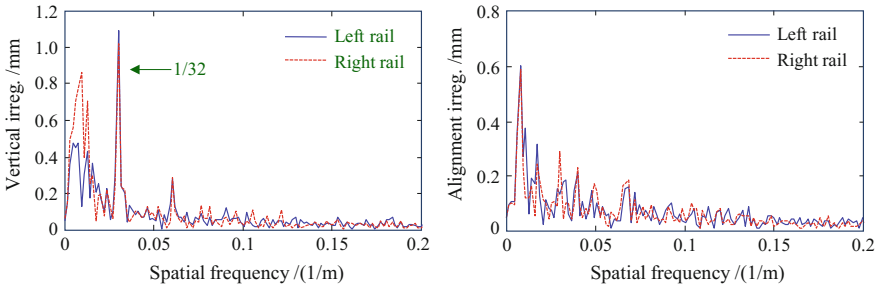

Fig. 10.4 Spatial spectra of the measured track irregularities

train runs on the bridge, such periodic excitation may intensify the vibrations of the train and the bridge and may even induce the resonance of them at certain speeds. Therefore, it is necessary to study the influences of concrete creep cambers on the track irregularity and on the running performance of the train on the bridge.

10.2.3 Analysis of Additional Track Unevenness Induced by PC Beam Creep Camber

With the increase of operation time, the additional deformations of PC beams caused by the concrete creep continue to develop. This additional deformation is gradually transmitted upwards through the track slabs and fasteners, which arouses additional internal forces in the track, causes additional unevenness of the track on the bridge, and even influences the running performance of the train. In order to study this influence, it is necessary to analyze the variation laws of the beam deformation and the additional track unevenness caused by the concrete creep.

10.2.3.1 FE Model of Creep Calculation for Beam-Track System

In China, bridges take a high proportion in HSR lines, which are mainly composed of 32 m simply-supported PC beams, and a few 24 m beams adopted to adjust the span arrangement. Herein, the 32 m and 24 m simply-supported PC box-beams (Design No. (2008) 2322A) are used to study the influence of additional unevenness of track caused by the beam creep cambers.

The CRTSIII ballastless slab track (Fig. 10.5) is the typical track structure with completely independent intellectual property rights in China. It is mainly composed of rail, fastener, PC slab, reinforced self-compact concrete (self-leveling concrete adjustment layer), positioning convex block, intermediate isolation layer (geotextile), and RC base.

The track adopts unit block structure with the size of 2400 mm × 190 mm. Positioning convex block is set for the track slab on the base, and the intermediate isolation layer is applied between the base and the self-leveling concrete layer. The WJ-8C fastener is used.

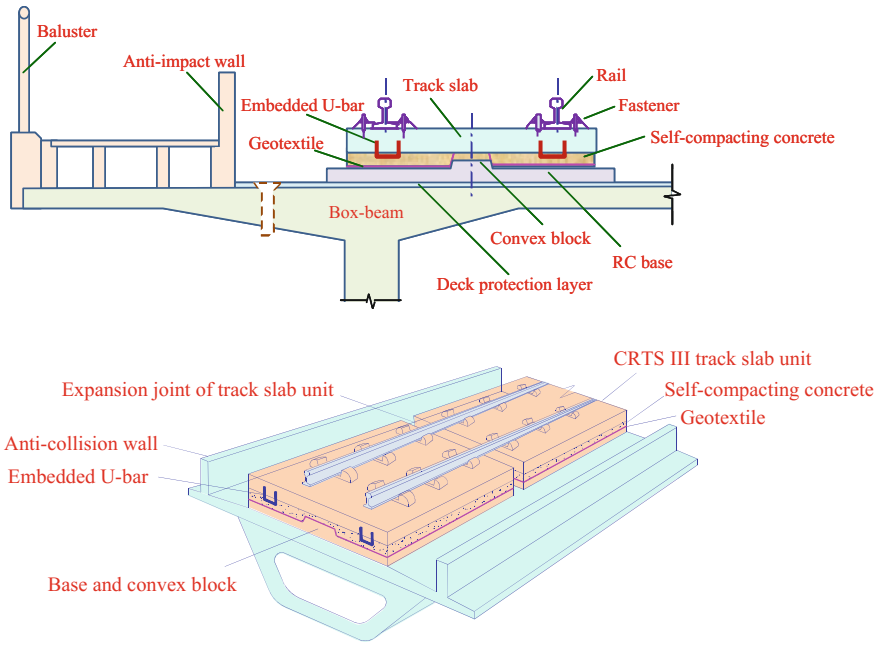

Fig. 10.5 Sketch of ballastless CRTSIII slab track

Shown in Table 10.3 are the layout plans of CRTSIII ballastless track slab units on 32 m and 24 m simply-supported beams, and in Figs. 10.6 and 10.7 are the corresponding specific slab layouts.

It can be seen that this layout allows the edge of the track slab to be justified with the beam end. The parameters of various components of CRTSIII ballastless slab track are listed in Table 10.4.

As shown in Fig. 10.8, the FE model of CRTSIII ballastless slab track on simply-supported beams is established. The model consists of two parts. The left part represents the subgrade, which is used to analyze the additional track unevenness in the beam-subgrade section under the creep camber of the side-span beam. The right part represents the beams, which is used to analyze the additional track unevenness on the beam including the connection section between the beams. In the analysis, it is assumed that the creep laws for all spans are identical.

Table 10.3 Layout plans of CRTSIII track slab units on 32 and 24 m beams (unit: mm)

Bridge span (m)	Slab unit layout	Fastener spacing	Slab joint	Fastener spacing cross slab joint	Fastener spacing cross beam end
32	4925 + 4 × 5600 + 4295	630	70	630/620	590
24	5 × 4856	617	80	617	637

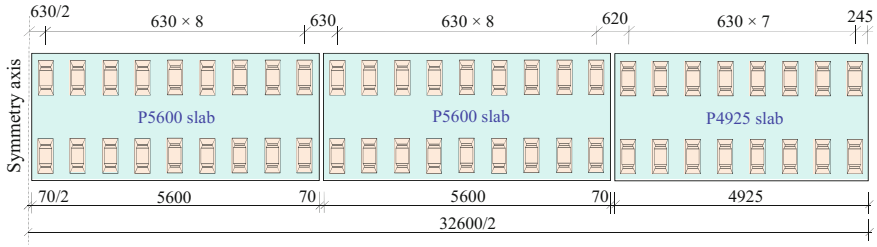

Fig. 10.6 Layout plan of CRTSIII track slab units on 32 m simply-supported beam (unit: mm)

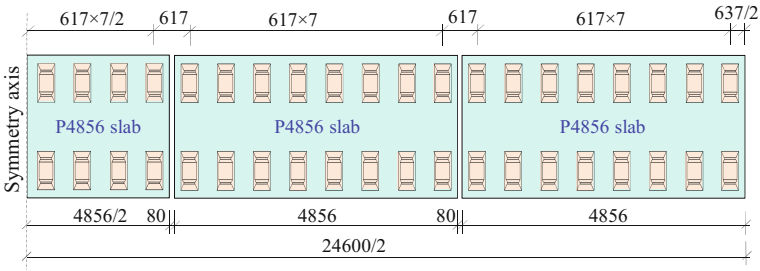

Fig. 10.7 Layout of CRTSIII track slab units on 24 m simply-supported beam (unit: mm)

Table 10.4 Parameters of CRTSIII ballastless slab track

Component	Parameter	Unit	Value
Rail	Section area	cm^2	77.45
	Moment of inertia about the horizontal axis	cm^4	3217
	Moment of inertia about the vertical axis	cm^4	524
	Elastic modulus	MPa	2.1×10^5
Fastener	Longitudinal fastening force/each group	kN	9
	Vertical static stiffness/each group	kN/mm	35
	Lateral static stiffness/each group	kN/mm	50
Track slab	Concrete grade	–	C60
	Density	kg/m^3	2500
	Elastic modulus	MPa	3.65×10^4
Self-compacting concrete	Concrete grade	–	C40
	Density	kg/m^3	2500
	Elastic modulus	MPa	3.4×10^4
Base	Concrete grade	–	C20
	Density	kg/m^3	2500
	Elastic modulus	MPa	2.8×10^4
	Shear bar	HRB335 ϕ28 steel bar, length 0.4 m	
	Supporting stiffness	Subgrade supporting stiffness: 76 MPa/m	

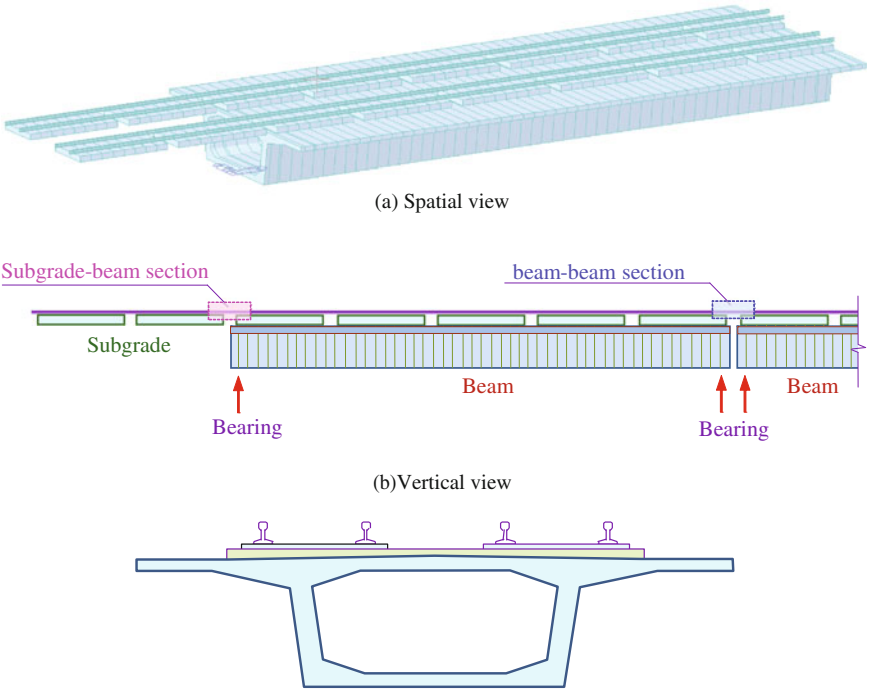

Fig. 10.8 Finite element model of the beam-track system

According to the Saint Venant's Principle, if the asymmetry of the outermost part of the track is ignored, the track deformation in the connection section of beams should be symmetric about the midpoint. Therefore, it is only needed to apply symmetry constraints on the right-side nodes of the model, by releasing the vertical displacement of the node and restricting the remaining DOFs. Thus, in the analysis, only one simply-supported beam is used to simulate the bridge.

According to the characteristics of CRTSIII ballastless slab track, some simplifications are adopted for the simulation of bridge track system:

(1) Due to the connection by embedded steel U-bars, the track slab and the self-compacting concrete layer can work together, so they are simplified as an equivalent slab.
(2) The geotextile between the self-compacting concrete layer and the RC base is modeled as a discrete compression spring with an equivalent stiffness of 400 MN/m^2. Because the creep only induces the vertical additional unevenness of the track, the compression spring is set on the center of the equivalent slab.
(3) The secondary dead load is adopted as 14.385 t/m.
(4) The prestressing loads are applied according to the actual arrangements of prestressing tendons in the beam.

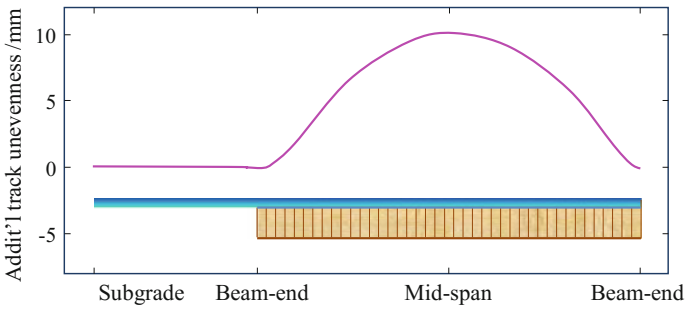

Fig. 10.9 Additional track unevenness caused by creep of simply-supported beam

10.2.3.2 Additional Track Unevenness Caused by Beam Creep

Based on the established analytical model and the assumed beam creep camber of 10 mm, the additional track unevenness caused by the creep of the simply-supported beams is calculated (Fig. 10.9).

It can be seen that due to the continuity of the track, the additional track unevenness curves in the subgrade-beam section and beam-beam section transit smoothly. The additional unevenness curve between the two beams shows a smooth break angle. Since the fastener stiffness (35 kN/mm) and the equivalent compression spring stiffness (400 MN/m^2) of the geotextile are very large, the maximum value of the track additional unevenness appears at the mid-span of the beam, which is approximately equal to the creep value of the beam-body.

10.2.3.3 Effects of Concrete Age and Track Laying Time

Concrete creep is affected by the loading age of the member. The dead loads on the simply-supported PC beam include two types: (1) the deadweights of the beam-body, secondary pavement, and accessory deck facilities; (2) the prestressing force applied on the beam by the prestressing tendons. To study the influence of concrete age on the creep of PC beams, the curing ages of concrete when applying prestressing forces are set as 7 d, 10 d, 14 d, and 21 d, respectively.

From applying prestressing forces on the beam, via beam erecting, to track laying, there is a time interval called track laying time. Only the beam creep after track laying can produce additional track unevenness. The positive moment generated by secondary loads can offset some of the negative moments caused by the creep camber due to the prestressing forces. Therefore, the *Code for Design of High-speed Railways* (TB10621 2014) requires that the accessory facilities be installed as early as possible before laying tracks. In the following analysis, it is assumed that the bridge accessory facilities are installed 20 days before laying the track, and the track laying times (the concrete age when the track is laid) are, respectively, 30 d, 60 d, 180 d, and 360 d.

The analysis results show that the normalized curves of the additional track unevenness under different track laying times are almost the same. Therefore, in the following analysis, it is assumed that the additional unevenness curve of the track is identical to the creep camber curve of the beam, and the amplitude increases with the creep development.

The maximum amplitudes of additional track unevenness for the 32 m and 24 m beams under various curing durations, track laying times, and operation periods after track laying are calculated, and the results are listed in Tables 10.5 and 10.6, respectively.

In the tables, the underlined negative values show that the beam develops negative creep in the early periods after track laying. This is because the moments produced by the secondary loads are opposite to those by prestressing forces, thus the tensile stress of the upper beam edge is reduced, which is equivalent to unloading of the upper edge concrete. The deformation recovery of concrete beams after unloading includes two parts: the immediate elastic recovery ε_{ce} and the elastic aftereffect ε_{cr} recovering gradually with time. Besides, there remains the residual deformation ε_{re}. Under the influence of elastic aftereffect, the creep due to unloading of secondary loads will be gradually recovered, so the negative creep growth appears.

It can be observed that the influence of beam creep on track smoothness is long-standing. Even after 5 years, the additional track unevenness can still develop by 1–2 mm. According to the *Code for Design of High speed Railways* (TB10621 2014), the residual creep of 32 m and 24 m simply-supported PC beams after laying the track should be no more than 10 mm, while the bold italic values in the tables are beyond the limit.

Shown in Figs. 10.10 and 10.11 are the influence of concrete curing duration M_d and track laying time L_d on the final deformation, where the final deformation refers to the additional unevenness of the track caused by beam creep after 20 years of service period.

The following conclusions can be drawn from the above analyses:

(1) Under the same working conditions, the additional track unevenness caused by 32 m beam creep is larger than that by 24 m beam. Under the same curing duration, longer concrete age before track laying is needed for 32 m beam to control the final deformation.
(2) Additional track unevenness decreases with the curing duration and the track laying time, and the latter has a larger influence. Concrete creep develops quickly in the early stage of loading, so the additional track unevenness can be reduced by delaying the track laying time, to release as much as possible the creep before laying track.

Table 10.5 Maximum amplitudes of additional track unevenness on 32 m beam under various conditions (unit: mm)

Curing duration/d	Track laying time/d	Operation period after track laying							
		3 months	6 months	1 year	2 years	5 years	10 years	15 years	20 years
7	30	4.51	6.96	9.54	***12.36***	***16.56***	***18.60***	***19.25***	***19.62***
	60	3.27	5.28	7.63	***10.43***	***14.67***	***16.75***	***17.42***	***17.81***
	180	0.79	1.76	3.41	5.88	9.72	***11.67***	***12.32***	***12.72***
	360	**−0.17**	0.32	1.52	3.55	6.78	8.48	9.10	9.50
10	30	4.16	6.43	8.83	***11.45***	***15.35***	***17.24***	***17.84***	***18.18***
	60	2.98	4.83	7.00	9.60	***13.52***	***15.45***	***16.06***	***16.42***
	180	0.65	1.53	3.06	5.34	8.90	***10.70***	***11.31***	***11.68***
	360	**−0.23**	0.20	1.30	3.17	6.16	7.74	8.31	8.68
14	30	3.84	5.96	8.19	***10.63***	***14.26***	***16.02***	***16.57***	***16.89***
	60	2.72	4.43	6.44	8.85	***12.46***	***14.28***	***14.85***	***15.18***
	180	0.53	1.33	2.73	4.86	8.16	9.83	***10.39***	***10.73***
	360	**−0.29**	0.09	1.09	2.83	5.60	7.06	7.59	7.93
21	30	3.49	5.43	7.48	9.71	***13.00***	***14.65***	***15.15***	***15.44***
	60	2.43	3.99	5.82	8.02	***11.31***	***12.93***	***13.44***	***13.74***
	180	0.40	1.10	2.37	4.30	7.31	8.83	9.33	9.64
	360	**−0.36**	**−0.04**	0.86	2.43	4.95	6.27	6.75	7.06

Table 10.6 Maximum amplitudes of additional track unevenness on 24 m beam under various conditions (unit: mm)

Curing duration/d	Track laying time/d	Operation period after track laying							
		3 months	6 months	1 year	2 years	5 years	10 years	15 years	20 years
7	30	2.58	3.96	5.41	7.00	9.32	***10.47***	***10.83***	***11.05***
	60	1.72	2.78	4.05	5.59	7.93	9.08	9.45	9.67
	180	0.56	1.13	2.06	3.43	5.55	6.64	7.01	7.23
	360	0.04	0.35	1.03	2.16	3.95	4.89	5.23	5.45
10	30	2.39	3.67	5.02	6.50	8.66	9.73	***10.06***	***10.26***
	60	1.74	2.79	4.01	5.45	7.63	8.70	9.05	9.25
	180	0.49	1.01	1.87	3.14	5.11	6.11	6.45	6.65
	360	0.01	0.28	0.91	1.96	3.62	4.49	4.81	5.01
14	30	2.22	3.41	4.67	6.04	8.07	9.06	9.37	9.55
	60	1.60	2.58	3.71	5.05	7.07	8.07	8.39	8.57
	180	0.43	0.90	1.70	2.88	4.71	5.64	5.95	6.14
	360	**−0.03**	0.22	0.80	1.77	3.31	4.12	4.42	4.60
21	30	2.02	3.12	4.28	5.53	7.39	8.30	8.59	8.75
	60	1.45	2.33	3.37	4.60	6.44	7.36	7.65	7.81
	180	0.35	0.78	1.50	2.58	4.25	5.10	5.38	5.55
	360	**−0.06**	0.15	0.68	1.56	2.96	3.70	3.97	4.14

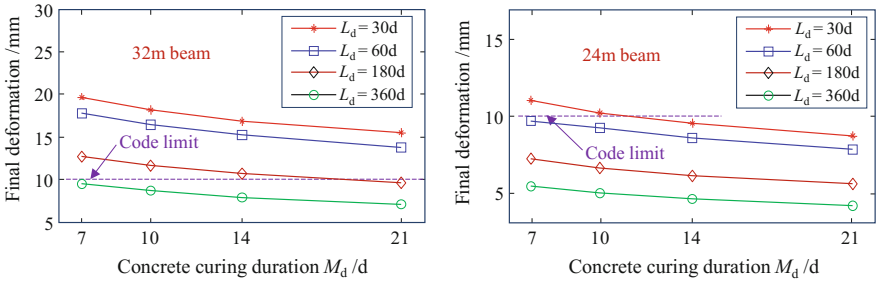

Fig. 10.10 Influence of concrete curing duration M_d on the final deformation under various track laying times

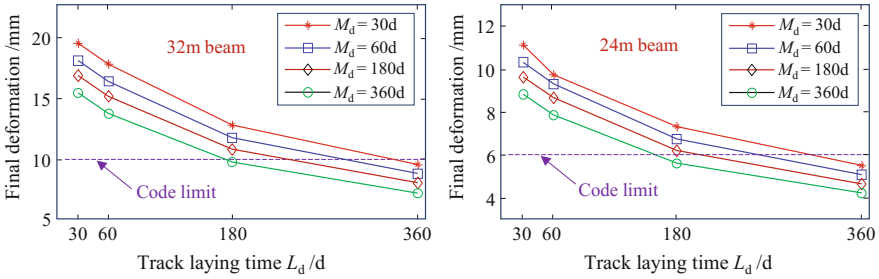

Fig. 10.11 Influence of track laying time L_d on the final deformation under various concrete curing durations

10.2.4 Simulation of Additional Track Unevenness Caused by Beam Creep Camber

In dynamic analysis of train-bridge system, the continuous additional track unevenness is needed, while the calculated results by the FE method are for a series of discrete points, so it is necessary to fit them to form a continuous curve. If the additional track unevenness curves caused by beam creep can be defined by the determinative shape with variable amplitudes, the normalized unevenness curves can be adopted for further analysis.

As shown in Fig. 10.12, the left part of the model is the subgrade and the right part is the simply-supported PC beams. The additional track unevenness curves caused by bridge creep are fitted in three sections, namely the subgrade-beam section, the beam section, and the beam-beam section. Shown in Fig. 10.13 are the fitted additional track unevenness curves normalized with 10 mm amplitude for 32 and 24 m simply-supported beams.

Due to the cantilevered length over beam-ends and the gap between beams, the real lengths for the 32 and 24 m simply-supported PC box-beams are 32.7 m and

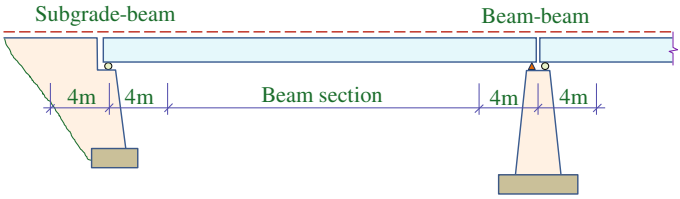

Fig. 10.12 Section partition for fitting simulation of additional track unevenness curves

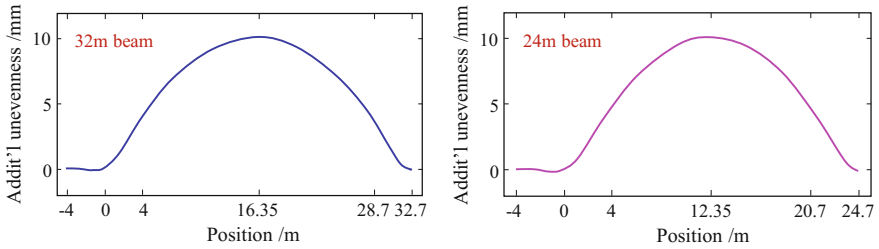

Fig. 10.13 Simulated additional track unevenness curves normalized with 10 mm amplitude

24.7 m, respectively. For easier expression, they are still simply called as 32 and 24 m beams in the following analysis.

Shown in Fig. 10.14 are the additional track unevenness curves of the 10×32 m and 10×24 m bridge with 30 mm creep amplitude. It can be seen that the creep cambers produce a series of concave corners on the additional track unevenness curves at the beam ends, forming a series of successive periodic half-sine waves.

The additional track unevenness curve may excite additional acceleration of the wheel when it moves along the track. Shown in Fig. 10.15 are the additional acceleration curves when the train passes the 10×32 m and 10×24 m bridges with 30 mm creep cambers at the speed of 360 km/h. The curves have the following

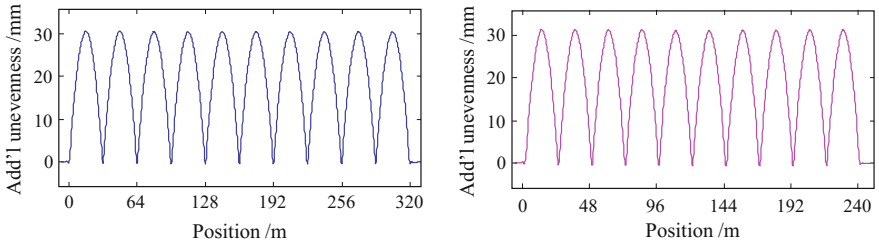

(a) 10×32m bridge (b) 10×24m bridge

Fig. 10.14 Additional track unevenness curves caused by beam creep cambers

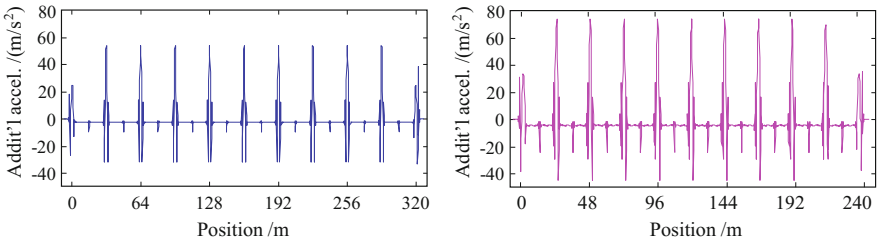

(a) 10×32m bridge (b) 10×24m bridge

Fig. 10.15 Time-histories of additional acceleration caused by additional track unevenness

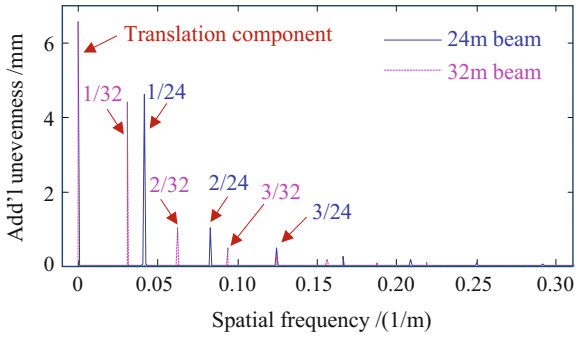

Fig. 10.16 Spatial spectra of additional track unevenness caused by beam creep camber

characteristics: (1) the acceleration peaks appear at the beam-ends; (2) the accelerations at the beam-beam sections are larger than those at the subgrade-beam sections; (3) the accelerations at the beam-ends are much greater than those at the beam centers; and (4) the accelerations on 24 m beams are larger than those on 32 m beams.

To better study the frequency features of the additional track unevenness caused by creep cambers, the additional track unevenness for 50×32 m and 50×24 m simply-supported beam bridges are calculated, and their spatial frequency spectra are analyzed and compared in Fig. 10.16.

As can be seen that in the spatial frequency spectra, only exist components at the frequency points of 0 and $n/32$ (corresponding to the 32 m beam) or $n/24$ (corresponding to the 24 m beam), (n = 1, 2, 3 …). The additional unevenness is composed of the translation component (0 Hz) and the harmonic components with spatial frequencies equal to integral times of $1/L$ (L is the span length), in which the harmonic component corresponding to n = 1 is the most obvious.

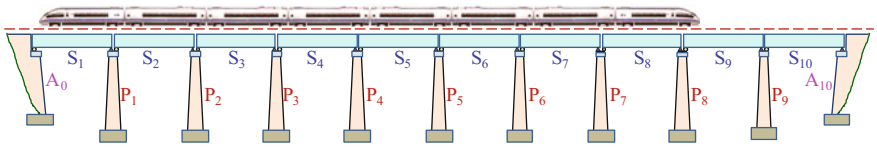

Fig. 10.17 Sketch of the train-bridge model

10.2.5 Influence of Beam Creep on Dynamic Responses of Train-Bridge System

The additional track unevenness caused by the creep cambers of simply-supported bridge with successive equi-span arrangement is periodical, which is equivalent to superposing a long-wave harmonic component on the original track irregularity. In this section, the 10×32 m and 10×24 m simply-supported beam bridges and the Germany ICE3 high-speed train are used to analyze the influences of beam creep on the dynamic responses of the train-bridge system. Shown in Fig. 10.17 is the sketch of the analysis model.

10.2.5.1 Parameters of the Train-Bridge System

The cross section of 32 m simply-supported box-beam is shown in Fig. 10.18, which is also applicable to the 24 m beam, except for the dimensions in brackets. The 6 m-high piers with round-ended section are used, whose bottoms are fixed on the ground. The first vertical natural frequencies for the 32 and 24 m beams are calculated as 4.65 Hz and 5.92 Hz, respectively.

The composition of the ICE3 train is (3M + 1T) × 2, with M denoting the motor-car and T the trailer-car. The parameters of the ICE3 vehicles can be found in Table 6.8 of Chap. 6.

Due to the randomness of track irregularity, when the additional track unevenness is superposed on the original irregularity, the local irregularity will also have

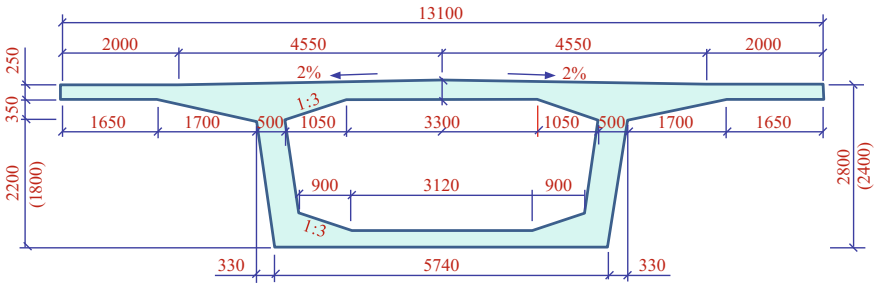

Fig. 10.18 Cross section of the 32 m (24 m) simply-supported PC box-beam (unit: mm)

randomness. Therefore, ten groups of track irregularity samples are generated based on the German low disturbance spectrum. The ten groups of irregularity samples are used to calculate the dynamic responses of the train-bridge system, and the results are averaged to analyze the influence of beam creep cambers.

In simulation analysis of the train-bridge system, the damping ratios for all modes are taken as 0.05, and the integration time step is 0.001 s.

10.2.5.2 Influence of Beam Creep on Car-Body Acceleration

Considering the train speed of 360 km/h, and beam creep amplitude as none and 30 mm, respectively, the whole histories of the train passing through the 10×32 m and 10×24 m simply-supported beam bridges are simulated. Shown in Figs. 10.19 and 10.20 are the calculated car-body acceleration time histories of the fifth vehicle on the two bridges. In the figures, the train position is located by its first wheel-set.

As shown in the figures, the car-body accelerations increase obviously when the additional track unevenness induced by 30 mm creep is considered, and the acceleration curves show the periodicity corresponding to the additional track unevenness.

It can also be seen that the car-body accelerations on the 10×24 m bridge are obviously greater than those on the 10×32 m bridge, and on both bridges, the car-end accelerations are significantly greater than the car-center's, especially when the additional track unevenness induced by 30 mm creep is considered. The frequency spectra of car-body accelerations are also analyzed, as shown in Figs. 10.21 and 10.22.

As can be seen from the figures, compared with the case of none creep, the frequency spectra of the car-body accelerations show predominant peaks at 3.12, 6.25, and 9.38 Hz when the train passes the 10×32 m bridge with 30 mm creep, and show predominant peaks at 4.17, 8.33 and 12.51 Hz when it passes the 10×24 m bridge with 30 mm creep. As analyzed in Chap. 2, the predominant frequencies are related to the span of the beam and the running speed of the train, expressed as

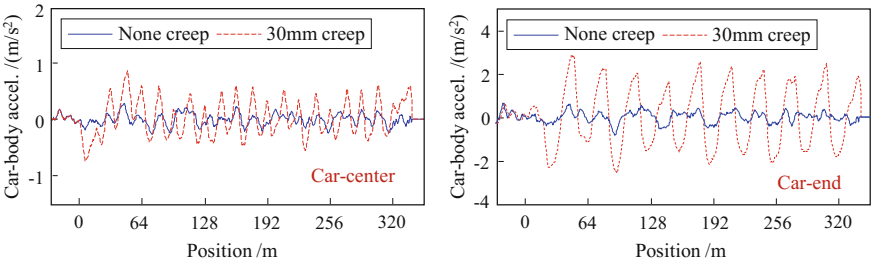

Fig. 10.19 Time histories of car-body acceleration (10×32 m bridge)

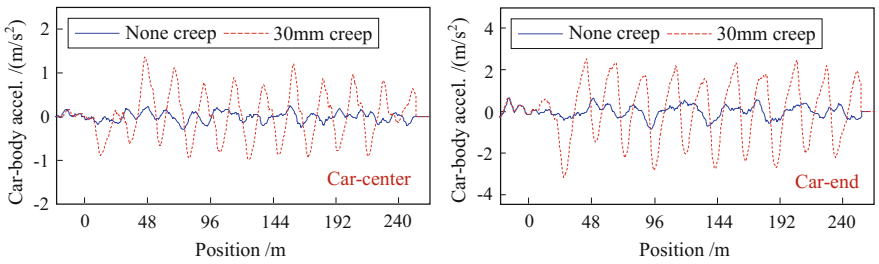

Fig. 10.20 Time histories of car-body acceleration (10×24 m bridge)

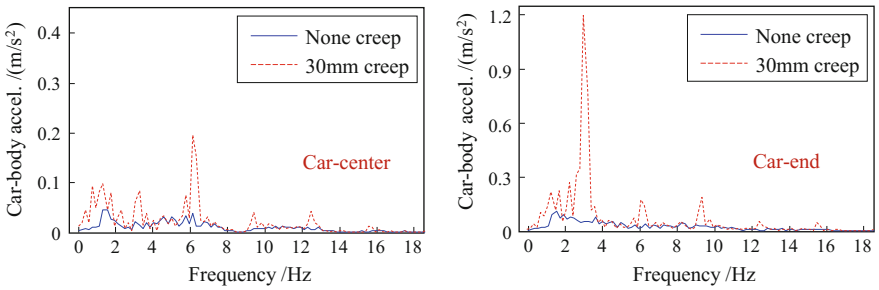

Fig. 10.21 Frequency spectra of car-body acceleration (10×32 m bridge)

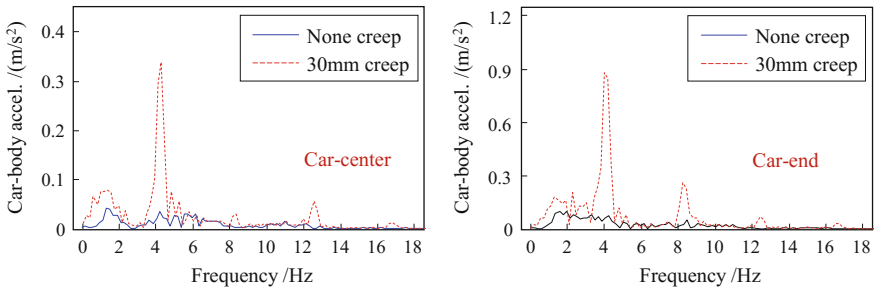

Fig. 10.22 Frequency spectra of car-body acceleration (10×24 m bridge)

$$f = \frac{nV}{3.6L} \quad (n = 1, 2, 3, \ldots) \tag{10.7}$$

where f is the predominant frequency (Hz); V is the train speed (km/h); L is the beam span (m).

The car-end accelerations of the vehicle are further calculated when the train passes the 10×32 m and 10×24 m bridges, considering the train speeds of 160–360 km/h and the beam creep amplitudes of 0–30 mm. Shown in Figs. 10.23 and 10.24 are the spatial distributions and contour graphs of the maximum car-body

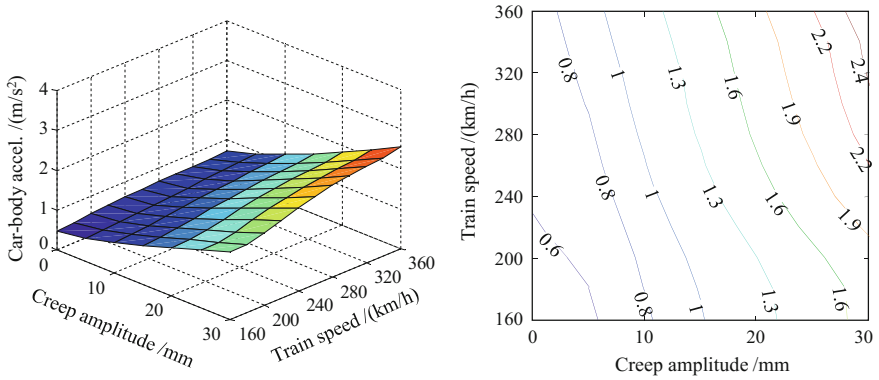

Fig. 10.23 Influence of train speed and creep amplitude on car-end acceleration (10×32 m)

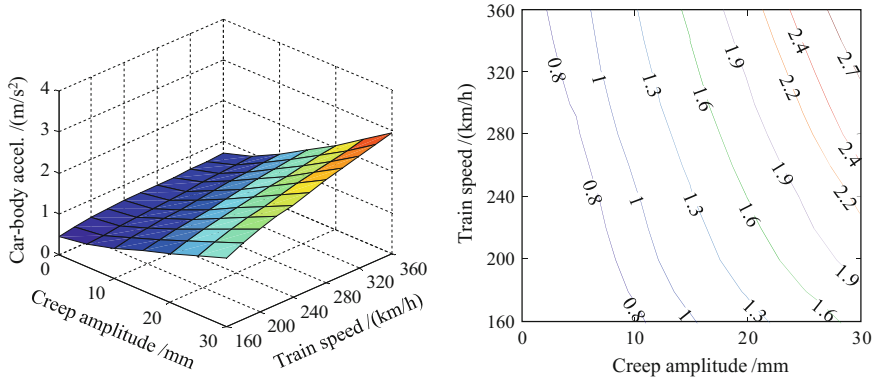

Fig. 10.24 Influence of train speed and creep amplitude on car-end acceleration (10×24 m)

accelerations versus train speed and creep amplitude, where the car-body accelerations are the average values under ten groups of track irregularity samples.

It is obvious that when the train passes the two bridges, the car-body accelerations of the train increase rapidly with train speed and creep amplitude, and the car-body accelerations on the 10×32 m bridge are greater than those on the 10×24 m bridge.

10.2.5.3 Influence of Beam Creep on Train Running Safety

Shown in Fig. 10.25 are the offload factor variation curves of the first wheel-set on the fifth vehicle when the train passes the 10×32 m bridge at the speed of 360 km/h, considering none creep and 30 mm creep of the beams.

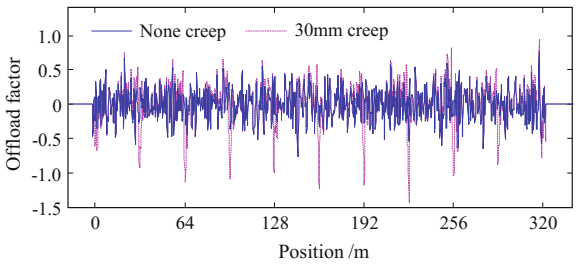

Fig. 10.25 Variation curves of offload factor

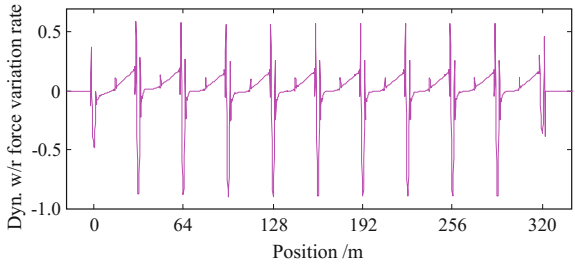

Fig. 10.26 Curves of dynamic wheel-rail force variation rate

To better describe the variations of vertical wheel-rail forces, Fig. 10.26 shows the curves of the dynamic wheel-rail force variation rate, defined as the ratio of dynamic wheel-rail force difference (between the values on creep and none creep beams) to static axle load.

It can be seen that the wheel-rail forces are significantly influenced by the additional track unevenness, especially at the beam-ends, the dynamic wheel-rail force variation rates increase dramatically, being as high as 0.9, while they change little at the beam centers, showing similar variations to the additional track acceleration curves in Fig. 10.15.

For the 10×24 m simply-supported bridge, the wheel-rail forces change more significantly, but the variation curves are similar to those of the 10×32 m bridge, so they are not given.

Compared in Figs. 10.27 and 10.28 are spatial distributions and contour graphs of maximum offload factors versus train speed and beam creep amplitude, when the train passes the beam-end and non-beam-end sections of the 10×32 m bridge and the 10×24 m bridge, respectively.

The following conclusions can be drawn from these figures:

(1) The offload factors increase rapidly with train speed and creep amplitude.
(2) When the train passes the beam-end sections, the offload factors increase more significantly with the creep amplitude than when the train passes non-beam-end Sects.
(3) When the train passes the 10×24 m bridge, the increase trend of offload factors is more obvious than that when the train passes the 10×32 m bridge. For example, in the case with creep amplitude of 30 mm and train speed of

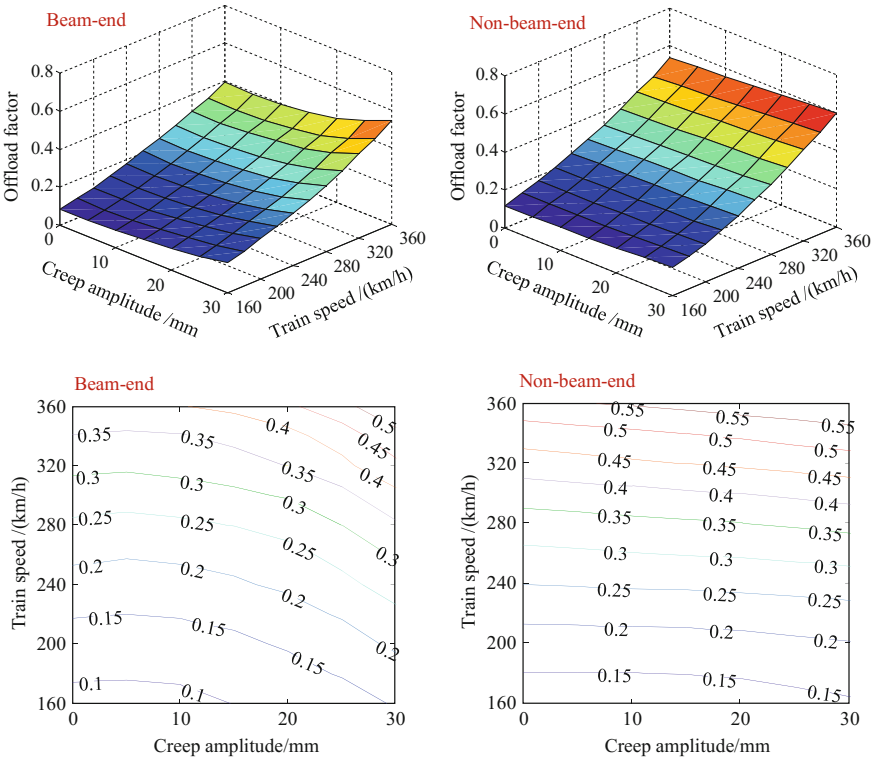

Fig. 10.27 Distributions of maximum offload factors versus train speed and beam creep amplitude (10×32 m bridge)

360 km/h, the offload factors of the train on the 32 m-span bridge increase from 0.393 to 0.545 at beam-ends and from 0.537 to 0.595 at non-beam-end sections. While on the 24 m-span bridge, the offload factors increase from 0.437 to 0.774 and from 0.471 to 0.609, respectively, which are beyond the limit of 0.6.

Shown in Figs. 10.29 and 10.30 are spatial distributions and contour graphs of maximum derailment factors versus train speed and creep amplitude when the train passes the beam-end and non-beam-end sections of the 10×32 m bridge and the 10×24 m bridge, respectively.

In the main trend, the maximum derailment factors increase gradually with train speed and beam creep amplitude. When the train passes the beam-end sections, the derailment factors are more easily affected by the beam creep. Because the derailment factor is simultaneously determined by the lateral force and vertical force between wheel and rail, it is not so much affected by beam creep as the offload factor which is only controlled by vertical wheel-rail force. Therefore, the variations of derailment factors are not elaborated herein in detail.

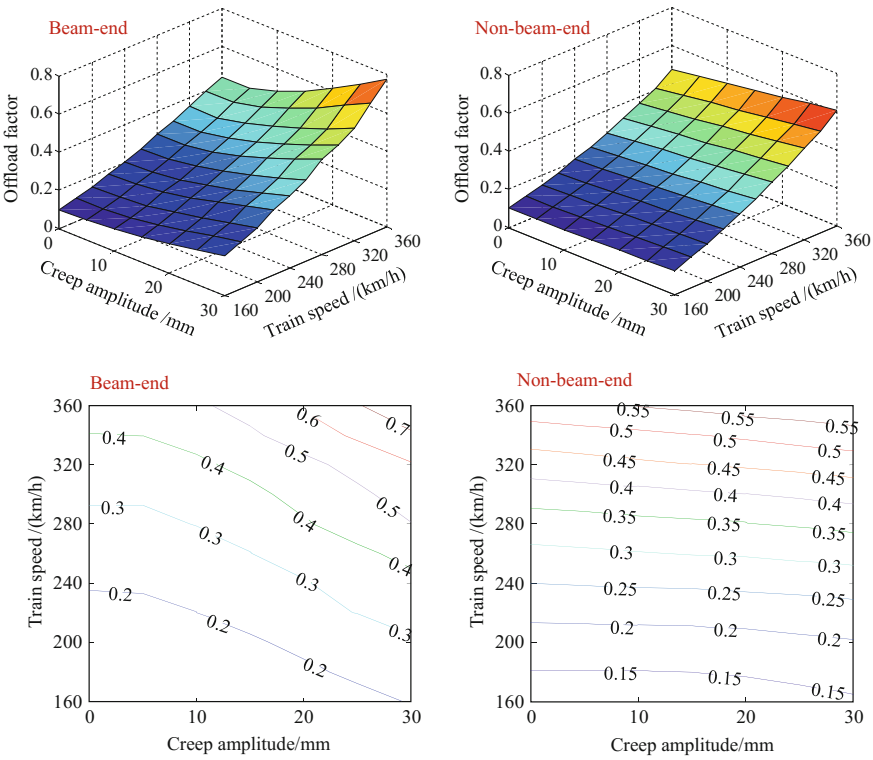

Fig. 10.28 Distributions of maximum offload factors versus train speed and beam creep amplitude (10×24 m bridge)

From the above analysis, it can be seen that under certain beam creep amplitudes and train speeds, the car-body accelerations and offload factors of the train exceed the limits given in the code, which are 1.3 m/s^2 and 0.6, respectively. This further confirms the necessity of studying the influence of beam creep deformation on the dynamic responses of train-bridge system.

Assume the dynamic responses of the train under different track irregularity samples obey the normal distribution, namely, the running safety indices or car-body accelerations have a 50% probability of exceeding the threshold based on the mean values. For the case of 30 mm creep, the maximum car-body accelerations and maximum offload factors under ten groups of track irregularity samples when the train passes the bridge at different train speeds are calculated, and the distributions of them are illustrated in Figs. 10.31 and 10.32.

It can be seen from the figures:

(1) Under low train speeds, the differences among the maximum car-body accelerations and among the maximum offload factors for 10 groups of track irregularity samples are small, and both of them increase with train speed.

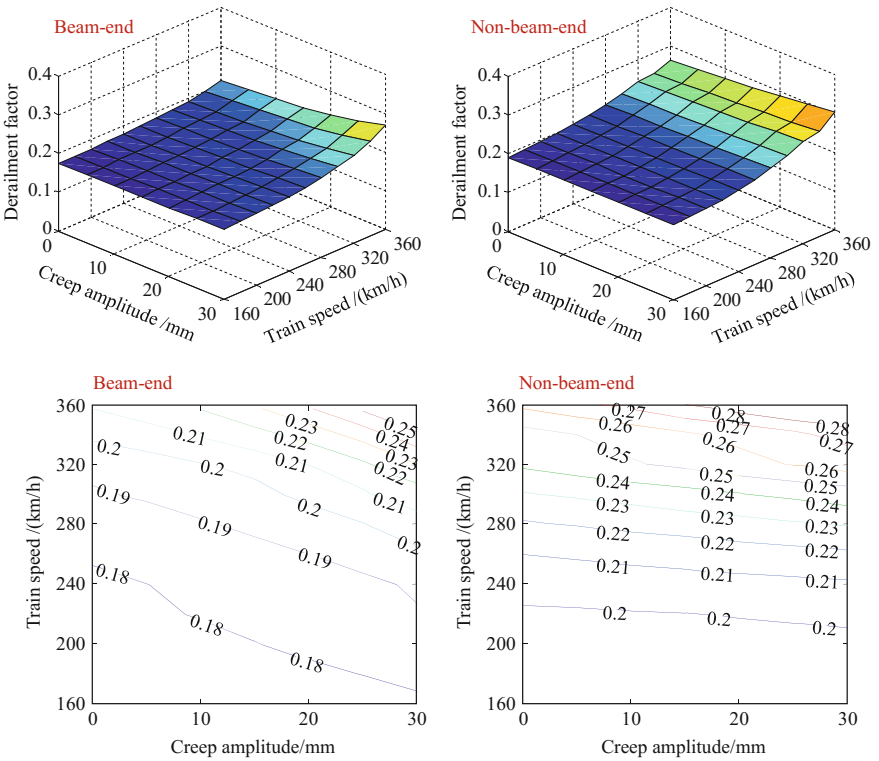

Fig. 10.29 Distributions of maximum derailment factors versus train speed and beam creep amplitude (10×32 m bridge)

(2) The maximum offload factors under different track irregularity excitations show greater discreteness than the maximum car-body accelerations, which is because the offload factors are mainly controlled by the short-wave irregularities, and the short-wave irregularities are more easily affected by the local randomness.

When the train speed is 360 km/h, the offload factors under several groups of track irregularity excitations are beyond the limit of 0.6. Under the tenth irregularity sample, the offload factor reaches 0.93 when the train passes through the 10×24 m bridge, while the average offload factor under the ten irregularity samples is 0.4, indicating that if the safety threshold is based on the average values, the safety factor may be underestimated.

When the train passes through the 10×32 m and 10×24 m bridges under the ten groups of track irregularity samples and various creep amplitudes, the maximum car-body accelerations and offload factors are calculated, based on which the safety and comfort thresholds are proposed, and according to Eq. (9.11), the threshold

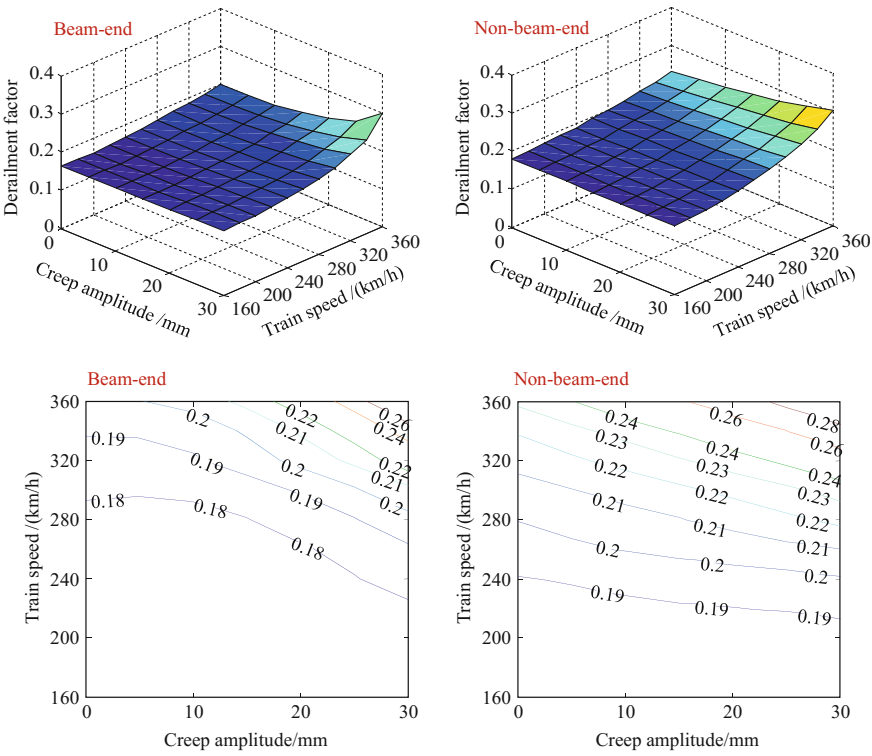

Fig. 10.30 Distributions of maximum derailment factors versus train speed and beam creep amplitude (10×24 m bridge)

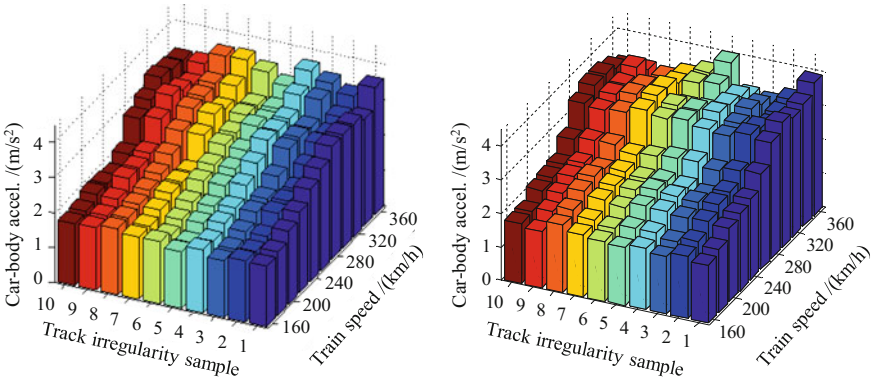

(a) 10×32m bridge (b) 10×24m bridge

Fig. 10.31 Distributions of maximum car-body accelerations under ten groups of track irregularity samples

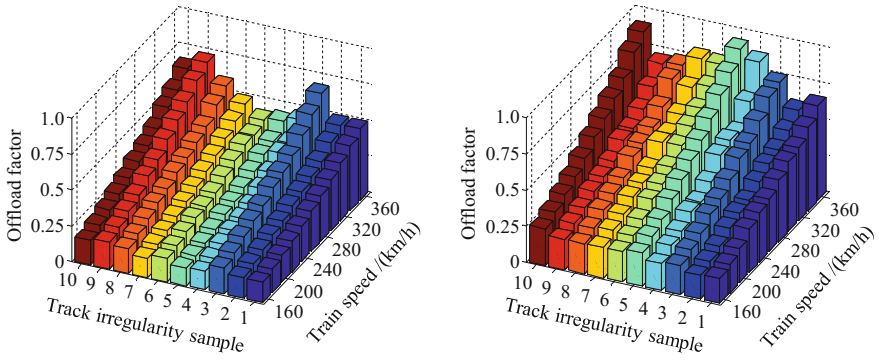

(a) 10×32m bridge (b) 10×24m bridge

Fig. 10.32 Distributions of maximum offload factors under ten groups of track irregularity samples

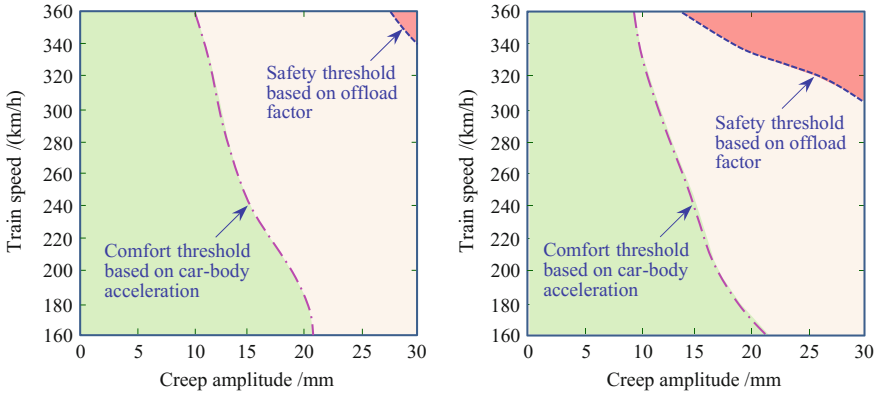

(a) 10×32m bridge (b) 10×24m bridge

Fig. 10.33 Threshold diagrams for running safety and comfort (95% confidence)

curves with 95% confidence are drawn in Fig. 10.33. In the figure, the dash-dotted line is used as the threshold to divide the comfort and uncomfortable zones based on car-body accelerations, and the dotted line is used as the threshold to divide the safety and unsafety regions based on the offload factors.

The following characteristics can be observed from the threshold diagrams:

(1) The safety region of offload factor for the 10×24 m bridge is smaller than that for the 10×32 m bridge, because the 24 m beam produces greater local excitations at the beam-ends.
(2) The safety region defined by acceleration threshold curve is much smaller than that by the offload factor threshold curve, showing that the beam creep affects

the passenger riding comfort (i.e., the car-body acceleration) more than the train running safety (offload factor).

Therefore, for the HSR bridges composed of successive equi-span arrangement PC beams, the additional track unevenness induced by creep cambers should be adjusted timely, to ensure the riding comfort and running safety of the train on bridges.

10.3 Influence of Temperature Deformation on Dynamic Responses of Train-Bridge System

10.3.1 Temperature Deformations of Bridge

For bridges, the temperature deformations consist of two types: the deformation caused by uniform temperature effect, and the deformation caused by the temperature gradient effect.

The bridge deformation under the uniform temperature effect is induced by the seasonal temperature variation in a year, which causes the bridge structures to evenly expand along their longitudinal axes.

The temperature gradient is the sunshine temperature difference due to the solar radiation along the structural height or width within a day (Kyle Buick 1981), whose forming mechanism is shown in Fig. 10.34. When a bridge member is exposed to the sunlight, the temperature in the sunny side becomes higher while in the shady side remains lower. Due to the poor thermal conductivity of concrete materials, most parts of the internal structure are insensitive to the temperature variation, thus forming a large temperature difference. Under the temperature gradient effects, the bridge will generate static deformation. For the ballasted-track beam, only the temperature gradient loads along the beam width need to be considered. While for the ballastless track beam, not only the temperature gradient loads along the beam height and width need to be separately considered, but also their combined effect should be concerned.

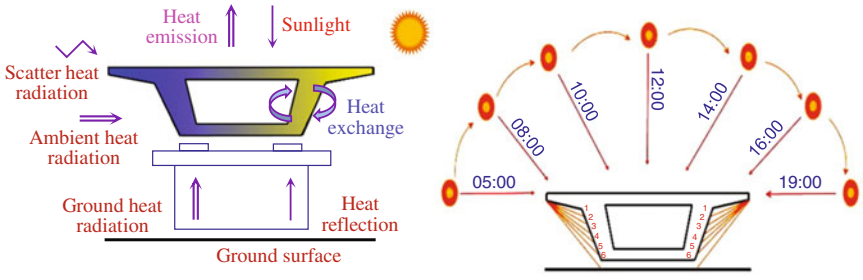

Fig. 10.34 Temperature effects on bridge structure

The uniform temperature effect can be determined by the meteorological data near the bridge site, whose fluctuation range is the difference between the extreme local temperature and the temperature for erection or closure of the bridge.

The range of temperature gradient effect is generally considered that the temperature at the beam top is 5 °C higher than that at the bottom.

According to the *Code for Design on RC and PC Structures of Railway Bridges and Culverts* (TB10002.3 2005), for the box-beam, the sunshine temperature difference curves along the beam height and width are expressed as

$$T_y = T_{01} \times \mathrm{e}^{-cy} \tag{10.8a}$$

$$T_x = T_{02} \times \mathrm{e}^{-cy} \tag{10.8b}$$

where T_{01} and T_{02} are, respectively, the temperature difference amplitudes along the beam height and width, and c is the coefficient of the exponential function, whose values are listed in Table 10.7. The distribution curves of temperature difference are shown in Fig. 10.35. In a practical design, the temperature differences can be calculated according to the temperature difference graph, with the values from 19 to 22 °C along the beam height, and from 12 to 16.5 °C along the width.

The position of the sun changes continuously in a day (and a year), and the heat exchange between the bridge and the environment is very complicated, so the assumed distributions of temperature gradient are usually different from the real temperature field. The track deformation induced by bridge temperature gradient, especially the local track deformation, has a great influence on the running safety of trains. In recent years, the temperature field and the temperature stress of bridge structure have been studied by theoretical analysis and experiments, and the related calculation theories well improved. The results show that the temperature stress in PC box-beams is mainly caused by the temperature difference along the vertical section. At present, there are many researches on the temperature deformations of bridge and track structures (Priestley 1976; Priestley 1978; Liu and DeWolf 2007; Bian 2009; Chen et al. 2010; He et al. 2012; He 2013; Shan 2014), but few attentions are paid to analyze the influence of them on the running safety of high-speed trains (Xia et al. 2006; Zhai 2007; Niu 2008; Zhang 2008; Sun 2013; Tian et al. 2015).

Table 10.7 Parameters for sunshine temperature difference curves along beam height and width

Beam type	Design type	Along beam height		Along beam width	
		$c(\mathrm{m}^{-1})$	T_{01} (°C)	$c(\mathrm{m}^{-1})$	T_{02}(°C)
Ballastless deck	Uni-direction	5	20	none	none
	Bi-direction	7	16	7	16
Ballasted deck	Uni-direction	none	none	7	16

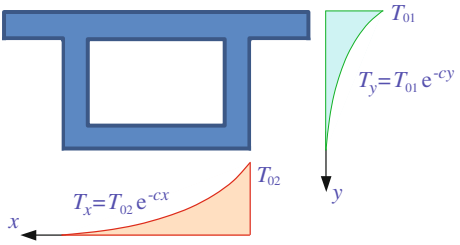

Fig. 10.35 Distribution diagram of temperature difference for box-beam

10.3.2 Numerical Simulation for Sidewise Bending of Beam

As mentioned previously, the temperature effect can cause vertical and transverse deformations of beams. The transverse deformation of the beam is called sidewise bending, which induces the additional transverse unevenness of the bridge. Because the vertical deformation rules of beams caused by temperature effect are similar to those by creep cambers, this section focuses on analyzing the influence of sidewise bending of beams on the train-bridge system.

For the HSR simply-supported bridge with constant-section beams, the sidewise-bending deformation of beam can be simulated with circular curves.

For the 2×32 m simply-supported PC box-beam bridge, the calculation span (distance between the bearings) for each beam is 31.5 m, and the distance between two adjacent beam bearings on the intermediate pier is 1.2 m. If the sidewise-bending amplitude is assumed to be 1, the sidewise-bending deformation is described by two types of circular curves, as expressed by Eq. 10.9a and shown in Fig. 10.36.

$$y_1(x) = \sqrt{\left(\frac{L_1^2}{8A} + \frac{A}{2}\right)^2 - \left(x - \frac{L_1}{2}\right)^2} - \left(\frac{L_1^2}{8A} - \frac{A}{2}\right), \quad (0 \le x \le L_1) \tag{10.9a}$$

$$y_1(\xi) = \sqrt{\frac{L_2^2}{L_1^2}\left(\frac{L_1^2}{8A} + \frac{A}{2}\right)^2 - \left(\xi - \frac{L_1}{2}\right)^2} + \frac{L_2}{L_1}\left(\frac{L_1^2}{8A} - \frac{A}{2}\right), \quad (0 \le \xi \le L_2) \tag{10.9b}$$

where A is the amplitude (maximum value) of the beam sidewise-bending deformation; L_1 is the calculation span of beam; L_2 is the center-to-center distance between the two adjacent beam bearings on the pier. The curves are continuous and first differentiable at the connecting points.

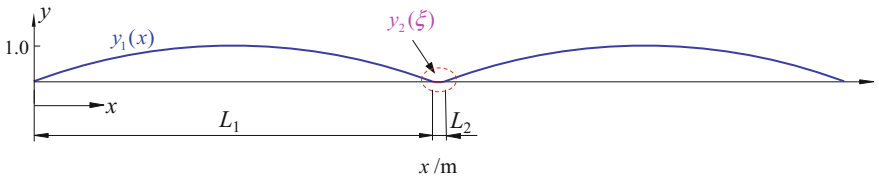

(a) Sidewise-bending curves of two-span simply-supported beams

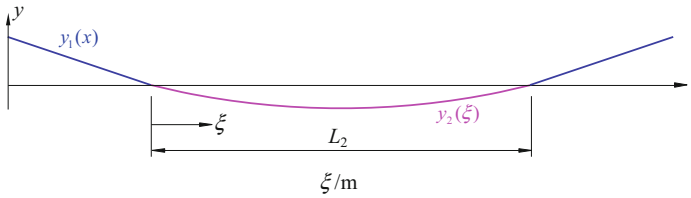

(b) Side-bending connection curve

Fig. 10.36 Simulation curves for temperature sidewise-bending deformation of 2×32 m simply-supported beams

10.3.3 Temperature Warping Deformation of Track Slab and Its Effect on Dynamic Responses of Train-Track System

The CRTSII ballastless slab track used on the Beijing-Shanghai HSR bridges is considered in the analysis. The CRTSII slab track adopts continuous-slab structure. It consists of rail, fastener, PC slab, CA mortar (cement asphalt mortar) layer, PC base (concrete supporting layer), lateral restriction (positioning) block, sliding layer, isolation layer, etc., as shown in Fig. 10.37. The track slabs on the bridge are longitudinally connected, under which are continuous RC base, a sliding layer is set between the base and the protection layer of the beam surface, and restriction blocks are set at the two sides on the base.

The CRTSII track slab is a partially prestressed concrete structure. The standard size of the track slab is 6450 mm × 2550 mm × 200 mm, with "V-shaped" pre-set notches of 4 cm depth at every 0.65 m along the longitudinal direction. Along the direction of the track, the slabs are connected at the ends by 6ϕ20 connecting bars. The section width of the RC base varies from 2.95 m (top) to 3.25 m (bottom). The 30 mm-thick high performance CA mortar is set between the slab and the base as the construction adjustment layer after erection.

The CRTSII track slab is prefabricated in factories with high quality standard. However, there occurred also some problems in construction and operation (Wang et al. 2009), such as the separations of track slab from the CA mortar and the sliding layer under the slab, and the warping and cracking of slab. Han and Sun (2011) found that these problems were related to the track slab temperature: When the track slab is exposed to the sunlight, the surface temperature rises rapidly, while most of

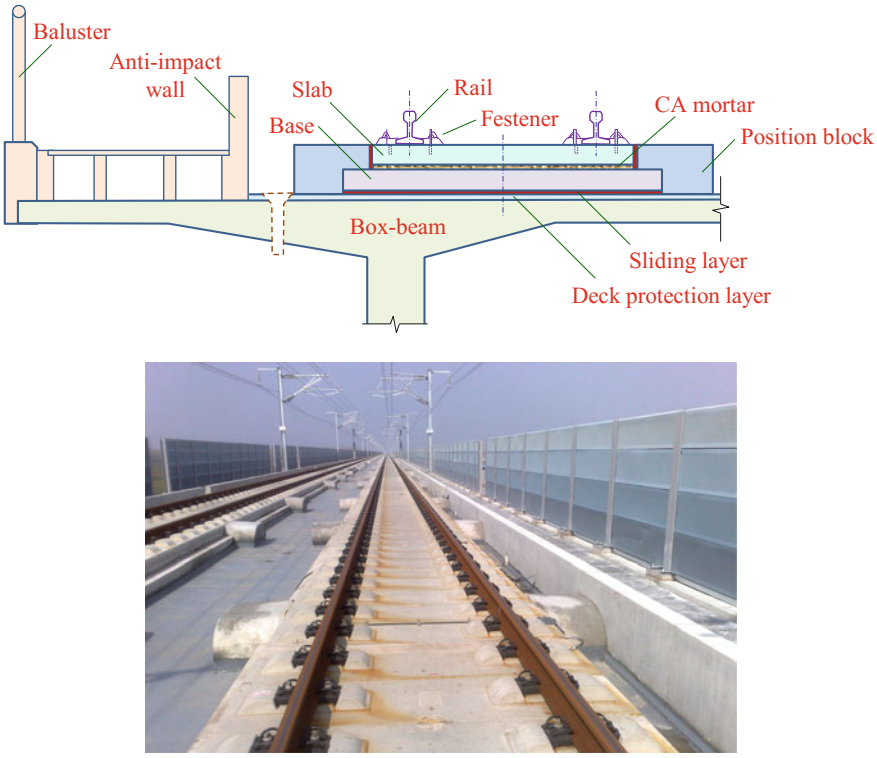

Fig. 10.37 CRTSII ballastless slab track on the bridge

the inner concrete still maintains the original state, as the result, uneven temperature gradient emerges in the slab along the depth.

Two kinds of temperature loads are considered for the track slab, i.e., the uniform temperature variation and the temperature gradient along the depth. The uniform temperature effect causes the longitudinal internal force and deformation of the track, and the temperature gradient along the depth causes the warping deformation of the slab, which leads to the separation between the slab and the CA mortar layer or between the CA mortar layer and the RC base. If the interlayer separation emerges in the construction stage, the track slab will repeatedly beat the CA mortar layer under the dynamic train loads in the operation stage, resulting in the damage of the CA mortar layer and even the failure of the whole track system (Liu and Zhao 2013; Liu et al. 2014).

The temperature field of track slab can be established either by numerical analysis based on the meteorology and heat transfer theories, or by statistical estimation based on a large number of measured data. At present, the researches on the temperature gradient of track slab have been in depth. Liu et al. (2014) investigated the variation characteristics of slab top and bottom temperatures and the temperature gradient, by surveying the slab temperatures of CRTSII tracks on

the Beijing-Shanghai HSR, and based on the measured temperature gradient field, calculated the warping deformation of track slab by FE analysis.

In reality, the variations of uniform temperature and the temperature gradient of track slab usually exist simultaneously, and the temperature deformation of the slab should be under the joint action of the two temperature effects. In order to investigate the temperature deformation of track slabs, a survey was conducted to measure the temperature of track slabs under the field environment, and then the track slab temperature field is simulated by applying nodal temperature loads. Further, the track deformation caused by the temperature loads is used as an additional track unevenness to analyze the dynamic response of the train-track system.

1. **Temperature measurement of track slabs**

On September 11, 2014 and September 13, 2014, the field survey was conducted at the beam yard near the Xiaogan North railway station, in which the temperatures of CRTSII track slabs were measured using the infrared point temperature gun. Shown in Fig. 10.38 are the arrangement of measuring points at slab top and bottom.

The survey was conducted on all measurement points by every half hour, and at each time 3 groups of readings were recorded, which are averaged as the adopted temperatures at that time. Considering several most unfavorable conditions, the measured temperatures of the track slab are analyzed as follows:

When analyzing the temperature gradient of the track slab, the temperature differences at various times in a day are calculated using the measured data of slab top and bottom at different positions. The maximum temperature difference among them and the corresponding slab top and bottom temperatures are adopted.

When analyzing the uniform temperature of the track slab, the maximum temperatures selected from the 9 measuring points on the top and the 6 points on the bottom of the slab in each day are adopted.

Listed in Table 10.8 are the maximum temperature differences and maximum slab temperatures of CRTSII track slab measured in the two-day survey.

2. **Numerical simulation of temperature warping deformation of track slab**

The FE model for temperature warping deformation of track slab is established, as shown in Fig. 10.39.

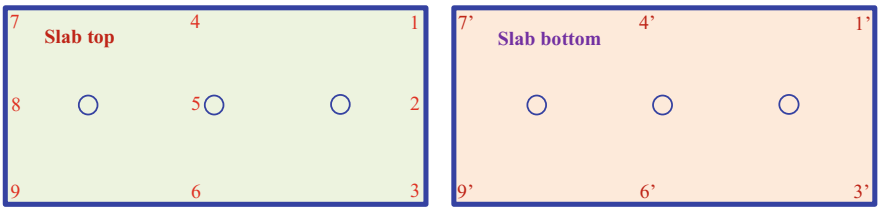

Fig. 10.38 Arrangement of temperature measuring points on the track slab

Table 10.8 Measured temperature results of CRTSII track slab

Date of survey	Maximum temperature difference of slab				Maximum temperature of slab		
	Time	Slab top (°C)	Slab bottom (°C)	Temperature difference (°C)	Time	Slab top (°C)	Slab bottom (°C)
11 Sept.	14:30	33.3	27	+6.3	15:00	35	32.8
13 Sept.	12:00	21.6	8.8	+12.8	12:30	27.6	21.4

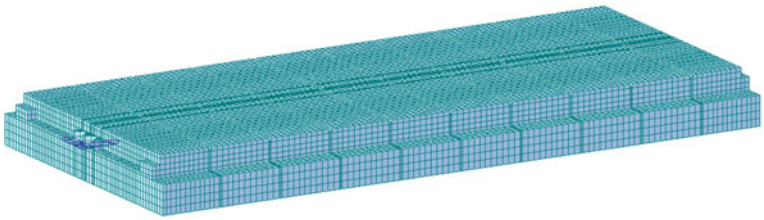

Fig. 10.39 FE model of CRTSII track with single slab

In the model, the track slab, CA mortar layer and RC base are simulated by solid elements; the track slab is supported on the CA mortar layer with nonlinear compression-only springs; the CA mortar layer and the RC base share common points; the connecting bars between the track slabs are simulated by beam elements; the rail is simulated by beam elements, and the fastener by spring elements. The material parameters of CRTSII track components are listed in Table 10.9.

In the calculation, the deadweight of the track slab needs to be considered, but the temperature fields of the CA mortar layer and the RC base can be ignored.

The track slab is loaded by the nodal temperature loads: the initial temperature is the stress-free temperature of the track construction, at which there is neither slab temperature difference nor slab deformation; the final temperature is the measured temperature at the concerned time.

In order to verify the analytical model, the temperature field in Han and Sun (2011), the temperature gradient of −0.275 °C/cm and the temperature difference −5.5 °C between slab top and bottom, is applied on the track slab model. The calculated maximum warping deformation of the slab is 0.4124 mm, which is close

Table 10.9 Material parameters of CRTSII ballastless track

Component	Elastic modulus E (MPa)	Poisson ratio	Linear expansion coefficient (°C)
Rail	2.1×10^5	0.3	1.2×10^{-5}
PC slab	3.6×10^4	0.2	1×10^{-5}
CA mortar	1×10^4	0.34	1.3×10^{-5}
RC base	2.2×10^4	0.2	1×10^{-5}

Table 10.10 Maximum vertical deformations of track slab under the most unfavorable temperature difference conditions

Temperature effect	Initial temperature (°C)	Final temperature (°C)		Temperature difference of track slab (°C)	Maximum vertical deformation of track slab (mm)
		Slab top	Slab bottom		
TG1	20	33.3	27	6.3	0.31
TG2	20	21.6	8.8	12.8	0.53
MT1	20	35	32.8	2.2	0.21
MT2	20	27.6	21.4	6.2	0.23

Note "TG1" denotes the maximum temperature gradient of track slab on the first day; "TG2" the maximum temperature gradient of track slab on the second day; "MT1" the maximum uniform temperature of track slab on the first day; "MT2" the maximum uniform temperature of the track slab on the second day

to the FE calculation value of 0.473 mm and the measured value of 0.45 mm in the reference.

(1) **Analysis of the Most Unfavorable Condition**

According to the temperature survey of the track slab, in the same day, the time with highest temperature is close to the time with maximum top-bottom temperature difference of the slab. The most unfavorable temperature warping deformation of track slab may appear at either of the two moments. Taking the positive temperature difference as an example, the maximum vertical deformations of the track slab under the most unfavorable temperature effects are calculated, and the results are listed in Table 10.10.

It can be seen from Table 10.10 that the maximum vertical deformation of track slab at the maximum temperature (35 °C) is 0.21 mm, which is smaller than 0.53 at the maximum temperature difference (12.8 °C). The higher the temperature difference is, the larger the maximum deformation becomes. Therefore, the most unfavorable temperature warping deformation of track slab occurs at the time with the maximum temperature gradient in a day.

Shown in Figs. 10.40 and 10.41 are, respectively, the temperature warping deformation nephograms of the single-track slab model at the maximum positive and negative temperature gradients. It can be seen that at the maximum positive temperature gradient, the center of the track slab shows an upward warping deformation, while at the maximum negative temperature gradient, the upward warping occurs at the four corners.

(2) **Influence of Uniform Temperature Variation of Track Slab**

Considering the positive and negative temperature gradient conditions, the temperature warping deformations of the track slab are calculated by using different initial temperatures, to analyze the effect of uniform temperature variation.

According to the regional meteorological records of the bridge site, the initial temperature range is set to be −5 °C ∼ 37 °C. For the positive temperature gradient

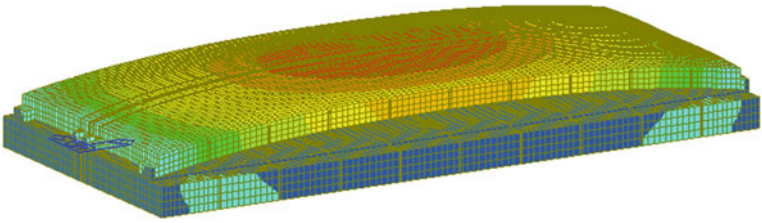

Fig. 10.40 Temperature warping deformation nephogram of track slab at the maximum positive temperature gradient

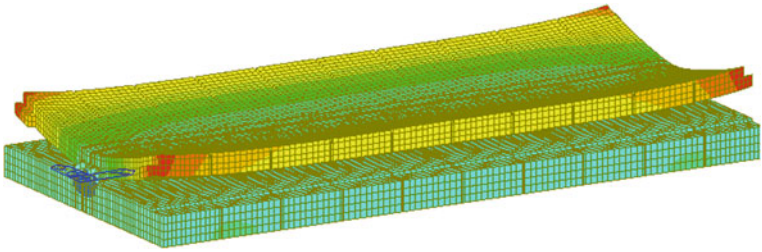

Fig. 10.41 Temperature warping deformation nephogram of track slab at the maximum negative temperature gradient

effect, the temperature difference is 12.8 °C, and the final temperature is 21.6 °C at slab top and 8.8 °C at bottom. For the negative temperature gradient effect, the temperature difference is −5.5 °C, and the final temperature is 30 °C at slab top and 35.5 °C at bottom. The warping deformations of the track slab with respect to different initial temperatures are shown in Fig. 10.42.

Under the positive temperature gradient, the maximum vertical displacement of track slab reaches a minimum value at the initial temperature of 22 °C (slightly higher than the final slab top temperature of 21.6 °C); under the negative temperature gradient, the maximum vertical displacement of track slab reaches a minimum

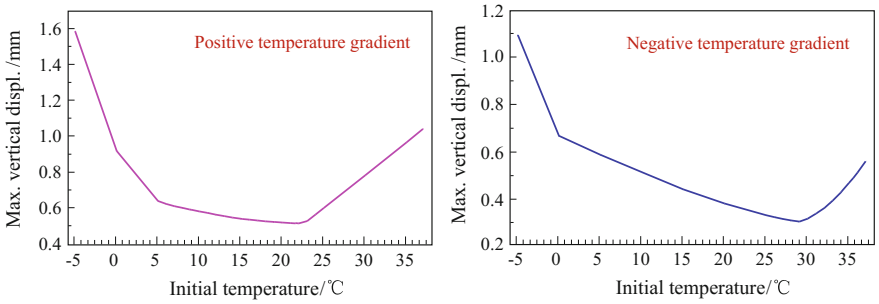

Fig. 10.42 Warping deformations of track slab with respect to different initial temperatures

value at the initial temperature of 29 °C (slightly lower than the final slab top temperature of 30 °C). It shows that the uniform temperature variation has influence on the warping deformation of the track slab. Under the same temperature gradient, the warping deformation of the track slab reaches a minimum value when the initial temperature is close to the slab top temperature.

(3) **Influence of Longitudinal Connection Between Slabs**

To analyze the influence of longitudinal connection on the temperature warping deformation of the track slab, a FE model with three slabs is established, as shown in Fig. 10.43.

In the analysis, the variation curves of the top temperature, bottom temperature, and top-bottom temperature difference of the slab in 24 h given in Han and Sun (2011) are used, as shown in Fig. 10.44.

When the initial temperature is 20 °C, the warping deformations of the single-slab model and the three-slab model in 24 h are calculated, using the temperature loads in Fig. 10.44, and the variation curves of them in 24 h are shown in Fig. 10.45.

It can be seen that at different times in a day, the longitudinal connection plays different roles on the temperature warping deformations of the slab. At 8:00 a.m. and at around 19:00, the temperature differences between slab top and bottom are small, when the warping deformations are increased by the connections. At around 14:00, the positive temperature difference between slab top and bottom reaches maximum, and at around 6:00 a.m., the negative temperature difference reaches maximum, when the warping deformations are decreased.

Fig. 10.43 FE model of CRTSII track with three slabs

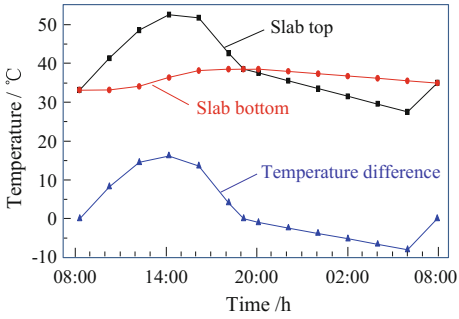

Fig. 10.44 Temperature variation of track slab in 24 h

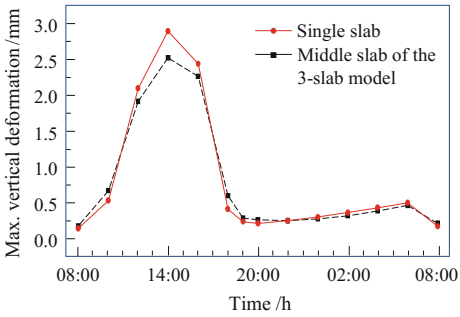

Fig. 10.45 Variations of temperature warping deformation of track slabs in 24 h

For different slab top temperatures at the maximum positive and negative temperature differences, the effects of longitudinal connections on the warping deformations of the track slabs are different. Therefore, the maximum vertical deformations of track slabs are analyzed considering three positive and three negative temperature differences, and the results are listed in Table 10.11.

The results show that the longitudinal connections can reduce the maximum vertical deformations of the track slab at both the positive and negative maximum temperature gradients; the difference between the initial temperature and the slab top temperature has the greater reduction effect than the temperature gradient on the warping deformation, and the bigger the difference, the greater the effect.

3. Dynamic analysis of train-track system under temperature loads

The track deformation under maximum temperature difference 16.2 °C (slab top temperature 52.6 °C, bottom temperature 36.4 °C) shown in Fig. 10.44 is adopted as additional track unevenness, which is added on the original track irregularity, to study the influence of slab temperature warping deformation on bridge track and train running performance. When a CRH2 train with eight vehicles passes through

Table 10.11 Maximum vertical deformations of track slab under various temperature gradients

Temp. effects	Initial temp. (°C)	Final temp. (°C)		Temp. difference (°C)	Max. deformation (mm)		Reduction (%)
		Slab top	Slab bottom		Single slab	Three slabs	
TG3	20	52.6	36.4	16.2	2.89	2.52	12.8
TG4	20	21.6	5.4	16.2	0.7	0.67	5.0
TG5	20	21.6	8.8	12.8	0.53	0.5	4.6
TG6	20	27.6	35.6	−8	0.5	0.47	6.9
TG7	20	30	38	−8	0.53	0.48	8.0
TG8	20	30	35.5	−5.5	0.37	0.32	11.5

Note "TG3" corresponds to the maximum temperature gradient (Fig. 10.40); "TG5" corresponds to "TG2" in Table 10.10; "TG4" corresponds to the positive temperature gradient of "TG3" and the slab top temperature of "TG5"; "TG6" corresponds to the maximum temperature gradient in Fig. 10.44; "TG8" corresponds to the temperature field in Han et al. (Han and Sun 2011); "TG7" corresponds to the negative temperature gradient of "TG6" and the slab top temperature of "TG8"

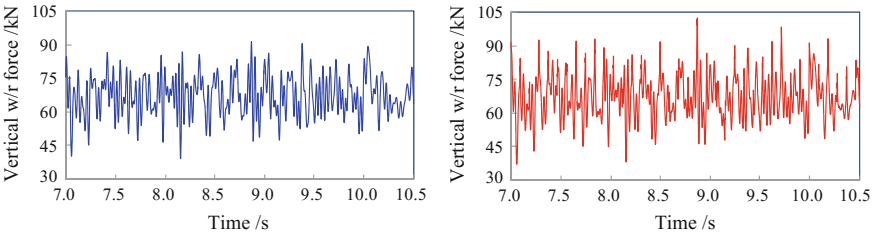

Fig. 10.46 Time histories of vertical wheel-rail forces of vehicle

the normal section and the temperature effect section of the track on the bridge, the dynamic responses, such as the vertical wheel-rail force, the fastener reaction force, the vertical rail acceleration, and slab acceleration, are calculated, and the dynamic response curves are shown in Figs. 10.46, 10.47, 10.48, and 10.49. In the analysis, the fastener stiffness is 22.5 kN/m, the original track irregularity is generated based on the German low interference spectrum, with the wavelength range between 1 m and 80 m, and the train speed of 250 km/h.

It can be seen from the figures that when the train runs on the track section with temperature warping deformation, the time histories of vehicle and track responses

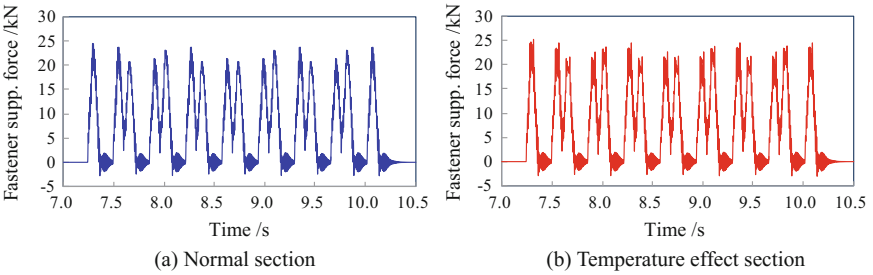

Fig. 10.47 Time histories of fastener support reaction forces

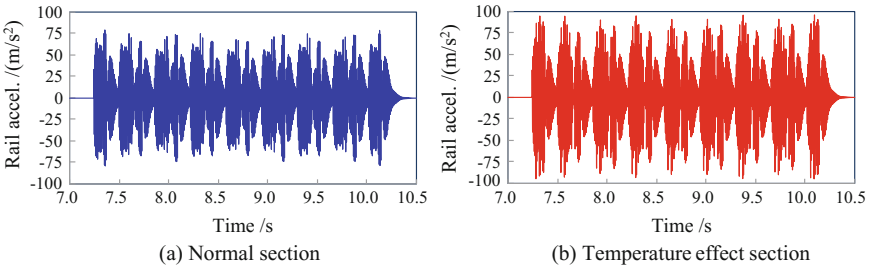

Fig. 10.48 Time histories of vertical rail accelerations

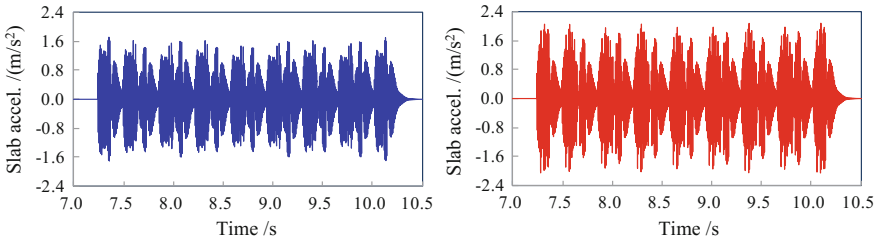

(a) Normal section (b) Temperature effect section

Fig. 10.49 Time histories of vertical slab accelerations

Table 10.12 Maximum dynamic responses of track and train vehicle

Dynamic response	Normal section	Temperature effect section	Increase ratio (%)
Wheel offload factor	0.3	0.318	6.0
Fastener support reaction force (kN)	24.39	25.25	3.5
Maximum vertical rail acceleration (m/s^2)	79.49	95.93	20.7
Maximum vertical slab acceleration (m/s^2)	1.72	2.08	20.7

are similar to those when it runs on the normal section, but the amplitude of the responses are increased.

The maximum dynamic responses of the vehicle and the track caused by the temperature deformation of track slab are listed in Table 10.12, where the responses of them on the normal track section are also given for comparison.

It can be seen that when the temperature deformation of the track slab is considered, the wheel offload factor is increased by 6.0%, the fastener support reaction force is increased by 3.5%, and the vertical accelerations of rail and slab are both increased by so high as 20.7%, which is disadvantageous to the track structure and the train running safety, thus it should be noticed.

References

ACI209 (1992) Prediction of creep, shrinkage and temperature effects in concrete structures [S]. American Concrete Institute committee

AASHTO (2012) LRFD bridge design specifications [S]. In: American association of state highway and transportation officials. Washington, D.C

Bazant ZP, Baweja S (1995) Creep shrinkage prediction model for analysis and design of concrete structures-model B3 [J]. Mater Struct 28:357–365

Bian MZ (2009) Study on temperature and shear lag effect experiment of PC box girder [D]. Chongqing Jiaotong University, Chongqing (in Chinese)

BS5400 (1990) BS5400: Part 4. Code practice for design of concrete bridges [S]. British Standard Institute

CEB-FIP (2010) Model code for concrete structures [S]. Fédération Internationale du Béton

Chai SF (2012) Research on the sensitivity analysis of monitoring and parameter affecting the large span continuous construction of passenger dedicated line [D]. Lanzhou Tiaotong University, Lanzhou (in Chinese)

Chen B, Zheng J, Wang JP (2010) State-of-the-art of the temperature effects of bridges [J]. J Wuhan Univ Technol 32(24):79–83 (in Chinese)

Duan XW (2014) Study on lateral displacement analysis of multiple factors on concrete curved continuous box-girder bridge [D]. Chang'an University, Xi'an (in Chinese)

Gardner NJ, Lockman MJ (2001) Design provisions for drying shrinkage and creep of normal-strength concrete [J]. ACI Mater J 98(2):159–167

Han ZG, Sun L (2011) Temperature measurement and deformation analysis for CRTSII ballastless track slabs [J]. Railw Stand Des 10:41–44 (in Chinese)

He SH (2003) Theory and calculation method of bridge structure [M]. People's Communication press, Beijing, p 2000

He X, Fang SS, Fang F (2012) Analysis of temperature effects of curved bridge under different gradient temperature load [J]. J Hefei Univ Technol (Nat Sci) 35(8):1088–1092 (in Chinese)

He JR (2013) The research on temperature field and temperature effect of the multi-cell concrete box-girder [D]. Hunan University, Changsha (in Chinese)

JTG D62 (2004) Code for design of highway RC and PC bridges and culverts [S]. The ministry of communications of PRC. China Communication Press, Beijing (in Chinese)

JTJ023 (1985) Code for design of highway RC and PC bridges and culverts [S]. The ministry of communications of PRC. China Communication Press, Beijing (in Chinese)

Kyle Buick F (1981) Influence of solar radiation on bridge structure [M]. China Railway Publishing House, Beijing (in Chinese)

Li GQ, Liu XB, Yang F (2014) Variation law and impact on dynamic performance of profile irregularity caused by creep of simply-supported beam on high-speed railway [J]. Sci Sin (Technologica) 44(7):786–792 (in Chinese)

Liu CY, DeWolf JT (2007) Effect of temperature on modal variability of a curved concrete bridge under ambient loads [J]. J Struct EngASCE 133(12):1742–1751

Liu H (2004) Research about lateral displacement and torsional distortion of PC continuous curved box-girder [D]. Southeast University, Nanjing (in Chinese)

Liu Y, Zhao GT (2013) Analysis of early gap between layers of CRTS II slab ballastless track structure [J]. China Railway Science 34(4):1–7 (in Chinese)

Liu Y, Chen P, Zhao GT (2014) Study on the characteristics of early temperature field of CRTS II slab ballastless track structure [J]. China Railway Science 35(1):1–6 (in Chinese)

Liu ZY (2005) Prefabrication and installation of high-speed railway double-track global-span simply-supported box-girder [D]. Southwest Jiaotong University, Chengdu (in Chinese)

Niu B (2008) A summary of China's high speed railway bridges [C]. In: The 18th national bridge academic conference, Changsha (in Chinese)

Priestley MJ (1976) Design thermal gradients for concrete bridges [J]. NZ Eng 31(9):213–219

Priestley MJ (1978) Design of concrete bridges for temperature gradients [J]. J Am Concr Inst 75 (5):209–217

Shan WW (2014) Two-dimensional temperature gradient effects and design methods of curved continuous box girder bridges [D]. Chang'an University, Xi'an (in Chinese)

Sun Q (2013) The temperature effect analysis on high-speed railway simply-supported beams running safety [D]. Beijing Jiaotong University, Beijing (in Chinese)

TB10002.1 (2005) Fundamental code for design on railway bridge and culvert [S]. The ministry of railways of PRC. China Railway Publishing House, Beijing

TB10002.3 (2005) Code for design on reinforced and prestressed concrete structure of railway bridge and culvert [S]. The ministry of railways of PRC. China Railway Publishing House, Beijing (in Chinese)

TB10621 (2014) Code for design of high-speed railway [S]. National railway administration of PRC. China Railway Publishing House, Beijing
Tian Y, Zhang N, Sun Q, Du XT, Xia H (2015) Temperature effect on running performance of steel railway bridge [J]. J Vib Shock 34(12):94–100 (in Chinese)
Wang SR, Sun L, Li QY (2009) Temperature measurement and temperature stress analysis of ballastless track slab [J]. J Railw Eng Soc 2:52–55 (in Chinese)
Xia H (2010) Maintenance and repair of railway bridges [M]. China Railway Publishing House, Beijing
Xia H, Ji WY, Han B, Zhang N (2011) Bridge engineering [M]. Higher Education Press, Beijing
Xia Y, Hao H, Zanardo G et al (2006) Long term vibration monitoring of a RC slab: temperature and humidity effect [J]. Eng Struct 28(3):441–452
Ye MX, Liu J (2009) Experimental research on creep deformation of high strength concrete of no-ballastless-track bridge [J]. J Shihezi Univ 27(1):84–86 (in Chinese)
Zhai WM (2007) Vehicle–track coupling dynamics (third edition) [M]. Science Press, Beijing
Zhang YH (2008) Research and application on shear lag effect and temperature effect theory of box girder bridge [D]. Southwest Jiao Tong University, Chengdu (in Chinese)
Zheng J (2008) High-speed railway bridges in China [M]. Higher Education Press, Beijing